Programa Doctorado
Ciencias de la Tierra

CSIC
CONSEJO SUPERIOR DE INVESTIGACIONES CIENTÍFICAS

IACT
INSTITUTO ANDALUZ DE CIENCIAS DE LA TIERRA

UNIVERSIDAD
DE GRANADA

Paleoredox conditions and productivity oscillations in the Mediterranean: implications for reconstructing deoxygenation dynamics and responses to ocean stressors

Ricardo David Monedero Contreras

Supervisors: Dr. Francisca Martínez Ruiz & Dr. Francisco J. Rodríguez Tovar

Tesis Doctoral

Paleoredox conditions and productivity oscillations in the Mediterranean: implications for reconstructing deoxygenation dynamics and responses to ocean stressors

Paleo-oxigenación y oscilaciones de productividad en el Mediterráneo: implicaciones en la reconstrucción de la dinámica de la desoxigenación y de las respuestas a los agentes estresantes de los océanos

Memoria de Tesis presentada por el Licenciado en Geología D. Ricardo David Monedero Contreras para optar al Grado de Doctor por la Universidad de Granada.

Esta Tesis Doctoral ha sido dirigida por la Dra. Dña. Francisca Martínez Ruiz, Investigadora Científica del CSIC, del Instituto Andaluz de Ciencias de la Tierra, y el Dr. D. Francisco Javier Rodríguez Tovar, Catedrático del Departamento de Estratigrafía y Paleontología de la Universidad de Granada.

Granada, 24 de abril de 2024

Vº Bº de los Directores

El Doctorando

Francisca Martínez Ruiz

Francisco J. Rodríguez Tovar

Ricardo D. Monedero Contreras

Programa Doctorado
Ciencias de la Tierra

CSIC
Consejo Superior de Investigaciones Científicas

Universidad de Granada

IACT
Instituto Andaluz de Ciencias de la Tierra

Doctoral Thesis

Paleoredox conditions and productivity oscillations in the Mediterranean: implications for reconstructing deoxygenation dynamics and responses to ocean stressors

Paleo-oxigenación y oscilaciones de productividad en el Mediterráneo: implicaciones en la reconstrucción de la dinámica de la desoxigenación y de las respuestas a los agentes estresantes de los océanos

Ricardo David Monedero Contreras

Editor: Universidad de Granada. Tesis Doctorales
Autor: Ricardo David Monedero Contreras
ISBN: 978-84-1195-394-8
URI: https://hdl.handle.net/10481/93127

Esta Tesis Doctoral es parte de los proyectos de I+D+i PID2019-104624RB-I00 y PID2019-104625RB-100 financiados por MICIU/AEI/10.13039/501100011033/, y del proyecto D TED2021-131697B-C22, financiado por MICIU/AEI/10.13039/501100011033 y por la Unión Europea NextGeneration EU/PRTR. También se desarrolló en el marco los de los Proyectos de Excelencia de la Junta de Andalucía P18-RT-3804 y P18-RT-4074 (cofinanciados por Fondos Europeos de Desarrollo Regional (FEDER) y financiación de la Consejería competente en materia de I+D+i de la Junta de Andalucía) y los Grupos de Investigación RNM-179 y RNM-178 (Junta de Andalucía). Para la realización de la tesis doctoral, el doctorando D. Ricardo David Monedero Contreras ha contado con un contrato predoctoral asociado al proyecto P18-RT-3804 (cofinanciado por Fondos Europeos de Desarrollo Regional (FEDER) y financiación de la Consejería competente en materia de I+D+i de la Junta de Andalucía) y con la Ayuda PRE2020-093259 financiada por MICIU/AEI/10.13039/501100011033 adscrita al proyecto del Plan Nacional PID2019-104624RB-I00.

Esta Tesis Doctoral se ha desarrollado en la unidad de Geociencias Marinas del Instituto Andaluz de Ciencias de la Tierra (IACT) del Consejo Superior de Investigaciones Científicas (CSIC). Además, se agradece al Departamento de Estratigrafía y Paleontología y al Centro de Instrumentación Científica (CIC) de la Universidad de Granada (UGR) por el uso de laboratorios y técnicas analíticas. También se agradece al Integrated Ocean Drilling Program (IODP) que ha proporcionado buena parte de las muestras analizadas en esta tesis, en particular al IODP Bremen Core Repository por su asistencia con la descripción y muestreo de los testigos del ODP Leg 160. Parte del trabajo de investigación se ha realizado durante dos estancias en centros extranjeros, cada una de tres meses de duración, en el *Department of Marine Palynology & Paleoceanography* de la Universidad de Utrecht (Países Bajos), bajo la supervisión de la Dra, Francesca Sangiorgi, y en el *Earth and Planetary Science Department* de la Universidad de California, Santa Cruz (Estados Unidos de América), bajo la supervisión de la Dra. Adina Paytan.

Junta de Andalucía

MINISTERIO
DE CIENCIA, INNOVACIÓN
Y UNIVERSIDADES

UNIÓN EUROPEA
Fondo Social Europeo
El FSE invierte en tu futuro

AGENCIA
ESTATAL DE
INVESTIGACIÓN

Viaje hacia lo Desconocido
Para avanzar, necesitas viajar,
tras cada partida, otra partida habrá.
Persiste, sigue adelante, sin descansar,
a pesar de errores, heridas, sin cesar.

El viaje es la esencia, la llegada, anhelo,
exploradores del alma en su vuelo.
Navegamos mares de sabiduría,
buscando la verdad con valentía

Anónimo

Science is organized knowledge.
Wisdom is organized life.

Immanuel Kant (1724–1804)

Table of Contents

Index of abbreviations **1**
Abstract **3**
Resumen **7**
Motivation, objectives and layout **11**

Chapter I. Introduction **21**
I.1. Climate Change and Ocean Stressors 23
I.2.The Mediterranean Sea 25
I.3. Eastern Mediterranean Sapropels and Western Mediterranean ORLs 27
I.4. Multiproxy paleoceanographic approach 31
    I.4.1. Geochemical proxies 33
    I.4.2. Ichnological analysis 36
    I.4.3. Dinoflagellates analysis 37
I.5. Materials and methods 38

Chapter II. *Role of climate variability on deep-water dynamics and deoxygenation during sapropel deposition: New insights from a palaeoceanographic empirical approach* **41**
Abstract 44
II.1. Introduction 45
II.2. Oceanographic and palaeoceanographic setting 46
II.3. Geochemical palaeoceanographic frameworks 49
II.4. Materials and methods 51
    II.4.1. Core description, sampling and chronology 51
    II.4.2. Geochemical analysis of sediments 52
        II.4.2.1. Major and trace elements 52
        II.4.2.2. Organic matter content 53
II.5. Results 53
II.6. Discussion 56
    II.6.1. Particulate shuttling and degree of oxygen depletion 57
    II.6.2. Degree of deep-water restriction 60
    II.6.3. Deep-water renewal frequency and $[Mo]_{aq}$ 61
II.7. Conclusions 67

Chapter III. *Redox geochemical signatures in Mediterranean sapropels: Implications to constrain deoxygenation dynamics in deep-marine settings* **69**
Abstract 72
III.1. Introduction 73
III.2. Oceanographic setting 75
III.3. Sapropel deposition 77
III.4. Material and methods 78
    III.4.1. Core description, sampling and chronology 78
    III.4.2. Geochemical analysis 79

III.4.3. Geochemical data normalization 80
III.4.4. Paleoenvironmental geochemical proxies 80
III.4.5. Multivariant statistical analyses 82
III.4.6. Redox thresholds calibration 82
III.5. Results 83
III.5.1. Geochemical data 83
III.5.2. Multivariate statistical analyses 85
III.6. Discussion 88
III.6.1. Characterization of distinctive geochemical intervals in sapropel layers 91
III.6.2. Redox thresholds calibration 100
III.6.3. Paleoenvironmental analysis of sapropel events 102
III.7. Conclusions 104

Chapter IV. *Evidence of postdepositional remobilization of redox-sensitive metals across sapropel boundaries: New insights from LA-ICP-MS and EDX mapping analyses* **106**

Abstract 110
IV.1. Introduction 111
IV.2. Methods and materials 113
IV.2.1. Study area 113
IV.2.2. Sediment samples analyses 115
IV.2.2.1. Geochemical analyses 115
IV.2.2.2. Scanning electron microscope (SEM) imaging and compositional maps 117
IV.2.3. Statistical analyses 117
IV.3. Results 118
IV.3.1. Discrete samples 118
IV.3.2. LA-ICP-MS analyses of sediment thin-section 122
IV.3.3. SEM images and SEM-EDX mapping 126
IV.4. Discussion 128
IV.4.1. S1 geochemical fractions 128
IV.4.2. Recognition and interpretation of S1 geochemical intervals 129
IV.4.3. Characterization and interpretation of RSTMs sub-mm signals 134
IV.4.4. TM postdepositional remobilization 135
IV.5. Conclusions 139

Chapter V. *Impact of Chondrites on trace metal distribution in the sapropel S7 (ODP Site 966): Implications for paleoenvironmental and paleoceanographic reconstructions* **141**

Abstract 144
V.1. Introduction 145
V.1.1. Assessed trace metals 147
V.2. Paleo-oceanographic setting and sediment record 148
V.3. Methodology approach 150

V.3.1. Geochemical analyses 150
V.3.2. High-resolution images 151
V.3.3. Bioturbation quantification 152
V.3.4. Scanning electron microscope (SEM) imaging and compositional maps 152
V.3.5. Data presentation and statistical analyses 153
V.4. Results 154
V.4.1. SEM and high-resolution optical images 157
V.4.2. EDX mapping 158
V.4.3. Bioturbation quantification 160
V.4.4. LA-ICP-MS spot-analyses 164
V.5. Discussion. Chondrites and micro-scale sediment disturbances 164
V.5.1. Chondrites: Lamination, texture and mineral composition 165
V.5.2. Chondrites: Trace elements distribution and geochemical signals 168
V.5.3. Multiproxy reconstruction of S7 evolution 173
V.6. Conclusions 178

Chapter VI. *Tracking productivity changes in the Alboran Sea during the past 13,000 years using a combination of palynological and geochemical tools: paleoperspectives on productivity responses to climate variability* **181**

Abstract 185
VI.1. Introduction 186
VI.2. Oceanographic and climatic setting 187
VI.3. Paleoceanographic and paleoenvironmental proxies 190
VI.3.1. Marine palynology: Dinocysts analysis for paleoproductivity 190
VI.3.2. Geochemical proxies for productivity 192
VI.3.3. Geochemical proxies for redox conditions 194
VI.3.4. Geochemical detrital proxies 195
VI.4. Material and methods 195
VI.4.1. Core description, chronology and sampling 195
VI.4.2. Dinoflagellate cysts 196
VI.4.3. Major and trace elements analyses 197
VI.4.4. Organic carbon analyses 197
VI.5. Results 198
VI.5.1. Dinocysts analysis 198
VI.5.2. Geochemical data 200
VI.6. Discussion 203
VI.6.1. Younger Dryas humid phase (~ 12.2 – 11.7 ka) 203
VI.6.2. Holocene humidity optimum (~ 10.5 – 8.5 ka) 209
VI.6.3. late Holocene (4.2 ka – present) 212
VI.7. Conclusions 215

Summary and Conclusions **217**
Epólogo y Conclusiones **223**
Future Research Perspectives **229**

Acknowledgment / Agradecimientos **237**

References **241**

Appendix I **271**
Appendix II **275**
Appendix III **279**
Appendix IV **287**

Index of abbreviations

ADWO: Adriatic Deep-Water Outflow
AMOC: Atlantic Meridional Overturning Circulation
AW: Atlantic Water
Corg: Organic carbon
DOPt: Degree of pyritization
E. Med.: Eastern Mediterranean
E. Smt.: Eratosthenes Seamount
EF: Enrichment Factor
EM: Eastern Mediterranean
EMDW: Eastern Mediterranean Deep-Water
ES: Eratosthenes Seamount
H_2S: Hydrogen Sulfide
HF: Hydrofluoric acid
HNO_3: Nitric Acid
ICP-MS: Inductively Coupled Plasma Mass Spectrometry
ICP-OES: Inductively Coupled Plasma Optical Emission Spectroscopy
IODP: Integrated Ocean Drilling Program
ITCZ: Intertropical Convergence Zone
ka: Thousands of years ago
kV: Kilovolts
kW: Kilowatt
Kyr: Thousands of years
LA-ICP-MS: Laser Ablation Inductively Coupled Plasma Mass Spectrometry
LIW: Levantine Intermediate Water
mA: milliamperes
Ma: Million years ago
MAW: Modified Atlantic Water
mbsl: meters below sea-level
Micro-CT: Micro-computed Tomography
MOW: Mediterranean Outflow Water
NAO: North Atlantic Oscillation
ODP: Ocean Drilling Program
OM: organic matter
ORL: Organic-Rich Layer
ppm: parts per million
RCP: Representative Concentration Pathway
RSTM: Redox-sensitive trace metal
SEM-EDX: Scanning Electron Microscope with Energy Dispersive X-ray Spectroscopy
SEM: Scanning Electron Microscopy
TM: Trace metal
TOC: Total organic carbon
W. Med.: Western Mediterranean
WM: Western Mediterranean
WMDW: Western Mediterranean Deep-Water
XRF: X-Ray Fluorescence Spectroscopy
yr: Year

Abstract

Resumen

Abstract

Climate change has significantly altered the ocean in recent decades, leading to declining oxygen levels in both open ocean and coastal waters. This decline is a major concern as it limits productivity, biodiversity, and affects biogeochemical cycles. This thesis investigates the drivers and long-term implications of marine deoxygenation and productivity changes in the Mediterranean Sea by integrating paleoceanographic reconstructions from marine paleoarchives. The Mediterranean's deep-marine paleoarchives offer exceptional examples of climate oscillations, resulting in the formation of sapropels and organic-rich layers (ORLs) corresponding to deoxygenation events. These events have occurred periodically over millions of years, impacting both Eastern and Western Mediterranean basins. This study employs diverse analytical techniques, principally geochemical analyses, coupled with ichnology, and dinoflagellate analysis, to better understand Mediterranean responses to deoxygenation events and climate variations, as well as to achieve a better comprehension of the geochemical signals produced in such scenarios.

The thesis analyzed five recent sapropels (S1, S5, S6, S7, and S8) from three Eastern Mediterranean locations (Eratosthenes Seamount, Ionian Abyssal Plain and Mediterranean ridge) using various paleoceanographic models derived from empirical geochemical data obtained from well-investigated modern marine systems. Findings reveal that regional climate conditions heavily influence the frequency and intensity of oxygen depletion, with deeper sites being more vulnerable to water-mass restriction and deoxygenation. During sapropel deposition, local intensity of particulate shuttling of organic and inorganic aggregates to deep-waters enhanced burial fluxes of trace metals (e.g., Mo, Cu, Co, Ni and V), affecting sediment composition and redox thresholds values of geochemical redox proxies. Additionally, water-mass exchange between the Western and Eastern Mediterranean (which is more intense during colder periods), influences dissolve trace metal budgets in Eastern Mediterranean deep basins. The comprehensive assessment of a large geochemical dataset gathered from the five sapropel layers at the three Eastern Mediterranean locations has allowed us a further understanding of the resulting redox geochemical signals and intervals produced in deep-marine settings during deoxygenation events as well as the associated early diagenesis processes across different local hydrogeographic conditions. Postdepositional processes significantly influenced the syndepositional redox signals, with Mn-oxyhydroxides and pyrite (FeS_2) playing crucial roles in trapping and scavenging dissolved redox-sensitive trace metals during early diagenesis. Mo is particularly efficiently trapped by Mn-oxyhydroxides and pyrite, highlighting the importance of considering postdepositional remobilization when interpreting Mo signals. Additionally, dissolved U, usually not linked with sulfides, may be trapped by underlying synsapropel pyrite framboids and large euhedral crystals during postdepositional oxidation, possibly via physical adsorption onto large pyrite surfaces. Analyzing sapropel S7 (deposited ~ 195 thousand years ago) at Eratosthenes Seamount as a case study has demonstrated how *Chondrites*, a common trace fossil in deep-marine and organic-rich sediments, can introduce oxygenated water beneath the sediment-water interface. This enhances bioirrigation and porewater ventilation, leading to postdepositional diffusion of trace metals. Results indicate that *Chondrites* bioturbation can dilute syndepositional concentrations of key paleoceanographic trace metals (e.g., Mo, U, and Ni) by over 10% and disrupt sedimentary features, altering mineral and organic-matter distribution. This highlights their significant influence on biogeochemical processes, sediment dynamics, and trace metal cycling in deep-marine environments.

A thorough analysis of oceanographic changes in Alboran Sea Basin over the past 13,000 years, using geochemical proxies and dinoflagellates analysis, has demonstrated the productivity response to regional climate variability at millennial and centennial timescale. Humid periods, controlled by both orbital (e.g., insolation cyclicity) and suborbital forcing factors as negative North Atlantic Oscillation (NAO) pattern, enhanced marine productivity by boosting nutrient availability through increased river discharges. Despite lower productivity during dry periods (e.g., last 4.2 thousand years), the region has maintained higher productivity in comparison with most Mediterranean regions due to active upwelling systems driven by a persistent positive NAO pattern. The positive NAO pattern results from the southward migration of the Intertropical Convergence Zone around 6.5 ka, in response to orbital forcing, shaping climatic patterns in the Westernmost Mediterranean, and subsequently marine productivity dynamics in Alboran Sea. These findings improve our understanding of marine ecosystem long-term responses to climate change and stress the importance of multiproxy approaches for accurate reconstructions in the Westernmost Mediterranean. Moreover, the multiproxy approach of this study highlights the limitations of using the Ba/Al ratio as a proxy for productivity in low productivity settings in which very high detrital input overprinted the relatively low pelagic barite accumulation rates. In contrast, the dinoflagellates analysis was revealed as a more robust proxy for marine productivity reconstructions in the Westernmost Mediterranean.

Overall, this thesis enhances our understanding of how deep-marine settings respond to changes in water-column circulation as a result of climatic variability. It offers new insights on the redox geochemical signals observed in organic-rich sediments deposited during deoxygenation events in deep-marine environments. Additionally, it elucidates the impacts of early postdepositional processes (e.g., oxidation and hydrogen sulfide diffusion) and bioturbation on redox geochemical signals. Furthermore, it provides paleoperspectives on the long-term primary productivity responses to climate change in the Mediterranean Sea.

Resumen

El cambio climático ha alterado considerablemente el océano en las últimas décadas, provocando un descenso de los niveles de oxígeno tanto en el océano abierto como en aguas costeras. Este descenso es motivo de gran preocupación, ya que limita la productividad y la biodiversidad y afecta a los ciclos biogeoquímicos. Esta tesis investiga los factores de control y las implicaciones a largo plazo de la desoxigenación marina y los cambios de productividad en el mar Mediterráneo mediante la integración de reconstrucciones paleoceanográficas obtenidas del análisis de paleoregistros marinos. En el caso del Mediterráneo, estos paleoregistros ofrecen ejemplos excepcionales de oscilaciones climáticas, que dieron lugar a la formación de sapropeles y capas ricas en materia orgánica (*Organic-Rich layers*, ORLs) caracterizados por episodios de desoxigenación. Estos sedimentos se han depositado periódicamente a lo largo de millones de años, tanto en las cuencas orientales como occidentales del Mediterráneo. Así, este estudio ha utilizado diversas técnicas analíticas, principalmente análisis geoquímicos, junto con estudios icnologicos y de dinoflagelados, para comprender mejor las respuestas del Mediterráneo a los eventos de desoxigenación y a las variaciones climáticas, además de alcanzar una mejor comprensión de las señales geoquímicas registradas en estos sedimentos.

En esta tesis se han analizado cinco sapropeles (S1, S5, S6, S7 y S8) recuperados en tres ambientes deposicionales diferentes en el Mediterráneo oriental (cima del monte submarino Eratóstenes, llanura abisal de la cuenca Jónica y Dorsal Mediterránea). Se han utilizado diversos modelos paleoceanográficos derivados de datos geoquímicos empíricos obtenidos en sistemas marinos actuales. Los resultados han puesto de manifiesto que las condiciones climáticas regionales influyen en gran medida en la frecuencia e intensidad del consumo de oxígeno, siendo los ambientes profundos los más vulnerables a la restricción de la masa de agua y a la desoxigenación. Durante el depósito de sapropeles, la intensidad local de la transferencia de partículas de agregados orgánicos e inorgánicos a aguas profundas conllevó el aumento de las tasas de enterramiento de metales traza (por ejemplo, Mo, Cu, Co, Ni y V), lo que afectó a la composición de los sedimentos y a los valores de los umbrales redox de los indicadores geoquímicos. Además, el intercambio de masas de agua entre el Mediterráneo occidental y oriental (más intenso durante los periodos más fríos), influye en los balances de metales traza disueltos en las cuencas profundas del Mediterráneo oriental. La integración de un amplio conjunto de datos geoquímicos procedentes de los sapropeles estudiados en los tres ambientes del Mediterráneo Oriental ha permitido comprender mejor las señales geoquímicas redox resultantes, así como las características del depósito en ambientes profundos durante eventos de desoxigenación. Asimismo, se han evaluado los procesos de diagénesis temprana asociados a diferentes condiciones hidrogeográficas locales. Los procesos postdeposicionales influyeron

significativamente en las señales redox sindeposicionales, desempeñando los Mn-oxihidróxidos y la pirita (FeS_2) un papel crucial como sumidero de metales traza disueltos durante la diagénesis temprana. El Mo suele ser atrapado eficientemente por oxihidróxidos de Mn y pirita, destacándose así la importancia de considerar la removilización postdeposicional para la correcta interpretación de las señales de Mo. Adicionalmente, el U disuelto, normalmente no ligado a sulfuros, puede ser atrapado por framboides de pirita y por los grandes cristales euhedrales subyacentes a la capa rica en materia orgánica durante la oxidación postdeposicional, posiblemente vía adsorción física sobre superficies cristalinas de pirita. El análisis detallado del sapropel S7 (depositado hace ~ 195.000 años) en el Monte submarino Eratóstenes (seleccionado como caso de estudio) ha demostrado cómo *Chondrites*, una traza fósil común en sedimentos marinos profundos y ricos en materia orgánica, pueden introducir agua con alto contenido en oxígeno bajo la interfaz sedimento-agua. Esto favorece la bioirrigación y la ventilación del agua intersticial, lo que provoca la difusión postdeposicional de metales traza. Los resultados obtenidos indican que la presencia de *Chondrites* puede diluir las concentraciones sindeposicionales de metales traza utilizados como indicadores geoquímicos (por ejemplo, Mo, U y Ni) en más de un 10% y así alterar las características sedimentarias, modificando la distribución de minerales y materia orgánica. Esto pone de relieve su influencia en los procesos biogeoquímicos, la dinámica de los sedimentos y el ciclo de los metales traza en los ambientes marinos profundos.

Un análisis exhaustivo de los cambios oceanográficos en la cuenca del Mar de Alborán durante los últimos 13.000 años, utilizando indicadores geoquímicos y análisis de dinoflagelados, ha demostrado la respuesta de la productividad a la variabilidad climática regional en escalas temporales de miles y cientos de años. Los periodos húmedos, controlados por factores de influencia orbital (por ejemplo, la ciclicidad de la insolación) y suborbital como el patrón negativo de la Oscilación del Atlántico Norte (NAO), dieron lugar a un aumento de la productividad marina debido a la mayor la disponibilidad de nutrientes derivada del incremento de la descarga fluvial. A pesar de la menor productividad durante los periodos secos (por ejemplo, los últimos 4.200 años), la región ha mantenido una mayor productividad relativa en comparación con otras regiones mediterráneas debido a la actividad de los sistemas de aporte marino durante periodos con un patrón positivo persistente de la NAO. Este patrón positivo de la NAO es el resultado de la migración hacia el sur de la Zona de Convergencia Intertropical en torno a 6,5 ka, en respuesta a la influencia orbital, lo que configura los patrones climáticos en el Mediterráneo más occidental, así como la dinámica de la productividad marina en el Mar de Alborán.

En conjunto, esta tesis contribuye al mejor entendimiento de la respuesta de los ambientes marinos profundos a la variabilidad climática y a los cambios en la circulación en la columna de agua. Además, proporciona evidencias para el mejor entendimiento de los indicadores geoquímicos

habitualmente utilizados en la reconstrucción de las condiciones de depósito de sedimentos ricos en materia orgánica durante episodios de desoxigenación en medios marinos profundos. Asimismo, se ha avanzado en el conocimiento del impacto de los procesos postdeposicionales tempranos (por ejemplo, oxidación y difusión de sulfuro de hidrógeno) y de la bioturbación en las señales geoquímicas. Por otra parte, proporciona paleoperspectivas sobre las respuestas a largo plazo de la productividad primaria al cambio climático en el Mediterráneo.

Motivation, objectives and layout

Motivation, objectives and layout

Climate change and its associated impacts on the ocean pose one of the greatest challenges to humanity. Over the past decades, the ocean has undergone significant physical and biogeochemical alterations in response to global climate change and anthropogenic impact, as evidenced by in-situ observations and remote sensing data (IPCC, 2023). These changes encompass a wide array of processes (Fig. 1), including ocean warming, variations in salinity, alterations in water mass structure and circulation, as well as an increase in dissolved inorganic carbon concentrations and a decrease in seawater pH and oxygen content (e.g., Bopp et al., 2013; Kwiatkowski et al., 2020; Reale et al., 2022). These physical and chemical modifications exert a profound effect on marine organisms and ecosystems (Deutsch et al., 2020).

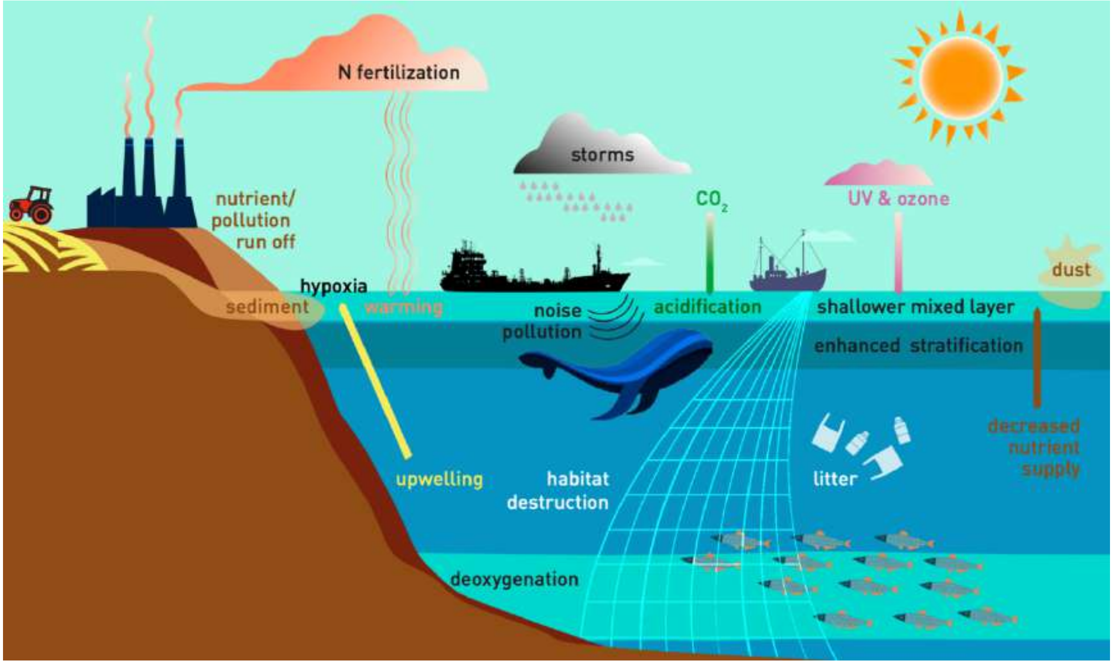
N fertilization
storms
CO_2
UV & ozone
nutrient/ pollution run off
dust
hypoxia
sediment
warming
noise pollution
acidification
shallower mixed layer
enhanced stratification
decreased nutrient supply
litter
upwelling
habitat destruction
deoxygenation

Figure 1. *Illustrative examples of global (warming, acidification), regional (ozone, litter, atmospheric pollutants) and local (sedimentation, pollution and nutrient runoff) stressors that can affect marine systems. Marine systems, from coastal areas to offshore waters, will encounter a unique combination of stressors, and ecosystems may be exposed to concurrent changes to multiple stressors simultaneously (from Beusen et al., 2022).*

In particular, oxygen levels have been declining in both the open ocean and coastal waters since at least the mid-20th century (Breitburg et al., 2018; Reale et al., 2022). This is considered one of the most significant changes occurring in the marine environment, as oceanic oxygen content limits productivity, biodiversity, and can disrupt biogeochemical cycles. In fact, some of the major extinction events (e.g., Toarcian Oceanic Anoxic Event; T-OAE, and Bonarelli Event; OAE-2) in Earth's history have been associated with warm climates and oxygen-depleted oceans (e.g., Jenkyns, 1985; Hetzel et al., 2009; Dickson et al., 2017; Fernández-Martínez et al., 2023). Current scenarios further support that climate change and anthropogenic activities could lead to widespread oxygen deficiency and decreased marine primary productivity over the next centuries, being more severe in vulnerable regions such as the Mediterranean (e.g., Bopp et al., 2013; Macias et al., 2015; Gong et al., 2021; IPCC, 2023).

Schmidtko et al. (2017) infer that, across the whole water column, just 15% of the oxygen loss is attributable to lower solubility caused by warmer water linked to increased carbon dioxide emissions produced by human activities. To explain the remaining 85% of oxygen loss, it is necessary to consider the complex combination of physical (e.g., water mixing) and biochemical (e.g., organic matter degradation) processes that affect oxygen concentrations in the ocean (e.g., Glibert et al., 2022). Therefore, understanding the mechanistic drivers (e.g., water-column dynamics), spatial extent and temporal variations of marine deoxygenation and marine productivity changes during episodes of rapid climate change is of utmost relevance for more robust projections. Yet, comprehending long-term (multidecadal and centennial) oceanographic responses of marine systems to climate variability necessitates insights beyond human timescales and instrumental records. In this regard, past climate changes, preserved as marine paleoarchives (e.g., deep-marine sediment records), offer valuable insights into the climatic and hydrogeographic factors influencing ocean deoxygenation and productivity changes, and provide critical long-term perspectives on the environmental and oceanographic changes induced by climate shifts, which can be incorporated into ocean models for more accurate future projections (e.g., Oschlies et al., 2018; Kiessling et al., 2023; Mancini et al., 2023a, b).

Past deoxygenation events are typically recorded in deep-marine settings as organic-rich facies, such as black shales and sapropels. These paleoarchives of rapid oxic-to-anoxic transitions provide key information about the interplay between climate change, oceanic dynamics, and biogeochemical cycles by offering a unique window into past environmental shifts and ecosystem responses (e.g., Cita et al., 1977; Marino et al., 2007; Grimm et al., 2015). Precisely, deep-marine paleoarchives in the Mediterranean provide good examples of recent climate oscillations involving radical redox and productivity changes. These climate oscillations resulted in the formation of so-called sapropels and organic-rich layers (ORLs), which occurred periodically throughout the last 13.5 million years (including the Holocene) in the eastern and Western Mediterranean basins, respectively (e.g., Malanotte-Rizzoli et al., 2014; Rohling et al., 2015). Hence, these marine paleoarchives of past deoxygenation events, intricately linked to climate variability, serve as a valuable source of information for understanding the long-term responses of contemporary marine systems facing oxygen loss and decreased primary productivity associated to the ongoing global warming and anthropogenic ocean perturbations (Hennekam et al., 2020; Kiessling et al., 2023; Mancini et al., 2023a, b).

In essence, the motivation behind this thesis is therefore the integration of paleoperspectives obtained through paleoceanographic reconstructions to advance knowledge and further comprehend the mechanistic drivers, dynamics and long-term implications of marine deoxygenation and primary productivity changes, which may have severe consequences for the future of oceans and marine ecosystems. Thus, by synthesizing insights from ancient Mediterranean deoxygenation events recorded in deep-sea sediments, this thesis seeks to:

(i) Provide a comprehensive understanding of the environmental and oceanographic drivers (e.g., water-column dynamics) of marine deoxygenation and primary productivity changes during rapid climate variations over the recent geological past (Pleistocene - Holocene) in the Mediterranean.

(ii) Contribute to a better understanding of the long-term impacts of climate variability on the Mediterranean marine productivity, thereby providing valuable insights that can be integrated to better constraint future ocean projections within the ongoing context of global warming.

The research has been conducted through an integrative and multidisciplinary analysis (i.e., geochemistry, mineralogy, micropaleontology, ichnology and sedimentology) of marine sedimentary records from the Mediterranean. These records, characterized in some cases by exceptional temporal resolution (centennial), allowed detailed reconstructions of past climate conditions. To address the main objectives of this thesis, the following specific objectives have been pursued:

1. Reconstruction of the oxygenation conditions (deoxygenation extent and intensity), marine productivity changes and water-column dynamics (water-column stability) during the deposition of organic-rich sediments in the Mediterranean – analyzing selected examples of sapropels – by using a combination of geochemical proxies.
2. Gain insights into the environmental and oceanographic significance of geochemical signals resulting from deoxygenation events in the Mediterranean and perform statistical calibration of redox geochemical proxies in the studied Eastern Mediterranean basins.
3. Explore the influence of postdepositional processes (e.g., oxidation and diffusion), and local hydrogeographic factors (e.g., water-depth and currents) on geochemical signals.
4. Evaluate benthic fauna response in deep-marine settings during the deposition of organic-rich sediments under low oxygen conditions and assess its potential impacts on both biogeochemical processes and geochemical record.

5. Reconstruction of oceanographic variability in the Western Mediterranean at millennial and centennial scale over the Holocene by integrating abiotic and biotic proxies to provide paleoperspectives on marine productivity responses to climate variability.
6. Assess the potential links between nutrient variability, water-column stability and climatic conditions as drivers to regional-scale marine deoxygenation and changes in primary productivity.

The findings achieved while pursuing these specific objectives have already been published or are currently under review in high-impact factor scientific journals. The five scientific papers are organized as separate chapters following the Introduction presented as Chapter I:

1. **Chapter I**. *Introduction*. The introduction presents an overview of the escalating impacts of climate change on marine ecosystems, stressing the urgency of understanding the interplay between climate change and deoxygenation, nutrient availability and water-column stability. It underscores the critical necessity of integrating modern observations with paleoperspectives to enhance the robustness of long-term (multidecadal and centennial) oceanographic projections, particularly regarding redox and productivity variability within the Mediterranean. The Mediterranean Sea is highlighted as a hotspot region for climate change. The significance of Eastern Mediterranean sapropels and Western Mediterranean ORLs as valuable paleoarchives documenting regional-scale deoxygenation events is introduced. A multidisciplinary approach, including geochemical proxies, ichnological analysis, and dinoflagellates information, is outlined for reconstructing past climate variability and paleoceanographic conditions. The materials and methods section details the selection of Mediterranean marine sediment cores and summarizes the applied analytical techniques, laying the foundation and setting the stage for the subsequent chapters.

2. **Chapter II**. *Role of climate variability on deep-water dynamics and deoxygenation during sapropel deposition: New insights from a palaeoceanographic empirical approach.* This chapter aims to link water-column dynamics and degree of deoxygenation across diverse deep-marine settings during rapid climate changes, employing analogical assessment based on contemporary observations from well-constrained modern marine systems. Various paleoceanographic conceptual models are applied to geochemical data representing different sapropel events. These conceptual models derived from empirical geochemical data, including trace metal concentrations and organic carbon content, gathered from well-investigated modern marine systems (e.g., the Black Sea and Cariaco Basin). Specifically, these models are employed to analyze five recent sapropels (S1, S5,

S6, S7, and S8) from three Eastern Mediterranean locations representing different oceanographic scenarios and climatic conditions. The findings offer insights into (i) the impacts of past climate variability on water-column dynamics and on the physicochemical properties of Eastern Mediterranean deep-water, (ii) the influence of local hydrogeographic features on bottom-water dynamics and redox conditions, (iii) the extent of deep-water restriction, and (iv) the intensity of deoxygenation during rapid climate changes in the Eastern Mediterranean. Additionally, the study provides long-term perspectives on modern deep-marine settings susceptible to experience deoxygenation due to a reduction in thermohaline circulation.

3. **Chapter III**. *Redox geochemical signatures in Mediterranean sapropels: Implications to constrain deoxygenation dynamics in deep-marine settings*. This chapter aims to elucidate the paleoenvironmental significance of geochemical redox signals stemming from regional-scale deoxygenation events in deep-marine environments. By integrating published and new data (this study) from five recent Quaternary sapropels (S1, S5, S6, S7, and S8) obtained from three Eastern Mediterranean deep-marine locations, the study examines a range of redox geochemical signals under varied environmental and hydrogeographic conditions. The research includes the calibration of redox proxies' thresholds at each location, crucial for accurately interpreting authigenic enrichment rates of redox-sensitive trace metals. The integrative methodology of this study provides valuable insights and geochemical tools for identifying and interpreting geochemical redox intervals in ancient and modern organic-rich sediments. This has contributed to a better understanding of geochemical signals resulting from deoxygenation dynamics and associated postdepositional processes in deep-marine environments. Additionally, it offers insights into potential biogeochemical changes in marine ecosystems transitioning towards anoxic conditions.

4. **Chapter IV**. *Evidence of postdepositional remobilization of redox-sensitive metals across sapropel boundaries: New insights from LA-ICP-MS and EDX mapping analyses*. This chapters presents novel findings on redox sensitive trace metals remobilization within sapropel layers at sub-mm scale. This study builds upon the results presented in Chapter III, where trace metals enrichments were observed in the sediments overlying and underlying some sapropels. This study aimed to conduct a more comprehensive and detailed analysis of the origin and nature of such enrichments and potential postdepositional alteration. This focuses on sapropel S1 at the Ionian Abyssal Plain, a well-preserved sapropel. High-resolution geochemical microanalyses were conducted, including Laser Ablation ICP-MS and SEM-EDX mapping to investigate the

postdepositional remobilization of redox sensitive trace metals within S1 and its surrounding sediments. The sub-mm scale analysis uncovered spatial heterogeneities in mineralogical composition and elemental distribution, highlighting the complexity of postdepositional geochemical reactions and providing new insights into what postdepositional processes are influencing the signals of commonly used redox proxies in deep-marine environments.

5. **Chapter V**. *Impact of Chondrites on trace metal distribution in the sapropel S7 (ODP Site 966): Implications for paleoenvironmental and paleoceanographic reconstructions*. The objective of this study is to assess how *Chondrites*, a trace fossil abundant in deep-sea sediments, impact the sediment texture and distribution of minerals, trace metals and organic matter in organic-rich sediments, which serve as valuable paleoarchives preserving crucial paleoceanographic changes and responses associated with past climate variations. We focused on sapropel S7 at the top of Eratosthenes Seamount (Eastern Mediterranean) as a case study. By employing high-resolution optical and scanning electron microscopy, as well as SEM-energy dispersive x-ray spectrometry (SEM-EDX) mapping and LA-ICP-MS analyses, we quantified the infill of *Chondrites* and the host sediment, and examined the resulting changes in the distribution and concentration of trace metals and organic matter. The results highlight the complex interplay between bioturbation, sedimentary processes, carbon and trace metals dynamics, and emphasizes the importance of considering *Chondrites*' impact on the geochemical record for accurate paleoenvironmental and paleoceanographic reconstructions.

6. **Chapter VI**. *Tracking productivity changes in the Alboran Sea during the past 13,000 years using a combination of palynological and geochemical tools: paleoperspectives on productivity responses to climate variability*. Marine productivity changes over the last millenniums in Eastern Mediterranean basins have been successfully reconstructed at high-resolution using pelagic barite content variability, which are normally detected using Ba/Al ratios. However, high sedimentation rates resulting from very high detrital input in the Westernmost Mediterranean (Alboran Sea Basin) induce Ba content dilution, which limits the use of the Ba/Al ratio as a productivity proxy. Therefore, the integration of dinoflagellates analysis has been used to better constrain centennial productivity changes in Westernmost Mediterranean over the last millennia. Within this context, this chapter focuses on reconstructing the paleoceanographic evolution of the Westernmost Mediterranean, emphasizing on productivity changes over the last 13,000 years at centennial resolution. A deep-sea sediment record from the Western Alboran Basin has been analyzed employing a comprehensive multiproxy approach, that integrates

dinoflagellates analysis and geochemical proxies. The results have facilitated an assessment of the influence of regional climatic conditions on fluvial inputs and water-column stability, which in turn affect nutrient availability and subsequently, marine primary productivity and oxygenation conditions in the Westernmost Mediterranean.

Following Chapter VI, the "**Summary and Conclusions**" section offers a comprehensive synthesis of the thesis's main findings and insights. It distills the research journey's essence into a structured recap, providing a synthesized overview of the key outcomes and conclusions. Additionally, a final section on "**Future Research Perspectives**" serves as a roadmap, outlining key emerging research areas of focus and methodologies, and exploring potential avenues for further interdisciplinary collaborative initiatives to deepen our understanding of marine environmental responses to climate change.

Chapter I

I. Introduction

I.1. Climate Change and Ocean Stressors

Ocean ecosystems play a crucial role in sustaining life on Earth. Covering two-thirds of the planet's surface, the ocean plays a key function in regulating global climate and environmental patterns by managing heat, water, and elemental cycles, including carbon and oligoelements (e.g., N, P, Fe and Si) (e.g., Levin and Le Bris, 2015; Glibert et al., 2022). However, the effects of climate change are increasingly evident across marine systems, exposing them to stressing environmental conditions such as ocean warming, acidification, deoxygenation, decreasing nutrient variability and others climatic impact-drivers (Fig. I.1) (e.g., Bopp et al., 2013; Oschlies et al., 2018; Gruber et al., 2021; Reale et al., 2022). Given the distinct spatio-temporal responses of ocean stressors, such as deoxygenation and nutrient availability changes, there is an urgent need for a comprehensive understanding of the drivers, triggers, and the interplay of these stressors for robust forecasting of future ocean scenarios under the current climate change and anthropogenic pressure.

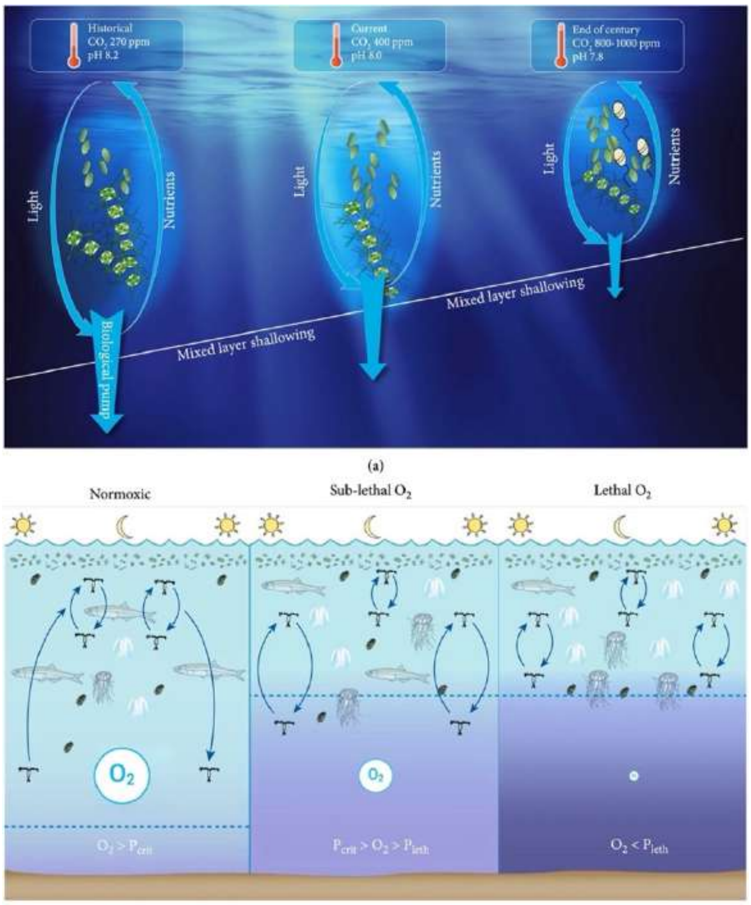
Historical
CO_2 270 ppm
pH 8.2
Current
CO_2 400 ppm
pH 8.0
End of century
CO_2 800-1000 ppm
pH 7.8
Light
Nutrients
Light
Nutrients
Light
Nutrients
Biological pump
Mixed layer shallowing
Mixed layer shallowing
(a)
Normoxic
Sub-lethal O_2
Lethal O_2
O_2
O_2
$O_2 > P_{crit}$
$P_{crit} > O_2 > P_{leth}$
$O_2 < P_{leth}$
(b)

Figure I.1. *Multiple stressors with ocean depth. (a) Global change effect on the surface oligotrophic ocean, including rising temperatures and atmospheric* CO_2 *levels, resulting effects on pH, shallowing of the mixed layer due to increased thermal stratification, lessening of nutrient availability but increased light availability, and the changing proportion of dominant cells in the euphotic zone. Note that an increased abundance of small-sized cells and mixotrophs is projected. (b) Conceptual diagram of food web changes that may occur over diel cycles between (i) normal oxic conditions (normoxic; left), (ii) sublethal deoxygenation conditions (center), and (iii) lethal conditions (right). The size of the symbol for* O_2 *and the color indicate the relative amount of dissolved oxygen under each condition (with light blue indicating high oxygen concentration and purple indicating lower oxygen concentration) (from Glibert et al., 2022).*

Projections indicate an alarming trend of oxygen loss ranging from 1 to 7% by the year 2100 across vast marine settings worldwide (Fig. I.2) (Breitburg et al., 2018; Kwiatkowski et al., 2020; Gong et al., 2021). This phenomenon, recognized as one of the most impactful stressors in modern marine ecosystems, not only disrupts fundamental processes such as primary productivity and biogeochemical cycles (Keeling et al., 2010; Schmidtko et al., 2017; Levin, 2018), but also triggers a cascade of complex ecological and environmental repercussions (e.g., loss of ecological diversity) (Deutsch et al., 2015, 2020; Gao et al., 2019; Glibert et al., 2022). Biogeochemical models outlined in the IPCC 2023 report support a global decline in primary production of 2.1% per decade attributed to the shoaling of the mixed layer and decreasing nitrate concentrations due to strengthening of the water-column stratification, based on instrumental data obtained from 1998 to 2015. This decrease in marine primary productivity has occurred more rapidly at low and mid latitudes (up to −3.0%) (IPCC, 2023). In this context, marine deoxygenation coupled with decreased primary productivity arise as critical and complex oceanic stressors with far-reaching implications on a global scale, underscoring the need for robust projections of these climatic impact-drivers across various spatial and temporal scales (e.g., Oschlies et al., 2020; Gruber et al., 2021).

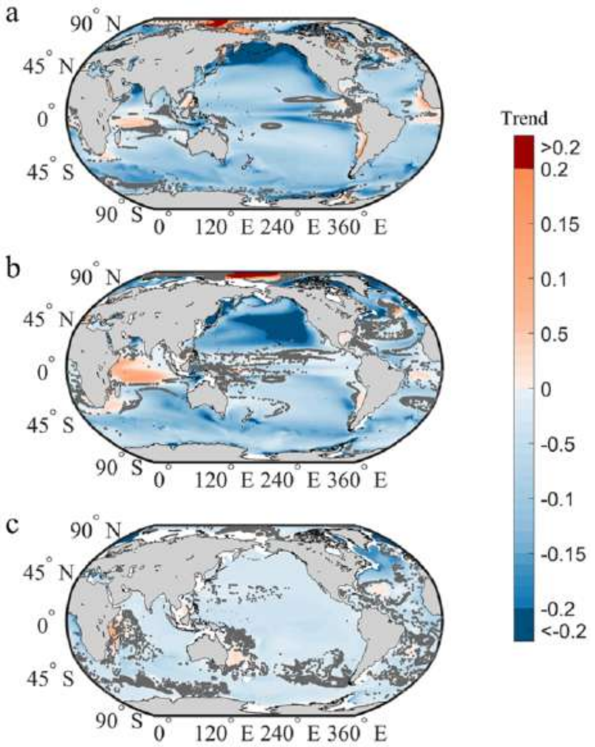

Figure I.2. *Global dissolved oxygen changes (mmol m*$^{-3}$ *per year) from 1920 to 2100 under the high-emission scenario (scenario RCP8.5). The linear trends of oceanic oxygen changes are estimated in the (a) epipelagic, (b) mesopelagic, and (c) bathypelagic zones. The blue and red color represent the deoxygenation and oxygenation, respectively. Note that the dark gray points indicate the slopes are not statistically significant at p = 0.05 level (from Gong et al., 2021).*

I.2.The Mediterranean Sea

The Mediterranean is a semi-enclosed (restricted) marginal sea, relatively small (~ 2,500,00 km^2), with a water-depth over 5,000 m, and with particular features such as high evaporation rate, complex land-sea distribution and seafloor morphology (Pinardi and Masetti, 2000; Millot and Taupier-Letage, 2005; Pinardi et al., 2015; Schroeder et al., 2016). It is often referred to as a "miniature ocean", as it has its own thermohaline circulation, deep-water formation, upwelling/downwelling processes, gyres and eddies, and represents a small-scale version of the meridional overturning circulation in the global ocean (Bethoux and Gentili, 1999; Lejeusne et al., 2010). These distinct hydrogeographic characteristics of the Mediterranean Sea, coupled with its relatively short water-mass residence time (of about one-tenth of the global ocean's) and latitudinal position, make it highly responsive to external forcing, such as global climate change (Giorgi, 2006; Lionello et al., 2006; Giorgi and Lionello, 2008; Malanotte-Rizzoli et al., 2014). Thus, the marine consequences of global climate variability are more evident and are manifested earlier in the Mediterranean Sea than in the global ocean (Fig. I.3) (e.g., Bopp et al., 2013; Macias et al., 2015; Turco et al., 2015). For this reason, the Mediterranean Sea stands out as a major hotspot for the current climate change, therefore, can be considered an exceptional natural laboratory to study the impacts of global climate change in marine settings (Krijgsman, 2002; Lejeusne et al., 2010; Mancini et al., 2023b).

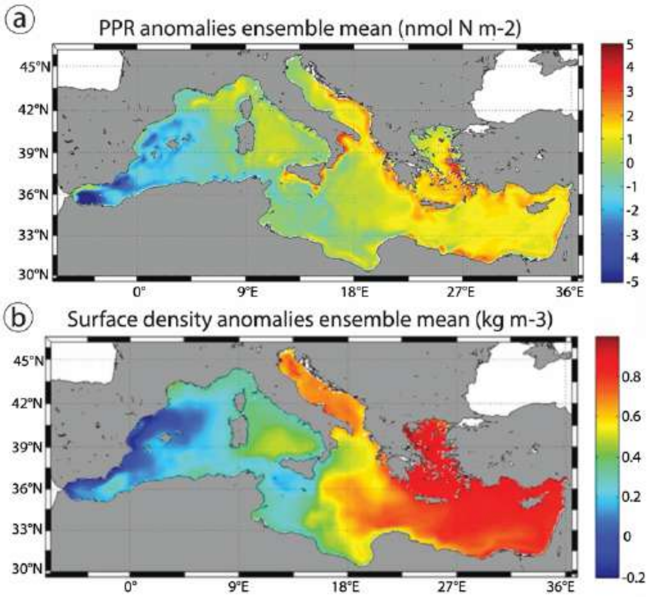
a
PPR anomalies ensemble mean (nmol N m-2)
45°N
42°N
39°N
36°N
33°N
30°N
0°
9°E
18°E
27°E
36°E
5
4
3
2
1
0
-1
-2
-3
-4
-5
b
Surface density anomalies ensemble mean (kg m-3)
0.8
0.6
0.4
0.2
0
-0.2

Figure I.3. *(a) Mean primary productivity rate (PPR; N m^{-2}) anomalies and (b) mean surface density (kg m^{-3}) anomalies expected for year ~ 2095 in the Mediterranean, according to simulations run under the different scenarios/models; from low to high emission (ENSEMBLE mean of models: MPI rcp45.5, EcEarth rcp4.5, MPI rcp8.5, EcEarth rcp8.5) (from Macias et al., 2015). West-east gradient can be observed for both surface-water properties.*

The enclosed nature of the Mediterranean basins allows to study the direct effects of changes in fluvial input and water-column stability on marine deoxygenation and productivity. On the other hand, oligotrophic areas with intermittent nutrient pulses at a regional scale, such as the Westernmost Mediterranean (e.g., Alboran Basin), are ideal to study productivity dynamics and to assess the climatic conditions (e.g., wet vs arid) and oceanographic factors (e.g., water-column stability) controlling such seasonal marine productivity increases (Siokou-Frangou et al., 2010; Bárcena et al., 2004; Mena et al., 2019). At present, the main mechanisms controlling Mediterranean Sea circulation are (i) wind stress, (ii) thermohaline forcing, and (iii) Atlantic - Mediterranean water-masses exchange (e.g., POEM Group, 1992; Zavatarelli and Mellor, 1995; Millot and Taupier-Letage, 2005; Amitai et al., 2018). Atlantic Water (AW) enters the Mediterranean Sea through the Strait of Gibraltar and mixes with saltier Mediterranean Intermediate Water (MIW), resulting in the formation of the Modified Atlantic Water (MAW) (e.g., Millot, 2009). Then MAW splits into a northward current and an eastward current. The northward current flows along the west coast of Italy towards the Gulf of Lions. The eastward current passes through the Strait of Sicily and reaches the Eastern Mediterranean. During winter-cooling, strong northern winds with dry and cold air masses evaporate Levantine Basin surface-water, increasing its salinity (i.e., density) and stimulating vertical convection, which result in the formation of the Levantine Intermediate Water (LIW; between ~ 150 and ~ 600 m water-depth) (e.g., Pinardi et al., 2015; Rohling et al., 2015) (Fig. I.4).

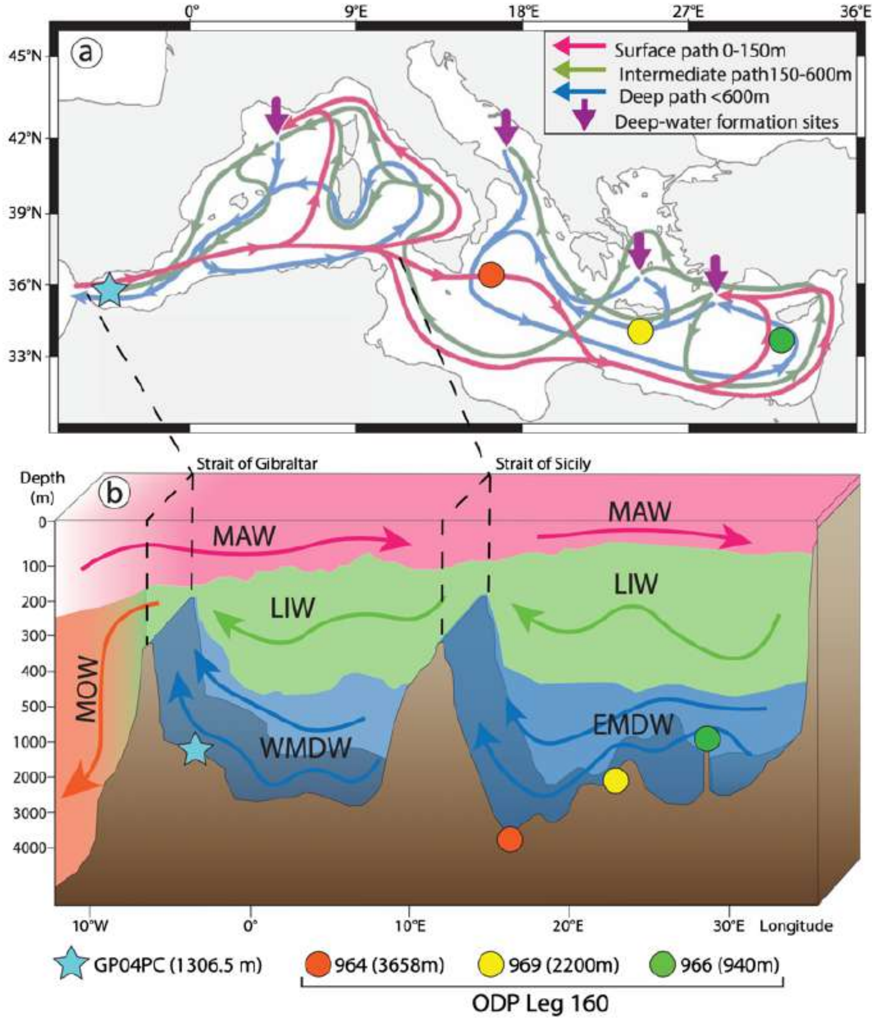

a
0°
9°E
18°E
27°E
36°E
45°N
42°N
39°N
36°N
33°N
Surface path 0-150m
Intermediate path 150-600m
Deep path <600m
Deep-water formation sites
b
Depth (m)
0
100
200
300
400
500
1000
2000
3000
4000
Strait of Gibraltar
Strait of Sicily
MAW
MAW
LIW
LIW
MOW
WMDW
EMDW
10°W
0°
10°E
20°E
30°E
Longitude
GP04PC (1306.5 m)
964 (3658m)
969 (2200m)
966 (940m)
ODP Leg 160

Figure I.4. *Mediterranean overturning circulation model. (a) Circulation patterns of surface water (pink arrows), intermediate water (green arrows) and deep water (blue arrows) in the Mediterranean. Deep-water formation sites are indicated in purple arrows (modified from Pinardi et al., 2022), (b) West-east Mediterranean bathymetry transect indicating the direction and depth interval of the different Mediterranean water-masses (modified from Zavatarelli and Mellor, 1995). MAW: Modified Atlantic Water (pink), LIW: Levantine Intermediate Water (green), WMDW: Western Mediterranean Deep Water (blue), EMDW: Eastern Mediterranean Deep Water (blue), MOW: Mediterranean Outflow Water (orange). The location of the studied marine cores is indicated. ODP Site 964 (orange circle) at a water-depth of 3658 m. ODP Site 966 (green circle) at a water-depth of 940 m. ODP Site 969 (yellow circle) at a water-depth of 2200 m. GP04PC (light blue star) at a water-depth of 1306.5 m. Studied ODP cores were recovered during expedition LEG 160.*

In recent decades, temperature, salinity and density of Mediterranean deep-water masses have increased, while deep-water convection and oxygen content have significantly decreased (e.g., Roether et al., 1996; Sparnocchia et al., 2006; Macias et al., 2015). Some of these oceanographic changes have been partially attributed to anthropogenic disturbances, such as the damming of the Nile in 1964, which has increased by ~ 30% the formation rate of LIW, explaining ~ 45% of the salinity increase in Eastern Mediterranean Deep Water (EMDW) and contributed to trigger the *Eastern Mediterranean Transient*; the most significant intermediate-to-deep Mediterranean overturning perturbation reported by instrumental records (Skliris and Lascaratos, 2004; Schroeder et al., 2006). The formation of EMDW primarily occurs in the Adriatic Sea, and Aegean Sea to a lesser extent, by vertical mixing during winter (Wüst, 1961; Miller, 1963; Lascaratos et al., 1999; Millot, 1999, 2009; Millot and Taupier-Letage, 2005; Rohling et al., 2015), whereas Western Mediterranean Deep Water (WMDW) is formed in the Gulf of Lions. Furthermore, the Mediterranean is an important component of the global circulation as saline water is injected into the North Atlantic through the Gibraltar Strait, known as the Mediterranean Outflow Water (MOW) (Fig. I.4.). The intensity WMDW and LIW circulation has a strong influence on the MOW strength, which, in turn, plays a critical role in the Atlantic meridional overturning circulation (AMOC), and subsequently, on the global ocean circulation and climate (e.g., Voelker et al., 2006; Hernández-Molina et al., 2014; Sierro et al., 2020).

I.3. Eastern Mediterranean Sapropels and Western Mediterranean ORLs

Assessing the potential oceanographic and environmental responses to climate variability (e.g., deoxygenation, weakened thermohaline circulation and primary productivity changes) requires a combination of approaches, including (i) laboratory- and field-based experiments, (ii) field observations (e.g., natural gradients, climate analogues), and (iii) the study of paleo-analogues (IPCC, 2023). The latter mentioned approach is the one applied in this thesis. Oceanographic data on timescales larger than those represented by instrumental records are essential for revealing the long-term (i.e., multidecadal to centennial scale) environmental and ocean responses to the current climate change (Kiessling et al., 2023). Therefore, paleoperspectives obtained through paleoceanographic reconstructions of past climate changes and oceanographic events are crucial to define the propensity of marine systems be adversely affected by the current climate change, and to constraint long-term projections of ocean stressors, including deoxygenation and decreased primary productivity, across different marine settings (Mancini et al., 2023a, b).

The Mediterranean deep sediment records have registered dramatic deoxygenation events during its complex environmental evolution, involving periods of (i) enhanced primary productivity, (ii) weakened termohaline circulation, and (iii) reduced water-column ventilation (e.g., Rohling et al., 2015). In the Eastern Mediterranean, past deoxygenation events are registered in deep-marine settings by the deposition of organic-rich sediments, so-called sapropels, while, in the Western Mediterranean, deoxygenation events are registered as organic-rich sediments known as ORLs (Fig. I.5.). Sapropels and ORLs do not occur synchronically (Fig. I.5.), implying that their deposition –in their respective Mediterranean basins– may derives from different oceanographic and climatic factors (Malanotte-Rizzoli et al., 2014).

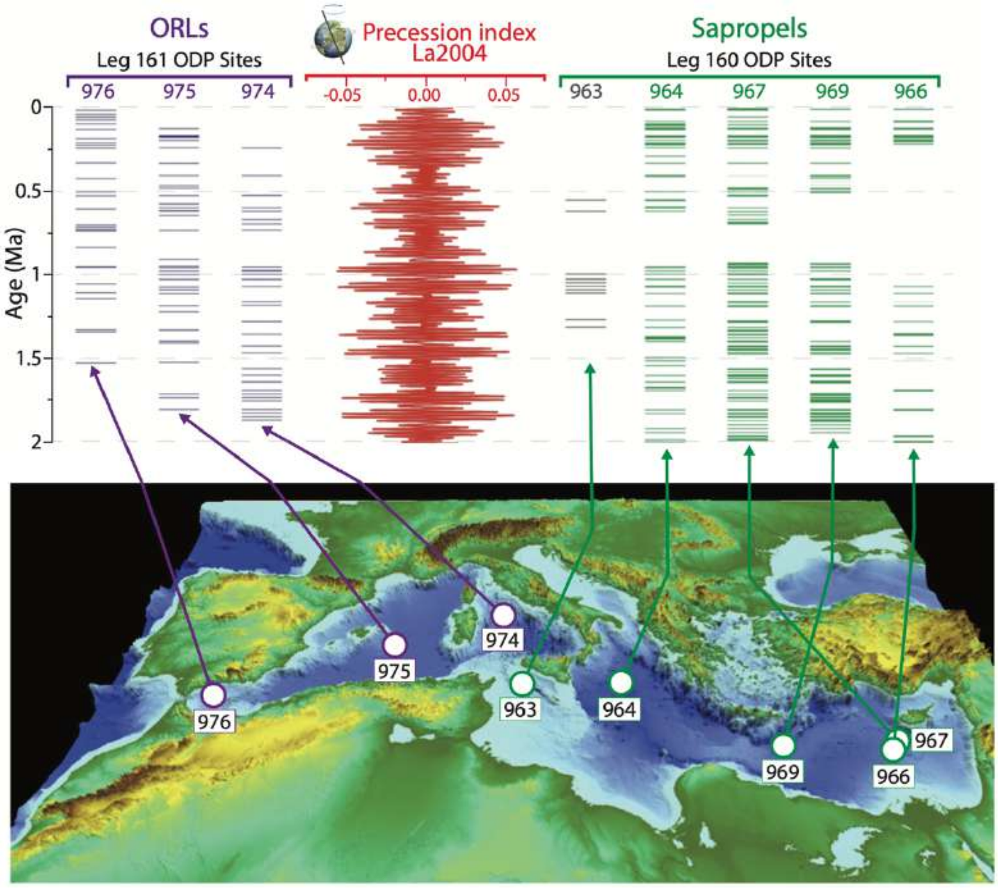

Figure I.5. *Timing of periodic deposition of ORLs and sapropels. Plot of sapropels and ORLs collected in the Mediterranean Sea over the last 3.5 million years by the ODP legs 160 and 161. ORLs and sapropels are not deposited synchronically in Western Mediterranean and Eastern Mediterranean, respectively. Sapropels are rarely deposited at the Strait of Sicily (modified from Malanotte-Rizzoli et al., 2014).*

Eastern Mediterranean sapropels are valuable marine paleoarchives, offering crucial insights into the impacts of climate conditions on ocean dynamics, particularly regarding the interplay between regional-scale deoxygenation, marine productivity, and water-column dynamics (Marino et al., 2007; Grimm et al., 2015; Benkovitz et al., 2020; Blanchet et al., 2020). Sapropels events represent rapid oxic-to-anoxic transitions induced by rapid climate variability (over time scales of hundreds of years or even decades). These events are rhythmically registered as organic-rich sediment layers since the Miocene –with total organic carbon content often above 2% and enriched in trace metals (Cita et al., 1977; Kidd et al., 1978; Calvert, 1983; Emeis et al., 1996, 2000). The rhythmic (quasi-cyclical) deposition of sapropels in the Eastern Mediterranean is influenced by astronomical precession minimum cycles (~ 21,000 years), inducing periods of maximum insolation in the Northern Hemisphere (Rohling et al., 2015; Dirksen and Meijer, 2022). Maximum insolation cyclicity in the Northern Hemisphere produced periodic northward migration of the Intertropical Convergence Zone (ITCZ) and periodic intensification of African monsoons (Fig. I.6.) (Lourens et al., 1996; Hennekam et al., 2014; Weldeab et al., 2014). This resulted in periods with increased freshwater and nutrient discharge into the Eastern Mediterranean, which caused periodic marine productivity increases (Rossignol-Strick, 1983, 1985; Casford et al., 2003; Marino et al., 2009: Gallego-Torres et al., 2010; Helmond et al., 2015; Zwiep et al., 2018).

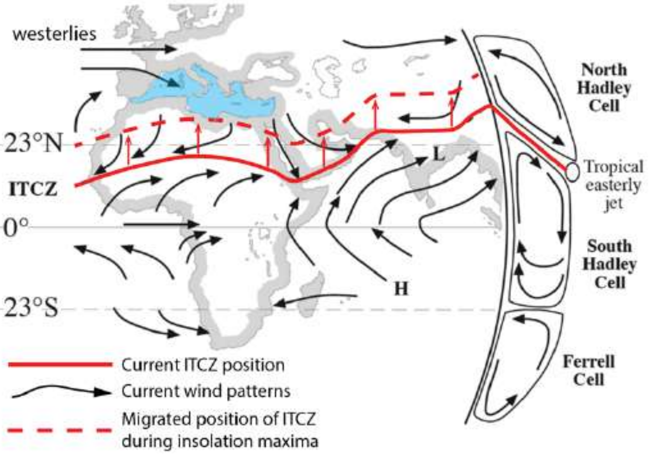

Figure I.6. *Current atmospheric circulation during Northern Hemisphere summer. The main winds patterns are indicated as black arrows. ITCZ = Intertropical Convergence Zone; H = areas of high sea-level pressure; L = areas of low sea-level pressure. The northward migrated position of the ITCZ during insolation maxima is indicated as dashed red line (modified from Rohling et al., 2015).*

The main freshwater inputs during sapropel deposition in the Eastern Mediterranean originate from the Nile River and paleo-African drainages, with additional contributions from northern Eastern Mediterranean margins (Gallego-Torres et al., 2007a; Tachikawa et al., 2015; Wu et al., 2016, 2018). The large freshwater inputs also increased surface-water buoyancy, creating a strong halocline that inhibited vertical mixing and deep-water formation in the Adriatic and Aegean Sea (Fig. I.7.). This resulted in deep-water restriction and upward migration of the redox chemocline from the sediment-water interface to the water-column, causing deoxygenation in deep and intermediate waters and the expansion of Oxygen Minimum Zones (Filippidi and de Lange, 2019; Zirks et al., 2019; Sweere et al., 2021).

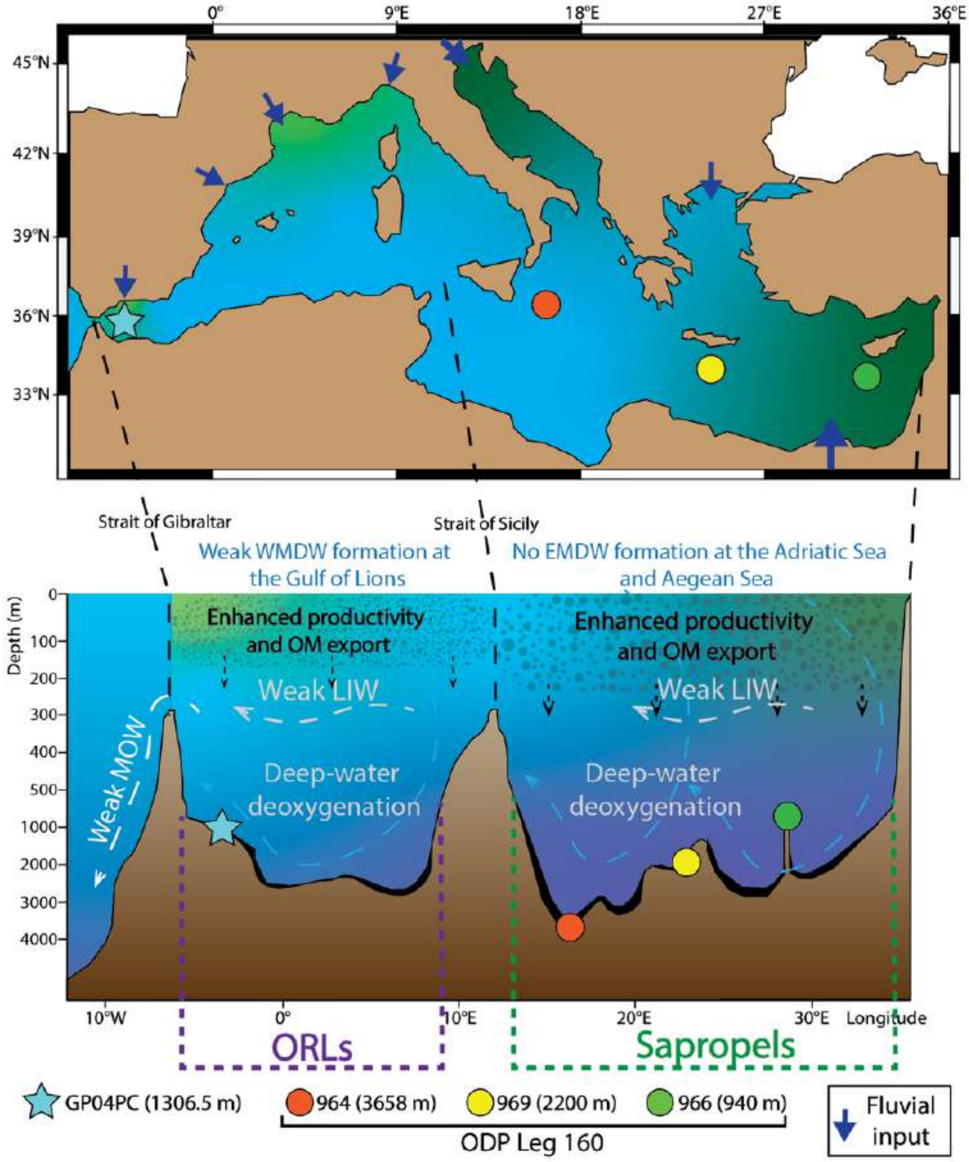
0°
9°E
18°E
27°E
36°E
45°N
42°N
39°N
36°N
33°N
Strait of Gibraltar
Strait of Sicily
Weak WMDW formation at the Gulf of Lions
No EMDW formation at the Adriatic Sea and Aegean Sea
Depth (m)
0
100
200
300
400
500
1000
2000
3000
4000
Enhanced productivity and OM export
Weak LIW
Enhanced productivity and OM export
Weak LIW
Weak MOW
Deep-water deoxygenation
Deep-water deoxygenation
10°W
0°
10°E
20°E
30°E
Longitude
ORLs
Sapropels
GP04PC (1306.5 m)
964 (3658 m)
969 (2200 m)
966 (940 m)
ODP Leg 160
Fluvial input

Figure I.7. *Typical sapropels and ORLs deposition models. In both scenarios occur: enhanced water-column stratification, decreased deep-water ventilation, increased organic matter export and preservation and decreased surface water salinity and buoyancy due to increased freshwater runoff (modified from Bulian et al, 2022 and Mancini et al., 2023a).*

Furthermore, over the Pleistocene-Holocene, sapropel deposition occurred during a similar land-sea distribution and Atlantic-Mediterranean gateway configuration (Fig. I.7.), facilitating inferences between paleoceanographic data and modern Mediterranean observations (Rohling et al., 2015). Consequently, Eastern Mediterranean sapropels have been extensively studied, providing a solid understanding of the behavior and sensitivity of the Eastern Mediterranean system to external forcing (Mancini et al., 2023a, b). In contrast, the occurrence and origin of ORLs in the Western Mediterranean have received comparatively little attention, despite being recognized since the early 1980s (Canals et al., 1982; Rogerson et al., 2008).

Western Mediterranean ORLs are recognized as sediment layers containing enhanced total organic carbon content (up to 0.9%), and extend throughout the Western Mediterranean deep basins, including the Tyrrhenian and Alboran Sea sub-basins (Cacho et al., 2002b; Martínez-Ruiz et al., 2003; Meyers and Arnaboldi, 2005; Pérez-Asensio et al., 2020). Although ORLs are linked to periods of enhanced organic matter preservation and oxygen-depleted deep-waters in the Western Mediterranean, they differ in deposition timing from sapropels (Malanotte-Rizzoli et al., 2014). While Eastern sapropels were deposited immediately following precession maxima over periods of 3 - 5.5 ka at the beginning of interglacial periods, the last two ORLs (ORL-1 and ORL-2) occurred at glacial Terminations over periods ~ 5 - 6 ka, during the orbital maximum. This difference suggests that ORL deposition is not forced by the same atmospheric, climatic and hydrogeographic factors as sapropels. Moreover, the timing of ORL deposition does not align with well-known pluvial maxima in North Africa, challenging the notion of an enhanced runoff mechanism associated with ITCZ northward migration (Larrasoaña et al., 2003; Rogerson et al., 2008). For instance, within the Alboran Sea, ORL-1 onset occurred at 14.5 ka, preceding the onset of sapropel S1 by around 4,500 years, and spanning multiple climatic events; including the Bølling-Allerød Younger Dryas and Holocene onset (Pérez-Asensio et al., 2020). Additionally, ORL-1 termination is associated with the ~ 8.2 ka cold climatic event, synchronously aligning with the interruption of S1a phase in the Eastern Mediterranean (Martínez-Ruiz et al., 2003; de Lange et al., 2008). Therefore, studying the different climatic and oceanographic interactions that led to the formation and termination of sapropels and ORLs is crucial for gaining insights into the Mediterranean system as a whole (Mancini et al., 2023a). This understanding is essential for assessing its sensitivity to external forces such as global warming, current regional aridification, and anthropogenic pressures like changes in nutrient availability.

The information provided by these marine paleoarchives on periods of enhanced deoxygenation and marine productivity in the Mediterranean (i.e., sapropels and ORLs) enables to study the potential reoccurrence of such extreme deoxygenation events in the future due to the current climate change, but also allows for the assessment of the potential environmental triggers and climatic drivers of regional deoxygenation (Hennekam et al., 2020). Additionally, they offer long-term perspectives (spanning multidecadal to centennial time scales) to modern global marine settings undergoing suffocation (oxygen depletion) due to climate change and anthropogenic pressure (Lionello et al., 2012; Mancini et al., 2023a).

I.4. Multiproxy paleoceanographic approach

Paleoenvironmental proxies –as indirect indicators of past climate, environmental and ecological conditions– provided by marine sediment records, are useful tools to unravel the oceanographic information prior to industrial times, covering long time-scale periods; from thousand to million years back in time (Kiessling et al., 2023). Over the past decades, significant progress has been made in the development of biotic and abiotic proxies and tools for assessing the marine environmental conditions (e.g., dissolved oxygen content, productivity changes, nutrient availability, and salinity) and the hydrogeographic conditions (e.g., ocean currents and water-column structure and stability) during the onset, evolution and termination of past climate changes (e.g., Calvert and Pedersen, 2007). Moreover, the integration of proxies of diverse nature (e.g., biotic and abiotic) allows a more comprehensive understanding of past climatic and oceanographic events (e.g., regional-scale deoxygenation) by mitigating potential biases inherent in using individual paleoceanographic proxies (Fig. I.8.). Thus, the multidisciplinary integrative approach employed in this thesis is essential for robust paleoceanographic reconstructions of past Mediterranean deoxygenation events (sapropels and ORLs events). Although the used paleoceanographic proxies are explained in the respective chapters, a brief overview of the applied biotic and abiotic proxies is presented in this section.

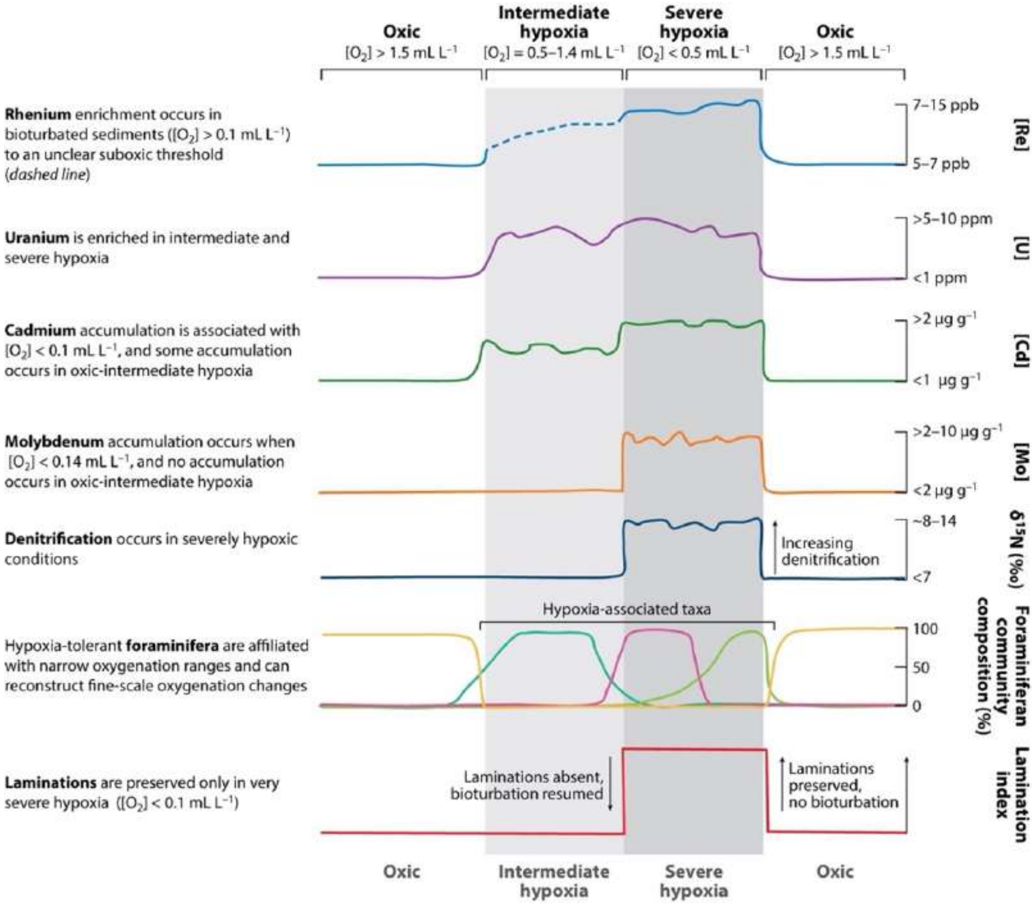
Oxic
[O2] > 1.5 mL L-1
Intermediate hypoxia
[O2] = 0.5–1.4 mL L-1
Severe hypoxia
[O2] < 0.5 mL L-1
Oxic
[O2] > 1.5 mL L-1
Rhenium enrichment occurs in bioturbated sediments ([O2] > 0.1 mL L-1) to an unclear suboxic threshold (dashed line)
7–15 ppb
5–7 ppb
[Re]
Uranium is enriched in intermediate and severe hypoxia
>5–10 ppm
<1 ppm
[U]
Cadmium accumulation is associated with [O2] < 0.1 mL L-1, and some accumulation occurs in oxic-intermediate hypoxia
>2 μg g-1
<1 μg g-1
[Cd]
Molybdenum accumulation occurs when [O2] < 0.14 mL L-1, and no accumulation occurs in oxic-intermediate hypoxia
>2–10 μg g-1
<2 μg g-1
[Mo]
Denitrification occurs in severely hypoxic conditions
Increasing denitrification
~8–14
<7
δ15N (‰)
Hypoxia-associated taxa
Hypoxia-tolerant foraminifera are affiliated with narrow oxygenation ranges and can reconstruct fine-scale oxygenation changes
100
50
0
Foraminiferan community composition (%)
Laminations are preserved only in very severe hypoxia ([O2] < 0.1 mL L-1)
Laminations absent, bioturbation resumed
Laminations preserved, no bioturbation
Lamination index
Oxic
Intermediate hypoxia
Severe hypoxia
Oxic

Figure I.8. *General example of a multiproxy assessment employing geochemical (e.g., redox-sensitive trace metals concentration, such as Mo and U) and biological (e.g., microfossils) proxies, and sedimentary structures (e.g., preserved lamination) derived from a deep marine sediment record. This approach allows for the inference of patterns and mechanisms underlying past deoxygenation events in marine environments (from Levin, 2018).*

I.4.1. Geochemical proxies

The paleoceanographic studies presented in this thesis rely predominantly on the utilization of geochemical proxies, such as diagnostic environmental trace elements (e.g., Ba, Mo and U; Tribovillard et al., 2006; Calvert and Pedersen, 2007). Marine sediments are typically conformed by a variable mixture of (i) lithogenous components (phases derived from continental sources; e.g., soils and rocks), (ii) biogenic components (skeletal materials and the degraded tissues of marine and terrestrial organisms), and (iii) authigenic minerals that precipitate from seawater due to specific environmental conditions (e.g., barite) and during diagenesis within sediments (e.g., Mn and Fe oxyhydroxides and iron sulfide). Therefore, the elemental composition of marine sediments –resulting from syndepositional physical, geochemical and biological processes coupled with postdepositional reactions– provides a wide range of information, including sediment nature (e.g., terrestrial vs marine), past climates and oceanographic conditions, organic production rate, bottom-water and sedimentary oxygenation and postdepositional (diagenetic) changes (Warning and Brumsack, 2000; Tribovillard et al., 2006; Calvert and Pedersen, 2007; Algeo and Maynard, 2008; Lyons et al., 2009; Algeo and Liu, 2020). In order to use geochemical elements as paleoenvironmental proxies, it is essential to assess whether they are relatively enriched or depleted in respect to the background values (Tribovillard et al., 2006). In this sense, the concentrations of elements of interest have to be normalized for adequate interpretation and comparison (Paul et al., 2023). The conservative behavior and uniform distribution in crustal rocks of aluminum (Al) has led to its use in sediment studies as a normalizing parameter for the assessment of the relative degrees of enrichment or depletion of specific elements in a given sample, or to estimate the background contribution of an element derived from crustal sources. Thus, elements analyzed in this thesis have been Al-normalized in order to use them as paleoclimatic and paleoceanographic proxies.

The chemical composition of the terrigenous fraction has been used to unravel the climatic variations in the Mediterranean over time as climate changes cause significant variations in the chemical and mineralogical composition of marine sediments (Calvert and Pedersen, 2007). Elemental ratios such as K/Al, Mg/Al and Rb/Al have been used to reconstruct the riverine supply of terrigenous material, while Ti/Al and Zr/Al ratios have been used to reconstruct the eolian input variations (e.g., Rodrigo-Gámiz et al., 2011). Thus, these elemental ratios allowed to differentiate arid from humid periods in the Mediterranean borderlands throughout the studied intervals. Qualitative productivity rates can also be reconstructed from geochemical data. In particular, the Ba/Al ratio has been commonly used as proxy for reconstructing marine export productivity since pelagic barite –an authigenic marine mineral ($BaSO_4$)– precipitates abundantly in the water-

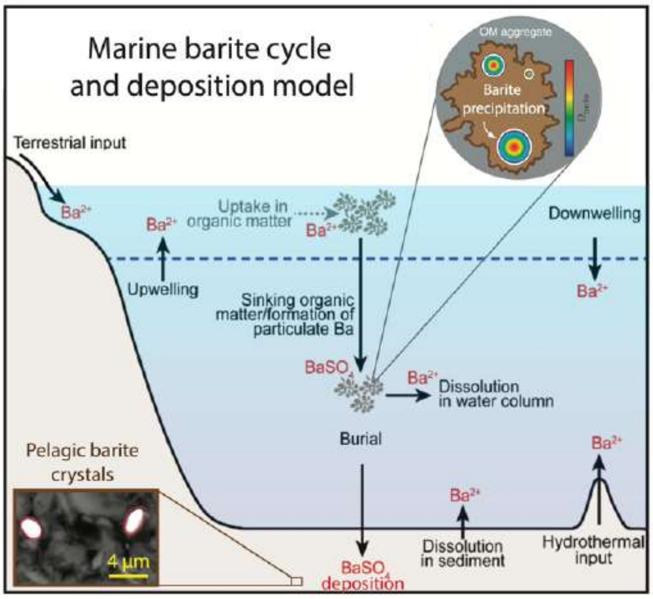
Marine barite cycle and deposition model
OM aggregate
Barite precipitation
Terrestrial input
Ba2+
Ba2+
Uptake in organic matter
Ba2+
Downwelling
Ba2+
Upwelling
Sinking organic matter/formation of particulate Ba
BaSO4
Ba2+
Dissolution in water column
Burial
Ba2+
Pelagic barite crystals
Ba2+
4 µm
BaSO4 deposition
Dissolution in sediment
Hydrothermal input

Figure I.9. *Simplified diagram of pelagic barite cycle and depositional model. Direction and sources of dissolved Ba fluxes are indicated in black arrows. Ba phases are indicated in red, with* Ba^{2+} *as the dissolved phase and* $BaSO_4$ *(barite) as the particulate phase. Light blue circle: organic matter aggregates creating Ba saturated microenvironments that favor barite precipitation in the water-column. Brown rectangle: SEM image of barite crystals is shown to illustrate pelagic barite in deep marine sediments (modified from Horner et al., 2017 and Carter et al., 2020).*

column during periods characterized by enhanced marine productivity and carbon export to the deep ocean, and subsequently enriches marine organic-rich sediments in Ba (Paytan and Griffith 2007; Martínez-Ruiz et al., 2015, 2018; Bridgestock et al., 2019; Carter et al., 2020). Pelagic barite precipitates in microenvironments enriched in Ba formed within sinking biogenic particulate matter in the water-column in close association with extracellular polymeric substances (EPS). During high productivity rates, large amounts of organic matter are subjected to bacterial degradation, producing large amounts of EPS that serve to bind and concentrate the necessary Ba to form nucleation sites for barite precipitation (Fig. I.9) (Martínez-Ruiz et al., 2019, 2020). Organic carbon content has also been used as qualitative paleoproductivity proxy, however, organic matter is susceptible to degradation during sinking in the water-column and particularly to postdepositional oxidation (Thomson et al., 1995; van Santvoort et al., 1996, 1997; Filippidi and de Lange, 2019). Thus, the final organic carbon content in marine sediments is not always proportional to surface-water productivity (Tribovillard et al., 2006).

Given the focus of this thesis on past deoxygenation events in the Mediterranean, the used approach involves the reconstruction of bottom-water and sediment oxygen conditions (paleoredox conditions) during the studied sedimentary intervals. Discerning paleoredox conditions requires determining whether conditions were oxidizing or reducing; typically categorized as oxic, suboxic, anoxic and euxinic conditions (Fig. I.10 a) (Tyson and Pearson, 1991). In oxic sediment settings, aerobic organisms utilize dissolved oxygen from overlying and interstitial waters for their metabolism (i.e., organic matter degradation). As dissolved oxygen is depleted, organic matter decomposition continues through secondary oxidant sources (nitrate, manganese and iron oxides and oxyhydroxides, and sulfate). When secondary oxidants are exhausted, methanogenic bacteria begin to break down organic matter (Tribovillard et al., 2006 and references therein). In the water-column, oxygen depletion (i.e., suboxic/anoxic conditions) may develop in stagnant or confined water masses where insufficient circulation prevents oxygen renewal (e.g., Black Sea and Cariaco Trench), or in places where intense organic matter degradation consumes oxygen faster than it is replenished due to high primary productivity and carbon export to the deep ocean, even in open-marine conditions where water-masses are not geographically restricted (e.g., Peru Shelf) (Algeo and Lyons, 2006; Algeo and Tribovillard, 2009; Scholz et al., 2013; Scholz, 2018).

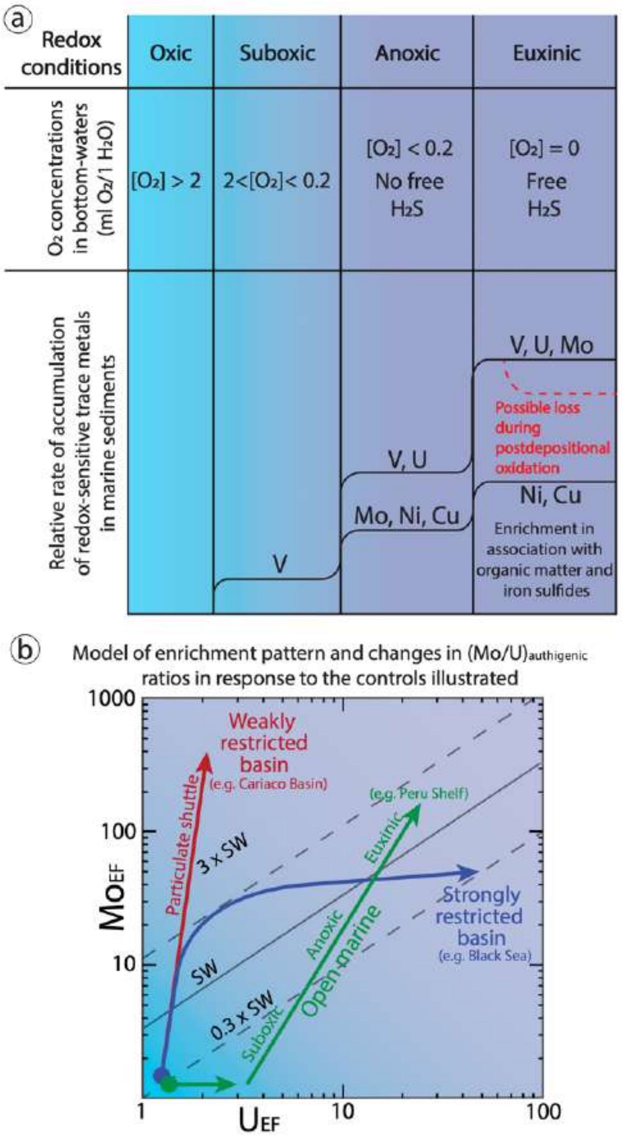
a
Redox conditions
Oxic
Suboxic
Anoxic
Euxinic
O₂ concentrations in bottom-waters (ml O₂/1 H₂O)
[O₂] > 2
2<[O₂]< 0.2
[O₂] < 0.2 No free H₂S
[O₂] = 0 Free H₂S
Relative rate of accumulation of redox-sensitive trace metals in marine sediments
V, U, Mo
Possible loss during postdepositional oxidation
V, U
Ni, Cu
Mo, Ni, Cu
Enrichment in association with organic matter and iron sulfides
V
b
Model of enrichment pattern and changes in (Mo/U)authigenic ratios in response to the controls illustrated
1000
100
10
1
10
100
MoEF
UEF
Weakly restricted basin
(e.g. Cariaco Basin)
Particulate shuttle
3 x SW
SW
0.3 x SW
(e.g. Peru Shelf)
Euxinic
Anoxic
Suboxic
Open-marine
Strongly restricted basin
(e.g. Black Sea)

Figure I.10. *Examples and interpretation of trace metals cross-plots used in this thesis. (a) Redox classification of the depositional environments, after Tyson and Pearson (1991) and schematic behavior of Ni, Cu, Mo, U and V as a function of the redox condition of the depositional environment. The values for O_2 concentrations in bottom-waters are valid for present-day ocean. Modified from Tribovillard et al. (2006). (b) Model of enrichment patterns and changes in $(Mo/U)_{authigenic}$ ratios in response to redox conditions, particulate shuttling intensity and degree of basin restriction. Conceptual model based on modern marine settings empirical observations. The diagonal dotted gray lines represent the seawater (SW) Mo/U molar ratio of ~ 7.5 - 7.9 and fractions thereof (3 x SW and 0.3 x SW) (modified from Algeo and Tribovillard et al., 2009).*

Within marine sediments, anoxia also occurs when the oxygen demand exceeds the supply, with the additional complexity that oxygen replenishment is also linked to the petrophysical properties of the sediments (e.g., grain size and permeability), sedimentation rate and the intensity of bioturbation (Tribovillard et al., 2006). Under suboxic conditions oxygen concentrations in the water-column are extremely low and hydrogen sulfide (H_2S; a catabolic by- product of sulfate-reducing bacteria) is confined to porewaters below the sediment-water interface (Scott and Lyons, 2012). Anoxic conditions may be nonsulfidic or sulfidic, the latter termed euxinic when hydrogen sulfide occurs within the water-column due to sulfate-reducing bacteria. In this regard, the concentration of redox sensitive elements (e.g., Mo, U, V, Ni, Co, Cu, and Mn) offer fundamental information about the redox conditions in bottom-water and porewater in organic-rich sediments (e.g., black shales and sapropels). These trace elements have varying sensitivities to redox conditions across an oxic to sulfidic gradient (Fig. I.10a.). For example, U, and V tend to be reduced and accumulate under denitrifying conditions (i.e., suboxic conditions;), while Ni, Co, Cu, Zn, Cd, and Mo are primarily enriched under sulfate-reducing conditions alone (i.e., euxinic conditions; Fig. I.10a.). Therefore, it is possible to discern redox gradients in ancient sedimentary systems by examining a suite of redox sensitive trace elements. For instance, the presence of U and V enrichment without Mo enrichment suggests suboxic/anoxic deposition without free H_2S. Conversely, sediments showing simultaneous enrichments in U, V, and Mo indicate euxinic conditions at the sediment-water interface or/and within the water-column (Fig. I.8). It is worth mentioning that these trace elements tend to be delivered to the seafloor by sinking organic aggregates and inorganic particulates (e.g., Mn-oxyhydroxides and clay minerals) (Tribovillard et al., 2006). Furthermore, they provide valuable information about water-column structure and dynamics –e.g., water-column stratification, particulate shuttling intensity, deep-water renewal frequency and stability of the chemocline (Fig. I.10b) (Algeo and Lyons, 2006; Algeo and Maynard, 2008; Algeo and Rowe, 2012; Scholz, 2018).

All these geochemical proxies have become powerful tools in paleoceanographic and paleoclimate research. However, paleoenvironmental interpretations require a profound understanding of the recognized geochemical signals, posing a significant challenge in accurately reconstructing paleoenvironmental conditions. As a result, extensive efforts have been made to comprehend the origin and environmental significance of geochemical signals observed in organic-rich sediments deposited in different deep pelagic environments (see Chapter III). Additionally, efforts have focused on assessing potential geochemical perturbations by deep-sea postdepositional processes, including early diagenetic ones (e.g., postdepositional oxidation and trace metals remobilization), and bioturbation –see Chapter IV and Chapter V, respectively. This contributes to enhancing the current understanding of geochemical signals generated by deoxygenation dynamics in deep-sea settings, as well as the potential alterations in the geochemical record caused by postdepositional processes.

I.4.2. Ichnological analysis

Trace fossils are geological records of biological activity, such as burrows, or trails, left behind by organisms in sedimentary rocks, or deep-marine sediments (Bromley et al., 1984, 1996). In recent decades, paleoichnological analysis (the study of trace fossils) has also emerged as a very powerful tool for paleoenvironmental and paleoceanographic reconstructions, mainly related to paleoclimatic variations. This is due to the relationship between the behavior of trace makers and the environmental conditions (e.g., salinity, oxygen content, nutrient availability, hydrodynamic energy, rate of sedimentation, and substrate, among others; Fig. I.11.) (Buatois and Mángano, 2011; Knaust and Bromley, 2012; Rodríguez-Tovar, 2021). Thus, trace fossils reflect the behavior of trace makers, recording their activity in response to the syndepositional environment, providing valuable paleoenvironmental (i.e., ecological and depositional) information (Ekdale et al., 2012; MacEachern et al., 2012). More specifically, ichnological features such as ichnodiversity, size of biogenic structures and bioturbation depth allow interpreting redox conditions in bottom-waters and below the sediment-water interface (Fig. I.11) (Savrda and Bottjer, 1989; Löwemark et al., 2006; Uchman et al., 2008; Buatois and Mángano, 2016; Baucon et al., 2020). Ichnology analysis is employed and further explained in the study presented in Chapter V.

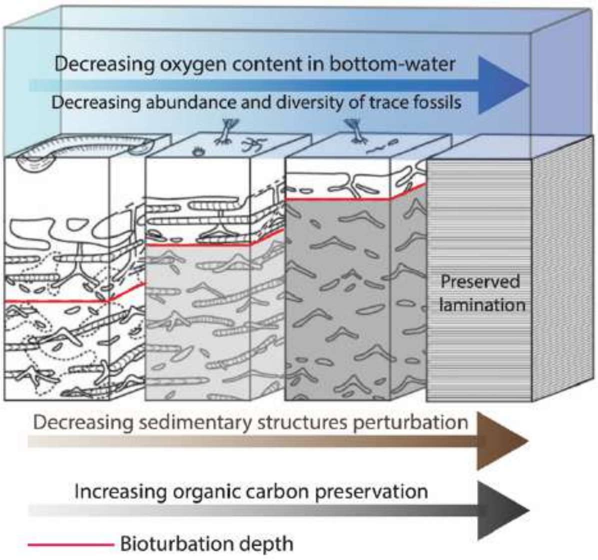
Decreasing oxygen content in bottom-water
Decreasing abundance and diversity of trace fossils
Preserved lamination
Decreasing sedimentary structures perturbation
Increasing organic carbon preservation
Bioturbation depth

Figure I.11. *Schematic block diagram illustrating abundance and diversity of trace fossils, burrow size, bioturbation depth, and tiering structure across a hypothetical seafloor oxygenation gradient and expected trace-fossil cross-cutting relationships in strata deposited at various sites along the redox gradient (modified from Savrda and Bottjer, 1989 and IchnoBioGeoScience research group (https://ichnology.ku.edu/poi/poi/models.html).*

I.4.3. Dinoflagellates analysis

Dinoflagellates analysis (also known as dinocysts analysis) was primarily considered to strengthen paleoproductivity reconstructions. Dinoflagellates are (predominantly) marine single-cell protists and an important component of the eukaryotic plankton community. During resting stages, they produce organic-walled hypnozygotic cysts, called dinocysts, that can be preserved in marine sediments (Taylor, 1987). Dinoflagellate communities are very sensitive and responsive to environmental and oceanographic changes (e.g., sea surface temperature, nutrient availability and water-column stability) (Dale and Fjellså, 1994; De Vernal and Marret, 2007; Taylor et al., 2008; Zonneveld et al., 2013; Zweip et al., 2018). Consequently, dinocysts abundance and assemblages serve for reconstructing marine primary productivity and others key oceanographic features, such as nutrient availability, salinity, and water-column stability (Fig. I.12.) (Zonneveld et al., 2001; Sluijs et al., 2005, 2006; Sangiorgi et al., 2021). Due to this and their frequent occurrence in marine sediments, dinocysts analysis has become a key tool in paleoenvironmental studies, providing insights into eukaryotic productivity responses to oceanographic changes linked to past climate variability (Sangiorgi et al., 2006; Sluijs et al., 2006; Penaud et al, 2011, 2016; van Helmond et al., 2015; Zwiep et al., 2018). Dinoflagellates analysis is employed and further explained in Chapter VI.

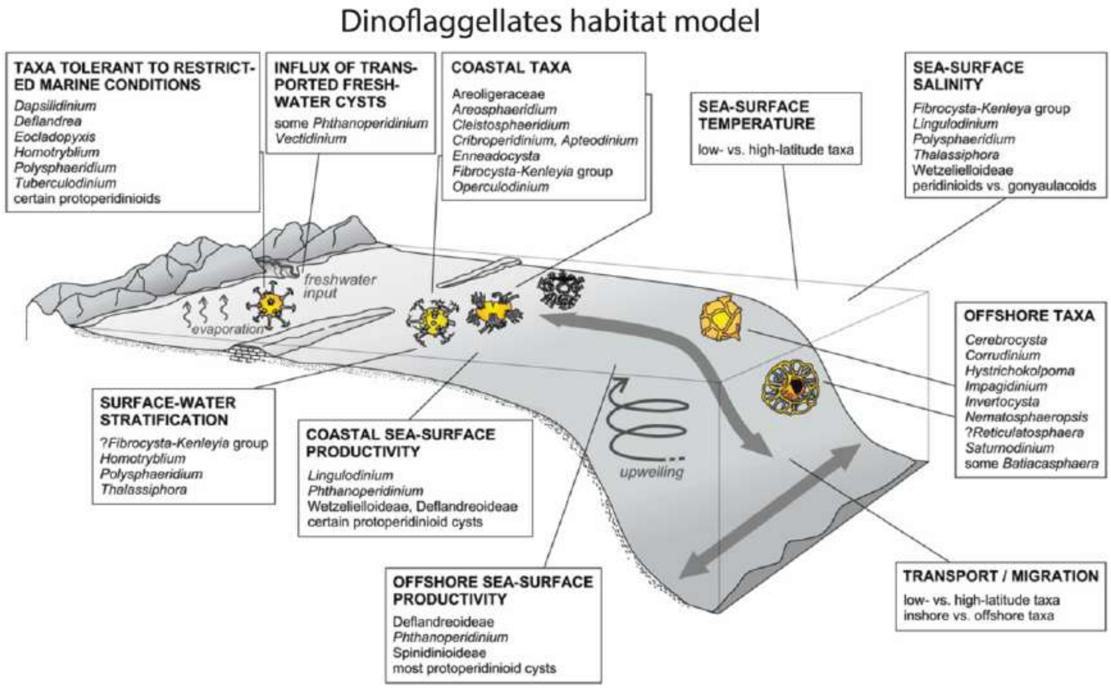
Dinoflaggellates habitat model
TAXA TOLERANT TO RESTRICTED MARINE CONDITIONS
Dapsilidinium
Deflandrea
Eocladopyxis
Homotryblium
Polysphaeridium
Tuberculodinium
certain protoperidinioids
INFLUX OF TRANSPORTED FRESHWATER CYSTS
some Phthanoperidinium
Vectidinium
COASTAL TAXA
Areoligeraceae
Areosphaeridium
Cleistosphaeridium
Cribroperidinium, Apteodinium
Enneadocysta
Fibrocysta-Kenleyia group
Operculodinium
SEA-SURFACE TEMPERATURE
low- vs. high-latitude taxa
SEA-SURFACE SALINITY
Fibrocysta-Kenleya group
Lingulodinium
Polysphaeridium
Thalassiphora
Wetzelielloideae
peridinioids vs. gonyaulacoids
freshwater input
evaporation
OFFSHORE TAXA
Cerebrocysta
Corrudinium
Hystrichokolpoma
Impagidinium
Invertocysta
Nematosphaeropsis
?Reticulatosphaera
Saturnodinium
some Batiacasphaera
SURFACE-WATER STRATIFICATION
?Fibrocysta-Kenleyia group
Homotryblium
Polysphaeridium
Thalassiphora
COASTAL SEA-SURFACE PRODUCTIVITY
Lingulodinium
Phthanoperidinium
Wetzelielloideae, Deflandreoideae
certain protoperidinioid cysts
upwelling
OFFSHORE SEA-SURFACE PRODUCTIVITY
Deflandreoideae
Phthanoperidinium
Spinidinioideae
most protoperidinioid cysts
TRANSPORT / MIGRATION
low- vs. high-latitude taxa
inshore vs. offshore taxa

Figure I.12. *Schematic model for the distribution of dinocysts associations along a proximal-distal marine platform transect during the Paleogene according to the specific environmental and oceanographic demands of dinocysts species (from Pross and Brinkhuis, 2005).*

I.5. Materials and methods

Among natural archives, marine records have been revealed as exceptional tools for past climate and oceanographic reconstructions, offering a unique, global and continuous signal of the ocean responses to climate change, also providing records of terrestrial and atmospheric processes (Bout-Roumazeilles et al., 2013; Kiessling et al., 2023; Mancini et al., 2023a). Marine sediment cores from different Mediterranean basins have been selected and analyzed to achieve the proposed objectives. To study the sediment and geochemical record of different sapropels events, three Ocean Drilling Program (ODP) sites from expedition Leg 160 were selected in a transect across the Eastern Mediterranean in order to represent different oceanographic regimes and water-depths (Fig. I.4.). The studied records are predominantly composed by nannofossil clay and nannofossil oozes, with sapropel layers periodically intercalated (Emeis et al., 1996). These background sediments exhibit a spectrum of colors ranging from brownish to greenish and grayish. Site 964 (36°15'37.4"N, 17°45'00.0"E) is located at the Ionian Basin at a water-depth of

3658 m. Site 966 (33°47'45.9"N, 32°42'05.4"E) is situated near the northern margin of the plateau area of the Eratosthenes Seamount at a water-depth of 940 m. Site 969 (33°50'23.9"N, 24°53'03.9"E) is situated on the Mediterranean Ridge at a water-depth of 2200 m (Fig. I.4.).

In the Western Mediterranean, a marine sediment piston core GP04PC was selected to study ORL-1 deposition and Westernmost Mediterranean marine responses to Holocene climatic variability. The GP04PC record was recovered in the West Alboran Sea Basin (35°47'13.6"N, 4°32'03.5"W) at a water-depth of 1306.5 m (Fig. I.4.), during the oceanographic cruise Gasalb onboard the R/V Pelagia in November 2011. According to the GP04PC age model (Morcillo-Montalbá et al., 2021), the 872.25 cm long core spans the last 35,000 years. Precise oceanographic setting and sampling details of the studied cores are included in the corresponding chapter.

A variety of analytical techniques and approaches have been utilized to comprehensively study the selected marine sediment records. While each methodology is thoroughly explained in its respective chapter, this section summarizes the main geochemical techniques employed in this thesis:

1. X-ray Fluorescence (XRF) and Inductively Coupled Plasma - Optical Emission Spectrometry (ICP-OES) for obtaining concentrations of major elements in bulk sediment samples (e.g., Si, Al, Mn, Fe, Ca, Mg, K). Some trace elements (e.g., Zr) were also determined by XRF.
2. Inductively Coupled Plasma - Mass Spectrometry (ICP-MS) for obtaining concentrations of trace elements (e.g., U, Mo, V, Co, Ni, Cu, Zn, Ba, Cr and Pb).
3. Rock-Eval pyrolysis for obtaining total organic carbon content in bulk sediment samples.
4. Elemental Analyzer (EA) for measuring total organic carbon and total nitrogen content (expressed as C_{org}% and N_{total}%) in decalcified sediment samples.
5. Laser Ablation - Inductively Coupled Plasma - Mass Spectrometry (LA-ICP-MS) for determining the concentration and distribution of trace elements in sediment thin-sections (resin-embedded sediments).
6. Scanning Electron Microscopy (SEM) for the observation of sediment samples at the micrometer scale and a SEM with Energy Dispersive X-ray Spectroscopy detector (SEM-EDX) for compositional analysis and identification of different mineral phases and sub-cm trace fossils in sediment thin-sections.
7. Isotope-Ratio Mass Spectrometry (IRMS) for measuring carbon stable isotopes for determining $\delta^{13}C$ values in organic matter and in planktonic foraminifer shells.
8. Optical microscope for dinoflagellates analysis and observation of trace fossils in sediment thin-sections

Furthermore, the interpretation of the obtained results has also required specific presentation and statistical treatments:

1. Data visualization, assessment and comparison through cross-plots and vertical plots.
2. Calibration of geochemical redox proxies using scatter-plots, following Algeo and Li (2020) methodology, to establish statistically robust numerical thresholds for oxygen conditions in the studied Mediterranean basins (Appendix I).
3. Multivariate statistical treatments of geochemical data, including Principal Component Analysis (PCA) and correlation matrices, using various software packages (e.g., Past 4.0 and R studio), to understand how elements behave and group for each set of data deriving from a specific Mediterranean basin and time interval (Appendix I).
4. Processing of high-resolution images of marine sediment cores and sediment thin-sections using Adobe Photoshop CS6 and following methodology developed by Dorador et al. (2014a, b) to highlight trace fossils (e.g., *Chondrites*) and sedimentary structures (e.g., lamination).

Chapter II

Role of climate variability on deep-water dynamics and deoxygenation during sapropel deposition: New insights from a palaeoceanographic empirical approach

Ricardo D. Monedero-Contreras, Francisca Martínez-Ruiz, Francisco J. Rodríguez-Tovar

Palaeogeography, Palaeoclimatology, Palaeoecology 622 (2023) 111601
doi: 10.1016/j.palaeo.2023.111601

Abstract

Modern marine settings are experiencing rapid deoxygenation mainly forced by global warming and anthropogenic eutrophication. Therefore, studies that assess the role of climate variability in large spatiotemporal deoxygenations during past climate changes are needed to better comprehend the consequences of the current global warming and ocean deoxygenation. In this respect, deep marine sediments associated to past oxic-to-anoxic transitions are useful palaeoarchives for understanding the interplay between climate variability, deep-water dynamics and large-scale deoxygenation. Moreover, they can offer long-term perspectives to modern marine settings that are suffering oxygen depletion due to climate change and anthropogenic pressure. In particular, sapropel layers from the Middle Pleistocene to the Holocene are excellent palaeoarchives of past large-scale deoxygenation events, since (i) they occurred during a similar Mediterranean hydrogeographic configuration to the present, (ii) have a robust chronological control, and (iii) previous studies have reconstructed the climate conditions that ruled during their deposition. In this work, we have applied empirical palaeoceanographic conceptual models to five sapropels (S1, S5, S6, S7 and S8) in three Eastern Mediterranean (EM) settings. The models suggest that the hydrographic regimes of all studied sapropels can be considered as analogues to those observed in certain modern marine restricted settings. The results obtained support the idea that climate and the degree of surface-water freshening are the primary factors that influence deep-water dynamics in marine restricted settings, that in turn control the frequency and intensity of bottom-water deoxygenation and the stability and depth of the chemocline. The deepest EM sites are the most vulnerable locations to develop bottom-water restriction and deoxygenation. Local hydrogeographic factors play an essential role in the extent and frequency of bottom-water deoxygenation. Particulate shuttling was very intense during sapropel deposition and water-mass exchange between EM and Western Mediterranean controlled the intensity of the basin reservoir effect and Mo budget in EM.

II.1. Introduction

An oxygen loss between 1 and 7% in oxygen is expected by 2100 in most marine areas around the globe (Breitburg et al., 2018). Deoxygenation is considered one of the most impacting ocean stressors in present marine systems, since a decrease in oxygen content alters productivity, biodiversity and biogeochemical cycles (Levin, 2018). Although deoxygenation can be linked to increased productivity, deep-water dynamics also play a major role in the intensity, duration and extent of deoxygenation (van Santvoort and de Lange, 1996; Warning and Brumsack, 2000; Gallego-Torres et al., 2007a; Algeo and Tribovillard, 2009; Gallego-Torres et al., 2012; Grimm et al., 2015; Levin, 2018; Algeo and Li, 2020; Lathika et al., 2021). Nonetheless, little is known about the interplay of climate conditions with large-scale deoxygenation and deep-water circulation, and about the influence of local hydrogeographic factors.

Palaeoceanographic reconstructions of past large-scale deoxygenations linked to climate variability are crucial to better understand the responses of modern marine systems vulnerable to experience oxygen loss due to the current climate change and anthropogenic pressure (Stocker et al., 2013; Levin, 2018; Dermawan et al., 2022). In this regard, sapropels, as layers with TOC (total organic carbon) content above 2%, represent rapid oxic-to-anoxic transitions induced by rapid climate variability (over time scales of hundreds of years or even decades) (Cita et al., 1977). Therefore, they can offer relevant insights about the role of climate change on large-scale deoxygenation and deep-water dynamics (Marino et al., 2007; Grimm et al., 2015; Benkovitz et al., 2020; Blanchet et al., 2020; Hennekam et al., 2020). Moreover, large-scale deoxygenations during sapropels deposition over the Pleistocene-Holocene occurred during a similar hydrogeographic configuration as today, thus allowing to make palaeooceanographic inferences from modern oceanographic observations (Rohling et al., 2015).

In the Eastern Mediterranean (EM), the deposition of sapropels is controlled by astronomical precession cycles (Kidd et al., 1978; Calvert, 1983; Emeis et al., 1996, 2000). Minimum astronomical precession periods caused periods of maximum insolation in the northern hemisphere, which produced an intensification and a northward migration of the African monsoons, resulting in greater discharge of fresh-water and nutrients into the EM (De Lange et al., 1989; Hilgen, 1991; Lourens et al., 1996; Hennekam et al., 2014; Weldeab et al., 2014; Rohling et al., 2015; Tachikawa et al., 2015). The increased marine productivity and weakened water-column circulation (reduced vertical mixing), resulting in oxygen depletion in the bottom-waters, promoted the deposition and preservation of organic-rich sapropels (Cita and Grignani, 1982; Rossignol-Strick, 1985; Rohling, 1994; Gallego-Torres et al., 2007a, 2007b, 2010; Marino et al., 2009; Rohling et al., 2015; Zwiep et al., 2018).

In this context, this work assesses the consequences of past climate variability on water-column dynamics and redox conditions in bottom-waters during sapropel deposition. This is achieved by applying different palaeoceanographic conceptual models based on empirical geochemical data (trace metal concentration and TOC%) obtained from well-studied modern marine systems (Algeo and Lyons, 2006; Algeo et al., 2007; Algeo and Maynard, 2008; McArthur et al., 2008; Algeo and Tribovillard, 2009; Tribovillard et al., 2012; Sweere et al., 2016; McArthur, 2019). These conceptual palaeoceanographic models have been applied to five recent sapropels (S1, S5, S6, S7 and S8) from three EM locations that represent different oceanographic regimes (Figs. II.1 and 2). The models provided key insights into (i) the consequences of past climate variability on water-column dynamics and physicochemical properties, (ii) the influence of local hydrogeographic features (i.e., water-depth, proximity to continental borderlands, local active currents) on bottom-water dynamics and redox conditions, (iii) the extent of deep-water restriction and intensity of deoxygenation in EM during rapid climate changes, and (vi) long-term perspectives about modern marine settings vulnerable to develop oxygen deficiency in the near future.

II.2. Oceanographic and palaeoceanographic setting

The Mediterranean Sea is a complex marine system with a strong thermohaline circulation that allows deep-water masses to renew and oxygenate (Pinardi and Masetti, 2000; Millot and Taupier-Letage, 2005; Pinardi et al., 2015; Rohling et al., 2015). In general, it represents an exceptional natural laboratory to study the impacts of past and current climate changes since: (i) it is one of the most vulnerable regions or hotspots to climate change on Earth, (ii) it is very responsive to external and climate forcing (e.g., orbital forcing, anthropogenic forcing), (iii) it amplifies and anticipates marine responses to global climate change (its turnover timescale is about one tenth of the global ocean's), and (iv) its sedimentary record has remarkably preserved marine responses to past climate changes (Calvert, 1983; Emeis et al., 1996, 2000; Giorgi, 2006; Lionello et al., 2006; Rohling et al., 2015; Turco et al., 2015; Schroeder et al., 2016). These features derive from its geographic and oceanographic setting; latitude (transitional zone), semi-enclosed (restricted) marginal sea, relatively small area (~2,500,000 km^2), deep water-depth (over 5000 m), hydrological balance (high evaporation rate), complex land-sea distribution and seafloor morphology.

Today, the main three mechanisms controlling Mediterranean Sea circulation are wind stress, thermohaline forcing and Atlantic water-exchange (POEM Group, 1992; Millot and Taupier-Letage, 2005; Amitai et al., 2018). Atlantic Water (AW) enters the Mediterranean Sea through the Strait of Gibraltar and mixes with upwelled and saltier Mediterranean Intermediate Water

(MIW), resulting in the formation of Modified Atlantic Water (MAW; upper 200 m to down to 600-1000 m water-depth) (Millot, 1999, 2009). Then MAW splits into a northward current and an eastward current. The eastward current passes through the Strait of Sicily (EM gateway; water-depth ~ 350 m) and reaches the EM (Fig. II.2; Millot, 1999, 2009; Millot and Taupier-Letage, 2005). During winter-cooling, strong northern winds with dry and cold air masses evaporate Levantine Basin surface-water, increasing its salinity (i.e., density) and stimulating vertical convection, resulting in the formation of the Levantine Intermediate Water (LIW; between ~150 and ~ 600 m water-depth) (Lascaratos et al., 1999; Millot, 1999, 2009; Millot and Taupier-Letage, 2005; Pinardi et al., 2015; Rohling et al., 2015 and references therein).

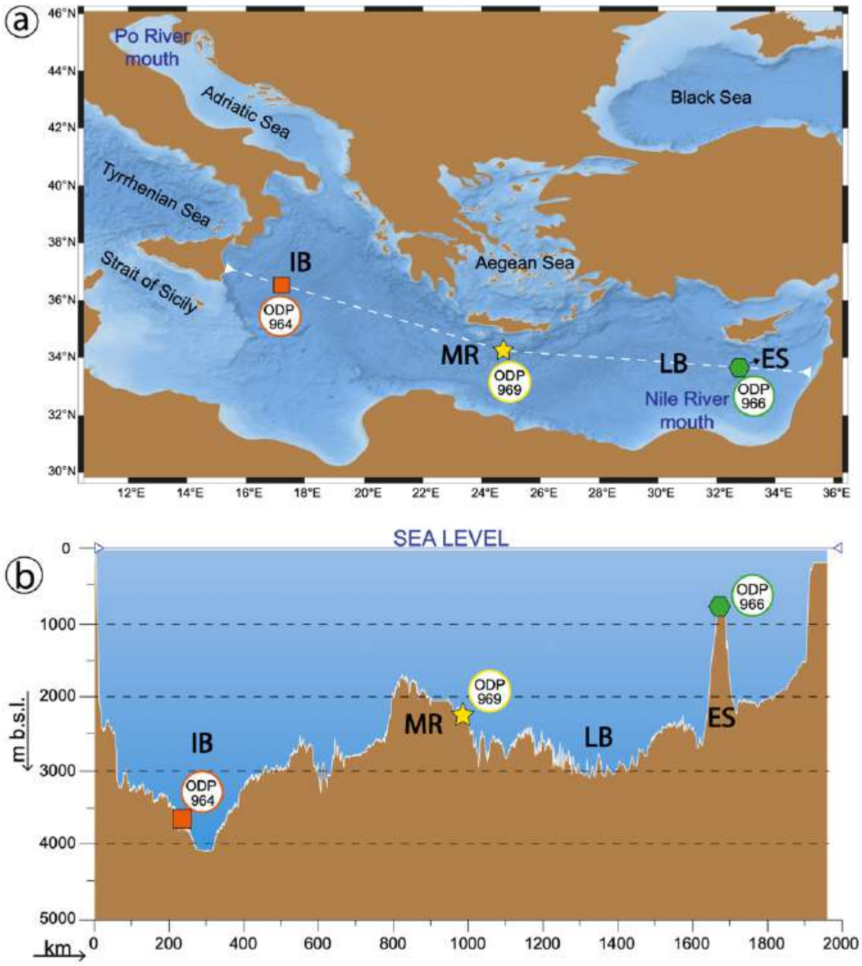
ⓐ
46°N
44°N
42°N
40°N
38°N
36°N
34°N
32°N
30°N
Po River mouth
Adriatic Sea
Black Sea
Tyrrhenian Sea
Strait of Sicily
IB
ODP 964
Aegean Sea
MR
ODP 969
LB
ES
Nile River mouth
ODP 966
12°E
14°E
16°E
18°E
20°E
22°E
24°E
26°E
28°E
30°E
32°E
34°E
36°E
ⓑ
SEA LEVEL
0
1000
2000
3000
4000
5000
m b.s.l.
IB
ODP 964
MR
ODP 969
LB
ES
ODP 966
km
0
200
400
600
800
1000
1200
1400
1600
1800
2000

Figure II.1. *(a) Satellite image showing the location of the three studied ODP sites (964, 966 and 969); (b) bathymetric section showing the depth of the three ODP sites; available under the European Marine Observation Data Network (EMODnet) Seabed Habitats initiative (http://www.emodnet-seabedhabitats.eu/). ES: Eratosthenes Seamount, IB: Ionian Basin, LB: Levantine Basin, MR: Mediterranean Ridge.*

LIW contributes to the formation of the Easter Mediterranean Deep Water (EMDW). However, EMDW is mainly formed in the Adriatic Sea region and to a lesser extent, in the Aegean Sea region (Fig. II.2; Wüst, 1961; Miller, 1963; Lascaratos et al., 1999; Millot and Taupier-Letage, 2005). In winter, Adriatic shelf water becomes cooler and its salinity increases under the action of cold and dry north-easterly winds (Ozsoy, 1981; Astraldi and Gasparini, 1992; Sparnocchia et al., 1994). Shelf waters sink towards the deep south of the Adriatic Basin, where it mixes with LIW and leads to the formation of the Adriatic Deep Water (ADW). ADW reaches the abyssal Ionian Basin, where it becomes the major contributor for EMDW circulation (Fig. II.2; POEM Group, 1992; Amitai et al., 2018).

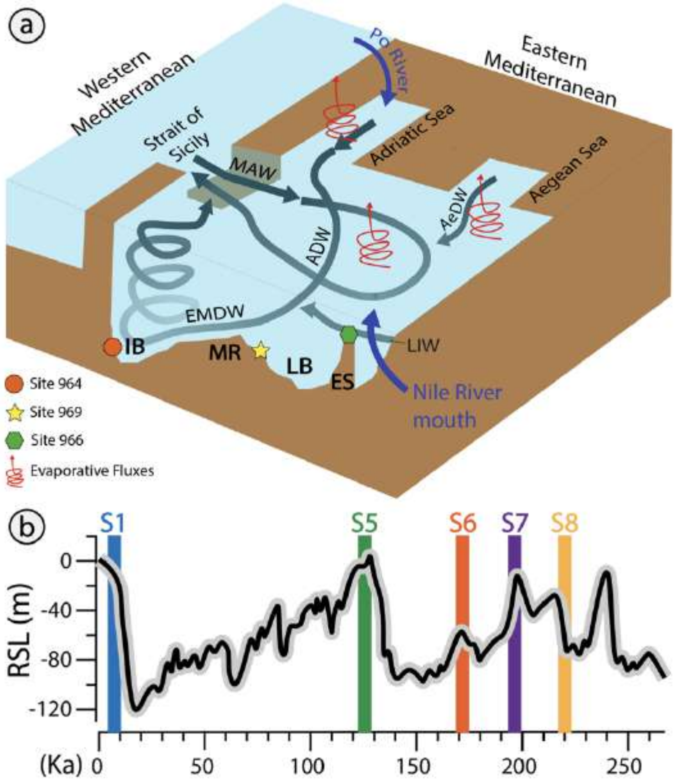

Figure II.2. *(a) 3D scheme (not to scale) of the modern EM circulation modified from Lascaratos et al. (1999), showing the main EM water-masses, currents and deep-water formation sites, and the main fresh-water inputs (fluvial inputs). IB: Ionian Basin (site 964), MR: Mediterranean Ridge (site 969), ES: Eratosthenes Seamount (site 966), LB: Levantine Basin. Water-masses: ADW (Adriatic Deep Water), AeDW (Aegean Deep Water), EMDW (Eastern Mediterranean Deep Water), LIW (Levantine Intermediate Water), and MAW (Modified Atlantic Water). (b) Approximate relative sea-level (RSL) for the last 250 ka from Grant et al. (2014). Time interval of each sapropel is indicated (Ziegler et al., 2010; Grant et al., 2016).*

In recent decades, temperature, salinity and density of Mediterranean deep-water masses have increased, while deep-water convection and oxygen content have significantly decreased (Roether et al., 1996; Sparnocchia et al., 2006). In fact, from 1950 to 2010, the Mediterranean below 1000 m underwent the strongest salinity gain anywhere in the world and have suffered important oceanographic changes that weakened deep-water circulation (e.g., *Western Mediterranean Transition* and *Eastern Mediterranean Transient*) (Lascaratos et al., 1999; Malanotte-Rizzoli et al., 1999; Skliris et al., 2014; Schroeder et al., 2016). These oceanographic changes have been partially attributed to anthropogenic disturbances, such as the damming of the Nile in 1964, which has increased by ~30% the formation rate of LIW, which explains ~45% of the salinity increase in Western Mediterranean Deep Water and contributed to triggered *Eastern Mediterranean Transient* (Skliris and Lascaratos, 2004).

In general, the present EM thermohaline circulation and low primary productivity promote oxic and ultra-oligotrophic conditions in the water-column, low TOC content in sediments (from 0.1 to 0.2%) and a conservative behavior of Mo and U as in global ocean ([U] ~3.23 ng/g, ([Mo] ~10 ng/g) (Abbott, 1977; Morford and Emerson, 1999; Delanghe et al., 2002; Rohling et al., 2015). However, during sapropel deposition weakened anti-estuarine circulation and increased fresh-water discharge, reduced vertical-mixing and decreased surface-water salinity (Rohling et al., 2015; Zirks et al., 2019). The main fresh-water inputs came from the Nile River and palaeo African drainages (Gallego-Torres et al., 2007a; Rohling et al., 2015; Tachikawa et al., 2015; Wu et al., 2016, 2018), although during some cold sapropel events (e.g., S6), fresh-water inputs from northern margins of the EM were also important (Gallego-Torres et al., 2007a). Large fresh-water inputs increased surface-water buoyancy and created a strong halocline, which decreased or even stop vertical mixing and deep-water formation in the Adriatic and Aegean Sea. This led to deep-water restriction and caused an upward migration of the redox chemocline from the sediment-water interface (SWI) to the water-column, which caused deoxygenation in deep-waters and in intermediate-waters due to an expansion of the Oxygen Minimum Zones (Zirks et al., 2019).

During sapropel events S1, S5 and S7, sea-level was comparable to the present sea-level, fluctuating just a few meters (<20 m below or above the present sea-level), but during cold sapropel events S6 and S8, large ice volumes trapped in the poles and continental glaciers led to a lower sea-level, >60 m below the actual level (Fig. II.2) (Grant et al., 2014; Rohling et al., 2014; Sainz de Murieta et al., 2021).

II.3. Geochemical palaeoceanographic frameworks

The reconstruction of chemical and physical conditions in the water-column during ancient deoxygenation events is not always straightforward from a direct interpretation of geochemical data. In this regard, empirical conceptual models based on geochemical patterns allow to use modern marine restricted settings as analogues hydrogeographic scenarios to the different sapropel events in EM. This can help to establish a wide spectrum of palaeoenvironmental and palaeohydrographic information, such as, robust differentiation between restricted and unrestricted settings, redox conditions in the water-column, stability of the chemocline, and degree of bottom-water restriction (Algeo and Lyons, 2006; Algeo et al., 2007; Algeo and Maynard, 2008; McArthur et al., 2008; Algeo and Tribovillard, 2009; Algeo et al., 2011; Tribovillard et al., 2012; Little et al., 2015; Sweere et al., 2016; McArthur, 2019).

Applied theorical palaeoceanographic models rely on the covariation patterns of trace metals and organic carbon empirically obtained from well-studied modern marine systems. The models applied are: (i) the Co_{EF} x Mn_{EF} vs. %Al plot model from Sweere et al. (2016) and modified by McArthur (2019), (ii) the Mo-U covariation plot model from Algeo and Tribovillard (2009), (iii) the Mo-TOC covariation plot model from Algeo and Lyons (2006), and (iv) the $[Mo]_{aq}$ - renewal time model from Algeo et al. (2007).

(i) The Co_{EF} x Mn_{EF} - Al% plot model from Sweere et al. (2016) and modified by McArthur (2019) allows to discriminate between restricted and unrestricted marine settings. The established Co_{EF} x Mn_{EF} threshold between restricted and unrestricted marine settings is 0.4, which was empirically determined by McArthur (2019). The limitation of this model is that it can only discriminate between extreme hydrographic scenarios, strong restriction or enhanced upwelling.

(ii) The Mo-U covariation plot model from Algeo and Tribovillard (2009) is a powerful tool to evaluate benthic redox conditions, stability of the chemocline, and the intensity of particulate shuttling and its influence on trace metals burial fluxes. The intensity of particulate shuttling in marine basins is obtained by the fact that the transfer of molybdenum (Mo) from the water-column to the sediments is boosted by particulate shuttling, unlike uranium (U), which is not influenced by this process (Tribovillard et al., 2006, 2012). The preferential transfer to the sediments of Mo over U due to particulate shuttling, allows Mo-U covariation plot patterns to assess the intensity of particulate shuttling and its influence on Mo burial fluxes in ancient marine settings (Berrang and Grill, 1974; Helz et al., 1996; Morford et al., 2005; Algeo and Tribovillard, 2009; Algeo et al., 2011; Tribovillard et al., 2012; Scholz et al., 2017; Scholz, 2018; Chiu et al., 2022).

The assessment of redox conditions using the Mo-U plot model is not straightforward for restricted marine settings due to the “basin reservoir effect”. The basin reservoir effect implies restricted trace metal resupply during water stagnation, which in turn drawdowns trace metals concentrations in bottom-waters and limits Mo and U authigenic uptake by seafloor sediments. However, the Mo/U trends observed in modern restricted marine settings allow to infer palaeo redox conditions and other parameters, such as, stability of the chemocline and intensity of the basin reservoir effect (Jacobs et al., 1985; Crusius et al., 1996; Algeo and Tribovillard, 2009; Paul et al., 2023).

(iii) The Mo-TOC plot model from Algeo and Lyons (2006) is a particularly helpful tool for establishing a qualitative degree of water-mass restriction in ancient marine systems with oxygen-depleted conditions (Algeo and Rowe, 2012). This conceptual model is supported by the fact that during restricted and oxygen-depleted conditions, Mo is scavenged from seawater into the underlying sediments by authigenic uptake (Bertine and Turekian, 1973; Tribovillard et al., 2006). This triggers Mo depletion, mainly in bottom-waters, until a future deep-water renewal event resupplies Mo to the bottom-waters. Hence, if restriction is intermittent and frequent deep-water renewal occurs, Mo is efficiently resupplied to deep-waters, which is evidenced as high Mo-TOC regression slope values. However, if deep-water restriction is more stable, the renewal of deep-waters decreases and euxinia becomes more recurrent and perennial. This causes a reduction of Mo resupply to the water-column and a more intense basin reservoir effect, which translates into lower Mo-TOC regression slope values (Algeo and Lyons, 2006; McArthur, 2019).

(iv) The $[Mo]_{aq}$-renewal time model from Algeo et al. (2007), which derives from the Mo-TOC plot model from Algeo and Lyons (2006), is a useful model to qualitatively estimate deep-water renewal frequency in ancient marine system. In modern marine restricted settings, aqueous Mo concentration ($[Mo]_{aq}$) and renewal time of bottom-waters have a linear relationship. Therefore, these parameters can be estimated (qualitatively) in ancient settings using a Mo-TOC regression slope (m) obtained from varied modern marine restricted settings (Black Sea, Framvaren Fjord, Cariaco Basin and Saanich Inlet). Consequently, qualitative bottom-water Mo concentration and renewal frequency are obtained for each sapropel event, at the three EM locations (i.e., Ionian Basin, Mediterranean Ridge and Eratosthenes Seamount), by plotting each sapropel m on the abscissa axis of the model. This conceptual model classifies sapropels as black shales categories. It is worth emphasizing that only qualitative estimation of deep-water renewal frequency can be achieved with this model. Marine settings tend to have different redox thresholds and trace metals dynamics due to different hydrogeographic factors (e.g., basin size, seafloor morphology and water-depth) and sedimentation rates. These factors limit a straightforward correlation between ancient and modern settings for the quantitative determination of deep-water renewal times (y) and $[Mo]_{aq}$ during sapropel events based on Mo-TOC covariation patterns (Liu and Algeo, 2020).

II.4. Materials and methods

II.4.1. Core description, sampling and chronology

Three ODP Leg 160 sites (964, 966 and 969) were selected in a transect across the EM in order to represent different oceanographic regimes and water-depths. Background sediments of the studied core sediments are principally composed by nannofossil clay, clayey nanno-fossil ooze and nannofossil ooze, varying in colour from brownish to more greenish and grayish (Emeis et al., 1996). Site 964 (36° 15.623′N, 17° 45.000′E) is located at the Ionian Basin and represents the deepest marine setting with a water-depth of 3658 m (Figs. II.1 and 2). This location is principally influenced by ADW and Western Mediterranean (WM) water masses. Site 966 (33° 47.765′N, 32° 42.090′E) is situated near the northern margin of the plateau area of the Eratosthenes Seamount, which represents a shallow pelagic setting with a water-depth of 940 m. This site offers the opportunity to evaluate the redox evolution and bottom-water restriction at a shallower water-depth. Site 969 (33° 50.399′N, 24° 53.065′E) has a water-depth of 2200 m. It is situated on the Mediterranean Ridge, and represents the centermost location of the EM, mainly influenced by the EMDW and the LIW (Emeis et al., 1996; Rohling et al., 2015) (Figs. II.1 and 2).

The five selected sapropels represent different environmental conditions and African monsoon intensities, and were deposited from the Middle Pleistocene to the Holocene. Their onset and termination ages have been previously established: S1: 10.5–6.1 ka (MIS 1), S5: 128.5–121.3 ka (MIS 5e), S6: 178.5–165.5 ka (MIS 6d), S7: 198.5–191.9 ka (MIS 7a), and S8: 224.1–209.5 ka (MIS 7c-7d) (Ziegler et al., 2010; Grant et al., 2016). Sapropels S3 (85.8–80.8 ka) and S4 (107.8–101.8 ka) exist in EM sedimentary record but were not the focus of this study (Fig. II.2b) (Grant et al., 2016). Sapropels intervals were sampled at 2 cm resolution, including the sapropels and the underlying and overlying sediments, which offers information on non-sapropel deposition and allows to determine the changes that EM hydrographic regime suffered during sapropels onset and termination. Base and top of sapropels were identified using Ba/Al ratio profiles since original TOC content signal is susceptible to be altered during post-depositional oxidation (Fig. II.4) (Higgs et al., 1994; van Santvoort et al., 1996; Gallego-Torres et al., 2007a, 2007b, 2010; Rohling et al., 2015).

II.4.2. Geochemical analysis of sediments

II.4.2.1. Major and trace elements

Samples were dried and then powdered in an agata mortar. Due to sample size limitation, XRF analysis for major elements quantification was only performed in S1 samples (prepared as fused beads) from Site 964. XRF was carried out at Instituto Andaluz de Ciencias de la Tierra (IACT), with a S4 Pioneer from BRUKER, equipped with a 4 kW wave-length dispersive X-ray fluorescence spectrometer (WDXRF) and a Rh anode X-ray tube (60 kV, 150 mA). XRF precision was better than ±0.3% for major elements. In the rest of samples, major elements were measured with an ICP-OES Perkin-Elmer Optima 8300 (Dual View) with an autosampler Perkin-Elmer. Certified standards (BR-N, GH, DR-N, UB-N, AGV-N, MAG-1, GS-N, and GA) were measured for element quantification. Trace elements, in all samples, were measured using an ICP-MS NexION 300d (Perkin Elmer) spectrometer using Rh as internal standard. For major elements, ICP-OES precision was better than ±1% and for trace elements ICP-MS precision was better than ±5% for analyte concentrations of 10 ppm (Bea, 1996).

ICP-MS and ICP-OES analyses were carried out at the Scientific Instrumentation Center (CIC, University of Granada) and measured using the same solutions, which were prepared in batches of 25 to 30 samples, and analytical blanks were introduced in each sample batch. Solutions were prepared with 0.1 g of powdered sample in Teflon vessels, where successive acid digestions using HNO_3 (ultra-pure with a 69% concentration) and HF (48% concentration) were performed at 130 °C until evaporation. A final acid digestion with HNO_3 and water at 80 °C for 1 h was also performed. Subsequently, the digested samples were diluted with Milli-Q water in 100 ml volumetric flasks (Bea, 1996).

II.4.2.2. Organic matter content

TOC content was measured by the Rock-Eval pyrolysis method, at the Institute of Earth Sciences (ISTE) of the University of Lausanne (UNIL). The Rock-Eval pyrolysis method consisted of a programmed temperature heating (from 200 °C to 850 °C, in successive steps), in a pyrolysis oven with an inert atmosphere (N_2). TOC% is calculated from the obtained thermograms using the following equation; TOC% = Pyrolysed Carbon (wt%) + Residual Carbon (wt%). Samples were calibrated using the IFP160000 standard with an instrumental precision
n of <0.1 wt% for TOC (Lafargue et al., 1998; Behar et al., 2001; Ordoñez et al., 2019).

II.5. Results

Results of the main geochemical parameters used for the construction of the palaeoceanographic conceptual models (TOC (%), Mo (ppm), U_{EF}, Mo_{EF}, Co_{EF} and Mn_{EF}) are presented in Figs. II.3 and 4. Trace metals Enrichment Factors (EFs) were obtained by applying the following equation: $TM_{EF} = (TM/Al)_{sample}/(TM/Al)_{reference}$, with the post-Archean Australian shale (PAAS) values from Taylor and McLennan (1995) as reference values to enable comparability with other studies, even when local background TM/Al values may be preferred over bibliographic reference values (Paul et al., 2023). The largest Mo and U enrichments are recognized in the Mediterranean Ridge (Site 969), followed by the Ionian Basin (Site 964), and the lowest Mo and U enrichments lowest at Eratosthenes Seamount (Site 966). Sapropels S5, S6 S7 are the sapropels most enriched in Mo and U (Figs. II.3 and 4) and have similar Mo concentrations. Sapropels S5 and S7 are more enriched in U than sapropel S6, while S6 is more enriched in Mo. S1 and S8 register the lowest U and Mo concentrations among all the studied sapropels, where S1 has the lowest U and Mo concentrations, but the highest Mn concentrations, especially at the Mediterranean Ridge. Co has similar concentrations in the three locations and in the five sapropels (mean Co_{EF} from 2 to 4.8), though it is slightly higher at the Mediterranean Ridge (Figs. II.3 and 4).

Regarding the TOC content, it is higher in the Ionian Basin and Mediterranean Ridge than in the Eratosthenes Seamount. S1 and S8 exhibit the lowest TOC content (below 1.5 mean TOC%), followed by S6 (below 2.1 mean TOC%). S5 and S7 present the highest TOC content, reaching up to 5% in S5 at the Mediterranean Ridge (Figs. II.3 and II.4).

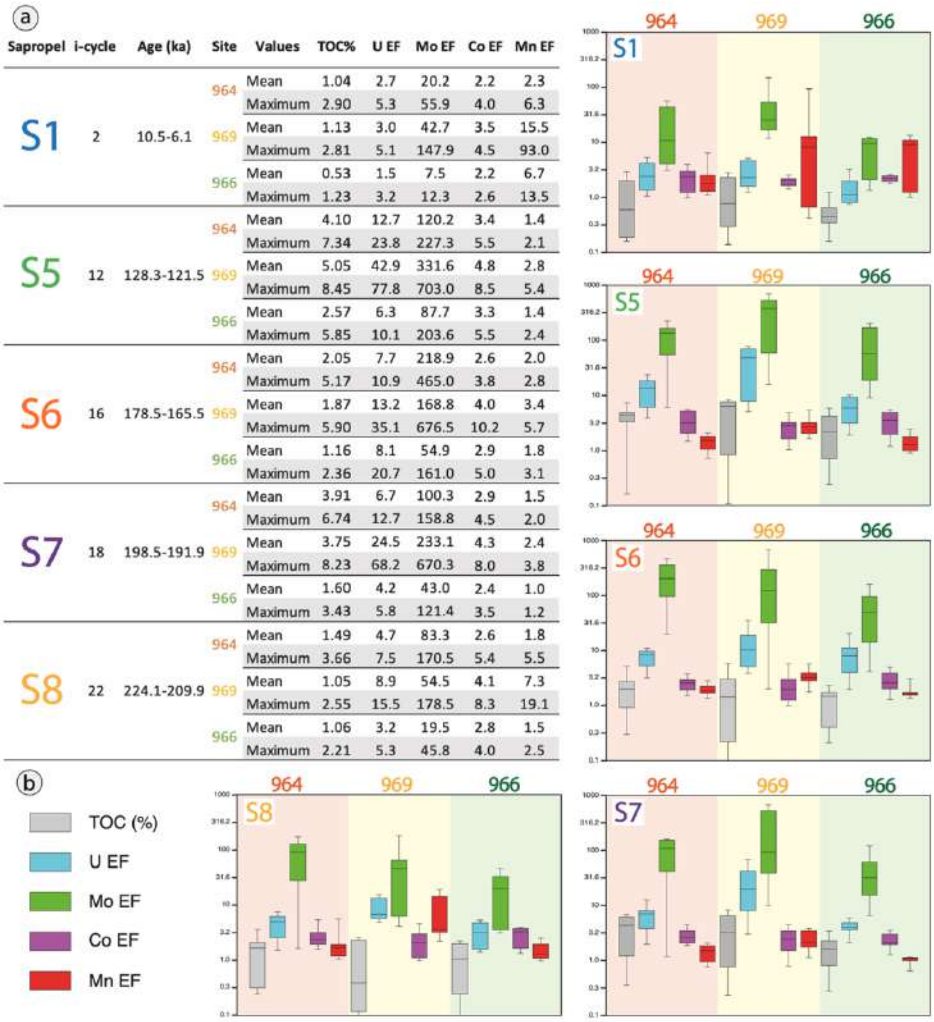

ⓐ

Sapropel	i-cycle	Age (ka)	Site	Values	TOC%	U EF	Mo EF	Co EF	Mn EF
S1	2	10.5-6.1	964	Mean	1.04	2.7	20.2	2.2	2.3
				Maximum	2.90	5.3	55.9	4.0	6.3
			969	Mean	1.13	3.0	42.7	3.5	15.5
				Maximum	2.81	5.1	147.9	4.5	93.0
			966	Mean	0.53	1.5	7.5	2.2	6.7
				Maximum	1.23	3.2	12.3	2.6	13.5
S5	12	128.3-121.5	964	Mean	4.10	12.7	120.2	3.4	1.4
				Maximum	7.34	23.8	227.3	5.5	2.1
			969	Mean	5.05	42.9	331.6	4.8	2.8
				Maximum	8.45	77.8	703.0	8.5	5.4
			966	Mean	2.57	6.3	87.7	3.3	1.4
				Maximum	5.85	10.1	203.6	5.5	2.4
S6	16	178.5-165.5	964	Mean	2.05	7.7	218.9	2.6	2.0
				Maximum	5.17	10.9	465.0	3.8	2.8
			969	Mean	1.87	13.2	168.8	4.0	3.4
				Maximum	5.90	35.1	676.5	10.2	5.7
			966	Mean	1.16	8.1	54.9	2.9	1.8
				Maximum	2.36	20.7	161.0	5.0	3.1
S7	18	198.5-191.9	964	Mean	3.91	6.7	100.3	2.9	1.5
				Maximum	6.74	12.7	158.8	4.5	2.0
			969	Mean	3.75	24.5	233.1	4.3	2.4
				Maximum	8.23	68.2	670.3	8.0	3.8
			966	Mean	1.60	4.2	43.0	2.4	1.0
				Maximum	3.43	5.8	121.4	3.5	1.2
S8	22	224.1-209.9	964	Mean	1.49	4.7	83.3	2.6	1.8
				Maximum	3.66	7.5	170.5	5.4	5.5
			969	Mean	1.05	8.9	54.5	4.1	7.3
				Maximum	2.55	15.5	178.5	8.3	19.1
			966	Mean	1.06	3.2	19.5	2.8	1.5
				Maximum	2.21	5.3	45.8	4.0	2.5

Figure II.3. *(a) Table showing mean and maximum values of TOC%, Mo concentration (ppm) and EFs of Mo, U, Co and Mn in each sapropel at the three EM locations. (b) Box-whisker plots showing a comparison between sites for the different sapropels. The box represents the inter-quartile range, the line in the box represents the median and the whiskers represent the 5th and 95th percentiles. Trace metal enrichments and TOC% are shown in log10 scale. Insolation cycles (i-cycles) and time intervals of each sapropel are also indicated. S1 and S5 ages from Grant et al. (2016) and S6, S7 and S8 ages from (Ziegler et al. (2010).*

Fig. II.4 shows the Mo, U and TOC enrichments in sapropels layers. Some Mo and U enrichment are associated to post-depositional processes and remobilization. (i) Downward oxidation caused Mo remobilization and subsequent Mo enrichments in the oxidation front in S1 at the Mediterranean Ridge and Eratosthenes Seamount (Fillippidi and De Lange, 2019), (ii) strong downward sulfidation caused Mo enrichments below S1 at the Mediterranean Ridge (Passier et al., 1996), and (iii) intense reoxygenation during reventilation caused downward migration of U enrichment in S1 at the Mediterranean Ridge and Eratosthenes Seamount (Zheng et al., 2002; Tribovillard et al., 2006) (Fig. II.4). Consequently, sapropels strongly affected by these post-depositional processes or with weak Mo and TOC enrichments due to weak oxygen depletion, generated unreliable Mo-TOC regression slopes. For these reasons, the degree of deep-water restriction using the Mo-TOC regression slopes will not be assessed for S1 at Eratosthenes Seamount and the Mediterranean Ridge, and for S8 and S6 at Eratosthenes Seamount.

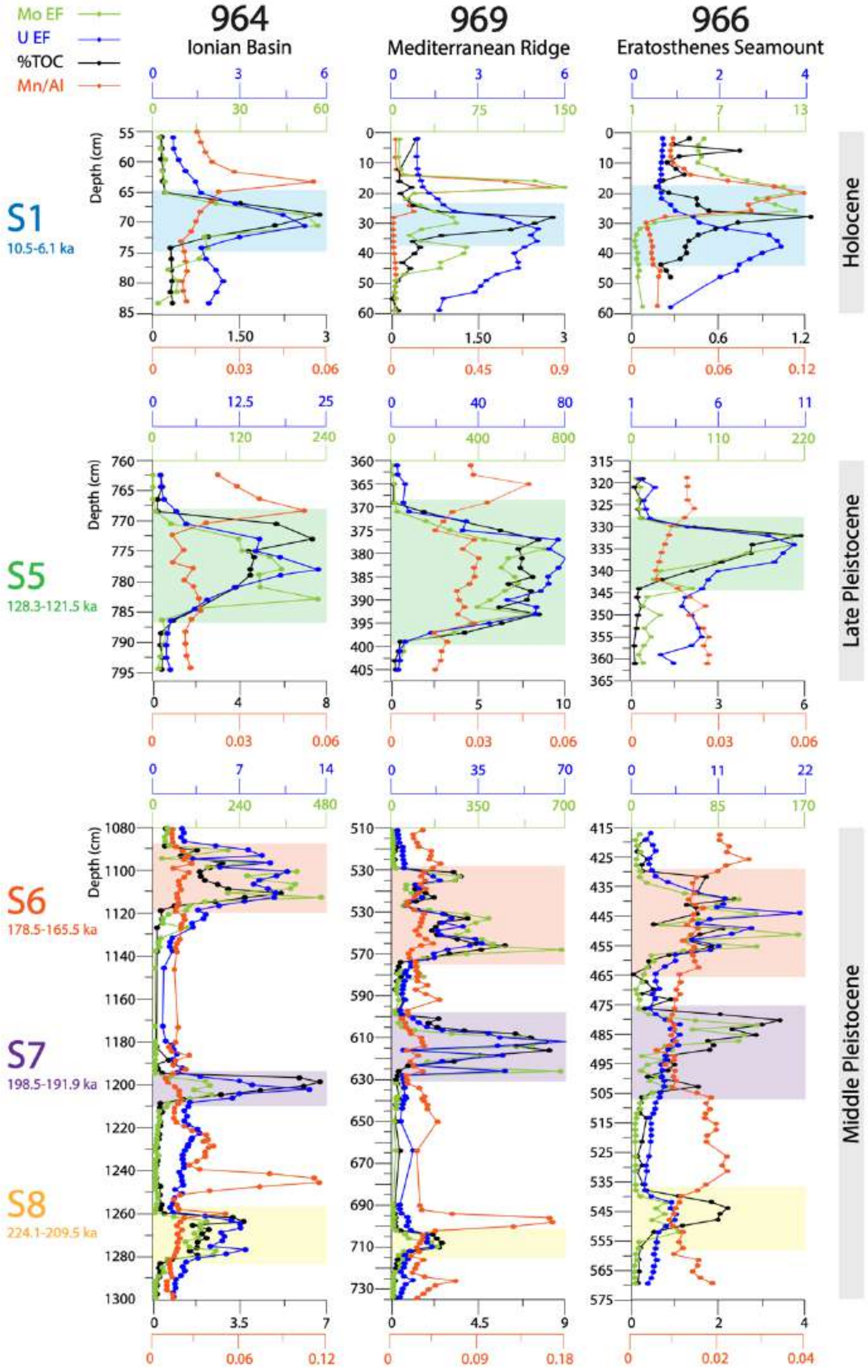

Figure II.4. Chemostratigraphic figure showing Mo$_{EF}$*, U*$_{EF}$*, TOC% and Mn/Al plotted in vertical dimension for sapropels S1, S5, S6, S7 and S8 from the Ionian Basin, Mediterranean Ridge and Eratosthenes Seamount. For sapropels time intervals references see Fig. II.3.*

II.6. Discussion

The Ionian Basin, Mediterranean Ridge and Eratosthenes Seamount represent very different hydrogeographic regimes. However, almost all sapropel values and non-sapropel values, at the three locations, fall in the "restricted" area of the Co_{EF} x Mn_{EF} - Al% plot model, even Eratosthenes Seamount, the shallowest location and the most susceptible to experience lateral advection (Fig. II.5c). Therefore, this model supports that EM sub-basins can be considered restricted marine settings since they have a similar behavior to the modern Baltic Sea or Black Sea in the Co_{EF} x Mn_{EF} - Al% plot model (McArthur, 2019). In these restricted settings, Co and Mn cannot escape the "closed" system due to reduced water-column circulation and enhanced trapping efficiency (Sweere et al., 2016; McArthur, 2019). Consequently, Co and Mn are permanently fixed in the sediments via redox cycling, where Co is typically fixed in pyrite (FeS) or as its own sulfide (CoS), while Mn is typically fixed as rhodochrosite ($MnCO_3$) or as Mn-oxyhydroxides depending on the redox conditions (Calvert and Pedersen, 1996, 2007; Tribovillard et al., 2006; Dellwig et al., 2010; Böttcher et al., 2012). Moreover, the data suggest that Co_{EF} x Mn_{EF} - Al% plot model responds better to regional than to local factors and does not discriminate sapropel from non-sapropel sediments since their values overlap (Fig. II.5).

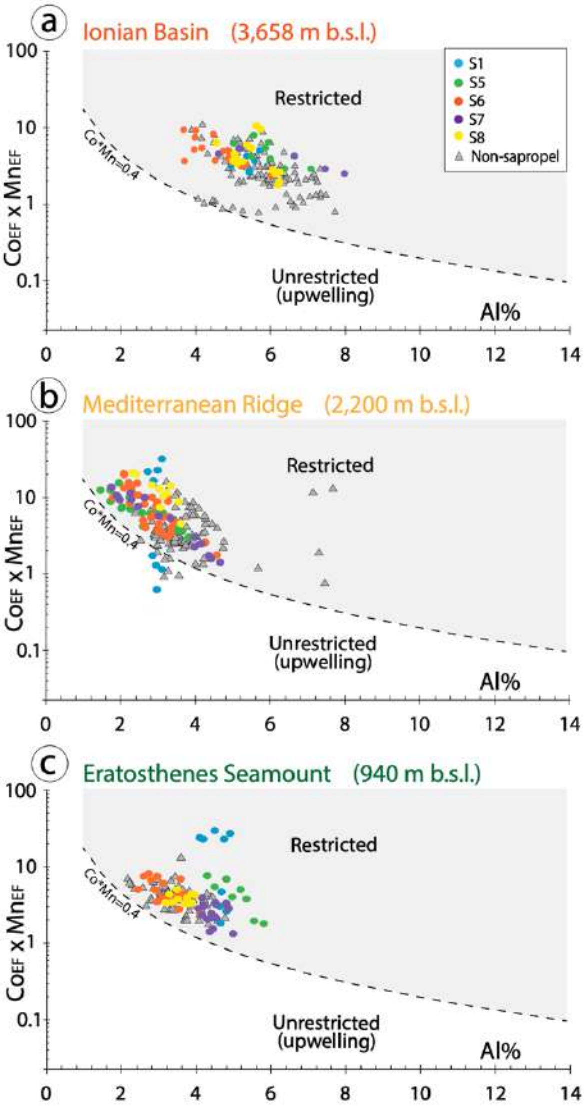

Figure II.5. *The Co_{EF} x Mn_{EF} vs. Al% conceptual model of Sweere et al. (2016) and modified by McArthur (2019) used to interpret depositional environments (restricted vs. unrestricted) at each location. Field divider (dashed line) is Co_{EF} x Mn_{EF} = 0.4. Sapropels and non-sapropel data are illustrated with different colors. (a) Ionian Basin (S1 n = 8, S5 n = 10, S6 n = 16, S7 n = 7, S8 n = 16, non-sapropel n = 108), (b) Mediterranean Ridge (S1 n = 9, S5 n = 20, S6 n = 34, S7 n = 15, S8 n = 11, non-sapropel n = 96), and (c) Eratosthenes Seamount (S1 n = 9, S5 n = 9, S6 n = 20, S7 n = 16, S8 n = 11, non-sapropel n = 65).*

II.6.1. Particulate shuttling and degree of oxygen depletion

In general terms, the Mo_{EF}-U_{EF} covariation patterns observed in EM during sapropel deposition indicate intense particulate shuttling, similar to the observed in the present Cariaco Basin. However, according to the Mo_{EF}-U_{EF} covariation patterns, each sapropel event presents specific hydrographic features. S5, at the Ionian Basin, and S5 and S7 at the Mediterranean Ridge, show deviating values from the rest of the sapropels ($U_{EF} > 20$ and $Mo_{EF} > 200$), which converge with the redox trend recorded in unrestricted marine settings (Fig. II.6). According to Tribovillard et al. (2012), in restricted marine settings this pattern is indicative of a restricted water-column with strong and stable euxinic conditions and intense particulate shuttling. The lower Mo/U ratios suggests progressive Mo drawdown due to poor Mo resupply to bottom-waters and the higher authigenic U concentrations in comparison to the rest of sapropels suggesting higher U fixation rate due to stronger and more stable anoxia/euxinia. Therefore, S5 and S7 deposition in EM occurred under strong and stable deep-water euxinia, as is also demonstrated by the covariation patterns of Fe, U and Mo isotopes in S5 and S7 (Andersen et al., 2018; Benkovitz et al., 2020; Sweere et al., 2021; Chiu et al., 2022).

Conversely, S1 and S8 have the lowest authigenic U and Mo concentrations, suggesting the weakest particulate shuttling activity and oxygen depletion at the three sites, where suboxic conditions in the water-column seem to have ruled during most of their deposition (Fig. II.6). Nevertheless, the Mo enrichment by itself in S1 and S8, demonstrate that during their deposition sulfidic conditions were reached, especially in EM deepest settings. This goes in agreement with recent studies that used Fe, U and Mo isotopes to support that sulfidic conditions were reached during S1 deposition (Azrieli-Tal et al., 2014; Matthews et al., 2017; Andersen et al., 2020; Sweere et al., 2021). Furthermore, S1 at the three locations and S8 at the Ionian Basin and Mediterranean Ridge, show abrupt "marker beds" evidenced by Mn peaks on the top of the sapropels (Fillippidi and De Lange, 2019), which in some cases are accompanied with Mo enrichments associated with Mn-oxyhydroxides (e.g., S1) (Figs. II.4 and 5). This demonstrates that strong and rapid bottom-water ventilation occurred in EM below 900 m after S1 and below 2000 m after S8.

S6 is the most influenced sapropel by particulate shuttling. Extremely high Mo concentrations ($Mo_{EF} > 200$) and low U concentrations ($U_{EF} > 25$) are indicative of marine systems with frequent fluctuations of the chemocline depth (from below the SWI to the water-column and vice versa) and high-frequency temporal redox variations (i.e., unstable bottom aoxia/euxinia), due to an unstable hydrographic regime with intense particulate shuttling and frequent deep-water renewal (Figs. II.8 and 9) (Algeo and Lyons, 2006; Algeo and Tribovillard, 2009; Scholz et al., 2017).

The fluctuating chemocline and the frequent deep-water renewal during S6 deposition vastly resupplied trace metals to bottom-waters and led to "Mo burial pumps" (Algeo and Tribovillard, 2009) (Figs. II.6 and 9).

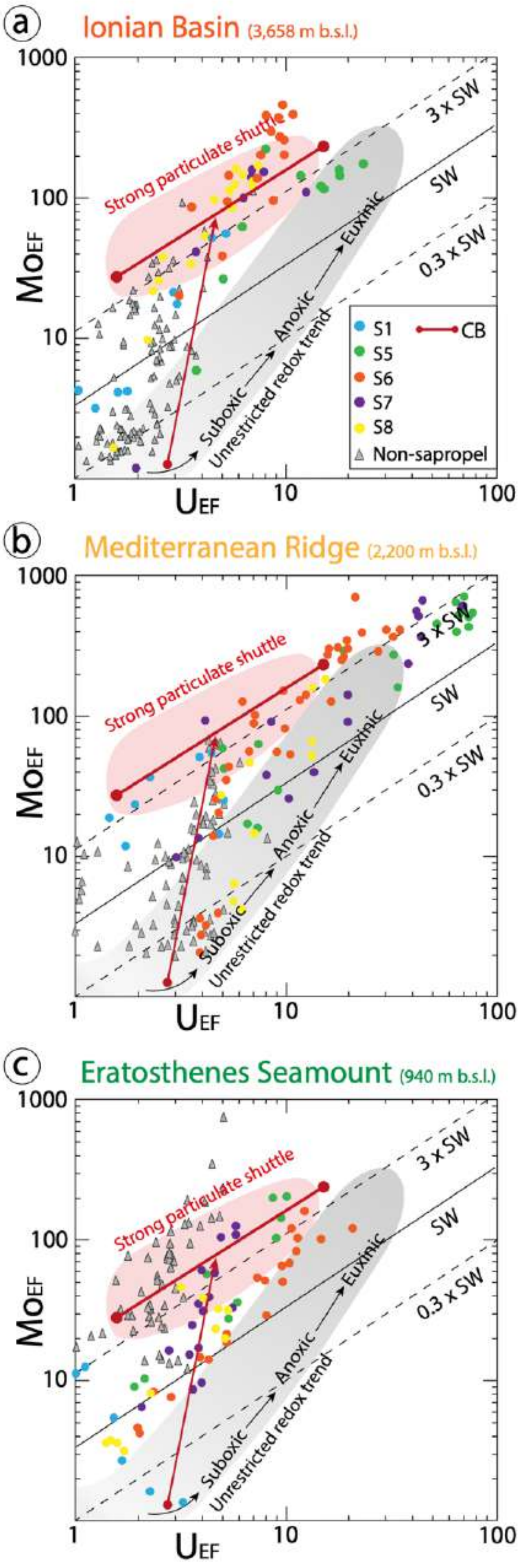

Figure II.6. *Mo_{EF}-U_{EF} conceptual model from Algeo and Tribovillard (2009). The plot model shows Mo_{EF}/U_{EF} covariation patterns of sapropels at the three locations. Sapropels and non-sapropel data is illustrated with different colors. Diagonal solid line represents seawater (SW) Mo/U molar ratio of ~7.5–7.9 and fractions thereof in dashed lines (3xSW and 0.3xSW). Red solid line: covariant Mo/U trend in modern Cariaco Basin (CB). Gray shaded area: redox trend of unrestricted marine (UM) settings. Red shaded area: intense particulate shuttling. Mo(ppm) - U(ppm) correlation coefficients at each location: (a) Ionian Basin (r = +0.69; p(α) < 0.01; n = 165), (b) Mediterranean Ridge (r = +0.85; p (α) < 0.01; n = 159), and (c) Eratosthenes Seamount (r = +0.58; p(α) < 0.01; n = 132).*

The principal source of Mo for authigenic uptake in EM is seawater (Nijenhuis et al., 1998), therefore, the high Mo concentrations and the palaeoceanographic models suggest that Mo was not depleted in EM water-masses during S6 deposition. This supports increased Mo resupply and high Mo concentrations in EM bottom-waters during S6, despite the lower sea-level and shallower basin sill between WM and EM, i.e., the Strait of Sicily, which had a depth of 250 m (Fig. II.9). This is probably associated to the fact that surface-water exchange between WM and EM was vigorous during S6 due to increased low-density Atlantic inflow into the Mediterranean, fueled by melted Atlantic ice sheets (Sierro and Andersen, 2022). Consequently, WM and EM water-mass exchange efficiently resupplied Mo and other trace metals to EM, where they were supplied to bottom-waters by intermittent deep-water formation during cold periods. Nevertheless, the low-density surface-waters that reached EM, probably weakened deep-water formation in the Adriatic Sea and Aegean Sea and promoted brief bottom-water stagnation and euxinia.

However, according to the applied theorical models, Mo was progressively depleted in EM water-masses during S5 and S7. This supports enhanced basin reservoir effect and weak surface-water exchange between EM and WM during S5 and S7 deposition, where Mo uptake rate by seafloor sediments was higher than the Mo input from WM, causing a progressive Mo drawdown in EM deep water-masses (Benkovitz et al., 2020; Sweere et al., 2021). During S1 and S8, Mo was not depleted in EM water-masses, probably because oxygen depletion was not strong enough to cause Mo burial rates to surpass Mo resupply in EM bottom-waters (Fig. II.6). In the case of S8, water-mass exchange between EM and WM was probably enhanced (i.e., higher Mo resupply) since it was deposited during a glacial period (i.e., colder temperatures), as occurred during S6 (Sierro and Andersen, 2022).

In respect to differences between locations, the Mediterranean Ridge and the Ionian Basin developed stronger oxygen depletion and more intense particulate shuttling (higher Mo and U concentrations) than Eratosthenes Seamount during sapropel deposition. However, the Mediterranean Ridge sediments have higher U concentrations than Ionian Basin sediments, indicating that the Mediterranean Ridge (at least below 2200 m) suffered stronger oxygen depletion than the Ionian Abyssal Plain. Weaker oxygen depletion at the Ionian Basin than at the Mediterranean Ridge, is probably due to its hydrogeographic location (i.e., local factors). The Ionian Abyssal Plain appears to be more responsive to the formation of EM deep-water masses (e.g., ADW Outflow and EMDW), which prevent it from experiencing stronger bottom-water deoxygenation despite being the location that develops earlier oxygen depletion. Eratosthenes seamount is the shallowest location (intermediate waters), hence, has a smaller overlying water-column for trace metals to be scavenged (i.e., smaller trace metals reservoir) and is more prone to experience bottom-water renewal (Zirks et al., 2019), therefore, it is the location with weaker particulate shuttling and oxygen depletion. However, particulate shuttling was still intense and similar to the modern Cariaco Basin (Fig. II.6c).

II.6.2. Degree of deep-water restriction

Mo-TOC regression slopes (*m*) obtained from modern marine settings with different degrees of deep-water restriction (i.e., Saanich Inlet, Cariaco Basin, Framvaren Fjord and Black), serve as an analogue hydrographic scenario to each sapropel event and allow to estimate a qualitative degree of deep-water restriction. There is congruence for the degree of deep-water restriction at regional scale for each sapropel event. However, local variability in particulate shuttling intensity and degree of bottom-water restriction during sapropel events caused differences in Mo burial fluxes between sites, and subsequent differences in the Mo-TOC regression slopes (Algeo and Lyons, 2006; Liu and Algeo, 2020). In this sense, the Mo-TOC regression slopes are more sensitive to local hydrographic factors than the Co_{EF} x Mn_{EF} vs. Al% plot model, which enables to mark out differences in the degree of deep-water restriction between sites during the deposition of each sapropel.

During each sapropel event, deep-water masses were restricted to different degrees. S1 slope at the Ionian Basin ($m \sim 11.3 \pm 1.3$) suggests a degree of deep-water restriction similar to the modern Framvaren Fjord. Hence, despite weak African monsoon intensity and low fresh-water input during S1 deposition (Rohling et al., 2015; Gallego-Torres et al., 2007a), S1 developed strong deep-water restriction and low-frequency temporal redox variations at the deepest EM settings (Figs. II.7a and 8). Conversely, S1 did not develop stable bottom-water restriction at shallower sites than the abyssal Ionian Basin (e.g., Mediterranean Ridge or Eratosthenes Seamount). Consequently, we can state that shallower sites than the Ionian Basin are less prone to develop stable deep-water restriction and subsequent bottom-water euxinia. This agrees with Fillippidi and De Lange (2019) who state that S1 deposition occurred under variable redox conditions at different water-depths. However, the results also suggest that once stable deep-water restriction is established at the Mediterranean Ridge, it develops stronger oxygen depletion (i.e., higher U enrichments) than the Ionian Basin, as occurred during S5, S6, S7 and S8 (Fig. II.9).

S5 and S7 show the lowest Mo-TOC slope values (Fig. II.7), therefore, represent sapropel events with the highest degree of water-mass restriction among the studied sapropels with similar hydrographic regime as that in the Framvaren Fjord ($m \sim 9\pm2$) or Black Sea ($m \sim 4.5\pm1$), as also previously suggested (Gallego-Torres et al., 2007a; Rohling et al., 2015; Andersen et al., 2018; Benkovitz et al., 2020; Sweere et al., 2021; Chiu et al., 2022). This means that during S5 and S7 deposition, deep-water restriction in EM was stronger and more perennial than during S1, S6 and

S8. This agrees with the Mo isotope results from Sweere et al. (2021), which indicate that among the studied sapropels in this study, S5 and S7 are the sapropel events with the strongest oxygen depletion (comparable to the modern Black Sea), followed by S6, S8 and S1, respectively. This is linked to the climatic conditions that ruled S5 and S7 events, which were characterized by exceptionally strong African monsoons that drastically increased fresh-water input and caused severe surface-water freshening and sluggish deep-water circulation (Nolet and Corliss, 1990; Casford et al., 2003; Capotondi et al., 2006; Gallego-Torres et al., 2007a; Marino et al., 2007; Osborne et al., 2010; Rohling et al., 2015; Benkovitz et al., 2020).

S5 and S7 seem to be the only sapropel events that developed perennial anoxia and stable bottom-water restriction and euxinia above 1000 m below sea-level (i.e., in intermediate-waters), since they are the only sapropels that reached relatively high Mo concentrations (between 50 and 100 ppm) at Eratosthenes Seamount. At this location, Mo-TOC slopes ($m \sim 17.9 \pm 2.6$; $m \sim 13 \pm 3.2$ respectively; Fig. II.7c) fall between the Cariaco Basin slope ($m \sim 25 \pm 5$) and the Framvaren Fjord slope, supporting moderate to strong bottom-water restriction and oxygen depletion in intermediate water-masses during their deposition.

At the Ionian Basin and Mediterranean Ridge, S6 and S8 have the highest slope values (Fig. II.7), therefore experienced the weakest deep-water restriction (i.e., the most frequent deep-water renewal) and had a similar degree of deep-water restriction as that in Saanich Inlet or Cariaco Basin, respectively. This could be linked to the fact that both sapropels were deposited under cold temperatures that promoted more frequent deep-water formation, which prevented stable euxinia in EM bottom-waters (Figs. II.9c). However, S6 Mo-TOC slope at Eratosthenes Seamount ($m \sim 13.6 \pm 3.2$) suggests the most restricted scenario among the three locations, being close to a Framvaren Fjord scenario (Fig. II.7). Nevertheless, Mo concentrations in sapropel S6 at this location are not high enough to make its respective Mo-TOC slope reliable to state this. Moreover, this statement would go in disagreement with the other two locations that indicate frequent deep-water renewal and with the lower water-depth, normally related to weaker bottom-water restriction.

II.6.3. Deep-water renewal frequency and $[Mo]_{aq}$

A qualitative deep-water renewal frequency is obtained for the sapropel layers at each location based on a comparison between Mo-TOC regression slopes (m) obtained from modern marine restricted settings. Empirical data suggest that high m values are characteristic of marine settings with weak deep-water restriction, frequent deep-water renewal, high Mo concentration in bottom-waters and high-frequency temporal redox variations (e.g., Saanich Inlet or Cariaco Basin), and the opposite for low *m* values (e.g., Black Sea or Framvaren Fjord). Therefore, modern marine restricted settings serve as analogues to determine more precise palaeohydrographic parameters, such as, qualitative deep-water renewal frequency and deep-water aqueous Mo concentration (Algeo et al., 2007; Little et al., 2015).

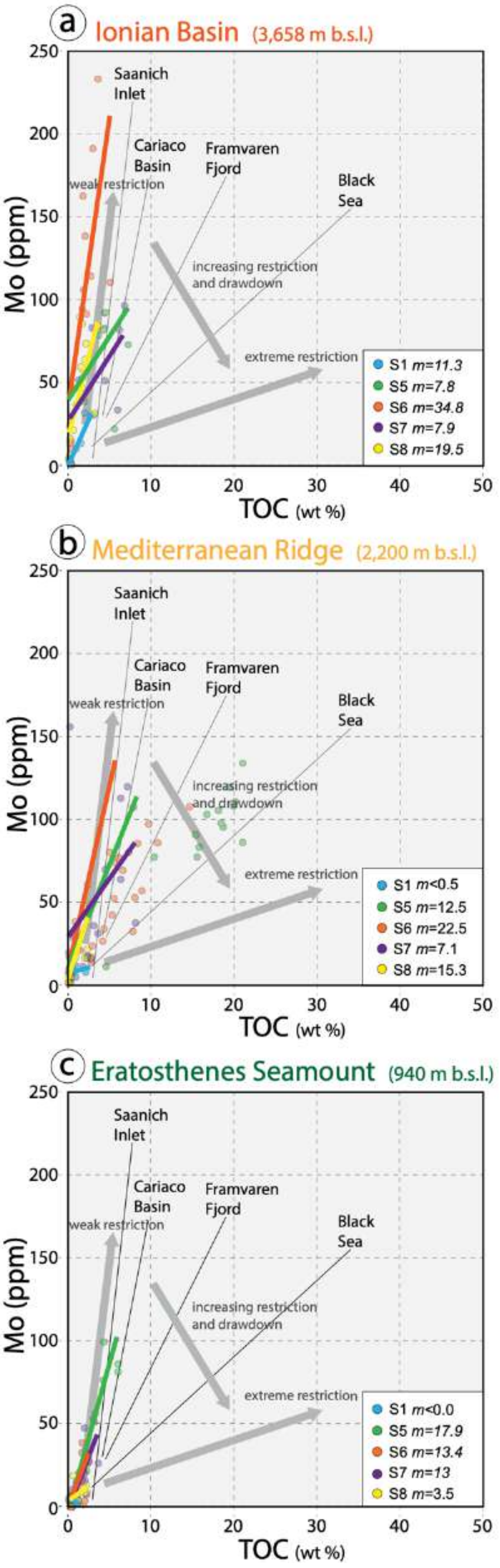

Figure II.7. *Mo-TOC conceptual model from Algeo and Lyons (2006) applied to studied sapropels at each location. Regression slopes from different modern anoxic silled-basins are shown on the conceptual model as modern analogues to the sapropels (Saanich Inlet, $m \sim 45 \pm 5$; Cariaco Basin, $m \sim 25 \pm 5$; Framvaren Fjord, $m \sim 9 \pm 2$ and Black Sea, $m \sim 4.5 \pm 1$). Gray arrows suggest degree of water-mass restriction. Slopes and slope values (m) of each sapropel are indicated in the figure. Mo(ppm) - TOC% correlation coefficients per location: (a) Ionian Basin ($r = +0.65$; $p(\alpha) < 0.01$; $n = 112$), (b) Mediterranean Ridge ($r = +0.80$; $p(\alpha) < 0.01$; $n = 121$), and (c) Eratosthenes Seamount ($r = +0.71$; $p(\alpha) < 0.01$; $n = 115$). Detailed Mo-TOC statistic parameters of each sapropel in Fig. II.8.*

S1 deep-water restriction signal was only recognized at the Ionian Basin, probably due to its greater water-depth that allowed rapid bottom-water restriction and deoxygenation (Azrieli-Tal et al., 2014). Therefore, stable euxinia during S1 occurred in the deepest EM settings with stable bottom-water restriction and under high export production areas (Casford et al., 2003). Consequently, the differences in EM settings exposed in the palaeoceanographic conceptual models suggest a limited extent of truly anoxic conditions in space, water-depth and time during S1 deposition due to local hydrogeographic features (Fig. II.9a) (Fillippidi and De Lange, 2019).

ⓐ

Sapropel	**Age (ka)**	**Location**	***n***	**Median** TOC%±1σ	**Median** Mo(ppm)±1σ	**Mo-TOC** ***m*±1σ** (x10-4)	***r2***	***r***	***p***
S1	10.5-6.1	Ionian Basin	8	1.1±0.6	6±13	11.3±1.3	0.93	0.96	<0.01
		Mediterranean Ridge	9	0.8±1.1	8±12	<0.5	-	-	-
		Eratosthenes Seamount	9	0.5±0.3	5±2	<0.0	-	-	-
S5	128.3-121-5	Ionian Basin	10	4.5±2.1	80±40	7.8±6.7	0.15	0.53	0.14
		Mediterranean Ridge	20	6.4±3.3	85±42	12.5±0.9	0.92	0.96	<0.01
		Eratosthenes Seamount	9	2.17±1.9	26±37	17.9±2.6	0.88	0.94	<0.01
S6	178.5-165.5	Ionian Basin	16	2.01±1.3	100±68	34.8±10.3	0.45	0.67	<0.01
		Mediterranean Ridge	34	1.7±1.6	33±42	22.2±2.5	0.7	0.83	<0.01
		Eratosthenes Seamount	20	1.4±0.7	17±13	<0.0	-	-	-
S7	198.5-191.9	Ionian Basin	7	4.3±2.5	52±33	7.9±4.7	0.36	0.6	0.16
		Mediterranean Ridge	15	3.2±2.9	36±48	7.1±4.2	0.18	0.43	<0.01
		Eratosthenes Seamount	16	1.6±0.1	14±17	<0.0	-	-	-
S8	224.1-209.5	Ionian Basin	16	1.7±1.1	50±30	19.5±5.3	0.49	0.7	<0.01
		Mediterranean Ridge	11	0.39±1.1	16±20	15.3±3.6	0.67	0.82	<0.01
		Eratosthenes Seamount	11	1.07±0.8	8±6	<0.0	-	-	-

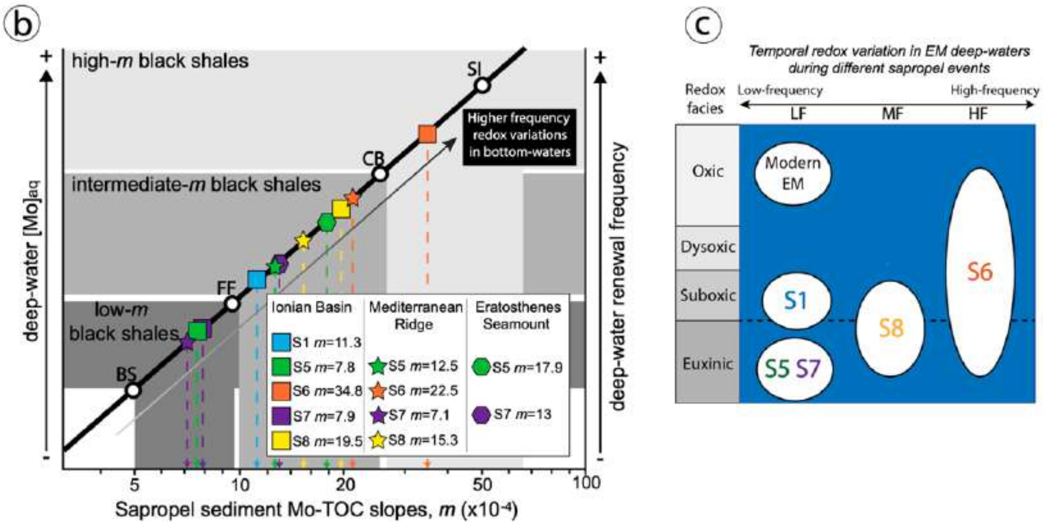

Figure II.8. *(a) Table showing Mo-TOC statistic parameters of each sapropel at the three locations. (b) [Mo]$_{aq}$-deep-water renewal time model from Algeo et al. (2007). This conceptual model allows qualitative deep-water renewal frequency and deep-water [Mo]aq during deposition of sapropels. Sapropels are categorized in "low-m black shales" (m < 10), "intermediate-m black shales" (10 < m < 25), and "high-m black shales" (m < 25). Most study sapropels fall in category of "intermediate-m black shales". (c) Modified conceptual redox classification scheme from Algeo and Li (2020) based on modern marine systems, where sapropel events are classified by the frequency of temporal redox variations, which can be low-frequency (LF), mid-frequency (MF), or high-frequency (HF). Modern analogues: BS: Black Sea, CB: Cariaco Basin, FF: Framvaren Fjord, and SI: Saanich Inlet. Sites water-depths: Ionian Basin: 3658 m, Mediterranean Ridge: 2200 m, and Eratosthenes Seamount: 940 m. Only sapropels with reliable Mo-TOC slopes were included in this model.*

For most sapropels, the Mo-TOC regression slopes range between 10 and 25, which correspond to intermediate-*m* black shales, however, some exceptions are observed. S7 and S5 at Mediterranean Ridge and S7 for the Ionian Basin are the only sapropels that fall in the low-*m* black shales category, indicating the highest deep-water renewal time among the studied sapropels and the lowest aqueous Mo concentrations in bottom-waters. This is in accordance with the high bottom-water renewal time for S5 (1030 + 820/− 520 years) obtained from U isotopes by Andersen et al. (2018). Therefore, S5 and S7 were deposited under a stable hydrographic regime with low-frequency redox variations in deep-water masses (Fig. II.9b). However, sporadic vertical mixing and associated resupply of trace-metals to bottom-waters could not have been totally absent since both sapropels reach high Mo concentrations in their sediments and only experience Mo depletion during its termination (Fig. II.8) (Sweere et al., 2021).

Another aspect that we suggest that should be to taken into consideration is that during stable deep-water stagnation in EM, brines derived from the dissolution of underlying evaporite deposits and mud diapirs can increase salinity in bottom-water masses (Emeis et al., 1996; van Santvoort and de Lange, 1996; Camerlenghi et al., 2019). Therefore, if deep-water masses are not frequently renovated, bottom-water salinity increases, especially in deep abyssal plains where brines tend to accumulate (van Santvoort and de Lange, 1996). Thus, we suggest that during periods of strong and stable water-column stratification, as occurred during S5 and S7 events, upward salinity fluxes from the sediments increased deep-water salinity increase. This in turn created a stronger halocline and pycnocline that inhibited vertical mixing and reinforced stagnation and trace metals depletion in bottom-waters. In contrast, during sapropel events characterized by more frequent deep-water renewal (e.g., S1, S6 and S8), such salinity fluxes did not drastically increase bottom-water salinity since bottom-water masses were reventilated and renewed by vertical mixing during episodes of thermohaline circulation reactivation, preventing trace-metals to suffer strong depletion in bottom-waters (Figs. II.9b).

S6 presents the highest *m* values and is the only sapropel that falls into the high-*m* black shales category, suggesting a hydrographic regime with more frequent deep-water renewal and higher concentrations of aqueous Mo in bottom-waters among the studied sapropels (Fig. II.8). This may relate to it being deposited during the end of a glacial climatic episode, as S8. Hence, they were deposited under colder temperatures than the average sapropel and lower sea-level that may have promoted upwelling currents and vertical convection, and subsequently, more frequent thermohaline reactivation and deep-water ventilation (Figs. II.9c) (Gallego-Torres et al., 2007a; (Melki et al., 2010; Grant et al., 2014).

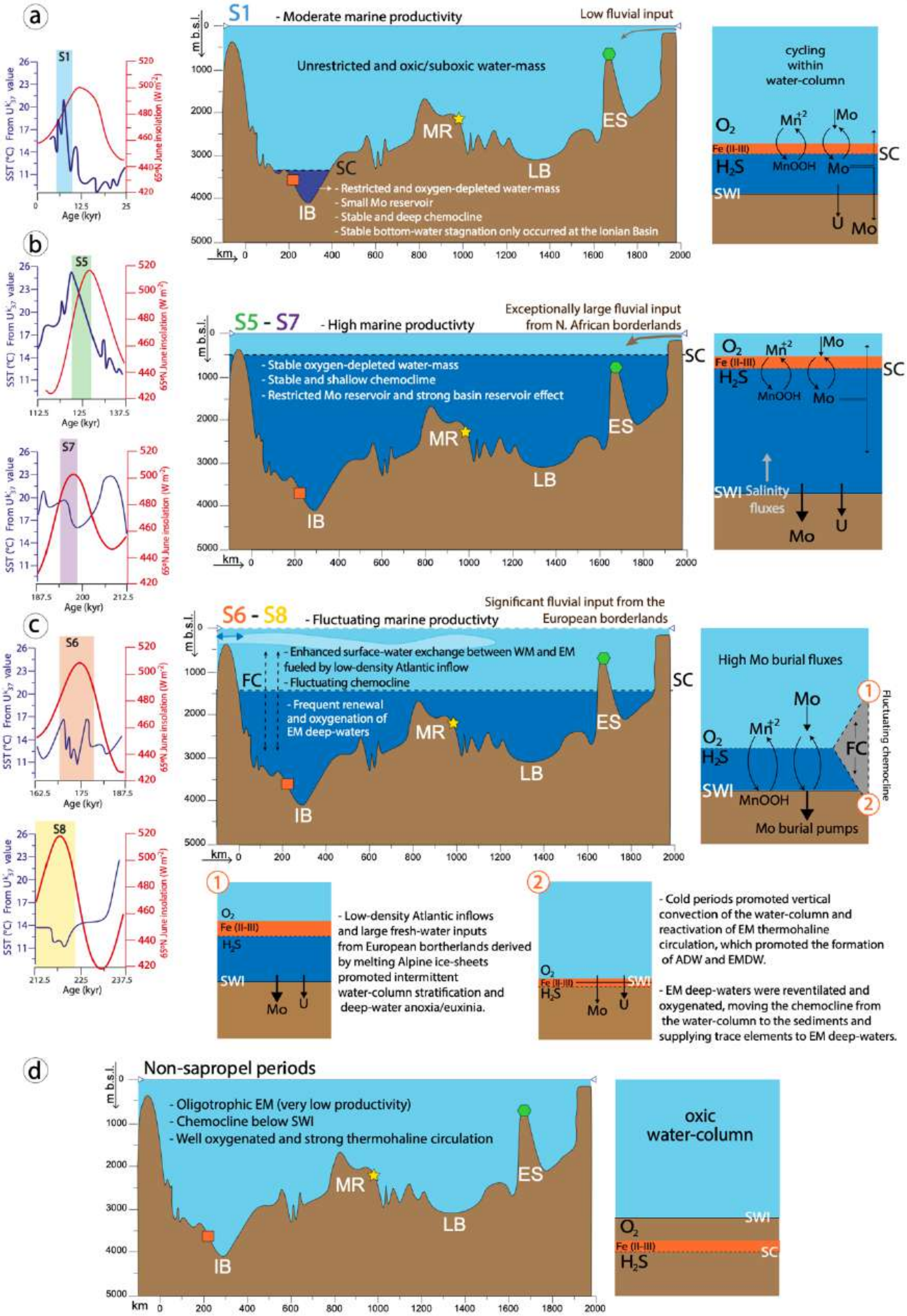
a
S1
SST (°C) From $U^{k'}_{37}$ value
65°N June insolation (W m^{-2})
Age (kyr)
S1 - Moderate marine productivity
Low fluvial input
Unrestricted and oxic/suboxic water-mass
MR
ES
LB
IB
SC
- Restricted and oxygen-depleted water-mass
- Small Mo reservoir
- Stable and deep chemocline
- Stable bottom-water stagnation only occurred at the Ionian Basin
cycling within water-column
O_2
Mn^{+2}
Mo
Fe (II-III)
H_2S
MnOOH
SWI
U
b
S5
S7
S5 - S7 - High marine productivty
Exceptionally large fluvial input from N. African borderlands
- Stable oxygen-depleted water-mass
- Stable and shallow chemocline
- Restricted Mo reservoir and strong basin reservoir effect
Salinity fluxes
c
S6
S8
S6 - S8 - Fluctuating marine productivty
Significant fluvial input from the European borderlands
- Enhanced surface-water exchange between WM and EM fueled by low-density Atlantic inflow
- Fluctuating chemocline
FC
- Frequent renewal and oxygenation of EM deep-waters
High Mo burial fluxes
Fluctuating chemocline
Mo burial pumps
1
2
- Low-density Atlantic inflows and large fresh-water inputs from European bortherlands derived by melting Alpine ice-sheets promoted intermittent water-column stratification and deep-water anoxia/euxinia.
- Cold periods promoted vertical convection of the water-column and reactivation of EM thermohaline circulation, which promoted the formation of ADW and EMDW.
- EM deep-waters were reventilated and oxygenated, moving the chemocline from the water-column to the sediments and supplying trace elements to EM deep-waters.
d
Non-sapropel periods
- Oligotrophic EM (very low productivity)
- Chemocline below SWI
- Well oxygenated and strong thermohaline circulation
oxic water-column
m b.s.l.
km
0
200
400
600
800
1000
1200
1400
1600
1800
2000
3000
4000
5000

Figure II.9. Synthetic and schematic depositional model during the deposition of S1 (a), S5 and S7 (b), S6 and S8 (c), and non-sapropel periods (d) across the EM transect at the three studied locations (Ionian Basin = IB, Mediterranean Ridge = MR and Eratosthenes Seamount = ES in the Levantine Basin = LB). The schemes show the hydrographic and geochemical processes that ruled during each the deposition of each sapropel. The schemes are based on hydrographic schemes from Algeo and Tribovillard (2009) and data obtained from the palaeoceanographic geochemical conceptual models applied in this study.

Qualitative productivity rate and relative fluvial inputs from Gallego-Torres et al. (2007a, 2010,). Temperature curve obtained by Emeis et al. (2003) from U37 (dark blue) at the Mediterranean Ridge and summer insolation curve (red) at 65°N obtained by Laskar et al. (1993) are shown for each sapropel. FC: fluctuating chemocline, SC: stable chemocline, SST: sea surface-temperature, SWI: sediment-water interface. Water-masses: light blue represents oxic conditions and unrestricted water-mass; orange represents anoxic (non-sulfidic) conditions (zones of Fe(III), Mn(IV) and nitrate reduction) and dark blue represents sulfidic conditions (sulfate reduction) and restricted water-mass. Size of arrows reflect relative magnitudes of authigenic Mo and U fluxes to the sediment. For sapropels time intervals references see Fig. II.3.

However, low-density Atlantic inflow was enhanced during this period, allowing low-density surface-waters to reach EM basin (Sierro and Andersen, 2022). Moreover, during S6 event, fresh-water inputs from northern borderlands (Europe) derived from melted Alpine ice sheets sourced large volumes of fresh-water into Adriatic Sea, which is the location where most EMDW is formed (Ozsoy, 1981; POEM Group, 1992; Lascaratos et al., 1999; Gallego-Torres et al., 2007a). Therefore, the interplay between the aforementioned factors during S6 event weakened EMDW formation, which caused intermittent deep-water restriction and associated intermittent anoxia/euxinia in deep EM settings (Fig. II.9c) (Sierro and Andersen, 2022).

EMDW intermittent circulation and enhanced water-mass exchange between EM and WM fluctuated the chemocline position from the water-column to below the SWI during the deposition of S6. This caused high-frequency temporal redox variations in EM deep settings and boosted Mo resupply to bottom-water, leading to higher aqueous Mo concentrations in bottom-waters that ultimately promoted the aforementioned "Mo burial pumps" (Fig. II.9c) (Algeo and Tribovillard, 2009). This explains why S6 shows the highest Mo concentrations, even though it is not the sapropel event associated to the strongest euxinia among the studied sapropels (Gallego-Torres et al., 2007a; Rohling et al., 2015; Sweere et al., 2021).

S8 represents a similar scenario to the modern Cariaco Basin, in terms of temporal redox variations and deep-water restriction and chemistry (Fig. II.9). The frequent deep-water renewal during S8 is associated to the fact that it was deposited during a glacial period, where cold temperatures and dry air masses stimulated more frequent deep-water formation, as occurred during S6. However, S8 has lower Mo and U concentrations (Fig. II.6), and higher Mn concentrations than S6, therefore S8 suffered weaker oxygen depletion, weaker surface-water freshening and lower primary productivity (Gallego-Torres et al., 2007a), and probably weaker influence of low-density Atlantic inflow on EM water-column stratification (Fig. II.9c).

II.7. Conclusions

The results obtained from the studied sapropels offer insights into the changes in deep-water circulation and redox conditions that EM experienced during different climate conditions. This offers palaeoperspectives to modern marine systems that are undergoing oxygen depletion due to the current global warming and anthropogenic pressure. Moreover, the exceptionally preserved oxic-to-anoxic transitions in EM contribute to better understand older regional-scale deoxygenation events (e.g., Paleozoic and Mesozoic Oceanic "Anoxic" Events).

1) It is shown that in restricted marine settings, climate and associated degree of surface-water freshening are the primary controls on deep-water dynamics, which in turn control the frequency and intensity of bottom-water deoxygenation, and the stability and depth of the chemocline. Warm and humid conditions (i.e., higher fresh-water inputs), as occurred during S5 and S7, promote more perennial restriction and stronger oxygen depletion in EM deep-waters than cooler and less humid conditions, as occurred during S6 and S8.

2) The deepest EM sites are the most vulnerable locations to develop deep-water restriction and deoxygenation. However, local hydrographic features (e.g., main active currents, proximity to continental borderlands, etc.) play an important role on the degree of deep-water restriction and deoxygenation. EM locations more influenced by ADW Outflow and EMDW currents develop weaker deep-water restriction and oxygen depletion than deep EM locations less influenced by these water-masses, which develop more stable deep-water restriction (i.e., less frequent deep-water renewal) and stronger deoxygenation.

3) Particulate shuttling was very intense in EM water-column during sapropel deposition, similar to the modern Cariaco Basin, which boosted burial fluxes of trace-metals influenced by this water-column process (e.g., Mo, Cu, Co, Ni, etc.).

4) Intensity in water-mass exchange between WM and EM plays a key role in EM deep-water oxygenation during sapropel deposition, controls Mo budget in EM water-masses (i.e., controls the intensity of the basin reservoir effect in EM) and is more intense during cold sapropel events.

Supplementary material

Supplementary data to this article can be found online at: https://ars.els-cdn.com/content/image/1-s2.0-S0031018223002195-mmc1.pdf

Acknowledgments

This study is part of R. Monedero PhD project, and has been supported by Grants PID2019-104624RB-I00, PID2019-104625RB-100, and TED2021-131697B-C22 funded by MCIN/AEI/ 10.13039/5011000110 33, Grants FEDER/Junta de Andalucía P18-RT-3804 and P18-RT- 4074, and by Research Groups RNM-179 and RNM-178 funded by Junta de Andalucía. We thank Prof. Adatte from Lausanne University (Switzerland) for Rock-eval analyses and TOC measurements. We are also grateful to the Center for Scientific Instrumentation (CIC, University of Granada) and the XRF Unit of the IACT (CSIC-UGR) for the ICP and XRF analyses, respectively. We are grateful to the Ocean Drilling Program for providing the analyzed samples as well as to the ODP Core Repository (Bremen, Germany) for assistance with sampling. We thank the Associate Editor, Dr. Mary Elliot, and the reviewer, Dr. Rick Hennekam, for their detailed and useful comments that significantly contributed to improve the manuscript.

Chapter III

Redox geochemical signatures in Mediterranean sapropels: Implications to constrain deoxygenation dynamics in deep-marine settings

Ricardo D. Monedero-Contreras, Francisca Martínez-Ruiz, Francisco J. Rodríguez-Tovar, Gert de Lange

Palaeogeography, Palaeoclimatology, Palaeoecology 634 (2024) 111953
doi: 10.1016/j.palaeo.2023.111953

Abstract

Global warming and anthropogenic activity are boosting marine deoxygenation in many regions around the globe. Deoxygenation is a critical ocean stressor with profound implications for marine ecosystems and biogeochemical cycles. Understanding the dynamics and evolution of past deoxygenation events can enhance our knowledge of present-day and future impacts of climate change and anthropogenic pressure on marine environments. Many studies have reconstructed the evolution redox conditions of past deoxygenation events using geochemical proxies. In this regard, the present work focuses on understanding the paleoenvironmental significance of geochemical redox signals derived from the onset, evolution and termination of regional-scale deoxygenations in deep-marine settings, with a specific focus on sapropels in the Eastern Mediterranean (EM). Sapropels, rhythmic organic-rich sediments deposited in EM, offer a unique opportunity to investigate recent deoxygenation events linked to past climate changes. Sapropels serve as paleoarchives of past deoxygenation events and can provide insights into the potential impacts of ongoing climate change on marine ecosystems and biogeochemical cycles. By integrating previous sapropel geochemical studies with a detailed analysis of new geochemical data from five Quaternary sapropels (S1, S5, S6, S7 and S8) in three different EM deep-marine settings, this study enhances our understanding of the paleoenvironmental significance of geochemical redox signals produced by deoxygenation dynamics and postdepositional processes in different deep-marine settings. The study supports that certain trace elements, such as Mo, V, U, Co, and Ni, are identified as more reliable redox proxies compared to Cr, Cu, Pb, and Zn. Four recurrent geochemical intervals attributed to specific redox conditions and postdepositional processes have been identified. Moreover, internal calibration of redox proxies thresholds has been performed and demonstrates how local environmental conditions (e.g., productivity rate) and hydrogeographic features (e.g., water-depth, particulate-shuttling intensity, deep-water renewal and fluvial input) play crucial roles in controlling the authigenic uptake rates of redox-sensitive trace metals, and subsequently, redox thresholds values of geochemical redox proxies. The results also emphasize the importance of postdepositional processes to accurately interpret geochemical signals in paleoenvironmental studies. This research enhances our overall understanding of geochemical signals associated with regional-scale deoxygenation events in deep-marine settings, offering new insights into predicting biogeochemical changes in marine environments undergoing a transition towards anoxia. By comprehending the dynamics of past and present deoxygenation, we acquire valuable knowledge regarding the potential effects of climate variability in marine ecosystems.

III.1. Introduction

Deoxygenation (reduction in oxygen levels) is an ocean stressor that alters biogeochemical cycles (e.g., C, N, P and trace metals) and with adverse effects on marine life (e.g., mass fish deaths). It is projected that deoxygenation will intensify in numerous marine regions worldwide by the year 2100, making it an escalating concern for human society (Keeling et al., 2010; Schmidtko et al., 2017; Breitburg et al., 2018). Marine deoxygenation may arise in different marine settings as a result of (i) reduced water-column mixing due to increased surface-water temperature and freshening (Levin, 2018; Monedero-Contreras et al., 2023a), and (ii) the expansion of Oxygen Minimum Zones resulting from increased nutrients inputs in coastal areas that enhance marine productivity (Zirks et al., 2021). Past deoxygenation events have drastically shaped marine environments throughout Earth's history. These deoxygenation events tend to be recorded in deep-marine settings as organic-rich sediments (e.g., black shales) enriched in redox-sensitive trace metals (RSTMs), as occurred during (i) the Toarcian Oceanic Anoxic Events (T-OAEs) (Jenkyns, 1985; Hetzel et al., 2009; Dickson et al., 2017; Fernández-Martínez et al., 2023), (ii) the Paleocene-Eocene Thermal Maximum (PETM) (Schulte et al., 2013) or (iii) the Eocene-Oligocene transition; EOT) (Dickson et al., 2021). Paleoceanographic reconstructions of these past deoxygenation events enhance our understanding of deoxygenation dynamics and marine responses. In this regard, the study of past episodes of marine deoxygenation offers valuable paleoperspectives to predict the potential impacts of deoxygenation on marine ecosystems and biogeochemical cycles derived from the current global warming and human-induced factors, such as nutrient pollution and habitat destruction (Hennekam et al., 2020; Mancini et al., 2023).

In general, black shales deposition occurred under very different Earth conditions and configuration than present. However, geologically "modern" analogs as the Eastern Mediterranean (EM) sapropels have recorded more recent regional-scale deoxygenation events (since the Miocene to the Holocene). These regional-scale deoxygenation events in EM can be considered as analogs for large-scale (i.e., global-scale) deoxygenation events (e.g., OAEs) since similar oceanographic processes are involved the Mediterranean and global ocean circulation (Giorgi and Lionello, 2008). In most cases, sapropel deoxygenation events are manifested in EM sedimentary record as rhythmic organic-rich sediment layers particularly enriched in trace metals (i.e., Mo, U, V, Cu, Co, Ba, etc.) (Cita et al., 1977; Kidd et al., 1978; Emeis et al., 1996, 2000; Warning and Brumsack, 2000; Gallego-Torres et al., 2007a; Rohling et al., 2015). The rhythmic deposition of sapropels in the EM is attributed to minimum astronomical precession cycles (orbital forcing) that promote cyclic periods of maximum insolation in the northern hemisphere. Consequently, African monsoons are intensified and forced to migrate northward, closer to the Mediterranean region (Lourens et al., 1996; Hennekam et al., 2014; Weldeab et al., 2014; Rohling et al., 2015). The intensified monsoons led to increased freshwater and nutrients inputs into the EM, which stimulated marine productivity. Simultaneously, these inputs slowed down or even stopped deep-water circulation. As a consequence, regional-scale deoxygenation occurred predominantly in bottom-waters, promoting the preservation of organic matter (OM) (Cita and Grignani, 1982; Rossignol-Strick, 1983, 1985; Casford et al., 2003; Gallego-Torres et al., 2007b, 2010; Marino et al., 2009; Rohling et al., 2015; Monedero-Contreras et al., 2023a).

Compared to older deoxygenation events, such as Paleozoic and Mesozoic Oceanic Anoxic Events (OAEs) recorded as black shales (Reershemius and Planavsky, 2021 and references therein), sapropels offer a better spatial and chronological control, and have been less affected by late diagenetic processes (Hennekam et al., 2020). Consequently, sapropels have been extensively used for paleoenvironmental and paleoclimatic reconstructions, providing paleoperspectives that enhance our understanding of deoxygenation dynamics and environmental responses during climate variability. Many of these studies have provided paleoredox reconstructions based on geochemical proxies. However, despite extensive research, and the existing literature on sapropels geochemical signatures, still open questions remain. Particularly regarding the interpretation of redox geochemical signals in organic-rich sediments that derived from the interplay of deoxygenation dynamics and associated postdepositional processes in deep-marine settings.

Compiling and synthetizing the existing knowledge coupled with new data presentation and interpretation can offer new insights to further understand the environmental/oceanographic significance of geochemical signals in modern and paleo marine settings. In this regard, the individual contributions from previous sapropel geochemical studies have provided crucial insights for the recognition and interpretation of recurring geochemical intervals and boundaries in the sapropels layers and surrounding sediments (e.g., marker bed, oxidized interval, unoxidized interval, oxidation front and synsapropel interval). These intervals, as identified and elucidated by various studies, reflect variations in redox conditions and postdepositional processes. Notably, the marker bed, characterized by shifts from euxinic/anoxic to suboxic/oxic conditions, has been recognized and interpreted by the work of Thomson et al. (1995, 1999), de Lange (1986), Pruysers et al. (1991, 1993), Reitz et al. (2006) and others, highlighting the significance of Mn-oxyhydroxide precipitation and its association with trace metals after sapropel termination (Filippidi and de Lange, 2019). The oxidized interval, where RSTMs are depleted due to mineral host phase oxidation due to the downward migration of the oxidation front, is informed by Wilson et al. (1986), de Lange et al. (1989) and van Santvoort et al. (1996, 1997). Additionally, studies by Passier et al. (1996, 1997) have contributed to our understanding of the synsapropel interval, where pyrite enrichment occurs through the reaction of downward HS^- fluxes.

Within this context, this work focuses on unraveling the paleoenvironmental significance of geochemical redox signals derived from regional-scale deoxygenations in deep-marine settings. This is achieved by integrating the outcomes of past geochemical studies and a detailed analysis of new geochemical data obtained from five recent Quaternary sapropels (S1, S5, S6, S7, and S8) recovered at three EM deep-marine settings (Ionian Basin, Mediterranean Ridge and Eratosthenes Seamount). These sapropels were deposited under different degrees of bottom-water stagnation and oxygen-depletion. Consequently, the assessment of these five sapropels deposited in three different EM locations, allows to assess a wide spectrum of redox geochemical signals derived from diverse environmental and hydrogeographic conditions in different deep-marine settings. Furthermore, a calibration of redox proxies' thresholds has also been performed at each location using the approach proposed by Algeo and Li (2020). This calibration is crucial as it has been demonstrated that the authigenic enrichment rate of RSTMs is not only attributed to bottom-water redox conditions (Warning and Brumsack, 2000; Algeo and Li, 2020). Moreover, the collected data facilitated the reconstruction of the paleoenvironmental and paleoceanographic evolution of the five examined sapropels in EM.

The integrative approach of this study provides key insights and geochemical tools for the identification and subsequent interpretation of geochemical redox intervals in organic-rich sediments (e.g., black shales). This contributes to enhance the current understanding of geochemical signals produced by deoxygenation dynamics and associated postdepositional geochemical processes in deep-marine settings. Furthermore, valuable information can be obtained regarding potential biogeochemical changes that may arise in marine environments transitioning towards anoxic conditions. Consequently, this knowledge aids in evaluating strategies to mitigate the consequences of deoxygenation on vulnerable marine ecosystems.

III.2. Oceanographic setting

The Mediterranean Sea is a semi-enclosed and evaporative marginal sea connected to the Atlantic Ocean by the Strait of Gibraltar. Despite its limited size (~2,500,000 km^2), the Mediterranean Sea exhibits a strong thermohaline circulation and a complex system of currents capable of maintaining oxic and ultra-oligotrophic conditions in the water-column and sediments with low total organic carbon content (TOC) (Pinardi and Masetti, 2000; Millot and Taupier-Letage, 2005; Pinardi et al., 2015; Rohling et al., 2015). The unique characteristics of the Mediterranean Sea make it highly sensitive to external forcing (e.g., astronomical oscillation, climate changes and anthropogenic pressure) and one of the most vulnerable regions to global climate change (Giorgi, 2006). Consequently, global climate variability and its consequences are manifested earlier in the Mediterranean Sea than in the global ocean (Lionello et al., 2006; Turco et al., 2015). Therefore, the Mediterranean Sea serves as an exceptional natural laboratory for studying the responses of marine environments to the current climate change, while its sedimentary record allows to study the nature and development of regional deoxygenation associated to past climate changes (Hennekam et al., 2020).

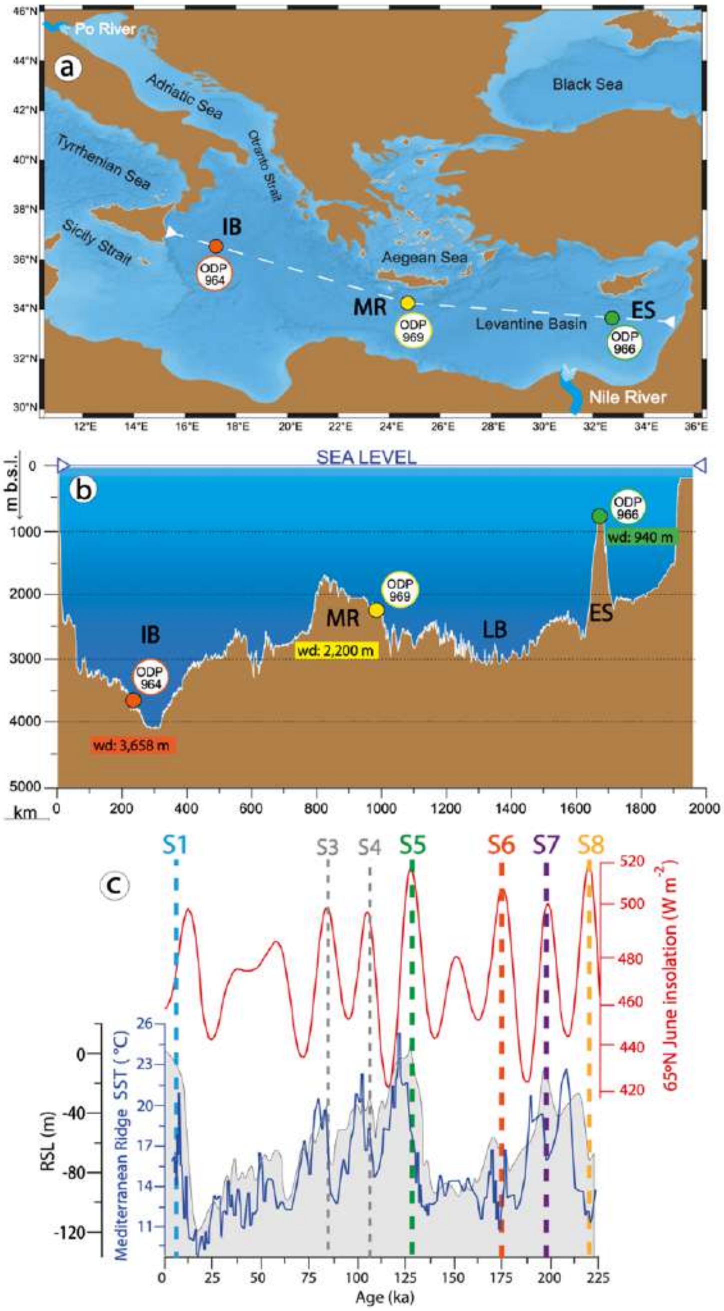

Figure III.1. *(a) Map showing the location of the three studied ODP sites (964, 966 and 969) and water-depths (wd). IB: Ionian Basin, MR: Mediterranean Ridge, ES: Eratosthenes Seamount. (b) Bathymetry of the transect. (c) Temperature curve (SST, blue) at the Mediterranean Ridge (core M40–4/71), obtained from U37 by Emeis et al. (2003). Summer insolation (red) at 65◦N from Laskar et al. (1993). Relative sea-level (RSL; light gray) from Grant et al. (2014). Sapropels under assessment are indicated with different colors that will be maintained henceforth in the following figs.*

Atlantic Water enters the Western Mediterranean through the Strait of Gibraltar, where it undergoes modifications, resulting in a water mass with higher salinity and temperature known as Modified Atlantic Water (MAW). MAW enters EM through the Strait of Sicily (Fig. III.1), where it keeps flowing eastward. As it flows to the Levantine Basin, MAW experience increases in salinity. During winter cooling, high evaporation rates caused by strong winds with dry air masses promote vertical mixing and the formation of Levantine Intermediate Water (LIW; between ~150 and ~ 600 m water-depth), which is then separated from the overlying MAW. The formation of Easter Mediterranean Deep Water (EMDW) primarily occurs in the Adriatic Sea by vertical mixing during strong winter winds from Europe, however, surface-water sinking at the Aegean Sea also contribute (Wüst, 1961; Miller, 1963; Lascaratos et al., 1999; Millot, 1999, 2009; Millot and Taupier-Letage, 2005; Rohling et al., 2015).

The five assessed sapropels (S1, S5, S6, S7 and S8), were sample in cores recovered from three ODP Leg 160 sites (964, 966 and 969). The sites describe an east-west transect across the EM and represent different deep-water regimes and water-depths. Site 964 is located at the Ionian abyssal plain and represents the deepest site (water-depth: 3658 m). This site is most influenced by the Adriatic Deep Water and Western Mediterranean water masses that come through Otranto Strait and Sicily Strait (Fig. III.1), respectively. Site 969 is situated at the Mediterranean Ridge and west to the Levantine Basin at a water-depth of 2200 m and represents the centermost location of the EM (Fig. III.1). Site 966 is the easternmost location, situated on the top of a pelagic high called Eratosthenes Seamount and the closest to the Nile River mouth. Site 966 represents the shallowest site at a water-depth of 940 m and is situated in the interface between LIW and EMDW.

III.3. Sapropel deposition

During sapropel deposition, circulation patterns and water masses dynamics were markedly different (Rohling et al., 2015; Andersen et al., 2020). Increased fresh-water discharge (mainly from the Nile River), due to monsoon intensification, weakened the anti-estuarine circulation, which resulted in decreased surface-water salinity and reduced vertical mixing (Gallego-Torres et al., 2007a; Tachikawa et al., 2015; Monedero-Contreras et al., 2023a). Increasing freshwater input led to enhanced nutrient input and marine productivity, and also to the formation of a strong halocline and restriction of deep-waters. In this situation, when deep-waters are not strongly restricted (intermittently ventilated), the redoxcline is normally located at the sediment-water interface (SWI), causing the porewater to become anoxic with euxinic confined microenvironments, even is sulfate is saturated (Martínez-Ruiz et al., 2000; Scott and Lyons, 2012; Tribovillard et al., 2008; Filippidi and de Lange, 2019). However, during strong water-column stratification, an upward migration of the redox chemocline (also known as the redoxcline) from below the SWI to the water-column can occur, allowing bottom-waters to reach anoxic or even euxinic conditions (Gallego-Torres et al., 2007a, 2010; Filippidi and de Lange, 2019; Benkovitz et al., 2020; Sweere et al., 2021).

During sapropels deposition, EM deep settings experienced varying degrees of bottom-water deoxygenation as a response to different oceanographic and climatic conditions (Monedero-Contreras et al., 2023a). Regarding the assessed sapropels, S1, S5 and S7 where deposited during interglacial periods, while S6 and S8 were deposited during glacial periods (Ziegler et al., 2010; Grant et al., 2016). However, sapropels S5 and S7 experienced the most intense bottom-water deoxygenation, followed by S6, S8 and S1, respectively (Gallego-Torres et al., 2007a; Wu et al., 2016, 2018; Sweere et al., 2021). The diverse sapropel scenarios derived in different degrees of OM preservation and rate of authigenic RSMTs uptake by seafloor sediments. The distribution and concentration of RSTMs and OM in sapropels have been used as geochemical signals to delimit the different sapropel deposition stages (i.e., pre-sapropel, onset, evolution, termination and early diagenesis) and evoke specific oceanographic processes and postdepositional disturbances, such as particulate-shuttling intensity, bottom-water reventilation and postdepositional oxidation and sulfidisation (Passier et al., 1996; van Santvoort et al., 1996; Reitz et al., 2006; Jilbert et al., 2010).

III.4. Material and methods

III.4.1. Core description, sampling and chronology

Background sediment of the analyzed records is mainly composed by nannofossil clay, with minor variations in clay content, displaying colors ranging from brownish to greenish and grayish (Emeis et al., 1996). Characteristic layers, such as foraminiferal sandy levels, discrete tephra layers and rhythmic dark layers (i.e., the sapropels), are intercalated into the background sediments (Emeis et al., 1996, 2000). Slump and tephra layers were visually and geochemically identified.

Sampling at 2 cm resolution includes the underlying and overlying intervals of sapropels S1, S5, S6, S7 and S8. Sapropels S3 (85.8–80.8 ka) and S4 (107.8–101.8 ka) exist in EM sedimentary record but were not the focus of this study (Fig. III.1c) (Grant et al., 2016). The onset and termination times of the selected sapropels are well established by previous studies: S1: 6.1–10.5 ka (MIS 1), S5: 121.5–128.3 ka (MIS 5e), S6: 165.5–178.5 ka (MIS 6d), S7: 191.9–198.5 ka (MIS 7a), and S8: 209.5–224.1 ka (MIS 7c-7d) (Fig. III.1c) (Ziegler et al., 2010; Grant et al., 2016). Top and base boundaries of sapropel events were delimited using Ba/Al ratio profiles (a productivity proxy, see Section 3.4) (Murat and Got, 1987; de Lange et al., 2008; Gallego-Torres et al., 2010; Rohling et al., 2015).

III.4.2. Geochemical analysis

For all geochemical analyses, dried sediment samples were powdered in an agata mortar. Due to sample size limitations, major elements quantification by XRF was only performed in sapropel S1 from Site 964 (Ionian Basin). In this case, sediment samples were prepared as fused beads. XRF analyses were done at Instituto Andaluz de Ciencias de la Tierra (IACT), with a S4 Pioneer from BRUKER, equipped with 4 kW wavelength dispersive X-ray fluorescence spectrometer (WDXRF) of BRUKER spectrometer and a Rh anode X-ray tube (60 kV, 150 mA). For major elements quantification, XRF precision was better than ±0.3%. In the rest of samples, major elements were measured with an ICP-OES Perkin-Elmer Optima 8300 (Dual View) with an autosampler Perkin-Elmer. Certified standards (BR-N, GH, DR-N, UB-N, AGV– N, MAG-1, GS-N, and GA) were measured for element quantification. Trace elements, in all samples, were measured using an ICP-MS NexION 300d (Perkin Elmer) spectrometer using Rh as internal standard. For major elements, ICP-OES precision was better than ±1% and for trace elements ICP-MS precision was better than ±5% for analyte concentrations of 10 ppm (Bea, 1996).

Both ICP-MS and ICP-OES were performed at the Scientific Instrumentation Center (CIC) of University of Granada. They both measured the same solutions, which were prepared in batches of 25 to 30 samples. Analytical blanks were introduced in each sample batch. Solutions were prepared with 0.1 g of powdered sample in Teflon vessels, where successive acid digestions using HNO_3 (ultra-pure with a 69% concentration) and HF (48% concentration) were performed at 130 °C until evaporation. A final acid digestion with HNO_3 and water at 80 °C for 1 h was performed until samples were completely dissolved. Subsequently, the digested samples were diluted with Milli-Q water in 100 ml volumetric flasks following standard procedures (Bea, 1996).

Total organic carbon content, expressed as TOC%, was measured in ~50 mg of powdered samples by the Rock-Eval pyrolysis method at the Institute of Earth Sciences (ISTE) of the University of Lausanne. The Rock-Eval pyrolysis method consisted of a programmed temperature heating (from 200 °C to 850 °C, in successive steps), in a pyrolysis oven with an inert atmosphere (N_2). TOC% is calculated from the obtained thermograms using the following equation; TOC% = Pyrolyzed Carbon(wt%) + Residual Carbon (wt%). Samples were calibrated using the IFP160000 standard with an instrumental precision of <0.1 wt% for TOC (Lafargue et al., 1998; Behar et al., 2001; Ordoñez et al., 2019).

III.4.3. Geochemical data normalization

Due to the conservative behavior of Aluminum, diverse studies support that Al-normalized trace metals (TM/Al) and trace metal Enrichment Factors (EFs) are the optimal normalization methods to evaluate trace metal variability and serve as reliable paleoenvironmental proxies (Brumsack, 2006; Tribovillard et al., 2006; Calvert and Pedersen, 2007; Algeo and Tribovillard, 2009; Algeo and Li, 2020; Algeo and Liu, 2020). Trace metals Enrichment Factors were obtained by applying the following equation: $TM_{EF} = (TM/Al)_{sample}/(TM/Al)_{reference}$, with the post-Archean Australian shale (PAAS) values from Taylor and McLennan (1995) as reference values to enable comparability with other studies, even if local background TM/Al values may be preferred over bibliographic reference values (Paul et al., 2023).

Vertical plots of environmental proxies allow to see variations in depth, delimit sapropels and stablish geochemical intervals within the sapropels and surrounding sediments (Figs. III.4, 5 and 6). On the other hand, cross-plots offer information about geochemical differences between the established geochemical intervals within the sapropels and surrounding sediments. The variables introduced in the cross-plots (i.e., Mo/Al-Mn/Al, Ba/Al-TOC% and DOPt-TOC%) were selected to evidence differences and anomalies in geochemical intervals. Mo/Al-Mn/Al cross-plots (Fig. III.7) evidence how some marker beds and synsapropel intervals the Mn-oxyhydroxides are enriched in Mo. RTSMs. Ba/Al-TOC% cross-plots (Fig. III.8) enable the observation and determination of oxidized intervals, which show high Ba/Al values but low TOC% values. Moreover, it enables to assess the correlation between barite content and preserved OM in the different geochemical intervals. DOPt-TOC% cross-plots (Fig. III.9) allow the observation of sapropels that developed synsapropel intervals, characterized by high DOPt values, but low TOC%. Consequently, cross-plots are an excellent tool to visually assess differences between geochemical intervals and sapropels.

III.4.4. Paleoenvironmental geochemical proxies

Diverse authigenic minerals precipitate during oxygen deficient conditions in marine systems, which enriched marine sediments in redox sensitive trace metals (i.e., Mo, U, V, Re, Cu, Co, Ni, Cr, Cu, Zn, Pb, Mn). Once normalized they can be used as redox proxies to determine different redox conditions in ancient marine environments (Figs. III.2, 4–6) (Berner, 1981; Tyson and Pearson, 1991; Calvert and Pedersen, 1993, 2007; Crusius et al., 1996; Warning and Brumsack, 2000; Tribovillard et al., 2006; Scheiderich et al., 2010; Little et al., 2015).

Diverse geochemical proxies based on trace metal concentrations have been used to identify paleoredox changes in EM bottom-waters during sapropel deposition and to recognize geochemical intervals that reflect specific conditions and processes that occurred during deoxygenation and early diagenesis. Used redox proxies are: Fe/Al, Mn/ Al, U_{EF}, Mo_{EF}, V_EF, Ni_{EF}, Cu_{EF}, Cr_{EF}, Co_{EF}, Zn_{EF}, Pb_EF, and degree of pyritization ($DOPt = S_T * (55.85/64.12) / Fe_T$), where S_T = total sulfur, Fe_T = total iron and 55.85/64.12 represents weight ratios of Fe/S in stoichiometric pyrite (Berner, 1970; Algeo and Li, 2020). Therefore, DOPt values reflect pyrite content in the sediments. Preestablished DOPt redox threshold values (e.g., DOPt >0.45 = euxinic bottom-water; Scott and Lyons, 2012) are not applied since the value of this threshold can vary depending on the hydrographic conditions of each marine setting (Algeo and Li, 2020).

Other geochemical proxies complemented additional paleoenvironmental information (e.g., productivity and climate variability). Ba/Al ratio and TOC% were used to determine productivity changes in sapropel intervals. Ba/Al ratio increases in marine sediments are associated to higher barite ($BaSO_4$) abundance. Barite precipitation in the water-column has been linked to periods of increased productivity and OM degradation, principally in the mesopelagic zone (Dehairs et al., 1987; Bishop, 1988; Paytan et al., 2002, 2004; Paytan and Griffith, 2007). Therefore, Ba/Al is a well-accepted qualitative proxy for paleoproductivity and have been successfully applied to sapropels (Passier et al., 1999; Arnaboldi and Meyers, 2007; Gallego-Torres et al., 2007a, 2010; Martínez-Ruiz et al., 2000; Hennekam et al., 2014; Filippidi and de Lange, 2019; Benkovitz et al., 2020).

Aeolian inputs in marine sediments can be tracked using geochemical proxies for gran-size, such as Zr/Al. Zr occurs in marine sediments primarily as zircon ($ZrSiO_4$), which is principally transported to the ocean by wind. K is mainly in association with clay minerals (e.g., illite) that are transported to the ocean by the rivers (Calvert and Pedersen, 2007 and references therein). Consequently, Zr/Al and K/Al were used to reconstruct aeolian and fluvial input respectively, which can offer information about climate variability. In the EM during dry periods, large aeolian inputs from the Sahara-Sahel region occurred. Conversely, during wet and warm climates (as occurs in most sapropel events), large fluvial inputs, mainly from African borderlands, are registered (Bout-Roumazeilles et al., 2013; Rohling et al., 2015; Wu et al., 2016, 2018). Nevertheless, it has been proven that European borderlands also play an important role in EM during sapropels deposited during glacial periods, such as S6 (Gallego-Torres et al., 2007a).

III.4.5. Multivariant statistical analyses

Multivariant statistical analyses (e.g., correlation matrixes and Principal Component Analysis, PCA) of the geochemical data are used to achieve a deeper understanding of the geochemical data and sediment composition of the three EM sites. Subsequently, a better interpretation of geochemical redox signals. Correlation matrixes have been obtained using the software "PAST 4.0" from Hammer et al. (2001). Mayor elements, trace metals and other variables that were considered the most important for this paleoenvironmental study (i.e., Al, Mg, Ca, Sr, K, Zr, Ti, Mo, U, V, Cu, Cr, Co, Ni, Pb, Zn, Mn, Fe, Ba DOPt, and TOC%), were introduced into the correlation matrix. A p-value of $(p) \leq 0.01$ was proposed as threshold to verify whether the established correlations were statistically significant or not. The correlations established in the correlation matrix of each location determined the variables introduced in the PCA.

PCA allowed the establishment of the principal geochemical affinities and fractions in each EM location. PCA was also performed with the software "PAST 4.0" from Hammer et al. (2001). Only variables that reached a moderate to strong correlation (correlation coefficient (r) between ±0.4 and ±1) in the correlation matrix were introduced in the PCA to reduce statistical noise. It is important to highlight that both multivariant statistical analyses (i.e., correlation matrix and PCA), were performed using non-normalized elements so there are no pre-induced correlations that could mask the real affinities and associations of the variables under assessment.

III.4.6. Redox thresholds calibration

Every depositional unit has specific depositional, geochemical, environmental and hydrographic features that control trace metal uptake rate by seafloor sediments (Algeo and Lyons, 2006; Algeo et al., 2007; Algeo and Tribovillard, 2009; Tribovillard et al., 2012; Sweere et al., 2016; Scholz et al., 2017; Scholz, 2018; McArthur, 2019; Algeo and Liu, 2020). The interplay of specific depositional features in a marine basin determines the redox thresholds values of the redox proxies (Algeo and Li, 2020). Therefore, applying redox thresholds values calibrated for a specific geological formation to another geological formation or depositional unit, is an inaccurate approach according to Algeo and Li (2020). These authors proposed that, if possible, redox thresholds should be calibrated for each paleodepositional unit. In the case of the present study, redox thresholds calibration was performed to the three EM sites to evaluate variations in RSTMs authigenic enrichment threshold and rate. It is important to note that postdepositional processes can affect the original concentration and position (i.e., depth) of RSTM and lead to inaccurate thresholds values calibration. For this reason, a prior assessment of the geochemical data is necessary to identify altered geochemical intervals and exclude them in the calibration cross-plots.

The “Compound covariant-sequential enrichment” approach optimized by Algeo and Li (2020) was applied to different redox proxies for the calibration of redox thresholds values. V_{EF}, U_{EF} and Mo_{EF} were used as calibrants, since the ionic couple reaction of V, U and Mo occur at a specific but different redox potential (pe) (Fig. III.11a). Mo, U, and V are reduced from specific oxyanions (e.g., MoO_4^{2-} , $UO_2(CO_3)_3^{4-}$, and $H_2VO_4^{-}$) into stable solid phase species at specific low-oxygen conditions (Crusius et al., 1996). Therefore, V, U and Mo enrichments in oxygen-depleted sediments represent a precise redox threshold according to their position in the redox ladder (Grundl et al., 2011; Algeo and Li, 2020). In order to specify positions in the redox ladder and respective redox thresholds, we employed the terminology proposed by Algeo and Li (2020) and Algeo and Liu (2020). Within this context, V enrichment is used to obtain the suboxidized-subreduced threshold value (T1). U enrichment is used to obtain the dysoxic-anoxic threshold value (T2), which indicates if ferruginous condition were reached. While Mo_{EF} is used to obtain the anoxic-euxinic redox threshold value (T3) (Fig. III.11a). Calibration of redox thresholds is only possible when the plotted redox proxies show a sequential enrichment and not a constant linear coenrichment. See Algeo and Li (2020) for detailed information about this calibration approach. Furthermore, the redox threshold values enable a qualitative comparison of RSTMs authigenic enrichments rates across different marine settings, offering valuable insights into the local dynamics of RSTMs in the water-column and porewater.

III.5. Results

III.5.1. Geochemical data

A comparison between the three EM locations reveals that Mo, U and V reach the highest concentrations at the Ionian Basin (Site 964), followed by the Mediterranean Ridge (Site 969). While the lowest concentrations occur at the Eratosthenes Seamount (Site 966). Mo is the RSTM with the highest enrichment of all at the three locations. Cr, Co, Cu, Ni, Pb Zn and Mn, which also correspond to RSTMs, are systematically more enriched at the Mediterranean Ridge, followed by the Eratosthenes Seamount and the Ionian Basin. Ba is most enriched in Mediterranean Ridge sediments. Conversely, Ba is least enriched in Eratosthenes Seamount sediments. TOC% and DOPt tend to be similar at the Ionian Basin and Mediterranean Ridge, but higher than at Eratosthenes Seamount. See Fig. III.2 and Table S1 in Supplementary material (Sup. mat.) for detailed results.

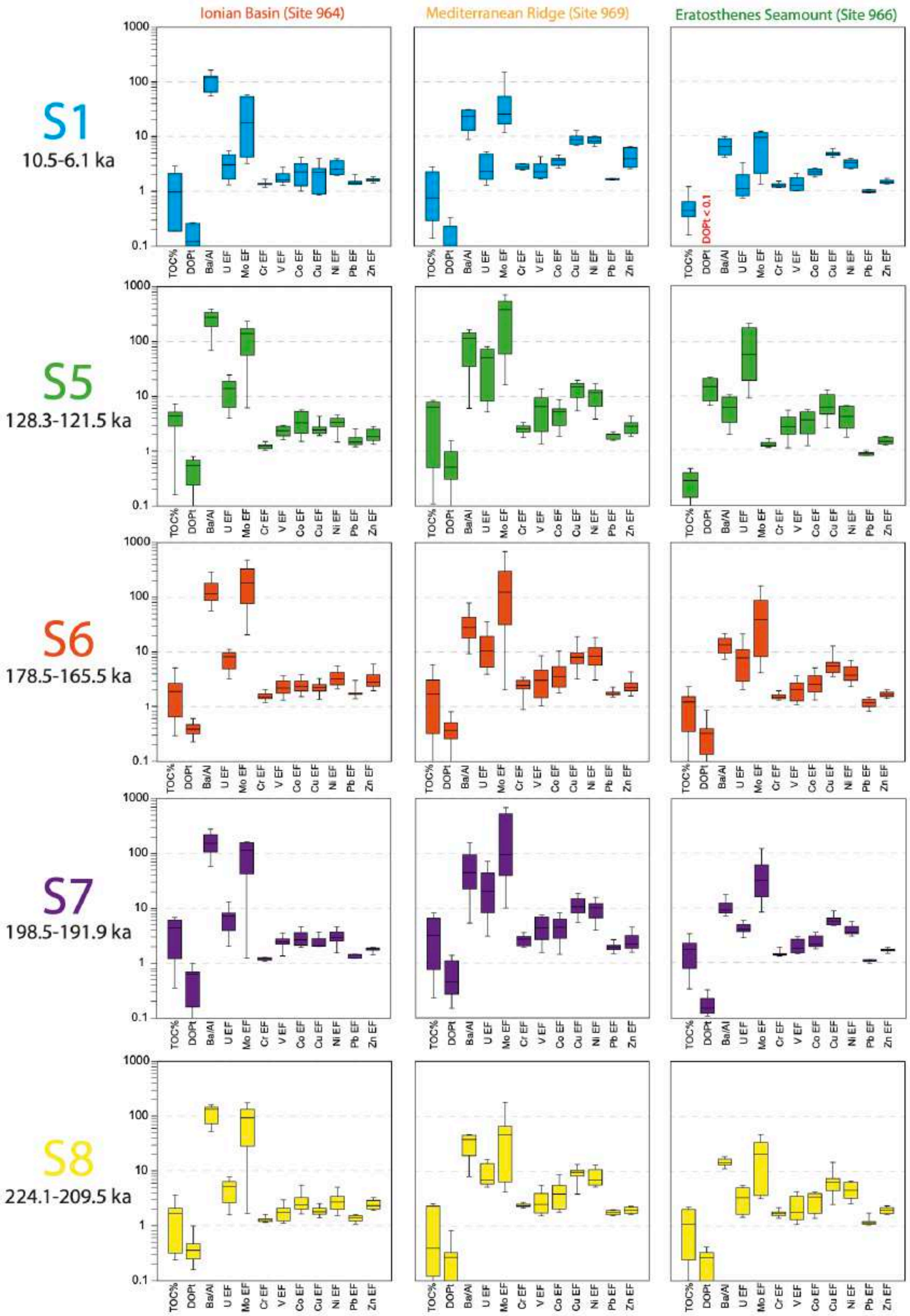

Figure III.2. *Box-plots showing redox and productivity proxies values in sapropel intervals delimited by Ba enrichment, at the three locations: Ionian Basin (Site 964), Mediterranean Ridge (Site 969) and Eratosthenes Seamount (Site 966). Ba concentrations are expressed as Ba/Al (ppm/%) and RSTMs as EFs.*

Regarding the sapropel layers, a comparison between sapropel values reveal that S5 and S7 are the sapropels most enriched in trace metals and have higher concentration in pyrite (i.e., higher

DOPt values). S6 sediments show strong enrichment in Mo, like S5 and S7. However, S6 exhibits more unstable trends of redox and productivity proxies in the vertical plots than the rest of sapropels at the three locations (Fig. III.6). S1 and S8 register lower enrichments in trace metals, and DOPt than the rest of sapropels (S5, S6, S7), being S1 the sapropel with the lowest values (Fig. III.2 and Table S1). Interestingly, even though S1 sediments show the lowest enrichments in most variables, is the most enriched sapropel in Mn, specially at Mediterranean Ridge (Fig. III.4). S1 and S8 also exhibit the lowest TOC% values (below 1.5% mean), followed by S6 (below 2% mean). Therefore, S5 and S7 show the highest TOC% values, but are systematically higher in S5 sediments (Fig. III.2 and Table S1). No evident signs of Ba remobilization or barite reprecipitation (e.g., Ba marked peak above or below organic-rich sediments) have been Recognized in the studied sapropel, enabling the use of Ba/Al as a paleoproductivity proxy (van Os and Middelburg, 1991: Martínez-Ruiz et al., 2000). See vertical plots of environmental proxies for variations in depth (Figs. III.4, 5 and 6) and cross-plots for differences in geochemical intervals (Figs. III.7, 8 and 9).

III.5.2. Multivariate statistical analyses

The correlation matrixes and the PC1 vs. PC2 scatterplots elucidated geochemical affinities and allowed the establishment of four statistical groups (GRPs), which represent the main geochemical fractions in each EM location. For detailed information about the Correlation Matrixes and PCA results, see Sup. mat. The four geochemical fractions are:

1) Terrigenous geochemical fraction (GRP1; red in Fig. III.3). Also named the detritic fraction, is principally constituted by elements enriched in minerals mainly supplied by rivers and wind, e.g., Al, K, Rb, Ti and Zr (Calvert and Pedersen, 2007). Pb and Cr are considered RSTMs that can precipitate in association with authigenic sulfides during oxygen depletion (Tribovillard et al., 2006). However, our data suggests that these two elements are mainly enriched in the terrigenous fraction at the three locations. Consequently, its respective EFs should not be used as reliable redox proxies. Mg is an element that is mainly supplied by continental runoff in detritic and clay minerals (Calvert and Pedersen, 2007 and references there in). However, the Ionian Basin is the only location where Mg is mainly in association with the fluvial fraction. Conversely, at Eratosthenes Seamount and Mediterranean Ridge, Mg is isolated from the rest of the geochemical fractions. This may indicate that Mg, in these two locations, is incorporated in other sediment fractions and minerals, such as in authigenic Mg-rich carbonates. Interestingly, at Eratosthenes Seamount the fluvial fraction (Al, Ti, K and Rb; Fig. III.3c), is better correlated than in the other two locations, probably due to its proximity to the Nile River mouth.

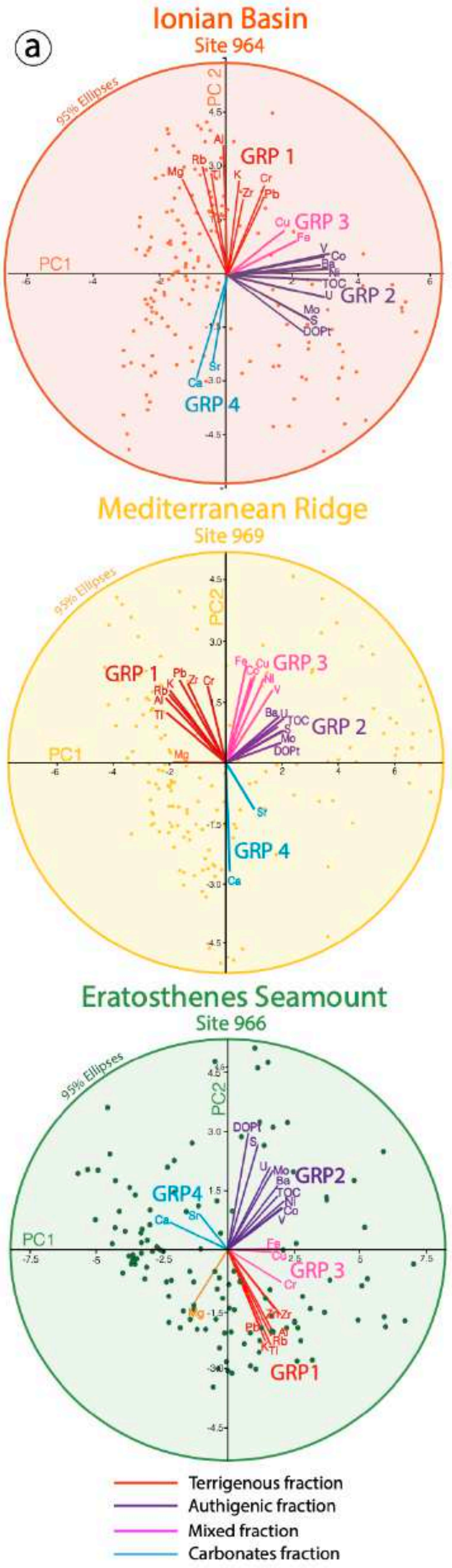

ⓑ

	Ionian Basin	Mediterranean Ridge	Eratosthenes Seamount
Variance% PC1	33.73	45.86	50.29
Variance% PC2	26.68	20.89	20.88
Variance% PC3	10.2	9.09	6.93
Variance% (PC1+PC2+PC3)	70.61	75.84	78.1
KMO	0.75	0.84	0.86

Figure III.3. *(a) Scatter plots using PCA (x = PC1; y = PC2) of geochemical data from each location: Ionian Basin, Mediterranean Ridge and Eratosthenes Seamount obtained using PAST 4.0 (Hammer et al., 2001). (b) PCA statical values obtained at each location. The Kaiser-Meyer-Olkin Test (KMO) is a statistical test that measures adequacy of the data for factor analysis. Values closer to 1, indicate better adequacy. Mn was not included in the PCA of Site 966, and Zn and Mn were not included in the PCA of Site 964 and Site 969, since they did not present relevant correlation with the rest of the variables in the correlation matrices. See Sup. mat. for detailed data.*

2) Authigenic geochemical fraction (GRP2; purple in Fig. III.3). This geochemical fraction is enriched during sapropel deposition. Is composed by elements that are strongly enriched in authigenic minerals (e.g., sulfides and sulfates) or in organometallic compounds than precipitate under oxygen deficient conditions and high marine productivity. Consequently, this fraction is mainly enriched during sapropel deposition. The elements that conformed this fraction can be divided in: (i) chalcophile and siderophile elements (e.g., Mo, S, Ni, Cu, Co, and Zn). These elements tend to be scavenged from the water-column to the seafloor by Mn and Fe oxyhydroxides and OM (Tribovillard et al., 2006; Scholz et al., 2013). Once in seafloor and in the presence of dissolved H_2S produced by sulfate-reducing bacteria, they are fixed in association with pyrite (FeS), as demonstrates the robust correlation with DOPt, or by forming their own sulfides (e.g., MoS, CuS, CuS_2, NiS and [Zn,Fe]S CoS, NiS). (ii) Elements that are enriched in association with OM and occur in seawater in at least two oxidation states and precipitate as the less soluble lower oxidation state during oxygen depleted conditions (e.g., U and V) (Helz et al., 1996; McManus et al., 2005). (iii) Elements that precipitate in authigenic minerals due to intense OM degradation in the water-column during periods of increased marine productivity, such as Ba in barite ($BaSO_4$; see Section III.4.4) (Bishop, 1988; Calvert and Pedersen, 2007; Paytan and Griffith, 2007; Martínez-Ruiz et al., 2018, 2019, 2020).

3) Mixed geochemical fraction (GPR3; magenta in Fig. III.3). Constituted by RSTMs that are under strong detritic influence, as shown by the PCA. Due to local factors this geochemical fraction varies at each location according to the influence of the detritic fraction on the authigenic enrichment of RSTMs. At the Ionian Basin, this geochemical fraction is only represented by Cu and Fe (Fig. III.3a), suggesting that these two elements are the RSTMs most influenced by the detritic fraction. In Eratosthenes Seamount sediments, the PCA suggests that Cr and Zn are also strongly influenced by the detritic fraction. While at the Mediterranean Ridge, the detritic fraction influences more RSTMs (e.g., Fe, Cu, Co, Ni and V; Fig. III.3a). V is an element that tends to be enriched in association with humic and fulvic acids (i.e., OM) and normally is minimally influenced by the terrigenous fraction (Tribovillard et al., 2006). However, at the Mediterranean Ridge, V enrichments seem to be highly influenced by the detritic fraction. This could be linked to stronger particulate-shuttling and RSTMs scavenging at the Mediterranean Ridge.

4) Carbonates geochemical fraction (GRP4; blue in Fig. III.3). Is constituted by Ca and Sr, which are characteristic elements of carbonate minerals, principally enriched under oxic conditions in the water-column and low productivity rates, i.e., during “non-sapropel” deposition.

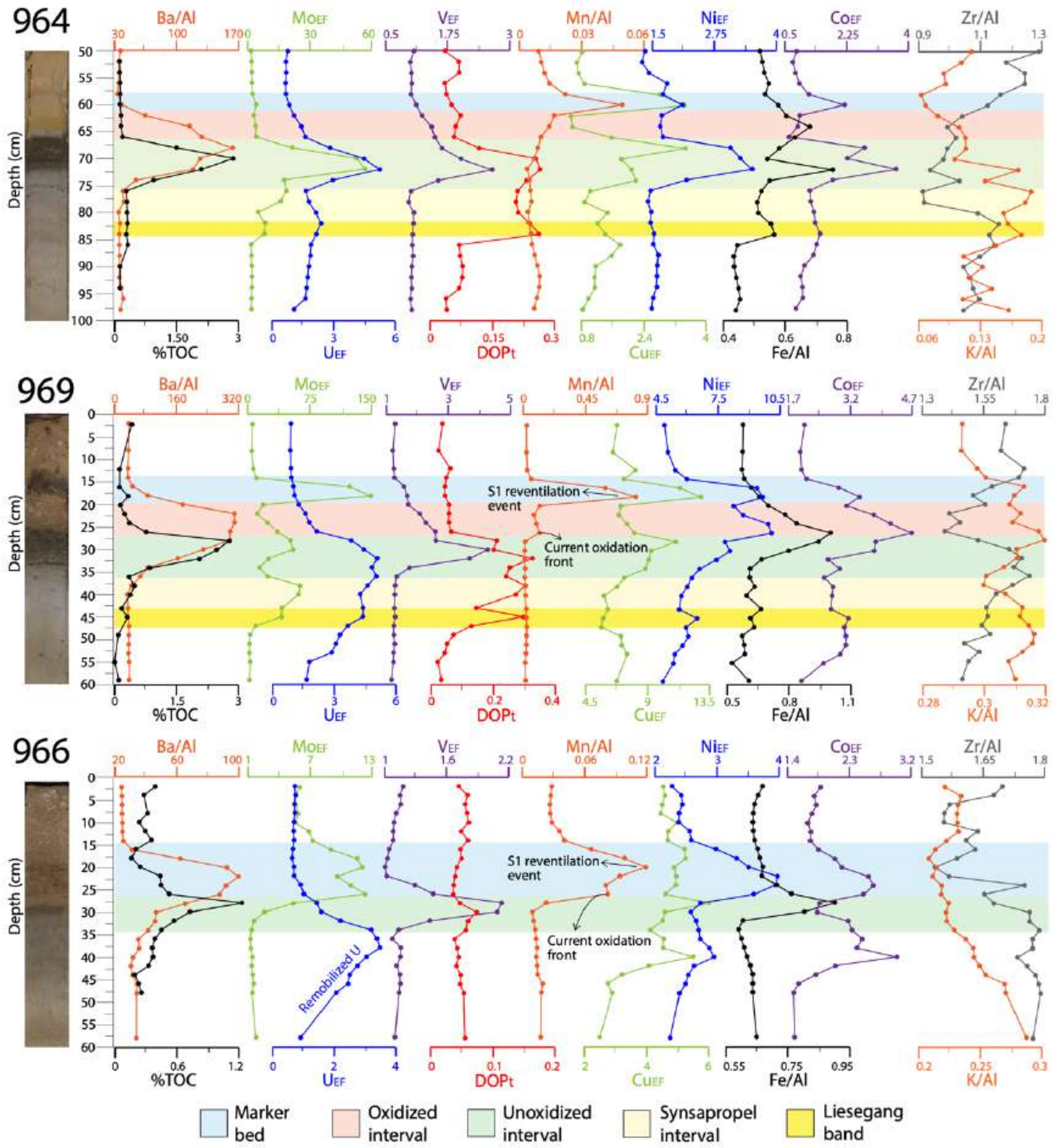

Figure III.4. *Vertical plots of different redox, productivity and environmental proxies from sapropel S1 at the three EM sites: Ionian Basin (Site 964), Eratosthenes Seamount (Site 966) and Mediterranean Ridge (Site 969). Fe/Al and Mn/Al in %/%, while Ba/Al and Zr/Al in ppm/% (x10− 4). To simplify the figure and facilitate data interpretation, vertical plots of Cr/Al, Zn/Al and Pb/Al for S1 are presented in a separate Sup. mat. figure, which includes all assessed TMs (Fig. S16 in Sup. mat.). Geochemical redox intervals and sedimentary layers in the sapropels are illustrated in different colors.*

III.6. Discussion

Geochemical records from EM sapropels have been exhaustedly studied. They represent exceptional paleoarchives for understanding regional oceanographic responses to past climatic changes (Hennekam et al., 2020; Mancini et al., 2023). Many of these studies have used variations in authigenic minerals (e.g., pyrite and barite), TOC and RSTMs distribution in the sapropel organic-rich sediments and surrounding sediments as geochemical signals for reconstruction of the environmental and physicochemical conditions in both the water-column and porewater during its deposition and early diagenesis (Passier et al., 1996; van Santvoort et al., 1996; Martínez-Ruiz et al., 2000; Reitz et al., 2006; Monedero-Contreras et al., 2023b).

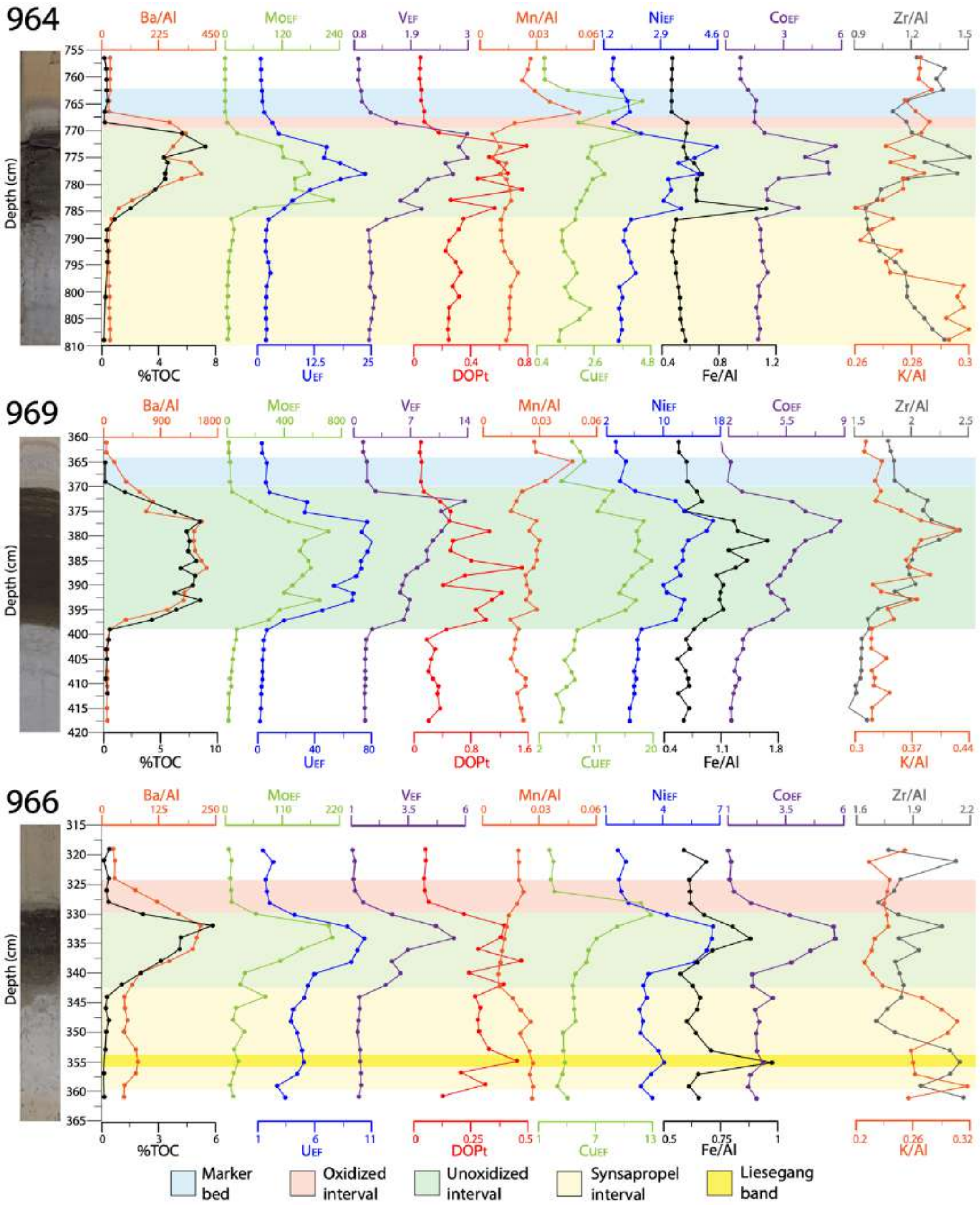

__Figure III.5.__ Vertical plots of different redox, productivity and environmental proxies from sapropel S5 at the three EM sites: Ionian Basin (Site 964), Eratosthenes Seamount (Site 966) and Mediterranean Ridge (Site 969). Geochemical redox intervals and sedimentary layers present in the sapropel sequence are illustrated in different colors. To simplify the figure and facilitate data interpretation, vertical plots of Cr/Al, Zn/Al and Pb/Al for S5 are presented in a separate Sup. mat. figure, which includes all assessed TMs (Fig. S17 in Sup. mat.). Fe/Al and Mn/Al in %/%, while Ba/Al and Zr/Al in ppm/% (x10^{-4}). See Fig. III.8 for legend.

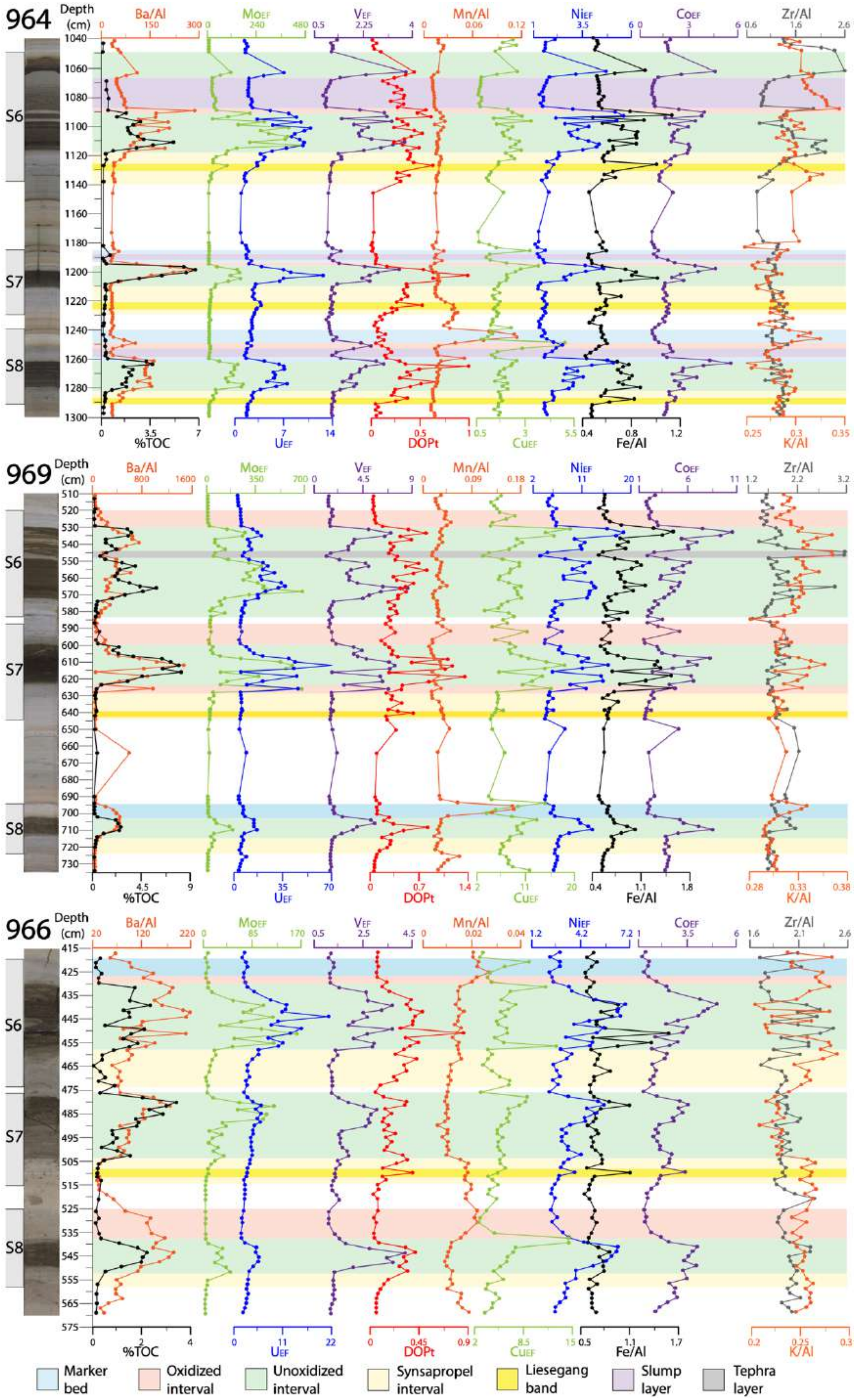
964
969
966
Depth (cm)
S6
S7
S8
%TOC
Ba/Al
MoEF
UEF
VEF
DOPt
Mn/Al
CuEF
NiEF
Fe/Al
CoEF
Zr/Al
K/Al
Marker bed
Oxidized interval
Unoxidized interval
Synsapropel interval
Liesegang band
Slump layer
Tephra layer

Figure III.6. *Vertical plots of different redox, productivity and environmental proxies from sapropels S6, S7 and S8 at the three EM sites: Ionian Basin (Site 964), Eratosthenes Seamount (Site 966) and Mediterranean Ridge (Site 969). Geochemical redox intervals and sedimentary layers present in the sapropel succession are illustrated in different colors. To simplify the figure and facilitate data interpretation, vertical plots of Cr/Al, Zn/Al and Pb/Al for S6, S7 and S8 are presented in a separate Sup. mat. figure, which includes all assessed TMs (Fig. S18 in Sup. mat.). Fe/Al and Mn/Al in %/%, while Ba/Al and Zr/Al in ppm/% (x10*$^{-4}$*). See Fig. III.8 for legend.*

III.6.1. Characterization of distinctive geochemical intervals in sapropel layers

Previous geochemical studies of sapropels, combined with a detailed analysis of new geochemical data obtained from five different sapropels (S1, S5, S6, S7 and S8) across three EM locations, have facilitated the recognition of recurring, yet distinct, geochemical patterns in sapropels and surrounding sediments, as previously explained in the introduction. Subsequently, these recurrent geochemical intervals and boundaries (i.e., marker bed, oxidized interval, oxidation front, unoxidized interval and synsapropel interval) have been interpreted in terms of redox conditions and postdepositional processes. However, it is important to acknowledge that these intervals are not uniformly present in all sapropels due to variations in environmental conditions and postdepositional processes.

- *Marker bed*. This geochemical interval is produced when the export of OM decreases and bottom-waters are reventilated, changing the redox regime in bottom-waters from euxinic/anoxic to suboxic/oxic (Fig. III.12). Bottom-water ventilation causes oxidant downward fluxes (e.g., O_2 and NO_3) to exceed reductant upward fluxes (e.g., Fe^{2+}, Mn^{2+} and NH_4) in the porewater system (Thomson et al., 1993; de Lange, 1986). This in turns oxidizes OM and sulfides (enriched in trace metals) in the sapropel layer, and releases trace metals into porewaters (e.g., Mo, Cu, Co and Ni) that can precipitate above the organic-rich sediments in association with Mn-oxyhydroxides (Berrang and Grill, 1974; Pruysers et al., 1991, 1993; van Os and Middelburg, 1991; van Os, 1993; Thomson et al., 1995, 1999; van Santvoort et al., 1997; Tribovillard et al., 2006; Reitz et al., 2006). Consequently, during the termination of oxygen-depleted condition and intense reventilation (as occurred during sapropel termination), large quantities of Mn-oxyhydroxides precipitate on the top of the organic-rich sediments and be recognized by a marked Mn/Al peak (Filippidi and de Lange, 2019). This feature was also reported by de Lange (1986) in turbidites sequences at the Nares Abyssal Plain (western North Atlantic).

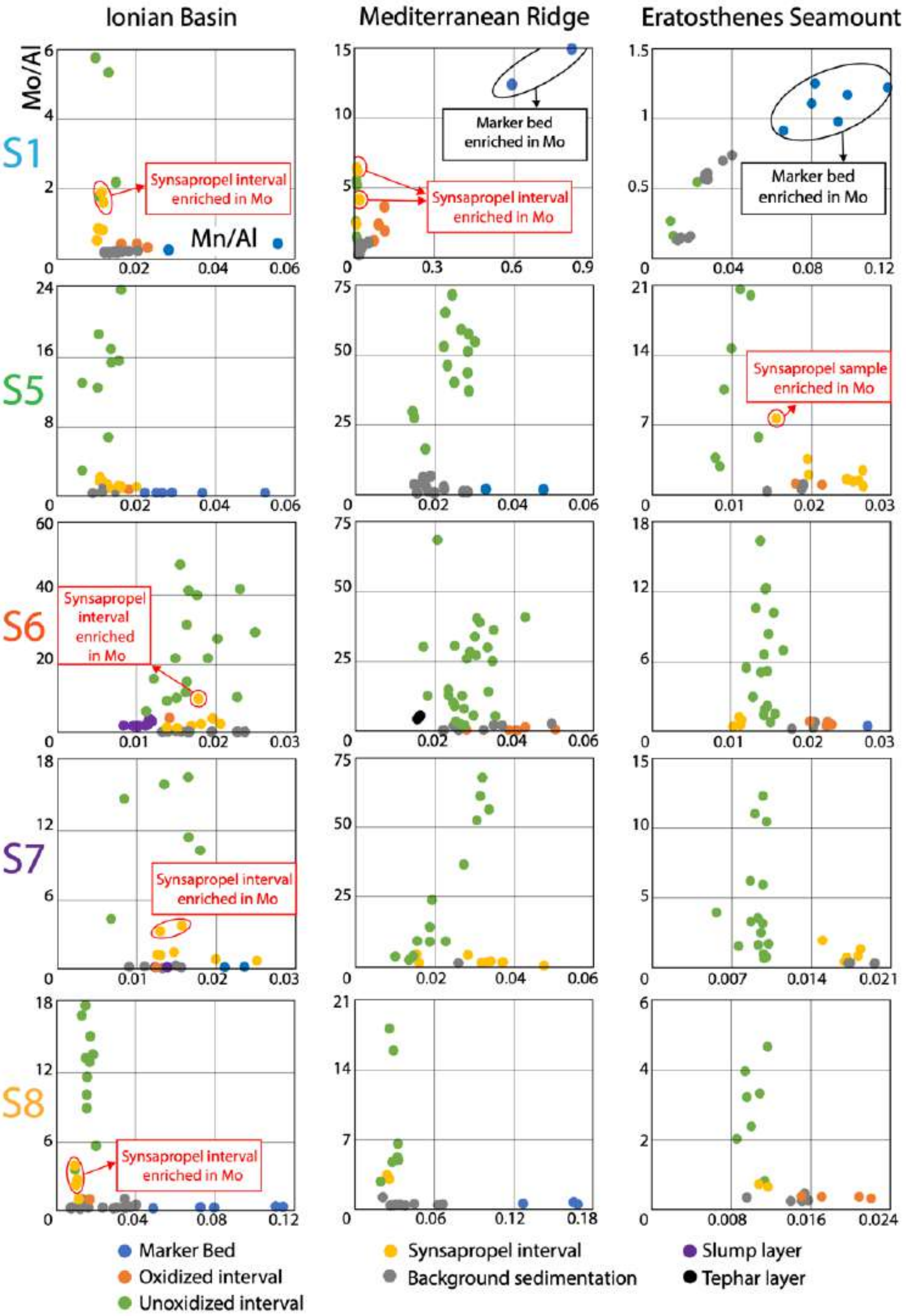

Figure III.7. *(a) Mo/Al - Mn/Al cross-plots of sampled sapropels (S1, S5, S6, S7, S8) at the three EM locations. Redox geochemical intervals are illustrated with different colors. y-axis: Mo/Al, x-axis: Mn/Al.*

The Mn/Al peak is sometimes accompanied by an increase in other trace metals, principally Mo, Co, Cu, Ni and to a lesser extent Pb, Cr and Zn (Fig. III.7). These elements precipitated in association with Mn-oxyhydroxides under suboxic conditions (during reventilation) and not as metal-organic ligands or in association with iron sulfides under euxinic conditions as there are no co-enrichments with DOPt, U, V or TOC in this interval (Figs. III.5, 8 and 9). In some sapropel layers, several of these trace metals (Mo, Co, Cu and Ni) present in their vertical profiles a "double-peak" pattern and in some exceptional cases a "triple-peak" pattern, as occurs with Mo and Cu in S1 at the Mediterranean Ridge. In the latter mentioned case, each peak is associated to a different geochemical interval (Fig. III.4). A similar case was recently observed by Filippidi and de Lange (2019), where a Mo enrichment in association with Mn-oxyhydroxides is observed on the top of S1 (delimited by Ba enrichment) at the Otranto Strait sill. A Mn and Mo coenrichment was also observed by Calvert and Pedersen (1993) at the deep continental margin of Baja California between the oxic/suboxic boundary at ~10 cm below the SWI. Consequently, the recognition of these postdepositional Mo enrichments is essential for accurate paleoredox interpretations since it evidences that a Mo enrichment by itself does not necessary imply a strong oxygen depletion. Hence, it is recommended that Mo, serving as a redox proxy (e.g., Mo_{EF}, Mo/Al, Mo ppm) should be employed in conjunction with the Mn/Al ratio and other established redox proxies within a multiproxy approach framework to prevent misinterpretations and explore diverse mechanisms contributing to RSTMs enrichment, extending beyond the singular influence of oxygen depletion (Algeo and Lyons, 2006; Algeo and Maynard, 2004; Tribovillard et al., 2006; Algeo and Tribovillard, 2009; Lyons et al., 2009).

- *Oxidized interval*. Trace metals are impoverished in this interval due to oxidation of their mineral host phases (e.g., sulfides or OM; Fig. III.10) during downward migration of the oxidation front (Fig. III.12) (Wilson et al., 1986; de Lange et al., 1989; Thomson et al., 1995; van Santvoort et al., 1996, 1997). Sulfide oxidation is evidenced by the abrupt decrease in pyrite content (i.e., DOPt) in this interval (Fig. III.9). The lower boundary of this geochemical interval, which represents the oxidation front, is recognized by a mismatch between the two productivity proxies (i.e., Ba/Al and TOC%). In this oxidized interval, Ba/Al values continue high, while TOC% values decrease (Fig. III.8) since OM is more susceptible to postdepositional oxidation than barite ($BaSO_4$), the main host mineral of Ba in sapropel sediments van Os and Middelburg, 1991; van Os, 1993; Nijenhuis et al., 1999; Martínez-Ruiz et al., 2000; Monedero-Contreras et al., 2023b). In this sense, the good preservation of biogenic barite in EM sediments have allowed the recognition of "ghost sapropels", which correspond to sapropel layers that have undergone total OM oxidation (Higgs et al., 1994; Wehausen and Brumsack, 2000).

The extent of the oxidized interval is closely related with bioturbation since it has been demonstrated that bioirrigation plays an important role in postdepositional oxidation of organic-rich sediments (Tribovillard et al., 2008; Löwemark et al., 2006). When deep-water circulation reactivates and oxic conditions returned to bottom-waters, opportunistic organisms (e.g., *Chondrites*-producers; recognized in sapropel layers Fig. S16 in Sup. mat.) colonize the substrate and stimulate bioirrigation (Löwemark et al., 2006). This promotes (i) deeper and more efficient penetration of oxygenated water in the sediments and (ii) dissolution of mineral phases that host RSTMs (Figs. III.10 and 12). Dissolved RSTMs diffuse from the oxidized interval back to the water-column and downward below the sapropel where they reprecipitate as anoxic/euxinic conditions still exist (Zheng et al., 2002; McManus et al., 2005; Tribovillard et al., 2006, 2008). Evidence of this postdepositional process is the isolated U enrichments below the organic-rich S1 sediments at the Mediterranean Ridge and Eratosthenes Seamount, where U (mainly hosted in association with OM) experienced downward migration and reprecipitation due to intense bioirrigation during bottom-water reventilation. (Fig. III.4).

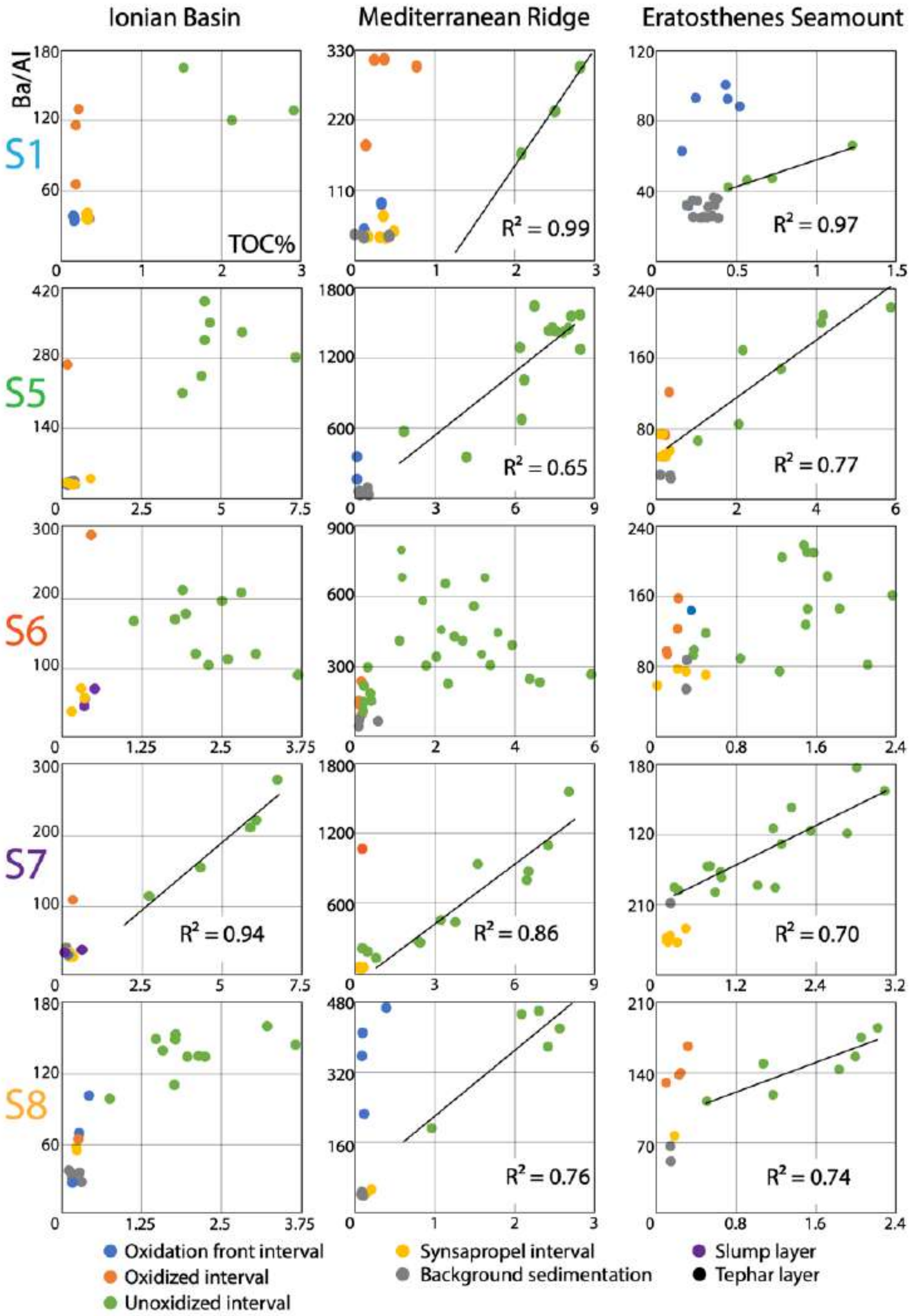

Figure III.8. Ba/Al (ppm/%; x10^{-4})-TOC% cross-plots of sampled sapropels (S1, S5, S6, S7, S8) at the three EM locations. Redox geochemical intervals are illustrated with different colors. Correlation coefficients (R^2) are shown in sapropels that have R^2 > 0.6. Dashed lines indicate the original TOC% prior to the oxidation according to the obtained correlation slope. y-axis: Ba/Al, x-axis: TOC%.

If bottom-water reventilation/reoxygenation occur progressively, passing from strong reducing conditions (euxinia/anoxia) to weak reducing conditions (dysoxia/suboxia), a preferential enrichment of V over U and Mo can occur on the top of the sapropel, as occurs on the top of S5 at the Ionian Basin (Fig. III.5). This is based on the fact that V can precipitate in weak reducing conditions, where neither Mo nor U authigenic enrichment occurs (Tribovillard et al., 2006). However, in most cases, sapropel termination seems to occur abruptly, i.e., with a synchronous drop in RSTMs. Furthermore, if a slump or tephra layer is immediately deposited on the top of a sapropel layer, it can act as “redox shield” that prevents oxygenated water to efficiently reach the underlying organic-rich sediments (Filippidi et al., 2016). This probably occurred in sapropels where slumps and tephra layers where recognized (e.g., S6 at the Ionian Basin and the Mediterranean Ridge; Fig. III.6).

- *Unoxidized interval*. This interval is characterized by the highest TOC and barite content in the sapropel sequence (Fig. III.8), and by the high and coeval enrichment of RSTMs and DOPt. Furthermore, anoxic/ euxinic porewater promote the dissolution of Mn-oxyhydroxides in this interval (see S5 at Site 966 and S7 at the three sites; Figs. III.5 and 6) (Monedero-Contreras et al., 2023b). This is corroborated in the Mo/ Al - Mn/Al cross-plots, where the data points belonging to the unoxidized interval tend to be impoverished in Mn (Fig. III.7). However, the rest of RSTMs, mainly associated to iron sulfides, did not suffer evident postdepositional oxidation or dissolution (Fig. III.10). Therefore, this geochemical interval is the most reliable for elucidating the syndepositional redox conditions during deoxygenation events and the most suitable for redox thresholds calibration. The high Mo concentrations in unoxidized sediments (over 200 ppm; Fig. III.2), principally at the two deep-marine settings, can be explained by intense particulate-shuttling that enhanced Mo transfer from the water-column to the seafloor, where is liberated in porewaters as MoO_4^{2-} . The molybdate ion is transformed to thiomolybdates in the presence of free H_2S/HS^-, where is finally fixed in association with sulfides (Berrang and Grill, 1974; Crusius et al., 1996; Helz et al., 1996; Zheng et al., 2000; Morford et al., 2005; Scholz et al., 2013, 2017).

The correlative enrichment of DOPt and Fe with Mo, Cu, Co, Ni, Pb, and to a lesser extent with Zn and Cr in this geochemical interval, suggest that these RSTMs precipitated in association with iron sulfides (i.e., pyrite) or by forming their own sulfides, which only occurs in successive sulfidation reactions that require persistent sulfidic conditions in pore-waters (Tribovillard et al., 2006). However, the PCA scatterplots show that in EM sediments Pb and Cr are strongly enriched in the detritic fraction. Accordingly, their enrichments in the unoxidized interval in sapropels characterized by large fluvial inputs from the Nile River such as S5 and S7 (Gallego-Torres et al., 2010; Wu et al., 2018), derive from the (i) increased detritic input and (ii) enhanced authigenic sulfides precipitation during euxinia.

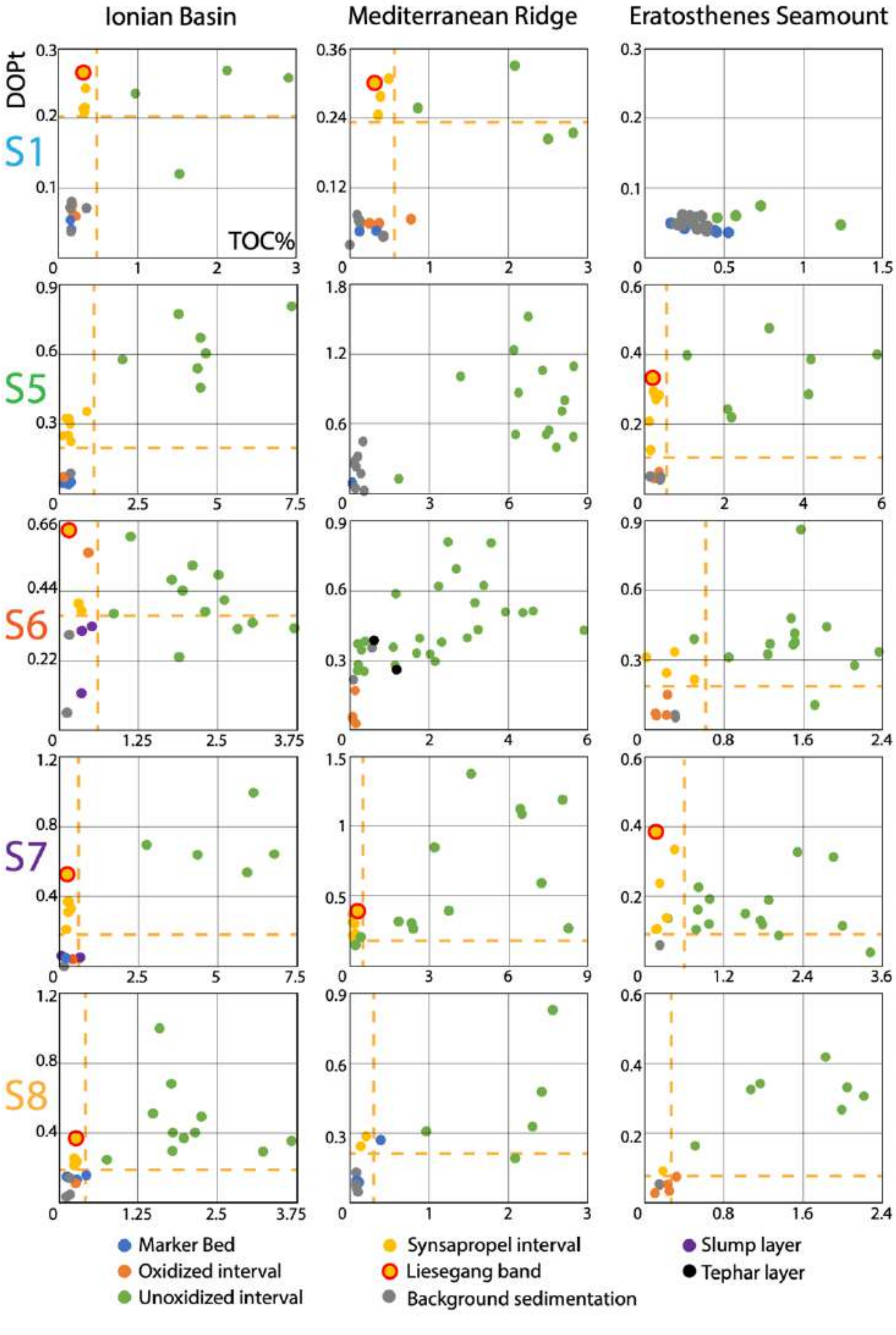

Figure III.9. *DOPt-TOC% cross-plots of sampled sapropels (S1, S5, S6, S7, S8) at the three EM locations. Redox geochemical intervals are illustrated with different colors. Yellow dashed lines are shown to delimit the high DOPt and TOC% values associated to the unoxidized interval from the high DOPt values with low TOC% associated to the synsapropel interval. y-axis: DOPt, x-axis: TOC%.*

Many sapropels in the unoxidized interval have linear regression coefficients over 0.65 ($r^2 \geq 0.65$) between Ba/Al and TOC%, emphasizing the good correlation and sometimes exceptional ($r^2 \geq 0.8$) between preserved OM and barite content (Fig. III.8). This supports that (i) Ba enrichment in sapropel sediments is indeed related to biogenic barite (Martínez-Ruiz et al., 2000), and (ii) that the increased production of OM aggregates during sapropel deposition may have played a vital role in preserving pelagic barite crystals as they sink through the oxygen-depleted water-column, even in deep-EM settings, such as the Ionian Abyssal plain, where the prolonged transit time to the seafloor makes barite crystals more susceptible to dissolution (Light et al., 2023). Furthermore, the positive linear correlation of Ba and OM supports that barite content in sapropels have not been significantly affected by diagenetic dissolution during porewater euxinia since this would have resulted in an evident Ba impoverishment in respect to TOC (Paytan et al., 2004). Passier et al. (1997) reported $\delta^{34}S$ pyrite values from − 37.3‰ to − 38.2‰ in S1 sapropel, indicating that SO_4^{2-} reduction took place in an open system with seawater exchange. Thus, the porewater sulfate-reduction did not lower sulfate concentrations enough for barite dissolution and remobilization of Ba (Martínez-Ruiz et al., 2000). The preservation of biogenic barite was also corroborated by SEM observations of barite crystals in different geochemical intervals of S1 (Fig. S15 in Sup. mat.), including the unoxidized interval which was under permanent anoxic conditions. However, this is not the case in other organic-rich deposits derived from high carbon export and low bottom-water oxygen, where sulfate-reducing conditions in the bottom-water and porewater promoted the dissolution of barite crystals (McManus et al., 1994, 1998). Dissolved barium can reprecipitate as euhedral diagenetic barite at the sulfate methane transition zone (SMTZ), as occurs in Paleozoic organic-rich strata (Torres et al., 1996; Grema et al., 2022) or above the oxidation front as occurs in modern Black Sea sediments (Henkel et al., 2012).

- *Synsapropel interval*. According to the DOPt-TOC% cross-plots, DOPt verticals plots and SEM images, many sapropels have pyrite enrichments below the organic-rich sediments (Figs. III.9 and 10). The precipitation of pyrite below some sapropels is controlled by the reaction of downward HS^- fluxes with the upward diffusing Fe from underlying sediments (Fig. III.12) (Passier et al., 1996). Sulfate reducing bacteria degrade the OM in the overlying organic-rich sediments and produce HS^-. If reactive iron (Fe_{HR}) in the unoxidized interval is exhausted by the formation of iron sulfides (principally pyrite) and HS^- production by sulfate reducing bacteria is greater than the up-ward Fe^{2+} flux, the excess of HS^- will diffuse out of the sapropel (Fig. III.10). The excess of HS^- can diffuse back to the water-column where it contributes to bottom-water euxinia or diffuse downwards below the organic-rich sediments, up to 20 cm below the unoxidized interval, where it promotes the precipitation of large pyrite framboids as large euhedral aggregates (>20 μm), principally into foraminifera chambers (Fig. III.10a), producing the so called "synsapropel interval" (Berner, 1970; Passier et al., 1996, 1997; Zhang et al., 2014; Liu et al., 2019). The precipitation of large pyrite aggregates probably occurs in confined euxinic microenvironments or microniches, as the ones facilitated by the foraminifera shells (Tribovillard et al., 2008). Certain pyrite aggregates underwent the formation of euhedral regrowths displaying a distinct "sunflower" texture (Fig. III.10a). Such textures are typically associated with late diagenesis processes (Lin et al., 2016; Chang et al., 2022). Similar pyrite textures have been observed at the paleo-SMTZ (submarine methane seepage zone) in select Paleozoic formations (Grema et al., 2022).

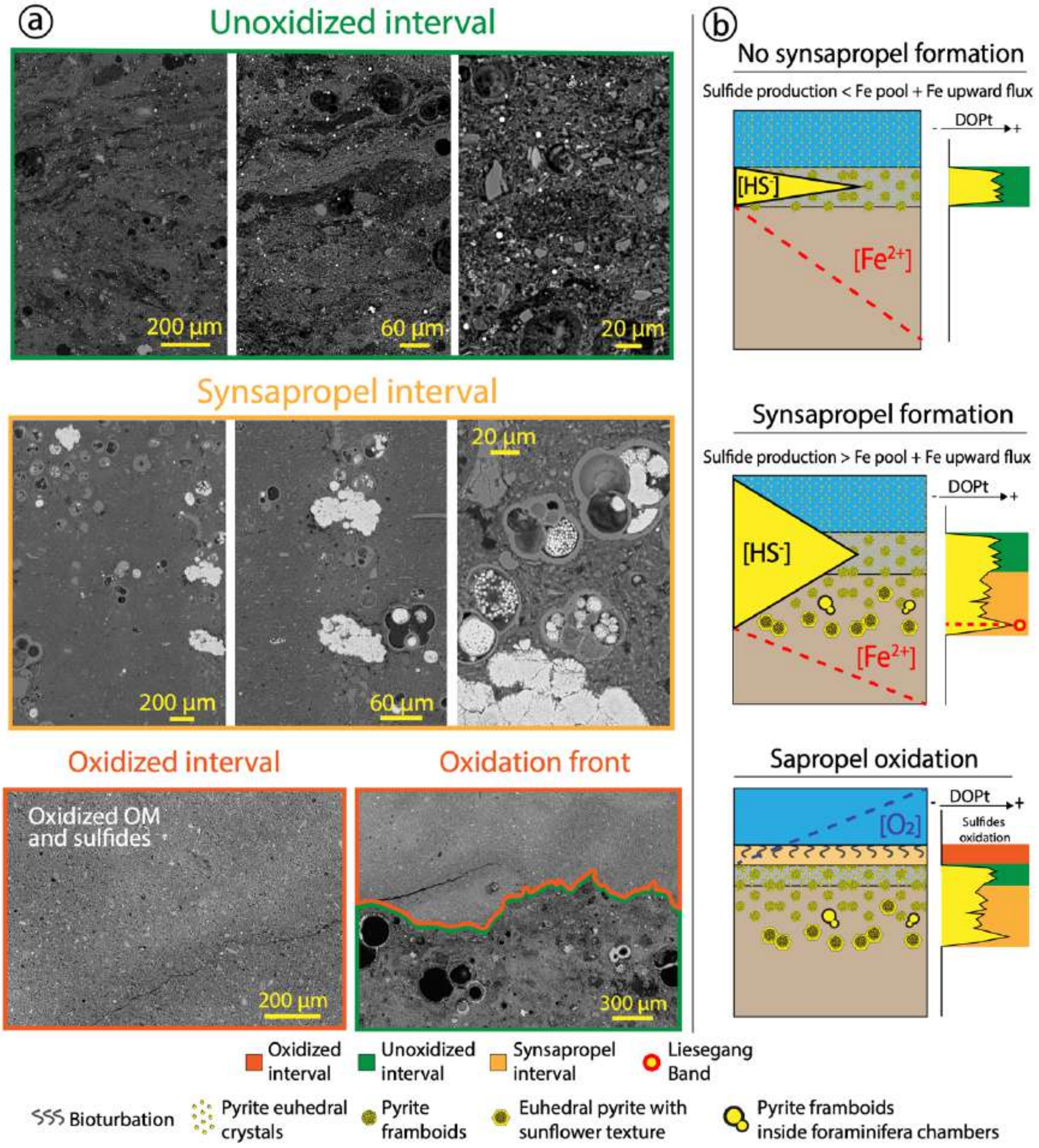
ⓐ
Unoxidized interval
200 µm
60 µm
20 µm
Synsapropel interval
20 µm
200 µm
60 µm
Oxidized interval
Oxidation front
Oxidized OM and sulfides
200 µm
300 µm
ⓑ
No synsapropel formation
Sulfide production < Fe pool + Fe upward flux
DOPt
[HS-]
[Fe2+]
Synsapropel formation
Sulfide production > Fe pool + Fe upward flux
DOPt
[HS-]
[Fe2+]
Sapropel oxidation
DOPt
[O2]
Sulfides oxidation
Oxidized interval
Unoxidized interval
Synsapropel interval
Liesegang Band
Bioturbation
Pyrite euhedral crystals
Pyrite framboids
Euhedral pyrite with sunflower texture
Pyrite framboids inside foraminifera chambers

Figure III.10. *Sample from sapropel S1 at the Ionian Basin (Site 964) (a) SEM images using backscattered electron detector (BSD) at different scales from different sapropel intervals (oxidized, unoxidized and synsapropel). Note that the oxidized interval shows no OM or pyrite crystals, the unoxidized sapropel interval shows small and scattered pyrite framboids and irregular OM laminae, and the synsapropel interval presents large pyrite framboids, principally inside foraminiferal shells, large euhedral pyrite crystals and no OM laminae. (b) Synsapropel formation scheme modified from Passier et al. (1997) showing expected DOPt signal (i) in subsaturated HS^- systems, (ii) in oversaturated HS^- system, and (iii) in oxidized sapropels. Different redox geochemical intervals are illustrated with different background colors in the simplified DOPt trends (green: unoxidized interval, dark yellow: synsapropel interval, orange: oxidized interval).*

If a synsapropel interval is absent, as occurs in S8 at the Ionian Basin (Fig. III.6), in S1 at Eratosthenes Seamount (Fig. III.4) and in S5 at the Mediterranean Ridge (Fig. III.5), we can infer that during its deposition and early diagenesis, the production of HS^- by sulfate reducing bacteria never exceeded the sum of the upward Fe^{2+} flux and the Fe_{HR} pool in the organic-rich sediments (Fig. III.10) (van Os and Middelburg, 1991; Passier et al., 1996, 1997). Therefore, a lack of synsapropel suggest that Fe_{HR} did not act as a limiting factor for pyrite precipitation and HS^- did not effectively diffuse out of the organic-rich sediments. Conversely, if a synsapropel interval exists, we can infer that: (i) Fe_{HR} acted as the limiting factor for pyrite precipitation in the organic-rich sediments, and (ii) HS^- downward diffusion exceeded the upward Fe^{2+} flux (Fig. III.10b). In respect to the timing of the synsapropel interval formation, downward sulfidisation developed as soon as the HS^- production exceeded the Fe availability for pyrite formation within the sapropel. Therefore, the formation of the synsapropel interval occurred during sapropel deposition and not before as suggested by its relative position in the sedimentary record (Passier et al., 1997).

In sapropels that developed a synsapropel interval, two different situations can be distinguished according to the patterns observed in DOPt vertical profiles. In the first situation the system remains HS^- dominated and the DOPt profile in the synsapropel interval shows a broad increase, but with no marked DOPt peaks (e.g., S5 at the Ionian Basin and S6 at Eratosthenes Seamount; Figs. III.5 and 6). In the second situation, at the lower boundary of a synsapropel interval, DOPt and Fe/ Al profile exhibit a peak recognized in previous studies as “Liesegang band” (Berner, 1969; Passier et al., 1996; Bektursunova and L’Heureux, 2011). In this band, DOPt can reach higher values than in the unoxidized interval, as occurs in S1, S6 and S7 at the Ionian Basin, in S5 and S7 at Eratosthenes Seamount and in S1 and S5 at the Mediterranean Ridge (Fig. III.9) (Berner, 1970; Passier et al., 1996, 1997). The Liesegang band indicates the stratigraphic position where the downward HS^- flux was balanced with the upward Fe^{2+} flux diffusing from the dissolution of Fe-oxides in the underlying sediments (Fig. III.10) (Berner, 1970; Passier et al., 1996, 1997).

Furthermore, the DOPt vertical plots indicate that Mo and to a lesser extent other RSTMs (e.g., Co, Cu, Ni, Cr, Zn and Pb) precipitated in association with iron sulfides in the synsapropel interval or were trapped by pyrite aggregates through surface absorption, creating in this way sub-mm RSTMs enrichments (Fig. III.7). Mo is the most efficiently trapped RSTM by the pyrite aggregates during early diagenesis (Tribovillard et al., 2008; Monedero-Contreras et al., 2023b) also noted that. These enrichments are more marked in the Liesegang bands where pyrite precipitation is more intense and present large recrystallized euhedral crystals with “sunflower” texture (Merinero et al., 2017; Chang et al., 2022). These types of syndepositional enrichment of RSTMs below the organic-rich sediments occurred in S1 at the Ionian Basin and the

Mediterranean Ridge and in S5 at Eratosthenes Seamount (Figs. III.4 and 5), as also observed by Filippidi and de Lange (2019) in S1 in deep and intermediate EM settings.

III.6.2. Redox thresholds calibration

The establishment of geochemical intervals in sapropel layers allowed the recognition of altered samples due to postdepositional processes (e.g., oxidation, bioirrigation, downward sulfidisation, etc.) that have affected the syndepositional concentration of the RSTMs. As previously stated, during sapropel termination Mn-oxyhydroxides precipitate and absorb RSTMs, such as Mo, Co, Cu and Ni, which then creates TMs enrichments that are not associated to oxygen-depleted conditions (Tribovillard et al., 2008; Filippidi and de Lange, 2019). In this regard, only samples corresponding to the unoxidized interval were incorporated into the calibration plots, considering that this particular interval is less affected by postdepositional processes and preserved better the syndepositional enrichments of RSTMs. It is worth mentioning that Pb_{EF} and Cr_{EF} did not present a marked enrichment in the calibration plots at any location (see Sup. mat.), inhibiting the calibration of the authigenic enrichment threshold. This is probably due to the fact that Pb and Cr enrichment in the unoxidized interval is not only in association with increased sulfides content, but also in association with increased detrital minerals content, as corroborated by the PCA geochemical fractions.

The calibrated redox proxies show identical values for all three redox thresholds (T1 = T2 = T3; Fig. III.11b), making it impossible to calibrate them separately. As a result, the values obtained from T1 and T2 correspond to the T3 value, which represents the anoxic-euxinic threshold. This indicates abrupt redox transitions in EM deep-waters during sapropels onsets and terminations. Such abrupt redox transition towards anoxic/euxinic EM bottom-waters promoted a synchronous co-precipitation of V, U and Mo, while inhibiting a progressive and preferential enrichment of V and U over Mo (Algeo and Li, 2020). This finding goes in agreement with previous studies that state a rapid onset of oxygen-depleted conditions in deep and intermediate EM settings (de Lange et al., 2008; Azrieli-Tal et al., 2014; Tesi et al., 2017; Filippidi and de Lange, 2019; Andersen et al., 2020; Zirks et al., 2019, 2021). The abrupt establishment of euxinic conditions is further supported by the synchronic and abrupt co-enrichment of Mo with U, V and other RSTMs observed in the vertical plots (Figs. III.4, 5 and 6) and by the linear covariation between Mo, U and V ($r^2 \geq 0.5$ and ≤ 0.8; see Sup. mat.).

Comparing the redox threshold values obtained for each EM deep-marine setting enables to assess local hydrogeographic factors on RSTMs uptake/burial rates. Among the three locations, the Mediterranean Ridge consistently exhibits higher redox thresholds values, while the Ionian Basin exhibit the lowest values (Fig. III.11; for detailed data see Sup. mat.). This indicates that the background concentrations of RSTMs are higher in the Mediterranean Ridge sediments (Fig. III.11b). Therefore, the authigenic enrichment of RSTMs due to euxinic conditions begins at lower concentrations in the Ionian Basin than in Eratosthenes Seamount and Mediterranean Ridge. Consequently, redox thresholds values differ between locations (Fig. III.11b). Moreover, this might suggest that the Ionian Abyssal plain is more prone to develop sulfidic bottom-waters due to rapid onset of deep-water stagnation since the T3 threshold is crossed at lower RSTMs concentrations. The highest redox thresholds values are found at the Mediterranean Ridge and could be associated to more vigorous particulate-shuttling and efficient RSTMs scavenging. Enhanced particulate-shuttling boosts trace metal transfer from the water-column, as occurs in the modern Black Sea (Dellwig et al., 2010; Algeo and Li, 2020). Therefore, intense particulate-shuttling promotes higher RSTMs concentrations in deep-marine sediments, and subsequently higher authigenic uptake rates. These findings go in accordance with Warning and Brumsack (2000) data, who also compared geochemical from different EM deep sites and stated that not only water-depths plays a key role on RSTMs authigenic enrichment, since they observed that EM sites with very different water-depths developed similar RSTMs enrichment. Moreover, our findings align with the Fernández-Martínez et al. (2023), who demonstrated that despite the global-scale impact of the T-OAE event, the local oceanographic and environmental features of each Toarcian basin were the main controls in the development of bottom-water euxinia.

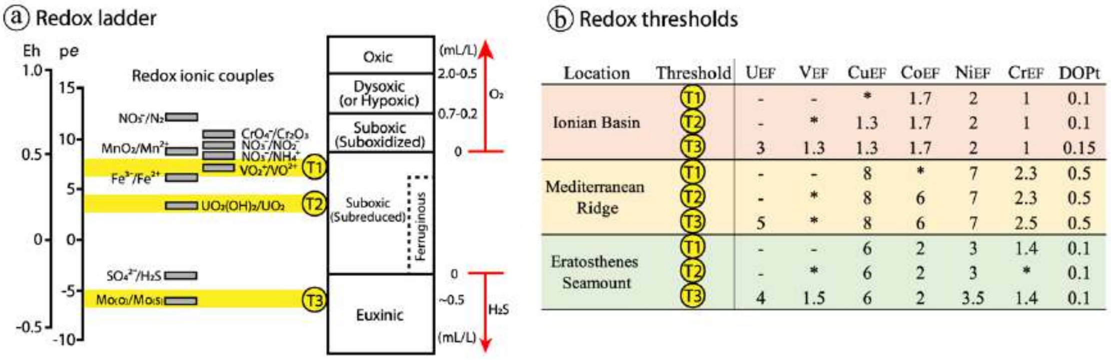

Location	Threshold	U_{EF}	V_{EF}	Cu_{EF}	Co_{EF}	Ni_{EF}	Cr_{EF}	DOPt
Ionian Basin	T1	-	-	*	1.7	2	1	0.1
	T2	-	*	1.3	1.7	2	1	0.1
	T3	3	1.3	1.3	1.7	2	1	0.15
Mediterranean Ridge	T1	-	-	8	*	7	2.3	0.5
	T2	-	*	8	6	7	2.3	0.5
	T3	5	*	8	6	7	2.5	0.5
Eratosthenes Seamount	T1	-	-	6	2	3	1.4	0.1
	T2	-	*	6	2	3	*	0.1
	T3	4	1.5	6	2	3.5	1.4	0.1

Figure III.11. *(a) Modified redox ladder scheme from Algeo and Li (2020) and Algeo and Liu (2020). Redox potentials (Eh) and electron activities (pe) of redox ionic couples at pH 7 are presented in the redox ladder. The yellow fields (T1, T2 and T3) represent the redox thresholds. (b) Table showing the redox thresholds values for different redox proxies at the three studied sites. (*) denotes where simple covariation pattern (i.e., co-enrichment) impeded redox thresholds calibration.*

While these redox thresholds values cannot be considered quantitative values, the observed variability among sites demonstrates that RSTMs concentration in marine sediments is not solely determined by bottom-water redox conditions and water-depth (Warning and Brumsack, 2000). Instead, RSTMs concentration can exhibit significant variations across oceanographic settings with equivalent redox conditions due to differences in particulate-shuttling intensity, bottom-water renewal frequency, fluvial input, and source material composition. This is supported in prior studies which conducted comparative analyses and empirical assessment of diverse anoxic to euxinic basins characterized by distinct oceanographic attributes, both in modern and ancient oceans, using geochemical cross-plots (e.g., U_{EF} - Mo_{EF} and RSTMs - TOC), to elucidate the main factors that control the enrichment of RSTMs in marine environments (Algeo and Lyons, 2006; Algeo and Maynard, 2004; Algeo and Tribovillard, 2009; Lyons et al., 2009; Algeo and Li, 2020; Algeo and Liu, 2020). Additionally, Tribovillard (2021), indicates that the geochemical properties of the sediment, such as availability of Fe_{HR} in the porewater and the rate of OM decomposition within sediments seem to also affect the authigenic enrichment rate of RSTMs, especially RSTMs that are strongly scavenged by OM, such as Ni and Cu. Overall, our results in conjunction with prior studies outline the importance of considering local hydrogeographic and environmental factors and geochemical properties of the sediments, since the interplay of these factors control the authigenic enrichment rate of TMs in organic-rich sediments that recorded past deoxygenation event, such as black shales or sapropels. This supports Algeo and Li (2020), who highlight the need for internal calibration for each individual depositional system in order to consider local variability and achieve more robust redox interpretations of RSTMs.

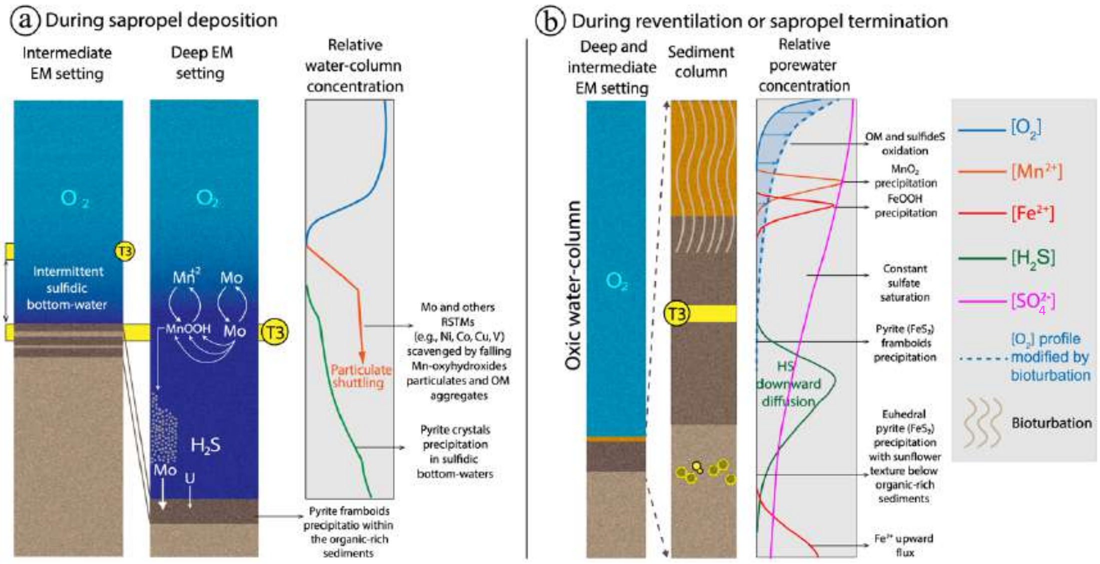
a
During sapropel deposition
Intermediate EM setting
Deep EM setting
Relative water-column concentration
O2
O2
T3
Intermittent sulfidic bottom-water
Mn+2
Mo
MnOOH
Mo
T3
H2S
Mo
U
Particulate shuttling
Mo and others RSTMs (e.g., Ni, Co, Cu, V) scavenged by falling Mn-oxyhydroxides particulates and OM aggregates
Pyrite crystals precipitation in sulfidic bottom-waters
Pyrite framboids precipitatio within the organic-rich sediments
b
During reventilation or sapropel termination
Deep and intermediate EM setting
Sediment column
Relative porewater concentration
Oxic water-column
O2
T3
HS downward diffusion
OM and sulfideS oxidation
MnO2 precipitation
FeOOH precipitation
Constant sulfate saturation
Pyrite (FeS2) framboids precipitation
Euhedral pyrite (FeS2) precipitation with sunflower texture below organic-rich sediments
Fe2+ upward flux
[O2]
[Mn2+]
[Fe2+]
[H2S]
[SO42-]
[O2] profile modified by bioturbation
Bioturbation

Figure III.12. *Redox schemes based on Passier et al. (1996), Algeo and Tribovillard (2009) and Canfield and Thamdrup (2009), showing redox ions profiles: (a) during sapropel deposition in intermediate and deep-marine settings, and (b) during reventilation events or sapropel termination. Ion water-column profile for deep-marine settings is based on the modern Black Sea water-column chemical profile from Canfield and Thamdrup (2009).*

III.6.3. Paleoenvironmental analysis of sapropel events

A number of conclusions regarding the paleoceanographic and paleoenvironmental conditions that ruled each sapropel event can be pointed in the light of previous studies. According to the Mo enrichments, deep-marine settings in EM developed sulfidic porewaters during all sapropel events; however, not all of them developed perennial sulfidic bottom-waters. The stability of sulfidic bottom-waters is controlled by the intensity of surface water freshening and productivity rate (Monedero-Contreras et al., 2023a). In this sense, sapropels with intense surface water freshening due to strong African monsoons (e.g., S5 and S7) are the ones that developed the most perennial sulfidic bottom-waters (Wu et al., 2018; Sweere et al., 2021). This is corroborated in this study, where S5 and S7 show the strongest oxygen depletion and highest productivity rates among the five studied sapropels. Moreover, in S5 and S7 the marker bed is less evident and in some cases absent (Figs. III.5 and 6), indicating weak postdepositional oxidation probably due to higher sedimentation rates (higher fluvial inputs) and less vigorous reventilation. However, during S7 deposition at the Mediterranean Ridge, two ventilation events seem to have occurred during its deposition, as suggested by two correlative decreases in RSTMs concentrations in S7 unoxidized interval at Eratosthenes Seamount and Mediterranean Ridge (Fig. III.6).

Conversely, in sapropels associated to weaker African monsoons, such as sapropels S1 and S8, redox proxies in the unoxidized interval indicate weaker oxygen depletion than during S5, S6 and S7 due to weaker surface water freshening and lower productivity rates (Gallego-Torres et al., 2007a, 2007b; Rohling et al., 2015; Sweere et al., 2021; Monedero-Contreras et al., 2023a). However, vigorous and abrupt reventilation and oxygenation of bottom-waters during S1 and S8 termination is evidenced by abrupt marker beds (Figs. III.4 and 6). In S1 layer at Eratosthenes Seamount (the shallowest setting), two Mn/Al peaks and associated Mo enrichments are observed (Fig. III.4). The upper Mn/Al peak was produced during S1 termination by intense reventilation, while the lower Mn/Al peak is still diagenetically forming due to downward migration of the current oxidation front where dissolved upward diffusing Mn^{2+} from the underlying anoxic sediments is reprecipitating as Mn-oxyhydroxides (van Santvoort et al., 1996; Filippidi and de Lange, 2019). Regarding sapropel S8, intense reventilation during its termination is only registered in the two deepest sea settings (i.e., Ionian Basin and Mediterranean Ridge), but not at Eratosthenes Seamount (Fig. III.6). This might occur because during S8, at Eratosthenes Seamount, bottom-waters were mainly under suboxic conditions, which did not allow intense Mn redox cycling in the overlying water-column and the subsequent massive precipitation of Mn-oxyhydroxides. However, intermittent and brief porewater euxinia at Eratosthenes Seamount needs to be evoked to explain the Mo enrichments in the unoxidized interval. This goes in agreement with Zirks et al. (2021) who state that intermediate EM settings during sapropels can develop bottom-water euxinia due to expansion of the Oxygen Minimum Zones.

S6 is an interesting sapropel since it was deposited during glacial period with lower sea-level. Its vertical plots present irregular and spiny trends (like a tooth-saw) in the redox and productivity proxies at the three locations. Key redox proxies (Mo_{EF}, U_{EF}, V_{EF} and DOPt) and productivity proxies (TOC% and Ba/Al) show correlative fluctuating trends within the unoxidized interval. Zr/Al and K/Al in S6 show abrupt changes in aeolian and fluvial input which indicates variable climatic conditions, which supported unstable hydrographic regime with strong productivity changes and redox fluctuations (Fig. III.6). S6 is the sapropel that presents the highest Mo concentration at the three locations, even though it is not associated to the strongest deep-water deoxygenation (Gallego-Torres et al., 2007a; Sweere et al., 2021). This could be associated to a more intense particulate-shuttling and a fluctuating chemocline that promoted frequent Mo resupply to bottom-waters and “Mo burial pumps” as occurs in the modern restricted Cariaco Basin and Saanich Inlet (Jacobs et al., 1985; Crusius et al., 1996; Algeo and Tribovillard, 2009; Monedero-Contreras et al., 2023a).

III.7. Conclusions

This study highlights the importance of improving our understanding of geochemical signals derived from redox transitions. The following findings contribute to the further understanding and interpretation of the paleoenvironmental significance of geochemical signals in sedimentary environments associated with regional-scale deoxygenation events in deep-marine settings:

1) By analyzing the large geochemical dataset obtained from different EM locations representing diverse oceanographic regimes, it is suggested that certain trace elements such as Mo, V, U, Co, and Ni are more reliable as redox proxies compared to other redox sensitive elements such as Cr, Cu, Pb, and Zn, since they show weaker detritic influence.

2) This study demonstrates the need for a precise understanding of postdepositional processes for accurate interpretations of geochemical signals, and subsequently a robust paleoenvironmental analysis since postdepositional remobilization can produce RSTMs enrichments above and/or below the organic-rich sediments. For example, caution must be exercised when interpreting Mo signals, as it has been demonstrated that dissolved Mo to can be readily scavenged by pyrite aggregates and Mn-oxyhydroxides during early diagenesis. Similarly, caution is necessary when considering U signals due to the potential downward migration of the syndepositional signal caused by intense bioirrigation.

3) The calibration plots and the synchronous enrichment of V, U, Mo, and other RSTMs in the vertical profiles provide support that deoxygenation in EM deep-marine settings during sapropel onsets occurred abruptly. Furthermore, the calibration plots underscore the significant influence of local environmental conditions (e.g., productivity rate) and

hydrogeographic features (e.g., water-depth, sedimentation rate, and particulate-shuttling intensity) in governing the authigenic rates of RSTMs by seafloor sediments and determining the redox thresholds of geochemical proxies. In this sense, deep-marine settings characterized by intense particulate-shuttling appear to exhibit higher redox threshold values (e.g., Mediterranean Ridge), whereas deep-marine settings with weaker particulate-shuttling and more prone to abrupt and early bottom-water stagnation seem to lead to lower redox thresholds values (e.g., Ionian Basin).

Overall, these findings demonstrate that a careful consideration of postdepositional processes and local hydrogeographic factors is essential for an accurate understanding and interpretation of geochemical signals derived from regional-scale deoxygenation events in deep-marine settings. Such findings are therefore crucial in advancing our understanding of past and present deoxygenation dynamics, contributing to better forecasting and management of marine environments facing the challenge of increasing marine deoxygenation.

Supplementary material

Supplementary data to this article can be found online at:
https://ars.els-cdn.com/content/image/1-s2.0-S0031018223005710-mmc1.pdf

Acknowledgments

This study has been funded by Grants PID2019-104624RB-I00, PID2019-104625RB-100, and TED2021-131697B-C22 funded by MCIN/ AEI/ 10.13039/501100011033, Grants FEDER/Junta de Andalucía P18- RT-3804 and P18-RT-4074, and by Research Groups RNM-179 and RNM-178 funded by Junta de Andalucía. We thank Prof. Adatte from Lausanne University (Switzerland) for Rock-eval analyses and TOC measurements. We are also grateful to the Center for Scientific Instrumentation (CIC, University of Granada) and the XRF Unit of the IACT (CSIC-UGR) for the ICP and XRF analyses, respectively. We are grateful to the Ocean Drilling Program for providing the analyzed samples as well as to the ODP Core Repository (Bremen, Germany) for assistance with sampling. We thank the Editor, Dr. Paul Hesse, and the two anonymous reviewers for their detailed and useful comments that significantly contributed to improve the manuscript. This study is part of R. Monedero PhD project.

Chapter IV

Evidence of postdepositional remobilization of redox-sensitive metals across sapropel boundaries: New insights from LA-ICP-MS and EDX mapping analyses

Ricardo D. Monedero-Contreras, Francisca Martínez-Ruiz, Francisco J. Rodríguez-Tovar

Chemical Geology 636 (2023) 121643
doi: 10.1016/j.chemgeo.2023.121643

Abstract

Deoxygenation in marine systems is globally increasing due to anthropogenic pressures and climate change impacts, leading to significant ecological and environmental consequences. Understanding past deoxygenation events is crucial for assessing the response of ocean stressors to climate variability and for predicting and managing the impacts of current and future changes. Deep-marine basins with organic-rich deposits serve as valuable palaeoarchives, preserving evidence of profound palaeoceanographic changes involving deoxygenation events. Such events have been broadly studied and reconstructed using redox-sensitive trace metals (RSTMs) as proxies for oxygenation conditions. Assessing these proxies is therefore crucial for further understanding deoxygenation events. To do so, this study focuses on RSTMs distribution across the most recent sapropel, S1, which is a well-preserved organic-rich sediment layer that represents the most recent large-scale deoxygenation event in the Eastern Mediterranean. High-resolution geochemical microanalyses, including Laser Ablation ICP-MS and SEM-EDX, were conducted to investigate sub-mm scale geochemical signals and post-depositional remobilization of RSTMs within S1 and surrounding sediments. Statistical analyses have also helped to identify the geochemical fractions within S1, including detritic, carbonate, and authigenic, enriched in RSTMs and organic matter. The study revealed distinct specific geochemical intervals, such as the marker bed, oxidized interval, unoxidized interval, and synsapropel interval. These intervals provided insights into the diagenetic processes and post-depositional reactions occurring within and across sapropel S1 boundaries. The enrichment of RSTMs within pyrite aggregates in the synsapropel interval was primarily attributed to post-depositional processes rather than the initial syndepositional conditions of S1. Large pyrite surfaces below S1 and the precipitation of Mn-oxyhydroxides over S1 played a significant role in the fixation and absorption of dissolved RSTMs derived from postdepositional oxidation. Furthermore, the sub-mm scale analysis revealed spatial heterogeneities in mineralogical composition and elemental distribution, providing valuable information on the complexity of post-depositional reactions and processes. The findings highlight the importance of microscale geochemical analyses for understanding the dynamics of RSTM fixation and enrichment processes in marine sediments. By differentiating between syndepositional and post-depositional geochemical signals, this study contributes to the interpretation of palaeoenvironmental conditions and enhances our understanding of the spatial complexity of deoxygenation processes. Such insights are crucial for accurately assessing the impacts of deoxygenation on biogeochemical cycling and ecosystem functioning in marine environments.

IV.1. Introduction

Global warming and anthropogenic pressure are inducing deoxygenation in many marine systems around the world, leading to a four-fold increase in the volume of anoxic ocean waters since the 1960s (Stocker et al., 2013; Breitburg et al., 2018). Deoxygenation boosts ocean acidification and alters biogeochemical cycles, posing threats to marine ecosystems and the dependent organisms and human populations (Keeling et al., 2010; Schmidtko et al., 2017; Levin, 2018). Past deoxygenation events have played a crucial role in shaping the Earth's environmental and ecological history. This has led many scientists to study past deoxygenation events linked to past climate variability in order to obtain palaeoperspectives and gain insights into the response of ocean stressors to climate changes (Mancini et al., 2023). In this sense, organic-rich deposits in deep-marine basins are considered valuable palaeoarchives of oceanographic conditions as they preserve evidence of profound palaeoceanographic changes often linked to past climate variations and marine oxygen depletion (Hennekam et al., 2020). Therefore, they have been extensively studied using various strategies. One widely employed approach involves studying the geochemical composition of these organic-rich sediment units, and particularly assessing oxygen conditions. Specifically, changes in concentrations of redox-sensitive trace metals (RSTMs) such as Mo, U, V, Co, Ni, and Cu have been broadly utilized to assess variations in bottom-water redox conditions (Berner, 1981; Tyson and Pearson, 1991; van Os and Middelburg, 1991; Calvert and Pedersen, 1993, 2007; Crusius et al., 1996; Martínez-Ruiz et al., 2000; Warning and Brumsack, 2000; Tribovillard et al., 2006; Scheiderich et al., 2010; Little et al., 2015; Monedero-Contreras et al., 2023). The downcore variations in these metals serve as tracers of evolving oceanographic conditions, and the higher the sediment sampling resolution, the greater the temporal resolution achieved (Jilbert et al., 2008; Jilbert et al., 2010; Hennekam et al., 2015).

Regarding the resolution of palaeoceanographic reconstructions, this has significantly increased over the last decades since sub-mm analytical techniques, such Laser Ablation ICP-MS (LA-ICP-MS) and SEM energy dispersive X-ray (SEM-EDX) techniques are becoming more sophisticated and available (Sylvester and Jackson, 2016). LA-ICP-MS enables the analysis of trace elements distribution and concentration at the microscale, including diagnostic palaeoenvironmental TMs (e.g., Mo, U, V, and Ba). Similarly, SEM-EDX allows for the examination of compositional profiles and maps of major elements (e.g., Al, Fe, Ca, K, S, and Si) and mineral phases at the sub-mm scale. However, to ensure robust interpretation of sub-mm geochemical signals in high-resolution palaeoceanographic reconstructions of deoxygenation events, it is crucial to assess potential diagenetic changes that may modify the primary geochemical composition of the sediment (Filippidi and de Lange, 2019). In this sense, it is critical to differentiate at the microscale, be-tween the diagenetic and the syndepositional geochemical signals. This is the case of TMs in organic-rich deposits which often undergo diagenetic remobilization following deposition, thereby biasing and altering the original signals reflecting the syndepositional environmental conditions (Pruysers et al., 1991, 1993; Passier et al., 1996, 1997; Zheng et al., 2002; Tribovillard et al., 2006; Andersen et al., 2018; Filippidi and de Lange, 2019).

Studies on RSTMs distribution and concentration at the sub-mm scale within sapropels precise the interpretation of high-resolution past or contemporary deoxygenation events (Jilbert et al., 2008, 2010; Hennekam et al., 2015, 2020). Sapropel layers characterized by their high organic carbon content (TOC > 2%; Cita et al., 1977) are rhythmically deposited in Eastern Mediterranean (EMed) and serve as exceptional palaeoarchives of past deoxygenation events, enabling high-resolution palaeoceanographic studies (Hennekam et al., 2020). The rhythmic deposition of sapropels is controlled by astronomical precession cycles, more precisely, minimum astronomical precession cycles (Olauson, 1961; Cita et al., 1977; Kidd et al., 1978; Murat and Got, 1987; de Lange et al., 1989; Hilgen, 1991; Lourens et al., 1996; Emeis et al., 2000). Minimum astronomical precession periods pro-moted maximum insolation in the northern hemisphere, resulting in the intensification and northward migration of the African monsoon. This, in turn, led to increased freshwater and nutrient input into the EMed, causing bottom-water stagnation and enhanced productivity (Rossignol-Strick, 1983, 1985; Ariztegui et al., 2000; Casford et al., 2003; Gallego-Torres et al., 2007a; Bout-Roumazeilles et al., 2013; Weldeab et al., 2014; Hennekam et al., 2014; Rohling et al., 2015; Wu et al., 2016, 2018; Monedero-Contreras et al., 2023).

Sapropel S1 holds particular relevance as it represents the most recent large-scale deoxygenation event in the Eastern Mediterranean, occurring between 10.5 and 6.1 ka (de Menocal et al., 2000; Grant et al., 2016). Therefore, S1 is well preserved and serves as an exceptional palaeoarchive for studying the geochemical signals derived from marine deoxygenation and associated postdepositional processes. In this sense, past studies have used S1 as a case study to assess the impact of postdepositional processes on TMs and organic matter (OM) distribution and cycling (Passier et al., 1996; van Santvoort et al., 1996, 1997; Rutten et al., 1999; Reitz et al., 2006; Filippidi and de Lange, 2019). However, to fully understand the pathways of TMs during postdepositional processes, a better comprehension of derived microscale geochemical signals in organic-rich sediments is needed. Thus, the present research uses geochemical microanalyses (e.g., LA-ICP-MS and SEM-EDX) for the recognition of sub-mm postdepositional geochemical signals and the assessment of potential remobilization of RSTMs across S1 and surrounding sediments deposited at the Ionian Abyssal Plain. The detailed assessment of S1 enables a comprehensive understanding of the biogeochemical cycling and distribution of RSTMs in deep marine sediments. This, in turn, provides crucial insights for accurately interpreting their signals in deep marine records.

IV.2. Methods and materials

IV.2.1. Study area

The Mediterranean is a semi-enclosed (restricted) marginal sea, relatively small (~2,500,00 km^2), with a water-depth over 5,000 m, and with particular features such as high evaporation rate, complex land-sea distribution and seafloor morphology, strong thermohaline circulation, and turnover timescale of about one-tenth of the global ocean's (Pinardi and Masetti, 2000; Millot and Taupier-Letage, 2005; Pinardi et al., 2015; Schroeder et al., 2016). These unique oceanographic features make the Mediterranean Sea an excellent natural laboratory highly sensitive and responsive to external forcing (e.g., astronomical oscillations and climate changes), and capable to amplify and anticipate marine responses to global climate change (Giorgi, 2006; Lionello et al., 2006; Giorgi and Lionello, 2008; Turco et al., 2015).

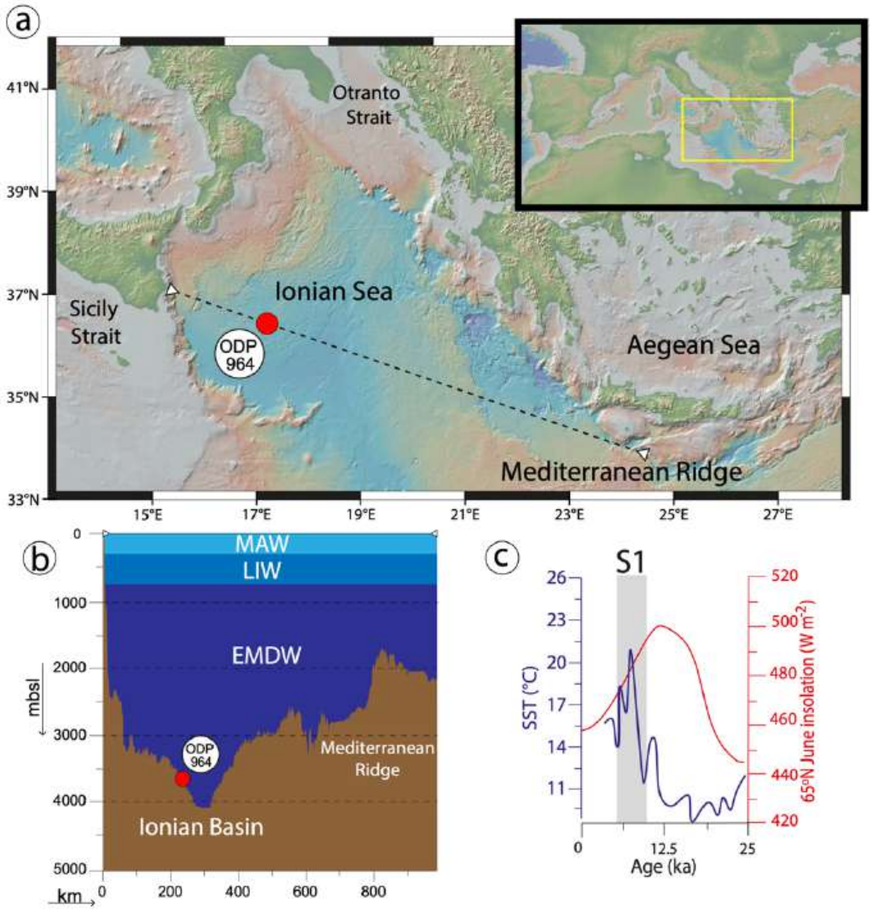
ⓐ
41°N
39°N
37°N
35°N
33°N
15°E
17°E
19°E
21°E
23°E
25°E
27°E
Otranto Strait
Sicily Strait
Ionian Sea
ODP 964
Aegean Sea
Mediterranean Ridge
ⓑ
0
1000
2000
3000
4000
5000
mbsl
km
0
200
400
600
800
MAW
LIW
EMDW
ODP 964
Mediterranean Ridge
Ionian Basin
ⓒ
S1
26
23
20
17
14
11
SST (°C)
520
500
480
460
440
420
65°N June insolation (W m^{-2})
0
12.5
25
Age (ka)

Figure IV.1. *(a) Base map generated using GeoMapApp, showing location of core 964B and the superficial expression of the bathymetric transect. (b) Bathymetric transect obtained by European Marine Observation Data Network (EMODnet) (http://www. emodnet-seabedhabitats.eu/). Location and depth of core 964B is indicated as a red circle. Depths of EMed water-masses (i.e., Modified Atlantic Water, WAW; Levantine Intermediate Water, LIW; Eastern Mediterranean Deep Water, EMDW) are indicated. (c) S1 time interval based on Grant et al. (2016) (10.5–6.1 ka). Sea surface temperature (SST) curve (dark blue line) obtained by Emeis et al. (2003) at the Mediterranean Ridge and summer insolation curve (red line) at 65∘N obtained by Laskar et al. (1993) are shown the last 25 ka.*

At present, two mechanisms control EMed circulation, wind stress and thermohaline forcing (POEM group, 1992; Malanotte-Rizzoli et al., 1999; Millot and Taupier-Letage, 2005; Amitai et al., 2018). During sapropel S1 deposition, sea-level was comparable to the present, however, water-column structure and currents dynamics were significantly different from the modern EMed (Fig. IV.1c) (Grant et al., 2014; Rohling et al., 2014, 2015; Filippidi and de Lange, 2019 and references therein). During S1 deposition, increased fresh-water input reduced surface-water salinity and enhanced surface-water buoyancy, which promoted sluggish thermohaline circulation and deep-water restriction and deoxygenation (Nolet and Corliss, 1990; Nijenhuis et al., 1999; Casford et al., 2003; Rohling et al., 2015). However, compared to previous sapropel events (e.g., S5 and S7), S1 was deposited during weaker African monsoons and lower fresh-water inputs (mainly from the Nile River) that promoted milder oxygen depletion and water-column stagnation, and lower productivity rates (Gallego-Torres et al., 2007a; Ziegler et al., 2010; Tachikawa et al., 2015; Wu et al., 2016, 2018; Sweere et al., 2021).

The studied record (ODP Leg 160964B 1H) was recovered in 1995 by the Ocean Drilling Program (ODP) during Leg 160. Site 964 (36° 15.623′N, 17° 45.000′E) is located at the Ionian Abyssal Plain representing a deep marine setting with a water-depth of 3,658 m (Fig. IV.1) (Emeis et al., 1996). This deep setting is highly influenced by Adriatic Deep-Water Outflow (ADWO) and northern Emed borderlands fresh-water input (Canals et al., 2009; Cantoni et al., 2016; Langone et al., 2016; Filippidi and de Lange, 2019), while the Nile River input has little influence due to the great distance. Overlying the Ionian Abyssal Plain, there are mainly three water-masses: (i) Modified Atlantic Water (MAW) from 0 to ~250 mbsl (meters below sea level) that come through the Strait of Sicily, (ii) Levantine Intermediate Water (LIW) from ~250 to ~900 mbsl that come from the Levantine Basin, and (iii) Eastern Mediterranean Deep Water (EMDW), which is principally formed in the Adriatic Sea (and to a lesser extent in the Aegean Sea) and occupies the rest of the water column (i.e., below ~900 mbsl) (Wüst, 1961; Miller, 1963; Astraldi and Gasparini, 1992; POEM group, 1992; Lascaratos, 1993; Sparnocchia et al., 1994; Wu and Haines, 1996; Lascaratos et al., 1999; Millot and Taupier-Letage, 2005; Amitai et al., 2018).

Sapropel layers (blackish layers) are imposed to the background sediment composition, which is mainly composed by nannofossil clay, clayey nannofossil ooze and nannofossil ooze, varying in colour from brownish to more greenish and grayish (Emeis et al., 1996, 2000). Sapropel S1 in core 964B 1H is clearly identified as a dark layer that is underlying and overlying lighter pelagic sediments.

IV.2.2. Sediment samples analyses

The sapropel interval and surrounding sediments were sampled at 2 cm resolution for discrete geochemical analyses of bulk sediment samples and for the preparation of resin-embedded thin-sections for geochemical microanalyses (i.e., at sub-mm scale).

Discrete bulk sediment samples were subjected to geochemical analysis to determine the concentrations of major, minor, and trace elements, as well as the total organic carbon (TOC) content. TMs concentrations across S1 were vertically plotted in order to recognize the different geochemical intervals and boundaries with specific environmental and diagenetic significance. Samples from the identified intervals and boundaries were selected for the preparation of resin-embedded-thin sections for geochemical analyses at sub-mm scale.

The poorly consolidated sediments were stabilized by resin embedding the 2 cm sediment samples, from which 100–120 μm thin-section were sliced. The sediment thin-section were utilized for: (i) SEM observation of sedimentary structures and minerals at sub-mm scale (with special attention to pyrite size and distribution), (ii) SEM-EDX mapping to visualize and analyze the distribution of major elements and authigenic minerals, (iii) LA-ICP-MS line-scans to determine sub-mm TMs variations across the thin-sections, and (iv) LA-ICP-MS spot-analyses for determining TMs concentrations in selected areas and minerals. This approach allowed the characterization of different geochemical signals at a sub-mm scale, enabling the differentiation between syndepositional redox signals and the diagenetic signals derived from the post-depositional remobilization of RSTMs. Additionally, statistical analyses were applied to enhance the visualization and interpretation of the geochemical data.

IV.2.2.1. Geochemical analyses

TOC content in discrete samples was measured by the Rock-Eval pyrolysis method, at the Institute of Earth Sciences (ISTE) of the University of Lausanne (UNIL). The Rock-Eval pyrolysis method consisted on heating the samples from 200 °C to 850 °C in successive steps in a pyrolysis oven with an inert atmosphere (N_2). TOC% is calculated from the obtained thermograms using the following equation:

$$\text{TOC\%} = \text{Pyrolysed Carbon (wt\%)} + \text{Residual Carbon (wt\%)}.$$

Samples were calibrated using the IFP160000 standard with an instrumental precision of <0.1 wt% for TOC (Lafargue et al., 1998; Behar et al., 2001; Ordoñez et al., 2019).

Major elements in discrete bulk sediment samples of S1 were analyzed in fused beads by using XRF. Analyses were carried out at Instituto Andaluz de Ciencias de la Tierra (IACT, CSIC-UGR), with a S4 Pioneer from BRUKER, equipped with a 4 kW wavelength dispersive X-ray fluorescence spectrometer (WDXRF) and a Rh anode X-ray tube (60 kV, 150 mA). XRF precision was better than ±0.3% for major elements. Trace elements in discrete sediment samples were measured at the Scientific Instrumentation Center (CIC, University of Granada) with an ICP-MS NexION 300d (Perkin Elmer) spectrometer using Rh as internal standard. For trace elements, ICP-MS precision was better than ±5% for analyte concentrations of 10 ppm (Bea, 1996). TMs have been normalized to aluminum (TM/Al) due to its conservative nature and since it is considered one of the optimal methods to evaluate TM variability because it takes into account the detrital input variability which may have a significant influence in TM concentration (Algeo and Maynard, 2004, 2008; Brumsack, 2006; Tribovillard et al., 2006; Calvert and Pedersen, 2007; Algeo and Tribovillard, 2009; Little et al., 2015; Scholz et al., 2017; Scholz et al., 2018; Algeo and Li, 2020; Paul et al., 2023).

For ICP-MS analyses, discrete bulk sediment samples were first oven-dried at 60 °C and then powdered in an agata mortar. Samples were processed in batches of 25 to 30 samples and an analytical blank was added to each batch. Solutions for ICP-MS analyses were prepared using 0.1 g of powdered sample in Teflon vessels, where successive acidifications using HNO_3 (69%) and HF (48%), were performed at 130 °C until evaporation. A final acid digestion with HNO_3 (69%) and water at 80 °C for 1 h was conducted to achieve a total acid dissolution of the sediment samples. Subsequently, dissolved samples were diluted with Milli-Q water in 100 ml flasks (Bea, 1996).

Trace elements concentrations at sub-mm in the thin-sections were determined by Laser ablation ICP-MS (LA-ICP-MS), which has been proven to have high potential for quantitative analysis of diagnostic environmental trace elements (e.g., Mo, V, U and Ba) in resin-embedded sediments (Jilbert et al., 2008, 2010; Hennekam et al., 2015; Sosa-Montes de Oca et al., 2018). LA-ICP-MS spot and line-scans analyses were performed at the Scientific Instrumentation Center (UGR). The LA-ICP-MS analyses were conducted using a 213 nm Mercantek Nd-YAG laser coupled to a NexION 2000b quadrupole ICP with a shielded plasma torch. The ablation was carried out in a He atmosphere, using a laser beam fixed at 60 μm diameter. The spot was pre-ablated for 45 s using a laser repetition rate of 10 Hz and 20% output energy. NIST-610 glass (ca. 450 ppm of each element) was employed as external standard (Pearce et al., 2007). In each analytical session of a single thin-section, the NIST-610 glass was analyzed at the beginning and at the end, and also after every nine spots to correct for drift. Concentration values were corrected using silicon as an internal standard. The precision, calculated on five to seven replicates of the NIST-610 glass measured in every session, was in the range ±3 to ±7% for most elements. Line-scanning for linear analyses of TMs concentration on thin-section surfaces was performed at 200 μm resolution (i.e., 5 spot-analyses per mm). The areas or minerals for LA-ICP-MS spot-analyses were visually selected using SEM-BSD images.

IV.2.2.2. Scanning electron microscope (SEM) imaging and compositional maps

Sediment thin-sections were coated with carbon for detailed observation under the SEM using an AURIGA FIB-FESEM Carl Zeiss SMT microscope of the Scientific Instrumentation Center (UGR). The SEM is equipped with an EDX (energy dispersive X-ray) detector system from Oxford Instruments and SE (secondary electrons), SE-inLens, BSE (backscattered secondary electrons), EsB (energy selective backscattered electrons) and STEM (scanning transmission electron microscopy) detectors. EDX was used to obtain spot microanalyses and compositional maps, and also profiles of major elements in selected areas and minerals of the sediment thin-sections. Moreover, unpolished fragments from different samples were also coated with carbon for observation under the SEM, and some samples were critical point dried in order to efficiently separate organic tissues from inorganic sediment and then carbon coated for SEM observations. Pyrite framboids were assessed in detail using SEM-BSD images since their morphology, texture and size provides important palaeoredox information for tracking microbial activities and diagenetic processes (Wilkin et al., 1996, 1997; Wilkin and Barnes, 1997; Lin et al., 2016; Liu et al., 2019; Chang et al., 2022).

IV.2.3. Statistical analyses

Multivariate statistical analyses, such as correlation matrices and Principal Component Analysis (PCA), were applied to the geochemical data obtained through various analysis techniques (ICP-MS, LA-ICP-MS, XRF, and Rock-Eval pyrolysis) to achieve a more comprehensive inter-pretation of the sapropel S1 deposition. PCA and correlation matrices were obtained using the software "PAST 4.0" from Hammer et al. (2001). Both multivariate statistical analyses were performed using non-normalized elements to avoid inducing correlations that could mask the real affinities and associations of the variables under assessment. DOPt (i.e., degree of pyritization) is the only calculated variable introduced in the multivariate statistical analyses since it serves to determine what RSTMs associate with pyrite. DOPt = S_T * (55.85/64.12) / Fe_T, where S_T = total sulphur, Fe_T = total iron and 55.85/64.12 represents weight ratios of Fe/S in stoichiometric pyrite. Therefore, a strong correlation between DOPt and S is expected.

Diagnostic palaeoenvironmental TMs (i.e., Mo, U, V, Cu, Co, Ni, Pb, Zn, and Ba) obtained by LA-ICP-MS analyses of thin-sections (e.g., line-scans and spot sub-mm results) were introduced into the correlation matrices to evaluate how these RSTMs associate at sub-mm scale. A *p*-value of 0.05 was proposed as the threshold to verify whether the established correlations were statistically significant (i.e., $(p) > 0.05$ no significant correlation). Moreover, a correlation matrix and a PCA were applied to the geochemical data derived from geochemical analyses of discrete samples to elucidate the main geochemical fractions in S1 and non-sapropel sediments above and below it. In this PCA, TOC%, concentrations of major elements (i.e., Al, Ca, Fe, K, Mg, Mn, S, and Ti) obtained through XRF, as well as Zr, Rb, and Sr concentrations obtained through ICP-MS, were introduced into the multivariate statistical analyses (Fig. IV.3). See the Supplementary material (Sup. mat) for detailed results of the multivariate statistical analyses.

IV.3. Results

IV.3.1. Discrete samples

Since barite ($BaSO_4$) is less affected by postdepositional oxidation than TOC (Dehairs et al., 1987; Bishop, 1988; Calvert and Pedersen, 2007), top and bottom boundaries of sapropel S1 were identified using Ba/Al vertical plot (Fig. IV.2). This allowed to identify the original thickness of the organic-rich interval of sapropel S1 before postdepositional oxidation occurred (Pruysers et al., 1991; Thomson et al., 1995; van Santvoort et al., 1996, 1997; Warning and Brumsack, 2000; Gallego-Torres et al., 2007a, 2007b; Filippidi and de Lange, 2019). Moreover, the $\delta^{34}S$ pyrite values in sapropel S1 obtained by Passier et al. (1997) suggest that sulphate reduction occurred in an open system with seawater exchange. Thus, during S1, porewater sulphate reduction was not sufficient enough to achieve efficient Barite dissolution and remobilization of Ba. Consequently, the Ba/Al ratio predominantly reflects the presence of authigenic barite and serves as a reliable indicator for determining the initial thickness of S1 (Martínez-Ruiz et al., 2020; Wehausen and Brumsack, 2000). The studied record, S1 original thickness is identified between 60 cm (S1 termination; 6.1 ka) and 76 cm (S1 onset; 10.5 ka) depth of core 964B 1H (S1 ages from Grant et al., 2016).

Two differentiated enrichments of some RSTMs (Mo, Co, Cu, Ni and Zn) are recognized in the vertical plots. The top RSTMs enrichment (from 58 to 62 cm) is correlative to a Mn enrichment and is above the Ba enrichment, while the lower enrichment (from 67 to 76 cm) is within the Ba enrichment and is correlative with high DOPt values and TOC content (~3%), but low Mn concentrations (Fig. IV.2 and Table IV.1). Below the organic-rich level, DOPt values remain high and enrichments of some RSTMs (e.g., Mo, U, Co, Cu and Zn) are observed (Fig. IV.2). These variations in S1 vertical plot allowed the recognition of four geochemical intervals, which are interpreted in section 4.2. Detailed results of discrete sample geochemical analyses are shown is Table IV.1 and Figs. IV.2 and 3.

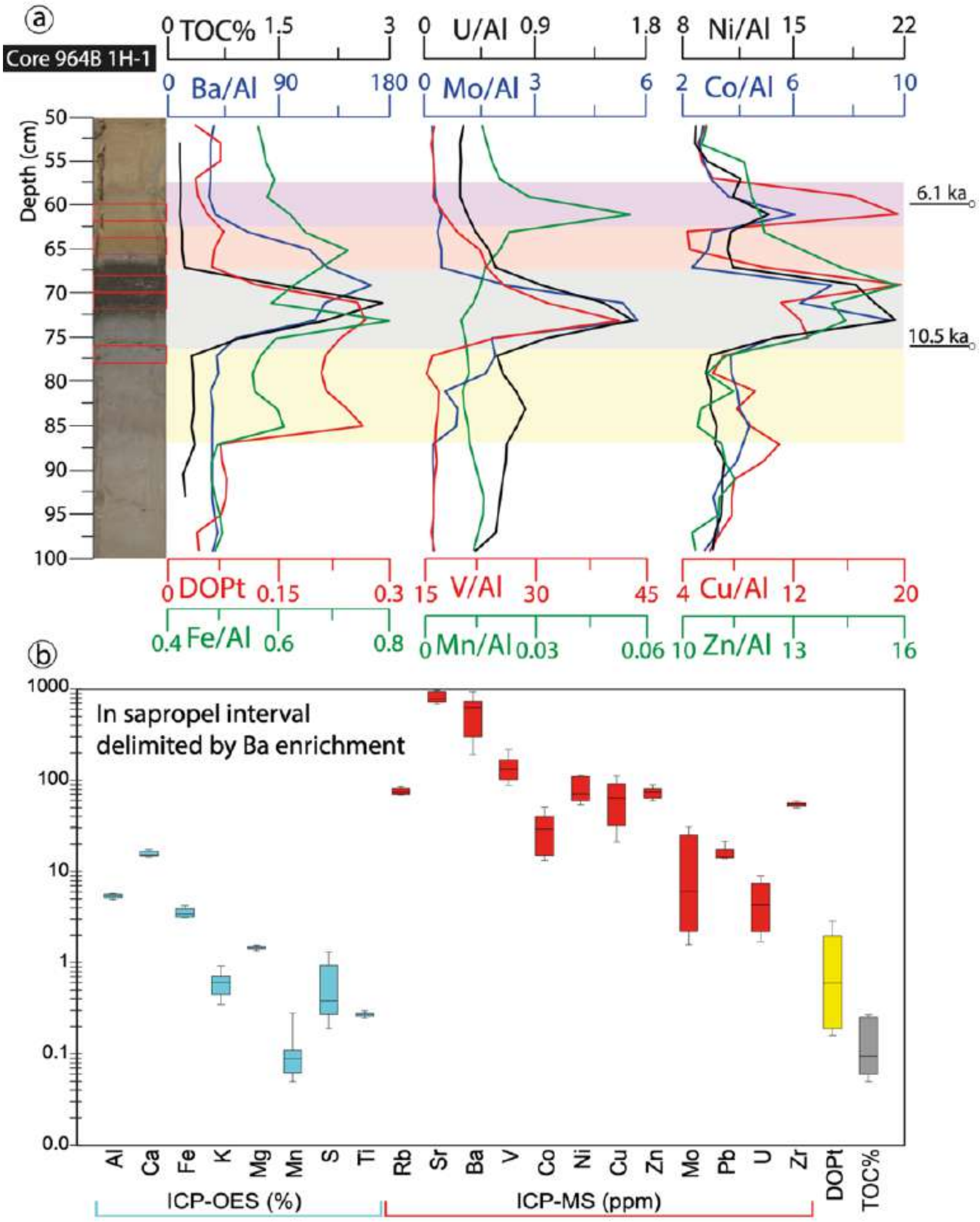

Figure IV.2. *Discrete samples geochemical data. (a) Chemostratigraphy of S1 unit, showing vertical plots of Al-normalized RSTMs (Mn, Mo, U, V, Co, Cu, Ni and Zn), Fe/Al, Ba/Al, DOPt and TOC%. S1 was delimited by the Ba/Al increase. Calculated Fe-oxides content plot of t is shown in Sup. mat. (Fig. S12). Onset and termination time of S1 is indicated according to Grant et al. (2016). Recognized geochemical intervals are indicated with different colours; marker bed (purple), oxidized interval (orange), unoxidized interval (gray), synsapropel interval (yellow). (b) Box-whisker plots showing major elements concentrations (in logarithmic scale), trace elements concentrations, TOC% and calculated DOPt values in the sapropel interval delimited by Ba enrichment. See Tables S1, S4-S10 in the Sup. mat. For detailed geochemical results.*

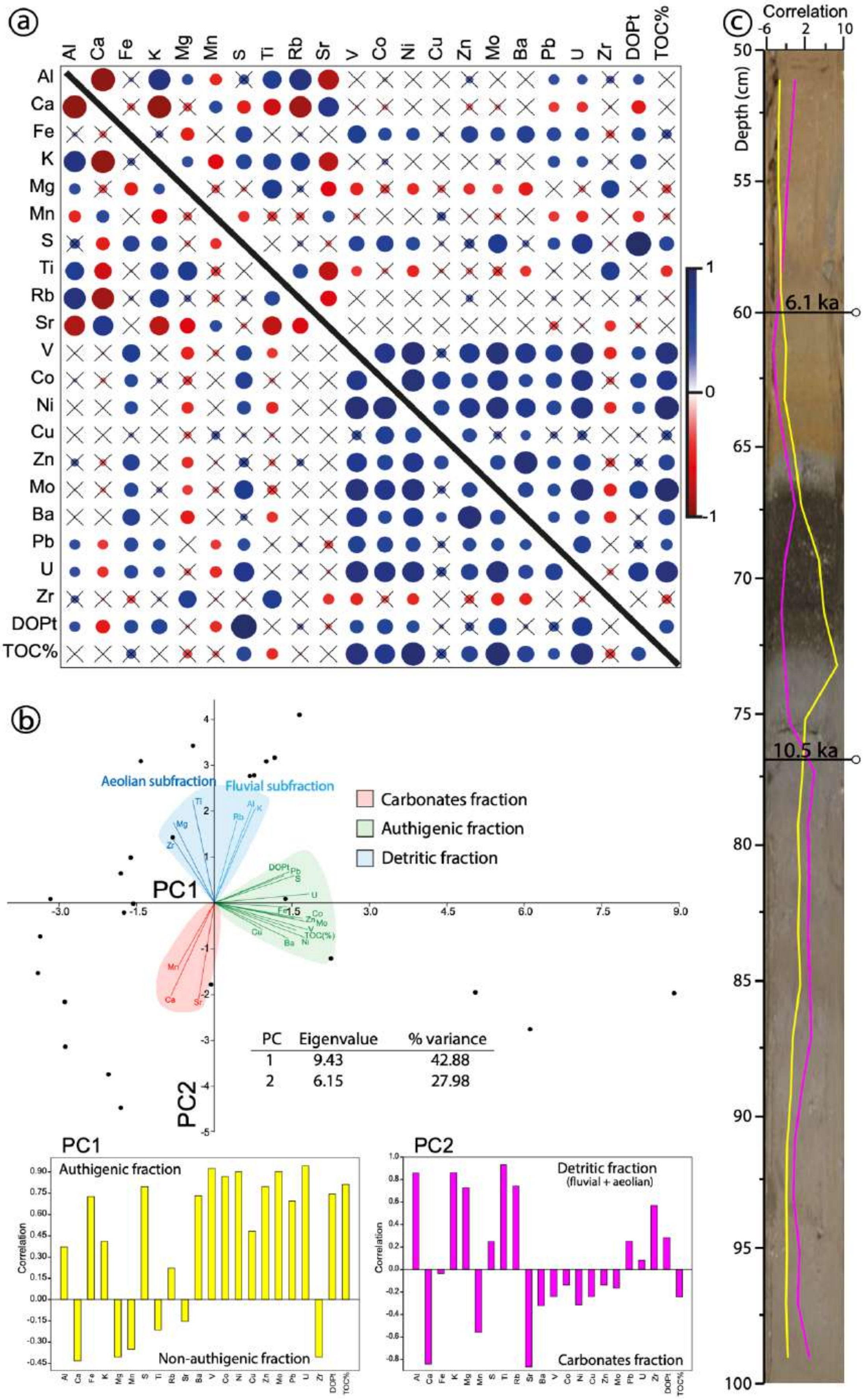

PC	Eigenvalue	% variance
1	9.43	42.88
2	6.15	27.98

Figure IV.3. *Multivariant statistical analyses of S1 discrete sediment samples obtained using PAST 4.0 from Hammer et al. (2001). The multivariant statistical analyses considered all analyzed discrete*

samples, i.e., from 50 to 100 cm. (a) Correlation matrix considering major and trace elements, DOPt and TOC%. Blue circles indicate positive correlation, and red circles negative. The size of the circle indicates the degree of correlation, the bigger the circle, the higher the correlation coefficient value. The cross indicates a correlation with a (p) > 0.05. (b) PCA results. On the top a PCA scatter-plot is illustrated; PC1: y-axis, PC2: x-axis. Identified geochemical fractions in different colours. Eigenvalue and %variance values of PC1 and PC2 are indicated. Loading plots of PC1 (yellow bars) and PC2 (pink bars). (c) Vertical plots of PC1 (yellow line) and PC2 (pink line) on a 964B core image. S1 time intervals is indicated (Grant et al., 2016). See Tables S2 and S3, and Fig. IV.S1 for detailed results of the PCA and correlation matrix performed to discrete samples results.

The correlation matrix of S1 shows (i) a strong positive correlation between RSTMs, Ba, DOPt and TOC%, and (ii) a strong to moderate negative correlation of Ca, Sr and Mn with Al, Mg, K, Fe, Rb, Ti and Zr (see Fig. IV.3a for detailed correlations). PC1 and PC2 group more that 70% of the total variance (Fig. IV.3b). The PCA scatter-plot suggests three main elemental associations or geochemical fractions present in S1 sediments (Fig. IV.3b), which are further discussed in section 4.1. The positive correlation of PC1 is principally controlled by Fe, S, Ba, V, U, Mo, Co, Cu, Ni, Zn, Pb, TOC% and DOPts, while the negative correlation of PC1 is controlled by Ca, Mg, Mn and Zr enrichments (Fig. IV.3b). PC2 positive correlation is mainly controlled by Al, K, Mn, Ti and Rb enrichments, while its negative correlation is mainly controlled by Ca, Mn and Sr enrichments (Fig. IV.3b). In this sense, the positive correlation of PC1 and the negative correlation of PC2 seem to be stronger in the organic-rich interval and just below it (Fig. IV.3c).

Table IV.1. *Geochemical data of selected S1 samples for LA-ICP-MS analyses. Results of bulk sediment sample analyses and LA-ICP-MS analyses (i.e., line-scans and spot-analyses) are given for each sample. Statistical values are indicated, i.e., mean, median and standard deviation (Std. Dev.) values. See Tables S1, S4-S10 in the Sup. mat. For detailed results of geochemical analyses results.*

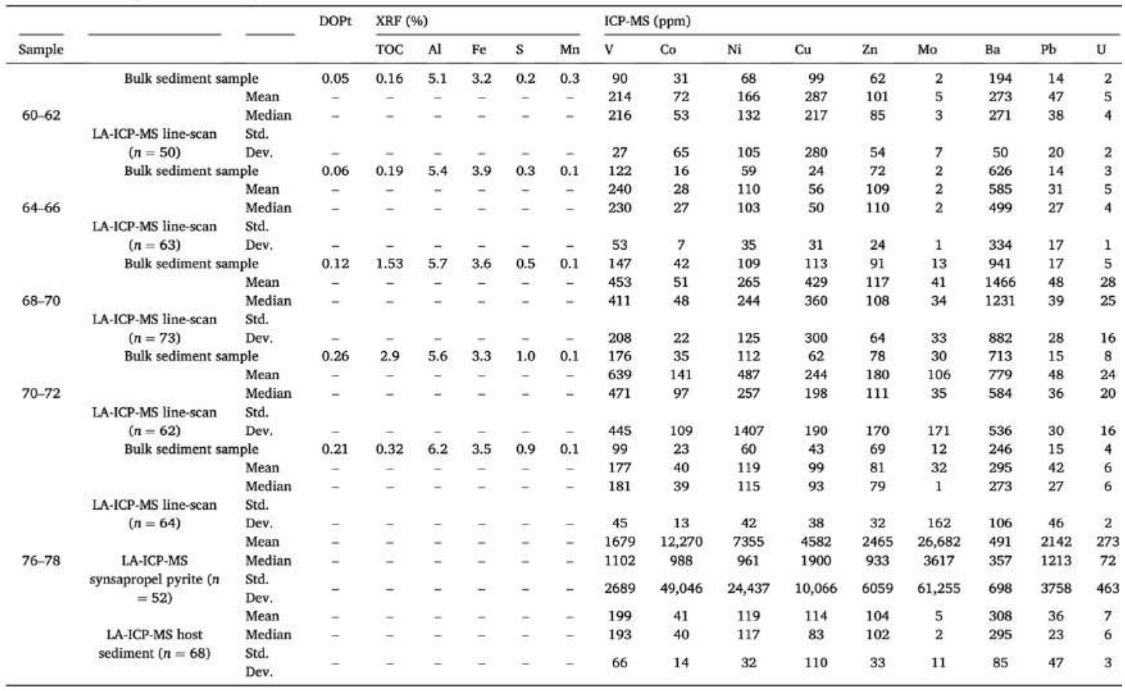

			DOPt	XRF (%)					ICP-MS (ppm)								
Sample				TOC	Al	Fe	S	Mn	V	Co	Ni	Cu	Zn	Mo	Ba	Pb	U
60–62	Bulk sediment sample		0.05	0.16	5.1	3.2	0.2	0.3	90	31	68	99	62	2	194	14	2
	LA-ICP-MS line-scan (n = 50)	Mean	–	–	–	–	–	–	214	72	166	287	101	5	273	47	5
		Median	–	–	–	–	–	–	216	53	132	217	85	3	271	38	4
		Std. Dev.	–	–	–	–	–	–	27	65	105	280	54	7	50	20	2
64–66	Bulk sediment sample		0.06	0.19	5.4	3.9	0.3	0.1	122	16	59	24	72	2	626	14	3
	LA-ICP-MS line-scan (n = 63)	Mean	–	–	–	–	–	–	240	28	110	56	109	2	585	31	5
		Median	–	–	–	–	–	–	230	27	103	50	110	2	499	27	4
		Std. Dev.	–	–	–	–	–	–	53	7	35	31	24	1	334	17	1
68–70	Bulk sediment sample		0.12	1.53	5.7	3.6	0.5	0.1	147	42	109	113	91	13	941	17	5
	LA-ICP-MS line-scan (n = 73)	Mean	–	–	–	–	–	–	453	51	265	429	117	41	1466	48	28
		Median	–	–	–	–	–	–	411	48	244	360	108	34	1231	39	25
		Std. Dev.	–	–	–	–	–	–	208	22	125	300	64	33	882	28	16
70–72	Bulk sediment sample		0.26	2.9	5.6	3.3	1.0	0.1	176	35	112	62	78	30	713	15	8
	LA-ICP-MS line-scan (n = 62)	Mean	–	–	–	–	–	–	639	141	487	244	180	106	779	48	24
		Median	–	–	–	–	–	–	471	97	257	198	111	35	584	36	20
		Std. Dev.	–	–	–	–	–	–	445	109	1407	190	170	171	536	30	16
76–78	Bulk sediment sample		0.21	0.32	6.2	3.5	0.9	0.1	99	23	60	43	69	12	246	15	4
	LA-ICP-MS line-scan (n = 64)	Mean	–	–	–	–	–	–	177	40	119	99	81	32	295	42	6
		Median	–	–	–	–	–	–	181	39	115	93	79	1	273	27	6
		Std. Dev.	–	–	–	–	–	–	45	13	42	38	32	162	106	46	2
	LA-ICP-MS synsapropel pyrite (n = 52)	Mean	–	–	–	–	–	–	1679	12,270	7355	4582	2465	26,682	491	2142	273
		Median	–	–	–	–	–	–	1102	988	961	1900	933	3617	357	1213	72
		Std. Dev.	–	–	–	–	–	–	2689	49,046	24,437	10,066	6059	61,255	698	3758	463
	LA-ICP-MS host sediment (n = 68)	Mean	–	–	–	–	–	–	199	41	119	114	104	5	308	36	7
		Median	–	–	–	–	–	–	193	40	117	83	102	2	295	23	6
		Std. Dev.	–	–	–	–	–	–	66	14	32	110	33	11	85	47	3

IV.3.2. LA-ICP-MS analyses of sediment thin-section

LA-ICP-MS line-scan analyses of thin-sections reveal that RSTMs associate and behave differently at sub-mm scale in each geochemical interval (Fig. IV.8):

In sample 60–62 cm (with low TOC% and high Mn concentrations), the background value or the baseline of Ba is ~250 ppm and does not present any localized enrichments, which is corroborated by the relatively low standard deviation in respect to the mean and median values. Mo and U have low concentrations (~5 ppm); however, Mo presents localized enrichments and U does not. Co, Cu, Pb, Zn and Ni present higher concentrations (between ~50 and 300 ppm) and localized enrichments, for the exception of V, which also has relatively low standard deviation. There is a positive strong to moderate correlation between Mo, Co, Cu, Ni, Zn and Pb, but U and V do not present significant correlations ($(p) > 0.05$).

In sample 64–66 cm (with low TOC%), the baseline of RSTMs is lower than in sample 60–62 cm and none of them present remarked peaks or localized enrichments, which is corroborated by the lower mean, median and standard deviations values. However, Ba has higher mean concentrations (~600 ppm), positioning its respective concentration line-scan above RSTMs. Mo, Co, U, V and Pb present a strong positive correlation, while Cu, Zn, Ni and Ba only present weak to moderate positive correlations with few RSTMs (Fig. IV.8).

In sample 68–70 cm (with high TOC%), the baseline of Ba is ~1,500 ppm. All RSTMs have higher concentrations than in the upper samples and numerous localized enrichments (i.e., marked peaks) of RSTMs are recognized and also evidenced by the high standard deviations. All RSTMs and Ba have strong to moderate positive correlation and most correlations have p-values ≤ 0.05.

Sample 70–72 cm (with high TOC%), has a similar behavior to sample 68–70 but with even higher concentrations in RSTMs, but bot in Ba (~700 ppm). However, sample 70–72 cm, localized RSTMs enrichments reach higher values and Ni only presents few weak positive correlations. Moreover, a generalized decrease in RSTMs in the middle of its line-scan is recognized.

Sample 76–78 cm (with low TOC% and Ba concentrations) has a low baseline of RSTMs and Ba (Ba ~250 ppm), but marked enrichments in most RSTMs (e.g., Mo, Co, Cu, Ni, Zn and Pb) are recognized, especially in Mo, which is also evidenced by their relatively high standard deviation values. U, V and Ba do not present localized enrichments. The respective correlation matrix shows moderate positive correlations between RSTMs, but not significant Ba correlations (Fig. IV.8).

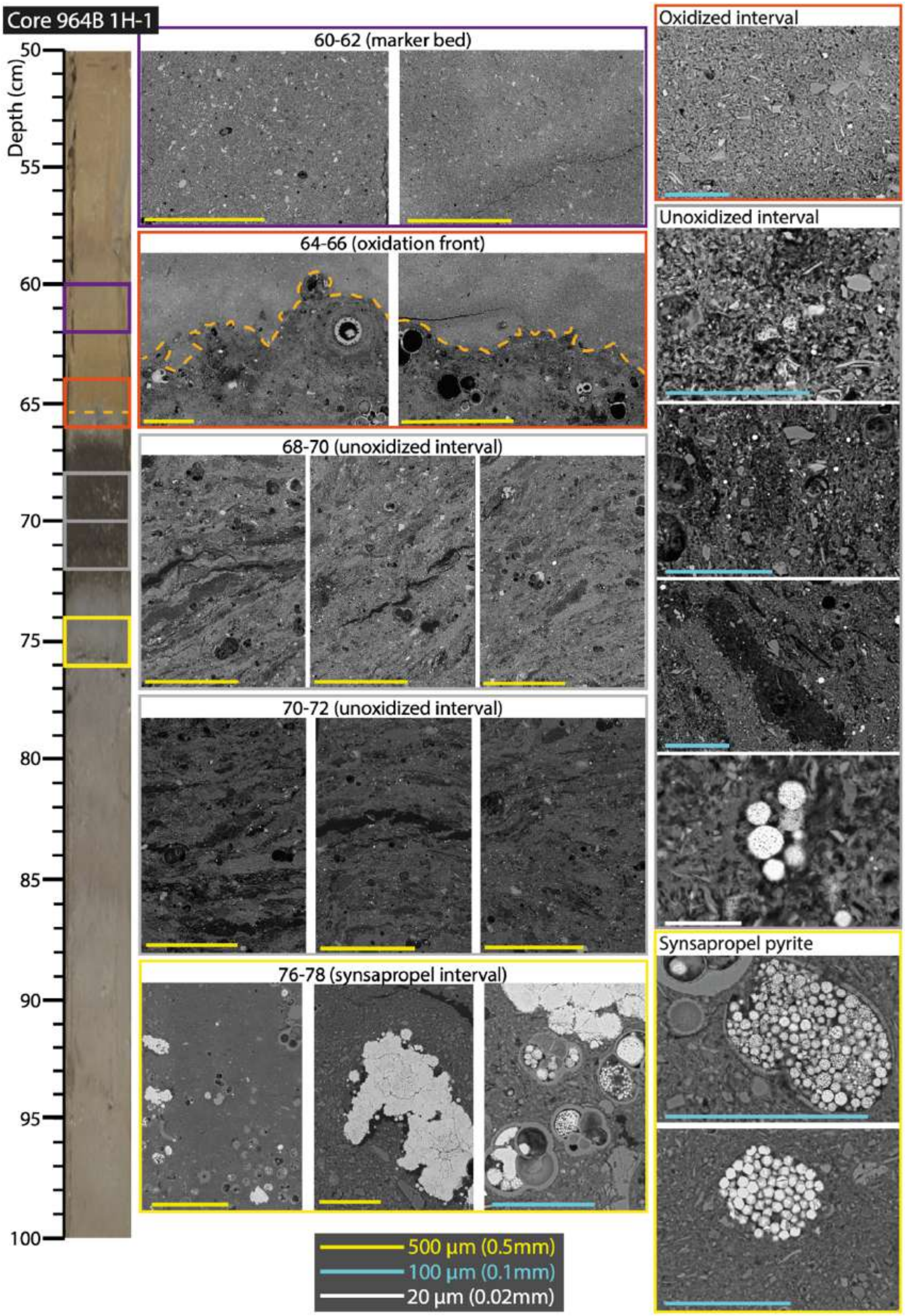
Core 964B 1H-1
Depth (cm)
50
55
60
65
70
75
80
85
90
95
100
60-62 (marker bed)
64-66 (oxidation front)
68-70 (unoxidized interval)
70-72 (unoxidized interval)
76-78 (synsapropel interval)
Oxidized interval
Unoxidized interval
Synsapropel pyrite
500 µm (0.5mm)
100 µm (0.1mm)
20 µm (0.02mm)

Figure IV.4. *SEM-BSD images at different scales of thin-sections of selected samples (60–62, 64–66, 68–70, 70–72, 76–78). Each sample represents a geochemical interval. The depths of the selected samples are indicated on the core image as red rectangles. Orange dashed line in sample 64–66 for the oxidation front. For more SEM images see figures in the Sup. mat.*

Besides the LA-ICP-MS line-scan analysis of 76–78 cm thin-section, selected sub-mm areas and minerals of 76–78 cm thin-section were analyzed with LA-ICP-MS spot-analyses. In this case, pyrite crystals/framboids and the host sediment were analyzed separately to compare RSTMs concentrations between these two sedimentary components (Table IV.1). The results show exceptionally high concentrations in RSTMs and Ba in the pyrite crystals/framboids below S1, in comparison with the host sediment which have very low concentrations in RSTMs and Ba. In pyrite crystals/ framboids below S1, all assessed RSTMs present strong positive correlation, except U which only presents the lowest concentrations and low to moderate positive correlations with the rest of the TMs.

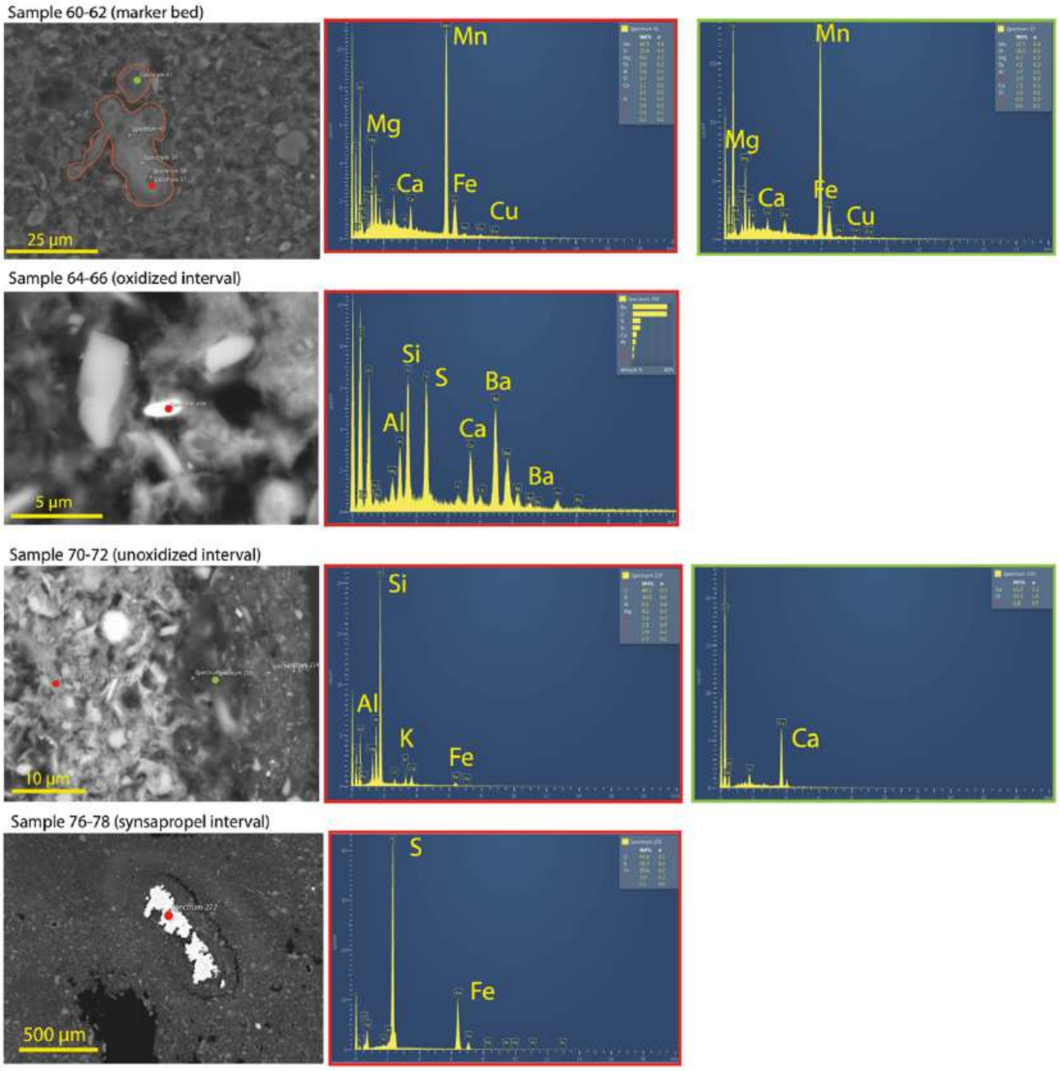

Figure IV.5. *SEM-EDX spot-analyses and respective elemental spectrums of minerals and areas in the different geochemical intervals recognized in S1 unit. Sample 60–62: Mn-enriched particle analysis; 64–66: barite crystal analysis; 70–72: irregular laminae alternation analyses; 76–78: pyrite aggregate analysis. All elemental spectrums of the SEM-EDX spot-analyses are shown in Sup. mat.*

LA-ICP-MS spot-analyses and line-scans in sample 76–78 produce distinct correlation matrices. In the case of the line-scan analysis, only pyrite aggregates within the scanned section are analyzed, resulting in a weaker signal and statistical representation of the trace elements within these pyrite aggregates. Conversely, separate spot-analyses of the host sediments and euhedral pyrite aggregates provide a better representation of both components. For more detailed LA-ICP-MS results and data, refer to Table IV.1 and Figs. IV.8 and 9, which display concentration box-plots, correlation matrices, and statistical values (i.e., mean, median, and standard deviation).

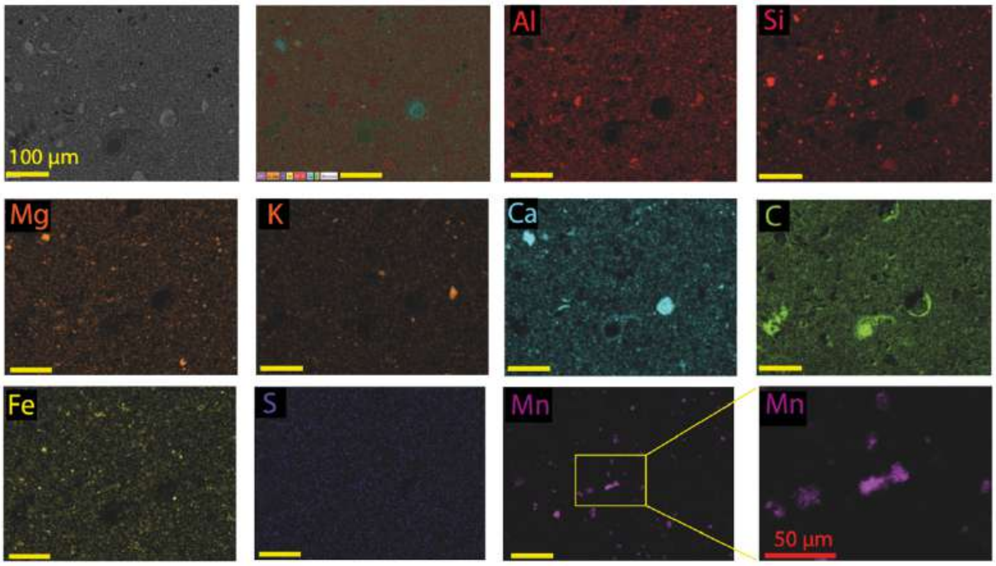
Sample 60-62 (marker bed)

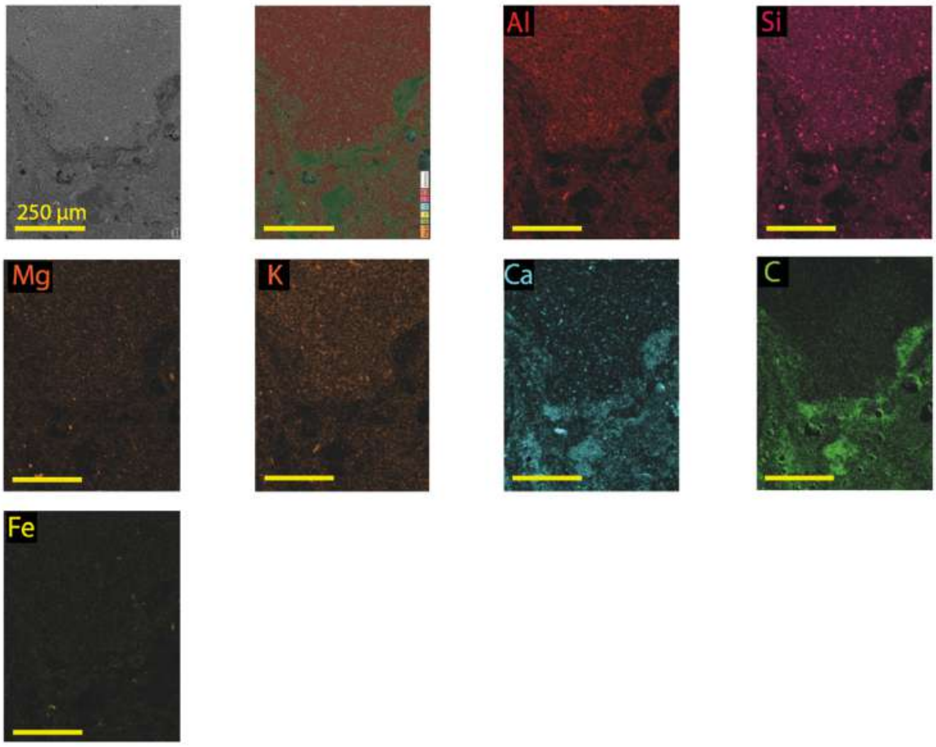
Sample 64-66 (oxidation front; unoxidized-oxidized boundary)

Figure IV.6. *SEM-EDX compositional maps of samples 60–62 and 64–66. Colour legend is indicated in the figure. Scalebars are indicated on each compositional map and its respective value is indicated on the SEM-BSD image. The first image of each sample corresponds to the SEM-BSD image, and the second to the composite map (map conformed by overlapping each elemental map). Additional SEM-EDX compositional maps of these samples are shown in Sup. mat. Mn is only shown in sample 60–62 since is the only sample where Mn has high enough concentrations to be detected by the SED-EDX detector.*

IV.3.3. SEM images and SEM-EDX mapping

SEM-BSD images and SEM-EDX maps of thin-sections reveal variations in composition and sedimentary structure at sub-mm scale (Figs. IV.4 - 7). As a general remark, the entire S1 unit is enriched in coccoliths and clay minerals. In sample 60–62, the sediment appears very homogenous, lacking barite or pyrite crystals/ framboids, as well as organic-rich laminae. However, abundant Mn-rich grains and scattered large angular detritic grains are observed (> 50 µm) (Figs. IV.4 - 6; Fig. S5 in the Sup. mat.). In sample 60–62 and in the upper part of sample 64–66 (i.e., above the oxidation front; Figs. IV.4 and 6), which correspond to the S1 interval with low RSTMs concentration and TOC content, the sediments appear to have undergone mixing, as the pseudo-lamination observed in the underlying interval is absent. Compositional maps of sample 60–62 indicate the presence of abundant amorphous Mn-rich grains featuring concentric growing layers. The Mn-rich grains vary in size, but can reach up to 20 µm. Sample 64–66 exhibits two distinct types of sediments delimited by a sharp boundary (Figs. IV.4 and 6). The upper section of sample 64–66 closely resembles sample 60–62, lacking organic-rich laminae, pyrite crystals, and the pseudo-lamination. In comparison with sample 60–62, oval barite crystals between ~0.3–2 µm are abundant (Fig. IV.6), while Mn-rich grains are less abundant. The compositions of these grains were corroborated by SEM-EDX spot-analyses (Fig. IV.5; Figs. S2 to S6 in the Sup. mat.). The lower section of sample 64–66 has abundant but small pyrite framboids (most between ~5–10 µm) and irregular OM laminae.

Samples 68–70 and 70–72 exhibit remarkable similarities (Figs. IV.4 and 7), with abundant and scattered small oval barite crystals (~0.5–2 µm), and octahedral pyrite crystals (~0.5–1 µm), with some pyrite crystals forming spherical euhedral framboids (5–10 µm diameter). Moreover, fossil bacteria were identified in SEM images of sample 68–70 after critical point drying (Fig. S11 in the Sup. mat.). The spherical and euhedral pyrite framboids in these samples are abundant and scattered throughout these samples (Figs. IV.4 and 7). Irregular OM laminae (~0.1–0.2 mm thick) are consistently present. SEM-EDX compositional maps reveal an alternation of laminae enriched in Al, Si and K with those in Ca and C. The laminae are irregular in shape and range between ~50–150 µm in thickness. The laminae enriched in Ca and C are mainly composed by coccoliths and amorphous OM. Also, large planktonic foraminifera shells (> 300 µm in diameter) are observed. Sample 70–72 in comparison with sample 68–70, contains higher abundance of pyrite framboids scattered in the sediments. Some of the foraminifera chambers in this sample are infilled by large euhedral pyrite framboids, where each crystal is ~5 µm and the diameter of the framboids is >30 µm. Therefore, in sample 70–72 there are three types of pyrite morphologies: (i) isolated octahedral pyrite crystals, (ii) euhedral pyrite framboids scattered in the sediments, and (iii) euhedral pyrite framboids inside foraminifera chamber (Figs. IV.4 and 7; Figs. S17-S21 in the Sup. mat.).

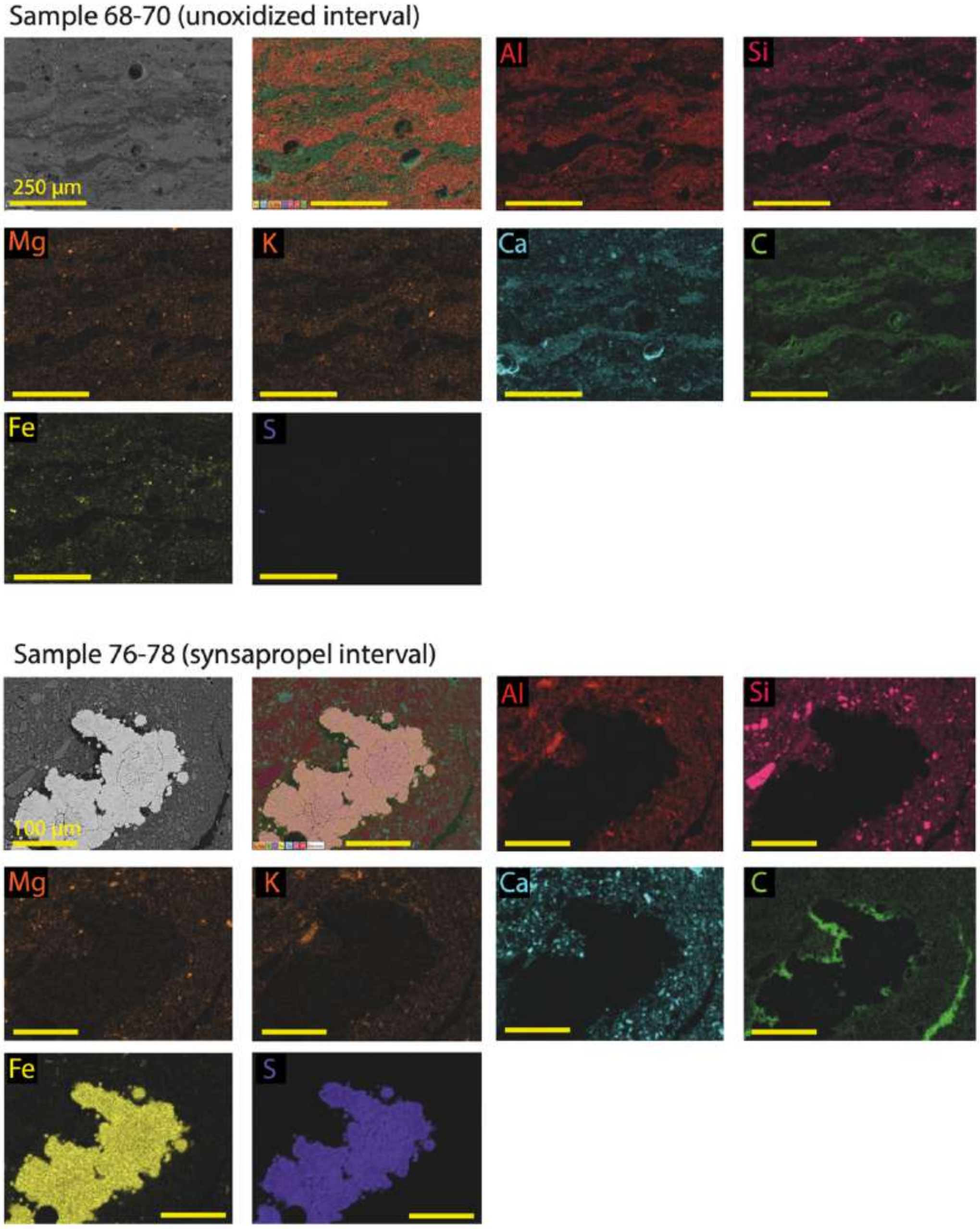
Sample 68-70 (unoxidized interval)

Sample 76-78 (synsapropel interval)

Figure IV.7. *SEM-EDX compositional maps of samples 68–70 and 76–78. Colour legend is indicated in the figure. Scalebars are indicated on each compositional map and its respective value is indicated on the SEM-BSD image. The first image of each sample corresponds to the SEM-BSD image, and the second to the composite map (map conformed by overlapping each elemental map). Additional SEM-EDX compositional maps of these samples are shown in Sup. mat.*

Sample 76–78 lacks organic-rich laminae and barite crystals. It features large pyrite framboids and euhedral aggregates ranging between ~0.1–0.3 mm. Many foraminifera shells are filled with these euhedral pyrite aggregates, although the largest aggregates are embedded in the sediment. However, it does not present the small pyrite crystals (~0.5–1 μm) observed in samples 64–66, 68–70 and 70–72. Some of the pyrite framboidal aggregates present euhedral overgrowths that confers them a “sunflower” texture (Figs. IV.4 and 7; Fig. S10 in the Sup. mat.) (Merinero et al., 2017; Chang et al., 2022).

IV.4. Discussion

IV.4.1. S1 geochemical fractions

The multivariate statistical analyses of the geochemical data (i.e., major elements and TMs concentration, TOC% and DOPt) derived from discrete geochemical analyses allowed the characterization of the geochemical fractions present across the S1 sapropel interval, enabling more accurate interpretations of the RSTMs signals and the subsequent recognition of diagenetic remobilization. According to the geochemical affinities observed in the multivariate statistical analyses, three geochemical fractions can be identified: (i) detritic, (ii) carbonate, and (iii) authigenic fraction (Fig. IV.3).

The detritic fraction is enriched Al, K, Rb, Ti, Zr and Mg, which are elements typically enriched in clays and other detrital minerals transported by rivers or wind (Calvert and Pedersen, 2007). The PCA analysis suggests that this fraction can be further subdivided into fluvial (Al, K, Rb) and aeolian (Ti, Zr and Mg) subfractions. The carbonate fraction is enriched in Ca, Sr and Mn, which are elements that tend to be associated to carbonate minerals (Calvert and Pedersen, 2007). The PC2 positive correlation is controlled by the detritic fraction, while the negative correlation is controlled by the carbonates fraction. Consequently, PC2 vertical plot suggests that the carbonate fraction is proportionally enriched after the onset of S1 (Figs. IV.2 and 3). This is corroborated by SEM-EDX compositional maps that show abundant irregular Ca-rich laminae in samples 68–70 and 70–72 (i.e., the unoxidized interval) (Figs. IV.6 and 7). The authigenic fraction is enriched in Mo, U, V, Co, Cu, Fe, Zn, Pb, Ba, DOPt and OM. Additionally, PC1 positive correlation is controlled by the authigenic fraction, while the negative correlation is controlled by the non-authigenic fraction. Therefore, the increase in PC1 in the vertical plot (Fig. IV.3c) suggests an increase in the authigenic fraction within the S1 and immediately below it, as also demonstrated by the compositional maps, which show high C and pyrite contents in S1, and high pyrite content just below it (Figs. IV.5 - 7).

The enrichments of different components within the authigenic fraction are attributed to several authigenic processes. All assessed RSTMs, are scavenged from the water-column to seafloor mainly by Mn-oxyhydroxides and/or OM (Calvert and Pedersen, 1996; Tribovillard et al., 2006; Filippidi and de Lange, 2019). During periods of bottom-water stagnation, such as during S1 in the Ionian Abyssal Plain, and due to the continuous presence of euxinic porewater resulting from extensive biotic sulphate reduction, RSTMs such as Mo, Co, Cu, Zn, Pb, and Ni, are fixed in the sediments in association with pyrite (FeS) or by forming their own sulphides (e.g., MoS, CuS, CuS_2, NiS and [Zn,Fe]S CoS, NiS) (Calvert and Pedersen, 1993, 2007; Crusius et al., 1996; Helz et al., 1996; Morford and Emerson, 1999; Zheng et al., 2000; Algeo and Maynard, 2004, 2008; Algeo and Lyons, 2006; Tribovillard et al., 2006; Dellwig et al., 2010; Algeo and Rowe, 2012; Scholz et al., 2017; Scholz, 2018). In regards to V, it can precipitate with Fe-sulphides as V^{3+} under euxinic condition, however, its fixation in organic-rich sediments is normally associated to organometallic compounds that promote the its precipitation in geoporphyrins or as solid oxide V_2O_3 or hydroxide $V(OH)_3$ (Tribovillard et al., 2006 and references therein). Conversely, U is not influenced by the redox cycling of Mn and Fe in the water-column and does not require free H_2S to precipitate, but as V under anoxic conditions, U precipitates as the less soluble lower oxidation state (normally as a stable oxide; UO_2) in association with humic and fulvic acids derived from OM degradation, (Zheng et al., 2002; Algeo and Maynard, 2004; McManus et al., 2005; Morford et al., 2005; Tribovillard et al., 2006; Calvert and Pedersen, 2007).

SEM observations reveal that Ba enrichments in S1 sediments are due to high abundance of barite oval crystals (see Fig. IV.5; Fig. S6 in the Sup. mat.). Size and morphology of these barite crystals indicate a biogenic mediated origin (Paytan et al., 2002; Paytan and Griffith, 2007). Biogenic barite nanocrystals precipitate more intensely in the water-column during periods of enhanced OM degradation in the mesopelagic zone, while increased TOC content in marine sediments is linked to periods of increased export productivity and OM preservation (Bishop, 1988; Calvert and Pedersen, 2007; Gallego-Torres et al., 2007a, 2010; Martínez-Ruiz et al., 2018, 2019, 2020; Filippidi and de Filippidi and de Lange, 2019). Overall, the proportional enrichment of the authigenic fraction in Ionian Abyssal sediments is associated with periods of oxygen-depleted bottom-waters, high export productivity and intense bacterial degradation (Fig. IV.3c).

IV.4.2. Recognition and interpretation of S1 geochemical intervals

For the detailed evaluation of postdepositional processes, a detailed assessment of sapropel geochemical boundaries and intervals is needed. S1 vertical plots of PC1, RSTMs, Ba, TOC% and DOPt, and SEM observations of samples allowed the recognition of four geochemical intervals in S1 sedimentary unit: (i) the marker bed, (ii) the oxidized interval, (iii) the unoxidized interval, and (iv) the synsapropel interval (Fig. IV.2a). Each geochemical interval represents different palaeoenvironmental conditions or postdepositional processes as previously recognized (Passier et al., 1996; Nijenhuis et al., 1999; Gallego-Torres et al., 2007a; Filippidi and de Filippidi and de Lange, 2019).

Marker bed (purple shaded interval in Fig. IV.2a): it is recognized by an abrupt Mn/Al peak and low TOC% and Ba concentrations. Moreover, it shows very low barite crystals abundance, and no organic-rich laminae or pyrite framboids, and abundant and scattered Mn-rich particles that are interpreted as Mn-oxyhydroxides. The absence of sulphides and OM is corroborated by PC1, that supports that this interval is impoverished in the authigenic fraction (Fig. IV.5). The stratigraphic position of this interval represents the time when reventilation of Ionian Basin deep-water occurred and oligotrophic conditions returned in surface-waters (Filippidi and de Filippidi and de Lange, 2019). During reventilation, the redoxcline in the water-column is transferred below the sediment-water interface (SWI), allowing the high levels of dissolved Mn^{2+} to rapidly precipitate as Mn-oxyhydroxides on the seafloor, resulting in prominent Mn enrichment easily recognized as dark layer or as a peak in the Mn/Al vertical plot (Figs. IV.5 - 7) (de Lange et al., 1989; Mangini et al., 1990; Thomson et al., 1993; Reitz et al., 2006; Filippidi and de Lange, 2019). Additionally, below the oxidation front (i.e., in the underlying anoxic sediments), Mn is released in the porewater as Mn^{2+} (Fig. IV.10) due to the utilization of Mn-oxides as electron acceptor during OM microbial degradation (Myers and Nealson, 1988). As a result, there is also a contribution from the upward diffusion and subsequent precipitation of dissolved Mn originating from the anoxic unoxidized interval. Consequently, the Mn-peak can be regarded as a fossilized redox front.

Oxidized interval (orange shaded interval in Fig. IV.2a): during the S1 termination, when oxic conditions returned to the Ionian Abyssal Plain, the redoxcline placed below the SWI acted as an oxidation front that progressively migrated downward, oxidizing the OM and sulphides (principally as pyrite framboids) (Fig. IV.6) (Thomson et al., 1995; van Santvoort et al., 1996, 1997; Reitz et al., 2006; Filippidi and de Lange, 2019). This oxidation is corroborated by the absence of pyrite framboids and OM laminae, and by abundant barite crystals more resistant to postdepositional oxidation (Fig. IV.5) (van Os and Middelburg, 1991; van Os, 1993; Nijenhuis et al., 1999; Passier et al., 1999; Martínez-Ruiz et al., 2000). A decrease in the authigenic fraction due to the postdepositional oxidation is further supported by the PC1 vertical plot (Fig. IV.3c). The progressive oxidation of the authigenic fraction liberated RSTMs in the porewater that were initially fixed in association with the OM and sulphides (Reitz et al., 2006; Filippidi and de Lange, 2019). The depth of the oxidation front was determined by the equilibrium of oxidant downward fluxes (e.g., O_2 and NO_3) with reductant upward fluxes (e.g., H_2S, Fe^{2+} and Mn^{2+}) in S1 porewater (Fig. IV.10) (Higgs et al., 1994; Thomson et al., 1995). Additionally, bioturbation seems to play an important role in the oxidized interval since all the sediments above the oxidation front are remobilized, as evidenced by the mottled background and the lack of pseudo-lamination (Figs. IV.4 - 6).

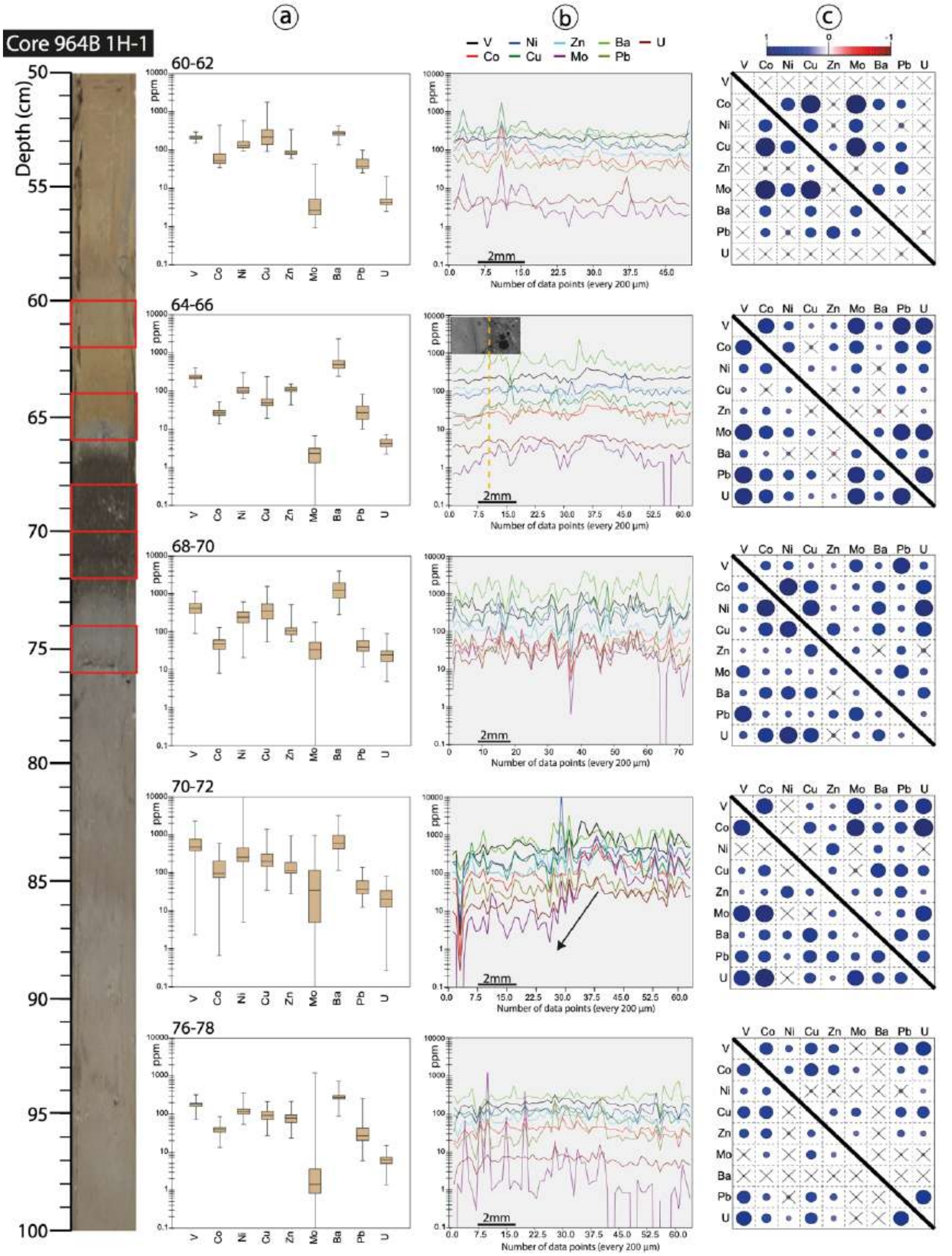

Figure IV.8. *LA-ICP-MS line-scans results of sediment thin-section of selected S1 samples. On the core image, the selected samples are indicated as red rectangles. (a) Box-whisker plots showing TMs concentrations (ppm in logarithmic scale) obtained by LA-ICP-MS line-scans of the thin-sections. (b) Linear plots of TMs concentration variations in the line-scans of thin-section. Each TM is indicated with a different colour. Spot-analyses in the line-scans were performed every 200 µm. y-axis: concentrations of TMs are expressed in ppm and in logarithmic scale. X-axis: number of data points. (c) Correlation matrices of TMs concentration obtained by the LA-ICP-MS line-scans. For interpretation of correlation matrices, read the caption of Fig. IV.3. For detailed results see Tables S4-S8 and Fig. S1 in Sup. mat.*

Unoxidized interval (gray interval area in Fig. IV.2a): it shows an enrichment in the authigenic geochemical fraction (i.e., OM, RSTMs and Ba), and abundant but scattered octahedral pyrite crystals and pyrite framboids, and also oval barite crystals (Figs. IV.4 and 7). The presence of pyrite framboids in this interval is indicative of euxinic porewaters, while the small sizes of scattered octahedral pyrite crystals in this interval are indicative of euxinic bottom-waters (Wilkin et al., 1996; Wilkin and Barnes, 1997; Liu et al., 2019; Chang et al., 2022). Moreover, this interval is characterized by irregular OM laminae enriched in coccolith, which probably decanted as OM flakes during increased seasonal productivity (Figs. IV.4 and 7). These irregular laminae consist of light gray laminae enriched in detritic elements (e.g., Si, Al, Mg and K) and darker layers enriched in Ca and OM (Fig. IV.7; Figs. S17-S21 in the Sup. mat.). The good preservation of OM and pyrite framboids indicates that the authigenic fraction has not been affected by postdepositional oxidation, and consequently, the concentrations of RSTMs and TOC content reflect the original syndepositional redox and productivity conditions. Moreover, texture and size of pyrite framboids do not indicate late diagenetic overgrowths or reprecipitation (e.g., sunflower texture) (Chang et al., 2022). The absence of diagenetic overgrowths is linked to the fact that reactive Fe^{+2} was depleted in this interval due to the intense precipitation of pyrite framboids during S1 deposition (Passier et al., 1996; Passier and de Lange, 1998). As a result, HS^{-} diffused out from this interval, facilitating the subsequent precipitation of pyrite below the unoxidized interval, specifically in the so-called “synsapropel interval” (Passier et al., 1996, 1997).

Synsapropel interval (yellow interval area in Fig. IV.2a): the sediments corresponding to the synsapropel interval were deposited before S1 under oxic/suboxic bottom-waters. This interval is characterized by high DOPt values, and low TOC% and Ba concentrations, due to the absence of barite crystals and organic-rich laminae, and the presence of large euhedral framboids aggregates (Figs. IV.4 and 7). This interval is also enriched in the authigenic fraction, but RSTMs are enriched in association with pyrite (Figs. IV.2 and 9). No abundant barite crystals or OM laminae were observed, indicating low productivity during the deposition of this interval (Fig. IV.7). Large pyrite framboids clusters, many infilling foraminifera shells and others embedded in the sediment, are typically formed just during intense H_2S downward diffusion (Fig. IV.10) (Zhang et al., 2014; Lin et al., 2016; Chang et al., 2022; Liu et al., 2022). During very early diagenesis, the downward diffusion of excess HS^{-} (mainly produced by sulphate-reducing bacteria) promoted the formation of confined euxinic sub-mm areas (i.e., “microniches”) (Tribovillard et al., 2008). These euxinic microniches allowed the precipitation of large pyrite framboids aggregates through sulphidisation of Fe-oxides within the sediments below the sapropel (Passier et al., 1996, 1997, 1999; Benkovitz et al., 2020; Matthews et al., 2017; Filippidi and de Lange, 2019). Some pyrite aggregates developed large pyrite overgrowth with a “sunflower” texture, which tends to occur during late diagenesis (Fig. IV.4; Fig. S10 in the Sup. mat.) (Lin et al., 2016; Chang et al., 2022).

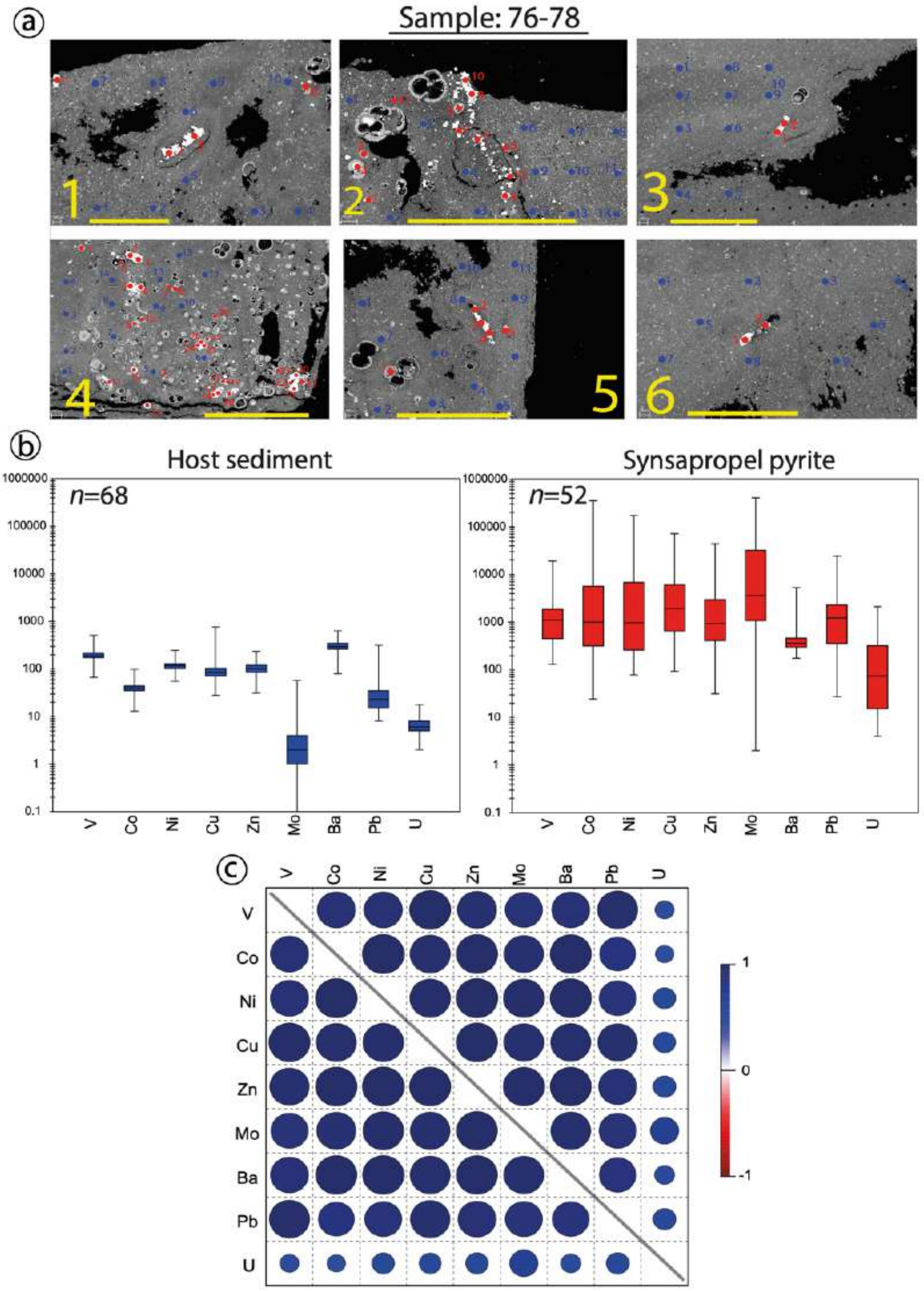

Figure IV.9. *LA-ICP-MS spot-analyses results of pyrite framboids and aggregates in the synsapropel layer (sample 76–78 thin-section). (a) Localization and number of the LA-ICP-MS spot-analyses. Pyrite framboids/aggregates in red, host sediment in blue. Yellow line represents a scale-bar of 100 µm. The yellow numbers correspond to the batch of LA-ICP-MS analysis. (b) Box-whisker plots showing TMs concentrations (ppm in logarithmic scale) obtained by LA-ICP-MS spot-analyses in the host sediments (blue box-whisker plot) and in the pyrite framboids/aggregates (red box-whisker plot) of the synsapropel interval. (c) Correlation matrix of TMs concentration obtained by LA-ICP-MS in the host sediments and in the pyrite framboids/aggregates. For interpretation of correlation matrices, read caption of Fig. IV.3. For detailed results of LA-ICP-MS spot-analyses and correlation matrices with values, see in the Sup. mat. Tables S9 - S11, and Fig. S8 for SEM-EDX spot-analyses of pyrite aggregates.*

Although some framboidal pyrite has undergone secondary growth, the maintenance of the diameter of the inner framboid sphere, allow interpret that these framboids precipitated below the SWI and not in the water-column (Liu et al., 2019; Chang et al., 2022). Thus, the pyrite framboids show a first growing phase during S1 deposition and early diagenesis, allowing precipitation below S1 due to intense H_2S downward diffusion, and a second phase during late diagenesis promoting overgrowths (Chang et al., 2022). Presence of euhedral pyrite framboids/aggregates infilling foraminifera chambers (Fig. IV.4; Fig. S8 in the Sup. mat.), can be related to microenvironments with different redox conditions from that of the surrounding sediment matrix (Fig. IV.10). These microenvironments are enriched in OM derived from the soft parts of foraminifera, which are degraded by sulphate-reducing bacteria. However, it is important to highlight that these microenvironments do not reflect the redox conditions of the porewater system.

IV.4.3. Characterization and interpretation of RSTMs sub-mm signals

The marker bed (sample 60–62, Figs. IV.6 and 8), present localized enrichments in Mo, Co, Cu, Zn, Ni and Pb, which are probably in association with Mn-oxyhydroxides that intensely precipitated during S1 termination. Some of the Mn-rich particles exhibit concentric layers, where, being the inner layer more enriched in Ca than the outer layer (Fig. S4 in the Sup. mat.). This seems to suggest a change in the host mineral of Mn during diagenesis. In this interval, the localized enrichments are more pronounced for Mo (Fig. IV.8), demonstrating that Mo is the RSTMs most efficiently fixed by Mn-oxyhydroxides during reventilation (Reitz et al., 2006). Conversely, V and U do not present enrichments in association with Mn-oxyhydroxides since these two elements tend to be enriched in association with OM, which in this interval is very low due to post depositional oxidation. Moreover, the low abundance of barite in this interval due to lower marine productivity promotes a low and almost univariable Ba sub-mm line-scan. In the oxidized interval (sample 64–66, Figs. IV.6 and 8), the lower concentrations of RSTMs are consequence of the oxidation of their host phases (i.e., sulphides and OM) (Nijenhuis et al., 1999; Tribovillard et al., 2006) (Fig. IV.7; Figs. S15 and S16 in the Sup. mat.). Ba line-scan is situated above the RSTMs line-scan due to the preservation of barite crystal to postdepositional oxidation.

In the unoxidized interval (samples 68–70 and 70–72, Figs. IV.7 and 8), RSTMs are characterized by high concentration and correlative increases due to their co-enrichments in association with pyrite and OM (Nijenhuis et al., 1999; Tribovillard et al., 2006). In most cases, U enrichments do not correlate with rest of RSTMs since are linked to metal-organic ligand complexes enriched in the sub-mm irregular organic-rich laminae, and not in association with the scattered pyrite framboids as most RSTMs (Tribovillard et al., 2006). Although, all RSTMs have high concentrations, Ba is the most enriched TM in this interval due to the high abundance of barite crystals. Moreover, a rapid shift of redox conditions in the Ionian Basin bottom-waters is interpreted since RSTMs show a correlative decrease in the middle of sample 70–72 (Fig. IV.8). However, Ba concentrations remained high throughout this sample, indicating that surface-water productivity and associated OM degradation were constant, while oxygen depletion Ionian Basin deep-water was weakened during the corresponding time interval. Thus, this sub-mm analysis demonstrates that deoxygenation in Emed deep settings during S1 does not only derive from increased marine productivity, and instead suggests that deep-water renewal frequency played a more important role in bottom-water deoxygenation than productivity. This shift in bottom-water redox conditions during S1, could be associated to the 8.2 ka cold event recognized in previous studies, which renewed and oxygenated the Emed deep-waters (Ariztegui et al., 2000; Rohling and P¨alike, 2005; Rohling et al., 2014; Rohling et al., 2015; Filippidi et al., 2016; Triantaphyllou et al., 2016; Filippidi and de Lange, 2019). These results highlight the potential of sub-mm high-resolution geochemical analyses for precise palaeoceanographic/palaeoenvironmental reconstructions.

The synsapropel interval (sample 76–78, Figs. IV.7 - 9) is characterized by low background concentrations of RSTMs and Ba. However, there are distinct localized areas with exceptionally high enrichments in all RSTMs, except for U and V, which exhibit almost univariable concentrations and weaker enrichments in the line-scan analysis. These enrichments are in association with the large synsapropel pyrite framboids/aggregate. This explains why U and V are the RSTMs with weaker sub-mm enrichments, since these two TMs do not tend to associate with pyrite (Tribovillard et al., 2006 and references therein). Mo is the RSTMs most enriched in the synsapropel pyrite aggregates (Figs. IV.2, 8 and 9), as is the most efficiently fixed RSTM by pyrite aggregates during early diagenesis, as also noted by Tribovillard et al. (2008) in Jurassic formations or by Filippidi and de Lange (2019) in S1 deposited in EMed deep settings.

IV.4.4. TM postdepositional remobilization

Dissolved RSTMs in the porewater derived from the postdepositional oxidation of OM and sulphides (i.e., oxidation of the authigenic fraction) can either be fixed again in the sediments through various mechanisms and interactions with different geochemical fractions, or they can diffuse upward to bottom-waters (Fig. IV.10). The upward diffusion of RSTMs is influenced by various factors such as concentration gradients, sediment properties, and bottom-water conditions. Once in the water column, these RSTMs can be transported and redistributed, potentially impacting water chemistry and biogeochemical processes. Overall, the fate of dissolved RSTMs in the porewater is determined by a complex interplay of sedimentary processes, geochemical interactions, and hydrodynamic conditions discussed below. Understanding these processes from macro to microscale is crucial for comprehending the cycling and distribution of RSTMs in marine sediments and their potential impact on the surrounding environment.

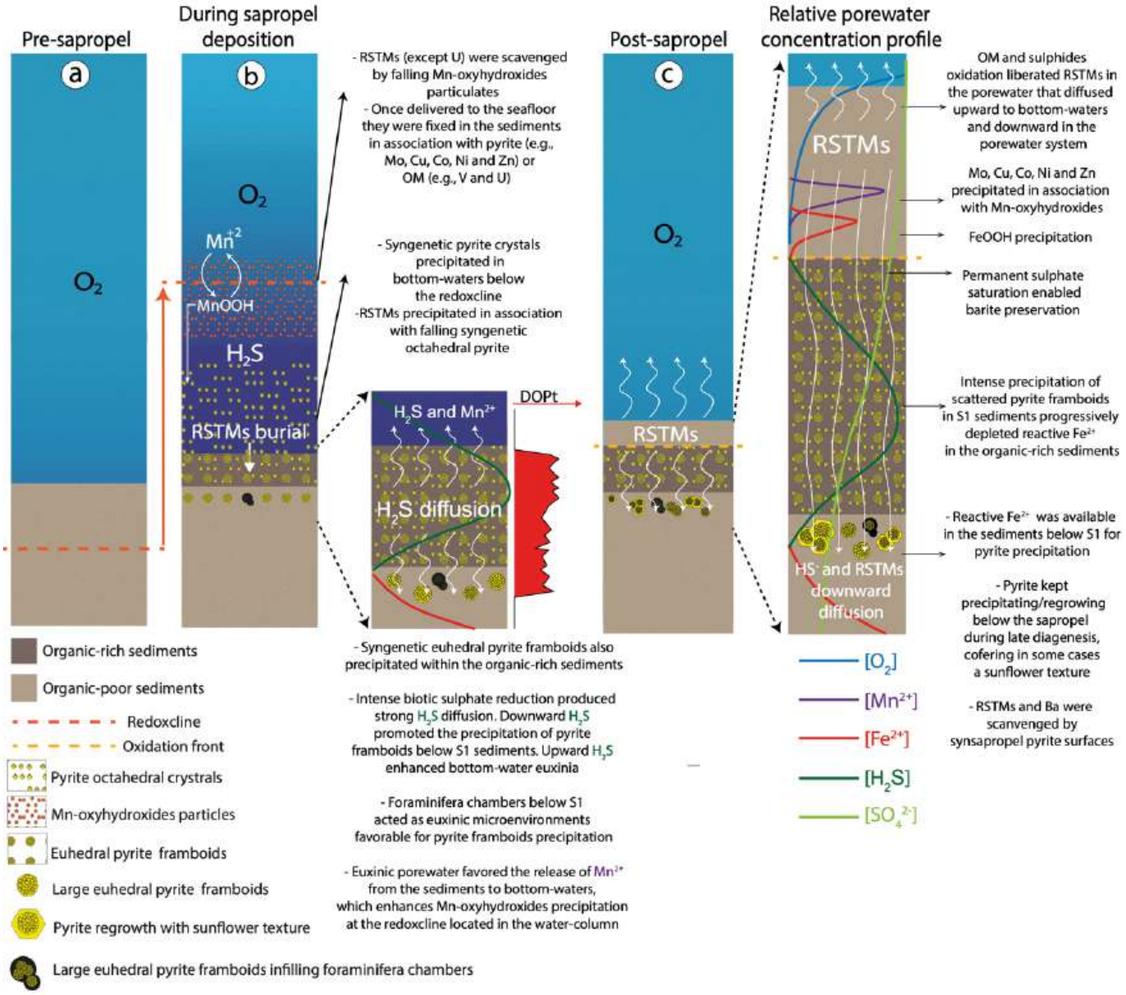
Pre-sapropel
a
O_2
During sapropel deposition
b
O_2
Mn^{+2}
MnOOH
H_2S
RSTMs burial
H_2S and Mn^{2+}
H_2S diffusion
DOPt
Post-sapropel
c
O_2
RSTMs
Relative porewater concentration profile
RSTMs
HS^- and RSTMs downward diffusion
$[O_2]$
$[Mn^{2+}]$
$[Fe^{2+}]$
$[H_2S]$
$[SO_4^{2-}]$
Organic-rich sediments
Organic-poor sediments
Redoxcline
Oxidation front
Pyrite octahedral crystrals
Mn-oxyhydroxides particles
Euhedral pyrite framboids
Large euhedral pyrite framboids
Pyrite regrowth with sunflower texture
Large euhedral pyrite framboids infilling foraminifera chambers

- RSTMs (except U) were scavenged by falling Mn-oxyhydroxides particulates
- Once delivered to the seafloor they were fixed in the sediments in association with pyrite (e.g., Mo, Cu, Co, Ni and Zn) or OM (e.g., V and U)

- Syngenetic pyrite crystals precipitated in bottom-waters below the redoxcline
-RSTMs precipitated in association with falling syngenetic octahedral pyrite

- Syngenetic euhedral pyrite framboids also precipitated within the organic-rich sediments

- Intense biotic sulphate reduction produced strong H_2S diffusion. Downward H_2S promoted the precipitation of pyrite framboids below S1 sediments. Upward H_2S enhanced bottom-water euxinia

- Foraminifera chambers below S1 acted as euxinic microenvironments favorable for pyrite framboids precipitation

- Euxinic porewater favored the release of Mn^{2+} from the sediments to bottom-waters, which enhances Mn-oxyhydroxides precipitation at the redoxcline located in the water-column

OM and sulphides oxidation liberated RSTMs in the porewater that diffused upward to bottom-waters and downward in the porewater system

Mo, Cu, Co, Ni and Zn precipitated in association with Mn-oxyhydroxides

FeOOH precipitation

Permanent sulphate saturation enabled barite preservation

Intense precipitation of scattered pyrite framboids in S1 sediments progressively depleted reactive Fe^{2+} in the organic-rich sediments

- Reactive Fe^{2+} was available in the sediments below S1 for pyrite precipitation

- Pyrite kept precipitating/regrowing below the sapropel during late diagenesis, cofering in some cases a sunflower texture

- RSTMs and Ba were scanvenged by synsapropel pyrite surfaces

Figure IV.10. *Schematic cartoons showing the paleoredox changes and processes that occurred in the porewater and water-column of the Ionian deep basin during the deposition of S1 at different stages (a: pre-sapropel, b: during sapropel deposition, c: post-sapropel). The legend and comments are indicated in the figure, not scale (modified from Algeo and Tribovillard, 2009; Canfield and Thamdrup, 2009).*

In S1, there are two distinct layers where dissolved RSTMs in the porewater can be fixed again (Fig. IV.10). The first layer is the marker bed, formed after S1 deposition, when rapid reventilation and reoxygenation of bottom-waters lead to the intense precipitation of Mn-oxyhydroxides (Fig. IV.6). Abundant Mn-oxyhydroxides in S1 top effectively trapped and immobilized upward diffusing RSTMs in the porewater. The other layer is the synsapropel layer, which is stratigraphically below the organic-rich interval, therefore, the downward diffusing fraction of RSTMs can reprecipitate in this layer (Passier et al., 1996, 1997; Passier and de Lange, 1998; Tribovillard et al., 2008; Reed et al., 2011; Matthews et al., 2017; Filippidi and de Lange, 2019).

The fraction of dissolved RSTMs that diffuses downward should precipitate immediately below the oxidation front, i.e., in the unoxidized interval, and not in the synsapropel interval. This could be attributed to the fact that reactive iron is depleted in the unoxidized interval due to the intense precipitation of pyrite framboids in the organic-rich sediments during S1 deposition (Fig. IV.10). Consequently, RSTMs keep diffusing downward until favorable conditions for permanent fixation are reached, i.e., where anoxic/ euxinic conditions and available reactive iron coincide. In most cases, these conditions occurred within euxinic microniches below the organic-rich interval, e.g., inside foraminifera shells (Passier et al., 1996, 1997; Tribovillard et al., 2008; Chang et al., 2022). As a consequence, post-depositional sub-mm scale RSTMs enrichments occurred below the organic-rich interval (Figs. IV.2, 8 and 9).

The presence of large euhedral pyrite framboids/aggregates below S1 played a crucial role in providing extensive reaction surfaces for pyrite regrowth and the trapping of RSTMs (Figs. IV.8 and 9). The dissolved RSTMs, mainly derived from the oxidation of OM and sulphides in the upper section of S1 after its termination, diffused downward into the porewater and reprecipitated on the surfaces of the pyrite aggregates within the synsapropel interval. Consequently, these sub-mm enrichments of RSTMs are postdepositional and do not reflect the syndepositional redox conditions of the surrounding sediment (Fig. IV.10). Nonetheless, these sub-mm RSTMs enrichments indicate the presence of confined euxinic or near-euxinic microenvironments within dysoxic sediments below S1. These microenvironments facilitated the sequestration of dissolved RSTMs that typically associate with pyrite, including Mo, Cu, Ni, Co, and Zn (Huerta-Diaz and Morse, 1991; Bostick et al., 2003; Vorlicek et al., 2004; Tribovillard et al., 2006, 2008).

Moreover, U and V, which are RSTMs that do not typically associate with pyrite (Tribovillard et al., 2006 and references therein), are enriched in the synsapropel pyrite framboids/aggregates (Table IV.1; Figs. IV.8 and 9). V exhibits a strong positive correlation with the other RSTMs (Fig. IV.9c), suggesting that remobilized V precipitated in association with pyrite, as most RSTMs. However, another possibility is that under euxinic conditions below the unoxidized interval, V in the form of V^{3+} precipitated as solid oxide V_2O_3 or hydroxide $V(OH)_3$ phase (Breit and Wanty, 1991; Wanty and Goldhaber, 1992). However, V sub-mm enrichments are found uniquely in pyrite framboids/aggregates, suggesting a primary origin associated with the synsapropel pyrite aggregates (Fig. IV.10). U is the only RSTMs that presents weak to moderate positive correlations with the rest of RSTMs in the sub-mm synsapropel pyrite framboids/aggregates and the least enriched RSTMs (Fig. IV.9). In anoxic/euxinic porewater U fixation is enhanced by organometallic ligands present in the OM and is mainly enriched in the sediments by the precipitation of uraninite (UO_2), a highly insoluble mineral (Crusius et al., 1996; Morford and Emerson, 1999; Zheng et al., 2000; McManus et al., 2005; Tribovillard et al., 2006; Bruggeman and Maes, 2010). Thus, these sub-mm U enrichments could be due to precipitation of U as uraninite nanoparticles in association with the OM inside of foraminifera chambers, since they represent the only microenvironments with high OM content in the synsapropel layer. However, U enrichments are not limited to pyrite aggregates inside foraminifera chambers. Hence, a more possible explanation is that dissolved U derived from post-depositional oxidation enhanced by bioirrigation (Zheng et al., 2002; Tribovillard et al., 2006; Morford et al., 2009), is adsorbed onto pyrite crystal surfaces by sorption reactions (Bruggeman and Maes, 2010).

Experimental studies have shown that U can be efficiently immobilized and scavenged by pyrite surfaces (Eglizaud et al., 2006; Scott et al., 2007; Bruggeman and Maes, 2010; Descostes et al., 2010; Wang et al., 2021). Therefore, all RSTMs enrichments in the synsapropel interval appear to be predominantly associated with pyrite aggregates, primarily through surface adsorption. A plausible pathway for these enrichments involves the oxidation of pyrite and OM in the upper section of S1, which releases RSTMs into the porewater and promotes the formation of colloidal and flocculated ferric hydroxides and low-crystallinity goethite precipitates. Consequently, these precipitates can then undergo chemical adsorption onto the surfaces of pyrite aggregates in the synsapropel interval, facilitating the co-precipitation of RSTMs (Duff et al., 2002; Wang et al., 2021). However, U absorption by pyrite surfaces is less efficient than for the rest of RSTMs, since the proportional enrichment in respect to the host sediment is the lowest. This would justify the weaker positive correlation of U.

Even though Ba is not considered a RSTMs, a similar fixation mechanism as the one proposed for U and V could justify the moderate Ba enrichments and its strong correlation with the rest of RSTMs in the synsapropel pyrite aggregates (Table IV.1; Fig. IV.9). As mentioned in section 4.1, Ba is enriched in superficial sediments due to the accumulation of oval barite nanocrystals, which precipitate in association with particulated OM (e.g., fecal pellets and OM flakes) and extracellular polymeric substances that rain down from the mesopelagic zone to the seafloor (Paytan et al., 2002; Gonzalez-Muñoz et al., 2012; Martínez-Ruiz et al., 2018, 2020). Upon burial, biogenic barite nanocrystals can undergo dissolution below the SWI if SO_2^{4-} is depleted due to intense euxinia, releasing Ba^{2+} in the porewater system (Fig. IV.10) (Torres et al., 1996; Grema et al., 2022). However, unlike in Black Sea sediments or Mesozoic and Paleozoic Black Shales, where SO_2^{4-} depletion resulted in the dissolution of authigenic barite and the formation of distinctive Ba peaks above the oxidation front or below the organic-rich sediments (Henkel et al., 2012; Grema et al., 2022), in the EMed, porewater SO_2^{4-} is not significantly depleted even during sapropel deposition (Passier et al., 1997). Consequently, the preservation of authigenic/biogenic barite is ensured (Paytan et al., 2004). This is corroborated by the morphology and size of barite crystals in the different S1 geochemical intervals which indicate authigenic nature and no significant signs of diagenetic recrystallization (see Fig. IV.5 and Fig. IV.S6) (Martínez-Ruiz et al., 2000). Furthermore, no evidence of diagenetic barite was observed, even above the oxidation front, where it would have reprecipitated if intense SO_2^{4-} depletion had occurred (Henkel et al., 2012). Nevertheless, some degree of barite dissolution needs to be evoked in order to explain the dissolved Ba that led to the moderate Ba enrichments in the synsapropel pyrite aggregates that formed during early diagenesis (Table IV.1).

IV.5. Conclusions

LA-ICP-MS and SEM-EDX analyses provided enhanced spatial resolution of geochemical redox and diagenetic signals across the S1 sapropel in the Ionian Basin. Geochemical microanalyses have allowed to: (i) enable the characterization of microscale geochemical heterogeneities, (ii) a precise spatial analysis of mineralogical composition and elemental distributions (including RSTMs) at a sub-mm scale, and (iii) identify sub-mm zones where redox reactions and diagenetic processes occurred within S1 and surrounding sediments due to postdepositional processes.

Three distinct geochemical fractions were identified and characterized across the S1 sapropel interval using multivariant statistical analyses, detritic, carbonate, and authigenic fractions. The proportional enrichment of the authigenic fraction is associated with oxygen-depleted bottom-waters, high export productivity, and intense bacterial degradation.

The S1 sapropel interval can be divided into four geochemical intervals: (i) the marker bed, (ii) the oxidized interval, (iii) the unoxidized interval, and (iv) the synsapropel interval. The marker bed and the synsapropel interval have been identified as significant geochemical intervals where dissolved RSTMs in the porewater can be re-precipitated. The intense precipitation of Mn-oxyhydroxides in the marker bed and the large pyrite surfaces in the synsapropel layer play key roles in trapping and scavenging dissolved RSTMs in the sediments. Among the RSTMs, Mo is the most efficiently trapped by Mn-oxyhydroxides and pyrite aggregates during early diagenesis.

The sub-mm RSTMs enrichments observed in the synsapropel pyrite aggregates are primarily attributed to postdepositional processes rather than the syndepositional conditions of the host sediment. The extensive reaction surfaces provided by large euhedral pyrite aggregates facilitated the trapping and absorption of RSTMs. However, the sub-mm enrichments of some RSTMs are not reflected in the bulk sediment composition obtained by discrete geochemical analyses, emphasizing in this way the importance of microscale analyses in detecting and assessing sub-mm geochemical signals derived from postdepositional processes.

Overall, this study underscores the importance of microscale geochemical analyses and highlights the complexity of RSTM fixation and enrichment processes in sediments, shedding light on the dynamic nature of postdepositional reactions and their implications for interpreting palaeoenvironmental conditions. Moreover, this level of detail is essential for understanding the spatial complexity of deoxygenation processes and their impacts on biogeochemical cycling.

Supplementary material

Supplementary data to this article can be found online at:
https://ars.els-cdn.com/content/image/1-s2.0-S0009254123003431-mmc1.docx

Acknowledgments

This study has been supported by Grants PID2019-104624RB-I00, PID2019-104625RB-100, and TED2021-131697B-C22 funded by MCIN/AEI/ 10.13039/501100011033, Grants FEDER/Junta de Anda- lucía P18-RT-3804 and P18-RT- 4074, and by Research Groups RNM- 179 and RNM-178 funded by Junta de Andalucía. We thank Prof. Adatte (Lausanne University, Switzerland) for Rock-eval analyses and TOC measurements. We are grateful to the Center for Scientific Instrumentation (CIC, University of Granada) and the XRF Unit of the IACT (CSIC-UGR) for the ICP, SEM-EDX and XRF analyses. We are also grateful to the Ocean Drilling Program for providing the analyzed samples as well as to the ODP Core Repository (Bremen, Germany) for assistance with sampling, and to the Department of Mineralogy and Petrology of University of Granada for the preparation of the sediment thin-sections. This study is part of Monedero PhD project.

Chapter V

Impact of *Chondrites* on trace metal distribution in the sapropel S7 (ODP Site 966): Implications for paleoenvironmental and paleoceanographic reconstructions

Ricardo D. Monedero-Contreras, Francisco J. Rodríguez-Tovar, Francisca Martínez-Ruiz

Global and Planetary Change 234 (2024) 104387
doi: 10.1016/j.gloplacha.2024.104387

Abstract

Organic-rich deposits are valuable paleoarchives, recording significant paleoceanographic changes linked to past climate variations and marine deoxygenation events. The deposition of organic-rich sediments stops when bottom-water reventilation/oxygenation occurs. This impedes organic matter preservation, enabling macro and micro burrowing-organisms to recover and bioturbate the seafloor. In this sense, highly bioturbated sediments require particular attention when sampling is done for geochemical analyses, as sediments can be considerably mixed. While avoiding trace fossils during sampling for geochemical analyses is easy for large traces (e.g., *Planolites, Thallasinoides,* and *Zoophycos*), it becomes challenging for smaller and complex traces (< 0.5 cm), as is the case with *Chondrites*. *Chondrites*-producers have an opportunistic behavior, being one of the first organisms to colonize the seafloor after an anoxic event. As a result, *Chondrites* are commonly and sometimes abundantly found in the upper layers of organic-rich sediments, including sapropels and black shales

This study focuses on sapropel S7, which was deposited between ~ 198.5 and 191.9 ka at the top of Eratosthenes Seamount and exhibits abundant *Chondrites*. For this sapropel, we demonstrated that *Chondrites*-producers can bioturbate significant volumes of organic-rich sediments (over 35%), introducing oxic/dysoxic material downward into anoxic sediments enriched in redox-sensitive trace metals and organic matter. This process can dilute up to 18% the original concentration of redox-sensitive trace metals (e.g., Mo, U and V). This dilution is especially important to consider when calculating trace metals and organic matter burial flux from bulk sediment data. Therefore, *Chondrites*-producers can play a crucial role in altering the sediment texture and distribution of minerals and organic matter at sub-cm scale, and may thus impact paleoenvironmental and paleoceanographic reconstructions based on geochemical signals. Furthermore, the subsequent redistribution of organic matter and redox-sensitive trace metals (including oligoelements) within the sediment can affect carbon and nutrient cycling, microbial activity, organic matter degradation in deep-marine sediments, and the overall sedimentary biogeochemistry.

V.1. Introduction

Organic-rich deposits are regarded as oceanographic paleoarchives of significant environmental importance because they record profound paleoceanographic changes typically associated with past climate variations. They are valuable tools for comprehending long-term oceanographic responses to contemporary climate change (Hennekam et al., 2020). The combination of sustained surface water eutrophication and water-column stagnation promotes expansion of the O_2-minimum zone into deeper settings and oxygen-depletion in deep bottom-waters, respectively (Zirk et al., 2019). In deep-marine settings, bottom-water deoxygenation leads to enhanced organic matter (OM) preservation and to the authigenic enrichment of redox-sensitive trace metals (RSTMs) such as Mo, U, and V (Tribovillard et al., 2006). Therefore, the concentrations of RSTMs in marine sediments are broadly utilized in geochemical paleoenvironmental studies as proxies for redox conditions (Warning and Brumsack, 2000; Tribovillard et al., 2006; Calvert and Pedersen, 1993, 2007; Algeo and Liu, 2020).

In this context, organic-rich deposits −such as sapropels− represent exceptional records of past deoxygenation events. Sapropels are quasi-cyclic organic-rich sediments deposited in the Eastern Mediterranean during periods of enhanced productivity and bottom-water restriction (Emeis et al., 2000). Their cyclic deposition is linked to astronomical precession cyclicity, whereby periods of minimum astronomical precession result in maximum insolation in the Northern Hemisphere (Fig. V.1c) (Hilgen, 1991; Lourens et al., 1996; Hennekam et al., 2014). This phenomenon triggers the intensification and northward migration of the African monsoon, leading to increased freshwater and nutrient input into the Eastern Mediterranean, and thereby promoting a decrease in surface water salinity and deep-water stagnation and deoxygenation (Weldeab et al., 2014; Tachikawa et al., 2015; Rohling et al., 2015; Wu et al., 2016, 2018; Andersen et al., 2020; Monedero-Contreras et al., 2023a).

Bottom-water deoxygenation ceases once ventilation occurs. Subsequently, during the reactivation of bottom-water circulation, oxygenated waters reach the seafloor and inhibit the accumulation/preservation of organic-rich sediments, as is the case during sapropel termination (Pruysers et al., 1991, 1993; Reitz et al., 2006; de Lange et al., 2008; Filippidi and de Lange, 2019). During bottom-water reoxygenation, both macro and micro benthic organisms rapidly colonize and repopulate the seafloor (Löwemark et al., 2006). Opportunistic burrowing organisms penetrate the underlying organic-rich sediments, leading to two potential outcomes: (i) discrete traces with marked outlines and differentiated infill, or (ii) a total remobilization and mixing of the sediment, determining a mottled background, consisting of biodeformational sedimentary structures, having no distinct outline (Rodríguez-Tovar, 2022). In either case, these processes may alter the original concentrations of RSTMs within the organic-rich sediment. Consequently, bioturbation is seen as a crucial factor when assessing RSTM concentrations in paleoenvironmental and paleoceanographic reconstructions. It is therefore essential to identify trace fossils to avoid the infilling material when sampling for geochemical analyses. Trace fossils are often visually distinguishable in organic-rich sediments due to their contrasting coloration when compared to the host sediment. Larger trace fossils frequently registered in deep-marine environments, such as *Planolites*, *Thallasinoides*, and *Zoophycos* (Rodríguez-Tovar, 2022), can usually be avoided during sampling for geochemical analyses. However, the same cannot be said for smaller trace fossils (< 0.5 cm), such as *Chondrites*, which are also very common in deep-marine environments and exhibit highly complex architecture (Baucon et al., 2020).

Chondrites normally exhibit a branching tunnel system, as a dendritic network, consisting of a small number of sub-vertical burrows, connected to the paleosediment-water interface (Baucon et al., 2020 and reference therein). *Chondrites*-producers exhibit opportunistic behavior, often being one of the first tracemakers to bioturbate the seafloor just after an anoxic event, e.g., a sapropel event (Löwemark et al., 2006; Löhr and Kennedy, 2015). Monogeneric or low-diversity assemblages with *Chondrites* are associated with dysoxic environments (Bromley and Ekdale, 1984; Bromley, 1996; Buatois and Mángano, 2011; Baucon et al, 2020). The producers of *Chondrites* appear to be capable of colonizing environments characterized by oxygen levels unfavorable for other tracemakers (Savrda and Bottjer, 1984; Löhr and Kennedy, 2015), being considered as an "extremotolerant" ichnotaxon (Baucon et al., 2020). As a result, they are frequent or even, in some cases, abundant in organic-rich sediments (see Baucon et al., 2020 for a review). This trace has been registered in black shale sediments through the fossil record linked to oceanic anoxic events such as the End Permian Mass Extinction (Rodríguez-Tovar et al., 2021), the Toarcian Oceanic Anoxic Event (Early Toarcian; i.e., Bromley and Ekdale, 1984; Rodríguez-Tovar and Uchman, 2010; Montero-Serrano et al., 2015; Fernández-Martinez et al., 2021; Rodríguez-Tovar, 2021a, b), the Bonarelli Event (Cenomanian-Turonian boundary; Schönfeld et al., 1991; Hilbrecht and Dahmer, 1994; Uchman et al., 2008, 2013a, 2013b; Rodríguez-Tovar et al., 2009a, 2009b, 2020; Rodríguez-Tovar and Uchman, 2011; Monaco et al., 2012, 2016), and the Faraoni Event (upper Hauterivian; Rodríguez-Tovar and Uchman, 2017).

Chondrites-producers can introduce significant volumes of overlying sediments downward into deeper sediments of different composition (Baucon et al., 2020). Discrete bulk sediment samples collected from organic-rich sediments with abundant *Chondrites* will exhibit a mixed geochemical signal resulting from the composition of both *Chondrites* infills and host sediments. Therefore, the RSTM concentrations obtained from bulk sediment samples do not reflect the syndepositional concentrations. Carbon isotope analysis of trace fossil infills −including

Chondrites− at the Agost section in southern Spain was used to distinguish between different phases of macrobenthic colonization during the K-Pg boundary period (Rodríguez-Tovar et al., 2004, 2006). Yet there are not many studies that specifically assess bioturbation impact on RSTM distribution and concentration within the sediment.

In this context, paleoenvironmental and paleoceanographic reconstructions require the assessment of *Chondrites'* influence on the original concentrations of RSTMs in organic-rich sediments that represent past deoxygenation events. The influence of *Chondrites* on the sub-cm distribution of RSTMs and OM in organic-rich sediments is examined in sapropel S7, deposited at the top of Eratosthenes Seamount. The aim of this study is to demonstrate the important role of discrete traces, particularly *Chondrites,* when using TMs as paleoceanographic proxies, while also assessing their potential impact on sedimentary biogeochemistry.

V.1.1. Assessed trace metals

Under oxygen-deficient conditions in marine systems, diverse authigenic minerals can precipitate, leading to the enrichment of marine sediments in RSTMs such as Mo, U, V, Re, Cu, Co, Ni, Cr, Zn, Pb, and Mn. Normalizing these metals allows them to be used as redox proxies, to infer different redox conditions in ancient marine environments (Berner, 1981; Calvert and Pedersen, 1993, 2007; Crusius et al., 1996; Tribovillard et al., 2006, 2008; Algeo and Tribovillard et al., 2009; Scheiderich et al., 2010; Little et al., 2015; Paul et al., 2023). In this study, we focus on the assessment of trace elements Mo, U, V, Co, Cu, Ni, Cr, Zn, Pb, and Ba, which are normally enriched in sapropel layers. Under oxygen-depleted conditions, Mo, V, Co, Cu, Ni, Cr, Pb, and Zn are scavenged from the water-column by manganese (Mn) and iron (Fe) oxyhydroxides, as well as OM, and are subsequently deposited on the seafloor (Scholz et al., 2013). If euxinic conditions occur in the bottom-water or porewaters, these metals become permanently fixed through association with pyrite (FeS) or by forming their own sulfides (e.g., MoS, CuS, CuS_2, NiS, and [Zn,Fe]S, CoS, NiS) or oxides in the case of V (e.g., V_2O_3) (Tribovillard et al., 2006 and references therein). U behaves differently, as it is not influenced by the redox cycling of Mn and Fe in the water-column. Instead, U precipitates as the less soluble lower oxidation state in association with humic and fulvic acids derived from OM degradation during anoxic conditions in bottom-waters (Zheng et al., 2002; McManus et al., 2005; Morford et al., 2005; Tribovillard et al., 2006; Calvert and Pedersen, 2007).

The Ba in sapropel sediments is primarily attributed to an increase in the abundance of marine barite (Martínez-Ruiz et al., 2000). The precipitation of barite in the water-column has been linked to periods of heightened productivity and degradation of OM in the mesopelagic zone (Bishop, 1988; Paytan et al., 2002, 2004; Calvert and Pedersen, 2007; Paytan and Griffith, 2007; Gallego-Torres et al., 2007a, 2010; Martínez-Ruiz et al., 2020; Filippidi and De Lange, 2019). Martínez-Ruiz et al. (2018, 2019) have demonstrated the significant role of bacteria and particularly Extracellular Polymeric Substances in promoting saturated microenvironments in which Ba precipitates. Due to its correlation with productivity, the Ba content is commonly employed as a qualitative proxy for assessing past oceanic productivity. Consequently, in this study, the potential Ba dilution resulting from the remobilization of *Chondrites* sediments was also evaluated.

V.2. Paleo-oceanographic setting and sediment record

The studied sediment record, containing the sapropel S7, was retrieved in 1995 during the Ocean Drilling Program (ODP) Leg 160 expedition at Site 966-Hole B, hereafter referred to as Site 966B (see Emeis et al., 1996 for Leg 160 expedition scientific report). Site 966B (33°47.765'N, 32°42.090'E) is located near the northern margin of the Eratosthenes Seamount plateau, at a depth of 927 m below sea level (mbsl) (Figs. V.V.1a and b). At present, circulation in the Eastern Mediterranean is controlled by two main mechanisms: wind stress and thermohaline forcing (POEM Group, 1992; Millot and Taupier-Letage, 2005; Amitai et al., 2018). The Eratosthenes Seamount lies beneath the present-day Levantine Intermediate Water (LIW) (Figs. V.V.1a and b). The depth of Site 966B corresponds to the lower limit of MIW and the upper limit of Eastern Mediterranean Deep-Water (EMDW), around 1000 mbsl (Wüst, 1961). Despite the close proximity of Eratosthenes Seamount to the Nile River mouth, Site 966B is not affected by fan deposition from the Nile Cone, and is not influenced by downslope gravity processes that could disturb the sediment record (Emeis et al., 1996). However, during sapropel events, the water-column structure and current dynamics differed significantly from those observed in the modern Eastern Mediterranean. Specifically, sapropel event S7 occurred between 198.5 and 191.9 ka, during Marine Isotope Stage 7a (Fig. V.1c; Ziegler et al., 2010). This period, in the Eastern Mediterranean, was characterized by exceptionally intense African monsoons and high freshwater input, which resulted in high marine productivity, stable water-column stratification, and anoxic/euxinic EMDW (Gallego-Torres et al., 2007a; Benkovitz et al., 2020; Sweere et al., 2021; Monedero-Contreras et al., 2023a).

The 966B sediment record consists mainly of nannofossil clay, clayey nannofossil ooze, and nannofossil ooze, with characteristic layers that include foraminiferal sandy levels, discrete tephra layers, and sapropels (dark layers) (Emeis et al., 1996, 2000). The 45 cm studied interval− spanning from 515 to 470 cm in core section 966B 1H-4− includes sediments from sapropel S7, as well as underlying and overlying sediments. The interval was sampled at 1-3 cm resolution, with a total of 25 discrete sediment samples for geochemical analyses (i.e., Rock- Eval, ICP-OES and ICP-MS; refer to section 3.1) (Table V.1). From this interval, eight samples belonging to S7 sediments were selected for sediment thin-section preparation. The sediment thin-sections were prepared by embedding 1-2 cm sediment samples in resin, and then slicing them into ~100 µm thick sections (Fig. V.2a). Sediment thin-sections were used for: (i) high-resolution images, (ii) bioturbation quantification, (iii) Laser ablation-ICP-MS analyses (LA-ICP-MS), and (iv) Scanning Electron Microscopy (SEM) observations.

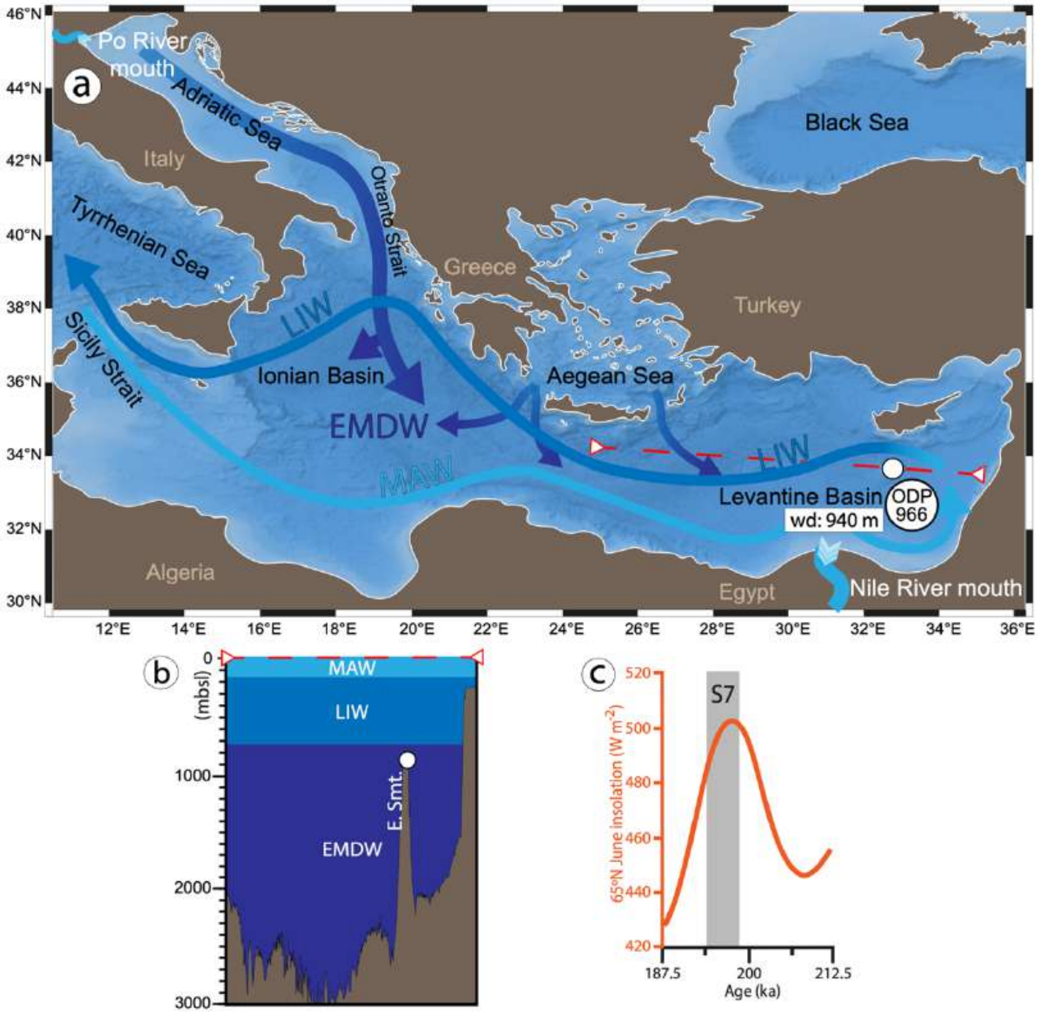
a
Po River mouth
Adriatic Sea
Otranto Strait
Italy
Tyrrhenian Sea
Sicily Strait
Greece
Turkey
Black Sea
LIW
Ionian Basin
Aegean Sea
EMDW
MAW
LIW
Levantine Basin
ODP 966
wd: 940 m
Algeria
Egypt
Nile River mouth
46°N
44°N
42°N
40°N
38°N
36°N
34°N
32°N
30°N
12°E
14°E
16°E
18°E
20°E
22°E
24°E
26°E
28°E
30°E
32°E
34°E
36°E
b
(mbsl)
0
1000
2000
3000
MAW
LIW
EMDW
E. Smt.
c
S7
65°N June insolation (W m⁻²)
520
500
480
460
440
420
187.5
200
212.5
Age (ka)

Figure V.1. *(a) Base map generated using GeoMapApp, showing location of core 966B, Eastern Mediterranean circulation pattern and the superficial expression of the bathymetric transect. (b) Bathymetric transect obtained by European Marine Observation Data Network (EMODnet) (http://www.emodnet-seabedhabitats.eu/). Location and depth of core 966B are indicated as a white circle at the top of Eratosthenes Seamount (E. Smt.). Eastern Mediterranean. water-masses are indicated. Modified Atlantic Water, WAW; Levantine Intermediate Water, LIW; Eastern Mediterranean Deep Water, EMDW. (c) S7 time interval (198.5 – 191.9 ka) based on Ziegler et al. (2010; 65°N summer insolation curve (in orange) from Laskar et al. (1993).*

V.3. Methodology approach

V.3.1. Geochemical analyses

Total organic carbon (TOC) content was measured in the 25 sediment samples by means of the Rock-Eval pyrolysis method, at the Institute of Earth Sciences (ISTE) of the University of Lausanne (UNIL). This method involved heating the samples from 200 °C to 850 °C in successive steps in a pyrolysis oven with an inert atmosphere (N_2). TOC (%) is calculated from the obtained thermograms using the following equation: TOC (%) = Pyrolyzed Carbon (wt%) + Residual Carbon (wt%). Samples were calibrated using the IFP160000 standard with an instrumental precision of <0.1 wt% for TOC (Lafargue et al., 1998; Behar et al., 2001; Ordoñez et al., 2019). ICP-MS and ICP-OES analyses were carried out at the Scientific Instrumentation Center of the University of Granada. For ICP analyses, discrete sediment samples were oven-dried at 60 °C and then powdered in an agata mortar. The 25 Samples were processed in one batch and an analytical blank was added. Solutions for ICP analyses were prepared using 0.1 g of powdered sample in Teflon vessels, where successive acidifications using HNO_3 (69%) and HF (48%) were performed at 130°C until evaporation. A final acid digestion with HNO_3 (69%) and water at 80 °C for 1 h was performed to achieve a total acid dissolution of the sediment samples. Subsequently, dissolved samples were diluted with Milli-Q water in 100 ml flasks following standard procedures (Bea, 1996).

Major elements in discrete sediment samples were measured with an Inductively Coupled Plasma Optical Emission Spectroscopy (ICP-OES) Perkin-Elmer Optima 8300 (Dual View) with a Perkin-Elmer autosampler. Certified standards (BR-N, GH, DR-N, UB-N, AGV-N, MAG-1, GS-N, and GA) were measured for element quantification. Trace elements in discrete sediment samples were measured by Inductively Coupled Plasma Mass Spectrometry (ICP-MS) −NexION 300d (Perkin Elmer) spectrometer− using Rh as the internal standard. For major elements, ICP-OES precision was better than 1%. For trace elements, ICP-MS precision was close to 2% and 5%, respectively on concentrations of 500 µg/g and 5 µg/g (Bea, 1996). Trace metals were normalized with aluminum (TM/Al) due to its conservative properties and since it is considered an optimal method for evaluating trace metal variability (Tribovillard et al., 2006; Calvert and Pedersen, 2007; Algeo and Li, 2020; Algeo and Liu, 2020; Paul et al., 2023).

LA-ICP-MS is known to have high potential for reliable quantitative analysis of diagnostic trace elements (e.g., Mo, V, U and Ba) in (laminated) resin-embedded sediments (Jilbert et al., 2008, 2010; Hennekam et al., 2015; Sosa-Montes de Oca et al., 2018). Therefore, trace element concentrations in selected locations on the sediment thin-sections were determined by laser ablation (LA-ICP-MS) at the Scientific Instrumentation Center, University of Granada. The LA-ICP-MS analyses were performed using a 213 nm Mercantek Nd-YAG laser coupled to an NexION 2000b quadrupole ICP with a shielded plasma torch. The ablation was carried out in a He atmosphere, with a laser beam fixed at 60 µm diameter. The spot was pre-ablated for 45 s at a laser repetition rate of 10 Hz and 20% output energy. A NIST-610 glass was employed as an external standard (see Pearce et al, 2007 for NIST-610 details). In each analytical session of a single thin-section, the NIST-610 glass was analyzed at the beginning and at the end, and also after every nine spots to correct for drift. Concentration values were corrected using silicon as an internal standard. The precision, calculated on five to seven replicates of the NIST-610 glass measured in every session, was in the range of 3% to 7% for most elements. Data reduction was carried out using software written by F. Bea (freely available upon request) in STATA programming language (StataCorp, 2007). Further details on LA-ICP-MS analysis can be found in Bea et al. (2005).

The locations of punctual analyses (i.e., spots) performed on each sample were visually determined using the high-resolution images. Because the aim of these analyses is to compare the geochemical composition of the host sediments versus the *Chondrites* infill material, the analyzed spots were selected and grouped as: (i) host sediment analyses (blue dots in Figs. V.10 and 12), and (ii) *Chondrites* infills (red dots in Figs. V.10 and 12) in each sample. It is worth mentioning that no LA-ICP-MS analyses were performed in areas where coring disturbances were observed. Refer to Figs. V.10-12 for statistical details of LA-ICP-MS punctual analyses of sediment thin-sections.

V.3.2. High-resolution images

High-resolution images of sediment thin-sections were captured using a Sony Alpha 7 MII camera attached to a Schneider-Kreuznach 50 mm Componon-S f 2.8 enlarging lens and closed bellows between the camera and lens. The high-resolution images were taken at the Scientific Instrumentation Center, University of Granada, by means of an automated motorized "Stack and Stitch" system designed for high-resolution panoramic views. This system utilizes focus stacking methods, combining a series of digital images captured from various quadrants and depths (i.e., focus levels) of the sediment thin-section. Utilizing a computer program, these images are merged to create a panoramic view of the entire thin-section offering exceptional high-definition. Consequently, the stacked and stitched gigapixel macro images can be zoomed into without a loss of resolution and pixelation, providing detailed insights into *Chondrites* disturbances and infills. In this specific case, the stacks were made every 80 µm and each panoramic image comprised

~25 photos, each photo being made up of 100 stacked images. The thin-section images are therefore made from ~2500 photos.

V.3.3. Bioturbation quantification

The quantification of bioturbation is a key feature of any ichnological analysis, traditionally accomplished through the use of indices such as the bioturbation index (%), assessed by visual observation (Taylor and Goldring, 1993). This implies that the assignment of the percentage of bioturbated area is, to some extent, subjective and semi-quantitative. However, by employing digital image processing techniques based on pixel analysis, an objective quantification of bioturbated areas can be achieved, thus enhancing the reliability of the assigned degree of bioturbation (Dorador et al., 2014a, 2017; Dorador and Rodríguez-Tovar, 2015, 2018).

Firstly, the images were cropped to exclude border regions where sediments were disturbed during coring. Discrete traces in the high-resolution images were then visually enhanced by adjusting optical parameters (e.g., contrast and brightness) using Adobe Photoshop CS6 software, following the methodology described by Dorador et al. (2014b). Once the visibility of traces was improved, the number of pixels corresponding to *Chondrites* and the pixels associated with the host sediment were separately determined (Table S1 in Supplementary material –Sup. mat.). The percentage of bioturbated areas was calculated as in Dorador et al. (2014a). "Similar Pixel Selection Method (SPSM)," was employed for pixel selection and subsequent quantification of bioturbation by *Chondrites*. For further details on image processing and digital bioturbation quantification, see Dorador et al. (2014a).

V.3.4. Scanning electron microscope (SEM) imaging and compositional maps

After capturing high-resolution optical images and conducting LA-ICP-MS analyses, sediment thin-sections were coated with carbon for detailed observation under the SEM using an AURIGA FIB-FESEM Carl Zeiss SMT microscope at the Scientific Instrumentation Center of the University of Granada. The SEM is equipped with various detectors, including an EDX (energy dispersive X-ray) detector system from Oxford Instruments, SE (secondary electrons), SE-inLens, BSE (backscattered secondary electrons), EsB (energy selective backscattered electrons) and STEM (scanning transmission electron microscopy) detectors. EDX served to obtain punctual microanalyses and compositional maps and profiles of major elements in selected areas of the sediment thin-sections. A composite EDX map was generated considering qualitative concentrations of Al, Si, Mg, Fe, S and Ca. Moreover, BSE images of selected areas were captured to facilitate comparison with the high-resolution optical images.

V.3.5. Data presentation and statistical analyses

Al-normalized trace metals (i.e., [trace metal]/[Al]) is the optimal normalization method to evaluate trace metal variability given the conservative behavior of Al in marine sediments (Paul et al., 2023). Consequently, for temporal and correlative assessment, trace metals concentrations in discrete samples were Al-normalized and then vertically plotted (Fig. V.2). Degree of pyritization (DOPt) values were also vertically plotted. This value indicates the abundance of authigenic pyrite in the sediments and it was calculated through the following equation: DOPt = S_t x (55.85/64.12) / Fe_t: where S_t: total sulfur (%), Fe_t: total iron, and the coefficient 55.85/64.12 represents the weight ratio of Fe/S in stoichiometric pyrite (Algeo and Li, 2020; Algeo and Liu, 2020).

Statistical analyses and box-plots were derived with the software PAST 4.0 (Hammer et al., 2001). Box-plots were used to compare major and trace elements concentrations (i) among different S7 subsections and (ii) between *Chondrites* infills and host sediments. Principal Components Analysis (PCA) was performed on the geochemical data obtained from discrete bulk sediments analyses (n = 25). The concentrations of Al, Si, Mg, Fe, K, Ca, Sr, Ti, Mn, S, Mo, U, V, Co, Cu, Ni, Zn, Pb, Cr, Ba, as well as DOPt and TOC (%) values, in S7 and surrounding sediments, were introduced in the PCA in order to obtain the main geochemical fractions in S7 sediments and elucidate the trace metals that are mainly enriched in the authigenic fraction. It is important to highlight that PCA was performed using non-normalized elements concentrations, ensuring there were no pre-induced correlations that could mask the real affinities and associations of the variables under assessment.

The PCA eigenvalues and eigenvectors were obtained from the correlation matrix, with the Singular Value Decomposition algorithm. A correlation matrix was used instead of a variance-covariance matrix because the variables are in different units; this implies normalizing all variables through division by their standard deviations (Hammer et al., 2001). The percentages of variance accounted for by Principal Component 1 (PC1) and Principal Component 2 (PC2) are given in Fig. V.2d, along with a scatter-plot for a 'Biplot' projection of the variables. The scatter-plot shows all data points plotted in the coordinate system given by PC1 and PC2. A Biplot projection of the original axes (variables) is shown onto the scatter-plot, facilitating visual assessment of any affinities among the variables. This procedure made it possible to identify subsets of components having similar relative variation patterns, which ultimately represent the main geochemical fractions in S7 sediments. Additionally, a Kaiser–Meyer–Olkin (KMO) test was conducted to determine the suitability of the data for factor analysis, assessing whether the variables are interrelated enough to state meaningful interpretations. The KMO test produces a value between 0 and 1, a higher KMO value indicating that the variables are better suited for factor analysis (refer to Fig. V.2d for KMO value).

To assess the influence of *Chondrites* bioturbation on the dilution of RSTMs within the organic-rich sediments, a qualitative dilution factor (df) was computed. It is noteworthy that the method for calculating this dilution factor of RSTMs by *Chondrites* bioturbation has not been proposed by previous studies, presenting a novel approach in the field. The calculation assumes that the median trace metal concentrations of the host sediment represent the syndepositional concentrations. Thus, the calculated df provides an estimation of the extent to which RSTMs are diluted by *Chondrites* in the organic-rich sediments. To obtain the df, a weighted average concentration ([wTM]) for each trace metal in every sample was determined, considering the *Chondrites* area (*Ch*%), host sediment area (hs%), median trace metal concentration in *Chondrites* infills ($[TM]_{Ch}$), and median trace metal concentration in host sediments ($[TM]_{hs}$). The formula to calculate [wTM] is as follows: $[wTM] = (([TM]_{hs} * hs\%) + ([TM]_{Ch} * Ch\%)) / 100\%$. The median was chosen over mean/average since it is less influenced by extreme values. The df is then calculated from the difference between the weighted average trace metal concentration, which considers *Chondrites* area, and the median trace metal concentration in the host sediment: $df\% = (([TM]_{hs} – wTM]) / [TM]_{hs})*100$.

V.4. Results

The top and bottom boundaries of sapropel S7 were determined in view of the Ba/Al trend (Fig. V.2a). The Ba/Al ratio serves to determine the original sapropel productivity signal if, eventually, OM is oxidized during reventilation (Gallego-Torres et al., 2007a, b; Filippidi and de Lange, 2019; Monedero-Contreras et al., 2024). Barite ($BaSO_4$), the primary host mineral for Ba, is less prone to postdepositional oxidation as compared to TOC, and the stable sulfate saturation in Eastern Mediterranean porewater enables its preservation during periods of oxygen-depleted bottom-waters (van Os et al., 1991; Passier et al., 1997; Nijenhuis et al., 1999; Martínez-Ruiz et al., 2000). This approach enabled the identification of the original thickness of the organic-rich interval of sapropel S7, even considering potential postdepositional oxidation. To this regard, the S7 interval is identified between 477 and 503.5 cm at Site 966B (Fig. V.2). Yet Ba/Al and TOC exhibit similar vertical trends, decreasing simultaneously at the top of S7, indicating that no relevant postdepositional oxidation occurred after S7 termination (Fig. V.2a). Therefore, in this case, TOC can also delimit the original thickness of S7.

Table V.1. *Major element concentrations (wt%), TMs concentrations (µg/g), TOC (%) and calculated DOPt values obtained from geochemical analyses of bulk sediment samples. S7 subsections are indicated.*

				ICP-MS (μg/g)										ICP-OES (wt%)							
	Depth (cm)	TOC (%)	DOPt	Ba	V	Co	Cr	Ni	Cu	Mo	U	Zn	Pb	Al	Ca	Fe	K	Mg	Mn	S	Ti
	470.0	0.49	0.21	260	67	16	58	56	45	1	4	55	9	3.68	17.62	2.52	0.96	1.60	0.04	0.61	0.28
	472.0	0.21	0.24	286	68	14	56	48	56	2	3	55	9	3.70	16.81	2.55	0.98	1.48	0.04	0.71	0.28
	474.0	0.89	0.09	265	68	16	59	55	56	3	3	56	9	3.74	16.29	2.38	0.95	1.59	0.04	0.25	0.28
	477.0	0.28	0.04	326	78	13	71	52	27	3	3	58	10	4.35	13.96	2.79	1.05	1.56	0.04	0.13	0.32
	479.0	2.04	0.12	616	96	20	93	76	88	7	4	72	9	4.30	14.37	2.95	0.98	1.35	0.04	0.40	0.28
	481.0	3.43	0.33	660	119	31	73	113	85	26	5	67	8	4.19	13.91	3.67	0.92	1.27	0.04	1.39	0.27
	482.0	3.01	0.32	736	157	35	67	120	76	51	8	65	9	4.15	13.96	4.66	0.96	1.29	0.04	1.69	0.27
S7b section	484.0	2.32	0.13	557	208	33	70	106	67	27	7	69	10	4.52	12.57	3.47	1.05	1.45	0.04	0.53	0.31
	486.0	2.87	0.19	582	204	37	75	127	73	53	9	70	11	4.81	11.86	3.36	1.11	1.49	0.04	0.74	0.33
	488.0	1.76	0.12	567	185	30	71	103	65	47	7	65	11	4.53	13.49	3.21	1.07	1.56	0.05	0.45	0.32
	489.5	1.88	0.11	544	202	33	76	112	72	16	9	73	11	4.86	12.37	3.30	1.09	1.53	0.04	0.41	0.34
	491.0	1.79	0.16	371	194	24	80	91	63	20	7	64	10	4.98	11.99	3.03	1.05	1.43	0.03	0.57	0.32
	493.0	0.78	0.12	422	110	21	68	71	51	4	6	67	11	4.54	14.75	3.24	1.07	1.56	0.04	0.46	0.33
	494.5	0.80	0.23	418	101	22	69	77	51	14	6	69	10	4.50	14.74	3.31	1.05	1.54	0.04	0.87	0.32
	496.0	0.97	0.14	391	104	19	72	70	58	7	5	64	10	4.45	13.59	2.90	1.00	1.42	0.03	0.46	0.30
S7a section	498.0	0.81	0.20	412	103	21	68	70	51	4	5	65	10	4.43	14.47	3.00	1.04	1.55	0.04	0.67	0.31
	500.0	0.34	0.15	300	103	21	69	73	48	10	5	57	9	4.15	14.53	2.73	0.95	1.58	0.04	0.48	0.29
	501.0	0.98	0.13	365	121	22	67	77	53	8	5	64	10	4.39	14.52	3.10	1.03	1.64	0.05	0.45	0.32
	503.5	1.53	0.29	312	116	26	68	88	55	14	5	61	9	4.08	14.42	3.15	0.94	1.52	0.04	1.06	0.28
	505.5	0.45	0.34	123	66	19	48	55	37	6	3	49	7	3.07	18.28	2.41	0.80	1.78	0.05	0.94	0.23
	507.0	0.22	0.24	97	67	18	41	47	35	4	3	44	7	2.87	20.23	2.26	0.77	2.05	0.05	0.62	0.21
	509.0	0.18	0.11	91	65	17	49	49	44	2	3	47	8	3.19	18.36	1.91	0.82	1.81	0.05	0.24	0.24
	511.0	0.16	0.39	87	59	24	40	59	34	2	3	44	7	2.97	19.28	3.36	0.79	2.02	0.05	1.50	0.23
	512.0	0.16	0.11	110	70	18	48	51	29	2	3	52	8	3.42	18.82	2.37	0.90	2.02	0.06	0.29	0.27
	514.0	0.32	0.14	90	61	16	46	47	32	1	2	44	7	3.20	18.90	2.13	0.81	1.90	0.05	0.34	0.24

The S7 interval is enriched in RSTMs such as Mo, U, V, Co, Cu, and Ni, and depleted in Mn (Figs. V.2a and b; Table V.1). Moreover, Mo, U, V, Cu, Co and Ni have similar vertical plots, while Pb and Zn differ from the rest and do not show significant enrichments (Fig. V.2a). Among the RSTMs, Mo exhibits the highest variability (i.e., highest standard deviation) within S7, whereas U has the lowest variability and the lowest concentration (Fig. V.2b). V presents the highest concentrations within S7 among the RSTMs (Fig. V.2b). However, it is not the most proportionally enriched RSTM relative to the background values (i.e., concentrations before the onset of S7). In this sense, Mo appears to be the RSTM that is most proportionally enriched relative to the background values, as it can increase by up to 1500% assuming background values of 3 μg/g. Interestingly, DOPt increases at the top and bottom of S7, where it reaches DOPt values around 0.3 (Fig. V.2a and Table V.1).

According to the vertical plots and mean concentration of trace metals and TOC, sapropel S7 can be subdivided into two sections, S7a and S7b (refer to Fig. V.2 and Table S3 in Sup. mat.) Section S7a has lower mean concentrations of RSTMs and Ba than section S7b (Fig. V.2c), indicating a change in bottom-water conditions during its deposition. Moreover, in section S7a (from 491 to 477 cm; Fig. V.2a), the mean TOC is relatively low (<1%). In section S7b (from 503.5 to 491 cm; Fig. V.2a), the TOC is higher (>3%) with mean values above 2% and presents a much lower variability in RSTMs concentration and Ba than section S7b (Fig. V.2c and Table V.1). The increase in TOC content is also made evident by the darkening of the sediments in the upper S7 half (i.e., from 491 to 479 cm depth; Fig. V.2a). See Fig. V.2. for more detailed results.

According to PCA, the PC1 and PC2 group >82% of the total variance. The KMO test gives a value of 0.7, indicating the data introduced in the PCA present a “good” adequacy for factor analysis (Fig. V.2d). The PCA analysis suggests that there are three main geochemical fractions in S7 sediments: (1) the detritic fraction, enriched in Al, Si, K, Ti, Cr, Zn and Pb, (2) the carbonate fraction, enriched in Ca, Mg and Mn, and (3) the authigenic fraction, enriched in Mo, U, V, Co, Cu, Ni, Ba, Fe and TOC. Even though pyrite is an authigenic mineral, in the authigenic fraction, pyrite is not well correlated with the rest of the RSTMs. Only the trace metals that are mainly enriched in the authigenic fraction (i.e., Mo, U, V, Co, Cu, Ni and Ba) are assessed in the comparison between *Chondrites* infills and host sediment composition derived from LA-ICP-MS analyses. For this reason, Zn, Pb and Cr are excluded from the assessment.

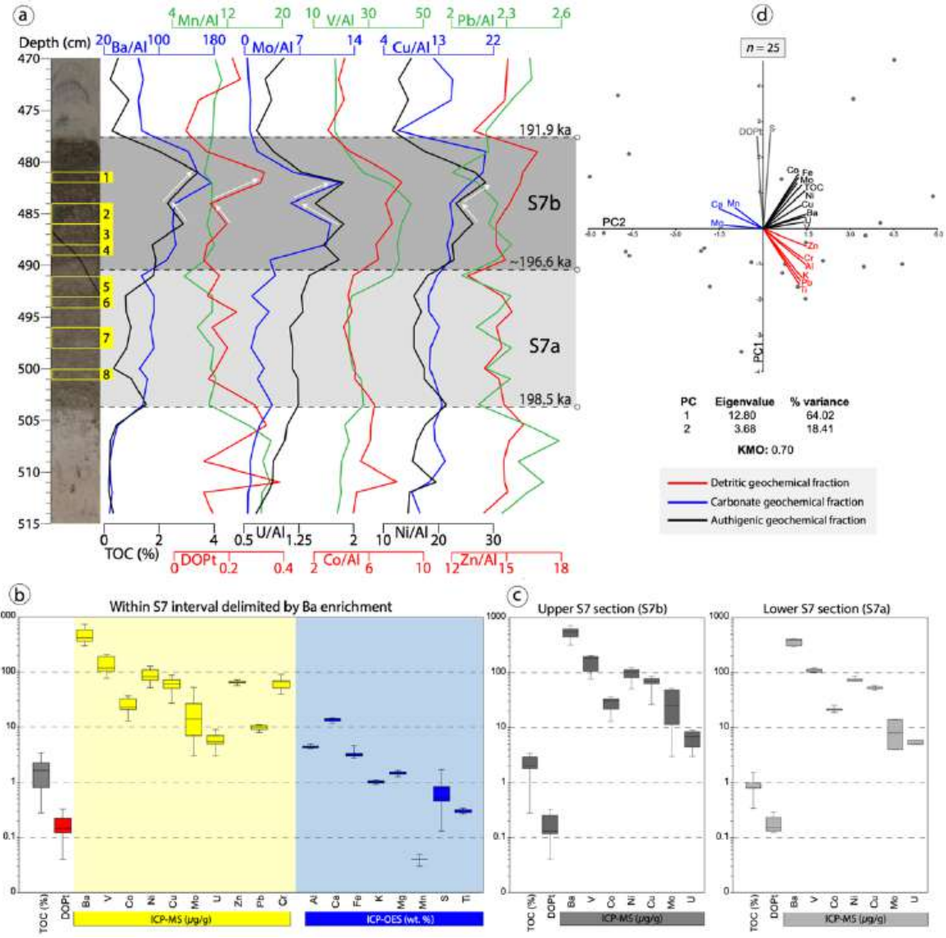

Figure V.2. *Results of geochemical analyses of bulk sediment samples. (a) Vertical plots of Al-normalized TMs concentrations ([TM]/[Al] x10^{-4}), TOC (%) and DOPt values. S7a and S7b subsections are indicated. Selected samples for thin-section preparation are indicated on the core image as yellow boxes. (b) Box-plots of major elements and TMs concentrations, TOC (%) and DOPt values within interval S7 delimited by Ba enrichment. (c) Box-plots of TMs concentrations, DOPt and TOC (%) of S7: top half (section S7b) and S7 bottom half (section S7a). All box-plots are presented in log$_{10}$ scale. (d) Principal Components scatter-plot (PC1: y-axis, PC2: x-axis) with a biplot projection of the variables. This allowed for a visual establishment of the main geochemical affinities and fractions in S7 sediments. Identified geochemical fractions are shown in different Eigenvalues, and variance (%) values of PC1 and PC2 are indicated. For details on Principal Components Analysis and the Kaiser-Meyer-Olkin Test (KMO) value see to section 3.6. For additional geochemical information about S7 at Site 966B, including calculated enrichment factors of assessed trace metals, consult Monedero-Contreras et al. (2024).*

V.4.1. SEM and high-resolution optical images

High-resolution optical images made it possible to assess sediment architecture, sediment disturbances and *Chondrites* infills at sub-mm and in natural colors, while SEM images allowed one to see compositional changes and sediment architecture, texture and distribution at higher resolution (Figs. V.V.3 - 5). In most samples, *Chondrites* are easily recognized as white subcircular branches between ~0.5 and 1 mm thick. However, in some samples, *Chondrites* infills appear to be altered by the presence of orange and brown haloes, as occurs in thin-sections 3, 4, 6 and 7. SEM images revealed a disturbance of *Chondrites* on sediment architecture in S7, specifically in the destruction of the syndepositional pseudolamination. In thin-section 1, situated at the top of S7, the host sediment is mixed/homogenized; therefore, it does not exhibit lamination and *Chondrites* are less evident and abundant than in the other samples. The host sediment in thin-section 1 is primarily composed of pyrite framboids with diameters > 10 µm (many infilling foraminifera chambers; Fig. V.3a). In thin-section 2, both optical and SEM images showed the presence of two types of *Chondrites*, with white infill and with dark brown infill, smaller in size (< 0.5 mm) (Fig. V.3b). The white *Chondrites* were observed in the rest of the thin-sections, although dark brown *Chondrites* appeared to be predominantly present in this particular sample. SEM images suggest that dark brown *Chondrites* also disrupt the original syndepositional architecture of S7 sediments (Fig. V.3b), but have composition a more similar to the host sediment than the white *Chondrites*, as the infilling material of these dark brown *Chondrites* has a color resembling that of the host sediment.

In thin-section 3 (Fig. V.4a), *Chondrites* displayed the most intense color alteration, having marked orange and brown shades and haloes. Interestingly, in this sample, some pyrite framboids clustered around *Chondrites*. In thin-section 4, *Chondrites* coloration is less altered, yet some orange haloes are still visible (Fig. V.4b). Contrasting with section S7b, section S7a (i.e., lower S7 section), lacks pseudolamination in the host sediment and exhibits lighter color, likely owing to the lower TOC content (Figs. V.5 and 6). The background sediments present a “mottled” texture upon which the white *Chondrites* are superimposed. In terms of texture, however, the background sediments of S7a section are similar to the *Chondrites* infills. White *Chondrites* in section S7a are similar in size, shape and color to the *Chondrites* from section S7b. In thin-section 5, light gray sediment patches can be observed, on which the white *Chondrites* are superimposed (Fig. V.5a). In thin-sections 6, 7 and 8, the white *Chondrites* also present orange haloes at the borders (Figs. V.5b and 6).

V.4.2. EDX mapping

SEM-EDX compositional maps reveal how the disturbance of *Chondrites* affects the distribution of major elements and minerals of S7 sediments at a sub-mm scale. The white *Chondrites* in all thin-sections are similar in terms of major element composition, suggesting a similar source for the infilling sediments. The infilling material of these white *Chondrites* furthermore exhibit a homogeneous mixture of grains and minerals. In general, the respective infilling material has larger grain size, abundant angular quartz grains and a higher proportion of Ca-rich minerals in comparison to the host sediments (Figs. V.7 and 8). Although pyrite framboids are absent in *Chondrites* infill, they are present (in some cases abundant) in the host sediment (thin-section 1 and 3; Fig. V.7).

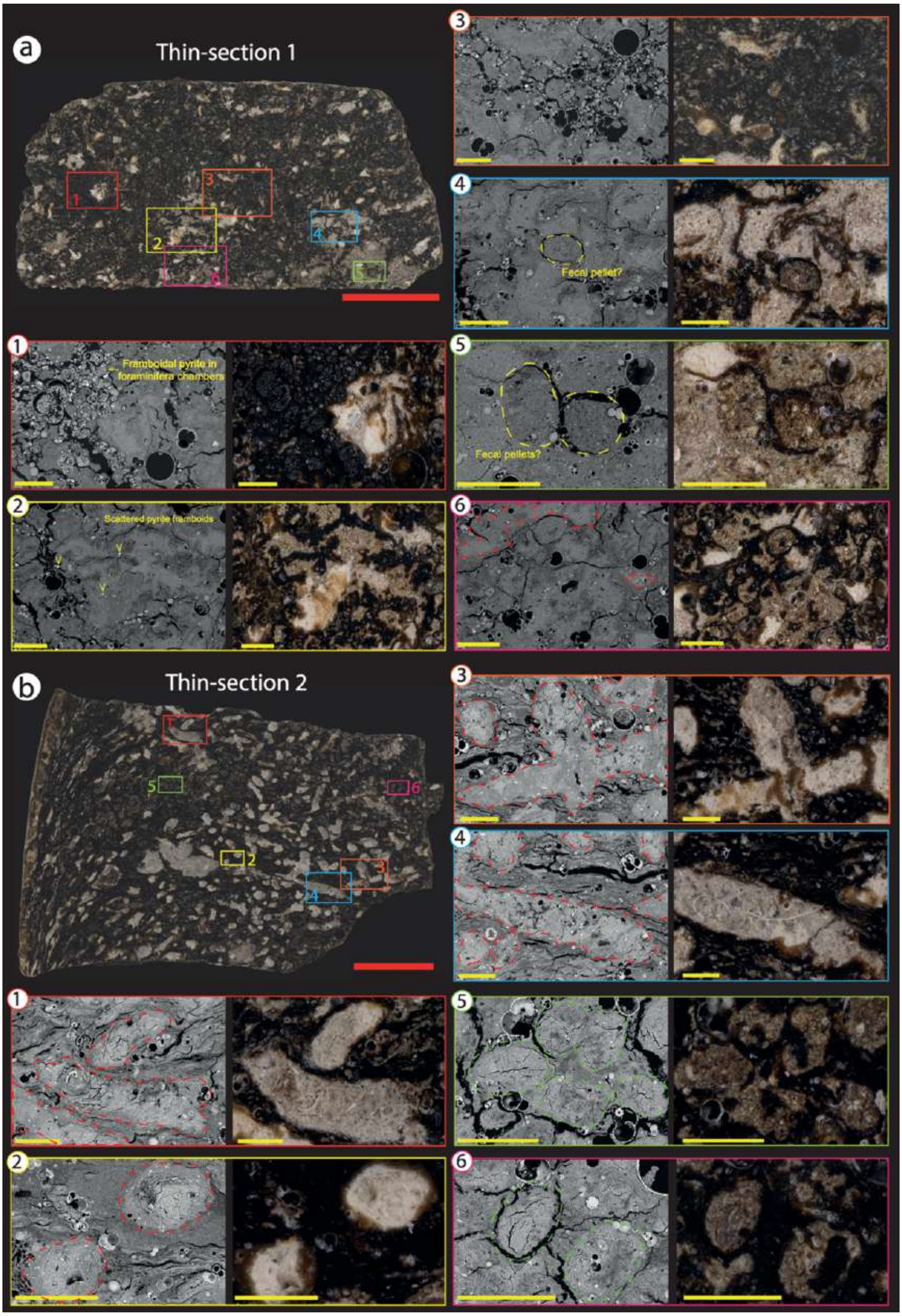
a
Thin-section 1
1
2
3
4
5
6
Framboidal pyrite in foraminifera chambers
Fecal pellet?
Fecal pellets?
Scattered pyrite framboids
b
Thin-section 2
1
2
3
4
5
6

Figure V.3. *High-resolution optical images of thin-sections 1 and 2, plus SEM images of selected areas (1-6). Red scale-bar: 5 mm; yellow scale-bar: 0.5 mm (500 µm). The amplified sections are shown as rectangles, each assigned a different color: (1) red, (2) yellow, (3) orange, (4) blue, (5) green, (6) magenta. White Chondrites are outlined with red dashed lines and dark Chondrites in green dashed lines.*

Certain differences between thin-sections can be underlined here. In thin-section 1, *Chondrites* are more difficult to distinguish since the *Chondrites* infill has a composition of major elements similar to the host sediment. The dark *Chondrites* in thin-section 2 likewise exhibit a composition of major elements similar to the host sediment (Fig. V.7). Therefore, they are not easily distinguished in SEM-EDX compositional maps. Still, it is evident that they disrupt host sediments and have marked contours. In thin-sections from section S7b, *Chondrites* destroy/break up the syndepositional pseudolamination within the host sediment and modify the syndepositional mineral and OM distribution (Fig. V.8). The orange shades observed in the high-resolution optical images of *Chondrites* infills, especially in thin-section 3 and 4, are not reflected in compositional maps of major elements (Fig. V.7). As shown by the high-resolution optical images, in thin-sections from section S7a, the host sediments do not present sub-mm lamination. *Chondrites* in section S7a have a composition, in terms of major elements, resembling *Chondrites* in section S7b (Fig. V.8).

V.4.3. Bioturbation quantification

Following the methodology described by Dorador et al. (2014a), the high-resolution optical images of thin-sections were processed, and *Chondrites* could be highlighted and isolated (Fig. V.9). Subsequently, the percentage of bioturbation was calculated based on the area (i.e., number of pixels) of these selected *Chondrites* (Fig. V.9). In thin-section 1 (S7 top), the selection of *Chondrites* was difficult due to significant sediment mixing. Thus, only well-defined *Chondrites* were chosen for bioturbation quantification in this sample, which probably determined the low bioturbation recorded. In the rest of thin-sections, *Chondrites* were well identified and selected for bioturbation quantification. In thin-section 2, the two types of *Chondrites* were selected and quantified independently (Fig. V.9). The dark brown *Chondrites* constitute only 4% and are only recognized in a 0.5 cm thick interval, while the white *Chondrites* represent 28%. Hence the total bioturbation percentage in this sample is 32% (Fig. V.9). This finding is in accordance with thin-sections 3, 4, 7 and 8, where white *Chondrites* range between 34 and 36% (Fig. V.9). In thin-sections 5 and 6, the bioturbation percentage attributed to *Chondrites* was lower, respectively ranging from 21% to 26% (Fig. V.9). In thin-section 5, the presence of white sediment patches hindered *Chondrites* identification and differentiation from the host sediment (Fig. V.9). It should be noted that variations in resin impregnation in thin-sections 6, 7, and 8 resulted in differences in surface brightness and color, impeding the automated selection of *Chondrites* (Fig. V.9). In these areas, the identification and isolation of *Chondrites* had to be done manually. However, the *Chondrites* infill area (i.e., the number of pixels) selected manually is comparable to the *Chondrites* infill area that would have been selected automatically.

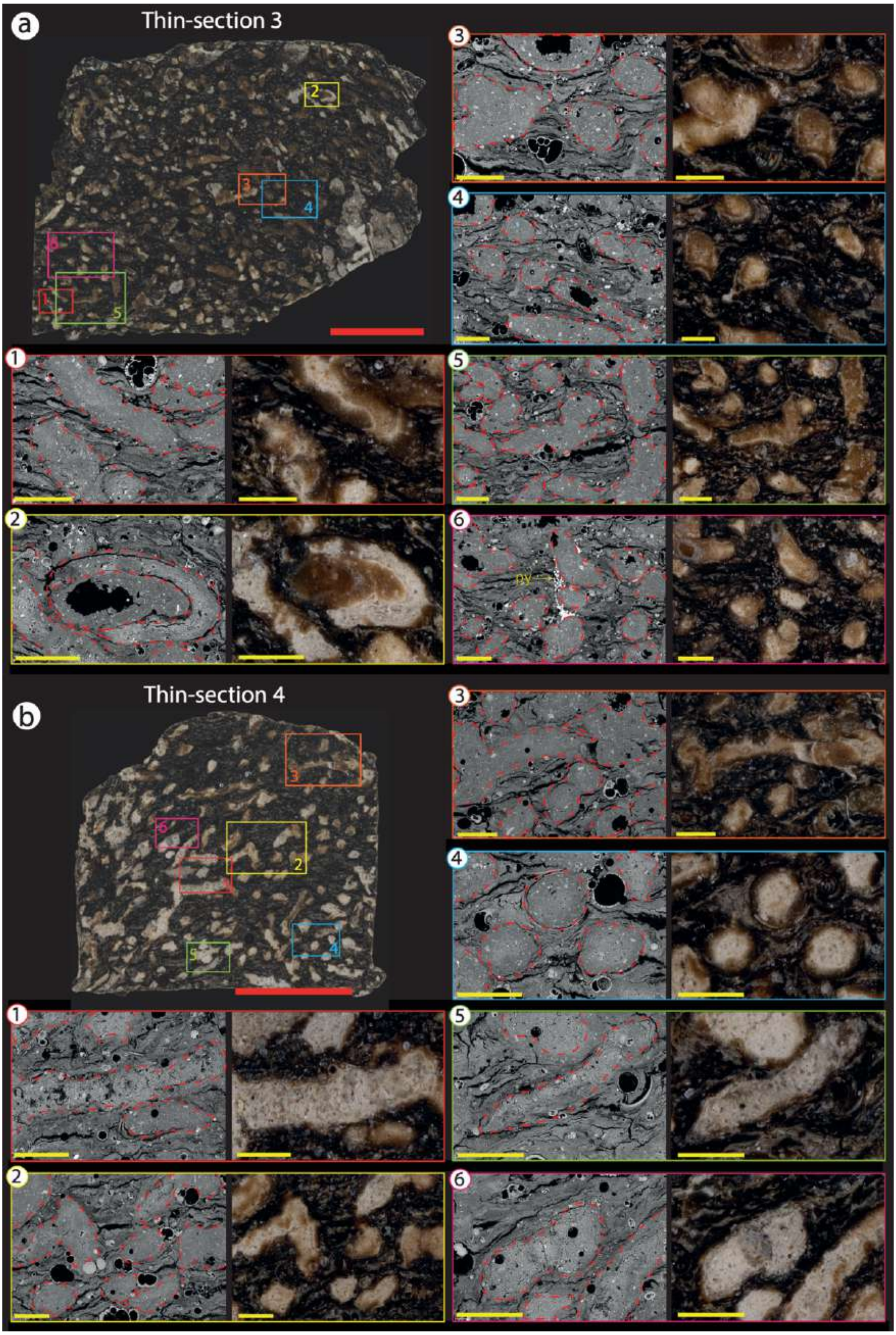
a
Thin-section 3
1
2
3
4
5
6
py
b
Thin-section 4

Figure V.4. *High-resolution optical images of thin-sections 3 and 4, plus SEM images of selected areas (1-6). Red scale-bar: 5 mm; yellow scale-bar: 0.5 mm (500 µm). The amplified sections are shown as rectangles, each assigned a different color: (1) red, (2) yellow, (3) orange, (4) blue, (5) green, (6) magenta. White Chondrites are outlined with red dashed lines.*

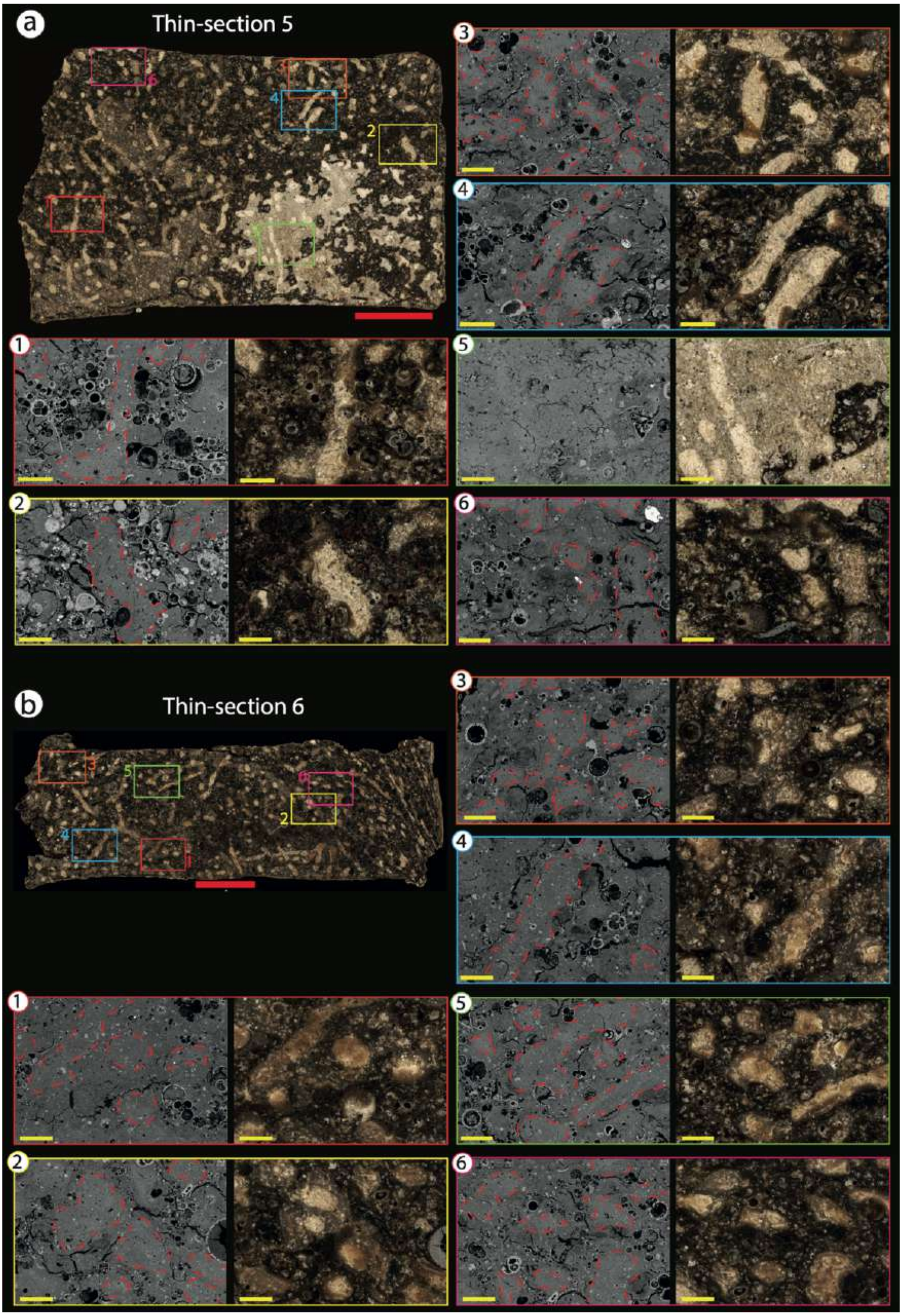

Figure V.5. *High-resolution optical images of thin-sections 5 and 6, plus SEM images of selected areas. Red scale-bar: 5 mm; yellow scale-bar: 0.5 mm (500 µm). The amplified sections are shown as rectangles, each assigned a different color: (1) red, (2) yellow, (3) orange, (4) blue, (5) green, (6) magenta. White Chondrites are outlined with red dashed lines.*

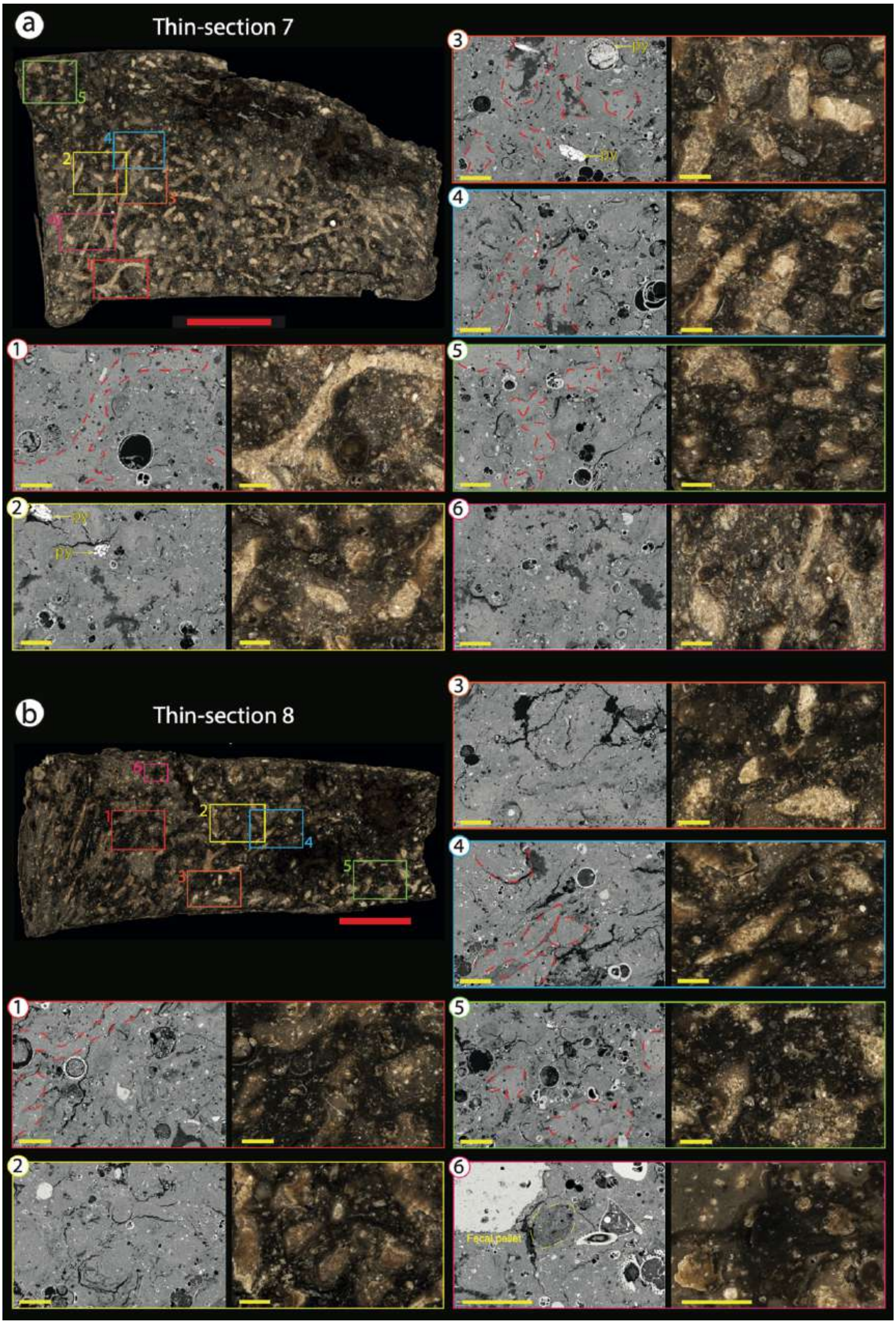
a
Thin-section 7
1
2
3
4
5
6
py
py
py
py
b
Thin-section 8
1
2
3
4
5
6
Fecal pellet

Figure V.6. *High-resolution optical images of thin-sections 7 and 8, plus SEM images of selected areas. Red scale-bar: 5 mm; yellow scale-bar: 0.5 mm (500 µm). The amplified sections are shown as rectangles, each assigned a different color: (1) red, (2) yellow, (3) orange, (4) blue, (5) green, (6) magenta. White Chondrites are outlined with red dashed lines.*

V.4.4. LA-ICP-MS spot-analyses

LA-ICP-MS spot-analyses were conducted on thin-sections to compare trace metal concentrations between *Chondrites* infills and host sediment. As previously stated, this comparison will focus exclusively on trace metals that exhibit a significant enrichment in the authigenic fraction and a weak influence from the detritic fraction (i.e., V, Co, Ni, Cu, Mo, Ba and U), as confirmed by the PCA (Fig. V.2d). Among all thin-sections, thin-section 1 exhibits the lowest trace metals concentrations (Fig. V.10b). Most trace metals (V, Co, Ni, Cu and U) have slightly higher concentrations in the host sediment than in the *Chondrites* infills, while Mo and Ba have similar values in both sediment fractions (Fig. V.10). In thin-section 2, dark *Chondrite*s show similar or higher trace metal concentrations than the host sediment, whereas white *Chondrites* show lower trace metal concentrations than the host sediment. Overall, thin-section 2 has the highest trace metals concentrations in the host sediment (Fig. V.10). In thin-section 3, where *Chondrites* appear more altered by the presence of orange shades, no significant differences exist in trace metals concentrations between the *Chondrites* infills and host sediment.

Interestingly, Cu and Ni have significantly higher concentrations in *Chondrites* infills than in the host sediment, while V, Co, Mo, Ba and U have similar concentrations in both sediment fractions (Fig. V.10). In thin-section 4, all trace metals exhibit higher concentrations in the host sediment than *Chondrites* infills, yet these differences are less marked for Co, Mo and U. In section S7a (thin-sections 5, 6, 7 and 8), trace metal concentrations in host-sediments and *Chondrites*-infills are systematically lower than in thin-sections from section S7b (Fig. V.11). This could be expected, since the bulk sediments analyses of section S7a, showed that trace metal concentrations and TOC content were significantly lower than in section S7b (Fig. V.2). Still, the tendency of higher concentrations of trace metals in the host-sediment than in *Chondrites*-infills is maintained, and in some cases, proportionally higher than in section S7b –as occurs with Ba, Cu and Ni (Fig. V.11 and Table V.2).

V.5. Discussion. *Chondrites* and micro-scale sediment disturbances

Bioturbation can disrupt sediment layers and mix different materials within the sediment from macro- to a microscale (Bromley, 1996). *Chondrite*s, being small traces relatively common in organic-rich sediments, may disrupt sedimentary architecture at the sub-cm scale, and thereby, affect the distribution of trace metals (including diagnostic RSTMs and oligoelements) and OM within the sediments (Löwemark et al., 2006; Baucon et al., 2020).

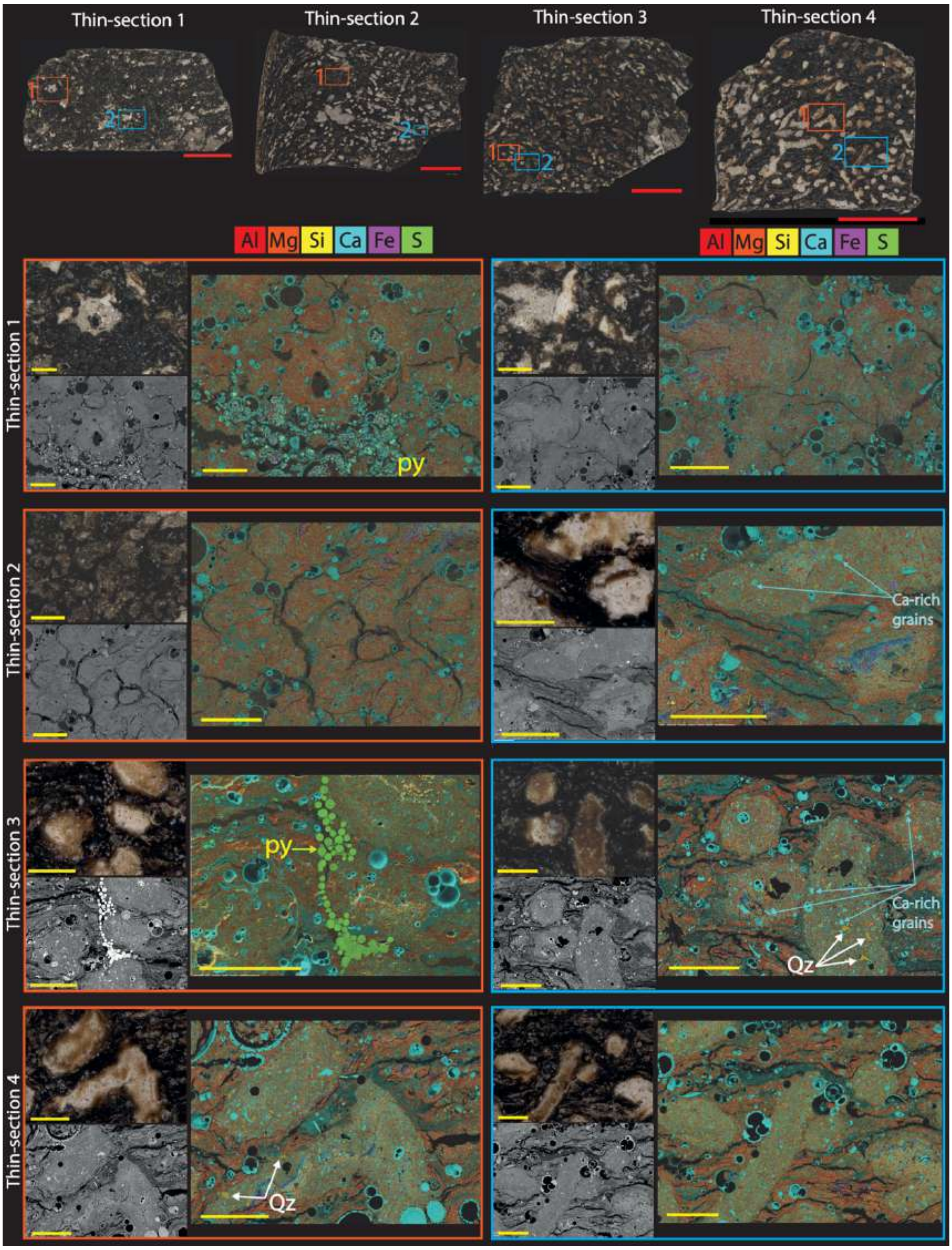
Thin-section 1
Thin-section 2
Thin-section 3
Thin-section 4
1
2
Al Mg Si Ca Fe S
py
Ca-rich grains
Qz

Figure V.7. *Selected SEM-EDX compositional maps of major elements of selected areas on thin sections 1, 2, 3 and 4 from section S7b. Mapped major elements: Al: red; Si: yellow; Mg: orange; Ca: blue; S: green and Fe: magenta. Red scale-bar: 5 mm; yellow scale-bar: 0.5 mm (500 µm). Qz: quartz grains, py: pyrite framboids. See Fig. S9 in Sup. mat. for additional SEM-EDX compositional maps of thin-sections 2 and 4.*

V.5.1. Chondrites: Lamination, texture and mineral composition

In S7 sediments at the top of Eratosthenes Seamount, *Chondrites*-producers bioturbated from 11% to 36% of the total volume of organic-rich sediments. Thus, despite its small size, the high abundance has a strong impact on the small-scale lamination, texture, and minerals, and OM distribution of the organic-rich sediments. A high abundance of *Chondrites* can produce disruption, or even destruction of sub-mm lamination or pseudolamination, which can serve as high-resolution paleoenvironmental archives (Jilbert et al., 2008, 2010; Hennekam et al., 2015; Sosa-Montes de Oca et al., 2018). Sediment bioturbation by *Chondrites*-producers can therefore alter valuable geochemical information used to reconstruct past redox conditions at high-temporal resolution (Figs. V.10 and 11).

Micro-scale disturbances can be recognized by the mineral distribution. The assessed white *Chondrites* infills exhibit a high abundance of angular quartz grains (typically associated with aeolian input) and Ca-enriched material, along with much lower TOC content than the host sediment, according to color contrast. Meanwhile, the host sediment is more enriched in OM and clay minerals enriched in Al, Mg and K (typically linked to fluvial input) (Figs. V.7 and 8). In this context, *Chondrites*-producers introduced overlying sediments, deposited during dryer climatic conditions and lower export productivity, into the S7 sediments deposited during high fluvial inputs. This resulted in alterations in mineral distribution at the sub-cm scale and a reduction in the overall TOC content (Figs. V.7 and 8), given that the sediments overlying S7 have an average lower TOC (~ 0.5%; Table S3 in Sup. mat.) and the light color of the white *Chondrites* infills indicates minimal organic carbon content.

OM and pyrite framboids are not equally distributed between *Chondrites* infills and the host sediment. Pyrite framboids and OM are present in the host sediment but absent in white *Chondrites* (Figs. V.3 to 8). The connection to overlying oxic waters through *Chondrites* burrows would promote higher oxygen levels within the *Chondrites* network than in the host sediment, where dysoxic-anoxic conditions prevailed (according to the enrichment of RSTMs; Fig. V.2). Nevertheless, the presence of pyrite framboids and Mo enrichments in the sediments suggest that intermittent euxinic conditions were reached in confined sub-cm microenvironments, e.g., inside foraminifera chambers (Figs. V.3 to 8) (Wilkin et al., 1996, 1997; Tribovillard et al., 2008; Scott and Lyons, 2012; Lin et al., 2016; Liu et al., 2019; Chang et al., 2022; Monedero-Contreras et al., 2023b). *Chondrites*, as open, actively ventilated burrows are expected to have less abundant (or absent) pyrite than the surrounding sediment (Baucon et al., 2020). Such observations allow us to state that *Chondrites* distribution, abundance and associated irrigation exerted control on OM, S and Fe distribution and chemistry within the sediment during early diagenesis pyrite precipitation (Phillips and McIlroy, 2010). The absence of pyrite framboids in *Chondrites* infills could also be related with the ethology of the organism; *Chondrites*-producers ingested the microbially degraded OM from which framboids would have originated (Baucon et al., 2020).

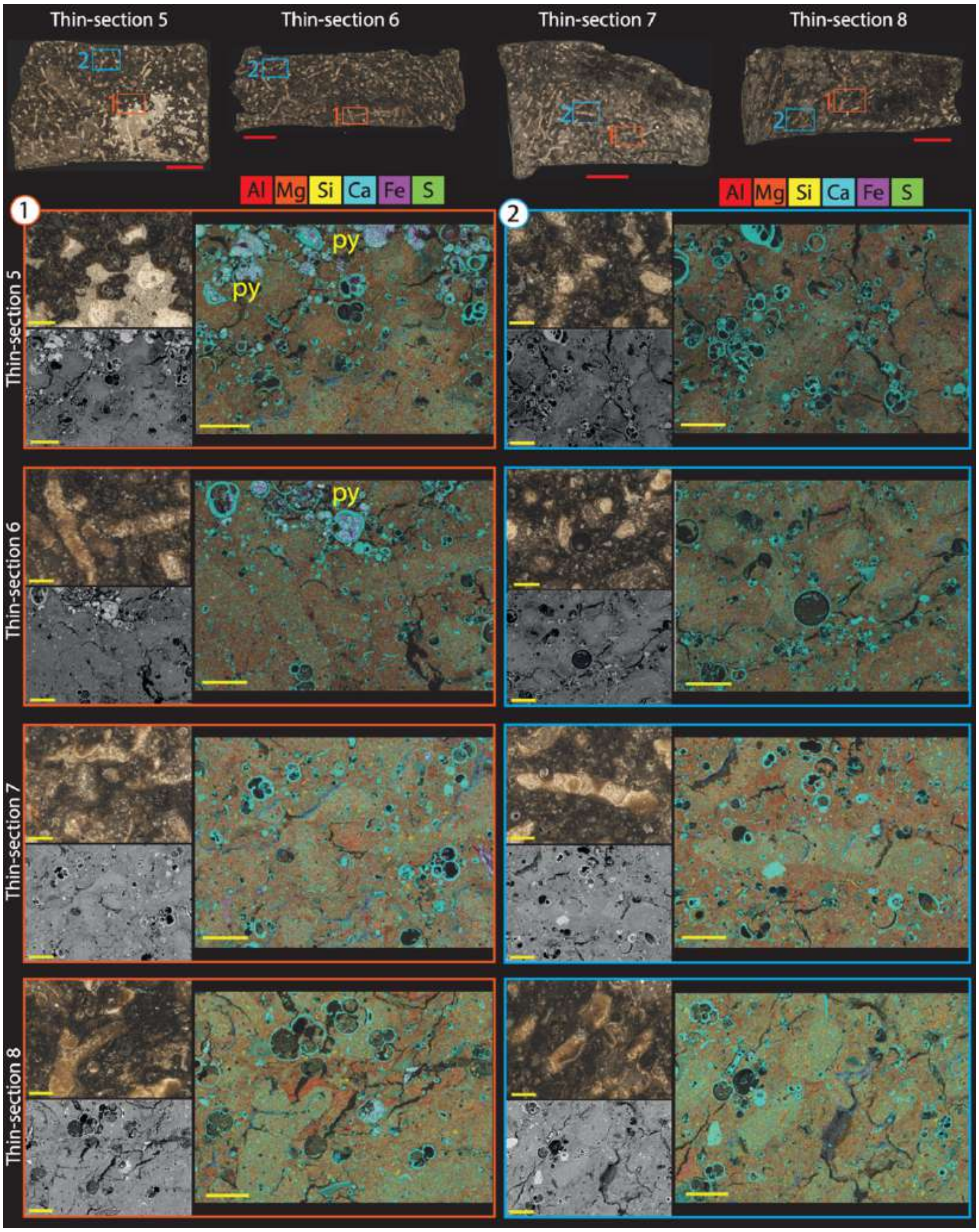

Figure V.8. *Selected SEM-EDX compositional maps of major elements of selected areas on thin sections 5, 6 ,7 and 8 from section S7a. Mapped major elements: Al: red; Si: yellow; Mg: orange; Ca: blue; S: green and Fe: magenta. Red scale-bar: 5 mm; yellow scale-bar: 0.5 mm (500 µm). See Table S9 and S10 in Sup. mat. for additional SEM-EDX compositional maps of thin-sections 5-8.*

Furthermore, research has revealed a correlation between elevated populations of benthic fauna and an increased occurrence of pyrite precipitation within the underlying sediment. This phenomenon is attributed to the augmented influx of sulfate-rich water into the oxygen-depleted sediments, which subsequently enhances the activity of sulfate-reducing bacteria and the precipitation of pyrite framboids (Hantsoo et al., 2023). This might explain the high abundance of pyrite framboids surrounding some *Chondrites* (Fig. V.7, thin-section 3). Yet, evidence from S isotopes indicates that during sapropel deposits in the Eastern Mediterranean, porewater was saturated in sulfate (Passier et al., 1996). Additional support for permanent sulfate saturation comes from the preservation of biogenic barite crystals in sapropel sediments (Martinez-Ruiz et al., 2000; Monedero-Contreras et al., 2023b). Therefore, *Chondrites*-producers would not significantly change sulfate saturation in Eastern Mediterranean porewater during sapropel termination. In deep-marine settings where sulfate is depleted in the porewater, *Chondrites*-producers would, however, bear a major impact by replenishing the depleted sulfate in the porewater.

The mixing and disturbance of sediments by benthic organisms through burrowing, feeding, and movement strategies can vary due to changes in redox conditions and OM content (Bromley and Ekdale, 1984; Bromley, 1996; Buatois and Mángano, 2011; Baucon et al, 2020). Such variations lead to differences in the degree of bioturbation and in the distribution of OM and oligoelements within the sediment. For instance, background sediments in section S7a present a different distribution of OM and sediment texture than section S7b owing to differences in bottom-water redox conditions (see section 4.3 and Fig. V.13). The section S7a background sediments show a scattered distribution of OM and a mottling texture, while in section S7b the OM is concentrated within sub-mm laminae. The different modifications in sediment texture and sub-mm architecture by *Chondrites*-producers and other benthic fauna can give rise to diverse distributions of oxygen, OM, S and Fe in the sediments and porewater (Fig. V.12). These differences imply a range of potential effects on nutrient cycling, sediment biogeochemistry, and overall macro to micro ecosystem dynamics. Bioturbation modelling and neoichnological studies in modern marine settings demonstrate how macrofauna (e.g., *thyasirid* burrows; Dufour and Felbeck, 2003; Dando et al., 2004) and meiofauna (e.g., nematodes; Moens et al., 2005) can enhance OM degradation, increase microbial and bacterial growth, increase solute transport and molecular diffusion, increase sulfide oxidation, shorten porewater turnover time, and alter the vertical distribution of sedimentary phosphorus (Kamp-Nielsen et al., 1982; Meadow et al., 1991; Neira et al., 2001; Löhr and Kennedy, 2015; Arndt et al., 2013; Jørgensen and Nelson, 2004; Jørgensen et al., 2022).

V.5.2. Chondrites: Trace elements distribution and geochemical signals

The preservation and distribution of trace metals in organic-rich sediments are influenced by various factors that include marine productivity, redox conditions in the water-column and porewater, detrital input, chemical diagenesis, and bioturbation (Bromley, 1996; Zheng et al., 2002; Tribovillard et al., 2006; Monedero-Contreras et al., 2023b, 2024). As mentioned before, *Chondrites*-producers may bioturbated considerable volumes (up to 36%) of organic-rich S7 sediments (Fig. V.9), which diluting the syndepositional concentration of trace metals, even trace oligoelements (e.g., Mo, V, Ni, Cu and Co) and TOC. The median dilution factor values of trace metals range from 4% to 9%, while the standard deviation values are from 3% to 7%. Cu and Mo exhibit the highest degree of dilution by *Chondrites*-producers, reaching up to 18% and 17%, respectively. This suggests significant variability in the dilution of different trace metals (Table V.2). The variable dilution for RSTMs and Ba could be attributed to differences in the speciation and mobility of trace metals under different redox conditions (Tribovillard et al., 2006; Calvert and Pedersen, 2007). Evident dilution of trace metals concentrations supports the interpretation that *Chondrites*-producers introduce oxic/dysoxic material impoverished in RSTMs, barite and OM downward into anoxic host sediments more enriched in RSTMs, barite and OM (Fig. V.12). Furthermore, as indicated above, the mixing of materials by *Chondrites* can impact trace metal speciation and mobility, thus influencing their bioavailability, and subsequently the microbial activity, efficiency of OM degradation and nutrient cycling within the sediment (Green and Chandler, 1994; Rysgaard et al., 2000).

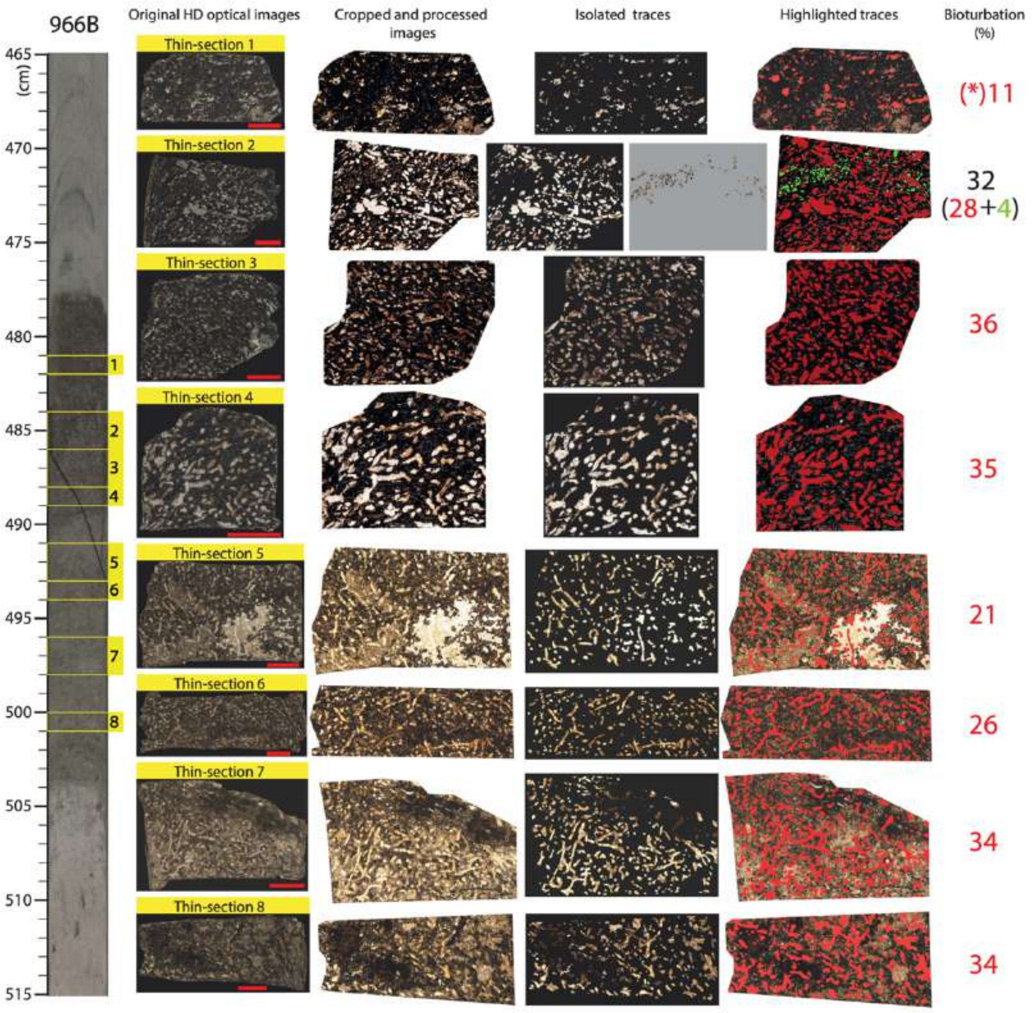
966B
(cm)
465
470
475
480
485
490
495
500
505
510
515
1
2
3
4
5
6
7
8
Original HD optical images
Cropped and processed images
Isolated traces
Highlighted traces
Bioturbation (%)
Thin-section 1
(*)11
Thin-section 2
32
(28+4)
Thin-section 3
36
Thin-section 4
35
Thin-section 5
21
Thin-section 6
26
Thin-section 7
34
Thin-section 8
34

Figure V.9. *Image treatment and bioturbation quantification using Photoshop CS6 methodology developed by Dorador et al., 2014a, b. Bioturbation index is indicated for each thin-section. Core image shown on the left to indicates the depth of each thin-section. Red scale-bar: 5 mm. (*) Bioturbation (%) obtained from quantification of irregular white Chondrites in thin-section 1 characterized by strong sediment mixing.*

In thin-section 2, the dark *Chondrites* appear in a limited ~5 mm thick interval (Figs. V.3 and 9). These *Chondrites* do not exhibit a strong color contrast and have a composition of major elements and trace metals similar to that observed in the host sediment (Figs. V.7 and 10). One explanation for the existence of these dark *Chondrites* is bioturbation by tracemakers during deposition of the sediments overlying thin-section 2, when a slight increase in oxygen levels occurred. Vertical plots reveal an increase in oxygen levels above thin-section 2 (at 484 cm; see Fig. V.2a), supported by a correlative decrease in TOC (%), DOPt values and certain Al-normalized RSTMs (e.g., Mo, U, Ni, and, to a lesser extent, Cu). In this case however, *Chondrites*-producers had to be highly resistant to low oxygen levels (slightly oxygenated during thin-section 2 deposition) because the infills reflect oxygen depleted bottom-waters and high productivity levels, as suggested by the high concentrations of RSTMs and Ba. An alternative explanation is that the infill of these *Chondrites* corresponds to fecal material introduced by active backfilling (Löhr and Kennedy, 2015); still, this possibility is controversial as such behavior has only been reported from uncertain *Chondrites* (Knaust, 2017; Baucon et al., 2020). At any rate, this hypothesis might explain the similarities in geochemical and mineral composition, as well as in texture (grain size) and color, with regard to those of the host sediment.

In thin-section 3, where *Chondrites* infills appear darkened with orange/brown shades and haloes, potentially indicating postdepositional alteration, the concentrations of trace metal are comparable to or even higher than those observed in the host sediment, with dilution factors ranging from 2% to -3% (Table V.2). This could be explained by the postdepositional oxidation and remobilization of trace metals in the near-burrow sediments, and the subsequent reprecipitation within *Chondrites* infills. *Chondrites* burrows open to the sediment-water interface allowed oxic water to flow into the *Chondrites* network. Oxygenated water, whether derived from the moment of deposition of the layer corresponding to thin-section 2 (deposited during an oxygen increase in bottom-water) or from S7 overlying sediments deposited after sapropel termination, could diffuse out of the *Chondrites* network into the anoxic sediments and create sub-mm oxic areas surrounding the burrows (Fig. V.12) (Jovanovic et al., 2014). This may lead to the oxidation of host mineral phases of RSTMs in the surrounding sediments, resulting in dissolved RSTMs in the porewater that can reprecipitate within the sediment or diffuse upwards to the oxic/dysoxic bottom-water. The precipitation of RSTMs in the *Chondrites* infills could occur in association with Mn and Fe oxyhydroxides under dysoxic conditions into the *Chondrites* burrows. Yet this suggestion does not fully account for U enrichments, as U tends to precipitate as uranite during anoxic conditions rather than in association with Fe or Mn oxyhydroxides under dysoxic conditions (McManus et al., 2005; Tribovillard et al., 2006; Calvert and Pedersen, 2007 and references therein). Moreover, SEM-EDX maps of altered *Chondrites* do not show Mn enrichments (Fig. V.7). An alternative mechanism for the reprecipitation of RSTMs must therefore be evoked to explain such enrichments. One potential explanation is that dissolved RSTMs reprecipitated within *Chondrites* infills, probably by absorption and/or co-precipitation into authigenic phases, once oxygen was depleted again due to aerobic bacterial activity along with OM and sulfides oxidation.

ⓐ

	Median values (µ g/g)	V	Co	Ni	Cu	Mo	Ba	U
Section S7b	**Thin-section 1 (B%=11)**							
	Host Sediment (*n* =41)	101	58	78	32	2	189	3
	Chondrites infill (*n* =76)	83	12	68	18	2	190	1
	Thin-section 2 (B%=28)							
	Host Sediment (*n* =23)	541	84	321	290	67	900	21
	White Chondrites infill (*n* =58)	460	77	269	228	51	782	18
	Dark *Chondrites* infill (*n* =12)	628	97	379	271	89	909	25
	Thin-section 3 (B%=36)							
	Host Sediment (*n* =20)	403	67	216	154	32	493	14
	Chondrites infill (*n* =51)	404	69	227	165	30	497	15
	Thin-section 4 (B%=35)							
	Host Sediment (*n* =44)	417	69	238	218	21	520	17
	Chondrites infill (*n* =100)	365	63	208	180	17	478	14

ⓑ

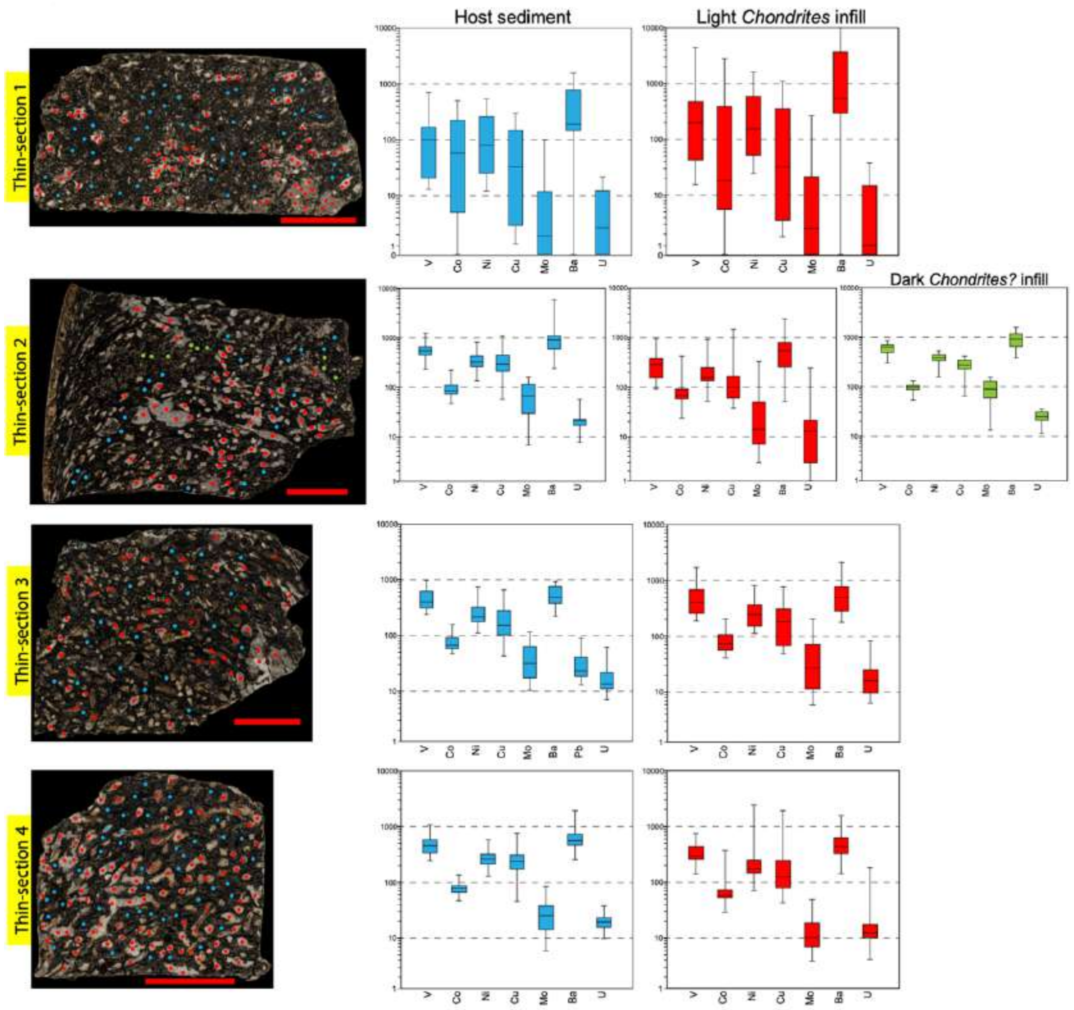

Figure V.10. *Box-plots of LA-ICP-MS spot-analysis results on thin-sections 1, 2, 3 and 4 from section S7b. (a) Table of TMs concentrations (µg/g) obtained by LA-ICP-MS spot-analyses in the host sediment and Chondrites infills. n = number of spot-analyses. (b) Box-plots of LA-ICP-MS spot-analyses results. The high-resolution optical images are indicated the locations of the LA-ICP-MS spot-analysis. Blue dots: host-sediment; red dots: Chondrites infills. Accordingly, blue box-plots indicate host-sediment results, while red box-plots indicate Chondrites infill results. LA-ICP-MS results of the dark Chondrites observed in thin-section 2 are shown in green. Red scale-bar: 5 mm. All box-plots have log*$_{10}$ *scale.*

ⓐ

	Median values (μ g/g)	V	Co	Ni	Cu	Mo	Ba	U
Section S7a	**Thin-section 5 (B%=21)**							
	Host Sediment (*n* =23)	268	50	172	174	8	376	15
	***Chondrites* infill (*n* =54)**	184	37	122	75	3	233	8
	Thin-section 6 (B%=26)							
	Host Sediment (*n* =26)	193	49	173	151	4	544	12
	***Chondrites* infill (*n* =50)**	182	44	138	79	4	335	9
	Thin-section 7 (B%=34)							
	Host Sediment (*n* =22)	220	48	173	151	7	393	11
	***Chondrites* infill (*n* =55)**	156	35	112	71	3	232	7
	Thin-section 8 (B%=34)							
	Host Sediment (*n* =23)	261	51	161	146	6	402	10
	***Chondrites* infill (*n* =34)**	219	47	144	86	4	355	8

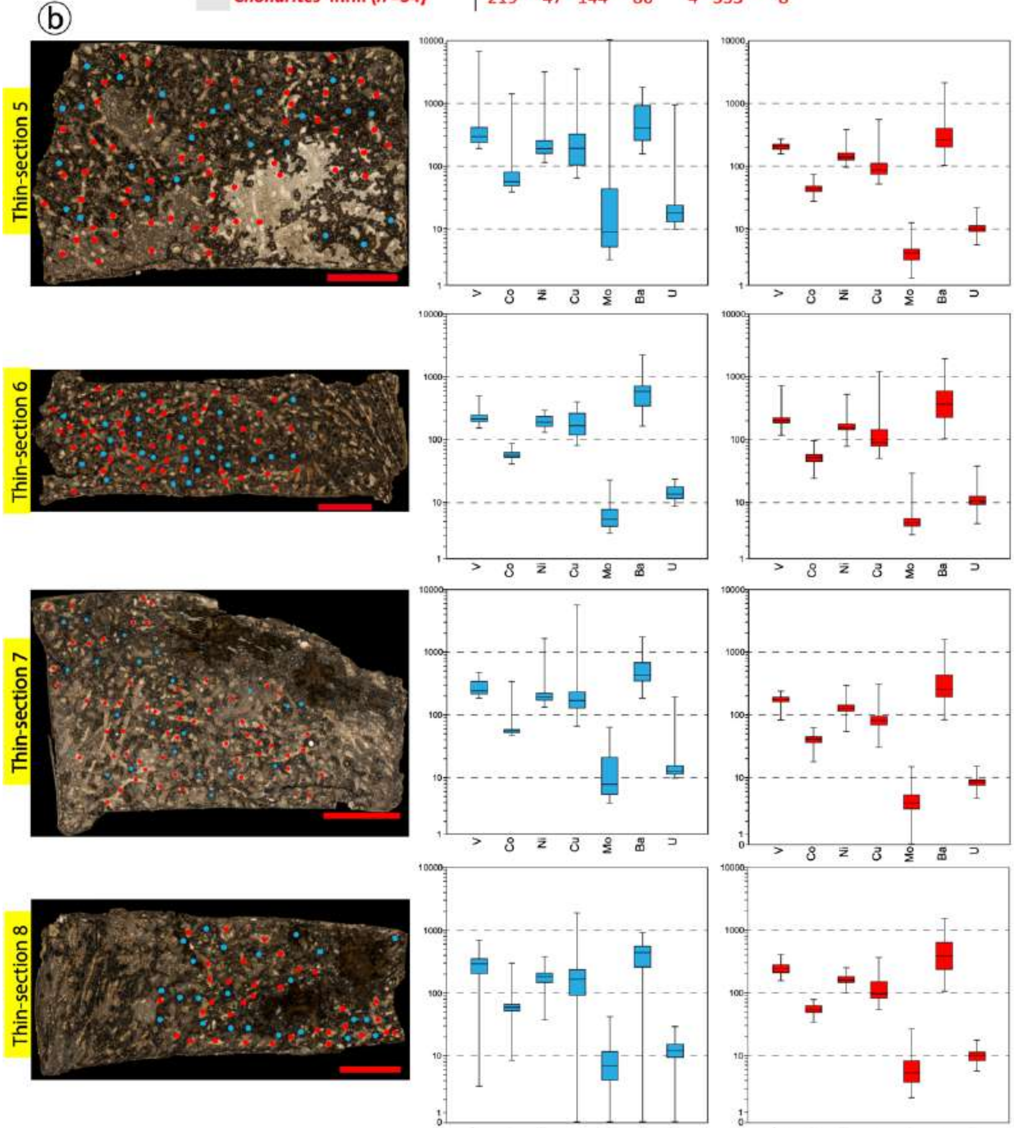

Figure V.11. *Box-plots of LA-ICP-MS spot-analysis results of thin-sections 5, 6, 7 and 8 from section S7a. (a) Table of TMs concentrations (μg/g) obtained by LA-ICP-MS spot-analyses in the host sediment and Chondrites infills. n = number of spot-analyses. (b) Box-plots of LA-ICP-MS spot-analysis results. The high-resolution optical images are indicated the locations of the LA-ICP-MS spot-analyses. Blue dots: host-sediment; red dots: Chondrites infill. Accordingly, blue box-plots indicate host-sediment results, while red box-plots indicate Chondrites infills results. Red scale-bar: 5 mm. All box-plots have log$_{10}$ scale.*

Table V.2. *Calculated weighted average TM concentration [wTM] and dilution factor (df). Mean and maximum dilution factor values are indicated at the bottom for each TM. [TM]$_{hs}$ = median TM in the host sediment.*

		LA-ICP-MS (μg/g)						
		V	Co	Ni	Cu	Mo	Ba	U
S7b section	**Thin-section 1**							
	[TM]hs	101	58	78	32	2	189	3
	[wTM]	99	53	77	31	2	189	2
	df (%)	2	9	1	5	-2	0	6
	Thin-section 2							
	[TM]hs	541	84	321	290	67	900	21
	[wTM]	522	83	309	272	64	867	20
	df (%)	4	2	4	6	5	4	3
	Thin-section 3							
	[TM]hs	403	67	216	154	32	493	14
	[wTM]	404	68	220	158	31	494	14
	df (%)	0	-1	-2	-3	2	0	-2
	Thin-section 4							
	[TM]hs	417	69	238	218	21	520	17
	[wTM]	399	67	228	205	20	505	16
	df (%)	4	3	4	6	7	3	5
S7a section	**Thin-section 5**							
	[TM]hs	268	50	172	174	8	376	15
	[wTM]	250	47	161	153	7	346	14
	df (%)	7	6	6	12	12	8	10
	Thin-section 6							
	[TM]hs	193	49	173	151	4	544	12
	[wTM]	190	48	164	132	4	490	11
	df (%)	1	3	5	12	3	10	6
	Thin-section 7							
	[TM]hs	220	48	173	151	7	393	11
	[wTM]	198	44	152	124	5	338	9
	df (%)	10	9	12	18	17	14	11
	Thin-section 8							
	[TM]hs	261	51	161	146	6	402	10
	[wTM]	247	50	155	126	5	386	9
	df (%)	5	3	4	14	8	4	5

	V	Co	Ni	Cu	Mo	Ba	U
Median df (%)	4	4	4	9	7	5	6
Maximum df (%)	10	9	12	18	17	14	11

In any case, *Chondrites*-producers are changing the redox conditions in confined sub-cm areas of the anoxic organic-rich sediments and the distribution of RSTMs, including some oligoelements such as Fe, S, Mo, Co, Cu, V and Ni (Fig. V.12). Aller (1994) stated that cyclic redox patterns are common within individual burrow structures and are accompanied by rapid switching in dominant metabolic processes, generating geometrically and temporally complex redox mosaics in the sediment matrix. This observation aligns with findings by Jørgensen et al. (2005) and Meysman et al. (2006), who state that oxic sub-cm microniches can occur along the burrow walls in anoxic sediments due to occasional oxic ventilation. Yin et al. (2017) further corroborated this by demonstrating how burrowing ragworms (polychaete *Nereis succinea*) oxidize the walls of the burrows in salt marsh sediments. Accordingly, the irrigation by *Chondrites*-producers creates a complex sub-cm redox mosaic within the sediments and can potentially enhances microbial productivity, involving sulfur-oxidizing and magnetotactic bacteria in the near-burrow sediments where the redox transition zones are located (Lefèvre and Bazylinski, 2013).

V.5.3. Multiproxy reconstruction of S7 evolution

The compiled geochemical dataset and ichnological assessments of S7 enable a multiproxy paleoenvironmental reconstruction of the S7 evolution, deposited between ~198.5 and 191.9 ka (Ziegler et al., 2010). S7 was deposited during very humid conditions with large nutrient-rich fluvial inputs from the African borderlands, primarily by the Nile River (Gallego-Torres et al., 2007a, b; Wu et al., 2018). Hence, the S7 sediments are enriched in OM as a result of increased export productivity and oxygen-depleted bottom-waters (Benkovitz et al., 2020; Sweere et al., 2021). As previously stated, the S7 event at the Eratosthenes Seamount can be divided in to two sub-sections tied to different redox and environmental conditions (Fig. V.2a). The deposition of section S7a (from 503.5 to 491 cm of core 966B; Fig. V.2) was accompanied by a moderate increase in productivity and weak deep-water restriction due to intermittent bottom-water ventilation/oxygenation, followed by low RSTMs authigenic enrichment. During the S7a period, oxic to dysoxic conditions most likely prevailed at the top of Eratosthenes Seamount. They allowed macro and micro-opportunistic organisms to intermittently colonize the seafloor and homogenize the sediments, erasing sub-mm lamination and producing a mottled texture (Fig. V.13) (Rodríguez-Tovar, 2022). Further evidence of syndepositional benthic activity lies in the presence of fecal pellets (see thin-section 8 in Fig. V.6b.6) (Löhr and Kennedy, 2015). In this framework, OM accumulation/preservation was not very efficient during S7a period; TOC content does not exceed 2%, supporting a weak oxygen-depletion at this water-depth in conjunction with moderate productivity (Fig. V.2). Nevertheless, intermittent and confined porewater euxinia must be evoked to explain the Mo enrichments and the presence of euhedral pyrite framboids in the host sediments of section S7a (Helz et al., 1996; Tribovillard et al., 2008; Scott and Lyons, 2012; Helz and Vorlicek, 2019).

The mixing and biodeformation of the sediments during period S7a probably took place through the interplay of two different bioturbational mechanisms, creating a distinctive "mottled" sediment texture (Fig. V.13): (i) in fine sediments with high water content, burrows created by macrotracemakers appear as biodeformational sedimentary structures, showing no distinct outline, leading to total sediment mixing without evident signs of well-defined burrows, outlines, or color contrasts (Rodriguez-Tovar, 2022), and (ii) meiofauna, despite their small size, could have actively mixed and homogenized the sediments. Furthermore, the bioturbation might have been a continuous process throughout S7a deposition, or else could have been limited to periods of increased bottom-water oxygenation. The grayish sediment patch in thin-section 5 (Fig. V.5) appears to be syndepositional because the presence of *Chondrites* “cuts” through it, and the irregular outline suggests it is not a biosedimentary structure. It can thus be interpreted as a partially erased oxic layer with low TOC (due to bioturbation) that was deposited during bottom-water ventilation. Even though brief bottom-water ventilations might have occurred, no apparent indications are seen in the geochemical record (e.g., Mn peak; Fig. V.2) (Filippidi and de Lange, 2019; Monedero-Contreras et al., 2023b). Still, we cannot be discarded the possibility that Mn-oxyhydroxides precipitating during ventilation might have undergone postdepositional dissolution as a result of the redox transition towards anoxic porewaters during the deposition of S7b section.

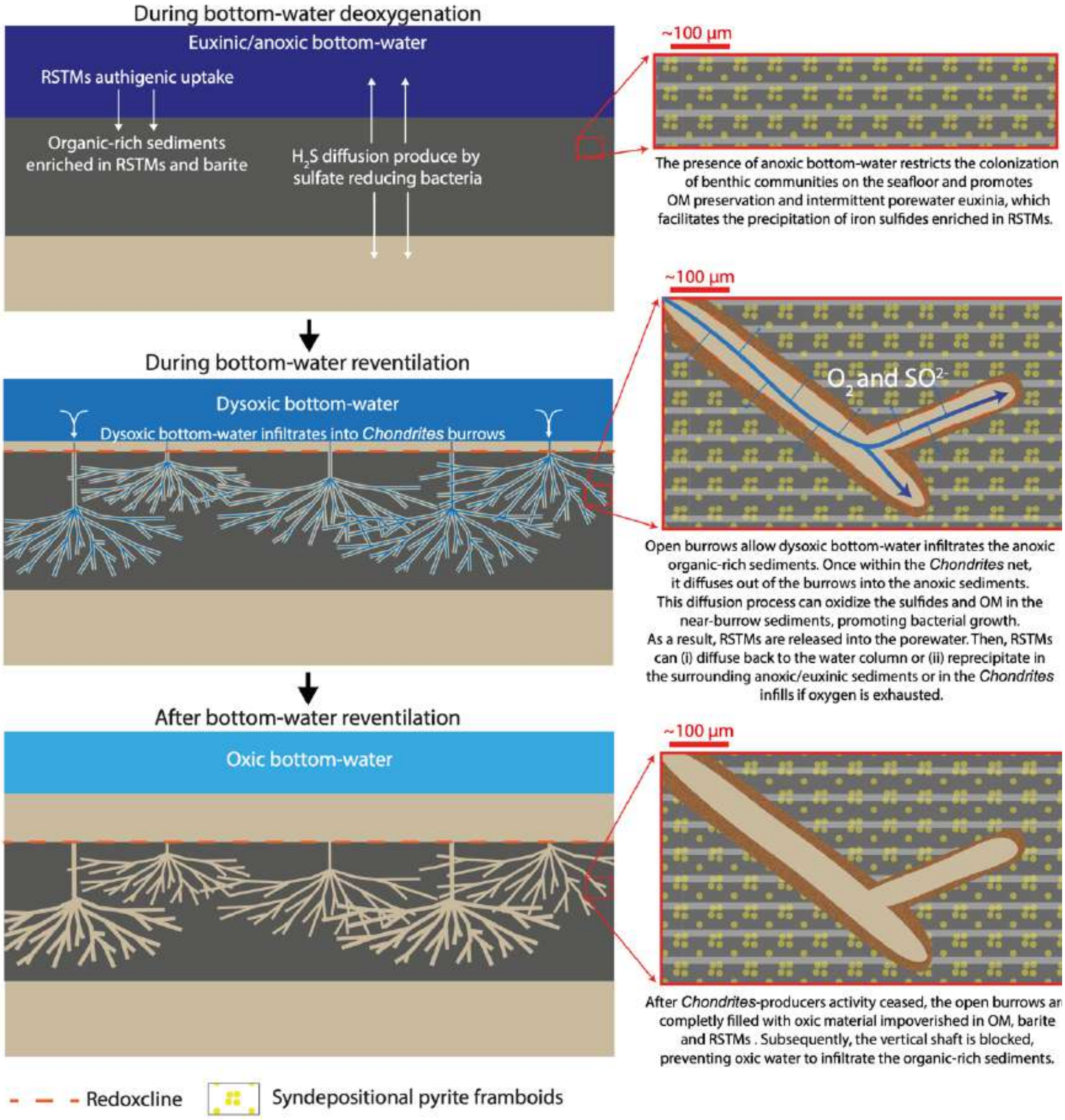
During bottom-water deoxygenation
Euxinic/anoxic bottom-water
RSTMs authigenic uptake
Organic-rich sediments enriched in RSTMs and barite
H_2S diffusion produce by sulfate reducing bacteria
~100 µm
During bottom-water reventilation
Dysoxic bottom-water
Dysoxic bottom-water infiltrates into *Chondrites* burrows
~100 µm
O_2 and SO^{2-}
After bottom-water reventilation
Oxic bottom-water
~100 µm
Redoxcline
Syndepositional pyrite framboids

The presence of anoxic bottom-water restricts the colonization of benthic communities on the seafloor and promotes OM preservation and intermittent porewater euxinia, which facilitates the precipitation of iron sulfides enriched in RSTMs.

Open burrows allow dysoxic bottom-water infiltrates the anoxic organic-rich sediments. Once within the *Chondrites* net, it diffuses out of the burrows into the anoxic sediments. This diffusion process can oxidize the sulfides and OM in the near-burrow sediments, promoting bacterial growth. As a result, RSTMs are released into the porewater. Then, RSTMs can (i) diffuse back to the water column or (ii) reprecipitate in the surrounding anoxic/euxinic sediments or in the *Chondrites* infills if oxygen is exhausted.

After *Chondrites*-producers activity ceased, the open burrows ar completly filled with oxic material impoverished in OM, barite and RSTMs . Subsequently, the vertical shaft is blocked, preventing oxic water to infiltrate the organic-rich sediments.

Figure V.12. *Chondrites evolution scheme in organic-rich sediments and induced geochemical processes at sub-cm scale.*

If a near-constant sedimentation rate is assumed for the entire S7 event −considering Ba enrichment as the complete sapropel event following Gallego-Torres et al. (2010) methodology− one may surmise that a change in water-column dynamics, redox conditions, and productivity rate occurred around 196.6 ka at the top of the Eratosthenes Seamount. This change marked the onset of the S7b period, characterized by (i) stronger deep-water stagnation, which boosted bottom-water deoxygenation at the top of Eratosthenes Seamount and enhanced adsorption and/or co-precipitation of RSTMs into authigenic phases by seafloor sediments, and (ii) increased productivity, that enhancing barite precipitation in the water-column (Fig. V.13). The accumulation/preservation of OM was thereby enhanced, which derived in higher TOC content in S7b section (TOC up to 3.4%; Fig. V.2a). Higher Mo concentrations and the high abundance of pyrite nanocrystals (> 1 µm) in the host sediments further supports that euxinic conditions may have been reached not only within confined microenvironments in the porewater-sediment system, but also sporadically in bottom-waters at the top of Eratosthenes Seamount (Wilkin et al., 1996, 1997; Wilkin and Barnes, 1997; Scott and Lyons, 2012; Lin et al., 2016; Liu et al., 2019; Chang et al., 2022). The existence of sub-mm lamination furthermore indicates that macro benthic organisms were absent from ~196.6 ka to 191.9 ka because of bottom-water anoxia (Fig. V.13). The existence of meiofauna that living between the grains, incapable of disturbing sub-mm lamination, cannot be ruled out, however (Löhr and Kennedy, 2015). Such insights would indicate that during period S7b the redoxcline in the Eastern Mediterranean was placed above ~ 900mbsl due to strong water-column stratification and deep-water deoxygenation (Benkovitz et al., 2020; Sweere et al., 2021; Monedero-Contreras et al., 2023a, 2024). A correlative decrease in various RSTMs concentrations at 484 cm deep points to a brief period of weakened bottom-water anoxia around 194-193 ka at Eratosthenes Seamount. This allowed small *Chondrites* tracemakers to colonize the seafloor for a short spell, until bottom-water anoxia returned (Fig. V.13); hence small dark *Chondrites* in the underlying sediment present a very similar composition to the host sediment and are only observed within a 0.5 cm thick interval (thin-section 2; see Figs. V.3 and 9).

After S7´s termination, dryer conditions ruled in the Eastern Mediterranean, meaning decreased fluvial input, increased aeolian influence, and lower OM accumulation/preservation. The end of S7 at Eratosthenes Seamount took place when deep-water formation/circulation was reactivated. The absence of a "marker bed" −an interval enriched in Mn-oxyhydroxides atop the S7 organic-rich sediments− does not support the occurrence of an abrupt reventilation during S7 termination at the Seamount (Wilson et al., 1986; Calvert and Pedersen, 1993; de Lange et al., 2008; Filippidi and de Lange, 2019). However, the immediate return of oxic bottom-waters after S7´s termination at the Eratosthenes Seamount is corroborated by the rapid colonization of the seafloor by opportunistic *Chondrites*-producers and by the synchronous drop in TOC, RSTMs and pyrite content at the top of S7 sediments. Since there are no signs of postdepositional sapropel burndown, e.g., a mismatch between Ba/Al and TOC (Fig. V.2a) (van Santvoort et al., 1997; Monedero-Contreras et al., 2023b), we can affirm that the redoxcline was never situated below the upper boundary of the organic-rich sediments during the deposition of section S7b (Fig. V.13). Despite the fact that porewater anoxia was maintained during S7 termination, *Chondrites*-

producers were able to bioturbate the organic-rich sediments, taking advantage of the oxygen from the overlying oxic/dysoxic bottom-waters due to the presence of a vertical shaft.

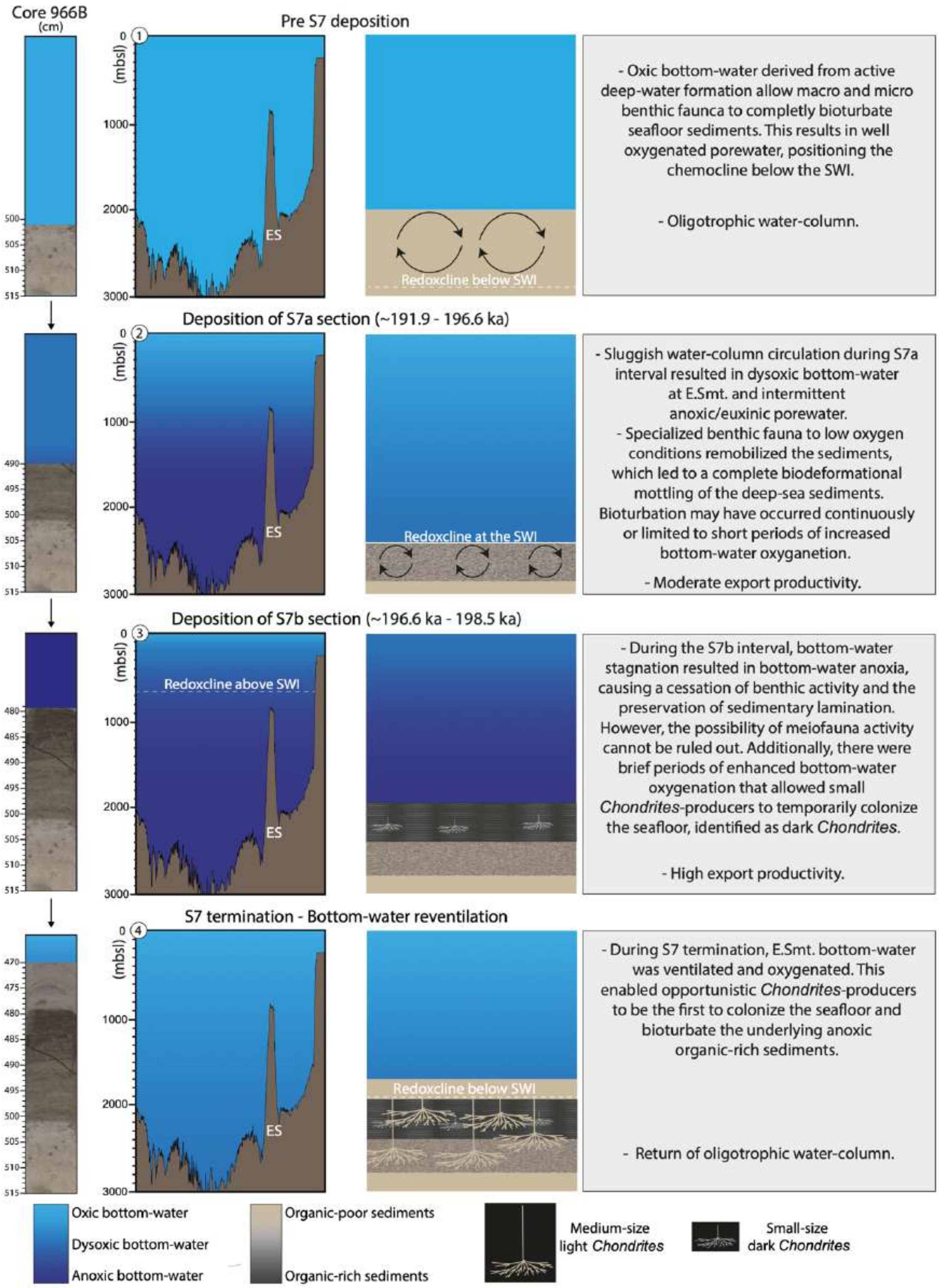
Core 966B
(cm)
Pre S7 deposition
Deposition of S7a section (~191.9 - 196.6 ka)
Deposition of S7b section (~196.6 ka - 198.5 ka)
S7 termination - Bottom-water reventilation
①
②
③
④
0
1000
2000
3000
(mbsl)
ES
Redoxcline below SWI
Redoxcline at the SWI
Redoxcline above SWI
470
475
480
485
490
495
500
505
510
515
Oxic bottom-water
Dysoxic bottom-water
Anoxic bottom-water
Organic-poor sediments
Organic-rich sediments
Medium-size
light *Chondrites*
Small-size
dark *Chondrites*

- Oxic bottom-water derived from active deep-water formation allow macro and micro benthic faunca to completly bioturbate seafloor sediments. This results in well oxygenated porewater, positioning the chemocline below the SWI.

- Oligotrophic water-column.

- Sluggish water-column circulation during S7a interval resulted in dysoxic bottom-water at E.Smt. and intermittent anoxic/euxinic porewater.
- Specialized benthic fauna to low oxygen conditions remobilized the sediments, which led to a complete biodeformational mottling of the deep-sea sediments. Bioturbation may have occurred continuously or limited to short periods of increased bottom-water oxyganetion.

- Moderate export productivity.

- During the S7b interval, bottom-water stagnation resulted in bottom-water anoxia, causing a cessation of benthic activity and the preservation of sedimentary lamination. However, the possibility of meiofauna activity cannot be ruled out. Additionally, there were brief periods of enhanced bottom-water oxygenation that allowed small *Chondrites*-producers to temporarily colonize the seafloor, identified as dark *Chondrites*.

- High export productivity.

- During S7 termination, E.Smt. bottom-water was ventilated and oxygenated. This enabled opportunistic *Chondrites*-producers to be the first to colonize the seafloor and bioturbate the underlying anoxic organic-rich sediments.

- Return of oligotrophic water-column.

Figure V.13. *Scheme of S7 evolution at Site 966B using geochemical and ichnological information. SWI: sediment-water interface; ES: Eratosthenes Seamount.*

The DOPt increases below S7 organic-rich sediments is indicative of authigenic pyrite enrichments, linked to the existence of a synsapropel interval, which corresponds to an interval with low TOC content but high pyrite content below a sapropel (Passier et al., 1996, 1997, 1999; Benkovitz et al., 2016; Matthews et al., 2017; Filippidi and de Lange, 2019; Monedero-Contreras et al., 2023b). The DOPt increase at the top of S7 corresponds to the synsapropel interval of the overlying sapropel (i.e., S6) (Monedero-Contreras et al., 2024). The precipitation of pyrite below some sapropels is controlled by the reaction of downward HS^{-} fluxes in contact with the upward diffusing Fe from underlying sediments (Passier et al., 1996). Thus, during S7 deposition, a downward diffusion of excess HS^{-} produced by sulfate-reducing bacteria promoted pyrite formation through sulfidisation of the sediments below S7 (Passier et al., 1996). This scenario implies that reactive Fe for pyrite precipitation was depleted in the organic-rich S7 sediments. Moreover, the vertical plots indicate that Co, Ni, and Cu, precipitated in association with the synsapropel pyrite (Monedero-Contreras et al., 2023b, 2024) (see Fig. V.2d).

V.6. Conclusions

Detailed ichnological analysis reveals the influence of *Chondrites* on the RSTMs enriched in sapropel S7 (~195ka), at the Eratosthenes Seamount (Levantine Basin, Eastern Mediterranean). *Chondrites* alter sedimentary features at a sub-cm scale, impacting lamination, texture and mineral distribution. The bioturbation of materials by *Chondrites*-producers also modifies the distribution and concentration of OM and trace elements, including oligoelements that are vital for macro and microorganisms (e.g., Fe, S, Mo, Co, Cu, V and Ni).

Chondrites-producers are able to bioturbate significant volumes of organic-rich sediments (from 11% to 35%). They can introduce overlying oxic/dysoxic material of low trace metals concentrations and OM content downward, into anoxic sediments more enriched in trace metals and OM. By doing this they can introduce oxic porewater below the sedimentary redoxcline. The whole of this process modifies redox conditions in the zones surrounding the *Chondrit*es burrows and remobilizes trace metals through the oxidation of sulfides and OM in the near-burrow sediments. Remobilized trace metals can reprecipitate within the sediment, or diffuse to bottom-waters. As a consequence, the change in trace metal speciation, mobility, and distribution influences the bioavailability of trace metals. In turn, *Chondrites* can impact carbon and nutrients cycling, microbial activity, and OM degradation, impacting in turn the overall sedimentary biogeochemistry of deep-marine sediments, where *Chondrites* tend to be abundant.

With respect to the implications for paleoceanographic/paleoenvironmental reconstructions based on geochemical signals, *Chondrites* bioturbation would dilute the overall TOC content and the concentration of paleoenvironmental diagnostic trace metals (e.g., Mo, U, V, Ba) in bulk sediment samples. Although the average dilution factor is between 5% and 6%, in some cases the dilution can be greater than 10% for key paleoceanographic trace metals (e.g., Mo, U and Ni); depending on the abundance, distribution and infilling material composition of *Chondrites*, and on the speciation and mobility of the trace metal under different redox conditions. If the distribution of *Chondrites* remains relatively constant throughout the sampled organic-rich section, vertical trends of RSTMs will not be substantially affected. At any rate, however, *Chondrites* presence must be considered for accurate sedimentary record comparisons and for calculating trace metals and OM burial fluxes. High-resolution redox reconstructions based on sub-cm analyses (e.g., LA-ICP-MS line-scanning and XRF core-scanning) should take into account the presence of *Chondrites*, as RSTMs variations might not be related to time variations but rather to *Chondrites* infills geochemical composition.

Based on the obtained geochemical data and ichnological information, the paleoenvironmental evolution of S7 was interpreted, leading us to characterize of two phases with different redox and environmental conditions. During the lower half of S7 (S7a), deep-water stagnation and deoxygenation was weak and marine productivity was low, then, as the upper S7 section (S7b) was deposited, deep-water stagnation strengthened and marine productivity increased. This enhanced deep-water deoxygenation, OM accumulation/preservation and trace metal authigenic uptake, in addition to shallowing the redoxcline above 900 mbsl and inhibiting the establishment of benthic organisms.

Overall, the sub-cm modifications caused by *Chondrites* have wide-ranging implications beyond mineral redistribution and trace metals dilution within organic-rich sediments. *Chondrites*-producers exert significant influences on biogeochemical processes, carbon and trace metals cycling, and the fate of organic carbon in deep-marine environments, highlighting the intricate and complex interplay between biological activity (i.e., bioturbation), sedimentary processes, and carbon and trace metal dynamics. Therefore, understanding the impacts of *Chondrites* bioturbation on sedimentary biogeochemistry by assessing its effect on trace metals distribution and OM preservation within the sediments is crucial for (i) accurately interpreting past oceanographic events (in particular deoxygenation events) from deep-sea records, and (ii) evaluating its potential impacts on carbon and trace metals cycling, as well as carbon sequestration in marine sediments.

Supplementary material

Supplementary data to this article can be found online at https://ars.els-cdn.com/content/image/1-s2.0-S0921818124000341-mmc2.docx

Geochemical data as Excel file can be found online at: https://ars.els-cdn.com/content/image/1-s2.0-S0921818124000341-mmc1.xlsx

Acknowledgments

This study has been funded by Grants PID2019-104625RB-100, PID2019-104624RB-I00 and TED2021-131697B-C22 through MCIN/AEI/ 10.13039/501100011033, Grants FEDER/Junta de Andalucía P18-RT-3804 and P18-RT-4074, and Research Groups RNM-179 and RNM-178 by Junta de Andalucía. We thank Prof. Adatte from Lausanne University (Switzerland) for Rock-eval analyses and TOC measurements. We thank the Center for Scientific Instrumentation (CIC, University of Granada) for the ICP analyses, especially to Dr. Olga Cazalla for her contribution to the numerous LA-ICP-MS analyses. We are also grateful to the Ocean Drilling Program for providing the analyzed samples and to the ODP Core Repository (Bremen, Germany) for assistance with sampling. We extend our gratitude to Jean Sanders for finally proofreading the text. Lastly, thanks to Dr. Jean-Carlos Montero-Serrano and Dr. Laurent Riquier for improving this article through their careful review, and to Dr. Fabienne Marret-Davies for his editorial work. This study is part of R. Monedero´s PhD project.

Chapter VI

Tracking productivity changes in the Alboran Sea during the past 13,000 years using a combination of palynological and geochemical tools: paleoperspectives on productivity responses to climate variability

Ricardo D. Monedero-Contreras, Francisca Martínez-Ruiz, Francisco J. Rodríguez-Tovar, Jose M. Mesa-Fernández, Francesca Sangiorgi

Submitted for publication in Quaternary Science Reviews

Abstract

Marine productivity is expected to globally decrease, posing a global-scale threat to marine ecosystems and seafood supplies, and decreasing export carbon to the deep-ocean. Integrating modern observations with paleoperspectives is crucial for enhancing the accuracy of long-term (centennial – multicentennial) productivity projections. This research delves into the paleoceanographic evolution of the Westernmost Mediterranean, with a specific focus on reconstructing productivity changes over the last 13,000 years from a high-resolution deep-marine sediment record in Western Alboran Basin (core GP04PC). At present, the Western Alboran Basin is one of the most productive marine areas in the Mediterranean, serving as an important regional carbon sink and key area for understanding marine productivity responses to past global climate variability. The sediment record was analyzed using a combination of palynological and geochemical tools, providing insights into centennial-scale marine productivity responses to climate variability. During the Younger Dryas humid phase (from ~ 12.2 to 11.7 ka) and the Holocene humidity optimum (from ~ 10.5 to 8.5 ka), high marine productivity was driven by surface water fertilization from enhanced local river discharges as a result of rapid melting of continental glaciers and an increase in regional precipitations. Additionally, during the late Holocene, intermittent marine productivity increases were associated with increases in fluvial input linked to short-term negative North Atlantic Oscillation (NAO) phases. Therefore, over the last 13,000 years wet regional conditions in the Westernmost Mediterranean, influenced by the interaction of orbital (e.g., insolation cycles) and suborbital (e.g., NAO patterns) factors, favor enhanced marine productivity in the Western Alboran Basin, with local river discharges playing a key role in primary productivity dynamics. The current oceanographic scenario in the Western Alboran Basin, characterized by active gyres and upwelling systems, has prevailed over the last ~ 4,200 years due to a persistent positive NAO phase, where water-column stability in the Western Alboran Basin appears to have a more significant effect on marine productivity than changes in fluvial inputs and sea surface temperature. The strong detrital influence on barium (Ba) concentrations in Western Alboran sediments limits the use of Ba/Al ratio for reconstructing of weak to moderate productivity changes, highlighting the importance of dinocyst analysis as a complementary tool for accurately reconstructing marine productivity in this region. Overall, this study advances our understanding of marine ecosystem responses to climate variability, providing valuable paleoperspectives for developing robust long-term productivity models essential for adapting to the ongoing environmental changes within this region.

VI.1. Introduction

Global warming and anthropogenic activities are affecting oceanographic processes (e.g., vertical mixing and thermohaline circulation) and biogeochemical cycles (e.g., nutrients cycling; C, N, P and Fe) (Gruber, 2011; Gruber et al., 2021), inducing important impacts on marine environments, including rising sea surface temperature (SST), decreasing oxygen content, and changing nutrient availability (Schmidtko et al., 2017; Breitburg et al., 2018). These impacts have led to variations in marine productivity, posing a global-scale threat to marine ecosystems and seafood supplies (Polovina et al., 2008; Lozier et al., 2011; Capotondi et al., 2012; Mena et al., 2019). Analyses of primary production derived from satellite data over the past two decades presented in the IPCC report from 2023 revealed a decrease in marine productivity (up to −3.0%) at low and mid latitudes. Biogeochemical models outlined in this report support a global decline in primary production of 2.1% per decade attributed to the shoaling of the mixed layer and decreasing nitrate concentrations, based on data obtained from 1998 to 2015. However, to achieve robust long-term projections (decades to centuries) of productivity responses to the current climate change, data on timescales larger than those represented by instrumental records is required. In this context, marine paleoarchives emerge as indispensable tools, as it has been demonstrated that marine environmental responses to past climate changes, obtained through paleoceanographic reconstructions, can be incorporated into future projections to better constrain centennial-scale environmental responses (including productivity changes), that may occur in different marine settings due to the current climate change (Oschlies et al., 2018; Kiessling et al., 2023; Mancini et al., 2023a, b).

Among the different regions around the globe, the Mediterranean Sea stands out as a major hotspot of climate change due to its unique characteristics –including its semi-enclosed nature, latitudinal position, relatively short water-mass residence time and complex seafloor morphology (Lionello et al., 2006; Malanotte-Rizzoli et al., 2014). These attributes make it highly responsive to climate impact-drivers such as warming, acidification, deoxygenation, and changes in nutrient availability, all of which significantly affect Mediterranean primary productivity (Lionello et al., 2018). Macias et al. (2015) demonstrate through hydrodynamic-biogeochemical models significant changes in marine productivity in the Mediterranean over the next century. Their findings indicate that the Western Mediterranean Basin is expected to become more oligotrophic, attributed to a decrease in surface density (increased stratification) influenced by low-salinity Atlantic water. Conversely, marine productivity in the Eastern Mediterranean Basin is expected to increase due to a density increase (less stratification and stronger vertical mixing) caused by the increasing evaporation rate of the Eastern Mediterranean surface waters. However, the integration of modern observations with paleoperspectives is critical for improving the robustness of modeled long-term productivity spatio-temporal patterns in the Mediterranean.

At present, the Alboran Sea (located in the Westernmost Mediterranean region) is one of the most productive areas in the Mediterranean due to seasonal upwelling systems in the northern margin (Moran and Estrada, 2001; Bárcena et al., 2004; Macias et al., 2015; Yebra et al., 2018; Mena et al., 2019). Its elevated sedimentation rates provide marine sediment records with exceptional temporal resolution, serving as ideal paleoarchives for reconstructing past climate variability and associated oceanic responses (including marine productivity changes) at centennial resolution (Cacho et al., 2002, 2006; Rodrigo-Gámiz et al., 2014a, b, 2015; Pérez-Asensio et al., 2020; Morcillo-Montalbá et al., 2021). Consequently, marine sediment records from the Alboran Sea region have enabled high-resolution productivity reconstructions throughout the different climatic events over the last millenniums (Ausín et al., 2015a, b; Pénaud et al., 2016).

To acquire key paleoperspectives on the long-term productivity responses to past climate variability, this study presents a multiproxy reconstruction of the oceanographic and environmental conditions in the Westernmost Mediterranean region over the last 13,000 years, focusing on reconstructing productivity changes at centennial resolution. This has been achieved using a combination of palynological and geochemical tools (see section 3) applied to the sediment record recovered from the Western Alboran Basin (Westernmost Mediterranean) at a water depth of 1306.5 m, and previously dated by Morcillo- Montalbá et al. (2021). Additionally, we compare our results with those from other sedimentary records, including continental ones (e.g., lake sediments), to support regional-scale interpretation.

VI.2. Oceanographic and climatic setting

The analyzed sediment record (GP04PC) is located in the Western Alboran Basin, which experiences pronounced seasonal productivity increases and represents one of the most productive areas in the Mediterranean (D'Ortenzio and Ribera d'Alcalà, 2009; Siokou-Frangou et al., 2010; Christaki et al., 2011; Basterretxea et al., 2018). The climate of the Alboran Sea region, located between Southern Iberia and North Africa in the Westernmost part of the Mediterranean Sea (see Fig. VI. 1), is influenced by the interaction of African subtropical, North Atlantic, and Mediterranean climate system (Rodó et al., 1997; Dünkeloh and Jacobeit, 2003). The current climate in the region is characterized by hot, arid summers and comparatively wetter winters controlled by an atmospheric high-pressure situated in the Atlantic Ocean, above the Azores archipelago (Sumner et al., 2001). The Alboran Sea experiences an annual mean SST of 19.5 ± 0.3°C, with a strong temperature seasonal contrast, ranging from 15°C in February to 25°C in August (Macias et al., 2016). Furthermore, it receives intermittent torrential riverine discharges from Morocco and Spain, as well as eolian dust inputs from the African margin, particularly the Sahara Desert, resulting in deep-sea sediments enriched in the lithogenic fraction (around 70%) (Liquete et al., 2005; Palanques et al., 2005; Zúñiga et al., 2008).

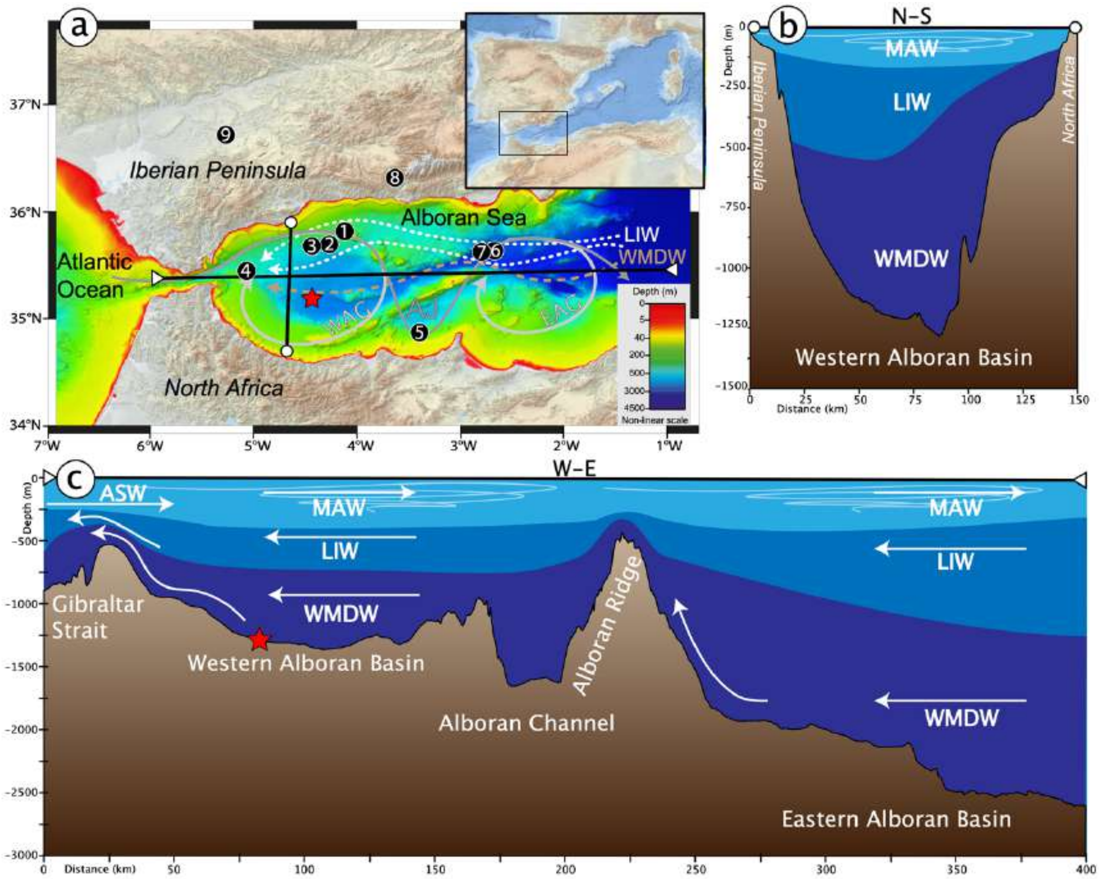
a
37°N
36°N
35°N
34°N
7°W
6°W
5°W
4°W
3°W
2°W
1°W
Iberian Peninsula
Alboran Sea
Atlantic Ocean
North Africa
LIW
WMDW
WAG
AJ
EAG
Depth (m)
Non-linear scale
b
N-S
MAW
LIW
WMDW
Iberian Peninsula
North Africa
Western Alboran Basin
Depth (m)
Distance (km)
c
W-E
ASW
MAW
LIW
WMDW
Gibraltar Strait
Western Alboran Basin
Alboran Ridge
Alboran Channel
Eastern Alboran Basin
Depth (m)
Distance (km)

***Figure VI.1**. Oceanographic setting of core GP04PC. Fig. VI. 1a. Bathymetric map of Alboran Sea. Black lines represent the superficial expression of the bathymetric transects in Figs. VI.1b and VI.1c. The location of core GP04PC (1306.5 mbsl) is indicated as red star. On this bathymetric map, the location of diverse cores from previous studies used for comparison in this study are indicated by numbered black circles: (1) HER-GC-T1 (659 mbsl; Ausín et al., 2015b); (2) TTR17-434G (1108 mbsl; Mesa-Fernández et al., 2022); (3) ODP 976 (1108 mbsl; Combourieu-Nebout et al., 1999, 2009; Dormoy et al., 2009); (4) CEUTA10PC08 (914 mbsl; Ausín et al., 2015a); (5) GeoB18131-1 (457 mbsl; Wang et al., 2019); (6) 4) MD95-2043 (1841 mbsl; Cacho et al., 1999, 2002; Fletcher et al., 2010; Panaud et al., 2011, 2016); (7) TTR12-293G (1840 mbsl; Rodrigo-Gamiz et al., 2011); (8) PADUL-15-05 (Padul wetland, Granada; Ramos-Román et al., 2018); (9) LB-15-01 (La Ballestera lake, Sevilla; García-Alix et al., 2022). Fig. VI. 1b. North to South (N-S) bathymetric transect of Western Alboran Basin. Fig. VI. 1c. West to East (W-E) bathymetric transect of Western and Eastern Alboran basins. The different water-masses are illustrated with different colors. Superficial currents: WAG (Western Alboran Gyre), EAG (Eastern Alboran Gyre), MAW (Modified Atlantic Water) and AJ (Atlantic Jet). Intermediate currents: LIW (Levantine Intermediate Water). Deep currents: WMDW (Western Mediterranean Deep Water). The directions of the currents are indicated with arrows.*

The modern oceanographic setting of the Alboran Sea features three distinct water-masses with varying physiochemical parameters, including temperature, salinity, and density. The upper part of the Alboran Sea water-column is occupied by the Modified Atlantic Water (MAW) between 0 and 200 m below sea level (mbsl), which flows eastward from the Gibraltar Strait and exhibits low salinity and density (Millot, 1999, 2009; Millot and Taupier-Letage, 2005). The MAW leads to the formation of two anticyclonic gyres: the quasi-permanent Western Alboran Gyre (WAG) and the seasonal (unstable) Eastern Alboran Gyre (EAG) (Millot, 1999; Fabres et al., 2002). Upwelling systems, characterized by cold waters and high productivity, occurs at the northern edge of WAG due to the offshore pushing of MAW by north-westerlies and WAG currents, (Tintoré et al., 1988; Sarhan et al., 2000; Sánchez-Vidal et al., 2004). An intense front, known as the Malaga Front, often develops at the northern edge of the WAG, where MAW meets upwelled Mediterranean water (Sarhan et al., 2000). The intensity of the WAG varies throughout the year, with weaker intensity in winter compared to summer and early autumn, possibly due to interannual variability in SST (García-Lafuente et al., 2017). WAG surface currents transport the upwelled nutrients, and associated biologically-mediated carbon, from the Iberian margin to the center of the Western Alboran Basin, where the vertical flux associated to the WAG downwelling favors its export to the deep ocean (Fabres et al., 2002; Yebra et al., 2018). Underlying the MAW, at intermediate depths (between 200 and 600 mbsl) in the Alboran Sea there is the Levantine Intermediate Water (LIW) produced in the Levantine Basin (Eastern Mediterranean) and characterized by high salinity. The deeper water-column part, underlying the LIW (i.e., below 600 mbsl), is occupied by the Western Mediterranean Deep Water (WMDW), which is formed in the Gulf of Lions during winter (Fig. VI. 1) (Millot, 2013, 2014). The Atlantic surface water inflow into the Alboran Sea is balanced by a deep-water outflow of the LIW and the WMDW across the Strait of Gibraltar (Masqué et al., 2003). Deep circulation in Western Alboran Basin is affected especially in by this outflow-inflow balance (Mesa-Fernández et al., 2022).

The natural climatic variability within the Westernmost Mediterranean region is modulated by the changes in insolation –primarily controlled by millennial-scale orbital precession cycles– as well as by suborbital changes, such as variations in the North Atlantic Oscillation (NAO) patterns (Rodrigo-Gámiz et al., 2011; Fletcher et al., 2013; Rita et al., 2018; Toney et al., 2020; García-Alix et al., 2021). The NAO is a decadal-scale atmospheric pattern driven by fluctuations in sea-level pressure between the Icelandic low and the Azores high-pressure centers (Hurrell, 1995). This phenomenon exerts significant control over present-day climate variability in the region (Rodó et al., 1997; Trigo et al., 2002). A positive NAO phase, characterized by a major pressure difference, results in stronger north-westerlies, and dry, cold winters in southern Europe, the Mediterranean Sea, and northern Africa. Conversely, a negative NAO phase, marked by a lower pressure difference, leads to weaker northwesterly winds and precipitation increases in southern Europe, the Mediterranean and North African regions (Wanner et al., 2001; Liisa Ilvonen et al., 2022; Benito et al., 2023).

VI.3. Paleoceanographic and paleoenvironmental proxies

The study integrates various palynological and geochemical tools to comprehensively understand the oceanographic and environmental conditions throughout the studied interval, with a particular focus on reconstructing productivity responses an over the last 13,000 years in the Western Alboran Basin. These proxies provide insights into the environmental factors influencing marine productivity such as, nutrient availability, redox conditions, temperature variations, water-column structure, currents dynamics and changes in fluvial and aeolian input, while mitigating potential biases associated with each proxy.

VI.3.1. Marine palynology: Dinocysts analysis for paleoproductivity

Dinoflagellates are (predominantly) marine single-cell protists and an important component of the eukaryotic plankton community. During their life cycle, they may produce organic-walled hypnozygotic cysts, called dinocysts (Taylor, 1987). Dinoflagellate communities are very responsive to changes in nutrient availability in surface waters (Taylor et al., 2008), hence changes in dinocyst assemblages in marine sediment records have been used to reconstruct changes in primary productivity (Combourieu-Neboutet al., 1999; Pénaud et al., 2011, 2016). Given their high abundances in marine sediments, dinocysts analysis (also known as dinoflagellate analysis) has become a key tool in paleoenvironmental studies for understanding eukaryotic productivity responses to oceanographic changes (e.g., nutrient availability, SST, surface current patterns, upwelling systems and water-mass mixing) linked to past climate variability (Sluijs et al., 2006; De Vernal and Marret, 2007; Sangiorgi et al., 2021).

Sea Surface Productivity (SSP) variations can be inferred from changes in the Protoperidinioid/Gonyaulacoid cysts ratio ($P/G = nP/(nP + nG)$), where n is the number of specimens counted belonging to the peridinioid (P) or gonyaulacoid (G) (Versteegh, 1994). The P/G ratio is also mentioned as Heterotrophic/Autotrophic ratio (H/A ratio; Dale and Fjellså, 1994; Sangiorgi and Donders, 2004; van Helmond et al., 2015; Pénaud et al, 2016; Zwiep et al., 2018) and is founded on the different feeding strategies in dinoflagellates producing peridinioid and gonyaulacoid cysts. P-cysts are almost exclusively formed by heterotrophic (H) dinoflagellates that thrive on phytoplankton like diatoms and organic matter (OM) (Jacobson and Anderson, 2008) and usually dominate areas with high annual productivity associated to high nutrient availability (Sangiorgi and Donders, 2004; De Vernal and Marret, 2007; Pospelova et al., 2008; Zonneveld et al., 2013). G-cysts consist exclusively of autotrophic (A) or mixotrophic dinoflagellates (Powell et al., 1992; Sangiorgi et al., 2006). The H/A ratio will be referred in this study as SSP index (Table VI.1.).

The species used to represent the P group (heterotrophs, H) belong to the genus *Brigantedinium*, *Dubridinium*, *Echinidinium*, *Lejeunecysta*, *Selenopemphix* and *Trinovantedinium*. G group includes all other dinocysts –autotrophic and mixotrophic, A (van Helmond et al., 2015; Zwiep et al., 2018). The H/A index can vary between 0 and 1, and in general, the higher the H/A ratio, the higher the productivity. However, it is important to note that protoperidiniod dinoflagellates are more prone to degradation/oxidation in the water-column and in the sediments than the G-cysts (e.g., Versteegh and Zonneveld, 2002; Zonneveld et al., 2007). Accumulation rates of total dinocysts, and also P-cysts, and G-cysts have shown to be better representative of the water column primary productivity patterns (Zonneveld et al., 2009). These rates are expressed as the number of cysts per cm² of sediment per year (*n* cysts/cm² × yr). Dinocyst accumulation rates were obtained using the mass accumulation rate data for core GP04PC from Morcillo-Montalbá et al. (2021) and vertically plotted. Additionally, the accumulation rate of specific G-cyst and P-cysts species were individually plotted to gather further paleoceanographic and environmental information according to their present hydrogeographic distribution and environmental affinities. These species include *Brigantedinium* spp., *Spiniferites* spp., *Nematosphaeropsis labyrinthus*, *Impagidinium* spp., *Operculodinium centrocarpum*, and *Lingulodinium machaerophorum*, as it has been demonstrated that these species are abundant in Alboran Sea sediments and mark important paleoceanographic changes in Westernmost Mediterranean (Pénaud et al., 2011, 2016).

Brigantedinium spp. cysts are generally the most abundant in high productivity, high nutrient environments (Dale and Fjellså, 1994; Zonneveld et al., 2001; De Vernal and Marret, 2007; Zonneveld et al., 2013). This heightened cyst production is often a response to increased nutrient availability, which can result from various factors such as upwelling, frontal activity, or the input of river and/or meltwaters (Montresor et al., 1998; De Vernal and Hillaire-Marcel, 2000; Zonneveld and Brummer, 2000; Fujii and Matsuoka, 2006; Pospelova et al., 2010). High relative *Lingulodinium machaerophorum* cysts concentrations are observed in sediments below (seasonal) upwelling cells or affected by river plumes (Sangiorgi and Donders, 2004; Zonneveld et al., 2013), but also in seasonally stratified, nutrient-rich environments (van Helmond et al., 2015; Pénaud et al., 2016; Zwiep et al., 2018). *Nematosphaeropsis labyrinthus* is a cosmopolitan species that can be present in high relative abundances in sediments deposited in cool/eutrophic marine environments and in ocean frontal systems or other areas with contrasting water parameters. *Impagidinium* cysts are typically found in warm oligotrophic open water (Pénaud et al., 2011, 2016; Zonneveld et al., 2013). In Alboran sediments, the increases in *Operculodinium centrocarpum* cysts are considered potential signs of increased inflow of nutrients-enriched Atlantic surface water (Pénaud et al., 2016). *Spiniferites* spp. is a cosmopolitan species found in temperate to equatorial coastal regions, but indicates enhanced in nutrient availability when its abundance increases (Zonneveld et al., 2013). Although the recognition of *Spiniferites* groups was not performed in this study, Pénaud et al. (2016) provides data on the accumulation rates of these *Spiniferites* groups throughout the study interval in core MD99-2339 located in the Gulf of Cadiz, with a 300 years resolution. These *Spiniferites* groups were principally applied to elucidate changes in the SST, where the groups *bentorii*, *delicatus*, and *mirablilis* are linked to warm SST, while the groups *elongates and lazus* are linked to cool SST (Pénaud et al., 2011, 2016).

VI.3.2. Geochemical proxies for productivity

Barium (Ba) content in marine sediments has been broadly used as a proxy to reconstruct past oceanic export productivity (e.g., Francois et al., 1995; McManus et al., 1998; Gingele et al., 1999; Paytan and Griffith 2007; Carter et al., 2020). Ba increases in Westernmost Mediterranean marine sediments have been associated to increases in pelagic barite ($BaSO_4$) content, and these increases in barite content has been linked to periods with increased productivity and OM degradation in the mesopelagic zone (e.g., Jiménez-Espejo et al., 2008; Martínez-Ruiz et al., 2015). In general, export productivity reconstructions have been achieved using pelagic barite content, even in cases where postdepositional oxidation has occurred (e.g., Monedero-Contreras et al., 2023a, b), as pelagic barite crystals are less susceptible to oxidation than OM (Table VI.1.). However, in sulfate-depleted porewater, pelagic barite can dissolve and reprecipitate at the oxidation front or at the sulfate-methane transition zone, recognized as marked Ba/Al peaks above or below the organic-rich section (e.g., Henkel et al., 2012; Grema et al., 2022). However, if pelagic barite dissolution and Ba remobilization is not observed, Ba/Al can be successfully applied as a qualitative paleoproductivity proxy (e.g., Martínez-Ruiz et al., 2000; Carter et al., 2020; Light et al., 2023).

The OM content in marine sediments, normally expressed as C_{org}% or TOC% (Total Organic Carbon weight %), has also been linked to productivity (Table VI.1.). C_{org} in marine sediments represents only a fraction of the total biological productivity in surface waters since only a small OM fraction “escapes” the efficient C-cycling and oxidation in the water-column and reaches the seafloor; this fraction is known as “export productivity” (Canfield, 1994; Tribovillard et al., 2006). During sinking and deposition, OM suffers degradation, consequently C_{org}% does not directly reflects surface water productivity, but rather the interplay between surface water productivity, accumulation rate and degree of preservation, since once deposited OM is still susceptible to suffer postdepositional oxidation. Despite this, changes in C_{org}% in marine sediments tend to reflect correlative changes in surface water productivity.

Table VI.1. *Proxies and interpretation synthesis used for the paleoceanographic reconstruction.*

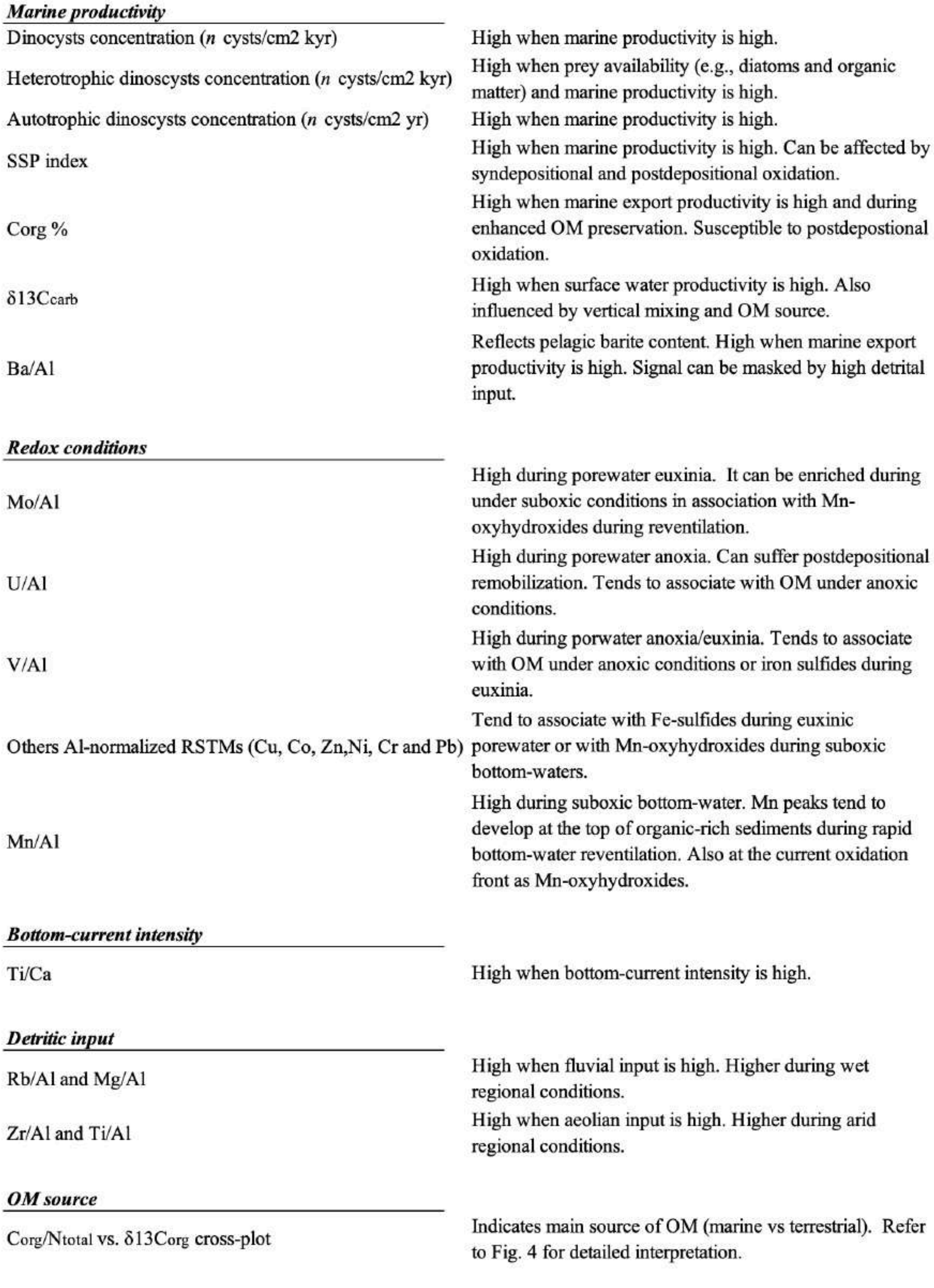

Marine productivity	
Dinocysts concentration (*n* cysts/cm2 kyr)	High when marine productivity is high.
Heterotrophic dinoscysts concentration (*n* cysts/cm2 kyr)	High when prey availability (e.g., diatoms and organic matter) and marine productivity is high.
Autotrophic dinoscysts concentration (*n* cysts/cm2 yr)	High when marine productivity is high.
SSP index	High when marine productivity is high. Can be affected by syndepositional and postdepositional oxidation.
Corg %	High when marine export productivity is high and during enhanced OM preservation. Susceptible to postdepostional oxidation.
$\delta 13C_{carb}$	High when surface water productivity is high. Also influenced by vertical mixing and OM source.
Ba/Al	Reflects pelagic barite content. High when marine export productivity is high. Signal can be masked by high detrital input.
Redox conditions	
Mo/Al	High during porewater euxinia. It can be enriched during under suboxic conditions in association with Mn-oxyhydroxides during reventilation.
U/Al	High during porewater anoxia. Can suffer postdepositional remobilization. Tends to associate with OM under anoxic conditions.
V/Al	High during porwater anoxia/euxinia. Tends to associate with OM under anoxic conditions or iron sulfides during euxinia.
Others Al-normalized RSTMs (Cu, Co, Zn,Ni, Cr and Pb)	Tend to associate with Fe-sulfides during euxinic porewater or with Mn-oxyhydroxides during suboxic bottom-waters.
Mn/Al	High during suboxic bottom-water. Mn peaks tend to develop at the top of organic-rich sediments during rapid bottom-water reventilation. Also at the current oxidation front as Mn-oxyhydroxides.
Bottom-current intensity	
Ti/Ca	High when bottom-current intensity is high.
Detritic input	
Rb/Al and Mg/Al	High when fluvial input is high. Higher during wet regional conditions.
Zr/Al and Ti/Al	High when aeolian input is high. Higher during arid regional conditions.
OM source	
C_{org}/N_{total} vs. $\delta 13C_{org}$ cross-plot	Indicates main source of OM (marine vs terrestrial). Refer to Fig. 4 for detailed interpretation.

$\delta^{13}C_{org}$ is a measure of the ratio of stable carbon isotopes (^{13}C:^{12}C) in the OM reported in parts per thousand (‰) and using a standard as reference. The main control on the $\delta^{13}C_{org}$ signature variation is the vegetation type (marine vs continental plants) from which the OM derive since marine algae are isotopically heavier than land plants (Fig. VI. 6) (Meyers, 1994 and references therein). Consequently, variations $\delta^{13}C_{org}$ help to recognize the main source of OM in export productivity in deep-marine basins. In this sense, C_{org}/N_{total} ratio is also used to identify variations in OM input and relative composition of land and marine derived components of sedimentary OM (Meyers, 1994). Algae typically have atomic C_{org}/N_{total} ratios between 4 and 10, whereas vascular land plants have C_{org}/N_{total} ratios of ≥20. However, selective degradation of OM components during early diagenesis might influence the original organic geochemical signals. But despite extensive early diagenetic losses of OM and of some of its important biomarker compounds, C_{org}/N_{total} ratio and $\delta^{13}C_{org}$ appear to undergo little change (Meyers, 1994; Tyson, 1995). Consequently, $\delta^{13}C_{org}$ vs C_{org}/N_{total} cross-plot is robust tool that allows to assess the main source of OM that reaches deep-marine basins.

On the other hand, variations in $\delta^{13}C$ in the shell of the planktonic foraminifera *Globigerina bulloides*, can indicate variations in marine productivity in the photic zone (Table VI.1.). The carbon isotopic composition of planktonic foraminifera shells (i.e., $\delta^{13}C_{carb}$) tend to reflect the carbon isotopic composition of the dissolved inorganic carbon in ambient water. *Globigerina bulloides* is a nonsymbiotic species; hence, photosynthesis would not influence the fractionation of carbon isotopes (Naidu and Niitsuma, 2004). *Globigerina bulloides* take carbon for shell growth in the $^{12}C/^{13}C$ ratio present in the upper water-column. The isotopic carbon composition in the upper water-column can vary as a function of biological processes and productivity intensity in photosynthetic zone. During kinetic fractionation, photosynthetic organisms take preferentially the lighter over the heavier isotope. Therefore, $\delta^{13}C_{carb}$ variations in *Globigerina bulloides* can be used to identify changes in marine productivity, where less negative $\delta^{13}C_{carb}$ values indicate more intense marine productivity. Additionally, it has been demonstrated that $\delta^{13}C_{carb}$ can also serve as an indicator of upwelling activity (Naidu and Niitsuma, 2004; Wang et al., 2019).

VI.3.3. Geochemical proxies for redox conditions

Under oxygen-deficient conditions in marine systems, authigenic minerals (e.g., sulfides and oxyhydroxides) enriched in trace metals precipitate, leading to an enrichment of redox-sensitive trace metals (RSTMs; e.g., Mo, U, V, Re, Cu, Co, Ni, Cr, Zn and Pb) in the sediments. In marine sediments Mo, Ni, Co, Cu, Cr, Zn and Pb can be authigenically fixed (i) in association with Mn and Fe oxyhydroxides under suboxic conditions or (ii) in association iron sulfides under euxinic conditions, while U tends to be enriched in association with OM under anoxic to euxinic conditions (Algeo and Maynard, 2004; Tribovillard et al., 2006, 2012; Monedero-Contreras et al., 2023b). Once normalized, these trace metals can serve as redox proxies to discern different redox conditions in modern and ancient marine environments (Berner, 1981; Tyson and Pearson, 1991;

Calvert and Pedersen, 1993, 2007; Crusius et al., 1996; Warning and Brumsack, 2000; Algeo and Maynard, 2004; Tribovillard et al., 2006; Little et al., 2015; Paul et al., 2023). Consequently, Aluminum-normalized metals (e.g., Fe/Al, Mn/Al, U/Al, V/Al, Mo/Al, Ni/Al, Cu/Al, Cr/Al, Co/Al, Zn/Al and Pb/Al) have been employed to identify paleoredox changes in the Westernmost Mediterranean deep-waters over the last 13,000 years and recognize potential geochemical processes during early diagenesis (e.g., postdepositional oxidation) (Table VI.1.).

VI.3.4. Geochemical detrital proxies

Aluminum-normalized detrital elements have been widely used to illustrate terrigenous fluctuations in the Mediterranean region (Martínez-Ruiz et al., 2000; Calvert and Pedersen, 2007; Frigola et al., 2007, 2008; Jiménez-Espejo et al., 2007, 2008; Rodrigo-Gámiz et al., 2011, 2018). Zr/Al and Ti/Al were used to assess variations in aeolian input, as enrichments in Zr and Ti in Mediterranean sediments are primarily associated with increased content of zircon and rutile minerals, respectively, predominantly supplied by Sahara dust during arid periods (Jiménez-Espejo et al., 2014). On the other hand, Rb/Al and Mg/Al are used to assess fluvial input variability. These elemental ratios were successfully employed to track fluvial input variability over the last 20 ka in Eastern Alboran Basin by Rodrigo-Gámiz et al. (2011), as Rb and Mg tend to be enriched in association with clay minerals that are delivered to the Western Mediterranean by rivers. Additionally, Ti/Ca has been used as proxy to assess Alboran Sea bottom-water dynamics throughout the Holocene (Mesa-Fernández et al., 2022) (Table VI.1.).

VI.4. Material and methods

VI.4.1. Core description, chronology and sampling

The studied marine sediment record is a piston core, GP04PC, 872.25 cm in length, recovered from the West Alboran Sea Basin at a water-depth of 1306.5 m mbsl during the oceanographic cruise Gasalb onboard the R/V Pelagia in November 2011 (Fig. VI. 1). The core site (35.7871° N, 4.5343° W) is located below the quasi-permanent anticyclonic gyre WAG. Core sediment lithology is very homogeneous and dominated by dark-greenish hemipelagic mud-clays with some foraminifera and shell fragments, with intervals with increased OM content (Morcillo-Montalbá et al., 2021).

GP04PC age model based in ^{14}C dates was obtained by Morcillo-Montalbá et al. (2021). They sampled 10 sediment horizons, extracting 10 mg of planktonic foraminifer *Globigerina bulloides* (size fraction >125 μm). The GP04PC chronology was generated using the R-code package rbacon 3.6.2 software (Blaauw and Christen, 2011) and the Marine20 calibration curve (Heaton et al., 2020). According to the GP04PC age model, the 872.25 cm long core covers the last 35,000 years (Fig. VI. 2). For detailed age model information, refer to Morcillo-Montalbá et al. (2021). This study focuses on the Younger Dryas (YD) and the Holocene in particular (past ~ 13 ka), which is represented by the top ~250 cm of the GP04PC core, with a mean sedimentation rate of 20cm/kyr (Fig. VI. 2). The studied interval was sample at 1.5 cm intervals for geochemical analysis (XRF and ICP-MS), with a total of 85 samples and a temporal resolution of ~145 years. Out of the 85 samples, 43 samples were selected for palynological and organic geochemical analyses, providing a resolution of ~ 250-300 years for dinocysts analysis for the last 13 ka.

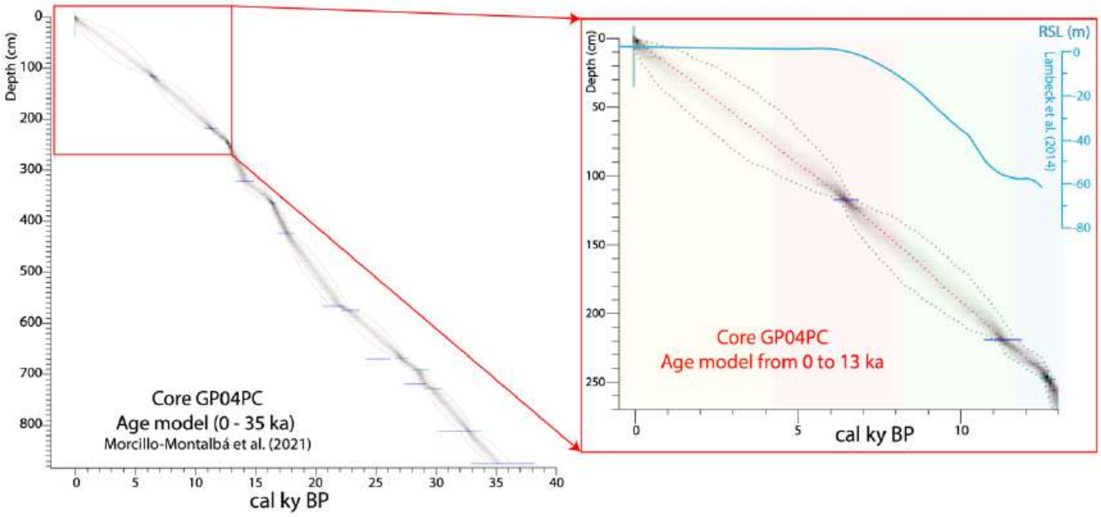

***Figure VI.2**. GP04PC age model from Morcillo-Montalbá et al. (2021). The studied time interval has been magnified and Relative Sea Level (RSL) from Lambert et al. (2014) is plotted for context.*

VI.4.2. Dinoflagellate cysts

Sediment samples for dincocysts analysis were prepared at the Utrecht University GeoLab using a standard palynological preparation technique. Each sample, consisting of ~ 2-4 g of dry-weight sediment, was oven-dried at 60°C and exactly weighted. One *Lycopodium clavatum* tablet (19,855, ± 829 spores) was added to each sample to ensure quantitative control (Wood et al., 1996; Mertens et al., 2012). Carbonates were removed by gradually adding hydrochloric acid (HCl, 30%), samples settled overnight, and were then rinsed with demineralized water to obtain a neutral pH. To remove silicates, the samples were processed with cold hydrofluoric acid (HF, 38%) and placed 2 hours on a shaker. Samples were decanted and any precipitated fluorosilicates were removed with HCl 30%. The remaining residues were sieved over a 10 µm nylon mesh screen. The sieved residues were diluted with deionized water in 1.5 ml safe-tubes and carefully poured over a cover slip using a Pasteur-pipette. Subsequently, a microscopic slide was mounted over the cover slip using transparent glue. A systematic count of a minimum of 280 dinoflagellate cysts (dinocysts) was conducted on each slide using an Olympus BX41 microscope at 40X magnification. Dinocyst taxonomy followed Williams et al. (2017) and dinocyst identification to was performed following Zonneveld and Pospelova (2015).

VI.4.3. Major and trace elements analyses

Major elements in discrete bulk sediment samples were analyzed in fused beads by using XRF. Analyses were carried out at Instituto Andaluz de Ciencias de la Tierra (IACT, CSIC-UGR, Spain), with a S4 Pioneer from BRUKER, equipped with a 4 kW wavelength dispersive X-ray fluorescence spectrometer (WDXRF) and a Rh anode X-ray tube (60 kV, 150 mA). XRF precision was better than ±0.3% for major elements. Trace elements in discrete sediment samples were measured at the Scientific Instrumentation Center (CIC, University of Granada, Spain) with an ICP-MS NexION 300d (Perkin Elmer) spectrometer using Rh as internal standard. For trace elements, ICP-MS precision was better than ±5% for analyte concentrations of 10 ppm (Bea, 1996). To assess the variability of trace metals (TMs), their concentrations have been normalized to aluminum (TM/Al). This normalization approach is favored because aluminum is considered conservative and accounts for the influence of detrital input variability, which can significantly affect TM concentrations (Tribovillard et al., 2006; Algeo and Li, 2020; Algeo and Liu, 2020; Paul et al., 2023).

For ICP-MS analyses, samples were oven-dried at 60°C and then powdered in an agata mortar. Samples were processed in batches of 25 to 30 samples and an analytical blank was added to each batch. Solutions for ICP-MS analyses were prepared using 0.1g of powdered sample in Teflon vessels, where successive acidifications using HNO_3 (ultra-pure with a 69% concentration) and HF (48% concentration), were performed at 130°C until evaporation. A final acid digestion with HNO_3 and water at 80°C for 1h was performed to achieve a total acid dissolution/digestion of the samples. Subsequently, dissolved samples were diluted with Milli-Q water in volumetric flasks of 100ml (Bea, 1996).

VI.4.4. Organic carbon analyses

The total organic carbon content (C_{org}%), total nitrogen content (N_{total}%) and stable carbon isotopic composition of the OM ($\delta^{13}C_{org}$) were obtained in GP04PC core samples at GeoLab of Utrecht University (The Netherland). Dried samples were powdered with an agata mortar and 1g of sample was weighted in a 50ml Greiner centrifuge tube. To remove carbonates, dried sediments were acidified with 25 ml of 1M HCl, followed by 4h of shaking, centrifugation and decanting. This procedure was repeated with 12h of shaking. Then, samples were washed twice with demineralized water to remove acids, and oven-dried for 72h at 60°C. The decalcified and dried sediments were weighted (about 15 to 20mg) in silver foils cup.

The C_{org}% and N_{total}% were obtained using an Elemental Analyzer (EA) IsoLink CN IRMS System from Thermo Scientific. This system includes the Flash IRMS Elemental Analyzer, a Delta V Advantage IRMS, and a ConFlo IV Universal Interface that allowed carbon isotope measurements of the sedimentary OM (i.e., $\delta^{13}C_{org}$). The C_{org}% and N_{total}% are expressed as weight percentage (wt %) of the dried sediment. Based on the standard deviation of replicate runs of laboratory standards (atropine, acetanilide and IVA), analyzed before and after the series, and after each 12 measurements, the analytical error (standard deviation) was on average <0.2 wt. % for C_{org}% and N_{total}%. The $\delta^{13}C_{org}$ values are reported relative to the Vienna Pee Dee Belemnite (V-PDB) standard and corrected for blank contribution. NBS-19 was used as the standard and the analytical reproducibility of $\delta^{13}C_{org}$ was usually better than 0.1 ‰.

$\delta^{13}C$ was also measured in the carbonate present in the shell of planktonic foraminifera ($\delta^{13}C_{carb}$) and calculated using the same equation. $\delta^{13}C_{carb}$ analysis was performed using ca. 10 specimens of *Globigerina bulloides* (size fraction >125 μm) picked from intervals of the 3 cm sediment samples. The carbon isotopic composition of foraminiferal samples was analyzed with an automated Finnigan-MAT Kiel Device Type I, coupled to a Finnigan-MAT 251 mass spectrometer at the Leibniz Laboratory for Radiometric Dating and Stable Isotope Research from the Christian Albrechts University of Kiel (Germany). Results were also calibrated to the V-PDB by means of the NBS-19 carbonate isotope standard and by calibrated lab standards. The analytical reproducibility of the instrument was ±0.07 ‰ for $\delta^{18}O$ and ±0.04 ‰ for $\delta^{13}C$ (Morcillo-Motalbá et al., 2021). Both $\delta^{13}C$ values (i.e., $\delta^{13}C_{org}$ and $\delta^{13}C_{carb}$) were obtained using the following equation: $\delta^{13}C_{org} = (([^{12}C]/[^{13}C])_{sample}/(([^{12}C]/[^{13}C])_{standard})-1)x1,000$ ‰.

VI.5. Results

VI.5.1. Dinocysts analysis

The GP04PC record contains abundant and well-preserved dinocysts. Their accumulation rates range from ~ 1,500 to over 30,000 cysts per kyr (Fig. VI. 3). Interestingly, some dinocysts have diagenetic pyrite crystals infilling their cavities, especially in samples corresponding to the YD and ORL-1a interval. Among the Protoperidinioid heterotrophic cysts (P-cysts), *Brigantedinium* spp. and *Selenopemphix quanta* are the most abundant. *Brigantedinium* cysts are the most abundant cysts of all, representing occasionally more that 75% of the total counted cysts. Among the G-cysts, *Spiniferites* spp. is the most abundant. However, *Impagidinium* spp., *Operculodinium* *centrocarpum* and *Lingulodinium machaerophorum* are present throughout the entire GP04PC core. During the YD there is a higher accumulation rate of P-cysts (around 18,000 cysts per kyr) and G-cysts (around 15,000 cysts per kyr), but it decreases rapidly during the onset of the Holocene (~ 11.7 ka). From ~ 12.2 to 11.7 ka *Operculodinium centrocarpum*, *Spiniferites* spp. and *Lingulodinium machaerophorum* cysts exhibit their highest accumulation rates. Moreover, *Nematosphaeropsis* spp. cysts are very high only during this period (over 4,000 cysts per kyr).

From ~ 10 to 8.5 ka (i.e., during Holocene humidity optimum, there is an increase in cysts accumulation rate (around 5,000 cysts per kyr), in both P-cysts (e.g., mainly *Brigantedinium* cysts; around 4,500 cysts per kyr) and G-cysts (e.g., mainly *Spiniferites* spp. and *Impagidinium* spp. cysts; around 1,000 and 250 cysts per kyr; respectively) (Fig. VI. 7). Right after this increase, total cysts flux decreased, reaching close to 1,500 cysts per kyr around 7.6 ka. From ~ 7.6 ka to the present, cysts accumulation rate is low. However, around 4.5 ka and throughput the late Holocene, an increase in *Lingulodinium machaerophorum* and *Spiniferites* spp. cysts accumulation rates occurs. Consult Supplementary material for detailed results.

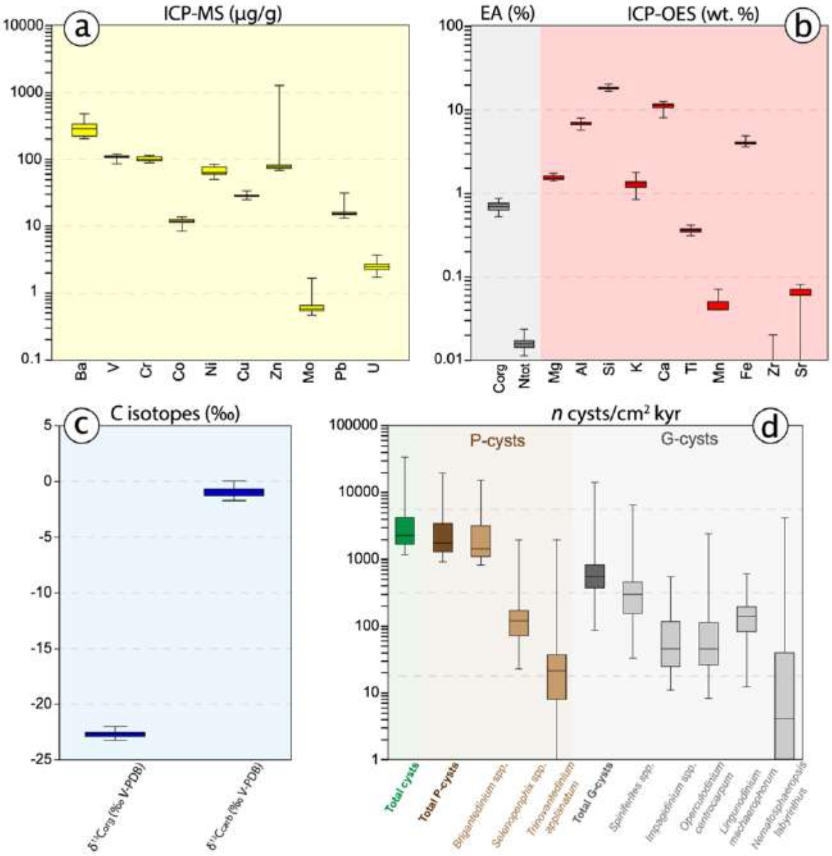

Figure VI.3. *Geochemical and dinocysts results shown as box-whisker. The box represents the inter-quartile range, the line in the box represents the median and the whiskers represent the 5th and 95th percentiles. (a) Trace metal concentrations expressed in µg/g log10 scale. (b) Major concentrations,* C_{org} *and* N_{tot} *expressed in wt.% log10 scale. (c)* $\delta^{13}C_{org}$ *and* $\delta^{13}C_{carb}$ *values expressed as ‰. (d) Dinocysts concentration expressed as number of cysts per gram of dried sediment (n-cysts/g).*

VI.5.2. Geochemical data

- *Aluminum-normalized trace metal contents*

The enrichment patterns of various trace metals in the studied record exhibit distinct trends over time. From 13 to 12.3 ka trace metals show relatively low concentrations. Notably, around 12.3 ka, Ba, Mo, Fe, U, Cu, and Zn concentrations exhibit a marked increase, which dropped abruptly ~ 11.7 ka (Fig. VI. 4). From ~11.7 to 6.8 ka, trace metals such as Ba, U, V, Cu, Co, Cr, Zn, and Pb maintained a moderate enrichment (Fig. VI. 4). During this period, Mo and Fe display only minor increases in concentration, occurring between ~ 10 and 8.5 ka. The enrichment of Mo and Fe from ~ 10 to 8.5 ka is accompanied by an increase in C_{org} content. After 6.8 ka, the concentrations of trace metals decrease. However, Cu and V exhibit significant variability from ~ 5 to 2 ka, while U maintained a low enrichment from ~ 4.5 to 1 ka. Within the uppermost interval of core GP04PC, Mn, Fe, Mo, Cu, Zn, and Pb exhibit a peak. It is noteworthy that this is the only interval where Mn exhibited a marked enrichment (Fig. VI. 4). The Ba record does not show evident peaks that might be liked associated to diagenetic remobilization.

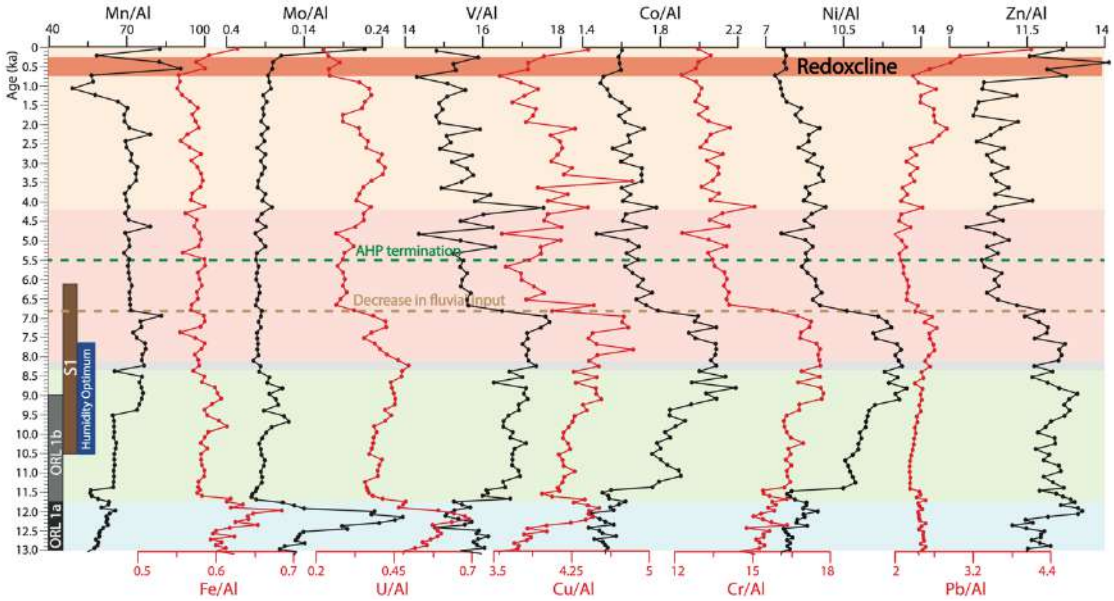

Figure VI.4. *Vertical-plots (also known as chemostratigraphic profiles) of Al-normalized RSTMs concentrations ([RSTMs]/[Al]) over the last 13 ka in core GP04PC. S1 interval from Grant et al. (2016). Values expressed as 10^{-4}.*

- *Aluminum-normalized detrital elements*

Regarding the detrital proxies, Ti/Al values are high throughout the entire YD period, while Rb/Al values are low. Zr/Al shows an increase from ~ 12.4 to 11.7 ka, which accompanied by an increase in Mg/Al values. From ~ 11.7 to 6.8 ka, Ti/Al values gradually decrease, while Rb/Al values gradually increase. Zr/Al shows a marked decrease ~ 11.7 ka that is maintained until ~ 0.5 ka, when it starts to increase accompanied by an increase in Ti/Al values. Around 6.8 ka, Mg/Al and Rb/Al values show a marked decrease, while Ti/Al values show a marked increase, that is maintain until present. Moreover, from ~ 6.8 to present, Rb/Al and Ti/Al present strong fluctuations. From ~ 3.5 to 1.5 ka, Mg/Al values show a minor increase, but from ~ 1.5 ka to present continue to decrease until the present.

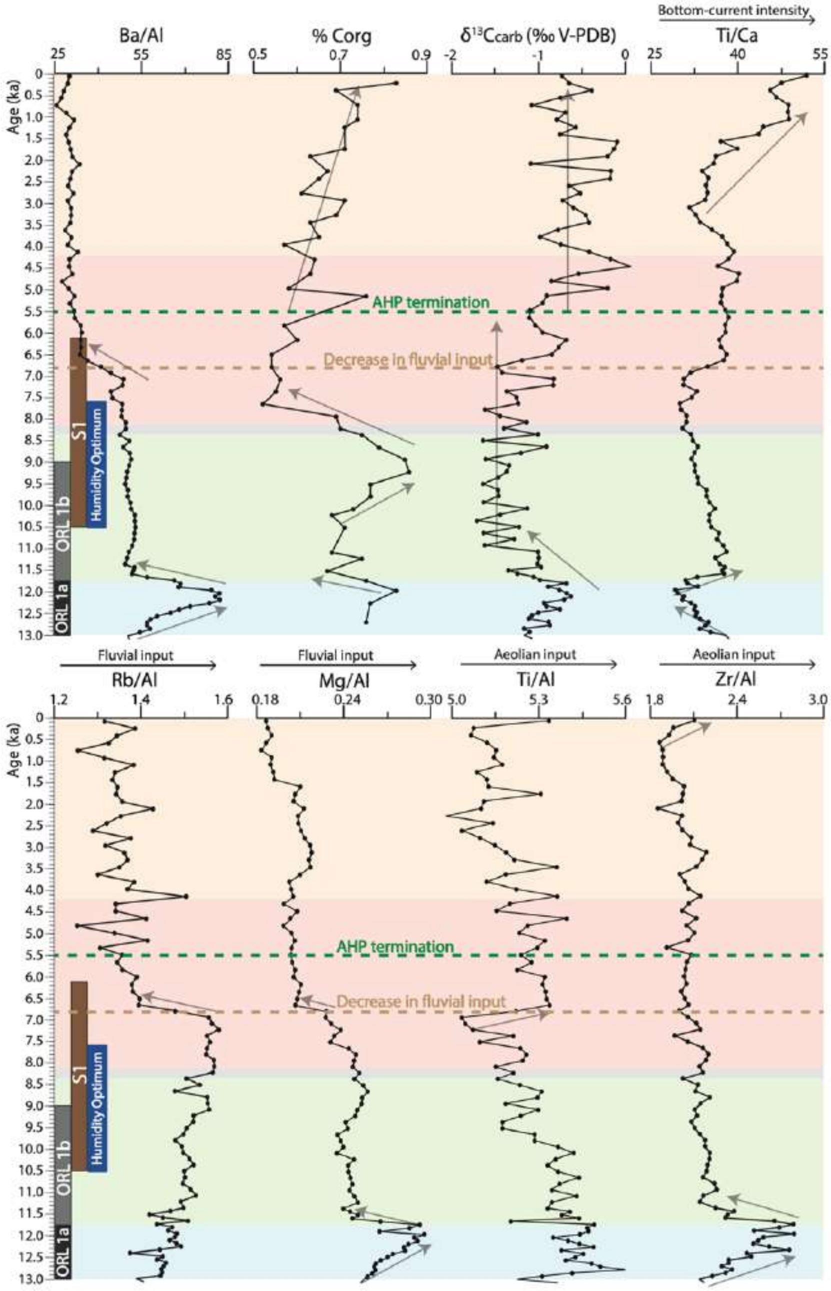

Figure VI.5. *Vertical-plots of different geochemical proxies for productivity (Ba/Al, %*C_{org} *and* $\delta^{13}C_{carb}$*), (ii) bottom currents intensity (Ti/Ca), (iii) fluvial input (Mg/Al and Rb/Al), and (iv) aeolian input (Zr/Al and Ti/Al) over the last 13 ka in core GP04PC. Arrows indicate the main trends. Ba/Al values expressed as* 10^{-4}*. Ti/Ca, Rb/Al, Mg/Al, Ti/Al and Zr/Al values expressed as* 10^{-3}*.*

Throughout the YD, Ti/Ca values decrease, reaching the lowest values at the end of the YD (~ 11.7 ka). During early Holocene onset Ti/Ca values raidly increase. Subsequently, during the early Holocene and part of the Middle Holocene (i.e., from ~ 11.7 to 7 ka), the Ti/Ca values exhibit a gradual decrease, with the lowest values within the Holocene. Following this period, from ~ 7 to 4.2 ka, Ti/Ca values increase (Fig. VI. 5). Around 4.2 ka, Ti/Ca decreases until ~ 3 ka, when it starts to progressively increase to the present, where it reaches its highest values (i.e., peak values).

- *Organic carbon content and organic matter source*

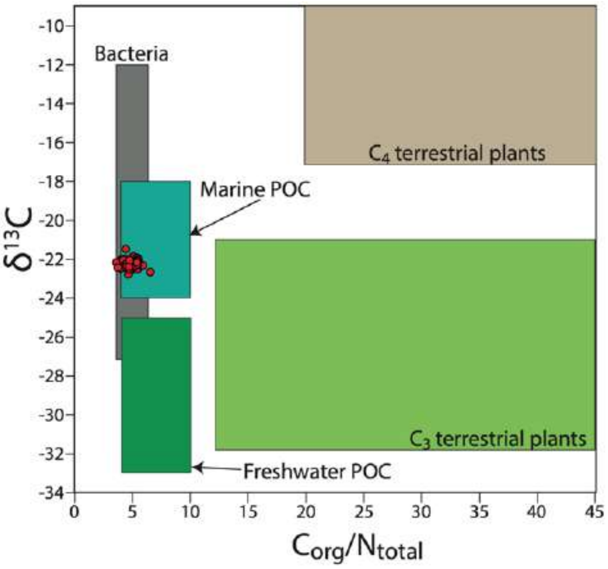

***Figure VI.6**. Modified cross-plot from Meyer (1994) showing distinctive source combinations of atomic C/N ratios and organic $\delta^{13}C_{org}$ values of marine algae, lacustrine algae, C3 land plants and Ca land plants. GP04PC data is shown as red circles. POC: particulate organic carbon.*

Throughout the last 13,000 years, sediment composition shows varying OM content. During the YD, OM content is relatively high (C_{org} > 0.8 % around 12 ka), but dropped to ~ 0.6 % during from ~ 11.7 to 8.5 ka. From ~ 10.0 to 8.5 ka sediments are notably enriched in OM, where C_{org} content reaches it maximum value (0.86 %). From ~ 8.5 to 7.5 ka C_{org} content progressively decreases. At 7.5 ka, marine sediments exhibit the lowest C_{org} content (~ 0.5%). Subsequently, from 6.8 ka to the present, C_{org} content progressively increases, reaching a value over 0.8% at the top of the core (Fig. VI. 5). Regarding the C_{org}/N_{total} ratio, most samples show values around 5, while $\delta^{13}C_{org}$, in most samples, exhibit values around -22‰ (Fig. VI. 3). Therefore, it is crucial to note that the OM, in all GP04PC samples, primarily originates from a marine source, as indicated by C/N and $\delta^{13}C_{org}$. Consequently, the OM in deep sediments of the Western Alboran Basin is predominantly a mixture of bacteria and marine particulate organic carbon (POC), with negligible terrestrial OM (Meyer, 1994; Fig. VI. 6).

- *$\delta^{13}C_{carb}$ values*

$\delta^{13}C_{carb}$ values vary from -2 to 0‰ and its vertical (i.e., temporal) trend can be divided in three phases. In the first phase, spanning from 13 to 11.7 (i.e., YD period), most values range from -0.5

to 0‰. In the second phase, from 11.7 to 6.8 ka, $\delta^{13}C_{carb}$ exhibits more negative values and relatively low variability, with most values ranging between -2 and -1.5‰. The third phase, from 6.8 ka to present, is characterized by a progressive increase $\delta^{13}C_{carb}$ values, from ~ -1.5 to 0.5 ‰. However, during the late Holocene (from ~ 4.2 ka to present) $\delta^{13}C_{carb}$ values exhibit abrupt variability (Fig. VI. 5).

VI.6. Discussion

Marine sediment records have provided relevant information to better constraint and model the climatic and oceanographic factors controlling the long-term (from several decades to centuries) marine productivity responses in the Mediterranean. With this aim, we have conducted a multiproxy paleoceanographic reconstruction, with an emphasis on reconstructing changes in nutrient availability and marine productivity, throughout the YD (13 – 11.7 ka) and different Holocene intervals: early Holocene (11.7 – 8.2 ka), middle Holocene (8.2 – 4.2 ka), and late Holocene (4.2 ka – present), as defined by Walker et al. (2012). Moreover, insights from terrestrial Holocene records from the southern Iberian Peninsula, as interpreted by prior studies, were also integrated with our data for regional scale interpretations and potential land-sea influences on productivity.

Our multiproxy analysis identified three distinct oceanographic scenarios of increased marine productivity and nutrient availability over the past 13,000 years: (i) during the YD humid/warmer phase (~ 12.2 – 11.7 ka) with exceptionally high productivity conditions, (ii) during the Holocene humidity optimum (~ 10.5 – 8.5 ka) with high productivity conditions, and (iii) throughout the late Holocene (~ 4.2 ka – present) with moderate productivity conditions. Each scenario of enhanced marine productivity is demonstrated to be governed by the interplay of distinct regional and local oceanographic and climatic conditions during its occurrence (Fig. VI. 9), as explained subsequently.

VI.6.1. Younger Dryas humid phase (~ 12.2 – 11.7 ka)

In the Westernmost Mediterranean, the YD can be divided into two phases with contrasting climatic conditions: a dry/cold phase (~ 13 to 12.2 ka) and a humid/warmer phase (~ 12.2 to 11.7 ka) (Combourieu-Neboutet al., 1999, 2009; Dormoy et al., 2009; Rodrigo-Gámiz et al., 2011, 2014b; Trias-Navarro et al., 2023). From ~ 13 to 12.2 ka, the Alboran Sea was characterized by cold SST (below ~ 15 °C; Cacho et al., 2002; Rodrigo-Gámiz et al., 2014a; Morcillo-Montalbá et al., 2021) and sea-level around 40 m below the present (Fig. VI. 2; Lambeck et al., 2014). During the YD onset (~ 13 ka), *Artemisia* pollen percentages surged by over 20% in the Alboran Sea sediments, indicating aridification in the Westernmost Mediterranean (Dormoy et al., 2009). Despite aridification, cold conditions promoted the re-advance of the glaciers that had persisted during the Bølling-Allerød, and even the appearance of new glaciers in the Alps and Pyrenees mountains (García-Ruiz et al., 2016 and references therein). During this YD cold/arid phase in Westernmost Mediterranean, marine productivity is moderate, according to the pelagic barite and OM content (Fig. VI. 5).

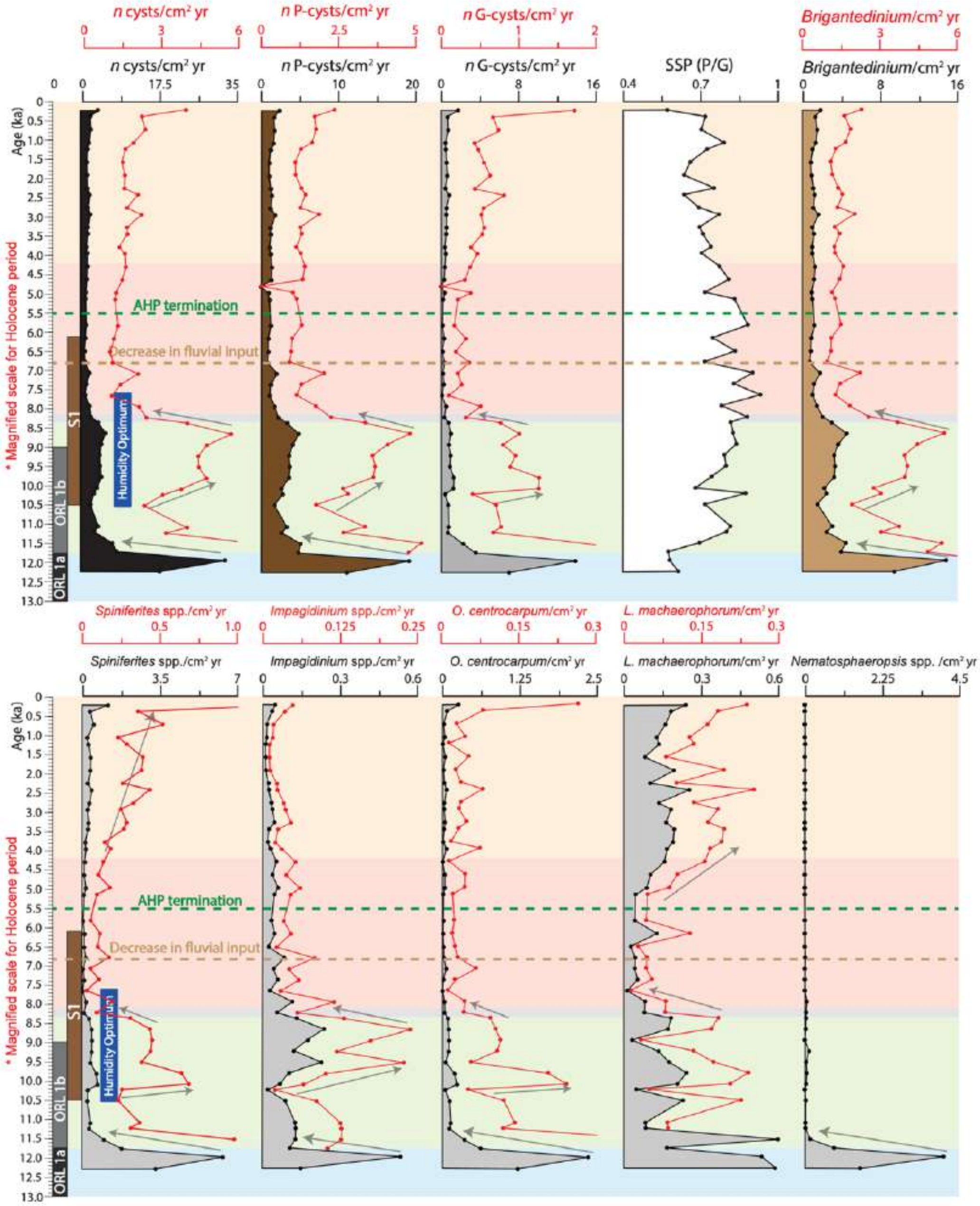

Figure VI.7. *Vertical-plots of cysts accumulation rates (expressed as n cysts/cm^2 yr) over the last 12.5 ka (yr = year). This includes the accumulation rates of total cysts, P-cysts, G-cysts and specific cysts species. Moreover, the P/G index is also plotted. Arrows indicate the main trends. Vertical plots with magnified scales are illustrated in red to highlight the changes throughout the Holocene period that are masked by the high dinocysts accumulation rates during the YD humid phase.*

However, during the YD humid phase (also known in Westernmost Mediterranean as interval YD-b; Ausín et al., 2015b), SST in the Alboran Sea experienced a marked increase in temperature of ~ 5 °C (from ~ 13 °C to ~ 18 °C) (Cacho et al., 2002; Rodrigo-Gámiz et al., 2014a; Morcillo-Montalbá et al., 2021). Our data suggest that this shift is accompanied by a drastic increase in export productivity, marked by the abrupt increase in pelagic barite and OM content (Fig. VI. 5). The high abundance of *Brigantedinium* cysts, and *Nematosphaeropsis* spp. cysts further supports seasonal eutrophic surface waters during YD humid phase. This aligns with Pénaud et al. (2016) observations of high accumulation rates of *Nematosphaeropsis labyrinthus* cysts, *Spiniferites elongatus* cysts and *Spiniferites lazus* cysts in the Gulf of Cadiz related with cool/eutrophic conditions. Furthermore, the high abundance of *Lingulodinium machaerophorum* cysts suggest seasonally stratified waters and enhanced fluvial run-off (and possibly lower surface water salinity) in Western Alboran Basin during YD humid phase. Interestingly, core GeoB18131-1, located at an intermediate water-depth (457 mbsl) in the North African margin (Fig. VI. 1), did not register enhanced planktonic foraminifera productivity during YD humid phase (Fig. VI. 8; Wang et al., 2019). Core CEUTA10PC08 (914 mbsl), located closer to the Iberian margin (Fig. VI. 1) did not register coccolithophores productivity during the period (Fig. VI. 8; Ausín et al., 2015a). This suggests strong spatial productivity variability within the Western Alboran Basin during YD humid phase and that primary productivity was dominated by dinoflagellates productivity.

In Western Alboran sediments the shift towards more humid conditions in Westernmost Mediterranean start to be registered around 12.4 ka, according to the increase in fluvial input marked by the increase Mg/Al ratios (Fig. VI. 5). Jiménez-Espejo et al. (2008) and Rodrigo-Gámiz et al. (2011) also detected fluvial input increases in Eastern Alboran Basin and Algero-Balearic Basin during this period, both basins influenced by the same regional climatic regime as the Western Alboran Basin. Furthermore, during YD humid phase, the Iberian Peninsula witnessed frequent extreme flood events, and Iberian Mountain glaciers underwent intense melting (García-Ruiz et al., 2016; Benito et al., 2023; Hernández et al., 2023). Additionally, during YD humid phase, enhanced influx of low-salinity nutrient-enriched AW through the Strait of Gibraltar into the Alboran Basin, coupled with increased freshwater input into the Gulf of Lyon derived from the rapid melting of Alpine, Pyrenees and west-central Europe glaciers inherited from the YD cold phase, weakened WMDW formation and vertical mixing, and subsequently, promoted deep-water stagnation in Westernmost Mediterranean deep basins (Bárcena et al., 2001; Jiménez-Espejo et al., 2008; Ausín et al., 2015b). Weakened bottom-current intensity in Western Alboran Basin deep-water during YD humid phase is revealed by the lower Ti/Ca values and goes in accordance with previous results from Mesa-Fernández et al. (2022); see Fig. VI. 8.

Therefore, the increase in local river run-off during the YD humid phase –originating from intense continental glaciers melting and increased regional precipitation– coupled with enhanced inflow of nutrient-enriched Atlantic water, would have supplied sufficient nutrients (e.g., N, P and Si) to sustain remarkably high productivity in the photic zone, as supported by previous studies (Bárcena et al., 2001; Jiménez-Espejo et al., 2008; Ausín et al., 2015b). This also caused Alboran Sea to experience a reduction in surface water salinity, resulting in increased surface water buoyancy and stratified water-column. Therefore, nutrient input from deeper water layers brought to surface waters by upwelling systems or vertical mixing can be discarded as a process responsible for the high marine productivity. The elevated Zr/Al values also support substantial aeolian input in the Western Alboran Basin during the YD humid phase. However, the high fluvial input signal during this period could be masking the Zr aeolian signal. Additionally, mountain glaciers (e.g., Sierra Nevada glaciers) in the surrounding drainage may have trapped significant volumes of aeolian dust (enriched in Zr) during the previous YD arid phase, which upon rapid melting during YD humid phase, the trapped aeolian dust could have been flushed into the Alboran Sea by local rivers (e.g., Gualdalfeo and Adra rivers), enriching Alboran marine sediments in Zr. In any case, aeolian input should not be dismissed as a potential additional nutrient source, as seasonality was a key climatic feature during the YD humid phase (Dormoy et al., 2009).

During YD humid phase, RSTMs trends indicate strong oxygen-depletion in Alboran deep-waters, enhancing OM preservation and supporting water-column stratification and sluggish deep-water circulation Western Alboran Basin during this period (Figs. VI.4 and VI.8) (Bárcena et al., 2001). Porewater anoxia/euxinia, produced by deep-water stagnation, promoted the authigenic precipitation of iron-sulfides in association with Mo, Cu and Zn within the sediments, and the authigenic enrichment of U in association with OM (Fig. VI. 4). As deep-water were oxygen-depleted during YD humid phase, RSTMs were likely transported from the Alboran Sea water-column to the sea-floor through Mn-particulate shuttling (i.e., Mn-redox cycling) and organic aggregates (Tribovillard et al., 2006, 2012, 2021). The coexistence of pelagic barite with iron sulfides in the sediments representing YD humid phase (~ 12.2 to 11.7 ka) suggest that sulfate depletion in the sediments was limited, as barite crystal did not dissolve under porewater euxinia (Passier et al., 1997; Sangiorgi et al., 2006; Monedero-Contreras et al., 2023a).

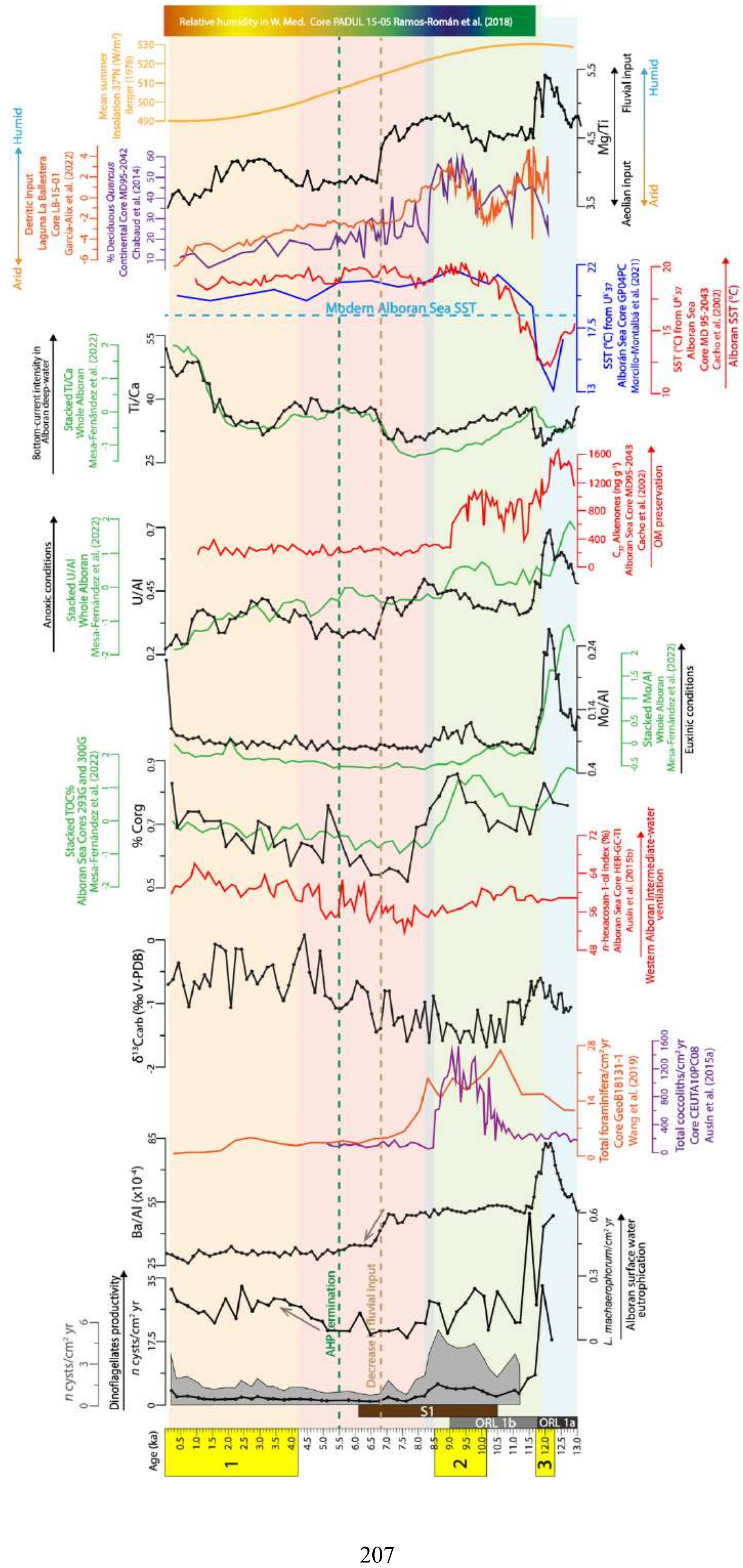
Relative humidity in W. Med. Core PADUL 15-05 Ramos-Román et al. (2018)
Mean summer Insolation 37°N (W/m²) Berger (1978)
Detritic input Laguna La Ballestera Core LB-15-01 García-Alix et al. (2022)
% Deciduous Quercus Continental Core MD95-2042 Chabaud et al. (2014)
Arid
Humid
Mg/Ti
Aeolian input
Fluvial input
SST (°C) from U$^{k'}_{37}$ Alborán Sea Core GP04PC Morcillo-Montalbá et al. (2021)
SST (°C) from U$^{k'}_{37}$ Alboran Sea Core MD 95-2043 Cacho et al. (2002)
Alboran SST (°C)
Modern Alboran Sea SST
Bottom-current intensity in Alboran deep-water
Stacked Ti/Ca Whole Alboran Mesa-Fernández et al. (2022)
Ti/Ca
C$_{37}$ Alkenones (ng g^{-1}) Alboran Sea Core MD95-2043 Cacho et al. (2002)
OM preservation
Anoxic conditions
Stacked U/Al Whole Alboran Mesa-Fernández et al. (2022)
U/Al
Mo/Al
Stacked Mo/Al Whole Alboran Mesa-Fernández et al. (2022)
Euxinic conditions
Stacked TOC% Alboran Sea Cores 293G and 300G Mesa-Fernández et al. (2022)
% Corg
n-hexacosan-1-ol index (%) Alboran Sea Core HER-GC-T1 Ausín et al. (2015b)
Western Alboran intermediate-water ventilation
δ^{13}C$_{carb}$ (‰ V-PDB)
Total foraminifera/cm²yr Core GeoB18131-1 Wang et al. (2019)
Total coccoliths/cm²yr Core CEUTA10PC08 Ausín et al. (2015a)
Ba/Al (x10^{-4})
Dinoflagellates productivity
n cysts/cm² yr
L. machaeropherum/cm² yr
Alboran surface water eutrophication
AHP termination
Decrease fluvial input
S1
ORL 1b
ORL 1a
Age (ka)
1
2
3

Figure VI.8. *Comparison with vertical-plots of diverse environmental and oceanographic proxies obtained by previous studies. These studies include marine and continental Holocene records from the Westernmost Mediterranean region covering the last 13 ka. Black vertical plots are proxies from this study. In solid gray we present dinocysts accumulation rats (n cysts/cm2 yr) with a magnified scale to highlight Holocene variability. Additionally, we propose the ratio Mg/Ti to summarize changes in fluvial input vs aeolian input, thereby reflecting changes in the regional climatic conditions. Colored vertical plots are proxies from other studies. Yellow rectangles indicate the different productivity scenarios illustrated in Fig. VI. 8. (1) late Holocene (last 4.2 kyr); (2) Holocene humidity optimum (from ~ 10.5 to 8.5 ka); (3) YD humid phase (from ~ 12.3 to 11.7 ka). See figure for refences and respective cores. Refer to Fig. VI. 1. for location of cores.*

The SSP dinocyst index does not support exceptionally high productivity during YD humid phase, contrary to what the geochemical productivity proxies and dinocyst abundance and assemblages indicate. This may be attributed to variations in the preservation of autotrophic and heterotrophic cysts under oxygenated conditions, as heterotrophic cysts are more prone to oxidation (Zonneveld et al., 2001; Reichart and Brinkhuis, 2003; Mertens et al., 2009). It has been demonstrated that *Brigantedinium* spp. and *Selenopemphix* spp. cysts are extremely sensitive to degradation under suboxic/oxic conditions, while *Nematosphaeropsis* spp. is very resistant (Zonneveld et al., 2001; Mertens et al., 2009 and references therein). However, the existence of oxygen-depleted conditions in Western Alboran Basin deep-water during the YD humid phase should not have had a substantial impact on the preservation of heterotrophic cysts (i.e., P-cysts), as OM preservation was enhanced during this period according to C_{37} alkenone trend (Fig. VI. 8) (Cacho et al., 2002). When potential biases attributed to preservation differences exist, total dinocysts and P-cysts accumulation rates, which support remarkably high productivity from ~ 12.2 to 11.7 ka (Fig. VI. 8), can be considered as more reliable proxies than SSP index to assess productivity changes (Reichart and Brinkhuis, 2003; Sangiorgi et al., 2006).

During the YD – early Holocene transition (from ~ 11.8 to 11.5 ka), dinoflagellates productivity decreased abruptly (affecting both autotrophs and heterotrophs dinoflagellates). This coincides with more negative $\delta^{13}C_{carb}$ values and an abrupt decrease in pelagic barite content (Fig. VI. 5). Between ~ 11.5 and 10.5 ka, Western Mediterranean experienced a shift towards more arid/cold conditions (Cacho et al., 2001; Fletcher et al., 2010; Rodrigo-Gámiz et al., 2011), which is corroborated by the decrease in fluvial input marked by the decrease in Mg/Al values. Weakened local river discharges due to more arid regional conditions reduced nutrient availability Western Alboran surface water, promoted the end of an exceptionally high productivity phase. Additionally, regional arid enhanced WMDW formation and Alboran deep-water ventilation, as evidenced by the abrupt decrease in RSTMs concentrations and increase in Ti/Ca values.

VI.6.2. Holocene humidity optimum (~ 10.5 – 8.5 ka)

From ~ 10.5 to 8.5 ka the Western Alboran Basin experienced an increase in marine productivity. This time interval coincides with the Holocene humidity optimum, a humid period in southern Europe often referred as the Holocene climatic optimum, which is attributed to a summer insolation maximum in the Northern Hemisphere during a precession minimum (Rohling and Rijk, 1999; Rossignal-Strick, 1999) (Fig. VI. 8). In the Westernmost Mediterranean region this period is characterized by warm and humid conditions with strong seasonality, as evidenced by pollen and geochemical records in lake sediments from the Padul wetland (Granada, Spain) and La Ballestera lake (Sevilla, Spain) (Figs. VI.1 and VI.8) (Ramos-Román et al., 2018a; García-Alix et al., 2022). Dinoflagellates productivity (including both autotrophs and heterotrophs dinoflagellates) and OM content increased from ~ 10.5 – 8.5 ka, after a continued between ~ 11.5 and 10.5 ka derived from reduced river discharges (Figs. VI.5– VI.8). Particularly, the observed increases in *Brigatedinium* cysts and *Lingulodinium machaerophorum* cysts, point to seasonal eutrophic surface waters. Additionally, the higher abundance of *Impagidinium* spp. cysts (mainly represented by *Impagidinium aculeatum* cysts) suggests warmer Alboran Sea surface waters during this period (Fig. VI. 8) (Pénaud et al., 2016). Cores CEUTA 10PC08 (914 mbsl, Fig. VI. 1; Ausín et al., 2015a) and GeoB18131-1 (457 mbsl, Fig. VI. 1; Wang et al., 2019) exhibit enhanced marine productivity in the Western Alboran Basin during this period, according to coccolith and planktonic foraminifera accumulation rates; respectively (Fig. VI. 8). An increase in OM content from ~ 10.5 to 9 ka also occurs in a marine core TTR17-434G, located close to the studied core (Figs. VI.1 and VI.7) (Mesa-Fernández et al., 2022). This points that enhanced marine productivity occurred in the entire Western Alboran Basin, including the North African margin area. Interestingly, the $\delta^{13}C_{carb}$ trend does not indicate increased marine productivity during this period, suggesting that $\delta^{13}C_{carb}$ values are strongly influenced by other factors, such as increased input of terrigenous material (characterized by with low C isotopes) due to rise continental run-off.

Low Ti/Ca values occurred during the Holocene humidity optimum, indicating that Western Alboran Basin experienced weakening of deep-currents during this period (Fig. VI. 8). The increase abundance of *Lingulodinium machaerophorum* cysts (an opportunistic dinocysts species) also supports (seasonally) stratified water-column in Western Alboran Basin from ~ 10.5 to 8.5 ka, and possibly reduced surface water salinity due to enhanced river run-off and seasonal thermal stratification (Pénaud et al., 2011, 2016) (see Fig. VI. 9). This increase in local fluvial discharges derived from the climatic shift towards more humid conditions in the Southern Iberian region around 10.5 ka (Dormoy et al., 2009; Mesa-Fernández et al., 2018; Camuera et al., 2020, 2021, 2022; García-Alix et al., 2021). In the geochemical record, the enhanced riverine discharge in Western Alboran Basin throughout the Holocene humidity optimum is supported by the increase in Rb/Al and Mg/Al values, the decrease in Ti/Al values, and the higher concentration of trace metals strongly influenced by the detritic fraction –e.g., Co, Ni, Cu and Cr; Tribovillard et al. (2006) (Figs. VI.4 and VI.5).

During the warmer Holocene humidity optimum, large freshwater volumes were released into the Atlantic Ocean due to melting of North Atlantic icebergs (Jiménez-Espejo et al., 2008). We suggest that enhanced low-salinity Atlantic inflows reached the Westernmost Mediterranean and reinforced reduced surface water salinity in Alboran Sea, as also occurred during Heinrich events and YD termination (Sierro et al., 2005; Grant et al., 2016). The Alps glaciers also experienced intense melting during the Holocene humidity optimum, reaching smaller sizes than in the late 20th century (Ivy-Ochs et al., 2009). This resulted in a significant release of freshwater into the Gulf of Lyon, weakening of WMDW formation and promoting deoxygenation of the Western Mediterranean deep settings (Jiménez-Espejo et al., 2008; Mesa-Fernández et al., 2022). Subsequently, sluggish WMDW circulation and weak or absent vertical-mixing cause oxygen depletion in Western Alboran deep-water from ~ 10 to 8.5 ka, as during this period Mo experienced an enrichment in association with iron sulfides, suggesting intermittent porewater euxinia that led to the precipitation of iron sulfides in association with Mo (Tribovillard et al., 2006; Scott and Lyons, 2012). Most RSTMs seems to be strongly influenced by the high detritic fluvial input, as most of these trace metals follow a trend similar to Rb/Al and Mg/Al (fluvial proxies), including U, a conservative RSTM that do not tend to be strongly influenced by detritic fraction variability (Tribovillard et al., 2006). The oxygen-depleted conditions in Alboran deep-water from ~ 10 to 8.5 ka enhanced OM preservation, as indicated by the obtained C_{org} trend and the C_{37} Alkenones trend (Cacho et al., 2002) and TOC% trend (Mesa-Fernández et al., 2022) (Fig. VI. 8). In this sense, in this interval the SSP index, which supports high marine productivity during this period, should be reliable and goes in accordance with the rest of proxies.

The humid and warm interval in Western Mediterranean (from ~ 10.5 to 8.5 ka) that led to increased dinoflagellates productivity and deep-water deoxygenation in Western Alboran Basin overlaps in time with the deposition of sapropel S1 in Eastern Mediterranean, more specifically with section S1a deposited before S1 interruption linked to the 8.2 ka cold event (de Lange et al., 2008; Jiménez-Espejo et al., 2015; Grant et al., 2016; Filippidi and de Lange, 2019). Consequently, during this period, LIW circulation in the Mediterranean was weaker and had lower oxygen content in the Western Mediterranean (Fig. VI. 8) (Ausín et al., 2015b; Fink et al., 2015; Wang et al., 2019; Zirks et al., 2019; Trias-Navarro et al., 2023). Weak LIW circulation promoted a strong reduction of Mediterranean Outflow Water flow during this period (Voelker et al., 2006).

Hence, from ~ 10.5 to 8.5 ka, the weak circulation of oxygen-depleted LIW reinforced OM preservation Western Alboran Basin. Consequently, enhanced OM accumulation/preservation and RSTMs fixation during the Holocene humidity optimum in the Western Alboran Basin, can be linked to the conjunction of different factors: (i) high marine productivity due to surface water fertilization by local rivers and enhanced flux of relatively fertilized Atlantic surface water, (ii) weak circulation of oxygen-depleted LIW due to Eastern Mediterranean deoxygenation during S1a deposition, favoring OM preservation during is transit through Western Alboran water-column, and (iii) decreased Alboran deep-water ventilation produced by weakened formation of WMDW at the Gulf of Lyon.

Intermittent porewater euxinia and deep-water deoxygenation, which started ~ 10 ka, ceased before the 8.2 ka cold event (also known as Bond event 5; Bond et al., 1997), characterized in the Westernmost Mediterranean region by arid and cold conditions (Rodrigo-Gámiz et al., 2011). The cold/arid regional conditions reduced local river discharges and promoted active WMDW formation and ventilation of the Western Mediterranean deep settings, including deep Alboran basins (Jiménez-Espejo et al., 2008; Rogerson et al., 2008; Rodrigo-Gámiz et al., 2011; Pérez-Asensio et al., 2020; Mesa-Fernández et al., 2022). As a result, the 8.2 ka cold event decreased marine productivity in the Western Alboran Basin (including planktonic foraminifera and coccolithophores productivity; Fig. VI. 8) and hindered OM preservation, marking the demise of ORL-1b in this basin. Conversely, in the Eastern Mediterranean basins (e.g., Levantine and Adriatic basins), high productivity and weak deep-water ventilation resumed after the 8.2 ka cold event, leading to the deposition of sapropel interval S1b from ~ 8.5 to ~ 6.1 ka (Fink et al., 2015; van Helmond et al., 2015; Zwiep et al., 2018). However, there is no Mn enrichment or signs of OM oxidation linked to a rapid reventilation of Western Alboran deep-water during the 8.2 ka cold event, as occurred during some sapropel reventilation events associated to abrupt Eastern Mediterranean deep-water renewal, where Mn-oxyhydroxides precipitated intensely due to the penetration of the oxidation front in the sediments (Thomson et al., 1993; Reitz et al., 2006; Filippidi and de Lange, 2019; Monedero-Contreras et al., 2023a, b).

The humid conditions in Western Alboran Basin ceased around 6.5 ka, based on the decrease in fluvial input and increase in aeolian input. This climatic transition occurred synchronically with key oceanographic changes: (i) an intensification of Western Alboran deep-currents (as revealed by the increase in Ti/Ca values; Fig. VI. 5), (ii) enhanced Alboran intermediate-water ventilation (Fig. VI. 8; Ausín et al., 2015b), and (iii) activation of vertical mixing at the Alboran Sea (as suggested by the increase in $\delta^{13}C_{carb}$ values; Fig. VI. 5). Therefore, the arid modern conditions in the south of the Iberian Peninsula emerged around 1000 years earlier than in Northern African and the Sahara region, where humid conditions persisted until the end of the African Humid

Period around 5.5 - 5 ka (Tierney et al., 2011; Bout-Roumazeilles et al., 2013). This observation is consistent with Menocal (2015) findings, indicating that the end of the African Humid Period progressed from north to south, with monsoon rains diminishing first in the north and gradually receding further south, in accordance with the expected southward migration of the Intertropical Convergence Zone (ITCZ) due to orbital forcing (Bout-Roumazeilles et al., 2013). Moreover, this observation is supported by South Iberian continental records, which registered the regional climatic shift towards more arid conditions around 7 – 6.5 ka using geochemical and pollen proxies (Fig. VI. 8) (Chabaud et al., 2014; Mesa-Fernández et al., 2018; Ramos-Román et al., 2018a, b; García-Alix et al., 2022; Jiménez-Moreno et al., 2022, 2023).

VI.6.3. late Holocene (4.2 ka – present)

The higher accumulation rate of *Lingulodinium machaerophorum* and *Spiniferites* spp. cysts support a moderate increase in nutrient content and productivity in Western Alboran surface water during the late Holocene, as these dinocysts species can be considered as eutrophication proxies in Westernmost Mediterranean (Pelauld et al., 2016). The higher $\delta^{13}C_{carb}$ and C_{org} values also support an increase in marine productivity during this period. However, this marine productivity increase is relatively low in comparison with the rise registered during the YD humid phase or Holocene humidity optimum. This moderate productivity increase during the late Holocene derived from the establishment of new oceanographic and environmental conditions in the Western Alboran Basin originating from the aforementioned regional climatic shift in response to the southward migration of the ITCZ. The low Mg/Al values and the increase in Ti/Al values support arid regional conditions during the late Holocene (specially over the last 1.5 ka). The arid regional conditions and strong north westerlies during the late Holocene facilitated active Ekman transport along the Iberian Peninsula coastline, which promoted active anticyclonic Alboran gyres (WAG and EAG; Fig. VI. 1) and inducing upwelling at the northern edge of the WAG (Sarhan et al., 2000; Ruiz et al., 2001; Pérez-Folgado et al., 2003; Ausín et al., 2015b, a; Garcia-Jove et al., 2022). Therefore, the increased nutrient availability during the late Holocene, and subsequent increase in marine productivity, seems to be controlled by the establishment of seasonal upwelling systems, as marked by the increase in *Lingulodinium machaerophorum* cysts accumulation rate (Pénaud et al., 2016).

NAO has been suggested as a key driver for several the suborbital climatic oscillations in the Western Mediterranean during the late Holocene (Jalut et al., 1997, 2000; Frigola et al., 2007; Fletcher and Zielhofer, 2011; Bout-Roumazeilles et al., 2013; Ausín et al., 2015b; Liisa Ilvonen et al., 2022). Despite regional aridification throughout the late Holocene, the Iberian Peninsula has experienced extreme flood events linked negative NAO incursions (Benito et al., 2023). In this regard, the marked increases in the irregular Rb/Al, $\delta^{13}C_{org}$ and C/N trends throughout the late Holocene suggest punctual fluvial input increases (see Fig. VI. 5 for Rb/Al trend and Supplementary material for $\delta^{13}C_{org}$ and C/N trends), possibly associated to short-periods with enhanced regional flood events linked to a negative NAO situation. In addition, *Concentricystes* (euglenoid cysts with a unique fingerprint shape and linked to eutrophic freshwater environments; Schootbrugge et al., 2024), have been documented since ~ 7.3 ka and throughout the late Holocene (see Supplementary material). *Concentricystes* have been found in marine sediments after events of enhanced river run-off (Yang et al., 2022). Therefore, their presence throughout the late Holocene suggests pulses of increased fluvial input in Western Alboran Basin, as well as effective transport of biomass from the northern continental margin to the center of the basin by active WAG and AJ currents during the late Holocene. This aligns with modern observations indicating that the seasonal but torrential nature of the relatively small rivers in the catchment basins around the Alboran Sea play a significant role as contributors of freshwater and nutrients (as large sediment plumes) during seasonal flood events (Fabres et al., 2002; Masqué et al., 2003; Liquete et al., 2005; Lobo et al., 2006). However, in a regional aridification context governed by a persistent positive NAO pattern, upwelling induced by strong north-westerlies seems to be the constant source of nutrients during the late Holocene and at present, where local rivers only act as fertilizers of the Alboran Sea during extreme flood events. Consequently, centennial-scale changes in marine productivity dynamics and nutrient availability throughout the late Holocene can be attributed to changes in the governing NAO-like pattern.

Regarding the Western Alboran deep-water dynamics, the increase in Ti/Ca values ~ 3 ka suggests a strengthening of the Bernoulli effect, which promoted more frequent Western Alboran deep-water renewal during the late Holocene, as previously interpreted by Mesa-Fernández et al., 2022 in Eastern Alboran Basin. The low concentration of RSTMs also supports active Western Alboran deep-water ventilation/oxygenation during the late Holocene. An increase in aeolian input is observed in the most recent sediments (Fig. VI. 5), indicating enhanced regional aridification over the last ~ 0.5 ka. This trend may be associated with deforestation and degradation due to anthropic activities, such as agriculture in the south of the Iberian Peninsula (Martín-Puertas et al., 2009; Mulitza et al., 2010; Gázquez-Sánchez et al., 2023). The significant decrease in water discharge and sediment supply of Western Alboran rivers since the first half of the 20th century, attributed to anthropogenic aridification and damming of local rivers, including the Guadalfeo River and the Adra River –two of the main rivers draining Sierra Nevada (Liquete et al., 2005; Bergillos and Ortega-Sánchez, 2017), raises concerns about the potential impacts on water-column dynamics and marine productivity (Ludwig et al., 2009). In this regard, achieving centennial resolution of dinocysts data for the last two centuries in the Western Alboran Basin would enable assessment of whether the anthropogenic reduction in freshwater and sediments supply has affected marine productivity, and discrimination between the pre- and post-industrial state of Western Alboran Sea, as in the Adriatic Sea (Sangiorgi and Donder, 2004).

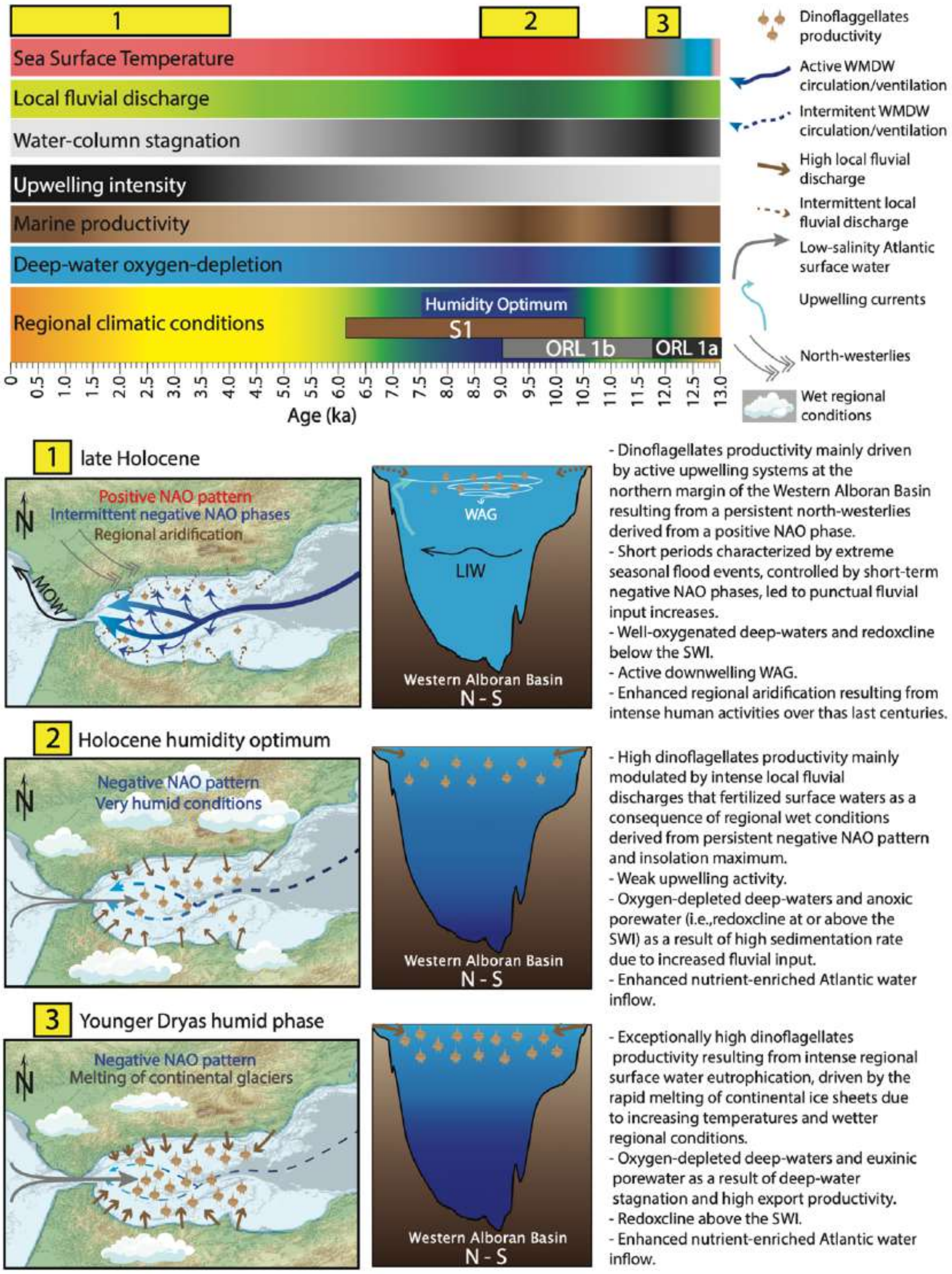
1
2
3
Sea Surface Temperature
Local fluvial discharge
Water-column stagnation
Upwelling intensity
Marine productivity
Deep-water oxygen-depletion
Regional climatic conditions
Humidity Optimum
S1
ORL 1b
ORL 1a
0
0.5
1.0
1.5
2.0
2.5
3.0
3.5
4.0
4.5
5.0
5.5
6.0
6.5
7.0
7.5
8.0
8.5
9.0
9.5
10.0
10.5
11.0
11.5
12.0
12.5
13.0
Age (ka)
Dinoflagellates productivity
Active WMDW circulation/ventilation
Intermitent WMDW circulation/ventilation
High local fluvial discharge
Intermittent local fluvial discharge
Low-salinity Atlantic surface water
Upwelling currents
North-westerlies
Wet regional conditions
1 late Holocene
N
Positive NAO pattern
Intermittent negative NAO phases
Regional aridification
MOW
WAG
LIW
Western Alboran Basin
N - S
2 Holocene humidity optimum
Negative NAO pattern
Very humid conditions
3 Younger Dryas humid phase
Negative NAO pattern
Melting of continental glaciers

- Dinoflagellates productivity mainly driven by active upwelling systems at the northern margin of the Western Alboran Basin resulting from a persistent north-westerlies derived from a positive NAO phase.
- Short periods characterized by extreme seasonal flood events, controlled by short-term negative NAO phases, led to punctual fluvial input increases.
- Well-oxygenated deep-waters and redoxcline below the SWI.
- Active downwelling WAG.
- Enhanced regional aridification resulting from intense human activities over thas last centuries.

- High dinoflagellates productivity mainly modulated by intense local fluvial discharges that fertilized surface waters as a consequence of regional wet conditions derived from persistent negative NAO pattern and insolation maximum.
- Weak upwelling activity.
- Oxygen-depleted deep-waters and anoxic porewater (i.e.,redoxcline at or above the SWI) as a result of high sedimentation rate due to increased fluvial input.
- Enhanced nutrient-enriched Atlantic water inflow.

- Exceptionally high dinoflagellates productivity resulting from intense regional surface water eutrophication, driven by the rapid melting of continental ice sheets due to increasing temperatures and wetter regional conditions.
- Oxygen-depleted deep-waters and euxinic porewater as a result of deep-water stagnation and high export productivity.
- Redoxcline above the SWI.
- Enhanced nutrient-enriched Atlantic water inflow.

Figure VI.9. *Scheme of the different oceanographic scenarios in Western Alboran basin over the last 13 ka. (1) late Holocene (last 4.2 kyr); (2) Holocene humidity optimum (from ~ 10.5 to 8.5 ka); (3) YD humid phase (from ~ 12.3 to 11.7 ka). The main factors controlling marine productivity at each stage are emphasized.*

Interestingly, Fe and Mn peaks are recognized at 10 cm of the core (~ 0.5 ka), marking the present position of the oxidation front (i.e., the redoxcline) (Fig. VI. 4). In this interval, Mn and Fe precipitated as Mn-Fe oxyhydroxides (Tribovillard et al., 2006), as occurs in some modern Eastern Mediterranean settings, such as Eratosthenes Seamount (Monedero-Contreras et al., 2023b) or Otranto Strait sill (South Adriatic Sea) (Filippidi and de Lange, 2019). RSTMs such as Zn, Pb and Mo precipitated in association with Mn and Fe oxyhydroxides, as occurred in the "marker bed" during sapropel termination/ventilation (Monedero-Contreras et al., 2023a). The enrichment in Pb, Cu and Zn, above the Mn-peak, might be attributed to mining of heavy metals sulfides in the South of Spain, a historically significant industry in the region over the last centuries (Leblanc et al., 2000; Olías and Nieto; 2015; Romero-Baena et al., 2018). The significant enrichment in Pb (a highly toxic metal) at the top of the core could also be linked to anthropogenic atmospheric pollution over the last century (Álvarez-Iglesias et al., 2012; García-Alix et al., 2020). In any case, dinocysts and geochemical results indicate that the sediment record of the Western Alboran Basin can serve as a valuable tool for studying the impacts of anthropogenic activities in the Iberian Peninsula over the past centuries.

VI.7. Conclusions

Beyond unraveling the paleoceanographic evolution of the Alboran Sea over the past 13,000 years, the obtained results provide paleoperspectives of marine productivity responses to suborbital climate variability, thereby providing valuable insights on the complex interactions of environmental and oceanographic factors influencing productivity dynamics in a changing climate crucial for developing more robust long-term (centennial - multicentennial) productivity models in the region.

During the Younger Dryas humid phase (from ~ 12.2 to 11.7 ka), characterized in Western Alboran Basin by water-column stratification, the remarkably high marine productivity was driven by surface water fertilization resulting from enhanced local river discharges, originating from rapid melting of surrounding mountain glaciers due to increasing global temperature and moderate increase in regional precipitations. Marine productivity in the Western Alboran Sea also increased during the Holocene humidity optimum (from ~ 10.5 to 8.5 ka). However, during this period, the primary factor contributing to the elevated local river discharges was the increased regional precipitations. Moreover, the punctual marine productivity increases during the late Holocene are associated to intermittent floods events linked to negative NAO incursions. These findings reveal that throughout the last 13,000 years, wet regional conditions in Westernmost Mediterranean, influenced by the interplay of orbital (e.g., insolation cycles) and suborbital factors (e.g., NAO patterns), favor enhanced marine productivity in Western Alboran Basin. Moreover, these observations highlight the key role that local river discharges play in dinoflagellates productivity dynamics within the Western Alboran Basin.

Marine productivity throughout the late Holocene in the Western Alboran Basin is controlled by upwelling systems produced by strong north-westerlies as a consequence of a persistent positive NAO phase. These active upwelling systems have promoted increased marine productivity in respect to most Mediterranean basins during the late Holocene, despite reduced river discharges due to the regional aridification. Therefore, under the current climate scenario, water-column dynamics seem to have a more important effect on marine productivity in Western Alboran Basin than the direct effect of decreased fluvial inputs and increasing SST. As a result, if Alboran upwelling systems cease, marine productivity would decrease as local rivers would not able to provide sufficient nutrients to sustained increased marine productivity, leading to a reduction of the biologically-mediated carbon export to the deep ocean in this region.

Throughout the Holocene, the Ba/Al trend mirrors the fluvial input trend, suggesting a strong detrital influence on Ba concentrations in Western Alboran sediments. Thus, fluctuations in the Ba/Al ratio may not accurately reflect changes in marine pelagic barite content as the strong Ba detrital signal deriving from the high detrital input characterizing Western Alboran Basin can mask the productivity signals derived from moderate increases in marine barite. In this context, dinocyst analysis emerges as an extraordinary complementary tool to reconstruct marine productivity in the Alboran Sea, as dinoflagellates community assemblages seem to be more sensitive to register minor changes in the environmental and oceanographic conditions (e.g., nutrient availability and water-column stability) than some geochemical signals (e.g., pelagic barite content and $\delta^{13}C$ in foraminifera shells and OM).

Acknowledgment

This study has been funded by Grants PID2019-104624RB-I00, PID2019-104625RB-100, and TED2021-131697B-C22 funded by MCIN/AEI/ 10.13039/501100011033, Grants FEDER/Junta de Andalucía P18-RT-3804 and P18-RT- 4074, and by Research Groups RNM-179 and RNM-178 funded by Junta de Andalucía. We thank the GeoLab staff from Utrecht University, more precisely to the Organic Geochemistry Lab, Stable Isotope Lab and Palynology Lab, for their valuable contributions to the organic matter analyses and their assistance in preparing palynomorph slides. We are also grateful to the Center for Scientific Instrumentation (CIC, University of Granada) and the XRF Unit of the IACT (CSIC-UGR) for the ICP and XRF analyses, respectively. All original data in this study is accessible via correspondence with the main author, who will willingly make them available for free to anyone upon request. This study is part of R. Monedero PhD project.

Supplementary material

Supplementary data to this article is presented as Appendix II.

Summary and Conclusions

Epílogo y Conclusiones

Summary and Conclusions

In this section, a summary of the results and conclusions is provided, offering a comprehensive synthesis of the main findings and general insights derived from the research conducted within this thesis.

The study of sapropels has provided valuable insights into bottom-water circulation and redox conditions in Eastern Mediterranean deep-marine settings under different climate conditions, offering paleoperspectives for understanding modern marine systems facing oxygen depletion. Key findings include:

- In Eastern Mediterranean basins, the degree of surface-water freshening associated with regional climate conditions has been a major control for deep-water formation and thermohaline circulation, which in turn control the frequency and intensity of deep-water deoxygenation, and the stability and depth of the chemocline.
- The deepest sites studied in the Eastern Mediterranean were identified as the most vulnerable locations prone to develop deep-water restriction and deoxygenation.
- Particulate shuttling of organic and inorganic aggregates was very intense in Eastern Mediterranean water-column during sapropel deposition, similar to the modern Cariaco Basin, which boosted burial fluxes of trace-metals (e.g., Mo, Cu, Co, Ni and V).
- Water-mass exchange between the Western and Eastern Mediterranean is particularly active during cold periods, such as during the deposition of sapropel S6. This water-mass exchange regulates the budget of dissolved Mo within Eastern Mediterranean basins, thereby controlling the intensity of the basin's reservoir effect on trace metals budget in Eastern Mediterranean deep-waters.

The study of sapropels across an Eastern Mediterranean transect including three different deep settings underscores the significant influence of local environmental conditions (e.g., productivity rate) and hydrogeographic features (e.g., water-depth, sedimentation rate, and particulate-shuttling intensity) in defining the extent of deep-water deoxygenation and the authigenic enrichment rates of redox-sensitive trace metals (RSTMs) by seafloor sediments. Deep-marine settings characterized by significant particulate-shuttling appear to exhibit higher redox threshold values (e.g., Mediterranean Ridge), whereas deep-marine settings with weaker particulate-shuttling present lower redox thresholds values (e.g., Ionian Basin). Moreover, by analyzing the large geochemical dataset obtained from different Eastern Mediterranean locations representing diverse oceanographic regimes, it is suggested that certain trace elements such as Mo, V, U, Co, and Ni are more reliable as redox proxies since they show weaker detritic influence in comparison to other redox sensitive elements such as Cr, Cu, Pb, and Zn.

The study of sub-cm geochemical signals within organic-rich sediments, conducted through SEM observation and LA-ICP-MS analyses of sediment thin-sections from sapropel S1 geochemical intervals (including the marker bed, and oxidized, unoxidized and synsapropel intervals; from top to bottom), highlights the importance of understanding postdepositional processes involving the dissolution and reprecipitation of RSTMs for accurate interpretation of the syndepositional geochemical redox signals. This study demonstrates that the Mn-oxyhydroxides (precipitated at the top of sapropels within the marker bed) and the large pyrite framboids and euhedral crystals (formed below the sapropels within the synsapropel layer) play crucial roles in trapping and scavenging dissolved RSTMs in porewater during early diagenesis. Mn-oxyhydroxides are formed due to the penetration of the oxidation front during rapid bottom-water reventilation, as observed during sapropel termination. Conversely, synsapropel pyrite precipitation occurs during sapropel deposition and is driven by the downward diffusion of hydrogen sulfide (H_2S) produced by intense sulfate-reducing bacterial activity within the overlying organic-rich interval. It is worth noting that diffusion of hydrogen sulfide only occurs if reactive iron is exhausted within the organic-rich interval, acting as limiting factor for pyrite precipitation and leading to hydrogen sulfide diffusion from the sapropel. While the downward diffusion of hydrogen sulfide promotes pyrite precipitation below the sapropel, the upward diffusion boosts bottom-water euxinia. Among the RSTMs, Mo is the most efficiently trapped by Mn-oxyhydroxides and pyrite aggregates during early diagenesis. Therefore, the interpretation of Mo signals (a key redox proxy) must consider the potential for postdepositional remobilization. Interestingly, dissolved U –a trace metal that does not tend to associate with sulfides– can also be scavenged by underlying synsapropel pyrite framboids and crystals during postdepositional oxidation, probably by physical adsorption by the large pyrite surfaces.

A detailed ichnological analysis of sapropel S7 (selected as a case study) at the Eratosthenes Seamount (~195 ka) using digital image treatments, SEM tools (e.g., SEM-EDX mapping) and LA-ICP-MS spot-analyses of sediment thin-sections allowed to evaluate the influence of *Chondrites*-producers in organic-rich sediments representing past deoxygenation events. The study revealed the following findings:

- The average dilution factor of RSTMs by *Chondrites* within the studied sapropel is between 5% and 6%. Although, in some cases, the dilution factor for key paleoceanographic trace metals (e.g., Mo, U and Ni) was greater than 10%.
- *Chondrites*-producers enable the introduction of oxic water (enriched in sulfate) below the sediment-water interface (and oxidation front) throughout open sub-cm

burrows, enhancing bioirrigation and porewater ventilation of underlying anoxic sediments, which promotes postdepositional oxidation and the remobilization of RSTMs fixed in association with organic-matter and iron sulfides.

- *Chondrites* significantly alter sub-cm sedimentary features by disrupting lamination and altering sub-cm mineral and organic-matter distribution, and subsequently, the distribution of trace metals and oligoelements vital for benthic macro and microorganisms.
- High-resolution redox reconstructions of past deoxygenation events in deep-sea records relying on sub-cm analyses (e.g., LA-ICP-MS line-scanning and XRF core-scanning) should acknowledge the presence of *Chondrites*, as sub-cm RSTMs variations could be due to *Chondrites* infills geochemical composition rather than syndepositional redox changes.

Overall, the sub-cm modifications associated to *Chondrites* in deep-sea sediments have wide-ranging implications beyond mineral redistribution and trace metals dilution within organic-rich sediments. *Chondrites* induce significant impact on biogeochemical processes, sediment hydrodynamics, trace metals cycling, and the fate of organic carbon in deep-marine environments, highlighting the intricate and complex interplay between biological activity (i.e., bioturbation), sedimentary processes, and carbon and trace metal dynamics.

The high-resolution reconstruction of the paleoceanographic evolution of the Alboran Sea over the last 13,000 years unveils the response of marine productivity to climate variability. Notably, during the Younger Dryas humid phase (~ 12.2 – 11.7 ka) and the Holocene humidity optimum (~ 10.5 – 8.5 ka), increased local river discharges, driven by melting mountain glaciers and increased regional precipitations, led to higher nutrient availability in the Alboran surface-waters, which promoted enhanced marine productivity. Intermittent flood events during the late Holocene (~ 4.2 ka – present) linked to North Atlantic Oscillation (NAO) negative incursions caused brief productivity increases. In essence, humid periods deriving from the interplay of orbital (e.g., insolation cycle) and suborbital (e.g., atmospheric patterns) factors promote enhanced marine productivity in the Westernmost Mediterranean. Marine productivity is usually lower during dry climatic conditions (as occurred throughout the late Holocene and at present), although it is higher in comparison with most Mediterranean basins due to active seasonal upwelling systems resulting from a persistent positive NAO pattern with strong north-westerlies. This persistent NAO pattern is the result of the southward migration of the Intertropical Convergence Zone (ITCZ), which occurred in Westernmost Mediterranean around 6.5 ka (according to geochemical detrital signals) in response to orbital forcing. Therefore, these results highlight the strong influence of both orbital and suborbital climatic factors on productivity dynamics in Westernmost Mediterranean.

Furthermore, the primary productivity reconstruction achieved using paleoceanographic proxies of different nature (abiotic and biotic) highlights limitations in using the Ba/Al ratio as a proxy for primary productivity in the Westernmost Mediterranean. This is due to the high detrital input and sedimentation rates, which can obscure the weak pelagic barite signals. Consequently, our findings advocate for dinoflagellate analysis as a more sensitive proxy for reconstructing marine productivity in this region. Overall, these findings advance our understanding of marine ecosystem responses to climate change, facilitating the development of long-term productivity models essential for adapting to ongoing environmental shifts.

The integration of modern observations with paleoperspectives obtained through the study of past deoxygenation and marine productivity changes driven by climatic factors is particularly valuable for developing more robust, long-term (centennial-scale) oceanographic projections under the ongoing rapid climate change. The 2023 IPCC report projected that, as general trend, the upper ocean will maintain high dissolved-oxygen levels due to air-sea exchange and photosynthesis, however mesopelagic waters and deep-waters may experience deoxygenation as is virtually certain that stratification in the upper 200 meters of the ocean has been increasing since 1970. Chapter II findings align with this projection, demonstrating that the deep Mediterranean settings were the first marine settings to experience oxygen-depletion during sapropel deposition due to water-column stratification and sluggish deep-water circulation deriving from enhanced surface-water buoyancy (i.e., decrease surface-water salinity). Furthermore, at present, Westernmost Mediterranean is one of the most productive areas in the Mediterranean (Macias et al., 2015). However, the paleoproductivity reconstruction of Western Alboran Basin suggests that, if Alboran upwelling systems cease due to the projected enhanced water-column stratification and weakened vertical mixing resulting from global warming, marine productivity would decrease in this region as local rivers would not able to supply sufficient nutrients to sustained increased marine productivity due to regional aridification. This would lead to a reduction of the biologically-mediated carbon export to the deep ocean in this region.

In summary, this thesis enhances our understanding of how oxygenation conditions in deep-marine settings react to changes in thermohaline circulation induced by climate variations. It also sheds light on the centennial- and multicentennial-scale marine productivity responses to rapid climate variability, enhancing our capacity to constraint marine changes (including ocean stressor) stemming from ongoing climate change, particularly in the Mediterranean Sea. Integration of theoretical constraints and paleoperspectives will also help top generate robust forecasts and projections of ocean changes, which play a crucial role in our efforts to adapt to and mitigate the impacts of environmental changes arising from current climate shifts and human activities.

Epílogo y Conclusiones

En esta sección se presenta un resumen de los resultados y conclusiones, ofreciendo una síntesis de los principales hallazgos y conocimientos derivados de la investigación llevada a cabo en esta tesis.

El estudio de los sapropeles ha proporcionado información muy valiosa sobre la circulación de las aguas profundas y las condiciones de oxigenación en ambientes marinos profundos del Mediterráneo Oriental durante diferentes condiciones climáticas, ofreciendo paleoperspectivas para el mejor entendimiento de ambientes actuales que sufren agotamiento del oxígeno. Entre las principales conclusiones cabe citar las siguientes:

- En las cuencas del Mediterráneo Oriental, el grado de salinidad de las aguas superficiales asociado a las condiciones climáticas regionales ha sido uno de los principales factores de control de la formación de aguas profundas, que a su vez controlan la frecuencia e intensidad de la desoxigenación de las aguas profundas, así como la estabilidad y profundidad de la quimioclina.
- Los medios más profundos en el Mediterráneo Oriental han sido los ambientes más vulnerables a desarrollar desoxigenación durante periodos húmedos.
- La transferencia de agregados orgánicos e inorgánicos fue muy intensa en la columna de agua del Mediterráneo Oriental durante el depósito de sapropeles, de forma similar a lo que ocurre actualmente en la Fosa de Cariaco (Mar Caribe), lo que potenció los flujos de enterramiento de metales traza (por ejemplo, Mo, Cu, Co, Ni y V).
- El intercambio de masas de agua entre el Mediterráneo Occidental y Oriental (particularmente activo durante los periodos fríos, por ejemplo, durante el depósito del sapropel S6) regula el balance de Mo disuelto dentro de las cuencas profundas del Mediterráneo Oriental.

Además, el estudio de sapropeles a lo largo de un transecto del Mediterráneo Oriental ha puesto de manifiesto la significativa influencia de las condiciones ambientales e hidrogeográficas locales (por ejemplo, productividad, profundidad del agua, tasa de sedimentación y la intensidad de transferencia de partículas) en las tasas de enriquecimiento autigénico de metales traza en los sedimentos del fondo marino. Los medios marinos profundos caracterizados por una alta tasa de transferencia de partículas inorgánicas (por ejemplo, oxihidróxidos de Mn) al fondo marino presentan umbrales de redox más elevados (por ejemplo, la Dorsal Mediterránea), mientras que los medios marinos profundos con una baja tasa transferencia de partículas inorgánicas presentan umbrales de redox más bajos (por ejemplo, la Cuenca Jónica). Además, analizando el amplio conjunto de datos geoquímicos obtenidos en diferentes localizaciones del Mediterráneo Oriental representativas de diversos regímenes oceanográficos, se ha podido establecer que ciertos metales trazas como Mo, V, U, Co y Ni son más fiables como indicadores redox ya que muestran una influencia detrítica más débil en comparación con otros elementos también sensibles a cambios en la oxigenación como Cr, Cu, Pb y Zn.

El estudio de las variaciones en las señales geoquímicas a escala subcentimétrica realizado mediante un análisis de SEM y LA-ICP-MS en láminas delgadas de sedimentos del sapropel S1 ha puesto de manifiesto la importancia de los procesos postdeposicionales, incluyendo la disolución y reprecipitación de los metales traza, en la interpretación de las señales redox geoquímicas sindeposicionales. Este estudio demuestra, además, que los oxihidróxidos de Mn (precipitados en el frente de oxidación del sapropel) y los grandes framboides y cristales euhedrales de pirita (formados por debajo de los sapropeles) desempeñan un papel esencial como sumidero de los metales trazas disueltos en el agua intersticial durante la diagénesis temprana. Los oxihidróxidos de Mn se forman debido a la penetración del frente de oxidación durante la reventilación del agua de fondo. Por el contrario, la precipitación de pirita en el sapropel se produce durante su depósito, pero se ve posteriormente intensificada por la difusión descendente de sulfuro de hidrógeno (H2S) producido por la actividad de bacterias sulfatoreductoras dentro del intervalo rico en materia orgánica suprayacente. Cabe destacar que la difusión de sulfuro de hidrógeno sólo se produce si el hierro reactivo se agota dentro del intervalo rico en materia orgánica, actuando como factor limitante para la precipitación de pirita y conduciendo a la difusión de sulfuro de hidrógeno desde el sapropel. Mientras la difusión descendente de sulfuro de hidrógeno promueve la precipitación de pirita por debajo del sapropel, la difusión ascendente potencia la euxinia del agua del fondo. Entre los metales traza, el Mo es retenido más eficientemente por los oxihidróxidos de Mn y los agregados de pirita durante la diagénesis temprana. Por lo tanto, para la interpretación de las señales de Mo (uno de los indicadores redox más fiables y utilizados) se debe considerar el potencial de removilización postdeposicional. Cabe destacar que el U disuelto –un metal traza que no tiende a asociarse con sulfuros– también puede ser atrapado en framboides y cristales de pirita subyacentes durante la oxidación postdeposicional, probablemente por adsorción física en las grandes superficies de pirita.

El análisis icnológico detallado del sapropel S7 (seleccionado como caso de estudio) en la cima del monte submarino Eratóstenes (~ 195 ka) realizado a partir del tratamiento digital de imágenes, análisis de SEM (por ejemplo, mapas composicionales obtenidos por SEM-EDX) y estudios mediante LA-ICP-MS de láminas delgadas de sedimentos, ha permitido evaluar la influencia de *Chondrites* (una traza fósil común en medios marinos profundos) en sedimentos ricos en materia orgánica que representan eventos pasados de desoxigenación. Este estudio ha permitido alcanzar los siguientes resultados:

- El factor medio de dilución de metales trazas por *Chondrites* dentro del sapropel estudiado se sitúa entre el 5% y el 6%. Aunque, en algunos casos, el factor de dilución para metales traza utilizados en estudios paleoceanográficos (por ejemplo, Mo, U y Ni) fue superior al 10%.
- Los organimos productores de *Chondrites* facilitan la introducción de agua rica en oxígeno (enriquecida en sulfato) por debajo de la interfase sedimento-agua (y frente de oxidación) a lo largo de las galerías abiertas de tamaño subcentimétrico, potenciando la bioirrigación y la ventilación del agua intersticial en los sedimentos anóxicos subyacentes, lo que da lugar a la oxidación postdeposicional y la removilización de metales traza asociados a la materia orgánica y sulfuros de hierro.
- Los *Chondrites* alteran significativamente las características sedimentarias a escala subcentimétrica alterando la laminación primaria y la distribución de minerales y materia orgánica y, posteriormente, la distribución de metales traza y oligoelementos vitales para los macro y microorganismos bentónicos.
- Las reconstrucciones redox de alta resolución de eventos pasados de desoxigenación registrados en ambientes marinos profundos, basadas en análisis subcentimétricos (por ejemplo, escaneo de líneas LA-ICP-MS y de núcleos XRF), deberían considerar la presencia de *Chondrites*. Las variaciones submilimétricas en las concentraciones de metales trazas podrían estar influenciadas, en parte, por la composición geoquímica del material que rellena los *Chondrites*, lo que podría enmascarar los cambios redox sincrónicos con la deposición.

En general, las modificaciones subcentimétricas asociadas a *Chondrites* en sedimentos de aguas profundas tienen implicaciones importantes más allá de la redistribución de minerales y la dilución de metales traza en sedimentos ricos en materia orgánica. Los *Chondrites* pueden tener un impacto significativo en los procesos biogeoquímicos, la hidrodinámica de los sedimentos, el ciclo de los metales traza y del carbono orgánico en ambientes marinos profundos, poniendo así de relieve la intrincada y compleja interacción entre la actividad biológica, los procesos sedimentarios y la dinámica del carbono y los metales traza.

La reconstrucción de alta resolución de la evolución paleoceanográfica del Mar de Alborán durante los últimos 13,000 años ha puesto de manifiesto la respuesta de la productividad marina a la variabilidad climática. En particular, durante la fase húmeda del Younger Dryas (~ 12.2 – 11.7

ka) y el óptimo de humedad del Holoceno (~ 10.5 – 8.5 ka), el aumento de las descargas fluviales locales, impulsado por el deshielo de los glaciares de montaña y el aumento de las precipitaciones regionales, dio lugar a una mayor disponibilidad de nutrientes en las aguas superficiales del Mar de Alborán, lo que contribuyó a un aumento de la productividad marina. Los periodos con inundaciones intermitentes durante el Holoceno tardío (~ 4.2 ka - actualidad) vinculadas a incursiones negativas de la Oscilación del Atlántico Norte (NAO de sus siglas en inglés) provocaron aumentos esporádicos de la productividad. En esencia, los periodos húmedos derivados de la interacción de factores orbitales (por ejemplo, variaciones en la insolación) y suborbitales (por ejemplo, los patrones atmosféricos) dieron lugar a un aumento de la productividad marina en el Mediterráneo más occidental. En general, la productividad marina suele ser más baja durante periodos áridos (como ocurrió a lo largo del Holoceno tardío y actualmente). Sin embargo, esta productividad es actualmente mayor en comparación con otras cuencas mediterráneas debido a los sistemas de surgencia de agua profunda (*upwelling systems* en inglés) generados en condiciones de NAO positiva con fuertes vientos del noroeste. Este patrón persistente de NAO positivo es el resultado de la migración hacia el sur de la Zona de Convergencia Intertropical (ITCZ de sus siglas en inglés), que se produjo en el Mediterráneo más occidental hace alrededor de 6.5 ka (según los indicadores geoquímicos) en respuesta al efecto orbital. Por tanto, estos resultados ponen de manifiesto la fuerte influencia de los factores climáticos, tanto orbitales como suborbitales, en la dinámica de la productividad del Mediterráneo más occidental. Además, la reconstrucción de productividad primaria obtenida a partir de la aplicación de diversos indicadores paleoceanográficos (abióticos y bióticos) muestra las limitaciones de la relación Ba/Al como un indicador de productividad primaria en el extremo oeste del Mediterráneo. Esto es debido al alto aporte detrítico y las altas tasas de sedimentación que diluyen significativamente la señal de la barita pelágica. Así, el análisis de dinoflagelados es en este caso un indicador más sensible para la reconstrucción de la productividad marina en esta región. En conjunto, estos resultados contribuyen a mejorar nuestra comprensión de las respuestas de los ecosistemas marinos al cambio climático, facilitando el desarrollo de modelos de productividad a largo plazo en el Mediterráneo, de especial importancia para la adaptación al cambio climático.

La integración de las observaciones en medios actuales con las paleoperspectivas obtenidas mediante el estudio de los cambios pasados en lo referido a desoxigenación y productividad marina derivados de variaciones climáticas resulta de particular importancia para la elaboración de proyecciones oceanográficas a largo plazo (a escala centenaria) en el marco del cambio climático actual. El informe del IPCC de 2023 mostraba que, como tendencia general, la superficie del océano mantendría altos niveles de oxígeno disuelto debido al intercambio aire-mar y a la fotosíntesis; sin embargo, las aguas mesopelágicas y las aguas profundas pueden experimentar una desoxigenación importante, ya que la estratificación en los 200 metros superiores del océano ha ido aumentando significativamente desde 1970. Los resultados presentados en el Capítulo II apoyan este aumento, demostrando que los medios profundos han sido los ambientes marinos que primero experimentaron el agotamiento del oxígeno durante el depósito de los sapropeles debido a la estratificación de la columna de agua y a la ralentización de la circulación en aguas profundas debido a la mayor flotabilidad del agua superficial debido a su menor salinidad. En la actualidad, el Mediterráneo más occidental es una de las zonas más productivas del Mediterráneo (Macias et al., 2015). Sin embargo, la reconstrucción de la paleoproductividad en la cuenca occidental de Alborán sugiere que si los sistemas de surgencia de agua profunda, responsables de esta productividad en el Mar de Alborán, cesaran debido al aumento previsto de la estratificación de la columna de agua y al debilitamiento de la mezcla vertical como resultado del calentamiento global, la productividad marina disminuiría significativamente en esta región. En general, la aridificación progresiva impediría que los ríos aportaran suficientes nutrientes para sostener el aumento de la productividad marina, lo que conduciría a una reducción significativa en los flujos de carbono a las zonas más profundas.

En resumen, esta tesis ha permitido comprender la respuesta de las condiciones de oxigenación en medios marinos profundos a los cambios en la circulación termohalina inducidos por variaciones climáticas. También arroja luz sobre las respuestas de la productividad marina (a escala centenaria y multicentenaria) a la variabilidad climática rápida, mejorando así nuestra capacidad para prever cambios en los ambientes marinos derivados del cambio climático actual, particularmente en el caso del Mar Mediterráneo. La integración de las paleoperspectivas también puede ayudar a generar previsiones y proyecciones de los cambios oceánicos, que juegan un papel importante en la adaptación y mitigación de los impactos de los cambios medioambientales derivados del cambio climático actual y de las actividades humanas.

Future Research Perspectives

Future Research Perspectives

This section outlines possible directions for future research, building on the results and findings of this thesis. These potential avenues involve state-of-the-art methodologies, techniques and approaches to try to address some of the open questions on the conducted research.

Deposition of aerosols and dust from continental sources brings bioavailable nutrients to the surface waters as iron, nitrate and phosphate that tend to control biological production. However, there are open questions regarding the role of aeolian dust input on ocean primary productivity dynamics. This issue is increasingly pertinent given projections that aridification will intensify in many regions around the globe in the coming decades, including the Mediterranean –see Fig. 1 (IPCC, 2023). The Mediterranean, adjacent to the Sahara-Sahel –the globe's major dust source– receives a substantial amount of aeolian dust, which plays a crucial role as a nutrient source, particularly under conditions of increasing regional aridification and reduced fluvial input

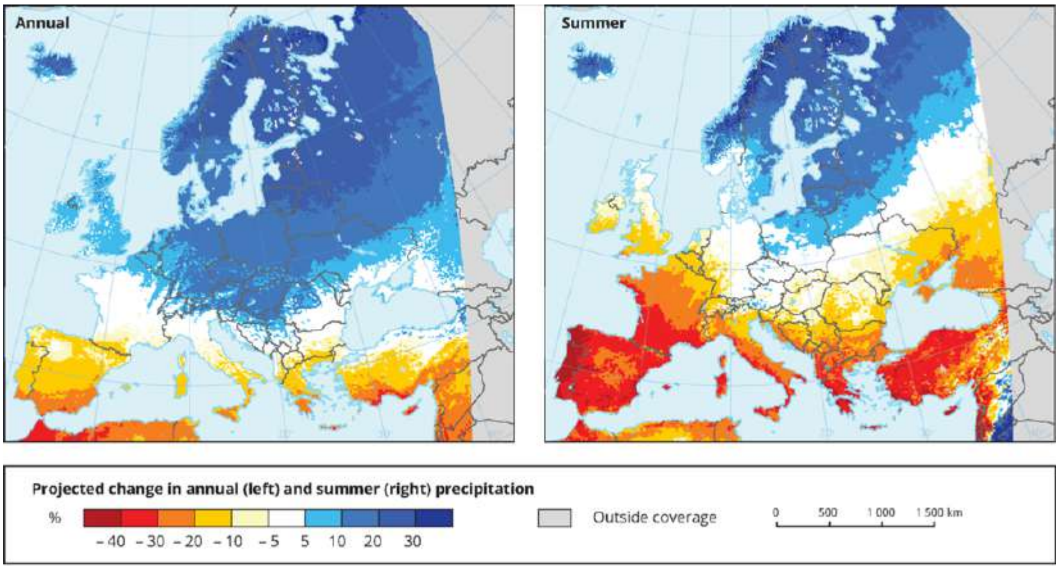

Figure 1. *Projected changes in annual (left) and summer (right) precipitation (%) in the period 2071-2100 compared to the baseline period 1971-2000 for the forcing scenario RCP 8.5. Model simulations from the EURO-CORDEX initiative of the European Environmental Agency (https://www.eea.europa.eu/data-and-maps/figures/projected-changes-in-annual-and-4).*

Despite the significant role of dust on marine productivity dynamics, few studies have delved into the consequences of dust deposition on nutrient budgets variability and marine productivity in the Mediterranean Sea (e.g., Richon et al., 2018a, b). In this regard, marine sediment intervals from the Mediterranean that correspond to arid periods, such as Heinrich events, provide valuable records for studying primary productivity responds to arid climatic conditions and aeolian dust variations. Consequently, through dinoflagellates analyses and geochemical proxies (e.g., Ba/Al, TOC and δ^{13}C) I intend to further study marine productivity responses during recent arid climatic events (i.e., Heinrich events) in the Mediterranean to better understand the links between aeolian input and marine productivity dynamics (refer to Fig. 2).

Moreover, gaining paleoperspectives on the long-term changes and spatial variability of marine productivity in the Mediterranean is crucial for developing more robust projections. To contribute to this understanding, I plan to analyze marine productivity responses to Holocene climate variability in both the Eastern and Western Mediterranean basins (Fig. 2). This analysis will include assessing differences in dinoflagellate assemblages, geochemical trends, and overall primary productivity patterns between the Alboran Basin and the Levantine Basin throughout the Holocene record (Fig. 2).

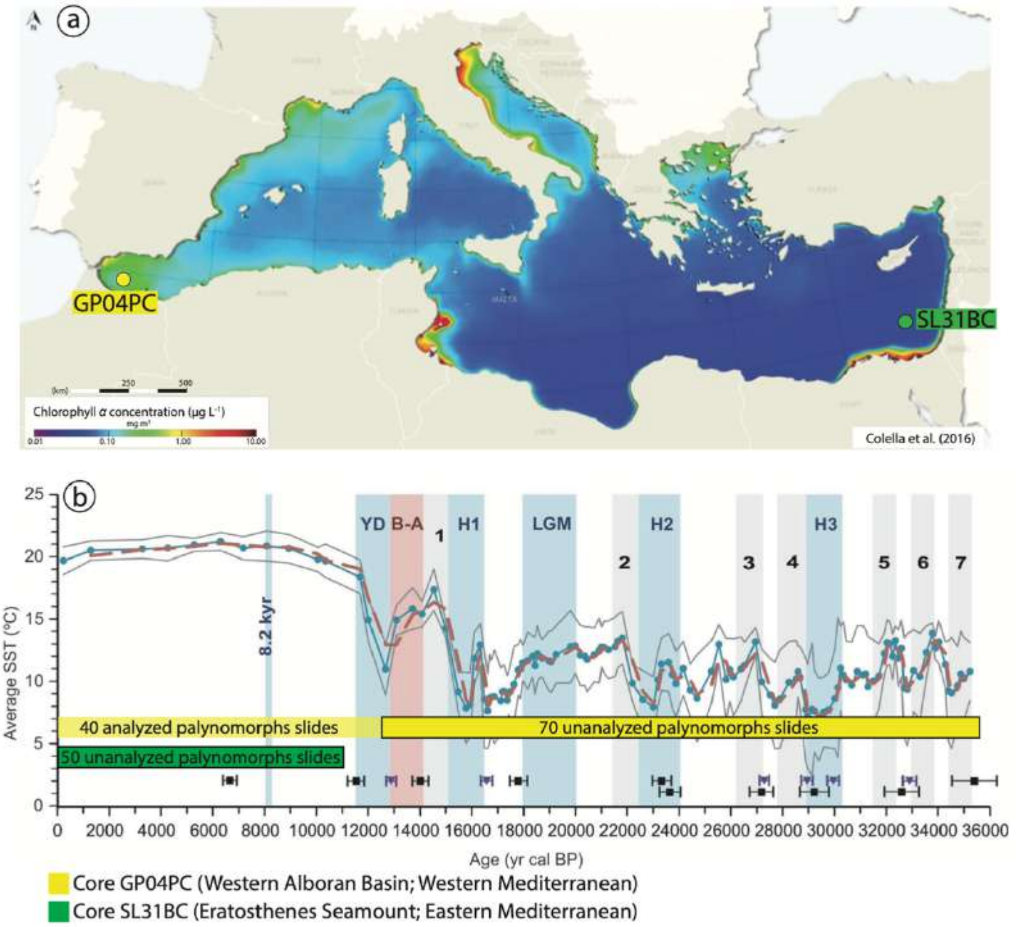

Figure 1. *(a) Location of cores GP04PC (Western Mediterranean, water-depth: 1306.5 m) and SL31BC (Eastern Mediterranean, water-depth: 1257 m) (modified from Colella et al., 2016). (b) Time intervals of analyzed and unanalyzed palynomorphs slides in both cores. 110 palynomorphs slides were prepare from core GP04PC (modified from Morcillo-Montalbá et al., 2021), covering the last 35 ka. Yet, only 40 palynomorphs slides, representing the Holocene period, were analyzed for the paleoproductivity reconstruction presented in Chapter VI. The remaining 70 palynomorphs slides –which expand from 12 ka to 35 ka at a resolution of 250-300 years and cover, the Last Glacial Maximum (LGM), the last three Heinrich events (H1, H2 and H3), the Dansgaard-Oeschger interstadials (1–7), and the Bölling-Alleröd event (B-A)– have not been analyzed yet. 50 palynomorph slides were prepared, but not analyzed, from core SL31BC, spanning the last 11 ka (i.e., the Holocene period), at a resolution of ~200 years.*

On the other hand, δ^{138}Ba$_{barite}$ stands out as a promising new geochemical tool in paleoproductivity reconstructions (Bridgestock et al., 2015, 2018; Horner et al., 2015, 2021; Hsieh and Henderson, 2017; Middleton et al., 2023). In this regard, barite was separated from S1 sediment samples at different Eastern Mediterranean settings (ODP sites 964, 966, 967, 968, 969, and 971; Fig. 3 and Table 1 in Appendix III) with the aim to measure δ^{138}Ba$_{barite}$ to assess the spatial variability of primary productivity in Eastern Mediterranean during the deposition of sapropel S1. In the same manner, pelagic barite has been separated from sapropels S5, S6, S7, S8, S17, S18, S29, S30, S31, S50, S51, S52, S53 and S54 deposited at the Ionian Basin abyssal plain (i.e., ODP Site 964) in order to assess variations in productivity during different sapropel events within the same marine setting (Fig. 3 and Table 1 in Appendix III). Some uncertainties regarding barium isotopic cycling in the water-column and sediments still remain unanswered. Therefore, results from these analyses would also help to better constraint the local hydrogeographic factors (e.g., local fluvial inputs and water-depth) influencing the Ba isotopic signature, such as productivity rate, local fluvial inputs, water-depth and diagenetic remineralization, in both modern and past marine environments.

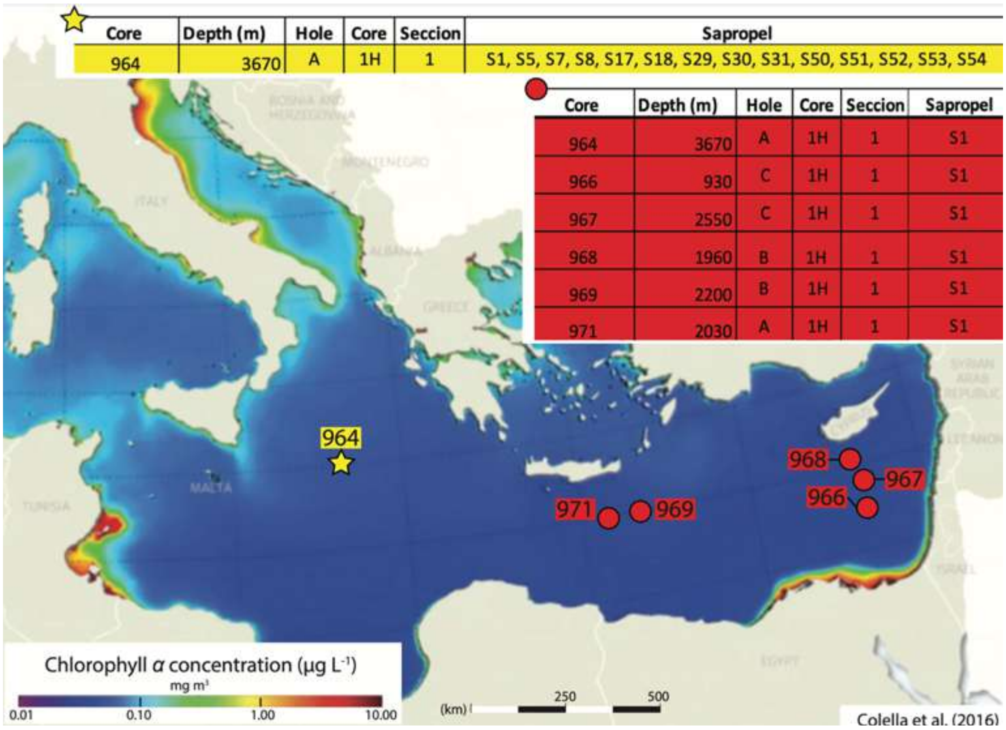

Core	Depth (m)	Hole	Core	Seccion	Sapropel
964	3670	A	1H	1	S1, S5, S7, S8, S17, S18, S29, S30, S31, S50, S51, S52, S53, S54

Core	Depth (m)	Hole	Core	Seccion	Sapropel
964	3670	A	1H	1	S1
966	930	C	1H	1	S1
967	2550	C	1H	1	S1
968	1960	B	1H	1	S1
969	2200	B	1H	1	S1
971	2030	A	1H	1	S1

Figure 3. *Locations of cores of sapropel samples for barite separation and δ^{138}Ba$_{barite}$ analysis. Sapropel S1 was sampled in all cores indicated in the figure (see red table for details). Holocene to Pliocene sapropels were sampled in core 964 (yellow star; see yellow table).*

Another important aspect regarding marine productivity oscillations in the Mediterranean is nitrogen cycle dynamics. Preliminary investigations focused on nitrogen isotopes in specific organic compounds extracted from various sapropels, ranging from the Pliocene to the Holocene sapropels, have been initiated. The main goals include assessing microbial and planktonic community differences and trophic dynamics across different sapropel events. I also intende to investigate nitrogen isotopes in sapropel S1 at varying depths along the Eratosthenes Seamount slope depths (~1000 m, 2000 m, and 3000 m) to understand nitrogen isotopic signal alterations during organic matter sinking and degradation in deep-marine basins, addressing a research gap. Furthermore, I intend to incorporate novel geochemical tools, such as isotopes of redox-sensitive trace metals (e.g., Fe, U, Mo, V and Cr isotopes; Dickson, 2017; Andersen et al., 2020; Benkovitz et al., 2020; Wei et al., 2020; Phillips and Xu, 2021; Sweere et al., 2021; Chiu et al., 2022; Li et al., 2023) for more precise paleoredox reconstructions of the studied sapropel events in this thesis.

Lastly, to gain deeper insights into the influence of benthic communities on the structural and functional dynamics of deep-marine sediments, intervals with abundant *Chondrites* (e.g., dark *Chondrites* below sapropel S8 at ODP Site 966; Fig. 4) were sampled for X-ray computerized axial microtomography analysis to study *Chondrites* 3D structure and its implications in modifying the sub-cm sedimentary architecture and petrophysical properties (e.g., permeability, porosity and connectivity), which in turn influence internal fluids dynamics and biogeochemical processes of deep-marine sediments. Moreover, sediment-thin sections are going to be prepared to further explore the consequences of sub-cm bioturbation in the distribution and biogeochemical cycling of trace elements in organic-rich sediments, continuing in this way the study presented in Chapter V.

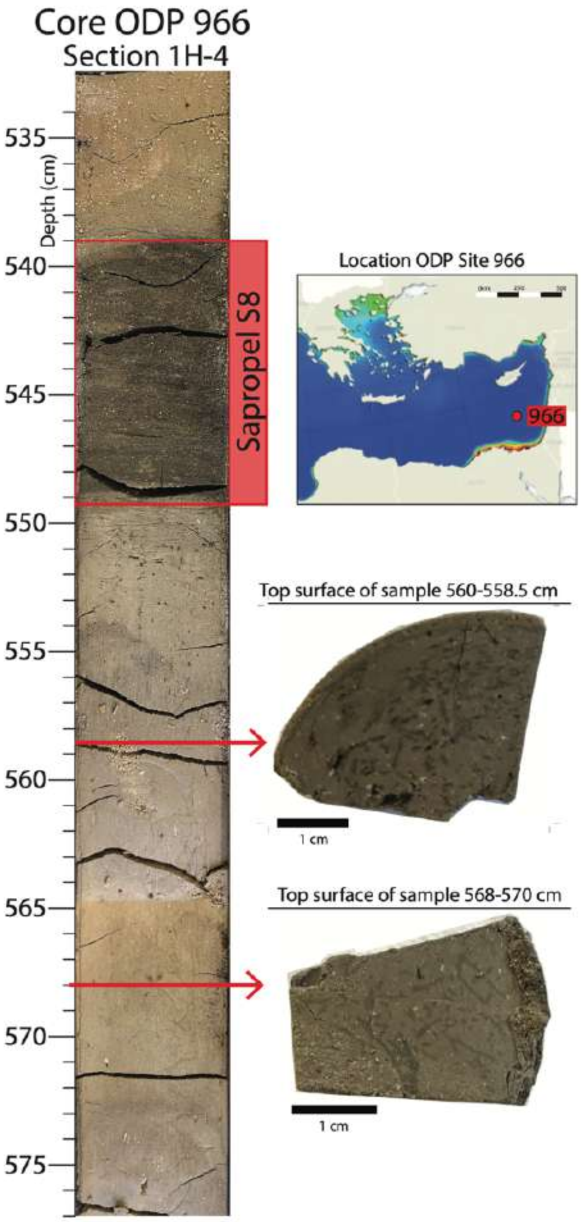
Core ODP 966
Section 1H-4
Depth (cm)
535
540
545
550
555
560
565
570
575
Sapropel S8
Location ODP Site 966
966
Top surface of sample 560-558.5 cm
1 cm
Top surface of sample 568-570 cm
1 cm

Figure 4. *Sapropel S8 from ODP Site 966 (Eratosthenes Seamount) sampled to study Chondrites architecture and sub-cm sedimentary disturbances using X-ray computerized axial microtomography. Dark Chondrites can be observed at the top of the 2 cm thick samples.*

Acknowledgements

Agradecimientos

Hace 3 años y medio, embarqué en el emocionante viaje de un doctorado con un corazón lleno de ilusión, pero también con la inevitable sensación de estar un tanto perdido en el mundo de la investigación científica. Sin embargo, en este trayecto, descubrí que más allá de los datos y las teorías, la verdadera fortaleza reside en la red de apoyo que nos rodea. Familiares, amigos y colegas profesionales se convirtieron en los pilares sobre los cuales construí mi camino hacia la culminación de esta tesis doctoral. A través de sus palabras de aliento y gestos de solidaridad, encontré el valor para enfrentar los desafíos, superar los obstáculos y persistir en la búsqueda del conocimiento

Quisiera comenzar expresando mi más sincero agradecimiento a mis distinguidos supervisores, la Dra. Francisca Martínez Ruiz y el Dr. Francisco Javier Rodríguez Tovar, por su apoyo incondicional, motivación constante y la confianza que depositaron en mí a lo largo de este arduo pero gratificante proceso. No tengo más que palabras de gratitud hacia ustedes; siempre han dedicado tiempo para mí y han respaldado mis ideas de manera incondicional.

No puedo pasar por alto el cálido recibimiento y la generosa hospitalidad brindada por la Dra. Francesca Sangiorgi y la Dra. Adina Paytan durante mis estancias en sus respectivos centros. Su amabilidad y apoyo fueron una parte integral de mi experiencia investigadora. Además, mi gratitud se extiende al Dr. Gert de Lange, cuyos fascinantes aportes científicos y conversaciones enriquecedoras han sido fundamentales para el desarrollo de mi investigación.

Deseo expresar mi agradecimiento a todos los técnicos de laboratorio del IACT y Centro de Instrumentación Científica de la Universidad de Granada, así como al personal técnico del Laboratorio de Palinología de la Universidad de Utrecht y del Laboratorio de Biogeoquímica Paytan de la Universidad de California (Santa Cruz). Su arduo trabajo y dedicación fueron esenciales para llevar a cabo los análisis que sustentan esta tesis. Su experticia y asistencia fueron invaluables en cada etapa del proceso investigador. También quiero agradecer al personal administrativo del IACT por su incansable ayuda en la gestión de documentos, trámites y logística, facilitando así el desarrollo fluido de este proyecto.

Un reconocimiento especial va dirigido a mis compañeros de Doctorado por los descansos de café compartidos, las discusiones enriquecedoras y el apoyo mutuo que nos brindamos a lo largo de esta travesía académica.

A mis padres, Elba Matilde Contreras y Carlos Monedero, les debo una deuda de gratitud que nunca podré saldar completamente. Su apoyo inquebrantable, su aliento constante y el sacrificio que hicieron para permitirme perseguir mis sueños personales y profesionales son la esencia misma de mi determinación y perseverancia.

A mis fieles compañeros caninos, Rocket y Rufus, les debo un agradecimiento especial por su constante apoyo emocional. Su presencia siempre reconfortante han sido un recordatorio constante de la importancia de encontrar alegría en los momentos más simples de la vida.

A mí mismo, quiero expresar un agradecimiento especial por mi perseverancia y determinación en lograr todos los objetivos planteados al iniciar este viaje académico y profesional. Cada obstáculo superado y cada meta alcanzada han sido testimonio de mi compromiso con la excelencia y mi pasión por el conocimiento.

Y, por último, pero no menos importante, quiero expresar mi profundo agradecimiento a mi esposa, Andrea Moreno Braña, por ser mi roca, mi inspiración y mi mayor apoyo. Su amor incondicional, paciencia y comprensión han sido la fuerza impulsora detrás de cada logro alcanzado.

A todos ustedes, mi más sincero agradecimiento. Este logro no habría sido posible sin su inestimable contribución y apoyo.

¡Esto solo es el inicio de una nueva aventura!

References

Abbott, O.J. (1977). The toxicity of ammonium molybdate to marine invertebrates. Mar. Pollut. Bull. 8, 204-205. https://doi.org/10.1016/0025-326X(77)90107-2.

Aguilera, M., Ferrio, J.P., Pérez, G., Araus, J.L., Voltas, J. (2012). Holocene changes in precipitation seasonality in the western Mediterranean Basin: a multi-species approach using $\delta^{13}C$ of archaeobotanical remains. J. Quat. Sci. 27, 192-202. https://doi.org/10.1002/jqs.1533.

Algeo, T.J., Li, C. (2020). Redox classification and calibration of redox thresholds in sedimentary systems. Geochim. Cosmochim. Acta 287, 8-26. https://doi.org/10.1016/j.gca.2020.01.055.

Algeo, T.J., Liu, J. (2020). A re-assessment of elemental proxies for paleoredox analysis. Chem. Geol. 540, 119549. https://doi.org/10.1016/j.chemgeo.2020.119549.

Algeo, T.J., Lyons, T.W., Blakey, C., Over, J. (2007). Hydrographic conditions of the Devono-Carboniferous north American Seaway inferred from sedimentary Mo-TOC relationships. Palaeogeogr. Palaeoclimatol. Palaeoecol. 256, 204-230. https://doi.org/10.1016/j.palaeo.2007.02.035.

Algeo, T.J., Lyons, T.W. (2006). Mo-TOC covariation in modern anoxic marine environments: implication for analysis of paleoredox and paleohydrographic conditions. Paleoceanography 21, PA1016. https://doi.org/10.1029/2004PA001112.

Algeo, T.J., Maynard, J.B. (2004). Trace-element behavior and redox facies in core shales of Upper Pennsylvanian Kansas-type cyclothems. Chem. Geol. 206, 289-318. https://doi.org/10.1016/j.chemgeo.2003.12.009.

Algeo, T.J., Maynard, J.B. (2008). Trace metal covariation as a guide to water-mass conditions in ancient anoxic marine environments. Geosphere 4, 872-887. https://doi.org/10.1130/GES00174.1.

Algeo, T.J., Morford, J., Cruse, A. (2011). New applications of trace metals as proxies in Marine Paleoenvironments. Chem. Geol. 307, 160-164. https://doi.org/10.1016/j.chemgeo.2012.03.009.

Algeo, T.J., Rowe, H. (2012). Paleoceanographic applications of trace-metal concentration data. Chem. Geol. 324-325, 6-18. https://doi.org/10.1016/j.chemgeo.2011.09.002.

Algeo, T.J., Tribovillard, N. (2009). Environmental analysis of paleoceanographic systems based on molybdenum-uranium covariation. Chem. Geol. 268, 211-225. https://doi.org/10.1016/j.chemgeo.2009.09.001.

Aller, R.C. (1994). Bioturbation and remineralization of sedimentary organic matter: effects of redox oscillation. Chem. Geol. 114, 331-345. https://doi.org/10.1016/ 0009-2541(94)90062-0.

Álvarez-Iglesias, P., Rubio, B., Millos, J. (2012). Isotopic identification of natural vs. anthropogenic lead sources in marine sediments from the inner Ría de Vigo (NW Spain). Sci. Total Environ. 437, 22-35. https://doi.org/10.1016/j.scitotenv.2012.07.063.

Amitai, Y., Ashkenazy, Y., Gildor, H. (2018). The effect of wind-stress over the Eastern Mediterranean on deep-water formation in the Adriatic Sea. Deep Sea Res. Part II Top. Stud. Oceanogr. 164, 5-13. https://doi.org/10.1016/j.dsr2.2018.11.015.

Andersen, M.B., Matthews, A., Bar-Matthews, M., Vance, D. (2020). Rapid onset of ocean anoxia shown by high U and low Mo isotope compositions of sapropel S1. Geochem. Perspect. Lett. 15, 10-14. https://doi.org/10.3929/ethz-b-000445569.

Andersen, M.B., Matthews, A., Vance, D., Bar-Matthews, M., Archer, C., de Souza, G.F. (2018). A 10-fold decline in the deep Eastern Mediterranean thermohaline overturning circulation during the last interglacial period. EPSL 503, 58-67. https://doi.org/ 10.1016/j.epsl.2018.09.013.

Araus, J.L., Febrero, A., Buxó, R., Camalich, M.D., Martín, D., Molina, F., Rodríguez-Ariza, M Romagosa, I. (1997). Changes in carbon isotope discrimination in grain cereals from different regions of the western Mediterranean Basin during the past seven millennia. Palaeoenvironmental evidence of a differential change in aridity during the late Holocene. Glob. Change Biol. 3, 107-118. https://doi.org/10.1046/j.1365-2486.1997.00056.x.

Ariztegui, D., Asioli, A., Lowe, J.J., Trincardi, F., Vigliotti, L., Tamburini, F., Chondrogianni, C., Accorsi, C.A., Bandini Mazzanti, M.B., Mercuri, A.M., van der Kaars, S., McKenzie, J.A., Oldfield, F. (2000). Palaeoclimate and the formation of sapropel S1: Inferences from late quaternary lacustrine and marine sequences in the Central Mediterranean region. Palaeogeogr. Palaeoclimatol. Palaeoecol. 158, 215-240. https://doi.org/10.1016/S0031-0182(00)00051-1.

Arnaboldi, M., Meyers, P. (2007). Trace element indicators of increased primary production and decreased water-column ventilation during deposition of latest Pliocene sapropels at five locations across the Mediterranean Sea. Palaeogeogr. Palaeoclimatol. Palaeoecol. 249, 425-443. https://doi.org/10.1016/j. palaeo.2007.02.016.

Arndt, S., Jørgensen, B., LaRowe, D.E., Middelburg, J., Pancost, R.D., Regnier, P. (2013). Quantifying the degradation of organic matter in marine sediments: a review and synthesis. Earth Sci. Rev. 123, 53-86. https://doi.org/10.1016/j. earscirev.2013.02.008.

Astraldi, M., Gasparini, G.P. (1992). The seasonal characteristics of the circulation in the North Mediterranean basin and their relationship with the atmospheric-climatic conditions. J. Geophys. Res. 97, 9531-9540. https://doi.org/10.1029/92JC00114.

Ausín, B., Flores, J.A., Sierro, F.J., Bárcena, M.-A., Hernández-Almeida, I., Francés, G., Gutiérrez-Arnillas, E., Martrat, B., Grimalt, J.O., Cacho, I. (2015a). Coccolithophore productivity and surface water dynamics in the Alboran Sea during the last 25kyr. Palaeogeogr. Palaeoclimatol. Palaeoecol. 418, 126-140. https://doi.org/10.1016/j. palaeo.2014.11.011.

Ausín, B., Flores, J.A., Sierro, F.J., Cacho, I., Hernández-Almeida, I., Martrat, B., Grimalt, J.O. (2015b). Atmospheric patterns driving Holocene productivity in the Alboran Sea (Western Mediterranean): a multiproxy approach. Holocene 25, 583-595. https://doi.org/10.1177/0959683614565952.

Ausín, B., Hodell, D.A., Cutmore, A., Eglinton, T.I. (2020). The impact of abrupt deglacial climate variability on productivity and upwelling on the southwestern Iberian margin. Quat. Sci. Rev. 230, 106139. https://doi.org/10.1016/j. quascirev.2019.106139.

Azrieli-Tal, I., Matthews, A., Bar-Matthews, M., Almogi-Labin, A., Vance, D., Archer, C., Teutsch, N. (2014). Evidence from molybdenum and iron isotopes and molybdenum-uranium covariation for sulphidic bottom waters during Eastern Mediterranean sapropel S1 formation. EPSL. 393, 231-242. https://doi.org/ 10.1016/j.epsl.2014.02.054.

Báez, J.C., Gimeno, L., Gómez-Gesteira, M., Ferri-Yáñez, F., Real, R. (2013). Combined Effects of the North Atlantic Oscillation and the Arctic Oscillation on Sea Surface Temperature in the Alborán Sea. PLOS ONE 8, e62201. https://doi.org/10.1371/journal.pone.0062201.

Baldini, L.M., McDermott, F., Baldini, J.U., Arias, P., Cueto, M., Fairchild, I.J., Hoffmann, D.L., Mattey, D.P., Müller, W., Nita, D.C., Ontañón, R., García-Moncó, Richards, D.A. (2015). Regional temperature, atmospheric circulation, and sea-ice variability within the Younger Dryas Event constrained using a speleothem from northern Iberia. Earth Planet. Sci. Lett. 419, 101-110. https://doi.org/10.1016/j.epsl.2015.03.015.

Bárcena, M.A., Cacho, I., Abrantes, F., Sierro, F.J., Grimalt, J.O., Flores, J.A. (2001). Paleoproductivity variations related to climatic conditions in the Alboran Sea (western Mediterranean) during the last glacial-interglacial transition: The diatom record. Palaeogeogr. Palaeoclimatol. Palaeoecol. 167, 337-357. https://doi.org/10.1016/S0031-0182(00)00246-7.

Bárcena, M.A., Flores, J.A., Sierro, F.J., Pérez-Folgado, M., Fabres, J., Calafat, A., Canals, M. (2004). Planktonic response to main oceanographic changes in the Alboran Sea (Western Mediterranean) as documented in sediment traps and surface sediments. Mar. Micropaleontol. 53, 423-445. https://doi.org/10.1016/j.marmicro.2004.09.009.

Bartolomé, M., Moreno, A., Sancho, C., Stoll, H.M., Cacho, I., Spötl, C., Belmonte, Á., Edwards, R.L., Cheng, H., Hellstrom, J.C. (2015). Hydrological change in Southern Europe responding to increasing North Atlantic overturning during Greenland Stadial 1. Proc. Natl. Acad. Sci. 112, 6568-6572. https://doi.org/10.1073/pnas.1503990112.

Barton, A.D., Lozier, M.S., Williams, R.G. (2015). Physical controls of variability in North Atlantic phytoplankton communities. Limnol. Oceanogr. 60, 181-197. https://doi.org/10.1002/lno.10011.

Basterretxea, G., Font-Muñoz, J.S., Salgado-Hernanz, P.M., Arrieta, J., Hernández-Carrasco, I. (2018). Patterns of chlorophyll interannual variability in Mediterranean biogeographical regions. Remote Sens. Environ. 215, 7-17. https://doi.org/10.1016/j.rse.2018.05.027.

Baucon, A., Bednarz, M., Dufour, S., Felletti, F., Malgesini, G., Neto de Carvalho, C., Niklas, K.J., Wehrmann, A., Batstone, R., Bernardini, F., Briguglio, A., Cabella, R., Cavalazzi, B., Ferretti, A., Zanzerl, H., McIlroy, D. (2020). Ethology of the trace fossil Chondrites: form, function and environment. Earth Sci. Rev. 202, 192989. https:// doi.org/10.1016/j.earscirev.2019.102989.

Bea, F. (1996). Residence of REE, Y, Th and U in granites and crustal protoliths: implications for the chemistry of crustal melts. J. Petrol. 37, 521-532. https://doi. org/10.1093/petrology/37.3.521.

Bea, F., Fershtater, G.B., Montero, P., Smirnov, V.N., Molina, J.F. (2005). Deformation- driven differentiation of granitic magma: the Stepninsk pluton of the Uralides, Russia. Lithos 81, 209-233. https://doi.org/10.1016/j.lithos.2004.10.004.

Bea, F., Montero, P., Stroh, A., Baasner, J. (1996). Microanalysis of minerals by an Excimer UV-LA-ICP-MS system. Chem. Geol. 133, 145-156. https://doi.org/10.1016/S0009-2541(96)00073-3.

Behar, F., Beaumont, V., De Penteado, H.L. (2001). Rock-Eval 6 technology: performances and developments. Oil Gas Sci. Technol. 56, 111-134. https://doi.org/10.2516/ogst: 2001013.

Bektursunova, R., L'Heureux, I. (2011). A reaction-transport model of periodic precipitation of pyrite in anoxic marine sediments. Chem. Geol. 287, 158-170. https://doi.org/10.1016/j.chemgeo.2011.06.004.

Benito, G., Greenbaum, N., Medialdea, A., Calle, M., Sánchez-Moya, Y., Machado, M., Ballesteros-Cánovas, J.A., Corella, J.P. (2023). Late Pleistocene-Holocene multi-decadal patterns of extreme floods in NW Iberia: The Duero River palaeoflood record. Quat. Sci. Rev. 321, 108356. https://doi.org/10.1016/j.quascirev.2023.108356.

Benkovitz, A., Matthews, A., Teutsch, N., Poulton, S.W., Bar-Matthews, M., Almogi- Labin, A. (2020). Tracing water column euxinia in Eastern Mediterranean Sapropels S5 and S7. Chem. Geol. 545, 119627. https://doi.org/10.1016/j. chemgeo.2020.119627.

Bergillos, R.J., Ortega-Sánchez, M. (2017). Assessing and mitigating the landscape effects of river damming on the Guadalfeo River delta, southern Spain. Landsc. Urban Plann. 165, 117-129. https://doi.org/10.1016/j.landurbplan.2017.05.002.

Berner, R.A. (1969). Migration of iron and sulfur within anaerobic sediments during early diagenesis. Am. J. Sci. 267, 19-42. https://doi.org/10.2475/ajs.267.1.19.

Berner, R.A. (1970). Sedimentary pyrite formation. Am. J. Sci. 268, 1-23. https://doi.org/ 10.2475/ajs.268.1.1.

Berner, R.A. (1981). A new geochemical classification of sedimentary environments. J. Sediment. Res. 51, 359-365. https://doi.org/10.1306/212F7C7F-2B24-11D7-8648000102C1865D.

Berrang, P.G., Grill, E.V. (1974). The effect of manganese oxide scavenging on molybdenum in Saanich inlet, British Columbia. Mar. Chem. 2, 125-148. https://doi.org/10.1016/0304-4203(74)90033-4.

Bertine, K.K., Turekian, K.K. (1973). Molybdenum in marine sediments. Geochim. Cosmochim. Acta 37, 1415-1434. https://doi.org/10.1016/0016-7037(73)90080-X.

Bethoux, J.P., Gentili, B. (1999). Functioning of the Mediterranean Sea: past and present changes related to freshwater input and climate changes. J. Mar. Syst. 20, 33-47. https://doi.org/10.1016/S0924-7963(98)00069-4.

Beusen, A., Boyd, P.W., Breitburg, D., Comeau, S., Dupont, S., Hansen, P.J., Isensee, K., Kudela, R., Lundholm, N., Otto, S., Schwing, F., Tilbrook, B. (2022). Multiple ocean stressors: a scientific summary for policy makers. https://doi.org/10.25607/OBP-1724.

Bianchi, G.G., McCave, N. (1999). Holocene periodicity in North Atlantic climate and deep- ocean flow south of Iceland. Nature 397, 515-517. https://doi.org/10.1038/17362.

Bishop, J. (1988). The barite-opal-organic carbon association in oceanic particulate matter. Nature 332, 341-343. https://doi.org/10.1038/332341a0.

Blaauw, M., Christen, J.A. (2011). Flexible paleoclimate age-depth models using an autoregressive gamma process. Bayesian Analysis 6, 457-474. https://doi.org/10.1214/ba/1339616472.

Blanchet, C.L., Tjallingii, R., Schleicher, A.M., Schouten, S., Frank, M., Brauer, A. (2021). Deoxygenation dynamics on the western Nile deep-sea fan during sapropel S1 from seasonal to millennial timescales. Clim. Past 17, 1025-1050. https://doi.org/10.5194/cp-17-1025-2021.

Bond, G., Kromer, B., Beer, J., Muscheler, R., Evans, M.N., Showers, W., Hoffmann, S., Lotti-Bond, R., Hajdas, I., Bonani, G. (2001). Persistent solar influence on North Atlantic climate during the Holocene. Science 294, 2130-2135. https://doi.org/10.1126/science.1065680.

Bond, G., Showers, W., Cheseby, M., Lotti, R., Almasi, P., de Menocal, P., Priore, P., Cullen, H., Hajdas, I., Bonani, G. (1997). A pervasive millennial-scale cycle in North Atlantic Holocene and Glacial climates. Science 278, 1257-1266. https://doi.org/10.1126/science.278.5341.1257.

Boni, L., Ceredi, A., Guerrini, F., Milandri, A., Pistocchi, R., Poletti, R., Pompei, M. (2000). Toxic Protoceratium reticulatum (Peridiniales, Dinophyta) in the north-western Adriatic Sea (Italy). In: Hallegraeff, G.M., Blackburn, S.I., Bolch, C.J., Lewis, R.J. (Eds.), Harmful Algal Blooms, Proceedings of the IX International Conference on Harmful Algal Blooms. UNESCO, Paris, pp. 137-140.

Bopp, L., Resplandy, L., Orr, J.C., Doney, S.C., Dunne, J.P., Gehlen, M., Halloran, P., Heinze, C., Ilyina, T., Séférian, R., Tjiputra J., Vichi, M. (2013). Multiple stressors of ocean ecosystems in the 21st century: projections with CMIP5 models. Biogeosciences 10, 6225-6245. https://doi.org/10.5194/bg-10-6225-2013.

Bostick, B.C., Fendorf, S., Helz, G.R. (2003). Differential Adsorption of Molybdate and Tetrathiomolybdate on Pyrite (FeS_2). Environ. Sci. Technol. 37, 285-291. https://doi.org/10.1021/es0257467.

Böttcher, M., Effenberger, H., Gehlken, P.L., Grathoff, G., Schmidt, B., Geprägs, P., Bahlo, R., Dellwig, O., Leipe, T., Winde, V., Deutschmann, A., Stark, A., Gallego- Torres, D., Martínez-Ruiz, F. (2012). $BaMn[CO_3]^{2-}$ a previously unrecognized double carbonate in low-temperature environments: Structural, spectroscopic, and textural tools for future identification. Chem. Erde 72, 85-89. https://doi.org/10.1016/j. chemer.2012.01.001.

Bout-Roumazeilles, V., Combourieu-Nebout, N., Desprat, S., Siani, G., Turon, J. L., Essallami, L. (2013). Tracking atmospheric and riverine terrigenous supplies variability during the last glacial and the Holocene in central Mediterranean. Clim. Past 9, 1065-1087. https://doi.org/10.5194/cp-9-1065-2013.

Breit, G.N., Wanty, R.B. (1991). Vanadium accumulation in carbonaceous rocks: a review of geochemical controls during deposition and diagenesis. Chem. Geol. 91, 83-97. https://doi.org/10.1016/0009-2541(91)90083-4.N.

Breitburg, D., Levin, L.A., Oschlies, A., Grégoire, M., Chavez, F.P., Conley, D.J., Garçon, V., Gilbert, D., Gutiérrez, D., Isensee, K., Jacinto, G.S., Limburg, K.E., Montes, I., Naqvi, S.W.A., Pitcher, G.C., Rabalais, N.N., Roman, M.R., Rose, K.A., Seibel, B.A., Telszewski, M., Yasuhara, M., Zhang, J. (2018). Declining oxygen in the global ocean and coastal waters. Science 359, 6371. https://doi.org/10.1126/ science.aam7240.

Bridgestock, L., Hsieh, Y.T., Porcelli, D., Henderson, G.M. (2019). Increased export production during recovery from the Paleocene-Eocene thermal maximum constrained by sedimentary Ba isotopes. Earth Planetary Sci. Lett., 510, 53-63. https://doi.org/10.1016/j.epsl.2018.12.036.

Broecker, W.S., Andree, M., Wolfli, W., Oeschger, H., Bonani, G., Kennett, J., Peteet, D. (1988). The chronology of the last deglaciation: Implications to the cause of the Younger Dryas event. Paleoceanography 3, 1-19. https://doi.org/10.1029/PA003i001p00001.

Broecker, W.S., Denton, G.H., Edwards, R.L., Cheng, H., Alley, R.B., Putnam, A.E. (2010). Putting the Younger Dryas cold event into context. Quat. Sci. Rev. 29, 1078-1081. https://doi.org/10.1016/j.quascirev.2010.02.019.

Bromley, R.G. (1996). Trace fossils: biology, taphonomy and applications, 2nd ed. Chapman & Hall, London. Geol. Mag. 134, 409-421. https://doi.org/10.1017/S0016756897316987.

Bromley, R.G., Ekdale, A.A. (1984). Chondrites: a trace fossil indicator of anoxia in sediments. Science 224, 872-874. https://www.jstor.org/stable/1692291.

Bruggeman, C., Maes, N. (2010). Uptake of uranium (VI) by pyrite under boom clay conditions: influence of dissolved organic carbon. Environ. Sci. Technol. 44, 4210-4216. https://doi.org/10.1021/es100919p.

Brumsack, H.J. (2006). The trace metal content of recent organic carbon-rich sediments: Implications for cretaceous black shale formation. Palaeogeogr. Palaeoclimatol. Palaeoecol. 232, 344-361. https://doi.org/10.1016/j.palaeo.2005.05.011.

Brun, P., Stamieszkin, K., Visser, A.W., Licandro, P., Payne, M.R., Kiørboe, T. (2019). Climate change has altered zooplankton-fuelled carbon export in the North Atlantic. Nat. Ecol. Evol. 3, 416-423. https://doi.org/10.1038/s41559-018-0780-3.

Buatois, L.A., Mángano, M.G. (2016). Ichnology: Organism-Substrate Interactions in Space and Time. Cambridge University Press, Cambridge/New York. https://doi.org/ 10.1017/CBO9780511975622.

Bulian, F., Kouwenhoven, T.J., Jiménez-Espejo, F.J., Krijgsman, W., Andersen, N., Sierro, F.J. (2022). Impact of the Mediterranean-Atlantic connectivity and the late Miocene carbon shift on deep-sea communities in the Western Alboran Basin. Palaeogeogr. Palaeoclimatol. Palaeoecol. 589, 110841. https://doi.org/10.1016/j.palaeo.2022.110841.

Cacho, I., Grimalt, J., Canals, M., Sbaffi, N., Schönfeld, R. (2001). Variability of the western Mediterranean Sea surface temperature during the last 25,000 years and its connection with the Northern Hemisphere climate changes. Paleoceanography 16, 40-52. https://doi.org/10.1029/2000pa000502.

Cacho, I., Grimalt, J.O., Canals, M. (2002). Response of the Western Mediterranean Sea to rapid climatic variability during the last 50,000 years: A molecular biomarker approach. J. Mar. Syst. 33, 253-272. https://doi.org/10.1016/S0924-7963(02)00061-1.

Cacho, I., Grimalt, J.O., Pelejero, C., Canals, M., Sierro, F.J., Flores, J.A., Shackleton, N. (1999). Dansgaard-Oeschger and Heinrich event imprints in Alboran Sea paleotemperatures. Paleoceanography 14, 698-705. https://doi.org/10.1029/1999PA900044.

Cacho, I., Grimalt, J.O., Sierro, F.J., Shackleton, N., Canals, M. (2000). Evidence for enhanced Mediterranean thermohaline circulation during rapid climatic coolings. Earth Planet. Sci. Lett. 183, 417-429. https://doi.org/10.1016/S0012-821X(00)00296-X.

Cacho, I., Shackleton, N., Elderfield, H., Sierro, F.J., Grimalt, J.O. (2006). Glacial rapid variability in deep-water temperature and $\delta^{18}O$ from the Western Mediterranean Sea. Quat. Sci. Rev. 25, 3294-3311. https://doi.org/10.1016/j.quascirev.2006.10.004.

Calvert, S.E. (1983). Geochemistry of Pleistocene sapropels and associated sediments from the Eastern Mediterranean. Oceanol. Acta 6, 255-267. https://archimer.ifremer.fr/doc/00114/22480/20161.pdf.

Calvert, S.E., Pedersen, T.F. (1993). Geochemistry of recent oxic and anoxic sediments: implications for the geological record. Mar. Geol. 113, 67-88. https://doi.org/10.1016/0025-3227(93)90150-T.

Calvert, S.E., Pedersen, T.F. (1996). Sedimentary geochemistry of manganese: implications for the environment of formation of manganiferous black shales. Econ. Geol. 91, 36-47. https://doi.org/10.2113/gsecongeo.91.1.36.

Calvert, S.E., Pedersen, T.F. (2007). Chapter Fourteen Elemental Proxies for Palaeoclimatic and Palaeoceanographic Variability in Marine Sediments: Interpretation and Application Dev. Mar. Geol. 567-644. https://doi.org/10.1016/S1572-5480(07)01019-6.

Camerlenghi, A., Ben, A., Huebscher, C., Forlin, E., Geletti, R., Brancatelli, G., Micallef, A., Saule, M., Facchin, L. (2019). Seismic markers of the Messinian salinity crisis in the deep Ionian Basin. Basin Res. 32, 716-738. https://doi.org/10.1111/bre.12392.

Camuera, J., Jiménez-Moreno, G., Ramos-Román, M.J., García-Alix, A., Jiménez-Espejo, F.J., Toney, J.L., Anderson, R.S. (2021). Chronological control and centennial-scale climatic subdivisions of the Last Glacial Termination in the western Mediterranean region. Quat. Sci. Rev. 255, 106814. https://doi.org/10.1016/j.quascirev.2021.106814.

Camuera, J., Ramos-Román, M.J., Jiménez-Moreno, G., García-Alix, A., Ilvonen, L., Ruha, L., Gil-Romera, G., González-Sampériz, P., Seppä, H. (2022). Past 200 kyr hydroclimate variability in the western Mediterranean and its connection to the African Humid Periods. Sci. Rep. 12, 9050. https://doi.org/10.1038/s41598-022-12047-1.

Canals, M., Danovaro, R., Heussner, S., Lykousis, V., Puig, P., Trincardi, F., Calafat, A.M., Durrieu de Madron, X., Palanques, A., S`anchez-Vidal, A. (2009). Cascades in Mediterranean submarine grand canyons. Oceanography 22, 26-43. https://doi.org/ 10.5670/oceanog.2009.03.

Canfield, D.E. (1994). Factors influencing organic carbon preservation in marine sediments. Chem. Geol. 114, 315-329. https://doi.org/10.1016/0009-2541(94)90061-2.

Canfield, D.E., Thamdrup, B. (2009). Towards a consistent classification scheme for geochemical environments, or, why we wish the term 'suboxic' would go away. Geobiology 4, 385-392. https://doi.org/10.1111/j.1472-4669.2009.00214.x.

Cantoni, C., Luchetta, A., Chiggiato, J., Cozzi, S., Schroeder, K., Langone, L. (2016). Dense water flow and carbonate system in the southern Adriatic: a focus on the 2012 event. Mar. Geol. 375, 15-27. https://doi.org/10.1016/j.margeo.2015.08.013.

Capotondi, A., Alexander, M.A., Bond, N.A., Curchitser, E. N., Scott, J.D. (2012). Enhanced upper ocean stratification with climate change in the CMIP3 models. J. Geophys. Res. Oceans 117, 1-23. https://doi.org/10.1029/2011JC007409.

Capotondi, L., Principato, M.S., Morigi, C., Sangiorgi, F., Maffioli, P., Giunta, S., Negri, A., Corselli, C. (2006). Foraminiferal variations and stratigraphic implications to the deposition of sapropel S5 in the eastern Mediterranean. Palaeogeogr. Palaeoclimatol. Palaeoecol. 235, 48-65. https://doi.org/10.1016/j. palaeo.2005.09.023.

Carlson, A.E. (2010). What caused the Younger Dryas cold event?. Geology 38, 383-384. https://doi.org/10.1130/focus042010.1.

Carter, S.C., Paytan, A., Griffith, E.M. (2020). Toward an improved understanding of the marine barium cycle and the application of marine barite as a paleoproductivity proxy. Minerals 10, 421. https://doi.org/10.3390/min10050421.

Casford, J.S.L., Rohling, E.J., Abu-Zied, R.H., Jorissen, F.J., Leng, M., Thomson, J. (2003). A dynamic concept for eastern Mediterranean circulation and oxygenation during sapropel formation. Palaeogeogr. Palaeoclimatol. Palaeoecol. 190, 103-119. https:// doi.org/10.1016/S0031-0182(02)00601-6.

Català, A., Cacho, I., Frigola, J., Pena, L.D., Lirer, F. (2018). Holocene hydrography evolution in the Alboran Sea: a multi-record and multiproxy comparison. Clim. Past 15, 927-942. https://doi.org/10.5194/cp-15-927-2019.

Chabaud, L., Sánchez Goñi, M.F., Desprat, S., Rossignol, L. (2014). Land-sea climatic variability in the eastern North Atlantic subtropical region over the last 14,200 years: atmospheric and oceanic processes at different timescales. The Holocene 24, 787-797. https://doi.org/10.1177/0959683614530439.

Chang, J., Li, Y., Lu, H. (2022). The morphological characteristics of authigenic pyrite formed in marine sediments. J. Mar. Sci. Eng. 10, 1533. https://doi.org/10.3390/ jmse10101533.

Chiu, C.F., Sweere, T.C., Clarkson, M.O., de Souza, G.F., Hennekam, R., Vance, D. (2022). Co-variation systematics of uranium and molybdenum isotopes reveal pathways for descent into euxinia in Mediterranean sapropels. EPSL. 585, 117527. https://doi.org/ 10.1016/j.epsl.2022.117527.

Chondrogianni, C., Accorsi, C.A., Bandini Mazzanti, M.B., Mercuri, A.M., van der Kaars, S., McKenzie, J.A., Oldfield, F. (2000). Palaeoclimate and the formation of sapropel S1: Inferences from late quaternary lacustrine and marine sequences in the Central Mediterranean region. Palaeogeogr. Palaeoclimatol. Palaeoecol. 158, 215-240. https://doi.org/10.1016/S0031-0182(00)00051-1.

Christaki, U., van Wambeke, F., Lefevre, D., Lagaria, A., Prieur, L., Pujo-Pay, M., Grattepanche, J.-D., Colombet, J., Psarra, S., Dolan, J.R., Sime-Ngando, T., Conan, P., Weinbauer, M.G., Moutin, T. (2011). Microbial food webs and metabolic state across oligotrophic waters of the Mediterranean Sea during summer. Biogeosciences 8, 1839-1852. https://doi.org/10.5194/bg-8-1839-2011.

Cita, M.B., Grignani, D. (1982). Nature and origin of Late Neogene Mediterranean sapropels. In: Academic, S.O., Schlanger, M.B. (Eds.), Nature and Origin of Cretaceous Carbon-Rich Facies, pp. 165-196. San Diego, California, USA.

Cita, M.B., Vergnaud-Grazzini, C., Robert, C., Chamley, H., Ciaranfi, N., Donofrio, S. (1977). Paleoclimatic record of a long deep-sea core from the eastern Mediterranean. Quat. Res. 8, 205-235. https://doi.org/10.1016/0033-5894(77)90046-1.

Colella, S., Falcini, F., Rinaldi, E., Sammartino, M., Santoleri, R. (2016). Mediterranean ocean colour chlorophyll trends. PloS one 11, e0155756. https://doi.org/10.1371/journal.pone.0155756.

Combourieu-Nebout, N., Londeix, L., Baudin, F., Turon, J. L., Von Grafenstein, R., Zahn, R. (1999). Quaternary marine and continental paleoenvironments in the western Mediterranean (Site 976, Alboran Sea): palynological evidence. In Proceedings of the Ocean Drilling Program. Scientific Results 161, 457-468. https://doi.org/10.2973/odp.proc.sr.161.238.1999.

Combourieu-Nebout, N., Peyron, O., Dormoy, I., Desprat, S., Beaudouin, C., Kotthoff, U., Marret, F. (2009). Rapid climatic variability in the west Mediterranean during the last 25 000 years from high resolution pollen data. Clim. Past 5, 503-521. https://doi.org/10.5194/cp-5-503-2009.

Cooley, S., Schoeman, D. Bopp, L., Boyd, P., Donner, S., Ghebrehiwet, D.Y., Ito, S.-I., Kiessling, W., Martinetto, P., Ojea, E., Racault, M.-F., Rost, B., Skern-Mauritzen, M. (2022). Oceans and Coastal Ecosystems and Their Services. In: Climate Change 2022: Impacts, Adaptation and Vulnerability. Contribution of Working Group II to the Sixth Assessment Report of the Intergovernmental Panel on Climate Change [H.-O. Pörtner, D.C. Roberts, M. Tignor, E.S. Poloczanska, K. Mintenbeck, A. Alegría, M. Craig, S. Langsdorf, S. Löschke, V. Möller, A. Okem, B. Rama (eds.)]. Cambridge University Press, Cambridge, UK and New York, NY, USA, pp. 379-550. https://doi.org/10.1017/9781009325844.005.

Crusius, J., Calvert, S., Pedersen, T., Sage, D. (1996). Rhenium and molybdenum enrichments in sediments as indicators of oxic, suboxic, and sulfidic conditions of deposition. Earth Planet. Sci. Lett. 145, 65-78. https://doi.org/10.1016/S0012-821X(96)00204-X.

D'Ortenzio, F., Ribera d'Alcalà, M. (2009). On the trophic regimes of the Mediterranean Sea: a satellite analysis. Biogeosciences 5,139-148. https://doi.org/10.5194/bg-6-139-2009.

Dale, B., Fjellså, A. (1994). Dinoflagellate cysts as paleoproductivity indicators: State of the Art, Potential, and Limits. In: Zahn, R., Pedersen, T.F., Kaminski, M.A., Labeyrie, L. (eds) Carbon Cycling in the Glacial Ocean: Constraints on the Ocean's Role in Global Change. NATO ASI Series 17, 521-537. https://doi.org/10.1007/978-3-642-78737-9_22.

Dale, B., Thorsen, T.A., Fjellså, A. (1999). Dinoflagellate cysts as indicators of cultural eutrophication in the Oslofjord, Norway. Estuar. Coast. Shelf Sci. 48, 371-382. https://doi.org/10.1006/ecss.1999.0427.

Dando, P.R., Southward, A.J., Southward, E.C. (2004). Rates of sediment sulphide oxidation by the bivalve mollusc Thyasira sarsi. Mar. Ecol. Prog. Ser. 280, 181-187. http://dx.doi.org/10.3354/meps280181.

Davis, B.A.S., Brewer, S., Stevenson, A.C., Guiot, J. (2003). The temperature of Europe during the Holocene reconstructed from pollen data. Quat. Sci. Rev. 22, 1701-1716. https://doi.org/10.1016/S0277-3791(03)00173-2.

de Lange, G.J. (1986). Early diagenetic reactions in interbedded pelagic and turbiditic sediments in the Nares Abyssal Plain (western North Atlantic): consequences for the composition of sediment and interstitial water. Geochim. Cosmochim. Acta 50, 2543-2561. https://doi.org/10.1016/0016-7037(86)90209-7.

de Lange, G.J., Middelburg, J.J., Pruysers, P.A. (1989). Discussion: Middle and Late Quaternary depositional sequences and cycles in the eastern Mediterranean. Sedimentology 36, 151-156. https://doi.org/10.1111/j.1365-3091.1989.tb00827.x.

de Lange, G.J., Thomson, J., Reitz, A., Slomp, C.P., Speranza Principato, M., Erba, E., Corselli, C. (2008). Synchronous basin-wide formation and redox-controlled preservation of a Mediterranean sapropel. Nat. Geosci. 1, 606-610. https://doi.org/ 10.1038/ngeo283.

de Menocal, P., Ortiz, J., Guilderson, T., Adkins, J., Sarnthein, M., Baker, L., Yarusinsky, M. (2000). Abrupt onset and termination of the African humid period: rapid climate responses to gradual insolation forcing. Quat. Sci. Rev. 19, 347-361. https://doi.org/10.1016/S0277-3791(99)00081-5.

De Menocal, P.B. (2015). End of the African Humid period. Nat. Geosci. 8, 86-87. https://doi.org/10.1038/ngeo2355.

de Vernal, A., Hillaire-Marcel, C. (2000). Sea-ice cover, sea-surface salinity and halo-/thermocline structure of the northwest North Atlantic: modern versus full glacial conditions. Quat. Sci. Rev. 19, 65-85. https://doi.org/10.1016/S0277-3791(99)00055-4.

de Vernal, A., Marret, F. (2007). Chapter nine organic-walled dinoflagellate cysts: tracers of sea-surface conditions. Developments in marine geology 1, 371-408. https://doi.org/10.1016/S1572-5480(07)01014-7.

Dehairs, F., Baeyens, W., Goeyens, L. (1992). Accumulation of suspended barite at mesopelagic depths and export production in the Southern Ocean. Science 258, 1332-1335. https://doi.org/10.1126/science.258.5086.1332.

Dehairs, F., Lambert, C.E., Chesselet, R., Risler, N. (1987). The biological production of marine suspended barite and the barium cycle in the Western Mediterranean Sea. Biogeochemistry 4, 19-139. https://doi.org/10.1007/BF02180151.

Delanghe, D., Bard, E., Hamelin, B. (2002). New TIMS constraints on the uranium-238 and uranium-234 in seawaters from the main ocean basins and the Mediterranean Sea. Mar. Chem. 80, 79-93. https://doi.org/10.1016/S0304-4203(02)00100-7.

Dellwig, O., Leipe, T., März, C., Glockzin, M., Pollehne, F., Schnetger, B., Yakushev, E.V., Böttcher, M.E., Brumsack, H.J. (2010). A new particulate Mn-Fe-P-shuttle at the redoxcline of anoxic basins. Geochim. Cosmochim. Acta 74, 7100-7115. https://doi. org/10.1016/j.gca.2010.09.017.

Dermawan, D., Wang, Y.F., You, S.J., Jiang, J.J., Hsieh, Y.K. (2022). Impact of climatic and non-climatic stressors on ocean life and human health: a review. Sci. Total Environ. 821, 153387. https://doi.org/10.1016/j.scitotenv.2022.153387.

Descostes, M., Schlegel, M.L., Eglizaud, N., Descamps, F., Miserque, F., Simoni, E. (2010). Uptake of uranium and trace elements in pyrite (FeS_2) suspensions. Geochim. Cosmochim. Acta 74, 1551-1562. https://doi.org/10.1016/j.gca.2009.12.004.

Deutsch, C., Ferrel, A., Seibel, B., Pörtner, H.O., Huey, R.B. (2015). Climate change tightens a metabolic constraint on marine habitats. Science, 348, 1132-1135. https://doi.org/10.1126/science.aaa1605

Deutsch, C., Penn, J.L., Seibel, B. (2020). Metabolic trait diversity shapes marine biogeography. Nature 585, 557-562. https://doi.org/10.1038/s41586-020-2721-y.

Di Rita, F., Fletcher, W.J., Aranbarri, J., Margaritelli, G., Lirer, F., Magri, D. (2018). Holocene forest dynamics in central and western Mediterranean: periodicity, spatio-temporal patterns and climate influence. Sci. Rep. 8, 8929. https://doi.org/10.1038/s41598-018-27056-2.

Dickson, A.J., Bagard, M.-L., Katchinoff, J.A.R., Davies, M., Poulton, S.W., Cohen, A.S. (2021). Isotopic constraints on ocean redox at the end of the Eocene. Earth Planet. Sci. Lett. 562, 116814. https://doi.org/10.1016/j.epsl.2021.116814.

Dickson, A.J., Gill, B.C., Ruhl, M., Jenkyns, H.C., Porcelli, D., Idiz, E., Lyons, T.W., van den Boorn, S.H.J.M. (2017). Molybdenum-isotope chemostratigraphy and paleoceanography of the Toarcian Oceanic Anoxic Event (early Jurassic). Paleoceanogr. 32, 813-829. https://doi.org/10.1002/2016pa003048.

Dirksen, J.P., Meijer, P. (2022). A mechanism for high-frequency variability in sapropels. Mar. Geol. 448, 106812. https://doi.org/10.1016/j.margeo.2022.106812

Dorador, J., Rodríguez-Tovar, F.J. (2015). Ichnofabric characterization in cores: a method of digital image treatment. Ann. Soc. Geol. Pol. 85, 465-471. https://doi.org/10.14241/asgp.2015.010.

Dorador, J., Rodríguez-Tovar, F.J. (2018). High-resolution image treatment in ichnological core analysis: initial steps, advances and prospects. Earth Sci. Rev. 177, 226-237. https://doi.org/10.1016/j.earscirev.2017.11.020.

Dorador, J., Rodríguez-Tovar, F.J., Hernández-Molina, F., Stow, D., Zarikian, C., Acton, G., Bahr, A., Balestra, B., Ducassou, E., Flood, R., Flores, J.A., Furota, S., Grunert, P., Hodell, D., Jiménez-Espejo, F., Kim, J.K., Krissek, L., Kuroda, J., Li, B., Xuan, C. (2014a). Quantitative estimation of bioturbation based on digital image analysis. Mar. Geol. 349, 55-60. https://doi.org/10.1016/j.margeo.2014.01.003.

Dorador, J., Rodríguez-Tovar, F.J., IODP Expedition 339 Scientists (2014b). Digital image treatment applied to ichnological analysis of marine core sediments. Facies 60, 39-44. https://doi.org/10.1007/s10347-013-0383-z.

Dormoy, I., Peyron, O., Combourieu Nebout, N., Goring, S., Kotthoff, U., Magny, M., Pross, J. (2009). Terrestrial climate variability and seasonality changes in the Mediterranean region between 15000 and 4000 years BP deduced from marine pollen records. Clim. Past. 5, 615-632. https://doi.org/10.5194/cp-5-615-2009.

Duff, M.C., Coughlin, J.U., Hunter, D.B. (2002). Uranium co-precipitation with iron oxide minerals. Geochim. Cosmochim. Acta 66, 3433-3547. https://doi.org/10.1016/S0016-7037(02)00953-5.

Dufour, S.C., Felbeck, H. (2003). Sulphide mining by the superextensile foot of symbiotic thyasirid bivalves. Nature 426 (6962), 65-67. https://doi.org/10.1038/ nature02095.

Dünkeloh, A., Jacobeit, J. (2003). Circulation dynamics of Mediterranean precipitation variability 1948-98. Int. J. Climatol. 23, 1843-1866. https://doi.org/10.1002/joc.973.

Eglizaud, N., Miserque, F., Simoni, E., Schlegel, M., Descostes, M. (2006). Uranium(VI) interaction with pyrite (FeS_2): chemical and spectroscopic studies. Radiochim. Acta 94, 651-656. https://doi.org/10.1524/ract.2006.94.9-11.651.

Emeis, K.C., Richter, C., Camerlenghi, A. (1998). Proceedings of the Ocean Drilling Program, Scientific Results, 160, pp. 249-259. https://doi.org/10.2973/odp.proc. sr.160.020.1998.

Emeis, K.C., Robertson, A.H.F., Richter, C., Shipboard Scientific Party (1996). Proceedings of Ocean Drilling Programs (ODP). Init. Repts. 160. https://doi.org/10.2973/odp. proc.ir.160.1996.

Emeis, K.C., Sakamoto, T., Wehausen, R., Brumsack, H.J. (2000). The sapropel record of the eastern Mediterranean Sea - results of Ocean Drilling Program Leg 160. Palaeogeogr. Palaeoclimatol. Palaeoecol. 158, 371-395. https://doi.org/10.1016/ S0031-0182(00)00059-6.

Emeis, K.C., Schulz, H., Struck, U., Rossignol-Strick, M., Erlenkeuser, H., Howell, M.W., Kroon, D., Mackensen, A., Ishizuka, S., Oba, T., Sakamoto, T., Koizumi, I. (2003). Eastern Mediterranean surface water temperatures and delta O-18 composition during deposition of sapropels in the late Quaternary. Paleoceanography 18, 1-18. https://doi.org/10.1029/2000PA000617.

Fabres, J., Calafat, A., Sánchez-Vidal, A., Canals, M., Heussner, S. (2002). Composition and spatio-temporal variability of particle fluxes in the Western Alboran Gyre, Mediterranean Sea. J. Mar. Syst. 33, 431-456. https://doi.org/10.1016/S0924-7963(02)00070-2.

Fenoglio-Marc, L., Mariotti, A., Sannino, G. Meyssignac, B., Carillo, A., Struglia, M.V., Rixen, M. (2013). Decadal variability of net water flux at the Mediterranean Sea Gibraltar Strait. Glob. Planet. Change. 100, 1-10. https://doi.org/10.1016/j.gloplacha.2012.08.007.

Fernández-Martínez, J., Martínez Ruíz, F., Rodríguez-Tovar, F.J., Piñuela, L., García- Ramos, J.C., Algeo, T.J. (2023). Euxinia and hydrographic restriction in the Tethys Ocean: Reassessing global oceanic anoxia during the early Toarcian. Glob. Planet. Change 221, 104026. https://doi.org/10.1016/j.gloplacha.2022.104026.

Fernández-Martínez, J., Rodríguez-Tovar, F.J., Piñuela, L., Martínez-Ruiz, F., García- Ramos, J.C. (2021). Bottom- and pore-water oxygenation during the early Toarcian Oceanic Anoxic Event (T-OAE) in the Asturian Basin (N Spain): Ichnological information to improve facies analysis. Sediment. Geol. 419, 105909. https://doi.org/10.1016/j.sedgeo.2021.105909.

Filippidi, A., de Lange, G.J. (2019). Eastern Mediterranean Deep Water formation during sapropel S1: A Reconstruction Using Geochemical Records Along a Bathymetric Transect in the Adriatic Outflow Region. Paleoceanogr. Paleoclimatol. 34, 409-429. https://doi.org/10.1029/2018PA003459.

Filippidi, A., Triantaphyllou, M.V., de Lange, G.J. (2016). Eastern-Mediterranean ventilation variability during sapropel S1 formation, evaluated at two sites influenced by deep-water formation from Adriatic and Aegean seas. Quat. Sci. Rev. 144, 95-106. https://doi.org/10.1016/j.quascirev.2016.05.024.

Fink, H.G., Wienberg, C., De Pol-Holz, R., Hebbeln, D. (2015). Spatio-temporal distribution patterns of Mediterranean cold-water corals (Lophelia pertusa and Madrepora oculata) during the past 14,000 years. Deep-Sea Res. I: Oceanogr. Res. Pap. 103, 37-48. https://doi.org/10.1016/j.dsr.2015.05.006.

Fletcher, W.J., Zielhofer, C. (2013). Fragility of Western Mediterranean landscapes during Holocene rapid climate changes. Catena 103, 16-29. https://doi.org/10.1016/j.catena.2011.05.001.

Francois, R., Honjo, S., Manganini, S.J., Ravizza, G.E. (1995). Biogenic barium fluxes to the deep sea: Implications for paleoproductivity reconstruction. Global Biogeochem. Cycles 9, 289-303. https://doi.org/10.1029/95GB00021.

Frigola, J., Moreno, A., Cacho, I., Canals, M., Sierro, F.J., Flores, J.A., Grimalt, J.O., Hodell, D.A., Curtis, J.H. (2007). Holocene climate variability in the western Mediterranean region from a deepwater sediment record. Paleoceanography 22, PA2209. https://doi.org/10.1029/2006PA001307.

Frigola, J., Moreno, A., Cacho, I., Canals, M., Sierro, F.J., Flores, J.A., Grimalt, J.O. (2008). Evidence of abrupt changes in Western Mediterranean Deep Water circulation during the last 50 kyr: a high-resolution marine record from the Balearic Sea. Quat. Int. 181, 88-104. https://doi.org/10.1016/j.quaint.2007.06.016.

Fujii, R., Matsuoka, K. (2006). Seasonal change of dinoflagellates cyst flux collected in a sediment trap in Omura Bay, West Japan. J. Plankton Res. 28, 131-147. https://doi.org/10.1093/plankt/fbi106.

Gallego-Torres, D., de Lange Martínez-Ruiz, G., Jiménez-Espejo, F., Ortega-Huertas, M. (2007a). Trace-elemental derived paleoceanographic and paleoclimatic conditions for Pleistocene Eastern Mediterranean sapropels. Palaeogeogr. Palaeoclimatol. Palaeoecol. 293, 76-89. https://doi.org/10.1016/j.palaeo.2010.05.001.

Gallego-Torres, D., Martínez-Ruiz, F., De Lange, G.J., Jiménez-Espejo, F.J., Ortega- Huertas, M. (2010). Trace-elemental derived paleoceanographic and paleoclimatic conditions for Pleistocene Eastern Mediterranean sapropels. Palaeogeogr. Palaeoclimatol. Palaeoecol. 293, 76-89. https://doi.org/10.1016/j. palaeo.2010.05.001.

Gallego-Torres, D., Martínez-Ruiz, F., Jiménez-Espejo, F., Ortega-Huertas, M. (2007b). Pliocene-Holocene evolution of depositional conditions in the eastern Mediterranean: Role of anoxia vs. productivity at time of sapropel deposition. Palaeogeogr. Palaeoclimatol. Palaeoecol. 246, 424-439. https://doi.org/10.1016/j. palaeo.2006.10.008.

Gao, K., Beardall, J., Häder, D.P., Hall-Spencer, J.M., Gao, G., Hutchins, D.A. (2019). Effects of ocean acidification on marine photosynthetic organisms under the concurrent influences of warming, UV radiation, and deoxygenation. Front. Mar. Sci. 6, 322. https://doi.org/10.3389/fmars.2019.00322.

García-Alix, A., Camuera, J., Ramos-Román, M.J., Toney, J.L., Sachse, D., Schefuß, E., Jiménez-Moreno, G., Jiménez-Espejo, F.J., López-Avilés, A., Anderson, R.S., Yanes, Y. (2021). Paleohydrological dynamics in the Western Mediterranean during the last glacial cycle. Glob. Planet. Change. 202, 103527. https://doi.org/10.1016/j.gloplacha.2021.103527.

García-Alix, A., Jiménez-Moreno, G., Gazquez, F., Monedero-Contreras, R., López-Avilés, A., Jiménez-Espejo, F.J., Rodríguez-Rodríguez, M., Camuera, J., Ramos-Román, M.J., Anderson, R.S. (2022). Climatic control on the Holocene hydrology of a playa-lake system in the western Mediterranean. Catena 214, 106292. https://doi.org/10.1016/j.catena.2022.106292.

García-Alix, A., Toney, J.L., Jiménez-Moreno, G., Pérez-Martínez, C., Jiménez, L., Rodrigo-Gámiz, M., Anderson, R.S., Camuera, J., Jiménez-Espejo, F.J., Peña-Angulo, D., Ramos-Román, M.J. (2020). Algal lipids reveal unprecedented warming rates in alpine areas of SW Europe during the industrial period. Clim. Past 16, 245-263. https://doi.org/10.5194/cp-16-245-2020.

García-Lafuente, J., Naranjo, C., Sammartino, S., Sánchez-Garrido, J.C., Delgado, J. (2017). The Mediterranean outflow in the Strait of Gibraltar and its connection with upstream conditions in the Alborán Sea. Ocean Sci. 13, 195-207. https://doi.org/ 10.5194/os-13-195-2017.

García-Ruiz, J.M., Palacios, D., González-Sampériz, P., De Andrés, N., Moreno, A., Valero-Garcés, B., Gómez-Villar, A. (2016). Mountain glacier evolution in the Iberian Peninsula during the Younger Dryas. Quat. Sci. Rev. 138, 16-30. https://doi.org/10.1016/j.quascirev.2016.02.022.

García-Jove, M., Mourre, B., Zarokanellos, N.D., Lermusiaux, P. F., Rudnick, D.L., Tintoré, J. (2022). Frontal dynamics in the Alboran Sea: 2. Processes for vertical velocities development. J. Geophys. Res. Oceans 127, e2021JC017428. https://doi.org/10.1029/2021JC017405.

Gázquez-Sánchez, F., Jiménez-Espejo, F., Rodríguez-Rodríguez, M., Martegani, L., Voigt, C., Ruíz-Lara, D, Moreno, A., Valero-Garcés, B., Morellón, M., Martín-Puertas, C. (2023). Roman water management impacted the hydrological functioning of wetlands during drought periods. Sci. Rep. 13, 18815. https://doi.org/10.1038/s41598-023-46010-5.

Gingele, F.X., Zabel, M., Kasten, S., Bonn, W.J., Nürnberg, C.C. (1999). Biogenic Barium as a Proxy for Paleoproductivity: Methods and Limitations of Application. In: Fischer, G., Wefer, G. (eds) Use of Proxies in Paleoceanography. Springer, Berlin, Heidelberg, 345-364. https://doi.org/10.1007/978-3-642-58646-0_13.

Giorgi, F. (2006). Climate change hot-spots. Geophys. Res. Lett. 33, L08707. https://doi. org/10.1029/2006GL025734.

Giorgi, F., Lionello, P. (2008). Climate change projections for the Mediterranean region. Glob. Planet. Chang. 63, 90-104. https://doi.org/10.1016/j.gloplacha.2007.09.005.

Glibert, P.M., Cai, W.J., Hall, E.R., Li, M., Main, K.L., Rose, K.A., Testa, J.M., Vidyarathna, N.K. (2022). Stressing over the complexities of multiple stressors in marine and estuarine systems. Ocean-Land-Atmos Res. https://doi.org/10.34133/2022/9787258.

Gong, H., Li, C., Zhou, Y. (2021). Emerging global ocean deoxygenation across the 21st century. Geophys. Res. Lett. 48, e2021GL095370. https://doi.org/10.1029/2021GL095370.

Grant, K.M., Grimm, R., Mikolajewicz, U., Marino, G., Ziegler, M., Rohling, E.J. (2016). The timing of Mediterranean sapropel deposition relative to insolation, sea-level and African monsoon changes. Quat. Sci. Rev. 140, 125-141. https://doi.org/10.1016/j. quascirev.2016.03.026.

Grant, K.M., Rohling, E.J., Ramsey, C.B., Cheng, H., Edwards, R.L., Florindo, F., Heslop, D., Marra, F., Roberts, A.P., Tamisiea, M.E., Williams, F. (2014). Sea-level variability over five glacial cycles. Nat. Commun. 5, 5076. https://doi.org/10.1038/ ncomms6076.

Green, A.S., Chandler, G.T. (1994). Meiofaunal bioturbation effects on the partitioning of sediment-associated cadmium. J. Exp. Mar. Biol. Ecol. 180, 59-70. https://doi.org/ 10.1016/0022-0981(94)90079-5.

Grema, H.M., Magnall, J.M., Whitehouse, M.J., Gleeson, S.A., Schulz, H.M. (2022). The Formation of Highly positive δ^{34}S Values in late Devonian Mudstones: Microscale Analysis of Pyrite (δ^{34}S) and Barite (δ^{34}S, δ^{18}O) in the Canol Formation (Selwyn Basin, Canada). Front. Earth Sci. 9, 784824. https://doi.org/10.3389/ feart.2021.784824.

Griffith, E.M., Paytan, A. (2012). Barite in the ocean-occurrence, geochemistry and palaeoceanographic applications. Sedimentology 59, 1817-1835. https://doi.org/10.1111/j.1365-3091.2012.01327.x.

Grimm, R., Maier-Reimer, E., Mikolajewicz, U., Schmiedl, G., Muller-Navarra, K., Adloff, F., Grant, K.M., Ziegler, M., Lourens, L.J., Emeis, K.C. (2015). Late glacial initiation of Holocene eastern Mediterranean sapropel formation. Nat. Commun. 6,7099. https://doi.org/10.1038/ncomms8099.

Gruber, N. (2011). Warming up, turning sour, losing breath: ocean biogeochemistry under global change. Philos. Trans. A Math. Phys. Eng. Sci. 369, 1980-1996. https://doi.org/10.1098/rsta.2011.0003.

Gruber, N., Boyd, P.W., Frölicher, T.L., Vogt, M. (2021). Biogeochemical extremes and compound events in the ocean. Nature, 600, 395-407. https://doi.org/10.1038/s41586-021-03981-7.

Grundl, T., Haderlein, S., Nurmi, J., Tratnyek, P. (2011). Introduction to aquatic redox chemistry. In: ACS Symp. Ser. Am. Chem. Soc, 1071, pp. 1-14. https://doi.org/ 10.1021/bk-2011-1071.ch001.

Hammer, Ø., Harper, D.A.T., Ryan, P.D. (2001). PAST: paleontological statistics software package for education and data analysis. Palaeontol. Electron. 4, 1-9. https://palaeo-electronica.org/2001_1/past/past.pdf.

Hantsoo, K., Gomes, M., Malkin, S., Brenner, D., Kenney, W.F. (2023). Sedimentary pyrite formation in a seasonally oxygen-stressed estuary: potential imprints of microbial ecology and position-specific isotope fractionation. Eur. J. Vasc. Endovasc. Surg. 128, e2022JG007324. https://doi.org/10.1029/2022JG007324.

Helz, G.R., Miller, C.V., Charnock, J.M., Mosselmans, J.F.W., Pattrick, R.A.D., Garner, C.D., Vaughan, D.J. (1996). Mechanism of molybdenum removal from the sea and its concentration in black shales: EXAFS evidence. Geochim. Cosmochim. Acta 60, 3631-3642. https://doi.org/10.1016/0016-7037(96)00195-0.

Helz, G.R., Vorlicek, T.P. (2019). Precipitation of molybdenum from euxinic waters and the role of organic matter. Chem. Geol. 509, 178-193. https://doi.org/10.1016/j. chemgeo.2019.02.001.

Henkel, S., Mogollón, J.M., Nöthen, K., Franke, C., Bogus, K., Robin, E., Bahr, A., Blumenberg, M., Pape, T., Seifert, R., März, C., de Lange, G., Kasten, S. (2012). Diagenetic barium cycling in Black Sea sediments - a case study for anoxic marine environments. Geochim. Cosmochim. Acta 88, 88-105. https://doi.org/10.1016/j. gca.2012.04.021.

Hennekam, R., Jilbert, T., Mason, P.R.D., de Lange, G.J., Reichart, G.-J. (2015). High-re- solution line-scan analysis of resin-embedded sediments using laser ablation-inductively coupled plasma-mass spectrometry (LA-ICP-MS). Chem. Geol. 403, 42-51. https://doi.org/10.1016/j.chemgeo.2015.03.004.

Hennekam, R., Jilbert, T., Schnetger, B., de Lange, G.J. (2014). Solar forcing of Nile discharge and sapropel S1 formation in the early to middle Holocene eastern Mediterranean. Paleoceanography 29, 343-356. https://doi.org/10.1002/ 2013PA002553.

Hennekam, R., van der Bolt, B., van Nes, E.H., de Lange, G.J., Scheffer, M., Reichart, G.J. (2020). Early-warning signals for marine anoxic events. Geophys. Res. Lett. 47, e2020GL089183. https://doi.org/10.1029/2020GL089183.

Hernández, A., Sáez, A., Santos, R. N., Rodrigues, T., Martin-Puertas, C., Gil-Romera, G., Abbot, M., Carballeira, R., Costa, P., Giralt, S., Gomes, S.D., Griffore, M., Ibañez-Insa, J., Leira, M., Moreno, J., Filipa, N., Oliveira, D., Raposeiro, P.M., Trigo, R.M., Vieira G., Ramos, A.M. (2023). The timing of the deglaciation in the Atlantic Iberian mountains: Insights from the stratigraphic analysis of a lake sequence in Serra da Estrela (Portugal). Earth Surf. Process. Landf. 48, 233-242. https://doi.org/10.1002/esp.5536.

Heslop, D., Marra, F., Roberts, A.P., Tamisiea, M.E., Williams, F. (2014). Sea-level variability over five glacial cycles. Nat. Commun. 5, 5076. https://doi.org/10.1038/ ncomms6076.

Hetzel, A., Böttcher, M.E., Wortmann, U.G., Brumsack, H.J. (2009). Paleo-redox conditions during OAE 2 reflected in Demerara rise sediment geochemistry (ODP Leg 207). Palaeogeogr. Palaeoclimatol. Palaeoecol. 273, 302-328. https://doi.org/ 10.1016/j.palaeo.2008.11.005.

Higgs, N.C., Thomson, J., Wilson, T.R.S., Croudace, I.W. (1994). Modification and complete removal of eastern Mediterranean sapropels by postdepositional oxidation. Geology 22, 423-426. https://doi.org/10.1130/0091-7613(1994)022<0423: MACROE>2.3.CO;2.

Hilbrecht, H., Dahmer, D.D. (1994). Sediment dynamics during the Cenomanian-Turonian (cretaceous) oceanic anoxic event in Northwestern Germany. Facies 30, 63-83. https://doi.org/10.1007/BF02536890.

Hilgen, F.J. (1991). Astronomical calibration of Gauss to Matuyama sapropels in the Mediterranean and implication for the geomagnetic polarity time scale. Earth Planet. Sci. Lett. 104, 226-244. https://doi.org/10.1016/0012-821X(91)90206-W.

Horner, T.J., Pryer, H.V., Nielsen, S.G., Crockford, P.W., Gauglitz, J.M., Wing, B.A., Ricketts, R.D. (2017). Pelagic barite precipitation at micromolar ambient sulfate. Nat. Commun. 8, 1342. https://doi.org/10.1038/s41467-017-01229-5.

Huerta-Diaz, M.A., Morse, J.W. (1991). Pyritization of trace metals in anoxic marine sediments. Geochim. Cosmochim. Acta 56, 2681-2702. https://doi.org/10.1016/0016-7037(92)90353-K.

Hurrell, J.W. (1995). Decadal trend in the North Atlantic Oscillation: regional temperatures and precipitations. Science 269, 676-679. https://doi.org/10.1126/science.269.5224.676.

Ilvonen, L., López-Sáez, J.A., Holmström, L., Alba-Sánchez, F., Pérez-Díaz, S., Carrión, J.S., Ramos-Roman, M.J., Camuera, J., Jiménez-Moreno, G., Ruha, L., Seppä, H. (2022). Spatial and temporal patterns of Holocene precipitation change in the Iberian Peninsula. Boreas 51, 776-792. https://doi.org/10.1111/bor.12586.

IPCC (2022). Climate Change 2022: Impacts, Adaptation and Vulnerability. Contribution of Working Group II to the Sixth Assessment Report of the Intergovernmental Panel of Climate Change (IPCC), H.-O. Pörtner et al., Eds. (Cambridge University Press, Cambridge, UK, 2022). https://www.ipcc.ch/report/ar6/wg2/.

IPCC (2023). Climate Change 2023: Synthesis Report. Contribution of Working Groups I, II and III to the Sixth Assessment Report of the Intergovernmental Panel on Climate Change [Core Writing Team, H. Lee and J. Romero (eds.)]. IPCC, Geneva, Switzerland, pp. 35-115. http://doi.org/10.59327/IPCC/AR6-9789291691647.

Ivy-Ochs, S., Kerschner, H., Maisch, M., Christl, M., Kubik, P. W., Schlüchter, C. (2009). Latest Pleistocene and Holocene glacier variations in the European Alps. Quat. Sci. Rev. 28, 2137-2149. https://doi.org/10.1016/j.quascirev.2009.03.009.

Jacobs, L., Emerson, S., Skei, J. (1985). Partitioning and transport of metals across the O_2/ H_2S interface in a permanently anoxic basin: Framvaren Fjord, Norway. Geochim. Cosmochim. Acta 49, 1433-1444. https://doi.org/10.1016/0016-7037 (85)90293-5.

Jacobson, D.M., Anderson, D.M. (1986). Thecate heterophic dinoflagellates: Feeding behavior and mechanisms 1. J. Phycol. 22, 249-258. https://doi.org/10.1111/j.1529-8817.1986.tb00021.x.

Jalut, G., Amat, A.E., Bonnet, L., Gauquelin, T., Fontugne, M. (2000). Holocene climatic changes in the Western Mediterranean, from south-east France to south-east Spain. Palaeogeogr. Palaeoclimatol. Palaeoecol. 160, 255-290. https://doi.org/10.1016/S0031-0182(00)00075-4.

Jalut, G., Amat, A.E., Mora, S.R., Fontugne, M., Mook, R., Bonnet, L., Gauquelin, T. (1997). Holocene climatic changes in the western Mediterranean: installation of the Mediterranean climate. C. R. Acad. Sci. Ser. II. 325, 327-334. https://doi.org/10.1016/S1251-8050(97)81380-8.

Jenkyns, H.C. (1985). The early Toarcian and Cenomanian-Turonian anoxic events in Europe: comparisons and contrasts. Geol. Rundsch. 74, 505-518. https://doi.org/10.1007/bf01821208.

Jilbert, T., de Lange, G., Reichart, G.-J. (2008). Fluid displacive resin embedding of la- minated sediments: preserving trace metals for high-resolution paleoclimate investigations. Limnol. Oceanogr. Methods 6, 16-22. https://doi.org/10.4319/ lom.2008.6.16.

Jilbert, T., Reichart, G.J., Mason, P., de Lange, G.J. (2010). Short-time-scale variability in ventilation and export productivity during the formation of Mediterranean sapropel S1. Paleoceanography 25, PA4232. https://doi.org/10.1029/2010PA001955.

Jiménez-Espejo, F. J., García-Alix, A., Jiménez-Moreno, G., Rodrigo-Gámiz, M., Anderson, R. S., Rodríguez-Tovar, F. J., Martínez-Ruiz, F., Giralt, S., Huertas, A.D., Pardo-Igúzquiza, E. (2014). Saharan aeolian input and effective humidity variations over western Europe during the Holocene from a high altitude record. Chem. Geol. 374, 1-12. https://doi.org/10.1016/j.chemgeo.2014.03.001.

Jiménez-Espejo, F.J., Pardos-Gené, M., Martínez-Ruiz, F., García-Alix, A., vande Flierdt, T., Toyofuku, T., Bahr, A., Kreissig, K. (2015). Geochemical evidence for intermediate water circulation in the Westernmost Mediterranean over the last 20 kyr BP and its impact on the Mediterranean Outflow. Glob. Planet. Change. 135, 38-46. https://doi.org/10.1016/j.gloplacha.2015.10.001.

Jiménez-Moreno, G., Anderson, R.S., Ramos-Román, M.J., Camuera, J., Mesa-Fernández, J.M., García-Alix, A., Jiménez-Espejo, F.J., Carrión, J.S., Lopez-Aviles, A. (2020). The Holocene Cedrus pollen record from Sierra Nevada (S Spain), a proxy for climate change in N Africa.

Quat. Sci. Rev. 242, 106468. https://doi.org/10.1016/j.quascirev.2020.106468.

Jiménez-Moreno, G., García-Alix, A., Anderson, R.S, Ramos-Román, M.J., Camuera, J., Mesa-Fernández, J.M., Toney, J.L., Jiménez-Espejo, F.J., Carrión, J.S., López-Avilés, A., Rodrigo-Gámiz, M., Webster, C.E. (2022). Reconstruction of Past Environment and Climate Using Wetland Sediment Records from the Sierra Nevada. In: Zamora, R., Oliva, M. (eds) The Landscape of the Sierra Nevada. Springer, Cham. 95-114. https://doi.org/10.1007/978-3-030-94219-9_7.

Jiménez-Moreno, G., López-Avilés, A., García-Alix, A., Ramos-Román, M.J., Camuera, J., Mesa-Fernández, J.M., Jiménez-Espejo, F.J., López-Blanco, C., Carrión, J.S., Anderson, R.S. (2023). Laguna Seca sediments reveal environmental and climate change during the latest Pleistocene and Holocene in Sierra Nevada, southern Iberian Peninsula. Palaeogeogr. Palaeoclimatol. Palaeoecol. 631, 111834. https://doi.org/10.1016/j.palaeo.2023.111834.

Jiménez-Espejo, F.J., Martínez-Ruiz, F., Rogerson, M., González-Donoso, J. M., Romero, O. E., Linares, D., Sakamoto, T., Gallego-Torres, D., Ruiz, L.R., Ortega-Huertas, M., Claros, J.A.P. (2008). Detrital input, productivity fluctuations, and water mass circulation in the Westernmost Mediterranean Sea since the Last Glacial Maximum. Geochem. Geophys. 9, Q11U02. https://doi.org/10.1029/2008GC002096.

Jørgensen, B.B., Glud, R.N., Holby, O. (2005). Oxygen distribution and bioirrigation in Artic fjord sediments (Svalbard, Barents Sea). Mar. Ecol. Prog. Ser. 292, 85-95. https://doi.org/10.3354/meps292085.

Jørgensen, B.B., Nelson, D. (2004). Sulfide oxidation in marine sediments: geochemistry meets microbiology. Spec. Pap. Geol. Soc. Am. 379, 63-81. https://doi.org/10.1130/0-8137-2379-5.63.

Jørgensen, B.B., Wenzhöfer, F., Egger, M., Glud, R.N. (2022). Sediment oxygenconsumption: Role in the global marine carbon cycle. Earth Sci. Rev. 228, 103987. https://doi.org/10.1016/j.earscirev.2022.103987.

Jovanovic, Z., Larsen, M., Quintana, C.O., Kristensen, E., Glud, R.N. (2014). Oxygen dynamics and porewater transport in sediments inhabited by the invasive polychaete Marenzelleria viridis. Mar. Ecol. Prog. Ser. 504, 181-192. https://doi.org/10.3354/ meps10737.

Kamp-Nielsen, L., Mejer, H., Jørgensen, S.E. (1982). Modelling the influence of bioturbation on the vertical distribution of sedimentary phosphorus in L. Esrom. Hydrobiologia 91, 197-206. https://doi.org/10.1007/BF00940110.

Keeling, R.A., Körtzinger, A., Gruber, N. (2010). Ocean deoxygenation in a warming world. Annu. Rev. Mar. Sci. 2, 199-229. https://doi.org/10.1146/annurev.marine.010908.163855.

Kidd, R.B., Cita, M.B., Ryan, W.B.F. (1978). Stratigraphy of eastern Mediterranean sapropel sequences recovered during Leg 42A and their paleoenvironmental significance. Initial Rep. Deep Sea Drill. Proj. 42A, 421-443. https://doi.org/ 10.2973/dsdp.proc.42-1.113-1.1978.

Kiessling, W., Smith, J.A., Raja, N.B. (2023). Improving the relevance of paleontology to climate change policy. Proceedings of the National Academy of Sciences 120, e2201926119. https://doi.org/10.1073/pnas.2201926119.

Knaust, D. (2017). Atlas of Trace Fossils in Well Core: Appearance, Taxonomy and Interpretation. Springer, Alphen aan den Rijn. https://doi.org/10.1007/978-3-319-49837-9.

Krijgsman, W. (2002). The Mediterranean: mare nostrum of earth sciences. Earth Planet. Sci. Lett. 205, 1-12. https://doi.org/10.1016/S0012-821X(02)01008-7

Kwiatkowski, L., Torres, O., Bopp, L., Aumont, O., Chamberlain, M., Christian, J.R., Dunne, J.P., Gehlen, M., Ilyina, T., John, J.G., Lenton, A., Li,H., Lovenduski, N.S., Orr, J.C., Palmieri, J., Santana-Falcón, Y., Schwinger, J., Séférian, R., Stock, C.A., Tagliabue, A., Takano, Y., Tjiputra, J., Toyama, K., Tsujino, H., Watanabe, M., Yamamoto, A., Yool, A., Ziehn, T. (2020). Twenty-first century ocean warming, acidification, deoxygenation, and upper-ocean nutrient and primary production decline from CMIP6 model projections. Biogeosciences 17, 3439-3470. https://doi.org/10.5194/bg-17-3439-2020.

Lafargue, E., Marquis, F., Pillot, D. (1998). Rock-Eval 6 applications in hydrocarbon exploration, production, and soil contamination studies. Oil Gas Sci. Technol. 53, 421-437. https://doi.org/10.2516/ogst:1998036.

Lambeck, K., Rouby, H., Purcell, A., Sun, Y., Sambridge, M. (2014). Sea level and global ice volumes from the Last Glacial Maximum to the Holocene. Proc. Natl. Acad. Sci. 111, 15296-15303. https://doi.org/10.1073/pnas.1411762111.

Langone, L., Conese, I., Miserocchi, S., Boldrin, A., Bonaldo, D., Carniel, S., Chiggiato, J., Turchetto, M., Borghini, M., Tesi, T. (2016). Dynamics of particles along the western margin of the Southern Adriatic: Processes involved in transferring particulate matter to the deep basin. Mar. Geol. 375, 28-43. https://doi.org/10.1016/j.margeo.2015.09.004.

Lascaratos, A. (1993). Estimation of deep and intermediate water mass formation rates in the Mediterranean Sea. Deep

Sea Res. Part II Top. Stud. Oceanogr. 40, 1327-1332. https://doi.org/10.1016/0967-0645(93)90072-U.

Lascaratos, A., Roether, W., Nittis, K., Klein, B. (1999). Recent changes in deep water formation and spreading in the eastern Mediterranean Sea: a review. Prog. Oceanogr. 44, 5-36. https://doi.org/10.1016/S0079-6611(99)00019-1.

Laskar, J. Joutel, F., Boudin, F. (1993). Orbital, precessional and insolation quantities for the Earth from -20 Myr to +10 Myr. Astronphys. 270, 522-533. https://adsabs.harvard.edu/full/1993A%26A...270..522L.

Lathika, N., Rahaman, W., Tarique, M., Gandhi, N., Kumar, A., Thamban, M. (2021). Deep water circulation in the Arabian Sea during the last glacial cycle: implications for paleo-redox condition, carbon sink and atmospheric CO_2 variability. Quat. Sci. Rev. 257, 106853. https://doi.org/10.1016/j.quascirev.2021.106853.

Leblanc, M., Morales, J.A., Borrego, J., Elbaz-Poulichet, F. (2000). 4,500-year-old mining pollution in southwestern Spain: long-term implications for modern mining pollution. Econ Geol. 95, 655-662. https://doi.org/10.2113/gsecongeo.95.3.655.

Lefèvre, C.T., Bazylinski, D.A. (2013). Ecology, diversity, and evolution of magnetotactic bacteria. Microbiol. Mol. Biol. Rev. 77, 497-526. https://doi.org/10.1128/ MMBR.00021-13.

Lejeusne, C., Chevaldonné, P., Pergent-Martini, C., Boudouresque, C.F., Pérez, T. (2010). Climate change effects on a miniature ocean: the highly diverse, highly impacted Mediterranean Sea. Trends Ecol. Evol. 25, 250-260. https://doi.org/10.1016/j.tree.2009.10.009.

Levin, L.A. (2018). Manifestation, drivers, and emergence of open ocean deoxygenation. Annu. Rev. Mar. Sci. 10, 229-260. https://doi.org/10.1146/annurev-marine- 121916-063359.

Levin, L.A., Le Bris, N. (2015). The deep ocean under climate change. Science 350, 766-768. https://doi.org/10.1126/science.aad012.

Lewis, J., Dodge, J., Powell, A. (1990). Quaternary dinoflagellate cysts from the upwelling system offshore Peru, Hole 686B, ODP leg 112. Proc. Ocean Drill. Prog., Sci. Results 112, 323-328. https://doi.org/10.2973/odp.proc.sr.112.162.1990.

Li, G., Cheng, L., Zhu, J. Trenberth, K.E., Mann, M.E., Abraham, J.P. (2020). Increasing ocean stratification over the past half-century. Nat. Clim. Chang. 10, 1116-1123. https://doi.org/10.1038/s41558-020-00918-2.

Li, S., Friedrich, O., Nielsen, S.G., Wu, F., Owens, J.D. (2023). Reconciling biogeochemical redox proxies: Tracking variable bottom water oxygenation during OAE-2 using vanadium isotopes. EPSL 617, 118237. https://doi.org/10.1016/j.epsl.2023.118237.

Light, T., Martínez-Ruiz, F., Norris, R. (2023). Marine barite morphology as an indicator of biogeochemical conditions within organic matter aggregates. Geochim. Cosmochim. Acta 358, 38-48. https://doi.org/10.1016/j.gca.2023.08.012.

Lin, Q., Wang, J., Algeo, T.J., Sun, F., Lin, R. (2016). Enhanced framboidal pyrite formation related to anaerobic oxidation of methane in the sulfate-methane transition zone of the northern South China Sea Mar. Geol 379, 100-108. https:// doi.org/10.1016/j.margeo.2016.05.016.

Lionello, P., Abrantes, F., Congedi, L., Dulac, F., Gacic, M., Gomis, D. Goodess, C., Hoff, H., Kutiel, H., Luterbacher, J., Planton, S., Reale, M., Schröder, K., Struglia, M.V., Toreti, A., Tsimplis, M., Ulbrich, U., Xoplaki, E. (2012). Introduction: Mediterranean climate: background information. In: Lionello P (ed) The Climate of the Mediterranean Region. From the Past to the Future. Elsevier (NETHERLANDS), Amsterdam, pp 1-50, ISBN: 9780124160422. https://doi.org/10.1016/B978-0-12-416042-2.00012-4.

Lionello, P., Malanotte-Rizzoli, P., Boscolo, R., Alpert, P., Artale, V., Li, L., Luterbacher, J., May, W., Trigo, R., Tsimplis, M., Ulbrich, U., Xoplaki, E. (2006). The Mediterranean climate: an overview of the main characteristics and issues. Dev. Earth Environ. Sci. 4, 1-26. https://doi.org/10.1016/S1571-9197(06)80003-0.

Lionello, P., Scarascia, L. (2018). The relation between climate change in the Mediterranean region and global warming. Regional Environ. Change 18, 1481-1493. https://doi.org/10.1007/s10113-018-1290-1.

Liquete, C., Arnau, P., Canals, M., Colas, S. (2005). Mediterranean river systems of Andalusia, southern Spain, and associated deltas: a source to sink approach. Mar. Geol. 222-223, 471-495. https://doi.org/10.1016/j.margeo.2005.06.033.

Lisa A. Levin, Le Bris N. (2015). The deep ocean under climate change. Science 350, 766-768. https://doi.org/10.1126/science.aad0126

Little, S.H., Vance, D., Lyons, T.W., McManus, J. (2015). Controls on trace metal authigenic enrichment in reducing sediments: insights from modern oxygen-deficient settings. Am. J. Sci. 315, 77-119. https://doi.org/10.2475/02.2015.01.

Liu, J., Algeo, T.J. (2020). Beyond redox: control of trace-metal enrichment in anoxic marine facies by watermass chemistry and sedimentation rate. Geochim. Cosmochim. Acta 287, 296-317. https://doi.org/10.1016/j.gca.2020.02.037.

Liu, J., Pellerin, A., Wang, J., Rickard, D., Antler, G., Zhao, J., Wang, Z., Barker, B., Ono, J.S. (2022). Multiple sulfur isotopes discriminate organoclastic and methane- based sulfate reduction by sub-seafloor pyrite formation. Geochim. Cosmochim. Acta 316, 309-330. https://doi.org/10.1016/j.gca.2021.09.026.

Liu, Z., Chen, D., Zhang, J., Lü, X., Wang, Z., Liao, W., Shi, X., Tang, J., Xie, G. (2019). Pyrite morphology as an indicator of paleoredox conditions and shale gas content of the Longmaxi and Wufeng Shales in the middle Yangtze Area, South China. Minerals 9, 428. https://doi.org/10.3390/min9070428.

Lobo, F.J., Fernández-Salas, L.M., Moreno, I., Sanz, J.L., Maldonado, A. (2006). The sea-floor morphology of a Mediterranean shelf fed by small rivers, northern Alboran Sea margin. Cont. Shelf Res. 26, 2607-2628. https://doi.org/10.1016/j.csr.2006.08.006.

Löhr, S.C., Kennedy, M.J. (2015). Micro-trace fossils reveal pervasive reworking of Pliocene sapropels by low-oxygen-adapted benthic meiofauna. Nat. Commun. 6, 1-8. https://doi.org/10.1038/ncomms7589.

Lourens, L.J., Antonarakou, A., Hilgen, F.J., van Hoof, A.A.M., Vergnaud-Grazzini, C., Zachariasse, W.J. (1996). Evaluation of the Plio-Pleistocene astronomical time-scale. Paleoceanography 11, 391-413. https://doi.org/10.1029/96PA01125.

Löwemark, L., Lin, Y., Chin, H.F., Yang, T.N., Beier, C., Werner, F., Lee, C.Y., Song, S.R., Kao, S.J. (2006). Sapropel burn-down and ichnological response to late Quaternary sapropel formation in two ~ 400 ky records from the eastern Mediterranean Sea. Palaeogeogr. Palaeoclimatol. Palaeoecol. 239, 406-425. https://doi.org/10.1016/j. palaeo.2006.02.013.

Lozier, M.S., Dave, A.C., Palter, J.B., Gerber, L.M., Barber, R.T. (2011). On the relationship between stratification and primary productivity in the North Atlantic. Geophys. Res. Lett. 38, 1-6. https://doi.org/10.1029/2011GL049414.

Ludwig, W., Dumont, E., Meybeck, M., Heussner, S. (2009). River discharges of water and nutrients to the Mediterranean and Black Sea: major drivers for ecosystem changes during past and future decades?. Prog. Oceanogr. 80(3-4), 199-217. https://doi.org/10.1016/j.pocean.2009.02.001.

Lyons, T.W., Anbar, A.D., Severmann, S., Scott, C., Gill, B.C. (2009). Tracking euxinia in the ancient ocean: a multiproxy perspective and Proterozoic case study. Annu. Rev. Earth Planet. Sci. 37, 507-534. https://doi.org/10.1146/annurev. earth.36.031207.124233.

Macias, D.M., García-Gorriz E., Stips, A. (2015). Productivity changes in the Mediterranean Sea for the twenty-first century in response to changes in the regional atmospheric forcing. Front. Mar. Sci. 2, 79. https://doi.org/10.3389/fmars.2015.00079.

Macias, D.M., García-Gorriz, E., Dosio, A., Stips, A., Keuler, K. (2016). Obtaining the correct sea surface temperature: Bias correction of region- al climate model data for the Mediterranean Sea. Clim. Dyn. 51, 1095-1117. https://doi.org/10.1007/s00382-016-3049-z.

Magny, M., Bégeot, C., Guiot, J., Peyron, O. (2003). Contrasting patterns of hydrological changes in Europe in response to Holocene climate cooling phases. Quat. Sci. Rev. 22, 1589-1596. https://doi.org/10.1016/S0277-3791(03)00131-8.

Magny, M., Miramont, C., Sivan, O. (2002). Assessment of the impact of climate and anthropogenic factors on Holocene Mediterranean vegetation in Europe on the basis of palaeohydrological records. Palaeogeogr. Palaeoclimatol. Palaeoecol. 186, 47-59. https://doi.org/10.1016/S0031-0182(02)00442-X.

Maher Jr., L.J. (1981). Statistics for microfossil concentration measurements employing samples spiked with marker grains. Rev. Palaeobot. Palynol. 32, 153-191. https://doi.org/10.1016/0034-6667(81)90002-6.

Malanotte-Rizzoli, P., Artale, V., Borzelli-Eusebi, G. L., Brenner, S., Crise, A., Gacic, M., Kress, N., Marullo, S., Ribera d'Alcalà, M., Sofianos, S., Tanhua, T., Theocharis, A., Alvarez, M., Ashkenazy, Y., Bergamasco, A., Cardin, V., Carniel, S., Civitarese, G., D'Ortenzio, F., Font, J., García-Ladona, E., García-Lafuente, J.M., Gogou, A., Gregoire, M., Hainbucher, D., Kontoyannis, H., Kovacevic, V., Kraskapoulou, E., Kroskos, G., Incarbona, A., Mazzocchi, M. G., Orlic, M., Ozsoy, E., Pascual, A., Poulain, P.-M., Roether, W., Rubino, A., Schroeder, K., Siokou-Frangou, J., Souvermezoglou, E., Sprovieri, M., Tintoré, J., Triantafyllou, G. (2014). Physical forcing and physical/biochemical variability of the Mediterranean Sea: a review of unresolved issues and directions for future research. Ocean Sci. 10, 281-322. https://doi.org/10.5194/os-10-281-2014.

Malanotte-Rizzoli, P., Manca, B.B., d'Alcalà, M.R., Theocharis, A., Brenner, S., Budillon, G., Ozsoy, E. (1999). The eastern Mediterranean in the 80s and in the 90s: the big transition in the intermediate and deep circulations. Dyn.

Atmos. Oceans 29, 365-395. https://doi.org/10.1016/S0377-0265(99)00011-1.

Mancini, A.M., Bocci, G., Morigi, C., Gennari, R., Lozar, F., Negri, A. (2023a). Past analogues of deoxygenation events in the mediterranean sea: a tool to constrain future impacts. J. Mar. Sci. Eng. 11, 562. https://doi.org/10.3390/jmse11030562.

Mancini, A.M., Lozar, F., Gennari, R., Capozzi, R., Morigi, C., Negri, A. (2023b). The past to unravel the future: Deoxygenation events in the geological archive and the anthropocene oxygen crisis. Earth-Science Reviews, 104664. https://doi.org/10.1016/j.earscirev.2023.104664.

Mangini, A., Eisenhauer, A., Walter, P. (1990). Response of manganese in the ocean to the climatic cycles in the Quaternary. Paleoceanography 5, 811-821. https://doi.org/10.1029/PA005i005p00811.

Marino, G., Rohling, E.J., Rijpstra, W.I., Sangiorgi, F., Schouten, S., Sinninghe-Damsté, J. S. (2007). Aegean Sea as driver for hydrological and ecological changes in the eastern Mediterranean. Geology 35, 675-678. https://doi.org/10.1130/G23831A.1.

Marino, G., Rohling, E.J., Sagiorgi, F., Sinninghe, D.J., Hayes, A., Casford, J.L., Lotter, A. F., Kucera, M., Brinkhuis, H. (2009). Early and middle Holocene in the Aegean Sea: interplay between high and low latitude climate variability. Quat. Sci. Rev. 28, 3246-3262. https://doi.org/10.1016/j.quascirev.2009.08.011.

Martín-Puertas, C., Valero-Garcés, B.L., Brauer, A., Mata, M.P., Delgado-Huertas, A., Dulski, P. (2009). The Iberian-Roman humid period (2600-1600 cal yr BP) in the Zoñar Lake varve record (Andalucía, southern Spain). Quat. Res. 71, 108-120. https://doi.org/10.1016/j.yqres.2008.10.004.

Martínez-Ruiz, F., Jroundi, F., Paytan, A., Guerra-Tschuschke, I., Abad, M.M., González-Muñoz, M.T (2018). Barium bioaccumulation by bacterial biofilms and implications for Ba cycling and use of Ba proxies. Nat. Commun. 9, 1619. https://doi.org/10.1038/s41467-018-04069-z.

Martínez-Ruiz, F., Kastner, M., Gallego-Torres, D., Rodrigo-Gámiz, M., Nieto-Moreno, V., Ortega-Huertas, M. (2015). Paleoclimate and paleoceanography over the past 20,000yr in the Mediterranean Sea Basins as indicated by sediment elemental proxies. Quat. Sci. Rev. 107, 25-46. https://doi.org/10.1016/j. quascirev.2014.09.018.

Martínez-Ruiz, F., Kastner, M., Paytan, A., Ortega-Huertas, M., Bernasconi, S.M. (2000). Geochemical evidence for enhanced productivity during S1 sapropel deposition in the eastern Mediterranean. Paleoceanography 15, 200-209. https://doi.org/10.1029/1999PA000419.

Martínez-Ruiz, F., Paytan, A., Gonzalez-Muñoz, M.T., Jroundi, F., Abad, M.M., Lam, P., Bishop, J.K.B., Horner, T.J., Morton, P., Kastner, M. (2019). Barite formation in the ocean: Origin of amorphous and crystalline precipitates. Chem. Geol. 511, 441-451. https://doi.org/10.1016/j.chemgeo.2018.09.011.

Martínez-Ruiz, F., Paytan, A., Gonzalez-Muñoz, M.T., Jroundi, F., Abad, M.D.M., Lam, P.J., Horner, T.J., Kastner, M. (2020). Barite precipitation on suspended organic matter in the mesopelagic zone. Front. Earth Sci. 8, 567714. https://doi.org/10.3389/feart.2020.567714.

Marzocchi, A. (2016). Modelling the impact of orbital forcing on late Miocene climate: implications for the Mediterranean Sea and the Messinian Salinity Crisis (Doctoral dissertation, University of Bristol).

Masqué, P., Fabres, J., Canals, M., Sánchez-Cabeza, J.A., Sánchez-Vidal, A., Cacho, I., Calafat, A.M., Bruach, J. M. (2003). Accumulation rates of major constituents of hemipelagic sediments in the deep Alboran Sea: a centennial perspective of sedimentary dynamics. Mar. Geol. 193, 207-233. https://doi.org/10.1016/S0025-3227(02)00593-5.

Matthews, A., Azrieli-Tal, I., Benkovitz, A., Bar-Matthews, M., Vance, D., Poulton, S.W., Teutsch, N., Almogi-Labin, A., Archer, C. (2017). Anoxic development of sapropel S1 in the Nile Fan inferred from redox sensitive proxies, Fe speciation, Fe and Mo isotopes. Chem. Geol. 475, 24-39. https://doi.org/10.1016/j.chemgeo.2017.10.028.

Mayewski, P.A., Rohling, E.E., Stager, J.C., Karlén, W., Maasch, K.A., Meeker, L.D., Meyerson, E.A., Gasse, F., van Kreveld, S., Holmgren, K., Lee-Thorp, J., Rosqvist, G., Rack, F., Staubwasser, M., Schneider, R.R., Steig, E.J. (2004). Holocene climate variability. Quat. Res. 62, 243-255. https://doi.org/10.1016/j.yqres.2004.07.001.

McArthur, J. (2019). Early Toarcian black shales: a response to an oceanic anoxic event or anoxia in marginal basins? Chem. Geol. 522, 71-83. https://doi.org/10.1016/j.chemgeo.2019.05.028.

McArthur, J., Algeo, T.J., van de Schootbrugge, B., Li, Q., Howarth, R.J. (2008). Basinal restriction, black shales, Re-Os dating, and the Early Toarcian (Jurassic) oceanic anoxic event. Paleoceanpgraphy 23, PA4217. https://doi.org/10.1029/ 2008PA001607.

McManus, J., Berelson, W.M., Klinkhammer, G.P., Hammond, D.E., Holm, C. (2005). Authigenic uranium: relationship to oxygen penetration depth and organic carbon rain. Geochim. Cosmochim. Acta 69, 95-108. https://doi.org/10.1016/j. gca.2004.06.023.

McManus, J., Berelson, W.M., Klinkhammer, G.P., Johnson, K.S., Coale, K.H., Anderson, R.F., Kumar, N., Burdige, D.J., Hammond, D.E., Brumsack, H.J., McCorkle, D.C., Rushdi, A. (1998). Geochemistry of barium in marine sediments: implications for its use as a paleoproxy. Geochim. Cosmochim. Acta 62, 21-22. https://doi.org/10.1016/S0016-7037(98)00248-8.

McManus, J., Berelson, W.M., Klinkhammer, G.P., Kilgore, T.E., Hammond, D.E. (1994). Remobilization of barium in continental margin sediments. Geochim. Cosmochim. Acta 58, 4899-4907. https://doi.org/10.1016/0016-7037(94)90220-8.

Meadows, P.S., Meadows, A., Zoological Society of London (1991). The Environmental Impact of Burrowing Animals and Animal Burrows: The Proceedings of a Symposium Held at the Zoological Society of London on 3rd and 4th May 1990. Published for the Zoological Society of London by Clarendon Press, Oxford. http://www.loc.gov/catdir/enhancements/fy0635/91024767-t.html.

Melki, T., Kallel, N., Fontugne, M. (2010). The nature of transitions from dry to wet condition during sapropel events in the Eastern Mediterranean Sea. Palaeogr. Palaeoclim. Palaeoecol. 291, 267-285. https://doi.org/10.1016/j.palaeo.2010.02.039.

Mena, C., Reglero, P., Hidalgo, M., Sintes, E., Santiago, R., Martín, M., Moya, G., Balbín, R. (2019). Phytoplankton community structure is driven by stratification in the oligotrophic Mediterranean Sea. Front. Microbiol. 10, 1698. https://doi.org/10.3389/fmicb.2019.01698.

Merinero, R., Cardenes, V., Lunar, R., Boone, M., Cnudde, V. (2017). Representative size distributions of framboidal, euhedral and sunflower pyrite from high-resolution X- ray tomography and scanning electron microscopy analyses. Am. Mineral. 102, 620-631. https://doi.org/10.2138/am-2017-5851.

Mertens, K.N., Gonzalez, C., Delusina, I., Louwye, S. (2009). 30 000 years of productivity and salinity variations in the late Quaternary Cariaco Basin revealed by dinoflagellate cysts. Boreas 38, 647-662. https://doi.org/10.1111/j.1502-3885.2009.00095.x.

Mertens, K.N., Price, A.M., Pospelova, V. (2012). Determining the absolute abundance of dinoflagellate cysts in recent marine sediments II: further tests of the Lycopodium marker-grain method. Rev. Palaeobot. Palynol. 184, 74-81. https://doi.org/10.1016/j.revpalbo.2012.06.012.

Mesa-Fernández, J.M., Jiménez-Moreno, G., Rodrigo-Gámiz, M., García-Alix, A., Jiménez-Espejo, F.J., Martínez-Ruiz, F., Anderson, R.S., Camuera, J., Ramos-Román, M.J. (2018). Vegetation and geochemical responses to Holocene rapid climate change in the Sierra Nevada (southeastern Iberia): the Laguna Hondera record. Clim. Past 14, 1687-1706. https://doi.org/10.5194/cp-14-1687-2018.

Mesa-Fernández, J.M., Martínez-Ruiz, F., Rodrigo-Gámiz, M., Jiménez-Espejo, F.J., García, M., Sierro, F.J. (2022). Paleocirculation and paleoclimate conditions in the western Mediterranean basins over the last deglaciation: New insights from sediment composition variations. Glob. Planet. Change 209, 103732. https://doi.org/10.1016/j.gloplacha.2021.103732.

Meyers, P.A. (1994). Preservation of elemental and isotopic source identification of sedimentary organic matter. Chem Geol. 114, 289-302. https://doi.org/10.1016/0009-2541(94)90059-0.

Meysman, F.J.R., Galaktionov, O.S., Gribsholt, B., Middelburg, J.J. (2006). Bioirrigation in permeable sediments: Advective pore-water transport induced by burrow ventilation. Limnol. Oceanogr. 51, 142–156. https://doi.org/10.4319/ lo.2006.51.1.0142.

Miller, A.R. (1963). Physical Oceanography of the Mediterranean Sea: a discourse. Rapp. Comm. Int. Mer Médit. 17, 857-887.

Millot, C. (1999). Circulation in the Western Mediterranean Sea. J. Mar. Syst. 20, 423-442. https://doi.org/10.1016/S0924-7963(98)00078-5.

Millot, C. (2009). Another description of the Mediterranean Sea outflow. Prog. Oceanogr. 82, 101-124. https://doi.org/10.1016/j.pocean.2009.04.016.

Millot, C. (2013). Levantine Intermediate Water characteristics: an astounding general misunderstanding!. Sci. Mar. 77, 217-232. https://doi.org/10.3989/scimar.03518.13A.

Millot, C. (2014). Heterogeneities of in-and out-flows in the Mediterranean Sea. Prog. Oceanogr. 120, 254-278. https://doi.org/10.1016/j.pocean.2013.09.007.

Millot, C., Taupier-Letage, I. (2005). Circulation in the Mediterranean Sea. In: The Mediterranean Sea (eds. Saliot A.). Springer, Berlin, Heidelberg. Handb. Environ. Chem. 5, 26-66. https://doi.org/10.1007/b107143.

Moens, T., Santos, G.A.P., Thompson, F., Swings, J., Fonsˆeca-Genevois, V., Vincx, M., De Mesel, I. (2005). Do nematode mucus secretions affect bacterial growth? Aquat. Microb. Ecol. 40, 77-83. https://doi.org/10.3354/ame040077.

Monaco, P., Rodríguez-Tovar, F.J., Uchman, A. (2012). Ichnological analysis of lateral environmental heterogeneity within the Bonarelli Level (uppermost Cenomanian) in the classical localities near Gubbio, Central Apennines, Italy. PALAIOS 27, 48-54. https://doi.org/10.2110/palo.2011.p11-018r.

Monaco, P., Rodríguez-Tovar, F.J., Uchman, A. (2016). The stratigraphic record of gubbio: integrated stratigraphy of the late Cretaceous-Paleogene Umbria-Marche Pelagic Basin. GSA Spec. Pap. 524, 97-103. https://doi.org/10.1130/SPE524.

Monedero-Contreras, R.D., Martínez-Ruiz, F., Rodríguez-Tovar, F.J. (2023a). Role of climate variability on deep-water dynamics and deoxygenation during sapropel deposition: new insights from a palaeoceanographic empirical approach. Palaeogeogr. Palaeoclimatol. Palaeoecol. 622, 111601. https://doi.org/10.1016/j.palaeo.2023.111601.

Monedero-Contreras, R.D., Martínez-Ruiz, F., Rodríguez-Tovar, F.J. (2023b). Evidence of postdepositional remobilization of redox-sensitive metals across sapropel boundaries: new insights from LA-ICP-MS and EDX mapping analyses. Chem. Geol. 636, 121643. https://doi.org/10.1016/j.chemgeo.2023.121643.

Monedero-Contreras, R.D., Martínez-Ruiz, F., Rodríguez-Tovar, F.J., de Lange, G. (2024). Redox geochemical signatures in Mediterranean sapropels: Implications to constrain deoxygenation dynamics in deep-marine settings. Palaeogeogr. Palaeoclimatol. Palaeoecol. 634, 111953. https://doi.org/10.1016/j.palaeo.2023.111953.

Montero-Serrano, J.C., Föllmi, K.B., Adatte, T., Spangenberg, J.E., Tribovillard, N., Fantasia, A., Suan, G. (2015). Continental weathering and redox conditions during the early Toarcian Oceanic Anoxic Event in the northwestern Tethys: Insight from the Posidonia Shale section in the Swiss Jura Mountains. Palaeogeogr. Palaeoclimatol. Palaeoecol. 429, 83-99. https://doi.org/10.1016/j.palaeo.2015.03.043.

Montresor, M., Zingone, A., Sarno, D. (1998). Dinoflagellate cyst production at a coastal Mediterranean site. J. Plankton Res. 20, 2291-2312. https://doi.org/10.1093/plankt/20.12.2291.

Morcillo-Montalbá, L., Rodrigo-Gámiz, M., Martínez-Ruiz, F., Ortega-Huertas, M., Schouten, S., Sinninghe Damsté, J.S. (2021). Rapid Climate Changes in the Westernmost Mediterranean (Alboran Sea) Over the Last 35 kyr: New Insights From Four Lipid Paleothermometers (UK'37, TEXH86, RI-OH', and LDI). Paleoceanogr. Paleoclimatol. Palaeoecol. 36, e2020PA004171. https://doi.org/10.1029/2020PA004171.

Moreno, A., Cacho, I., Canals, M., Grimalt, J.O., Sánchez-Vidal, A. (2004). Millennial-scale variability in the productivity signal from the Alboran Sea record, Western Mediterranean Sea. Palaeogeogr. Palaeoclimatol. Palaeoecol. 211, 205-219. https://doi.org/10.1016/j.palaeo.2004.05.007.

Moreno, T., Querol, X., Castillo, S., Alastuey, A., Cuevas, E., Herrmann, L., Mounkaila, M., Elvira, J., Gibbons, W. (2006). Geochemical variations in aeolian mineral particles from the Sahara-Sahel Dust Corridor. Chemosphere 65, 261-270. https://doi.org/10.1016/j.chemosphere.2006.02.052.

Morford, J.L., Emerson, S. (1999). The geochemistry of redox sensitive trace metals in sediments. Geochim. Cosmochim. Acta 63, 1735-1750. https://doi.org/10.1016/S0016-7037(99)00126-X.

Morford, J.L., Emerson, S.R., Breckel, E.J., Kim, S.H. (2005). Diagenesis of oxyanions (V, U, Re, and Mo) in pore waters and sediments from a continental margin. Geochim. Cosmochim. Acta 69, 5021-5032. https://doi.org/10.1016/j.gca.2005.05.015.

Morford, J.L., Martin, W.R., François, R., Carney, C.M. (2009). Model for uranium, rhenium, and molybdenum diagenesis in marine sediments based on results from coastal locations. Geochim. Cosmochim. Acta 73, 2938-2960. https://doi.org/ 10.1016/j.gca.2009.02.029.

Mulitza, S., Heslop, D., Pittauerova, D., Fischer, H.W., Meyer, I., Stuut, J.B., Zabel, M., Mollenhauer, G., Collins, J.A., Kuhnert, H., Schulz, M. (2010). Increase in African dust flux at the onset of commercial agriculture in the Sahel region. Nature 466, 226-228. https://doi.org/10.1038/nature09213.

Murat, A., Got, H. (1987). Middle and late Quaternary depositional sequences and cycles in the eastern Mediterranean. Sedimentology 34, 885-889. https://doi.org/10.1111/j.1365-3091.1987.tb00810.x.

Myers, C.R., Nealson, K.H. (1988). Bacterial manganese reduction and growth with manganese oxide as the sole electron acceptor. Science 240, 1319-1321. https://doi.org/10.1126/science.240.4857.1319.

Naidu, P.D., Niitsuma, N. (2004). Atypical $\delta^{13}C$ signature in Globigerina bulloides at the ODP site 723A (Arabian Sea): implications of environmental changes caused by upwelling. Marine Micropaleontology 53, 1-10. https://doi.org/10.1016/j.marmicro.2004.01.005.

Neira, C., Sellanes, J., Levin, L.A., Arntz, W.E. (2001). Meiofaunal distributions on the Peru margin: relationship to oxygen and organic matter availability. Deep Sea Res. Part

I Oceanogr. Res. Pap. 48, 2453-2472. https://doi.org/10.1016/S0967-0637 (01)00018-8.

Nieto-Moreno, V., Martínez-Ruiz, F., Giralt, S., Jiménez-Espejo, F., Gallego-Torres, D., Rodrigo-Gámiz, M., García-Orellana, J., Huertas-Ortega, M., de Lange, G.J. (2011). Tracking climate variability in the western Mediterranean during the late Holocene: a multiproxy approach. Clim. Past 7, 1395-1414. https://doi.org/10.5194/cp-7-1395-2011.

Nijenhuis, I.A., Bosch, H.J., Damsté, J.S., Brumsack, H.J., de Lange, G.J. (1999). Organic matter and trace element rich sapropels and black shales: a geochemical comparison. Earth Planet. Sci. Lett. 169, 277-290. https://doi.org/10.1016/S0012-821X(99) 00083-7.

Nijenhuis, I.A., Brumsack, de Lange, G.J. (1998). The trace element budget of the eastern mediterranean during pliocene sapropel formation. In: Proceedings of the Ocean Drilling Program, Scientific Results 160, 199-206. https://doi.org/10.2973/odp.proc. sr.160.019.1998.

Nolet, G.J., Corliss, B.H. (1990). Benthic foraminiferal evidence for reduced deep-water circulation during sapropel deposition in the eastern Mediterranean. Mar. Geol. 94, 109-130. https://doi.org/10.1016/0025-3227(90)90106-T.

Olauson, E. (1961). Studies of deep-sea cores. Reports Swedish Deep-Sea Expedit. 1947- 1948 (8), 337-391.

Olías, M., Nieto, J.M. (2015). Background Conditions and Mining Pollution throughout History in the Río Tinto (SW Spain). Environments 2, 295-316. https://doi.org/10.3390/environments2030295.

Ordoñez, L., Vogel, H., Sebag, D., Ariztegui, D., Adatte, T., Russell, J.M., Kallmeyer, J., Vuillemin, A., Friese, A., Crowe, S.A., Bauer, K.W., Simister, R., Henny, C., Nomosatryo, S., Bijaksana, S. (2019). Empowering conventional Rock-Eval pyrolysis for organic matter characterization of the siderite-rich sediments of Lake Towuti (Indonesia) using End-Member Analysis. Org. Geochem. 134, 32-44. https://doi.org/ 10.1016/j.orggeochem.2019.05.002.

Osborne, A., Marino, G., Vance, D., Rohling, E.J. (2010). Eastern Mediterranean surface- water Nd during Eemian sapropel S5: monitoring northerly (mid latitude) versus southerly (sub tropical) freshwater contributions. Quat. Sci. Rev. 29, 2473-2483. https://doi.org/10.1016/j.quascirev.2010.05.015.

Oschlies, A., Brandt, P., Stramma L., Schmidtko S. (2018). Drivers and mechanisms of ocean deoxygenation. Nat. Geosci. 11, 467-473. https://doi.org/10.1038/s41561-018-0152-2.

Özsoy, E. (1981). On the atmospheric factors affecting the Levantine Sea. European Centre for Medium Range Weather Forecasts Reading, UK. Technical Report 25, 29. https://www.ecmwf.int/sites/default/files/elibrary/1981/11461-atmospheric-factors-affecting-levantine-sea.pdf.

Palanques, A., El Khatab, M., Puig, P., Masqué, P., Sánchez-Cabeza, J.A., Isla, E. (2005). Downward particle fluxes in the Guadiaro submarine canyon depositional system (north-western Alboran Sea), a river flood dominated system. Mar. Geol. 220, 23-40. https://doi.org/10.1016/j.margeo.2005.07.004.

Passier, H.F., Bosch, H.J., Nijenhuis, I., Lourens, L., Böttcher, M., Leenders, A., Sinninghe-Damste, J., de Lange, G., de Leeuw, J. (1999). Sulphic Mediterranean surface waters during Pliocene sapropel formation. Nature 397, 146-149. https:// doi.org/10.1038/16441.

Passier, H.F., de Lange, G.J. (1998). Sedimentary sulfur and Iron chemistry in relation to the formation of Eastern Mediterranean Sapropels 1. In Proceedings of the Ocean Drilling Program, Scientific Results 160, 249-259. https://doi.org/10.2973/odp.proc.sr.160.020.1998.

Passier, H.F., Middelburg, J., de Lange, G., Böttcher, M. (1997). Pyrite contents, microtextures, and sulfur isotopes in relation to formation of the youngest eastern Mediterranean sapropel. Geology 25, 519-522. https://doi.org/10.1130/0091-7613 (1997)025<0519:PCMASI>2.3.CO;2.

Passier, H.F., Middelburg, J.J., van Os, B.J.H., de Lange, G.J. (1996). Diagenetic pyritisation under eastern Mediterranean sapropels caused by downward sulphide diffusion. Geochim. Cosmochim. Acta 60, 751-776. https://doi.org/10.1016/0016- 7037(95)00419-X.

Paul, K.M., van Heldmond, N.A.G.M., Slomp, C.P., Jokinen, S.A., Virtasalo, J.J., Filipsson, H.L., Jilbert, T. (2023). Sedimentary molybdenum and uranium: Improving proxies for deoxygenation in coastal depositional environments. Chem. Geol. 615, 121203. https://doi.org/10.1016/j.chemgeo.2022.121203.

Paytan, A., Averyt, K., Faul, K., Gray, E., Thomas, E. (2007). Barite accumulation, ocean productivity, and Sr/Ba in barite across the Paleocene-Eocene Thermal Maximum. Geology 35, 1139-1142. https://doi.org/10.1130/G24162A.1.

Paytan, A., Griffith, E.M. (2007). Marine Barite: Recorder of Variations in Ocean export Productivity. Deep Sea Res. Part Topical Stud. Oceanogr. 54, 687-705. https://doi.org/10.1016/j.dsr2.2007.01.007.

Paytan, A., Kastner, M., Chavez, F.P. (1996). Glacial to interglacial fluctuations in productivity in the equatorial

Pacific as indicated by marine barite. Science 274, 1355-1357. https://doi.org/10.1126/science.274.5291.13.

Paytan, A., Martínez-Ruiz, F., Eagle, M., Ivy, A., Wankel, S. (2004). Using sulfur isotopes to elucidate the origin of barite associated with high organic matter accumulation events in marine sediments. Geol. Soc. Am. Spec. Paper 379, 151-160. http://dx.doi.org/10.1130/0-8137-2379-5.151.

Paytan, A., Mearon, S., Cobb, K., Kastner, M. (2002). Origin of marine Barite deposits: Sr and S isotope characterization. Geol 30, 747-750. https://doi.org/10.1130/0091-7613(2002)030<0747:oombds>2.0.co;2.

Pearce, N.J.G., Perkins, W.T., Westgate, J.A., Gorton, M.P., Jackson, S.E., Neal, C.R., Chenery, S.P. (2007). A compilation of new and published major and trace element data for NIST SRM 610 and NIST SRM 612 glass reference materials. Geostandards Newslet. J. Geostand. Geoanal. 21, 115-144. https://doi.org/10.1111/j.1751-908X.1997.tb00538.x.

Pénaud, A., Eynaud, F., Sánchez-Goñi, M., Malaizé, B., Turon, J.L., Rossignol, L. (2011). Contrasting sea-surface responses between the western Mediterranean Sea and eastern subtropical latitudes of the North Atlantic during abrupt climatic events of MIS 3. Mar. Micropaleontol. 80, 1-17. https://doi.org/10.1016/j.marmicro.2011.03.002.

Pénaud, A., Eynaud, F., Voelker, A.H.L., Turon, J.L. (2016). Palaeohydrological changes over the last 50 ky in the central Gulf of Cadiz: complex forcing mechanisms mixing multi-scale processes. Biogeosciences 13, 5357-5377. https://doi.org/10.5194/bg-13-5357-2016.

Pérez-Asensio, J.N., Frigola, J., Pena, L.D., Sierro, F.J., Reguera, M.I., Rodríguez-tovar, F.J., Dorador, J., Asioli, A., Kuhlmann, J., Huhn, K., Cacho, I. (2020). Changes in western Mediterranean thermohaline circulation in association with a deglacial Organic Rich Layer formation in the Alboran Sea. Quat. Sci. Rev. 228, 106075. https://doi.org/10.1016/j.quascirev.2019.106075.

Pérez-Folgado, M., Sierro, F.J., Flores, J.A., Cacho, I., Grimalt, J.O., Zahn, R., Shackleton, N. (2003). Western Mediterranean planktonic foraminifera events and millennial climatic variability during the last 70 kyr. Mar. Micropaleontol. 48, 49-70. https://doi.org/10.1016/S0377-8398(02)00160-3.

Phillips, C., McIlroy, D. (2010). Ichnofabrics and Biologically Mediated changes in Clay Mineral Assemblages from a Deep-water, Fine-grained, Calcareous Sedimentary Succession: an example from the Upper cretaceous Wyandot Formation, Offshore Nova Scotia. Bull. Can. Petrol. Geol. 58, 203–218. https://doi.org/10.2113/ gscpgbull.58.3.203.

Pinardi, N., Masetti, E. (2000). Variability of the large scale general circulation of the Mediterranean Sea from observations and modelling: a review. Palaeogeogr. Palaeoclimatol. Palaeoecol. 158, 153-173. https://doi.org/10.1016/S0031-0182 (00)00048-1.

Pinardi, N., Zavatarelli, M., Adani, M., Coppini, G., Fratianni, C., Oddo, P., Simoncelli, S., Tonani, M., Lyubartsev, V., Dobricic, S., Bonaduce, A. (2015). Mediterranean Sea large-scale low-frequency ocean variability and water mass formation rates from 1987 to 2007: a retrospective analysis. Progress. Oceanogr. 132, 318-332. https:// doi.org/10.1016/j.pocean.2013.11.003.

Pistocchi, R.; Guerrini, F., Pezzolesi, L., Riccardi, M., Vanucci, S., Ciminiello, P., Dell'Aversano, C., Forino, M., Fattorusso, E., Tartaglione, L., Milandri, A., Pompei, M., Cangini, M., Pigozzi, Riccardi, E. (2012). Toxin Levels and Profiles in Microalgae from the North-Western Adriatic Sea—15 Years of Studies on Cultured Species. Mar. Drugs 10, 140-162. https://doi.org/10.3390/md10010140.

POEM group (1992). General circulation of the eastern Mediterranean Sea. Earth Sci. Rev. 32, 285-308. https://doi.org/10.1016/0012-8252(92)90002-B.

Polovina, J.J., Howell, E.A., Abecassis, M. (2008). Ocean's least productive waters are expanding. Geophys. Res. Lett. 35, L03618. https://doi.org/10.1029/ 2007GL031745.

Pospelova, V., de Vernal, A., Pedersen, T.F. (2008). Distribution of dinoflagellate cysts in surface sediments from the northeastern Pacific Ocean (43-25 N) in relation to sea-surface temperature, salinity, productivity and coastal upwelling. Mar. Micropaleontol. 68, 21-48. https://doi.org/10.1029/2007GL031745.

Pospelova, V., Esenkulova, S., Johannessen, S.C., O'Brien, M.C., Macdonald, R.W. (2010). Organic-walled dinoflagellate cyst production, composition and flux from 1996 to 1998 in the central Strait of Georgia (BC, Canada): a sediment trap study. Mar. Micropaleontol. 75, 17-37. https://doi.org/10.1016/j.marmicro.2010.02.003.

Powell, A.J., Lewis, J., Dodge, J.D. (1992). The palynological expressions of post-Palaeogene upwelling: a review. Geol. Soc. Spec. Publ. 64, 215-226. https://doi.org/10.1144/GSL.SP.1992.064.01.1.

Pross, J., Brinkhuis, H. (2005). Organic-walled dinoflagellate cysts as paleoenvironmental indicators in the Paleogene; a synopsis of concepts. Paläontologische Zeitschrift 79, 53-59. https://doi.org/10.1007/BF03021753.

Pruysers, P.A., de Lange, G.J., Middelburg, J.J. (1991). Geochemistry of eastern Mediterranean sediments: primary sediment composition and diagenetic alterations. Mar. Geol. 100, 137-154. https://doi.org/10.1016/0025-3227(91)90230-2.

Pruysers, P.A., de Lange, G.J., Middelburg, J.J., Hydes, D.J. (1993). The diagenetic formation of metal-rich layers in sapropel-conatining sediments in the eastern Mediterranean. Geochim. Cosmochim. Acta 57, 527-536. https://doi.org/10.1016/0016-7037(93)90365-4.

Ramos-Román, M.J., Jiménez-Moreno, G., Camuera, J., García-Alix, A., Anderson, R.S., Jiménez-Espejo, F.J., Sachse, D., Toney, J.L., Carrión, J.S., Webster, C., Yanes, Y. (2018a). Millennial-scale cyclical environment and climate variability during the Holocene in the western Mediterranean region deduced from a new multi-proxy analysis from the Padul record (Sierra Nevada, Spain). Glob. Planet. Change 168, 35-53. https://doi.org/10.1016/j.gloplacha.2018.06.003.

Ramos-Román, M.J., Jiménez-Moreno, G., Camuera, J., García-Alix, A., Anderson, R.S., Jiménez-Espejo, F.J., Carrión, J.S. (2018b). Holocene climate aridification trend and human impact interrupted by millennial-and centennial-scale climate fluctuations from a new sedimentary record from Padul (Sierra Nevada, southern Iberian Peninsula). Clim. Past 14, 117-137. https://doi.org/10.5194/cp-14-117-2018.

Reale, M., Cossarini, G., Lazzari, P., Lovato, T., Bolzon, G., Masina, S., Solidoro, C., Salon, S. (2022). Acidification, deoxygenation, and nutrient and biomass declines in a warming Mediterranean Sea. Biogeosciences 19, 4035-4065. https://doi.org/10.5194/bg-19-4035-2022.

Reddin, C.J., Nätscher, P.S., Kocsis, Á.T., Pörtner, H.O., Kiessling, W. (2020). Marine clade sensitivities to climate change conform across timescales. Nat. Clim. Change. 10, 249-253. https://doi.org/10.1038/s41558-020-0690-7.

Reed, D.C., Slomp, C.P., de Lange, G.J. (2011). A quantitative reconstruction of organic matter and nutrient diagenesis in Mediterranean Sea sediments over the Holocene. Geochim. Cosmochim. Acta 75, 5540-5558. https://doi.org/10.1016/j. gca.2011.07.002.

Reershemius, T., Planavsky, N.J. (2021). What controls the duration and intensity of ocean anoxic events in the Paleozoic and the Mesozoic? Earth Sci. Rev. 221, 103787. https://doi.org/10.1016/j.earscirev.2021.103787.

Reichart, G.J., Brinkhuis, H. (2003). Late Quaternary Protoperidinium cysts as indicators of paleoproductivity in the northern Arabian Sea. Mar. Micropaleontol. 49, 303-315. https://doi.org/10.1016/S0377-8398(03)00050-1.

Reitz, A., Thomson, J., de Lange, G.J., Hensen, C. (2006). Source and development of large manganese enrichments above eastern Mediterranean sapropel S1. Paleoceanography 21, PA3007. https://doi.org/10.1029/2005PA001169.

Richon, C., Dutay, J. C., Dulac, F., Wang, R., Balkanski, Y., Nabat, P., Aumony, O., Desboeufs, K, Laurent, B., Guieu, C., Raimbault, P., Beuvier, J. (2018). Modeling the impacts of atmospheric deposition of nitrogen and desert dust-derived phosphorus on nutrients and biological budgets of the Mediterranean Sea. Prog. Oceanogr. 163, 21-39. https://doi.org/10.1016/j.pocean.2017.04.009.

Richon, C., Dutay, J.C., Dulac, F., Wang, R., Balkanski, Y. (2018). Modeling the biogeochemical impact of atmospheric phosphate deposition from desert dust and combustion sources to the Mediterranean Sea. Biogeosciences 15, 2499-2524. https://doi.org/10.5194/bg-15-2499-2018.

Rochon, A., Vernal, A.D., Turon, J.L., Matthiessen, J., Head, M.J. (1999). Distribution of recent dinoflagellate cysts in surface sediments from the North Atlantic Ocean and adjacent seas in relation to sea-surface parameters. AASP Contribution Series 35, 1-146.

Rodó, X., Baert, E., Comin, F.A. (1997). Variations in seasonal rainfall in Southern Europe during the present century: relationships with the North Atlantic Oscillation and the El Niño-Southern Oscillation. Clim. Dyn. 13, 275-284. https://doi.org/10.1007/s003820050165.

Rodrigo-Gámiz, M., Martínez-Ruiz, F., Chiaradia, M., Jiménez-Espejo, F.J., Ariztegui, D. (2015). Radiogenic isotopes for deciphering terrigenous input provenance in the western Mediterranean. Chem. Geol. 410, 237-250. https://doi.org/10.1016/j. chemgeo.2015.06.004.

Rodrigo-Gámiz, M., Martínez-Ruiz, F., Jiménez-Espejo, F.J., Gallego-Torres, D., Nieto- Moreno, V., Romero, O., Ariztegui, D. (2011). Impact of climate variability in the western Mediterranean during the last 20,000 years: Oceanic and atmospheric responses. Quat. Sci. Rev. 30, 2018-2034. https://doi.org/10.1016/j. quascirev.2011.05.011.

Rodrigo-Gámiz, M., Martínez-Ruiz, F., Rampen, S.W., Schouten, S., Sinninghe Damsté, J.S. (2014a). Sea surface temperature variations in the western Mediterranean Sea over the last 20 kyr: a dual-organic proxy UK′37 and LDI) approach. Paleoceanography 29, 87-98. https://doi.org/10.1002/2013PA002466.

Rodrigo-Gámiz, M., Martínez-Ruiz, F., Rodríguez-Tovar, F.J., Jiménez-Espejo, F.J., Pardo-Igúzquiza, E. (2014b). Millennial-to centennial-scale climate periodicities and forcing mechanisms in the Westernmost Mediterranean for the past 20,000 yr. Quat. Res. 81, 78-93. https://doi.org/10.1016/j.yqres.2013.10.009.

Rodríguez-Tovar, F.J. (2021a). Ichnology of the Toarcian Oceanic Anoxic Event: an underestimated tool to assess palaeoenvironmental interpretations. Earth Sci. Rev. 216, 103579. https://doi.org/10.1016/j.earscirev.2021.103579.

Rodríguez-Tovar, F.J. (2021b). Toarcian Oceanic Anoxic Event in the Iberian Massif: the ichnological record. Geol. Today 37, 134-140. https://doi.org/10.1111/gto.12361.

Rodríguez-Tovar, F.J. (2022). Ichnological analysis: a tool to characterize deep-marine processes and sediments. Earth Sci. Rev. 228, 104014. https://doi.org/10.1016/j.earscirev.2022.104014.

Rodríguez-Tovar, F.J., Dorador, J., Zuchuat, V., Planke, S., Hammer, Ø. (2021). Response of macrobenthic trace maker community to the end-Permian mass extinction in Central Spitsbergen, Svalbard. Palaeogeogr. Palaeoclimatol. Palaeoecol. 581, 110637. https://doi.org/10.1016/j.palaeo.2021.110637.

Rodríguez-Tovar, F.J., Martínez-Ruiz, F., Bernasconi, S.M. (2004). Carbon isotope evidence for the timing of the Cretaceous-Palaeogene macrobenthic colonization at the Agost section (Southeast Spain). Palaeogeogr. Palaeoclimatol. Palaeoecol. 203, 65-72. https://doi.org/10.1016/S0031-0182(03)00660-6.

Rodríguez-Tovar, F.J., Martínez-Ruiz, F., Bernasconi, S.M. (2006). Use of high resolution ichnological and stable isotope data for assessing completeness of a K-P boundary section, Agost, Spain. Palaeogeogr. Palaeoclimatol. Palaeoecol. 237, 137-146. https://doi.org/10.1016/j.palaeo.2005.11.019.

Rodríguez-Tovar, F.J., Uchman, A. (2010). Ichnofabric evidence for the lack of bottom anoxia during the lower Toarcian Oceanic Anoxic Event in the Fuente de la Vidriera section, Betic Cordillera, Spain. PALAIOS 25, 576-587. https://doi.org/10.2110/ palo.2009.p09-153r.

Rodríguez-Tovar, F.J., Uchman, A. (2011). Ichnological data as a useful tool for deep-sea environmental characterization: a brief overview and an application to recognition of small-scale oxygenation changes during the Cenomanian-Turonian anoxic event. Geo-Mar. Lett. 31, 525-536. https://doi.org/10.1007/s00367-011-0237-z.

Rodríguez-Tovar, F.J., Uchman, A. (2017). The Faraoni event (latest Hauterivian) in ichnological record: the Rio Argos section of southern Spain. Cretac. Res. 79, 109-121. https://doi.org/10.1016/j.cretres.2017.07.018.

Rodríguez-Tovar, F.J., Uchman, A., Martín-Algarra, A. (2009a). Oceanic anoxic event at the Cenomanian-Turonian boundary interval (OAE-2): ichnological approach from the Betic Cordillera, southern Spain. Lethaia 42, 407-417. https://doi.org/10.1111/ j.1502-3931.2009.00159.x.

Rodríguez-Tovar, F.J., Uchman, A., Martín-Algarra, A., O'Dogherty, L. (2009b). Nutrient spatial variation during intrabasinal upwelling at the Cenomanian-Turonian oceanic anoxic event in the Westernmost Tethys: an ichnological and facies approach. Sediment. Geol. 215, 83-93. https://doi.org/10.1016/j.sedgeo.2009.01.006.

Rodríguez-Tovar, F.J., Uchman, A., Reolid, M., Sánchez-Quiñónez, C.A. (2020). Ichnological analysis of the Cenomanian-Turonian boundary interval in a collapsing slope setting: a case from the Rio Fardes section, southern Spain. Cretac. Res. https://doi.org/10.1016/j.cretres.2019.104262.

Roether, W., Manca, B.B., Klien, B., Bregant, D., Georgopoulos, D., Beitzel, V., Kovacevic, V., Luchetta, A. (1996). Recent changes in Eastern Mediterranean deep waters. Science 271, 333-335. https://doi.org/10.1126/science.271.5247.333.

Rogerson, M., Cacho, I., Jiménez-Espejo, F., Reguera, M.I., Sierro, F.J., Martínez-Ruiz, F., Frigola, J., Canals, M. (2008), A dynamic explanation for the origin of the western Mediterranean organic-rich layers, Geochem. Geophys. Geosyst. 9, Q07U01. https://doi.org/10.1029/2007GC001936.

Rohling, E.J. (1994). Review and new aspects concerning the formation of Mediterranean sapropels. Mar. Geol. 122, 1-28. https://doi.org/10.1016/0025-3227(94)90202-X.

Rohling, E.J., De Rijk, S. (1999). The Holocene climate optimum and last glacial maximum in the Mediterranean: the marine oxygen isotope record. Mar. Geol. 153, 57-75. https://doi.org/10.1016/S0025-3227(98)00020-6.

Rohling, E.J., Den Dulk, M., Pujol, C., Vergnaud-Grazzini, C. (1995). Abrupt hydrographic change in the Alboran Sea (western Mediterranean) around 8000 yrs BP. Deep. Res. Part I 42, 1609-1619. https://doi.org/10.1016/0967-0637(95)00069-I.

Rohling, E.J., Foster, G.L., Grant, K.M., Marino, G., Roberts, A.P., Tamisiea, M.E., Williams, F. (2014). Sea-level and deep-sea-temperature variability over the past 5.3 million years. Nature 508, 477-482. https://doi.org/10.1038/nature13230.

Rohling, E.J., Marino, G., Grant, K.M. (2015). Mediterranean climate and oceanography, and the periodic development of anoxic events (sapropels). Earth-Sci. Rev. 143, 62-97. https://doi.org/10.1016/j.earscirev.2015.01.008.

Rohling, E.J., Pälike, H. (2005). Centennial-scale climate cooling with a sudden cold event around 8.200 years ago. Nature 434, 975-979. https://doi.org/10.1038/ nature03421.

Romero-Baena, A.J., González, I. Galán, E. (2018). Soil pollution by mining activities in Andalusia (South Spain)—the role of Mineralogy and Geochemistry in three case studies. J. Soils Sediments 18, 2231-2247. https://doi.org/10.1007/s11368-017-1898-7.

Rossignol-Strick, M. (1983). African monsoons, an immediate climate response to orbital insolation. Nature 304, 46-49. https://doi.org/10.1038/304046a0.

Rossignol-Strick, M. (1985). Mediterranean Quaternary sapropels, an immediate response of the African monsoon to variations of insolation. Palaeogeogr. Palaeoclimatol. Palaeoecol. 49, 237-263. https://doi.org/10.1016/0031-0182(85)90056-2.

Rossignol-Strick, M. (1999). The Holocene climatic optimum and pollen records of sapropel 1 in the eastern Mediterranean, 9000-6000 BP. Quat. Sci. Rev. 18, 515-530. https://doi.org/10.1016/S0277-3791(98)00093-6.

Ruiz, J., Echevarrıa, F., Font, J., Ruiz, S., García, E., Blanco, J.M., Jiménez-Gómez, F., Prieto, L., González-Alaminos, A., García, C.M., Cipollini, P., Snaith, H., Bartual., A., Reul, A., Rodríguez, V. (2001). Surface distribution of chlorophyll, particles and gelbstoff in the Atlantic jet of the Alborán Sea: from submesoscale to subinertial scales of variability. J. Mar. Syst. 29, 277-292. https://doi.org/10.1016/S0924-7963(01)00020-3.

Rutten, A., de Lange, G.J., Hayes, A., Rohling, E.J., de Jong, A.F.M., van der Borg, K. (1999). Deposition of sapropel S1 sediments in oxic pelagic and anoxic brine environments in the eastern Mediterranean: differences in diagenesis and preservation. Mar. Geol. 153, 319-335. https://doi.org/10.1016/S0025-3227(98) 00076-0.

Rysgaard, S., Christensen, P.B., Sørensen, M.V., Funch, P., Berg, P. (2000). Marine meiofauna, carbon and nitrogen mineralization in sandy and soft sediments of Disko Bay, West Greenland. Aquat. Microb. Ecol. 21, 59-71. https://doi.org/10.3354/ ame021059.

Sainz de Murieta, E., Cunha, P., Cearreta, A., Murray, A., Buylaert, J.P. (2021). The Oyambre coastal terrace: a detailed sedimentary record of the Last Interglacial Stage in northern Iberia (Cantabrian coast, Spain). J. Quat. Sci. 36, 570-585. https://doi. org/10.1002/jqs.3317.

Sánchez-Vidal, A., Calafat, A., Canals, M., Frigola, J., Fabres, J. (2005). Particle fluxes and organic carbon balance across the Eastern Alboran Sea (SW Mediterranean Sea). Cont. Shelf Res. 25, 609-628. https://doi.org/10.1016/j.csr.2004.11.004.

Sangiorgi, F., Capotondi, L., Combourieu Nebout, N., Vigliotti, L., Brinkhuis, H., Giunta, S., Lotter, A.F., Morigi, C., Negri, A., Reichart, G.J. (2003). Holocene seasonal sea-surface temperature variations in the southern Adriatic Sea inferred from a multiproxy approach. J. Quat. Sci. 18, 723-732. https://doi.org/10.1002/jqs.782.

Sangiorgi, F., Dinelli, E., Maffioli, P., Capotondi, L., Giunta, S., Morigi, C., Principato, M.S., Negri, A., Emeis, K.-C., Corselli, C. (2006). Geochemical and micropaleontological characterisation of a Mediterranean sapropel S5: a case study from core BAN89GC09 (south of Crete). Palaeogeogr. Palaeoclimatol. Palaeoecol. 235, 192-207. https://doi.org/10.1016/j.palaeo.2005.09.029.

Sangiorgi, F., Donders, T.H. (2004). Reconstructing 150 years of eutrophication in the north-western Adriatic Sea (Italy) using dinoflagellate cysts, pollen and spores. Estuar. Coast. Shelf Sci. 60, 69-79. https://doi.org/10.1016/j.ecss.2003.12.001.

Sangiorgi, F., Quaijtaal, W., Donders, T.H., Schouten, S., Louwye, S. (2021). Middle Miocene temperature and productivity evolution at a Northeast Atlantic shelf site (IODP U1318, Porcupine Basin): Global and regional changes. Paleoceanogr Paleoclimatol. 36, e2020PA004059. https://doi.org/10.1029/2020PA004059.

Sarhan, T., Lafuente, J.G., Vargas, M., Vargas, J.M., Plaza, F. (2000). Upwelling mechanisms in the northwestern Alboran Sea. J. Mar. Syst. 23, 317-331. https://doi.org/10.1016/S0924-7963(99)00068-8.

Satake, M., MacKenzie, L., Yasumoto, T. (1997). Identification of Protoceratium reticulatum as the biogenetic origin of yessotoxin. Nat. Toxins 5, 164-167. https://doi.org/10.1002/nt.7.

Savrda, C.E., Bottjer, D.J. (1984). Trace-fossil model for reconstruction of paleo- oxygenation in bottom waters. Geology 14, 3-6. https://doi.org/10.1130/0091-7613(1986)14<3:TMFROP>2.0.CO;2.

Savrda, C.E., Bottjer, D.J. (1989). Trace-fossil model for reconstructing oxygenation histories of ancient marine bottom waters: application to Upper Cretaceous Niobrara Formation, Colorado. Palaeogeogr. Palaeoclimatol. Palaeoecol. 74, 49-74. https://doi.org/10.1016/0031-0182(89)90019-9.

Scheiderich, K., Zerkl, A.L., Helz, G.R., Farquhar, J., Walker, R.J. (2010). Molybdenum isotope, multiple sulfur isotope, and redox-sensitive element behavior in early. Pleistocene Mediterranean sapropels. Chem. Geol. 279, 134-144. https://doi.org/ 10.1016/j.chemgeo.2010.10.015.

Schmidtko, S., Stramma, L. Visbeck, M. (2017). Decline in global oceanic oxygen content during the past five decades. Nature 542, 335-339. https://doi.org/10.1038/nature21399.

Scholz, F. (2018). Identifying oxygen minimum zone-type biogeochemical cycling in Earth history using inorganic geochemical proxies. Earth-Science Reviews, 184, 29-45. https://doi.org/10.1016/j.earscirev.2018.08.002.

Scholz, F., Maum, M., Siebert, C., Eroglu, S., Dale, A.W., Naumann, M., Sommer, S. (2018). Sedimentary molybdenum cycling in the aftermath of seawater inflow to the intermittently euxinic Gotland deep, Central Baltic Sea. Chem. Geol. 491, 27-38. https://doi.org/10.1016/j.chemgeo.2018.04.031.

Scholz, F., McManus, J., Sommer, S. (2013). The manganese and iron shuttle in a modern euxinic basin and implications for molybdenum cycling at euxinic ocean margins. Chem. Geol. 355, 56-68. https://doi.org/10.1016/j.chemgeo.2013.07.00.

Scholz, F., Siebert, C., Dale, A.W., Frank, M. (2017). Intense molybdenum accumulation in sediments underneath a nitrogenous water column and implications for the reconstruction of paleo-redox conditions based on molybdenum isotopes. Geochim. Cosmochim. Acta 213, 400-417. https://doi.org/10.1016/j.gca.2017.06.048.

Schönfeld, J., Schiebel, R., Timm, S. (1991). The Rotpläner (Upper Cenomanian to lower Turonian) of Baddecken-stedt (North-Western Germany): lithology, geochemistry, foraminifers, and stratigraphic correlations. Meyniana 43, 73-95. https://doi.org/ 10.2312/meyniana.1991.43.73.

Schroeder, K., Chiggiato, J., Bryden, H., Borghini, M., Ismail, S.B. (2016). Abrupt climate shift in the Western Mediterranean Sea. Sci. Rep. 6, 23009. https://doi.org/ 10.1038/srep23009.

Schroeder, K., Gasparini, G.P., Tangherlini, M., Astraldi, M. (2006). Deep and intermediate water in the western Mediterranean under the influence of the Eastern Mediterranean Transient. Geophys. Res. Lett. 33, L21607. https://doi.org/10.1029/2006GL027121.

Schulte, P., Schwark, L., Stassen, P., Kouwenhoven, T.J., Bornemann, A., Speijer, R.P. (2013). Black shale formation during the Latest Danian Event and the Paleocene-Eocene Thermal Maximum in central Egypt: Two of a kind? Palaeogeogr. Palaeoclimatol. Palaeoecol. 371, 9-25. https://doi.org/10.1016/j. palaeo.2012.11.027.

Scott, C., Lyons, T.W. (2012). Contrasting molybdenum cycling and isotopic properties in euxinic versus non-euxinic sediments and sedimentary rocks: Refining the paleoproxies. Chem. Geol. 324-325, 19-27. https://doi.org/10.1016/j.chemgeo.2012.05.012.

Scott, T.B., Riba, T.O., Allen, G.C. (2007). Aqueous uptake of uranium onto pyrite surfaces; reactivity of fresh versus weathered material. Geochim. Cosmochim. Acta 71, 5044-5053. https://doi.org/10.1016/j.gca.2007.08.017.

Sierro, F.J., Andersen, N. (2022). An exceptional record of millennial-scale climate variability in the southern Iberia margin during the MIS 6: impact on the formation of sapropel S6. Quat. Sci. Rev. 286, 107527. https://doi.org/10.1016/j. quascirev.2022.107527.

Sierro, F.J., Hodell, D.A., Curtis, J.H., Flores, J.A., Reguera, I., Colmenero-Hidalgo, E., Bárcene, M.A., Grimalt, J.O., Cacho, I., Frigola, J., Canals, M. (2005). Impact of iceberg melting on Mediterranean thermohaline circulation during Heinrich events. Paleoceanography 20, PA2019. https://doi.org/10.1029/2004PA001051.

Siokou-Frangou, I., Christaki, U., Mazzocchi, M.G., Montresor, M., Ribera d'Alcalá, M., Vaqué, D., Zingone, A. (2010). Plankton in the open Mediterranean Sea: a review. Biogeosciences 7, 1543-1586. https://doi.org/10.5194/bg-7-1543-2010.

Skliris, N., Lascaratos, A. (2004). Impacts of the Nile River damming on the thermohaline circulation and water mass characteristics of the Mediterranean Sea. J. Mar. Syst. 52, 121-143. https://doi.org/10.1016/j.jmarsys.2004.02.005.

Skliris, N., Marsh, R., Josey, S.A., Good, S.A., Liu, C., Allan, R.P. (2014). Salinity changes in the World Ocean since 1950 in relation to changing surface freshwater fluxes. Clim. Dyn. 43, 709-736. https://doi.org/10.1007/s00382-014-2131-7.

Sluijs, A., Pross, J., Brinkhuis, H. (2005). From greenhouse to icehouse; organic-walled dinoflagellate cysts as paleoenvironmental indicators in the Paleogene. Earth Sci Rev. 68, 281-315. https://doi.org/10.1016/j.earscirev.2004.06.001.

Sluijs, A., Schouten, S., Pagani, M., Woltering, M., Brinkhuis, H., Damsté, J.S.S., Dickens, G.R., Huber, M., Reichart, G.J, Stein, R., Matthienssen, J., Lourens, L.J., Pedentchouk, N., Backman, J., Moran, K., Expedition 302 Scientists. (2006). Subtropical Arctic Ocean temperatures during the Palaeocene/Eocene thermal maximum. Nature 441, 610-613. https://doi.org/10.1038/nature04668.

Sosa-Montes de Oca, C., de Lange, G.J., Martínez-Ruiz, F., Rodríguez-Tovar, F.J. (2018). Application of laser ablation-ICP-MS to determine high-resolution elemental profiles across the cretaceous/Paleogene boundary at Agost (Spain). Palaeogeogr. Palaeoclimatol. Palaeoecol. 497, 128-138. https://doi.org/10.1016/j. palaeo.2018.02.012.

Sparnocchia, S., Manzella, G.M.R., Violette, P.E.L. (1994). The interannual and seasonal variability of the MAW and

LIW core properties in the western Mediterranean Sea. Coast. Estuar. Stud. 46, 177-194. https://doi.org/10.1029/ce046p0177.

Sparnocchia, S., Schiano, E., Picco, P., Bozzano, R., Cappelletti, A. (2006). The anomalous warming of summer 2003 in the surface- layer of the Central Ligurian Sea (Western Mediterranean). Ann. Geophys. 24, 443–452. https://doi.org/10.5194/angeo-24-443-2006.

StataCorp, L.P. (2007). Tata Multivariate Statistics: Reference Manual. Stata Press Publication. https://www.stata.com/manuals/mv.pdf.

Stocker, T.F., Qin, D., Plattner, G.K., Tignor, M., Allen, S.K., Boschung, J., Nauels, A., Xia, Y., Bex, V., Midgley, P.M. (2013). In: IPCC, 2013: Climate Change 2013: The Physical Science Basis. Contribution of Working Group I to the Fifth Assessment Report of the Intergovernmental Panel on Climate Change. Cambridge Univ. Press, Cambridge, United Kingdom and New York, USA, p. 1535.

Sumner, G., Homar, V., Ramis, C. (2001). Precipitation seasonality in Eastern and Southern coastal Spain. Int. J. Climatol. 21, 219-247. https://doi.org/10.1002/joc.600.

Sweere, S., van den Boorn, S., Dickson, A.J., Reichart, G.J. (2016). Definition of new trace- metal proxies for the controls on organic matter enrichment in marine sediments based on Mn Co, Mo and Cd concentrations. Chem. Geol. 441, 235-245. https://doi.org/10.1016/j.chemgeo.2016.08.028.

Sweere, T., Hennekam, R., Vance, D., Reichart, G.-J. (2021). Molybdenum isotope constraints on the temporal development of sulfidic conditions during Mediterranean sapropel intervals. Geochem. Persp. Let. 17, 16-20. https://doi.org/ 10.7185/geochemlet.2108.

Sylvester, P.J., Jackson, S.E. (2016). A brief history of laser ablation inductively coupled plasma mass spectrometry (LA-ICP-MS). Elements 12, 307-310. https://doi.org/ 10.2113/gselements.12.5.307.

Tachikawa, K., Vidal, L., Cornuault, M., García, M., Pothin, A., Sonzogni, C., Bard, E., Ménot, G., Revel, M. (2015). Eastern Mediterranean Sea circulation inferred from the conditions of S1 sapropel deposition. Clim. Past 11, 855-867. https://doi.org/ 10.5194/cp-11-855-2015.

Taylor, A.M., Gawthorpe, R.L., Goldring, R. (1993). Description and analysis of bioturbation and ichnofabric. J. Geol. Soc. Lond. 150, 141-148. https://doi.org/ 10.1144/gsjgs.150.1.0141.

Taylor, F.J.R. (1987). Dinoflagellate ecology: General and marine ecosystems. Chapt. 11A In Taylor, F.J.R. (ed.) The Biology of Dinoflagellates 80, 398-502.

Taylor, F.J.R., Hoppenrath, M., Saldarriaga, J.F. (2008). Dinoflagellate diversity and distribution. Biodivers. Conserv. 17, 407-418. https://doi.org/10.1007/s10531-007-9258-3.

Taylor, S.R., McLennan, S.M. (1995). The geochemical evolution of the continental crust. Rev. Geophys. 33, 241-265. https://doi.org/10.1029/95RG00262.

Tesi, T., Asioli, A., Minisini, D., Maselli, V., Dalla Valle, G., Gamberi, F., Langone, L., Cattaneo, A., Montagna, P., Trincardi, F. (2017). Large-scale response of the Eastern Mediterranean thermohaline circulation to African monsoon intensification during sapropel S1 formation. Quat. Sci. Rev. 159, 139-154. https://doi.org/10.1016/j.quascirev.2017.01.020.

Thomson, J., Higgs, N.C., Croudace, I.W., Colley, S., Hydes, D.J. (1993). Redox zonation of elements at an oxic/post-oxic boundary in deep-sea sediments. Geochim. Cosmochim. Acta 57, 579-595. https://doi.org/10.1016/0016-7037(93)90369-8.

Thomson, J., Higgs, N.C., Wilson, T.R.S., Croudace, I.W., de Lange, G.J., van Santvoort, J. M. (1995). Redistribution and geochemical behavior of redox-sensitive elements around S1, the most recent easter Mediterranean sapropel. Geochim. Cosmochim. Acta 59, 3487-3501. https://doi.org/10.1016/0016-7037(95)00232-O.

Thomson, J., Mercone, D., de Lange, G.J., van Santvoort, J.M. (1999). Review of recent advances in the interpretation of eastern Mediterranean sapropel SI from geochemical evidence. Mar. Geol. 153, 77-89.

Tierney, J.E., Lewis, S.C., Cook, B.I., LeGrande, A.N., Schmidt, G.A. (2011). Model, proxy and isotopic perspectives on the East African Humid Period. Earth Planet. Sci. Lett. 307, 103-112. https://doi.org/10.1016/j.epsl.2011.04.038.

Tintoré, J., La Violette, P.E., Blade, I., Cruzado, A. (1988). A study of an intense density front in the Eastern Alboran Sea: the Almeria-Oran front. J. Phys. Oceanogr. 18, 1384-1397. https://doi.org/10.1175/1520-0485(1988)018<1384:ASOAID>2.0. CO;2.

Torres, M.E., Brumsack, H.J., Bohrmann, G., Emeis, K.C. (1996). Barite fronts in continental margin sediments: a new look at barium remobilization in the zone of sulfate reduction and formation of heavy barites in diagenetic fronts. Chem. Geol. 127, 125-139. https://doi.org/10.1016/0009- 2541(95)00090-9.

Triantaphyllou, M.V., Gogou, A., Dimiza, M.D., Kostopoulou, S., Parinos, C., Roussakis, G., Geraga, M., Bouloubassi, I., Fleitmann, D., Zervakis, V., Velaoras, D., Diamantopoulou, A., Sampatakaki, A., Lykousis, V. (2016).

Holocene climatic optimum centennial-scale paleoceanography in the NE Aegean (Mediterranean Sea). Geo-Mar. Lett. 36, 51–66. https://doi.org/10.1007/s00367-015-0426-2.

Tribovillard, N. (2021). Re-assessing copper and nickel enrichments as paleo-productivity proxies. Bull. Soc. Géol. Fr. 192, 54. https://doi.org/10.1051/bsgf/2021047.

Tribovillard, N., Algeo, T.J., Baudin F., Riboulleau A. (2012). Analysis of marine environmental conditions based on molybdenum-uranium covariation Applications to Mesozoic paleoceanography. Chem. Geol. 325, 46-58. https://doi.org/10.1016/j.chemgeo.2011.09.009.

Tribovillard, N., Algeo, T.J., Lyons, T., Riboulleau, A. (2006). Trace metals as paleoredox and paleoproductivity proxies: An update. Chem. Geol. 232, 12-32. https://doi.org/10.1016/j.chemgeo.2006.02.012.

Tribovillard, N., Lyons, T.W., Riboulleau, A., Bout-Roumazeilles, V. (2008). A possible capture of molybdenum during early diagenesis of dysoxic sediments. Bull. Soc. Geol. Fr. 179, 3-12. https://doi.org/10.2113/gssgfbull.179.1.3.

Trigo, R.M., Osborn, T.J., Corte-Real, J.M. (2002). The North Atlantic Oscillation influence on Europe: climate impacts and associated physical mechanisms. Clim. Res. 20, 9-17. https://doi.org/10.3354/cr020009.

Turco, M., Palazzi, E., Von Hardenberg, J., Provenzale, A. (2015). Observed climate change hotspots. Geophys. Res. Lett. 42, 3521-3528. https://doi.org/10.1002/2015GL063891.

Tyson, R., Pearson, T. (1991). Modern and ancient continental shelf anoxia: An overview. Geol. Soc. Spec. Publ. 58. 1-24. https://doi.org/10.1144/GSL.SP.1991.058.01.01.

Tyson, R.V. (1995). Bulk geochemical characterization and classification of organic matter: Stable carbon isotopes ($\delta^{13}C$). Sedimentary Organic Matter: Organic Facies and Palynofacies, 395-416. https://doi.org/10.1007/978-94-011-0739-6_23

Uchman, A., Bąk, K., Rodríguez-Tovar, F.J. (2008). Ichnological record of deep-sea palaeoenvironmental changes around the Oceanic Anoxic Event 2 (Cenomanian-Turonian boundary): an example from the Barnasiówka section, Polish Outer Carpathians. Palaeogeogr. Palaeoclimatol. Palaeoecol. 262, 61-71. https://doi.org/10.1016/j.palaeo.2008.02.002.

Uchman, A., Rodríguez-Tovar, F.J., Machaniec, E., Kędzierski, M. (2013a). Ichnological characteristics of late cretaceous hemipelagic and pelagic sediments in a submarine high around the OAE-2 event: a case from the Rybie section, Polish Carpathians. Palaeogeogr. Palaeoclimatol. Palaeoecol. 370, 222-231. https://doi.org/10.1016/j. palaeo.2012.12.013.

Uchman, A., Rodríguez-Tovar, F.J., Oszczypko, N. (2013b). Exceptionally favourable life conditions for macrobenthos during the late Cenomanian OAE-2 event: ichnological record from the Bonarelli Level in the Grajcarek Unit. Polish Carpathians Cretac. Res. 46, 1-10. https://doi.org/10.1016/j.cretres.2013.08.007.

van de Schootbrugge, B., Koutsodendris, A., Taylor, W., Weston, F., Wellman, C., Strother, P. K. (2024). Recognition of an extended record of euglenoid cysts: implications for the end-Triassic mass extinction. Rev. Palaeobot. Palynol. 322, 105043. https://doi.org/10.1016/j.revpalbo.2023.105043.

van Helmond, N.A., Hennekam, R., Donders, T.H., Bunnik, F.P., de Lange, G.J., Brinkhuis, H., Sangiorgi, F. (2015). Marine productivity leads organic matter preservation in sapropel S1: palynological evidence from a core east of the Nile River outflow. Quat. Sci. Rev. 108, 130-138. https://doi.org/10.1016/j.quascirev.2014.11.014.

van Os, B.J.H. (1993). Primary diagenesis signals in Mediterranean sapropels and North Atlantic turbidities. Geo. Ultraiectina 109, 1-127.

van Os, B.J.H., Middelburg, J.J., de Lange, G.J. (1991). Possible diagenetic mobilization of barium in sapropelic sediment from the eastern Mediterranean. Mar. Geol. 100, 125-136. https://doi.org/10.1016/0025-3227(91)90229-W.

van Santvoort, P.J.M., de Lange, G.J. (1996). Messinian salt fluxes into the present-day. Eastern Mediterranean: implications for budget calculations and stagnation. Mar. Geol. 132, 241-251. https://doi.org/10.1016/0025-3227(95)00164-6.

van Santvoort, P.J.M., de Lange, G.J., Langereis, C.G., Dekkers, M.J., Paterne, M. (1997). Geochemical and Paleomagnetic evidence for the occurrence of “missing” sapropels in eastern Mediterranean sediments. Paleoceanography 12, 773-786. https://doi.org/10.1029/97PA01351.

van Santvoort, P.J.M., de Lange, G.J., Thomson, J., Cussen, H., Wilson, T.R.S., Krom, M.D., Strohle, K. (1996). Active post-depositional oxidation of the most recent sapropel (S1) in the eastern Mediterranean. Geochim. Cosmochim. Acta 60, 4007-4024. https://doi.org/10.1016/S0016-7037(96)00253-0.

Versteegh, G.J., Zonneveld, K.A. (2002). Use of selective degradation to separate preservation from productivity.

Geology 30, 615-618. https://doi.org/10.1130/0091-7613(2002)030<0615:UOSDTS>2.0.CO;2.

Versteegh, G.J.M. (1994). Recognition of cyclic and non-cyclic environmental changes in the Mediterranean Pliocene: a palynological approach. Mar. Micropaleontol. 23, 147-183. https://doi.org/10.1016/0377-8398(94)90005-1.

Voelker, A.H., Lebreiro, S.M., Schönfeld, J., Cacho, I., Erlenkeuser, H., Abrantes, F. (2006). Mediterranean outflow strengthening during northern hemisphere coolings: a salt source for the glacial Atlantic?. Earth Planet. Sci. Lett. 245, 39-55. https://doi.org/10.1016/j.epsl.2006.03.014.

Vorlicek, T.P., Kahn, M.D., Kasuya, Y., Helz, G.R. (2004). Capture of molybdenum in pyrite-forming sediments: role of ligand-induced reduction by polysulfides. Geochim. Cosmochim. Acta 68, 547-556. https://doi.org/10.1016/S0016-7037(03) 00444-7.

Walker, M.J., Berkelhammer, M., Björck, S., Cwynar, L.C., Fisher, D.A., Long, A.J., Lowe, J.J., Newnham, R.M., Rasmussen, S.O., Weiss, H. (2012). Formal subdivision of the Holocene Series/Epoch: a Discussion Paper by a Working Group of INTIMATE (Integration of ice-core, marine and terrestrial records) and the Subcommission on Quaternary Stratigraphy (International Commission on Stratigraphy). J. Quat. Sci. 27, 649-659. https://doi.org/10.1002/jqs.2565.

Wang, H., Lo Iacono, C., Wienberg, C., Titschack, J., Hebbeln, D. (2019). Cold-water coral mounds in the southern Alboran Sea (western Mediterranean Sea): internal waves as an important driver for mound formation since the last deglaciation. Mar. Geol. 412, 1-18. https://doi.org/10.1016/j.margeo.2019.02.007.

Wang, S., Shen, J., Du, B., Xu, K., Zhang, Z., Liu, C. (2021). The relationship between natural pyrite and impurity element semiconductor properties: a case study of vein pyrite from the zaozigou gold deposit in China. Minerals 11, 596. https://doi.org/ 10.3390/min11060596.

Wanner, H., Brönnimann, S., Casty, C., Gyalistras, D., Luterbacher, J., Schmutz, C., Stephenson, D.B., Xoplaki, E. (2001). North Atlantic Oscillation-concepts and studies. Surv. Geophys. 22, 321-381. https://doi.org/10.1023/A:1014217317898.

Wanty, R.B., Goldhaber, M.B. (1992). Thermodynamics and kinetics of reactions involving vanadium in natural systems: accumulation of vanadium in sedimentary rocks. Geochim. Cosmochim. Acta 56, 1471-1483. https://doi.org/10.1016/0016-7037 (92)90217-7.

Warning, B., Brumsack, H.J. (2000). Trace metal signatures of eastern Mediterranean sapropels. Paleogeogr. Paleoclimatol. Paleoecol. 158, 293-309. https://doi.org/10.1016/S0031-0182(00)00055-9.

Wehausen, R., Brumsack, H.J. (1998). The formation of Pliocene Mediterranean sapropels: constraints from high-resolution major and minor element studies. Proceedings-Ocean Drilling Program: Scientific Results 160, 207-218. https://doi.org/10.2973/odp.proc.sr.160.004.1998.

Wehausen, R., Brumsack, H.J. (2000). Chemical cycles in Pliocene sapropel-bearing and sapropel-barren eastern Mediterranean sediments. Paleogeogr. Paleoclimatol. Paleoecol. 158, 325-352. https://doi.org/10.1016/S0031-0182(00)00057-2.

Wei, W., Klaebe, R., Ling, H.F., Huang, F., Frei, R. (2020). Biogeochemical cycle of chromium isotopes at the modern Earth's surface and its applications as a paleo-environment proxy. Chem. Geol. 541, 119570. https://doi.org/10.1016/j.chemgeo.2020.119570.

Weldeab, S., Menke, V., Schmiedl, G. (2014). The pace of East African monsoon evolution during the Holocene. Geophys. Res. Lett. 41, 1724-1731. https://doi.org/10.1002/2014GL059361.

Wilkin, R.T., Arthur, M.A., Dean, W.E. (1997). History of water-column anoxia in the Black Sea indicated by pyrite framboid size distributions. Earth Planet. Sci. Lett. 148, 517-525. https://doi.org/10.1016/S0012-821X(97)00053-8.

Wilkin, R.T., Barnes, H.L. (1997). Formation processes of framboidal pyrite. Geochim. Cosmochim. Acta 61, 323-339. https://doi.org/10.1016/S0016-7037(96)00320-1.

Wilkin, R.T., Barnes, H.L., Brantley, S.L. (1996). The size distribution of framboidal pyrite in modern sediments: an indicator of redox conditions. Geochim. Cosmochim. Acta 60, 3897-3912. https://doi.org/10.1016/0016-7037(96)00209-8.

Williams, G.L., Fensome, R.A., MacRae, R.A. (2017). The Lentin and Williams index of fossil dinoflagellates 2017 edition. American Association of Stratigraphic Palynologists Contributions Series no. 48. https://palynology.org/wp-content/uploads/2017/01/AASP-Contribution-Series-No.48.pdf.

Wilson, T.R.S., Thomson, J., Hydes, D.J., Colley, S., Culkin, E., Sorensen, J. (1986). Oxidation fronts in pelagic sediments: Diagenetic formation of metal-rich layers. Science 232, 972-975. https://doi.org/10.1126/science.232.4753.972.

Wood, G.D. (1996). Palynological techniques-processing and microscopy. In. Jasonius, J. and McGregor, DC eds., Palynology: Principles and Application. American association of stratigraphic palynologists foundation 1, 29-50.

Wu, J., Böning, P., Pahnke, K., Tachikawa, K., de Lange, G. (2016). Unraveling North- African riverine and eolian contributions to Central Mediterranean sediments during Holocene sapropel S1 formation. Quat. Sci. Rev. 152, 31-48. https://doi.org/ 10.1016/j.quascirev.2016.09.029.

Wu, J., Filippidi, A., Davies, G.R., de Lange, G. (2018). Riverine supply to the eastern Mediterranean during last interglacial sapropel S5 formation: a basin-wide perspective. Chem. Geol. 485, 74-89. https://doi.org/10.1016/j. chemgeo.2018.03.037.

Wu, P., Haines, K. (1996). Modeling the dispersal of Levantine Intermediate Water and its role in Mediterranean deep water formation. J. Geophys. Res. 101, 6591-6607. https://doi.org/10.1029/95JC03555.

Wüst, G. (1961). On the vertical circulation of the Mediterranean Sea. J. Geophys. Res. 66, 3261-3271. https://doi.org/10.1029/JZ066i010p03261.

Yang, Y., Wang, W.M., Shu, J.W., Chen, W., Shi, G.L. (2022). Disruption of terrestrial plant ecosystem in Miocene (sub) tropics: A palynological perspective from Fotan Formation, Southeast China. Rev. Palaeobot. Palynol. 304, 104715. https://doi.org/10.1016/j.revpalbo.2022.104715.

Yebra, L., Herrera, I., Mercado, J.M., Cortés, D., Gómez-Jakobsen, F., Alonso, A., Sánchez, A., Salles, S., Valcárcel-Pérez, N. (2018). Zooplankton production and carbon export flux in the western Alboran Sea gyre (SW Mediterranean). Prog. Oceanogr. 167, 64-77.https://doi.org/10.1016/j.pocean.2018.07.009.

Yin, H., Zhu, Q., Aller, R.C. (2017). An irreversible planar optical sensor for multi- dimensional measurements of sedimentary H_2S. Mar. Chem. 195, 143-152. https:// doi.org/10.1016/j.marchem.2017.03.005.

Zavatarielli, M., Mellor, G.L. (1995). A numerical study of the Mediterranean Sea circulation. J. Phys. Oceanogr. 25, 1384-1414. https://doi.org/10.1175/1520-0485(1995)025<1384:ANSOTM>2.0.CO;2.

Zhang, M., Konishi, H., Xu, H., Sun, X., Lu, H., Wu, D., Wu, N. (2014). Morphology and formation mechanism of pyrite induced by the anaerobic oxidation of methane from the continental slope of the NE South China Sea. J. Asian Earth Sci. 92, 293-301. https://doi.org/10.1016/j.jseaes.2014.05.004.

Zheng, Y., Anderson, R.F., van Geen, A., Fleisher, M.Q. (2002). Preservation of particulate non-lithogenic uranium in marine sediments. Geochim. Cosmochim. Acta 66, 3085-3092. https://doi.org/10.1016/S0016-7037(01)00632-9.

Zheng, Y., Anderson, R.F., van Geen, A., Kuwabara, J. (2000). Authigenic molybdenium formation in marine sediments: a link to pore water sulfide in the Santa Barbara Basin. Geochim. Cosmochim. Acta 64, 4165-4178. https://doi.org/10.1016/S0016- 7037(00)00495-6.

Ziegler, M., Tuenter, E., Lourens, L.J. (2010). The precession phase of the boreal summer monsoon as viewed from the eastern Mediterranean (ODP Site 968). Quat. Sci. Rev. 29, 1481-1490. https://doi.org/10.1016/j.quascirev.2010.03.011.

Zirks, E., Krom, M., Schmiedl, G., Katz, T., Xiong, Y., Alcott, L.J., Poulton, S.W., Goodman-Tchernov, B. (2021). Redox evolution and the development of oxygen minimum zones in the Eastern Mediterranean Levantine basin during the early Holocene. Geochim. Cosmochim. Acta 297, 82-100. https://doi.org/10.1016/j. gca.2021.01.009.

Zirks, E., Krom, M.D., Zhu, D., Schmiedl, G., Goodman-Tchernov, B.N. (2019). Evidence for the presence of oxygen-depleted sapropel intermediate water across the Eastern Mediterranean during Sapropel S1. ACS Earth Space Chem. 3, 2287-2297. https://doi.org/10.1021/acsearthspacechem.9b00128.

Zonneveld, K.A., Brummer, G.A. (2000). (Palaeo-) ecological significance, transport and preservation of organic-walled dinoflagellate cysts in the Somali Basin, NW Arabian Sea. Deep Sea Res. Part II Top. Stud. Oceanogr. 47, 2229-2256. https://doi.org/10.1016/S0967-0645(00)00023-0.

Zonneveld, K.A., Chen, L., Möbius, J., Mahmoud, M.S. (2009). Environmental significance of dinoflagellate cysts from the proximal part of the Po-river discharge plume (off southern Italy, Eastern Mediterranean). J. Sea Res. 62, 189-213. https://doi.org/10.1016/j.seares.2009.02.003.

Zonneveld, K.A., Marret, F., Versteegh, G.J.M., Bogus, K., Bonnet, S., Bouimetarhan, I., Crouch, E., de Vernal, A., Elshanawany, R., Edwards, L., Esper, O., Forke, S., Grøsfjeld, K., Henry, M., Holzwarth, U., Kielt, J.F., Kim, S.Y., Ladouceur, S., Ledu, D., Chen, L., Limoges, A., Londeix, L., Lu, S.H., Mahmoud, M.S., Marino, G., Matsouka, K., Matthiessen, J., Mildenhal, D.C., Mudie, P., Neil, H.L., Pospelova, V., Qi, Y., Radi, T., Richerol, T., Rochon, A., Sangiorgi, F., Solignac, S., Turon, J.L., Verleye, T., Wang, Y., Wang, Z., Young, M. (2013). Atlas of modern dinoflagellate cyst distribution based on 2405 data points. Rev. Palaeobot. Palynol. 191, 1-197. https://doi.org/10.1016/j.revpalbo.2012.08.003.

Zonneveld, K.A., Pospelova, V. (2015). A determination key for modern dinoflagellate cysts. Palynology 39, 387-409. https://doi.org/10.3389/fmars.2022.915755.

Zonneveld, K.A., Versteegh, G.J., de Lange, G.J. (2001). Palaeoproductivity and post-depositional aerobic organic matter decay reflected by dinoflagellate cyst assemblages of the Eastern Mediterranean S1 sapropel. Mar. Geol. 172, 181-195. https://doi.org/10.1016/S0025-3227(00)00134-1.

Zúñiga, D., Calafat, A., Heussner, S., Miserocchi, S., Sánchez-Vidal, A., García- Orellana, J., Canals, M., Sánchez-Cabeza, J.A., Carbonne, J., Delsaut, N., Saragoni, G. (2008). Compositional and temporal evolution of particle fluxes in the open Algero-Balearic basin (Western Mediterranean). J. Mar. Syst. 70, 196-214. https://doi.org/10.1016/j.jmarsys.2007.05.007.

Zwiep, K.L., Hennekam, R., Donders, T.H., van Helmond, N.A., De Lange, G.J., Sangiorgi, F. (2018). Marine productivity, water column processes and seafloor anoxia in relation to Nile discharge during sapropels S1 and S3. Quat. Sci. Rev. 200, 178-190. https://doi.org/10.1016/j.quascirev.2018.08.026.

Appendix I

Supplementary material for Chapter I

ⓐ Redox ladder

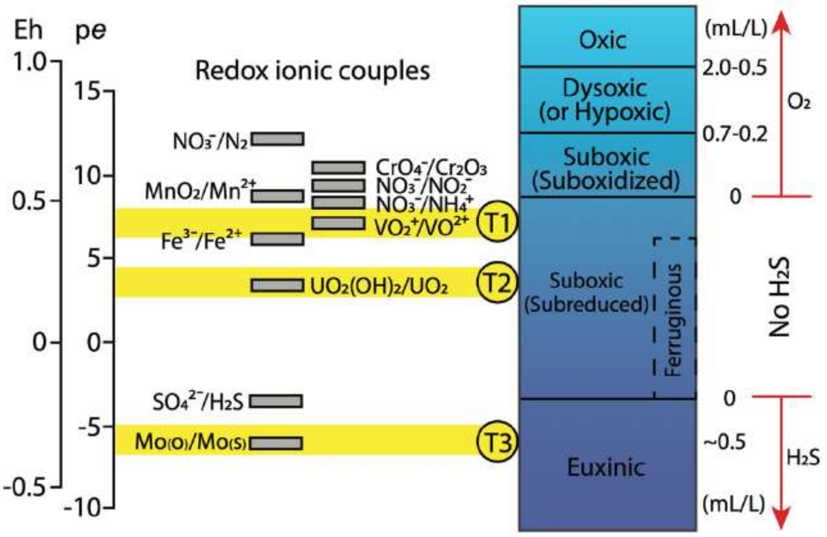
Eh
pe
1.0
0.5
0
-0.5
15
10
5
0
-5
-10
Redox ionic couples
NO_3^-/N_2
MnO_2/Mn^{2+}
Fe^{3+}/Fe^{2+}
CrO_4^-/Cr_2O_3
NO_3^-/NO_2^-
NO_3^-/NH_4^+
VO_2^+/VO^{2+}
$UO_2(OH)_2/UO_2$
SO_4^{2-}/H_2S
$Mo_{(O)}/Mo_{(S)}$
T1
T2
T3
Oxic
Dysoxic (or Hypoxic)
Suboxic (Suboxidized)
Suboxic (Subreduced)
Ferruginous
Euxinic
(mL/L)
2.0-0.5
0.7-0.2
0
0
~0.5
(mL/L)
O_2
No H_2S
H_2S

ⓑ Calibration of redox thresholds based on proxy covariation

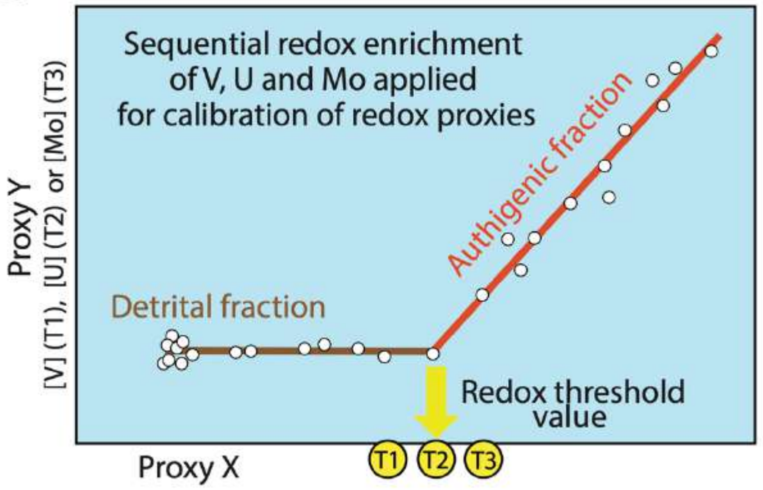

Figure S1. *Algeo and Li (2020) methodology for redox thresholds calibration for geochemical proxies. (a) Redox ladder and thresholds (at pH = 7). Redox potential is an intensity factor reported as the measured potential versus the standard hydrogen electrode (Eh) or as the negative logarithm of electron activity (pe). The yellow fields (T1 to T3) are three redox thresholds that are the focus of the present analysis. Note that the exact threshold for any given redox couple depends on additional environmental factors such as pH. The ferruginous field is approximately co-extant with the subreduced facies, although it extends only to the* Fe^{3+}/Fe^{2+} *couple. (b) Compound covariation of proxies X and Y, reflecting sequential enrichment, i.e., initial enrichment of X at a higher redox threshold than Y, with the sharp bend (yellow arrow) representing the redox threshold at which enrichment of Y began (i.e., T1, T2 or T3). The concentrations of X and Y in the detrital fraction are shown as a cluster of points close to the graph origin, representing an absence of authigenic enrichment of both X and Y under relatively oxidizing conditions.*

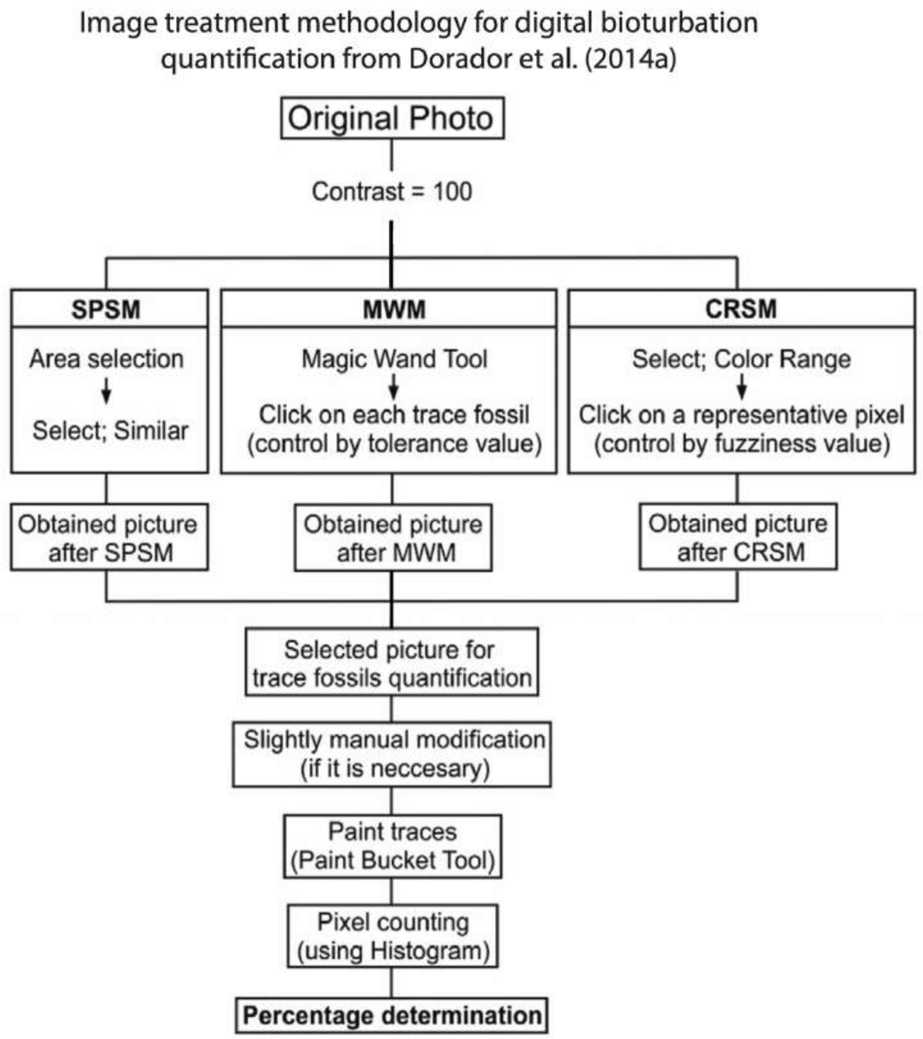
Image treatment methodology for digital bioturbation quantification from Dorador et al. (2014a)
Original Photo
Contrast = 100
SPSM
Area selection
Select; Similar
MWM
Magic Wand Tool
Click on each trace fossil (control by tolerance value)
CRSM
Select; Color Range
Click on a representative pixel (control by fuzziness value)
Obtained picture after SPSM
Obtained picture after MWM
Obtained picture after CRSM
Selected picture for trace fossils quantification
Slightly manual modification (if it is neccesary)
Paint traces (Paint Bucket Tool)
Pixel counting (using Histogram)
Percentage determination

Figure S2. *Flowchart showing sequential of processes conforming IDIAP (Ichnological Digital Analysis Image Package) methodology applied in Chapter V. SPSM: Similar Pixel Selection Method, MWM: Magic Wand Method and CRSM: Color Range Selection Method (modified from Dorador et al., 2014a).*

Appendix II

Supplementary material for Chapter VI

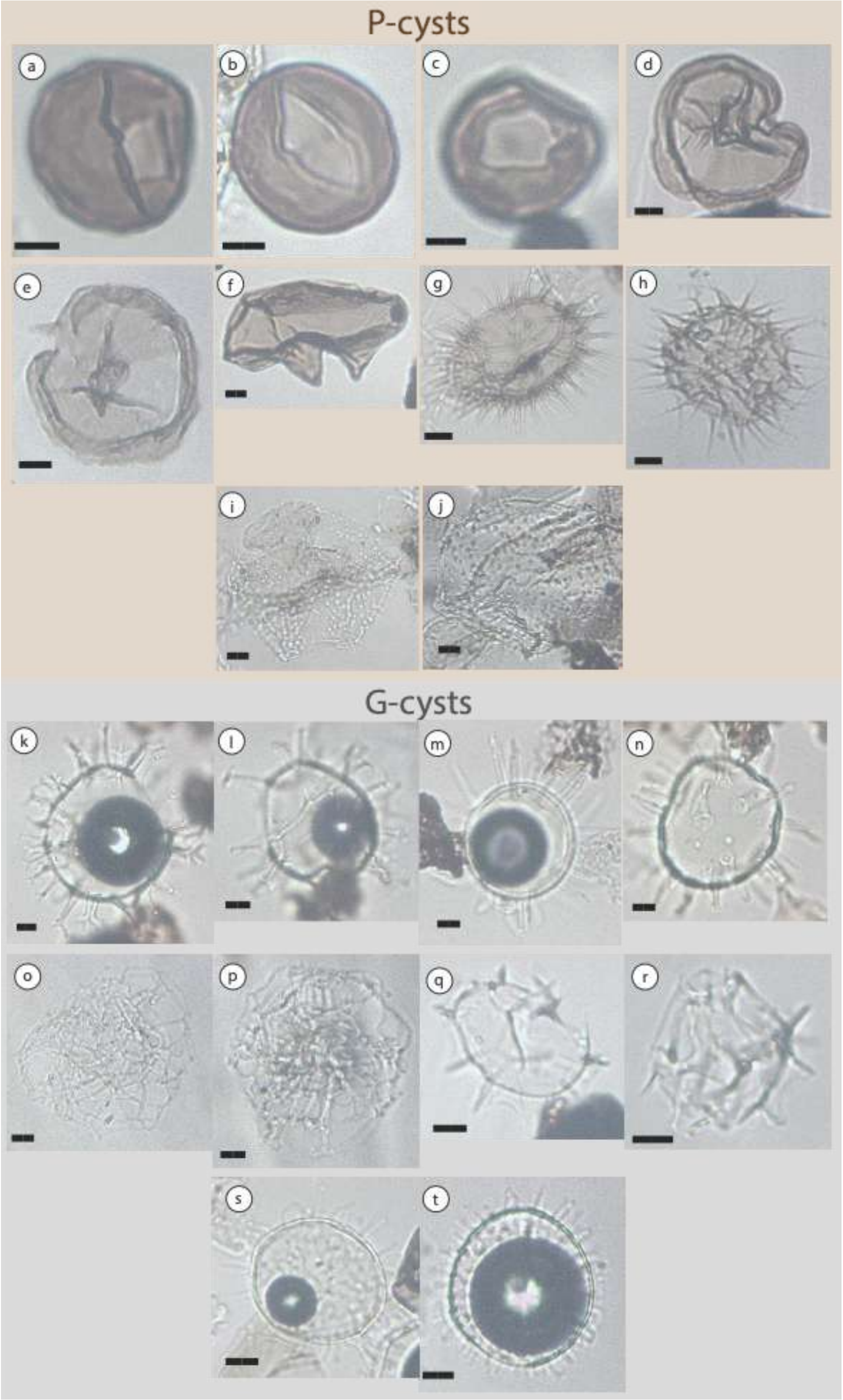

Figure S1. *Photo of most abundant dinocysts species recognized in Western Alboran sediments over the last 13000 years for the dinocysts analysis presented in Chapter VI. P-cysts: a-j (brown background), k-t: G-cysts (gray background). (a-c) Brigantedinium spp, (d-e). Selenopemphix nephroides, (f) Quinquecuspis concreta, (g-h) Selenopemphix quanta, (i-j) Trinovantedinium applanatum, (k-l) Spiniferites bentorii, (m-n) Lingulodinium machaerophorum, (o-p) Nemaosphaeropsis labyrinthus, (q-r) Impagidinium aculeatum, (s-t) Operculodinium centrocarpum. Diagenetic pyrite is infilling cysts in photos k, l, m, s and t. Scalebar (black line): 10 µm. Palynomorphs slides prepared at Utrecht University at the Palynology and Paleoceanography Department.*

Appendix III

Pelagic barite separation performed at Paytan Biogeochesmistry Lab at University of California, Santa Cruz (UCSC) under the supervision of Dr. Adina Paytan.

Table 1. *SEM observation of solid residue obtained after barite separation procedure performed to sediment samples belonging to different sapropels for* $\delta^{138}Ba_{barite}$ *analysis. The white crystals correspond to pelagic barite crystals.*

Sapropel	Samples	Aprox. [Ba] ppm	Weight after ashing (mg)	SEM images	Observation
S1	964A 1H1 63.5-65.5	500	15	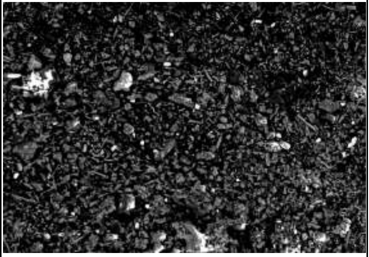	Highly enriched in Rutile grains. Presents few barite crystals (low barite content)
S1	964A 1H1 68-70	900	24.5	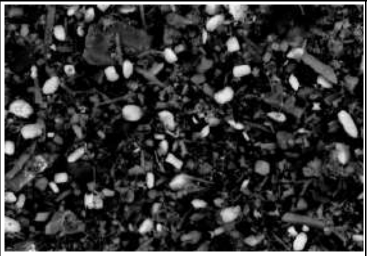	Enriched in barite crystals and rutile elongated crystals.
S1	969B 1H1 22-24	900	20.8	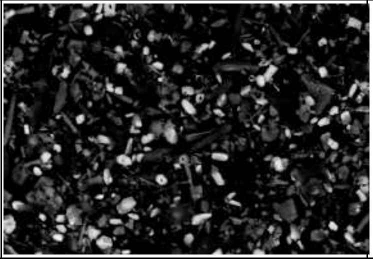	Enriched in barite crystals and rutile elongated crystals.
S1	969B 1H1 27-29	850	18.4	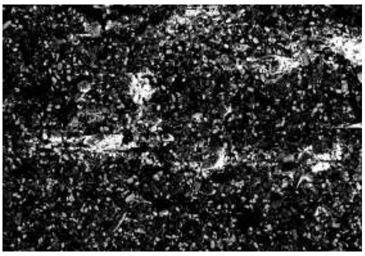	Highly enriched in barite crystals.
S51	964A 9H4 136-138	3500	84.6	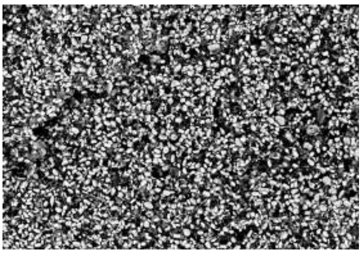	Highly enriched in barite. Almost everything is barite.
S52	964A 9H5 32.5-38.5	2000	32.9	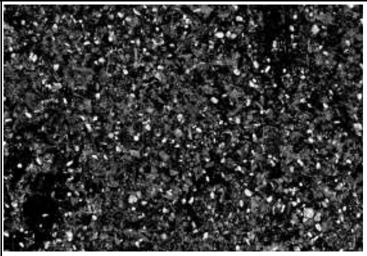	Highly enriched in barite crystals. Clay minerals can be observed.

S53	964A 9H5 92-95	2000	66	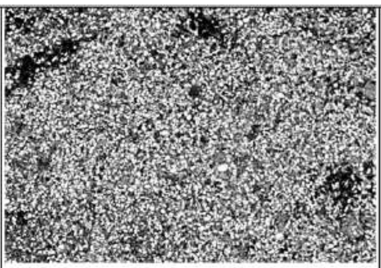	Highly enriched in barite crystals. Almost everything is barite.
S54	964A 9H6 14-18	1500	1751.7	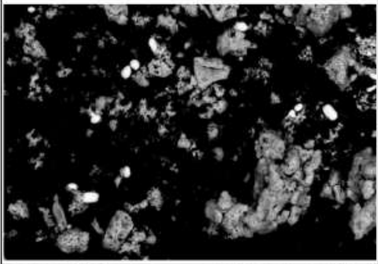	Barite crystals can be observed despite dark reddish color of the smple. Amorphous material is enriched in Fe and O. Probably, iron oxides that seem to be enriched in Zn, Ni and Co.
S1	969B 1H1 33-35	300	25.5	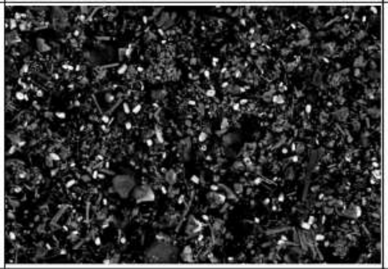	Barite crystals can be observed. Moderate barite content. Enriched in elongated rutile crystals.
S7	964A 2H4 70-74	1000	34.9	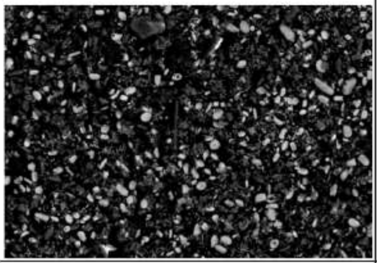	Enriched in barite cystals. High barite content.
S17	964B 4H3 32-36.5	2000	64.8	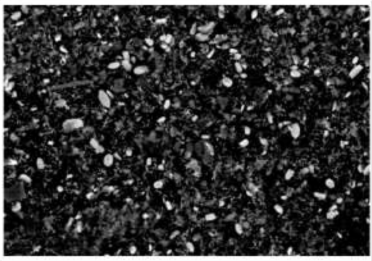	Enriched in barite cystals. High barite content.

S18	964B 4H3 120-122	1200	0.2	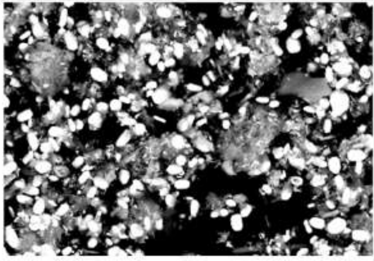	High barite content despite litle amount of sample. Highly pure sample.
S29	964B 6H2 30-35	3500	183.4	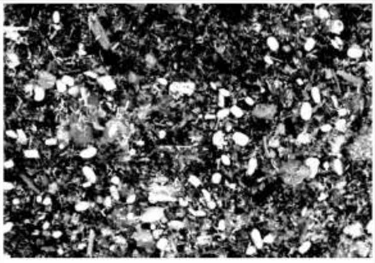	High barite content. High clay content.
S30	964B 6H2 91-98	2000	141.4	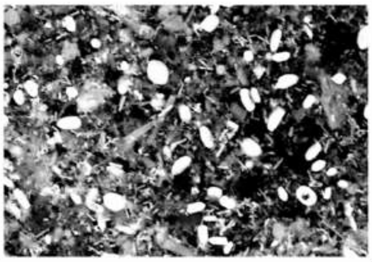	High barite content. High clay content.
S31	964B 6H2 145-149	unknown	57.8	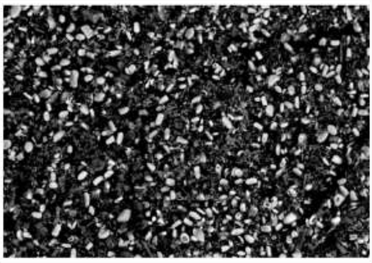	Very high barite content. Almost pure barite crystals.
S50	964A 9H4 0-2	800	57.6	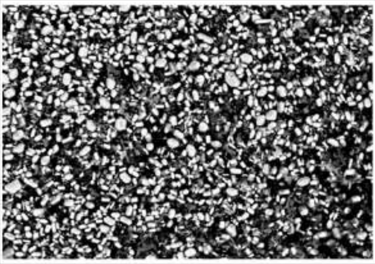	High barite content.

S5	964A 2H1 94-96	1600	27.2	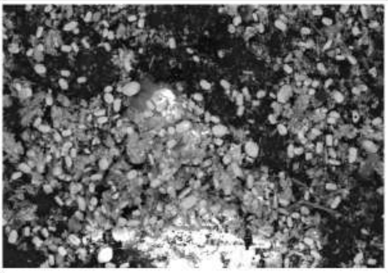	High barite content. Almost pure barite crystals.
S5	964A 2H1 97-99	2000	32.8	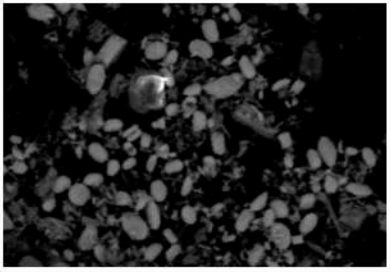	High barite content. Almost pure barite crystals.
S8	964A 2H4 138-142	700	4.6	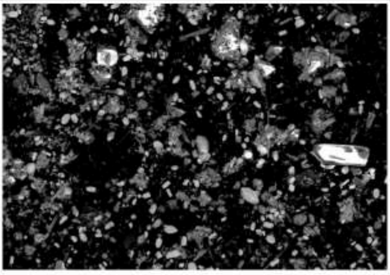	High barite content. Abundant barite crystals.
S8	964A 2H4 148-149.5	800	8.0	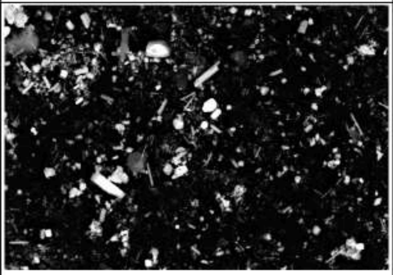	Moderate to low barite abundance. Enrched rutile crystals.
S1	968B 1H1 55-57	unknown	1.6	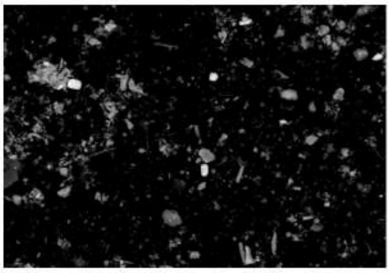	Moderate to low barite abundance. Enrched rutile crystals.
S1	968B 1H1 60-62, 64-66	unknown	5.2	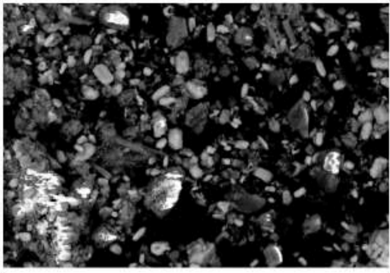	High barite content. Moderate abundance of rutile crystals.

S1	971A 1H1 28-30, 30-32	unknown	23.5	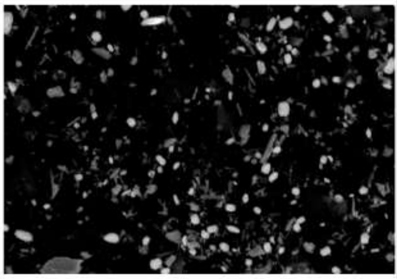	Moderate barite content.
S1	971A 1H1 22-24, 26-28	unknown	8.6	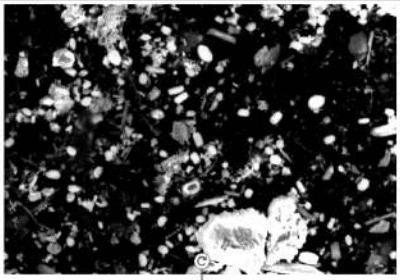	Moderate to high barite content.
S1	967C 1H1 63-65, 67-69	unknown	8.1	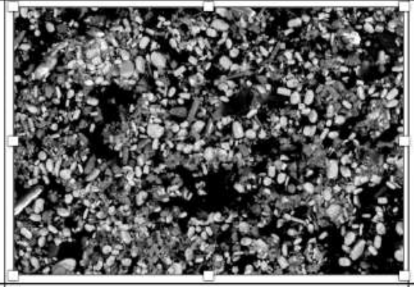	Moderate to high barite content.
S1	968B 68-70, 71-73	unknown	63.2	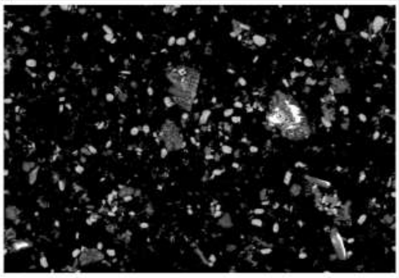	Moderate to high barite content.
S6	964A 2H3 117-119, 123-125	700	74.6	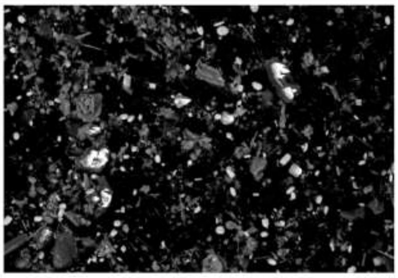	Moderate barite content. Some clay minerals and rutile crystals.

11		**S6**	964A 2H3 117-119, 123-125	700	74.6	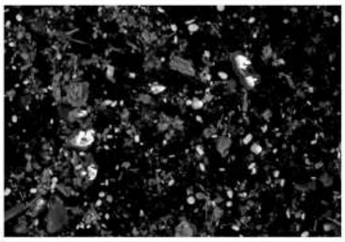	Moderate barite content. Some clay minerals and rutile crystals.
12		**S6**	964A 2H3 133-135, 137-138.5	700	136.7	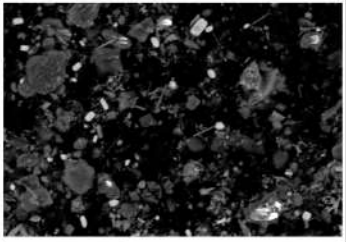	Moderate barite content.
13		**S1**	966C 1H1 32.5-35.5, 37-40, 43-45	400	102.2	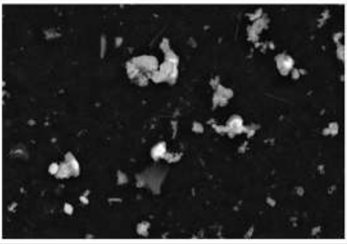	Very low barite content. Enriched in rutile crystals, clay minerals and amorphous silica (see SEM image below). 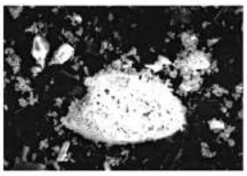

Appendix IV

Other peer reviewed publications –JCR (SCI)– indexed journal papers.

- García-Alix, A., Jiménez-Moreno, G., Gázquez, F., **Monedero-Contreras, R.**, López-Avilés, A., Jiménez-Espejo, F.J., Rodríguez-Rodríguez, M., Camuera, J., Ramos-Román, M.J., Anderson, R.S. (2022*). Climatic control on the Holocene hydrology of a playa-lake system in the western Mediterranean*. Catena 214, 106292. https://doi.org/10.1016/j.catena.2022.106292. Journal Impact Factor: 6.2.

- Casanova-Arenillas, S., Martínez-Ruiz, F., Rodríguez-Tovar, F.J., Pérez-Asensio, J.N., **Monedero-Contreras, R.**, Villasante-Marcos, V. Reconstructing *Deep-Sea Palaeoenvironments in the Western Alboran Sea Basin over the end of the Last Glacial Period and the Holocene: Insights from a multiproxy approach*. Accepted with revisions in Palaeogeography, Palaeoclimatology, Palaeoecology. Journal Impact Factor: 3.0

Thesis results were published in the following national and international conferences:

- 2023 _ Poster _ Goldschmidt23. *Assessing redox sensitive elements concentrations as deoxygenation proxies in sapropel layers: influence of bioturbation and sediment mixing*. **Monedero-Contreras, R.**, Martinez-Ruiz, F., Rodríguez-Tovar, F. J., de Lange, G. On-site: Lyon, France.

- 2023 _ Poster _ CLIVAR 2023. *Deoxygenation dynamics in the Mediterranean: new paleo-perspectives from empirical models based on modern anoxic basins*. **Monedero-Contreras, R.**, Martinez-Ruiz, F., Rodríguez-Tovar, F. J., de Lange, G. On-site: Madrid, Spain.

- 2022 _ Poster _ 14th International Conference on Paleoceanography (ICP). *Role of deep-water circulation and related redox variability during sapropel deposition: new insights into marine deoxygenation dynamics*. **Monedero-Contreras, R.**, Martinez-Ruiz, F., Rodríguez-Tovar, F. J., de Lange, G. On-site: Berger, Norway.

- 2022 _ Oral presentation (flash talk, 3 min.) _ Ocean Sciences Meeting (OSM). *Barite precipitation and preservation in the Mediterranean during sapropel deposition: implications for paleoproductivity reconstructions.* **Monedero-Contreras, R.**, Martinez-Ruiz, F., Rodríguez-Tovar, F. J., Paytan, A., de Lange, G. Online.

- 2021 _ Oral presentation (flash talk, 3 min.) _ EGU21. *Rapid changes in primary productivity and oxygen depletion during sapropel deposition: implications for reconstructing seawater oxygen levels*. **Monedero-Contreras, R.**, Martinez-Ruiz, F., Rodríguez-Tovar, F. J., Gallego-Torres, D., de Lange, G. Online.

- 2021 _ Oral presentation (flash talk, 3 min.) _ Goldschmidt21. *Oxygen depletion during sapropel deposition: Reassessing redox proxies for reconstructing surface and bottom water oxygen conditions*. **Monedero-Contreras, R.**, Martinez-Ruiz, F., Rodríguez-Tovar, F. J., Gallego-Torres, D., de Lange G. Online.

- 2021 _ Oral presentation (long talk, 20 min.) _ 1st edition of CSIC-UGR Young Scientist Seminars. *Paleoredox conditions and productivity oscillations in the Mediterranean: implications for reconstructing deoxygenation dynamics and responses to ocean stressors*. **Monedero-Contreras, R.** On-site: Granada, Spain.

- 2021 _ Oral presentation (short talk, 10 min.) _ *Jóvenes investigadores del mar (CEIMAR). Eventos de desoxigenación en el registro sedimentario del Mediterráneo*. **Monedero-Contreras, R.**, Martinez-Ruiz, F., Rodríguez-Tovar, F. J. On-site: Motril (Granada), Spain.